APPLICATION OF NODAL EQUIVALENCE THEORY TO THE NEUTRONIC ANALYSIS OF PWRS

(Vol. I)

by

Christopher Lloyd Hoxie

B. S., University of Florida (1975)

M. E., University of Florida (1978)

SUBMITTED IN PARTIAL FULFILLMENT

OF THE REQUIREMENTS FOR THE

DEGREE OF

DOCTOR OF PHILOSOPHY

AT THE

MASSACHUSETTS INSTITUTE OF TECHNOLOGY

JUNE 1982

Signature of Author . . . . .
Department of Nuclear Engineering
June 1982

Certified by . . . . . .
Allan F. Henry
Thesis Supervisor

Accepted by . . . . . .
Allan F. Henry
Chairman, Department Graduate Committee

APPLICATION OF NODAL EQUIVALENCE THEORY TO THE NEUTRONIC ANALYSIS OF PWRs

by

Christopher Lloyd Hoxie

Submitted to the Department of Nuclear Engineering on May 21, 1982 in partial fulfillment of the requirements for the Degree of Doctor of Philosophy in the field of Nuclear Engineering

ABSTRACT

The objective of this research is to apply the analytic nodal method and nodal equivalence theory as embodied in the nodal code, QUANDRY, to the neutronic analysis of pressurized water reactors (PWRs). This includes applying QUANDRY to the calculation of normalized assembly power distributions for PWRs and devising, implementing and testing a heterogeneous PWR flux reconstruction scheme for QUANDRY.

In this research equivalence parameters are derived from heterogeneous assembly calculations. These parameters are then employed in QUANDRY calculations. For realistic PWR problems it was found that this procedure leads to maximum errors in normalized assembly power densities of about 2%. The use of assembly equivalence parameters did not lead to any consistent improvement in the accuracy of calculated power distributions as compared to conventional flux-weighting methods of spatial homogenization. However, it was found that the use of assembly equivalence parameters leads to more accurate prediction (less than 2% error) of the heterogeneous surface fluxes than the flux-weighting methods (about 7% error). This is an important result since such surface fluxes are input into heterogeneous flux reconstruction schemes.

A method of heterogeneous flux reconstruction is introduced called the form function method. This technique uses node-averaged information from the nodal code QUANDRY to construct an approximate form function which is then multiplied into a detailed flux shape from an inexpensive assembly criticality calculation to yield the reconstructed global heterogeneous flux within an assembly. For nodes near the steel baffle at the edge of a PWR core, extended assembly criticality calculations are employed in which the baffle and water reflector are included.

Use of the form function method on realistic PWR cores leads to maximum errors in the pointwise reconstructed flux of 3.5% for assemblies in the interior of the PWR core. For points in the core adjacent to the steel baffle, the maximum error may be 5.9%. Pin powers are calculated to within 4% maximum error.

Thesis Supervisor: Allan F. Henry
Title: Professor of Nuclear Engineering

TABLE OF CONTENTS

ACKNOWLEDGMENTS

The author expresses his sincerest appreciation to his thesis supervisor, Professor Allan F. Henry, for his guidance, support and encouragement throughout the course of this thesis work. Thanks are also due to Professor Michael J. Driscoll who served as reader for this thesis. Their numerous efforts on my behalf throughout my stay at M.I.T. are appreciated.

This research was funded by the Electric Power Research Institute (EPRI) whose financial support is gratefully acknowledged.

All computation was performed on an IBM 370/168 computer at the M.I.T. Information Processing Center.

It's much more fun to learn reactor physics by discussing it with fellow members of a research group. In this regard, I am indebted to Greg Greenman, Kord Smith, Jean Koclas, Rich Loretz, Alex Cheng, Hussein Khalil, Philippe Finck and Kent Parsons.

Finally, the author extends his deepest gratitude to his parents, Mr. and Mrs. Don L. Hoxie, and to his sister, Mrs. Donna Comarow, for their constant moral support. Thanks also goes to the author's wife, Robin, for her continual encouragement and for her help in typing and proofreading this thesis.

LIST OF FIGURES

LIST OF TABLES

Chapter 1

INTRODUCTION

1.1 OVERVIEW

There are strong economic and safety incentives in the utility industry to perform accurate and reasonably inexpensive multidimensional reactor calculations. By accurately calculating the multidimensional behavior of reactors, the utilities can gain safety benefits from an increased confidence in plant safety margins. Direct economic gains may accrue from improved fuel management and the possible relaxation of some plant margins due to increased confidence in the knowledge of plant operating conditions.

Finite-difference solutions of the group diffusion equations [1, pgs. 156-168] are commonly employed in the nuclear industry for the calculation of spatial power distributions within reactors. Such finite-difference methods have been automated within many computer codes. The utility industry standard is probably the PDQ-7 code [2] which was originally developed at Bettis Atomic Power Laboratory for use in the US Navy reactor program. Unfortunately, for realistic three-dimensional thermal-reactor problems, with accuracy requirements for average

assembly powers of one percent, these methods require a huge number of spatial mesh points. This leads to excessive computing times which preclude the use of routine, three-dimensional PDQ-7 calculations in the utility industry. Planar, two-dimensional PDQ-7 calculations are routinely performed. However, even here the computing cost quickly runs into the thousands of dollars. Thus more efficient and faster methods would surely be welcomed.

It is conceivable that as computers become more efficient and with further advances in parallel processors that routine three-dimensional PDQ-7 calculations will become a reality and two-dimensional PDQ-7 calculations may be made considerably less expensive [3]. In the interim, a number of other approaches are being used to derive the multidimensional behavior of operating reactors. These approaches include synthesis methods [4], finite element techniques [5], response matrix methods [6], nodal methods [7] and combinations of these techniques [8]. It is the use of nodal methods to supplement fine-mesh finite-difference calculations in the analysis of PWRs which is the topic of this thesis.

1.2 HISTORICAL REVIEW OF NODAL METHOD DEVELOPMENTS

The term, nodal method, is a broad one. However, most nodal methods have the following salient features. In the nodal approach the reactor core is partitioned into large (~ 20 cm x 20 cm x 20 cm) homogeneous nodes. The essential characteristic of nodal methods is to regard as unknowns, node-integrated quantities such as volume-averaged fluxes and surface-averaged currents. When the multigroup neutron diffusion equation is integrated over a typical node, a rigorous mathematical statement of neutron conservation is derived. Unfortunately, this one mathematical equation contains more than one unknown. It contains the volume-averaged flux and surface-averaged currents. Thus, auxiliary spatial-coupling equations are generally developed to solve for all the unknowns. There appears to be a myraid of ways to write the spatial-coupling equations and then solve the resulting set of coupled equations. This accounts for the large number of nodal methods in the literature. Some of these methods will now be reviewed.

One of the oldest nodal methods is FLARE [9]. The FLARE method is usually implemented in one energy group. Spatial coupling is expressed in terms of leakage probabilities which are found from a crudely derived transport kernel. Even though the FLARE methodology lacks a rigorous theoretical foundation, there is much experience in the utility industry in using FLARE-based codes such as EPRI-Node B and EPRI-Node P [10].

An improved class of nodal techniques are the one-and-a-half group methods. These methods were first developed in the late 1960's and early 1970's. They are incorporated in the computer codes, TRILUX, PRESTO and CETRA [11]. In these codes, various artful methods, some of which involve auxiliary fine-mesh calculations, have been devised to determine coupling parameters. These coupling parameters relate surface currents to nodal fluxes and thus have the effect of eliminating the surface currents, leaving only a system of equations involving nodal fluxes to be solved iteratively. These methods are of limited accuracy because only the nodal fluxes are involved in the global solution, when in fact both the nodal

fluxes and surface currents (or coupling parameters) should be updated as the iterative global solution proceeds. One-and-a-half group methods are also widely used by utilities.

During the last ten years, a third class of nodal methods have been developed which Professor Dorning [7] labels as "modern nodal methods". These methods differ from their predecessors in that they are based upon systematic, rigorous mathematical foundations. These include the nodal collision probability method, nodal synthesis method, partial current balance method, flux expansion method, nodal expansion method, polynomial method, nodal Green's function method and the analytic nodal method.

In this thesis, the analytic nodal method is utilized. It originated at M.I.T. in the work of Shober and Henry [12], although variations of the M.I.T. work have recently appeared in the literature [13]. In the analytic nodal method, a one-dimensional diffusion equation is derived for each of the three coordinate directions by integrating the multigroup diffusion equation over the two directions transverse to the direction of interest. The required flux-current,

spatial-coupling relationships are found by solving these one-dimensional diffusion equations. Unfortunately, to do this an assumption must be made concerning the transverse leakages from the nodes. It is the treatment of the transverse leakages that is the one clearly identified approximation inherent in the analytic nodal method. As originally implemented by Shober and Henry the analytic nodal method was limited to two dimensions and used a flat transverse leakage approximation. Greenman, Smith and Henry [14, 15, 16] extended the analytic nodal method to three dimensions. They also incorporated a quadratic transverse leakage approximation as suggested by Finneman [17]. The resulting computer code was called QUANDRY [16].

Thus, with the advent of modern nodal codes like QUANDRY, the tools were at hand to solve nodal reactor problems quickly and efficiently. Such nodal problems are ones in which the reactor is represented as large homogenized nodes, either by design, or through the use of equivalent diffusion theory parameters [1, pgs. 427-457]. To avoid the whole question of spatial homogenization and the generation of equivalent diffusion theory parameters several nodal benchmark problems were developed.

These included the two- and three-dimensional IAEA problems [18], the two-dimensional LRA problem [19], and the three-dimensional LMW problem [20]. The modern nodal methods were applied to these problems [7, 16] with impressive results. The nodal methods proved to be at least two orders of magnitude more computationally efficient than standard finite-difference techniques. Furthermore, this gain in computational speed was accomplished without sacrificing accuracy. Nodal powers for these benchmarks were found to within a few percent.

1.3 A REVIEW OF SPATIAL HOMOGENIZATION OF PWR ASSEMBLIES

In this thesis the analytic nodal method in QUANDRY is applied to the neutronic analysis of pressurized water reactors (PWRs). To do this for realistic cases, a method of spatial homogenization had to be applied to the fuel assemblies making up the PWRs. In this section, the spatial homogenization problem is discussed.

The first part of the spatial homogenization problem is called pin-cell homogenization. A typical PWR assembly is square and contains 15x15, 16x16 or 17x17 pins. Each fuel pin is made of Zircaloy tubes which have an outer diameter of about 1 cm. The tubes are typically about 4 m long and they are filled with about 3.8 m of sintered uranium dioxide pellets. A pin-cell is made up of the uranium pellets, the Zircaloy rod and the coolant-moderator associated with the fuel rod. In general, the pin-cell homogenization consists of finding equivalent diffusion theory parameters for each pin-cell. This is usually done through the use of collision theory methods [21]. Pin-cell homogenization is a science in itself and it is not the intent of this thesis to examine pin-cell homogenization methods. Thus, this analysis starts with a reasonable set of pin-cell homogenized cross sections for two fuel types, water, control rod and a steel baffle. See Appendix 1.

By assigning one of the reference, pin-cell-homogenized cross section sets in Appendix 1 to each homogenized pin-cell in a typical PWR assembly, a heterogeneous assembly configuration is derived. See Figure 1.1.

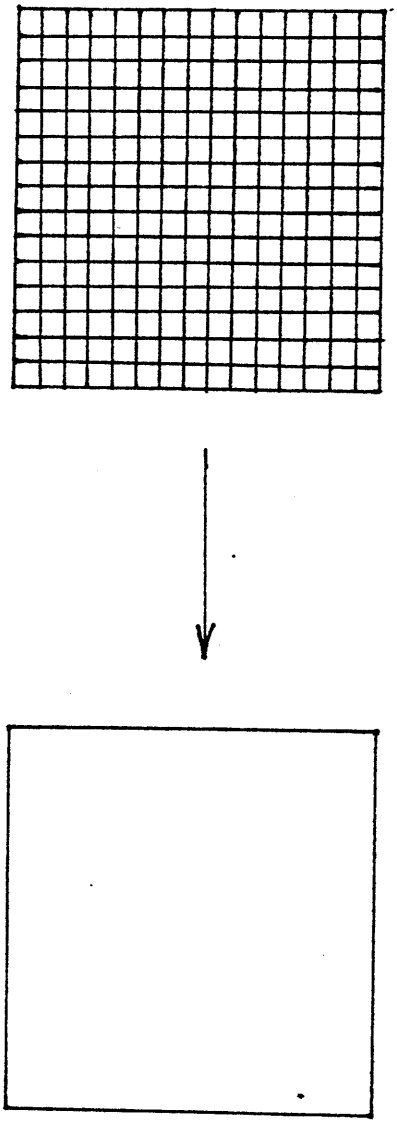

Figure 1.1: A Second Level of PWR Assembly Spatial Homogenization

To utilize a nodal code like QUANDRY, a second level of homogenization must be performed. The heterogeneous assembly configuration must be spatially homogenized. For PWRs this can be done by performing two-dimensional assembly criticality calculations based on zero-net-current boundary conditions. The assembly geometry for these calculations is heterogeneous as shown at the top of Figure 1.1. Each fuel-element-cell, control-rod-cell, water hole, etc., within the assembly is represented as a homogenized pin-cell. The result of this procedure is a single set of homogenized parameters which represent the entire PWR assembly. The assembly calculation also yields the heterogeneous assembly flux, $A_g(x,y)$, $g = 1,2$. Once this has been done for each unique assembly type in a PWR, then a nodal code may easily be employed.

The reactor physics community realized the importance of finding a systematic method to accomplish this second level of spatial homogenization and much work was performed throughout the 1970's on this topic [22, 23, 24, 25]. In this thesis, the spatial homogenization method used is that of Koebke [26] as extended by Smith [27]. This spatial homogenization method is called nodal equivalence theory. This theory suggests how the

assembly calculations described in the previous paragraph can be advantageously employed to perform the spatial homogenization. This is described in Chapter 2.

Smith incorporated nodal equivalence theory (NET) into the computer code QUANDRY and then applied it to several boiling water reactor (BWR) benchmark problems [28]. Cheng and Henry [29] incorporated response matrix techniques into nodal equivalence theory as a practical approach to iterative BWR assembly homogenization. Also, Henry and the author [29] applied NET to some rodded PWR benchmark problems. In this thesis, NET is applied to several rodded and unrodded PWR benchmark problems and results are presented. See Chapter 3.

Thus, when Smith completed his work, the nodal code QUANDRY looked fairly complete. It was computationally efficient and a consistent spatial homogenization scheme had been incorporated into QUANDRY. The next step was to apply QUANDRY to depletion problems. Unfortunately, to perform a detailed depletion of a PWR core, one must have pointwise, heterogeneous fluxes for each assembly in the core. QUANDRY supplies only volume- and surface-averaged fluxes. Clearly, if QUANDRY was to be enabled to perform a detailed core depletion and be able to pick out the hottest pin in a PWR assembly, a method would have to be devised to allow

QUANDRY to reconstruct the pointwise heterogeneous fluxes in a core. Devising and implementing a heterogeneous flux reconstruction scheme for PWR analysis is a major part of this thesis. The next section gives an overview of this problem.

1.4 RECONSTRUCTION OF HETEROGENEOUS PWR FLUXES FROM NODAL CALCULATIONS

Figure 1.2 illustrates a global heterogeneous PWR problem. The problem is heterogeneous because a cross section set from Appendix 1 is specified for each pin-cell in each assembly making up the reactor. Thus, spatial heterogeneities such as water holes are explicitly represented in this problem.

A planar PDQ-7 calculation is commonly employed in the utility industry [30] to find the two-group, heterogeneous fluxes for problems of this type. In this thesis, such fine-mesh PDQ-7 calculations will serve as reference calculations of the two-group, heterogeneous fluxes, $\phi_g(x,y)$, $g = 1,2$. However, the goal is to find a close approximation to $\phi_g(x,y)$ without ever having to perform such relatively expensive global PDQ-7 calculations. This is done by combining the results of relatively inexpensive

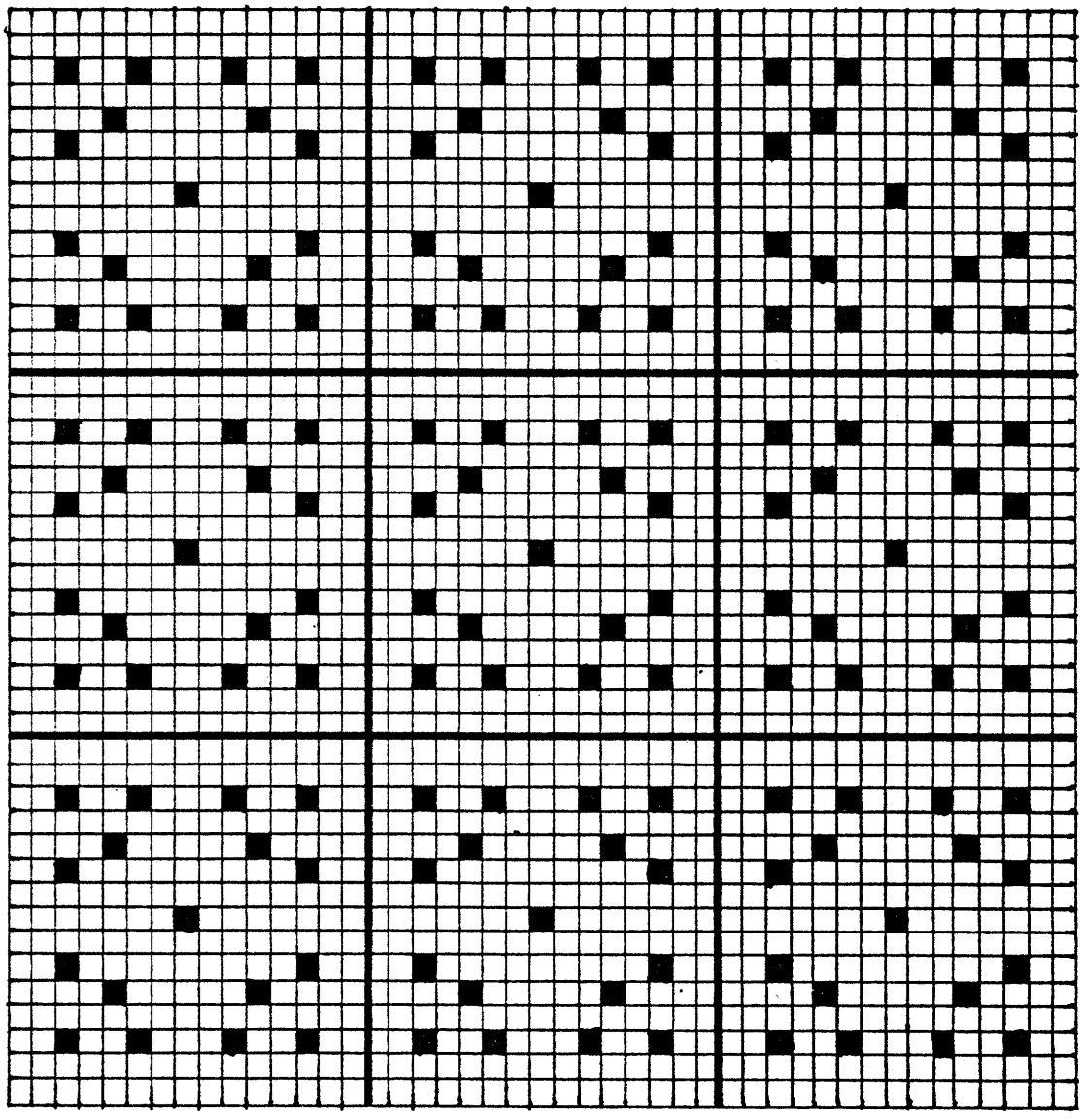

Figure 1.2 A Global Heterogeneous Problem

heterogeneous PDQ-7 assembly calculations for each unique assembly type in the core with the results from the global homogeneous problem calculated by QUANDRY. See Figure 1.3.

The reconstruction of detailed fluxes and pin powers from nodal calculations is not a new idea [31, 32]. However, the approach that has been pursued at M.I.T. [33] is different in that the Koebke/Smith equivalence theory ideas allow heterogeneous flux and current information from the homogenized global problem to be input into the flux reconstruction techniques.

Koebke and Wagner present two basic approaches to flux reconstruction [31]. These approaches are the imbedded heterogeneous assembly calculation method and the modulation method. The most accurate and expensive method of these two is the imbedded heterogeneous assembly calculation. Such imbedded calculations can be performed in two ways. The first way is to use information from the nodal calculation and heterogeneous assembly calculation to infer logarithmic boundary conditions at the assembly faces. An assembly eigenvalue problem using this logarithmic boundary condition then yields the reconstructed flux. The second way is to use information from the nodal calculation and heterogeneous assembly calculation to infer an inhomogeneous boundary source at the assembly

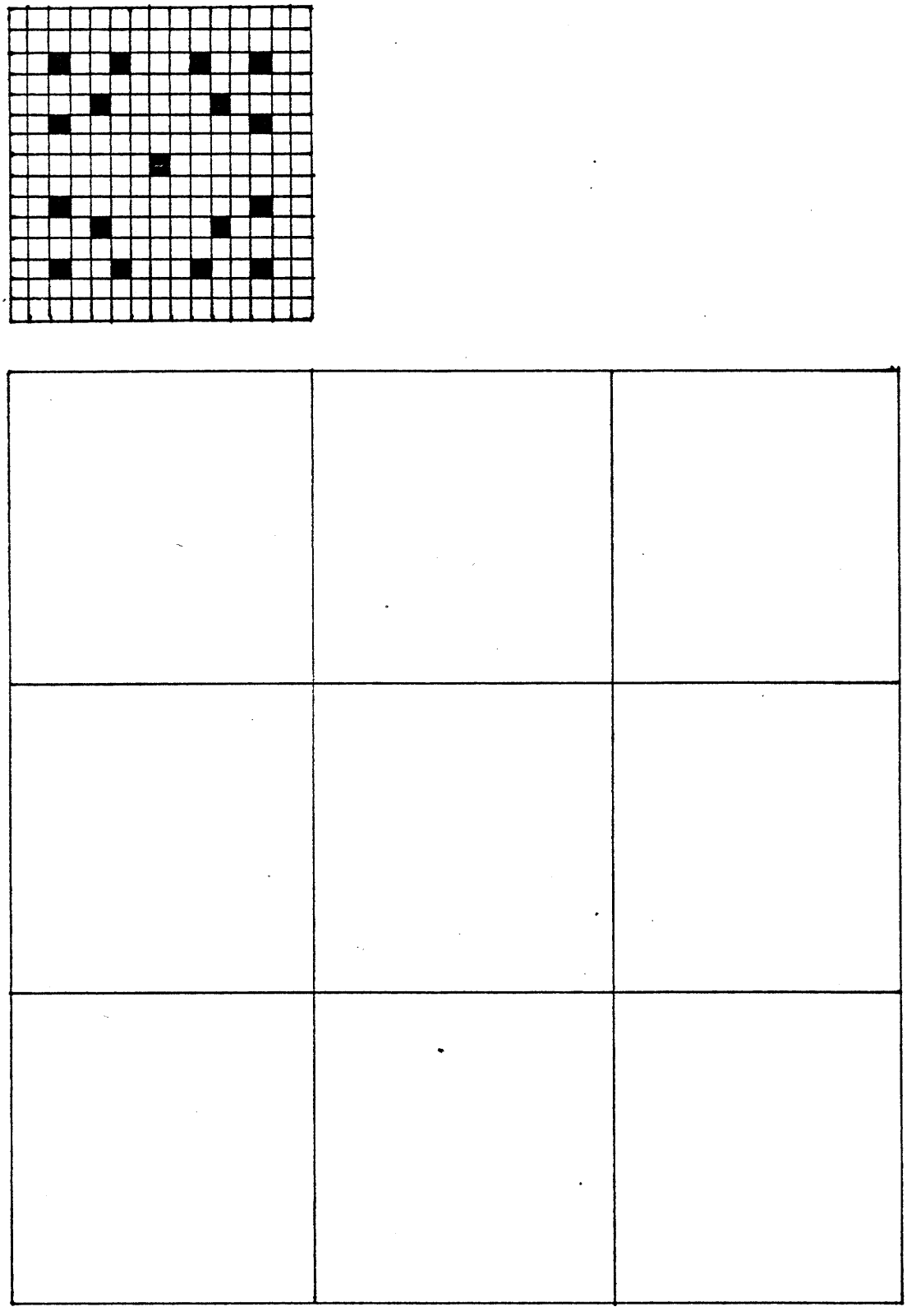

Figure 1.3: A Heterogeneous Assembly Problem and a Global Homogeneous Problem

surface. An inhomogeneous boundary source problem then yields the reconstructed flux. Clearly, the accuracy of the imbedded heterogeneous assembly approach depends entirely on how accurately the logarithmic boundary condition or inhomogeneous boundary source is inferred.

Koebke and Wagner [31] and Jonsson, Grill and Rec [32] report excellent flux reconstruction results by using partial in-currents from the nodal calculations to derive boundary sources for an inhomogeneous boundary source problem. This appears to be due to their success at accurately approximating the reference partial in-current distributions from information from the nodal calculations and heterogeneous assembly calculations. Partial out-current distributions are not well fit and thus the logarithmic boundary condition approach, which requires both partial in- and out-currents, did not fare as well [31].

At M.I.T. Parsons [34] has successfully calculated the inhomogeneous boundary source by assuming that fluxes on the surfaces of PWR assemblies are quadratic. Parsons' quadratic surface fluxes are inferred using only information from the nodal calculation. Finck [35] has calculated the inhomogeneous boundary source by

assuming that the ratio, $\phi_g(x,y)/A_g(x,y)$, on the surfaces of BWR bundles is quadratic. Thus, Finck uses information from both the nodal calculation and the heterogeneous assembly calculation.

Imbedded heterogeneous assembly calculations appear to yield reconstructed heterogeneous pin power distributions to within a few percent. However, they are relatively expensive since they require auxiliary, fine-mesh assembly calculations.

The second approach to flux reconstruction is called the modulation method by Koebke and Wagner [31]. For each assembly they find a pin power distribution from a heterogeneous assembly calculation. Information from the global nodal calculation is used in a local interpolation to find a smooth power distribution. The product of the pin power distribution and the smooth power distribution yields the shape of the modulated heterogeneous power distribution. A renormalization is applied so the assembly average of the final modulated heterogeneous power distribution matches the assembly average power from the nodal calculation.

In this thesis, the approach taken to heterogeneous PWR flux reconstruction is called the form function method.

It is closer to the modulation method than it is to the imbedded heterogeneous assembly calculation method. Its essence is to search for a form function, $F_g(x,y)$, that multiplicatively corrects the assembly flux, $A_g(x,y)$, such that the product $A_g(x,y) * F_g(x,y)$ reconstructs the global heterogeneous flux, $\phi_g(x,y)$, within the assembly. The equation,

$$\phi_g(x,y) = A_g(x,y) * F_g(x,y) \qquad (1.1)$$

defines the reference form function, $F_g(x,y)$. However, this equation is useless in helping to find approximations to $F_g(x,y)$ since $\phi_g(x,y)$ is not known (without having done the expensive reference global calculation). Since the effects of local heterogeneities on flux shapes are represented in both the global heterogeneous flux, $\phi_g(x,y)$, and the assembly flux, $A_g(x,y)$, the form function, $F_g(x,y)$, is spatially smooth. Thus, the form function method consists of finding analytic functions to approximate the reference $F_g(x,y)$ in equation 1.1. The reconstructed analytic form function is called $F_g^R(x,y)$. Once $F_g^R(x,y)$ is found, the reconstructed heterogeneous flux, $\phi_g^R(x,y)$, is

$$\phi_g^R(x,y) = A_g(x,y) * F_g^R(x,y) \qquad (1.2)$$

In general, the analytic form function, $F_g^R(x,y)$ contains coefficients whose magnitudes are determined by forcing the reconstructed flux in equation 1.2 to match heterogeneous global flux information derived from the global homogeneous QUANDRY problem. Specifically, for each assembly, QUANDRY yields good approximations of the heterogeneous volume-averaged group-flux and the heterogeneous surface-averaged group-currents and group-fluxes.

It was found that using only these integral quantities was not enough information to determine all the coefficients of some analytic form functions. Thus in Chapter 4 of this thesis, methods of interpolating the heterogeneous corner point fluxes at each of the four corners of a PWR assembly are presented. These interpolation methods are tested on several benchmark problems and results are presented.

In Chapter 5, the analytic form function, $F_g^R(x,y)$, is expressed in terms of various polynomial functions. Pointwise flux reconstructions are performed and results are presented for several PWR benchmark problems.

In Chapter 6, the group diffusion equations are used to derive a coupled set of differential equations for the reference form functions, $F_g(x,y)$, $g = 1,2$. A solution technique is employed to solve the coupled set of equations in an approximate fashion. The resulting solution yields a non-polynomial, analytic form function, $F_g^R(x,y)$, $g = 1,2$. Pointwise flux reconstructions are performed and results are presented for several PWR benchmark problems.

Chapter 7 contains conclusions and recommendations for future work.

1.5 SUMMARY AND OBJECTIVE

This chapter has reviewed nodal method developments. Modern nodal methods were first developed in the 1970's. To benchmark these methods, nodal problems were devised in which the homogenized diffusion theory parameters were assumed known. The nodal code employed in this thesis is QUANDRY. The next step was to develop methods for finding homogenized diffusion theory parameters. The nodal equivalence ideas of Koebke as extended and implemented into QUANDRY by Smith are used. The reconstruction of the heterogeneous flux was the next problem that needed to be solved to make QUANDRY more useful for PWR analysis.

It is the objective of this thesis to apply the analytic nodal method and nodal equivalence theory as embodied in QUANDRY to the neutronic analysis of PWRs. This includes applying QUANDRY to the calculation of normalized assembly power distributions for PWRs and devising, implementing and testing a heterogeneous PWR flux reconstruction scheme for QUANDRY.

Chapter 2

A REVIEW OF THE ANALYTIC NODAL METHOD AND NODAL EQUIVALENCE THEORY

2.1 INTRODUCTION

The purpose of this chapter is to review the analytic nodal method and nodal equivalence theory as implemented in QUANDRY. The theory described in this chapter is not new. However, the concepts in this chapter form the foundation for understanding the theory and results that make up the rest of this thesis. A more complete treatment of the analytic nodal method is in Smith's N. E. Thesis [16]. Nodal equivalence theory is described in Smith's Ph.D. Thesis [27].

The QUANDRY nodal balance equation is presented and the QUANDRY spatial coupling equations are discussed in section 2 of this chapter. Section 3 describes nodal equivalence theory and a cross section homogenization method through which reference diffusion theory parameters may be found. Section 4 presents inexpensive methods for finding close approximations of the reference parameters based on fine-mesh assembly calculations. Section 5 summarizes this chapter.

The generalized notation employed by Smith [16,27] is used in this chapter. The global reactor problem is treated in three-dimensional Cartesian geometry, where x, y and z represent the three coordinate directions and u, v and w serve as generalized coordinate subscripts. The spatial domain of all problems is divided into an array of right rectangular parallelopipeds (nodes) with grid indices defined by u_ℓ, v_m, w_n where

$$\ell, m, n = \begin{cases} i = 1, 2, \ldots, I; & u, v, w = x \\ j = 1, 2, \ldots, J; & u, v, w = y \\ k = 1, 2, \ldots, K; & u, v, w = z. \end{cases}$$

The node (i,j,k) is defined by

$$x \in [x_i , x_{i+1}]$$
$$y \in [y_j , y_{j+1}]$$
$$z \in [z_k , z_{k+1}].$$

The node widths are expressed as

$$h_\ell^u = u_{\ell+1} - u_\ell ; \qquad u = x, y, z.$$

The volume of node (i,j,k) is

$$V_{i,j,k} = h_i^x h_j^y h_k^z.$$

2.2 THE QUANDRY EQUATIONS

2.2.1 Introduction

The QUANDRY computer code may be used to solve a global homogeneous reactor problem as represented in Figure 1.3 of Chapter 1. The spatial domain of such homogeneous problems is divided into an array of rectangular nodes which have homogeneous compositions. Associated with each homogenized node is a single set of node-homogenized diffusion theory parameters which are spatially constant within each node. In this section it is assumed that these parameters are known. The problem of finding these parameters for the general case when the reactor problem is heterogeneous is deferred until later sections of this chapter. The superscript "hom" is used in this section as a mnemonic device to indicate that a given quantity is related to the homogeneous reactor problem.

This section presents four equations that are fundamental to the theory upon which QUANDRY is based. The first is the QUANDRY nodal balance equation for a homogeneous node (i,j,k). The second is the differential equation for the QUANDRY one-dimensional homogeneous fluxes. The third and fourth are equations for the homogenized QUANDRY surface fluxes at a nodal interface u_ℓ.

2.2.2 The Nodal Balance Equation

The three-dimensional, multigroup neutron diffusion equation for the global homogeneous problem is

$$- \sum_{u=x,y,z} \frac{\partial}{\partial u} D^{u,hom}_{g_{i,j,k}} \frac{\partial}{\partial u} \phi^{hom}_g(x,y,z) +$$

$$\Sigma^{hom}_{Rg_{i,j,k}} \phi^{hom}_g(x,y,z) =$$

$$\sum_{g' \neq g}^{G} [\Sigma^{hom}_{gg'_{i,j,k}} + \chi^{hom}_{g_{i,j,k}} \frac{1}{\lambda^{hom}} \nu\Sigma^{hom}_{fg'_{i,j,k}}] \phi^{hom}_{g'}(x,y,z)$$

$$g = 1, 2, \ldots, G$$

$$(x,y,z) \subset node(i,j,k) \qquad (2.1)$$

where

G = total number of neutron energy groups

$D^{u,hom}_{g_{i,j,k}}$ = diffusion coefficient for group g, direction u and in node (i,j,k), (cm^{-1})

$\phi^{hom}_g(x,y,z)$ = scalar neutron flux in group g (cm^{-2} sec^{-1})

$$\Sigma^{hom}_{Rg_{i,j,k}} = \Sigma^{hom}_{ag_{i,j,k}} + \Sigma^{hom}_{sg_{i,j,k}} - \Sigma^{hom}_{gg_{i,j,k}} + \chi^{hom}_{g_{i,j,k}} \frac{1}{\lambda^{hom}} \nu\Sigma^{hom}_{fg_{i,j,k}}$$

$\Sigma^{hom}_{ag_{i,j,k}}$ = macroscopic absorption cross section for group g in node (i,j,k), (cm^{-1})

$\Sigma^{hom}_{sg_{i,j,k}}$ = macroscopic scattering cross section for group g in node (i,j,k), (cm^{-1})

$\chi^{hom}_{g_{i,j,k}}$ = fission spectrum for group g in node (i,j,k)

λ^{hom} = reactor eigenvalue for the global homogeneous problem (k_{eff})

$\nu\Sigma^{hom}_{fg_{i,j,k}}$ = the mean number of neutrons released per fission times the macroscopic fission cross section for group g in node (i,j,k), (cm^{-1})

$\Sigma^{hom}_{gg'_{i,j,k}}$ = macroscopic transfer cross section from group g' to group g (cm^{-1}).

The integration of equation 2.1 over the volume of the homogeneous node (i,j,k) yields

$$h^y_j \; h^z_k \; L^{x,hom}_{g_{i,j,k}} + h^x_i \; h^z_k \; L^{y,hom}_{g_{i,j,k}} +$$

$$h^x_i \; h^y_j \; L^{z,hom}_{g_{i,j,k}} + V_{i,j,k} \; \Sigma^{hom}_{Rg_{i,j,k}} \; \bar{\bar{\phi}}^{hom}_{g_{i,j,k}} =$$

$$V_{i,j,k} \sum_{g' \neq g}^{G} [\Sigma^{hom}_{gg'_{i,j,k}} + \frac{1}{\lambda^{hom}} \; \chi^{hom}_{g_{i,j,k}} \; \nu\Sigma^{hom}_{fg'_{i,j,k}}] \bar{\bar{\phi}}^{hom}_{g'_{i,j,k}}$$

$$g = 1, 2, \ldots, G. \qquad (2.2)$$

In equation 2.2, the volume-averaged flux in group g for the homogeneous node (i,j,k) is

$$\bar{\bar{\phi}}^{hom}_{g_{i,j,k}} = \frac{1}{V_{i,j,k}} \int_{x_i}^{x_{i+1}} dx \int_{y_j}^{y_{j+1}} dy \int_{z_k}^{z_{k+1}} dz \; \phi_g^{hom}(x,y,z) \tag{2.3}$$

The nodal face-averaged, u-directed, net leakage is

$$L^{u,hom}_{g_{\ell,m,n}} = \left(J^{u,hom}_{g_{\ell+1,m,n}} - J^{u,hom}_{g_{\ell,m,n}} \right) \tag{2.4}$$

where the nodal face-averaged, u-directed net current for the homogeneous node (i,j,k) is

$$J^{u,hom}_{g_{i,j,k}} = \frac{-D^{u,hom}_{g_{i,j,k}} \frac{\partial}{\partial u} \int_{v_m}^{v_{m+1}} dv \int_{w_n}^{w_{n+1}} dw \; \phi_g^{hom}(u_\ell,v,w)}{h_m^v \cdot h_n^w}$$

$$u = x, \; y, \; z$$

$$v \neq u$$

$$w \neq u \neq v. \tag{2.5}$$

Equation 2.2 is a rigorous statement of neutron conservation within node (i,j,k). However, the utility of equation 2.2 is limited unless additional relationships can be specified which involve both the nodal face-averaged net leakages, $L^{u,hom}_{g_{i,j,k}}$, and the nodal volume-averaged fluxes, $\bar{\bar{\phi}}^{hom}_{g_{i,j,k}}$. The required relationships are called spatial coupling equations.

The first step in deriving the QUANDRY spatial coupling equations is to formulate a differential equation which can be solved for the one-dimensional, homogeneous QUANDRY fluxes. That differential equation is presented in the next subsection of this chapter.

2.2.3 Differential Equation for the One-Dimensional Homogeneous Fluxes

The differential equation for the one-dimensional homogeneous fluxes in QUANDRY is determined by integrating the diffusion equation over the two directions transverse to the direction of interest. This yields for the direction u (= x, y, z) and node (ℓ,m,n)

$$
\begin{aligned}
&- h_m^v \, h_n^w \, D_{g_{\ell,m,n}}^{u,hom} \frac{\partial^2}{\partial u^2} \phi_{g_{\ell,m,n}}^{u,hom}(u) \quad + \\
&h_m^v \, h_n^w \, \Sigma_{Rg_{\ell,m,n}}^{hom} \phi_{g_{\ell,m,n}}^{u,hom} \quad = \\
&h_m^v \, h_n^w \sum_{g' \neq g}^{G} [\Sigma_{gg'_{\ell,m,n}}^{hom} + \frac{1}{\lambda^{hom}} \chi_{g_{\ell,m,n}} \nu\Sigma_{fg'_{\ell,m,n}}^{hom}] \phi_{g'_{\ell,m,n}}^{u,hom}(u) + \\
&D_{g_{\ell,m,n}}^{v,hom} \int_{v_m}^{v_{m+1}} dv \int_{w_n}^{w_{n+1}} dw \frac{\partial^2}{\partial v^2} \phi_{g_{\ell,m,n}}^{hom}(u,v,w) \quad + \\
&D_{g_{\ell,m,n}}^{w,hom} \int_{v_m}^{v_{m+1}} dv \int_{w_n}^{w_{n+1}} dw \frac{\partial^2}{\partial w^2} \phi_{g_{\ell,m,n}}^{hom}(u,v,w)
\end{aligned}
$$

$$
\begin{aligned}
&u = x, y, z \\
&v \neq u \\
&w \neq v \neq u
\end{aligned}
\qquad (2.5)
$$

where

$$\phi^{u,hom}_{g_{\ell,m,n}}(u) = \frac{1}{h^v_m \, h^w_n} \int_{v_m}^{v_{m+1}} dv \int_{w_n}^{w_{n+1}} dw \; \phi^{hom}_{g_{\ell,m,n}}(u,v,w) \qquad (2.6)$$

is the one-dimensional homogenized QUANDRY flux in group g and in direction u for node (ℓ,m,n).

Equation 2.5 may be written in a more compact form by defining the directionally dependent transverse leakages

$$L^{v,hom}_{g_{\ell,m,n}}(u) = \frac{- D^{v,hom}_{g_{\ell,m,n}} \int_{v_m}^{v_{m+1}} dv \int_{w_n}^{w_{n+1}} dw \; \frac{\partial^2}{\partial v^2} \phi^{hom}_{g_{\ell,m,n}}(u,v,w)}{h^w_n}$$

$$u = x, \; y, \; z$$

$$v \neq u$$

$$w \neq v \neq u. \qquad (2.7)$$

Note that when the transverse leakage in equation 2.7 is integrated over $[u_\ell \; , \; u_{\ell+1}]$ and divided by h^u_ℓ it yields

$$L^{v,hom}_{g_{\ell,m,n}} = \frac{1}{h^u_\ell} \int_{u_\ell}^{u_{\ell+1}} du \; L^{u,hom}_{g_{\ell,m,n}}(u)$$

$$= \left(J^{v,hom}_{g_{\ell,m+1,n}} - J^{v,hom}_{g_{\ell,m,n}} \right)$$

$$u = x, y, z$$

$$v \neq u \qquad (2.8)$$

which is the nodal face-averaged, v-directed, net leakage.

The sum of two net leakages transverse to the direction u, per unit u, divided by $h^v_m \; h^w_n$ is

$$S^{u,hom}_{g_{\ell,m,n}}(u) = \frac{1}{h^v_m} L^{v,hom}_{g_{\ell,m,n}}(u) + \frac{1}{h^w_n} L^{w,hom}_{g_{\ell,m,n}}(u)$$

$$u = x, y, z$$

$$v \neq u$$

$$w \neq u \neq v. \qquad (2.9)$$

By using the definitions in equations 2.7 and 2.9, the differential equation 2.5 becomes

$$- D^{u,hom}_{g_{\ell,m,n}} \frac{\partial^2}{\partial u^2} \phi^{u,hom}_{g_{\ell,m,n}}(u) + \Sigma^{hom}_{Rg_{\ell,m,n}} \phi^{u,hom}_{g_{\ell,m,n}}(u) =$$

$$RHS^{u,hom}_{g_{\ell,m,n}}(u) \equiv$$

$$\sum_{g' \neq g}^{G} [\Sigma^{hom}_{gg'_{\ell,m,n}} + \frac{1}{\lambda^{hom}} \chi^{hom}_{g_{\ell,m,n}} \nu\Sigma^{hom}_{fg'_{\ell,m,n}}] \phi^{u,hom}_{g'_{\ell,m,n}}(u) -$$

$$S^{u,hom}_{g_{\ell,m,n}}(u)$$

$$u = x, y, z$$

$$v \neq u$$

$$w = v = u. \qquad (2.10)$$

Thus, the right-hand side of the differential equation 2.1o is composed of the difference of the out-of-group source term and the total transverse leakage term.

An analytic solution for the one-dimensional homogeneous group-flux, $\phi^{u,hom}_{g_{\ell,m,n}}(u)$, would be possible if the right-hand side of equation 2.10 were known. Such a solution could then be utilized to provide the required spatial coupling relationships between homogenized net leakages and node-averaged fluxes. Unfortunately, $RHS^{u,hom}_{g_{\ell,m,n}}(u)$ in equation 2.10 is not known. Thus an approximation is required.

At this point, the nodal analysis can take many branches. For example, Smith [36] indicates that if $RHS^{u,hom}_{g_{\ell,m,n}}(u)$ could be represented as spatially flat, then a multigroup approach to the solution of equation 2.10 could be taken in which each group is treated sequentially. Such an approach would be invaluable if the total number of groups, G, is much greater than two. However, the purpose of this thesis is to perform neutronic analysis of PWRs. For that purpose, G = 2 is satisfactory for many calculations. Thus, in QUANDRY, a two-group approach is taken in which the group-fluxes are solved for simultaneously, not sequentially. This is accomplished by moving the out-of-group source term on the right-hand side of equation 2.10 to the left-hand side, leaving only the total transverse leakage term on the right.

The resulting differential equation for the one-dimensional homogenized QUANDRY fluxes is written in matrix form as

$$- [D^{u,hom}_{\ell,m,n}] \frac{\partial^2}{\partial u^2} [\phi^{u,hom}_{\ell,m,n}(u)] + [\Sigma^{hom}_{\ell,m,n}] [\phi^{u,hom}_{\ell,m,n}(u)] = - [S^{u,hom}_{\ell,m,n}(u)]$$

$$u = x, y, z$$

$$v \neq u$$

$$w \neq v \neq u \qquad (2.11)$$

where

$[\phi^{u,hom}_{\ell,m,n}(u)]$ is a column vector of length G containing homogenized one-dimensional fluxes

$[D^{u,hom}_{\ell,m,n}]$ is a diagonal G x G matrix containing directionally dependent, homogenized diffusion coefficients

$[S^{u,hom}_{\ell,m,n}(u)]$ is a column vector of length G containing homogenized total net leakages transverse to the direction u

$$[\Sigma^{hom}_{\ell,m,n}] = [\Sigma^{hom}_{a_{\ell,m,n}}] + [\Sigma^{hom}_{s_{\ell,m,n}}] - [\Sigma^{hom}_{gg'_{\ell,m,n}}] - \frac{1}{\lambda^{hom}} [\chi^{hom}_{\ell,m,n}] [\nu\Sigma^{hom}_{f_{\ell,m,n}}]^T$$

and is a full G x G matrix in the general case.

The meanings of the terms making up the $[\Sigma^{hom}_{\ell,m,n}]$ matrix are

$[\Sigma^{hom}_{a_{\ell,m,n}}]$	is a diagonal G x G matrix containing macroscopic absorption cross sections
$[\Sigma^{hom}_{s_{\ell,m,n}}]$	is a diagonal G x G matrix containing macroscopic scattering cross sections
$[\Sigma^{hom}_{gg'_{\ell,m,n}}]$	is a full G x G matrix containing macroscopic scattering cross sections for scattering from group g' to group g
λ^{hom}	is the eigenvalue of the homogeneous global reactor problem
$[\chi^{hom}_{\ell,m,n}]$	is a column vector of length G containing the fission neutron spectrum
$[\nu\Sigma^{hom}_{f_{\ell,m,n}}]$	is a column vector of length G containing nu, the mean number of neutrons emitted per fission, times the macroscopic fission cross section.

Unfortunately, the net transverse leakage term, $[S^{u,hom}_{\ell,m,n}(u)]$, is still not known. Thus, an approximation concerning it must be made so that the differential equations 2.11 can be solved for the one-dimensional

fluxes, $[\phi^{u,hom}_{\ell,m,n}(u)]$. In this thesis, the approximation that is made for the transverse leakage term, $[S^{u,hom}_{\ell,m,n}(u)]$, is that it can be expanded in a quadratic polynomial [17]. For the direction u, the quadratic chosen is such that the integrals of the quadratic transverse leakage approximation over the node (ℓ,m,n) and the two adjacent nodes $(\ell-1,m,n)$ and $(\ell+1,m,n)$ preserve the average transverse leakage of the nodes. Thus $[S^{u,hom}_{\ell,m,n}(u)]$ is approximated as

$$[S^{u,hom}_{\ell,m,n}(u)] \cong [S^{u,hom}_{\ell,m,n}] + \left([S^{u,hom}_{\ell-1,m,n}] - [S^{u,hom}_{\ell,m,n}] \right) \rho^{\ell-1}_{u_\ell}(u) + \left([S^{u,hom}_{\ell+1,m,n}] - [S^{u,hom}_{\ell,m,n}] \right) \rho^{\ell+1}_{u_\ell}(u)$$

$$u = x, y, z. \qquad (2.12)$$

In equation 2.12, $[S^{u,hom}_{\ell,m,n}]$ is defined by

$$[S^{u,hom}_{\ell,m,n}] = \frac{1}{h^m_v} [L^{v,hom}_{\ell,m,n}] + \frac{1}{h^n_w} [L^{w,hom}_{\ell,m,n}]$$

$$u = x, y, z \qquad (2.13)$$

where the components of the column vectors $[L^{v,hom}_{\ell,m,n}]$ and $[L^{w,hom}_{\ell,m,n}]$ are defined by equations 2.4 and 2.5. The quadratic expansion functions, $\rho^{\ell-1}_{u_\ell}(u)$ and $\rho^{\ell+1}_{u_\ell}(u)$, are defined in Appendix 1 of Reference 16.

Once a suitable approximation for the shape of $[S^{u,hom}_{\ell,m,n}(u)]$ has been made, the differential equation 2.11 can be solved for the one-dimensional homogeneous fluxes. Boundary conditions for equation 2.11 are specified in terms of both fluxes and currents. The homogeneous one-dimensional fluxes, $[\phi^{u,hom}_{\ell,m,n}(u)]$, are related to the homogeneous currents in direction u, $[J^{u,hom}_{\ell,m,n}(u)]$, by the equation

$$[J^{u,hom}_{\ell,m,n}(u)] = - [D^{u,hom}_{\ell,m,n}] \frac{\partial}{\partial u} [\phi^{u,hom}_{\ell,m,n}(u)]$$

$$u = x, y, z. \qquad (2.14)$$

The actual solution of the differential equation 2.11 has been extensively documented by Smith [16, 27] and will not be repeated here. Instead, the next subsection describes how the solution to equation 2.11 can be used to derive equations for the homogeneous QUANDRY surface fluxes at a nodal interface u_ℓ.

2.2.4 Equations for Homogeneous Surface Fluxes At a Nodal Interface u_ℓ

The nodal balance equation 2.2 for the homogeneous problem relates net leakages and volume-averaged fluxes. The global QUANDRY solution method consists of finding spatial coupling equations which also relate homogeneous net leakages and volume-averaged fluxes and then solving a combined system of equations involving both net leakages and volume-averaged fluxes as unknowns. The first step in the derivation of the spatial coupling equations is the formulation and solution of the differential equation 2.11 for the one-dimensional homogeneous fluxes. How these one-dimensional flux solutions are used to derive the spatial coupling equations will be described in this section.

Figure 2.1 shows three adjacent QUANDRY nodes. The differential equation 2.11 is solved for the homogeneous node (ℓ-1,m,n) subject to the boundary conditions

$$\left.\phi^{u,hom}_{g_{\ell-1,m,n}}(u)\right|_{u=u_\ell} = \phi^{u,hom}_{g_{\ell-1,m,n}}(u_\ell)$$

$$\left.J^{u,hom}_{g_{\ell-1,m,n}}(u)\right|_{u=u_\ell} = J^{u,hom}_{g_{\ell-1,m,n}}(u_\ell)$$

$$u = x,\ y,\ z. \qquad (2.15)$$

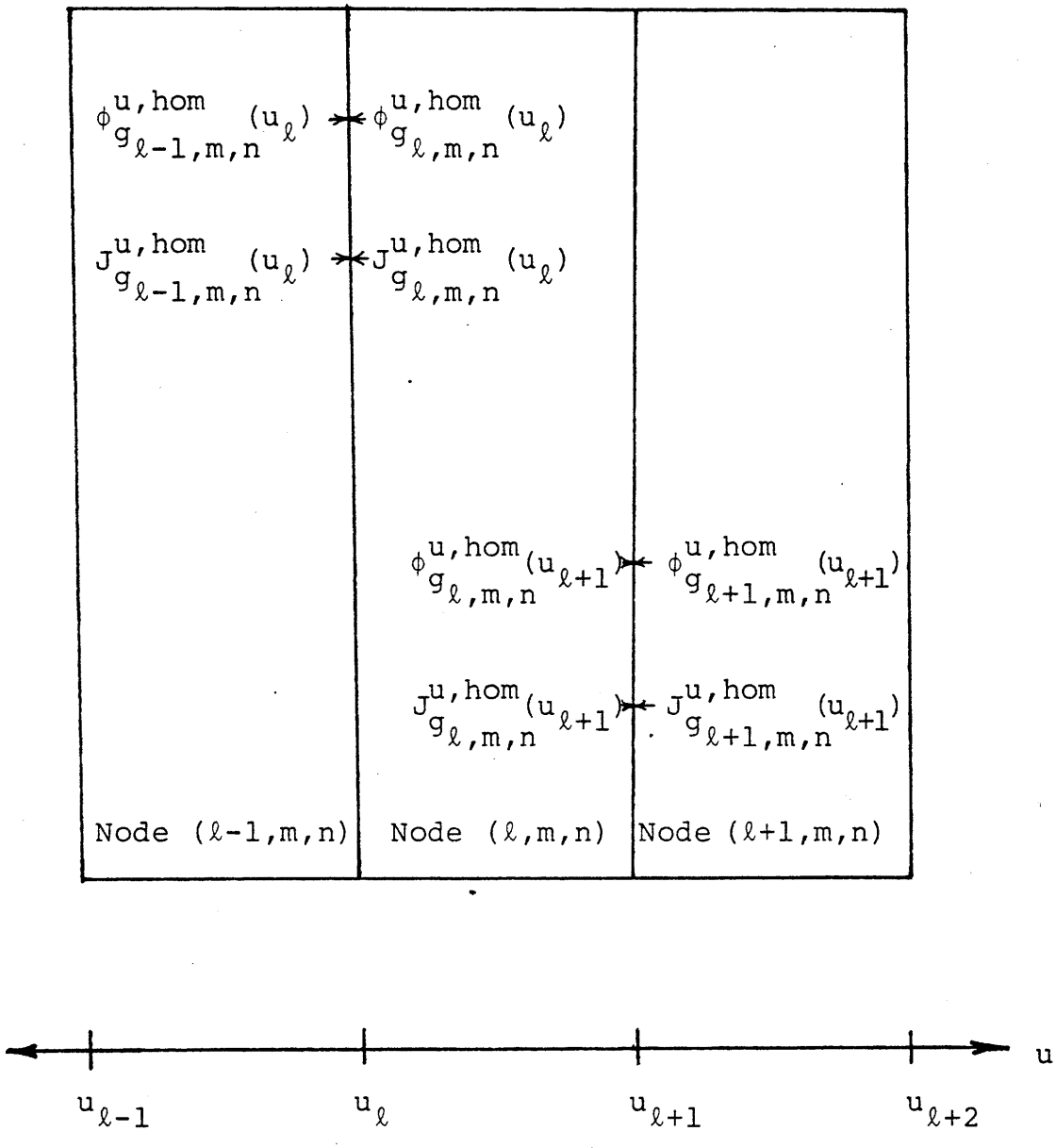

Figure 2.1 QUANDRY Nodes (ℓ-1,m,n), (ℓ,m,n) and (ℓ+1,m,n)

This solution is integrated over the node width $(u_{\ell-1}, u_\ell)$ to yield an equation involving node-surface-averaged net leakages and node-volume-averaged fluxes for the homogeneous node $(\ell-1,m,n)$ in terms of the homogeneous, surface-averaged net current at u_ℓ, $J^{u,hom}_{g_{\ell-1,m,n}}(u_\ell)$, and the homogeneous, surface-averaged fluxes at u_ℓ, $\phi^{u,hom}_{g_{\ell-1,m,n}}(u_\ell)$. In matrix form, the resulting equation is

$$
\begin{aligned}
[\phi^{u,hom}_{\ell-1,m,n}(u_\ell)] = &-[A^{u,hom}_{\ell-1,m,n}]\ [J^{u,hom}_{\ell-1,m,n}(u_\ell)] \\
&+[B^{u,hom}_{\ell-1,m,n}]\ [\bar{\bar{\phi}}^{hom}_{\ell-1,m,n}] \\
&-\left[[C^{u^+,hom}_{\ell-1,m,n}]\ a^{u^-}_{\ell-1} + [D^{u^+,hom}_{\ell-1,m,n}]\ b^{u^-}_{\ell-1} + [E^{u^+,hom}_{\ell-1,m,n}]\ c^{u^-}_{\ell-1} \right] [S^{u,hom}_{\ell-2,m,n}] \\
&-\left[[C^{u^+,hom}_{\ell-1,m,n}]\ (1 - a^{u^-}_{\ell-1} - a^{u^+}_{\ell-1}) + [D^{u^+,hom}_{\ell-1,m,n}]\ (-b^{u^-}_{\ell-1} - b^{u^+}_{\ell-1}) \right. \\
&\left. +[E^{u^+,hom}_{\ell-1,m,n}]\ (-c^{u^-}_{\ell-1} - c^{u^+}_{\ell-1}) \right] [S^{u,hom}_{\ell-1,m,n}] \\
&-\left[[C^{u^+,hom}_{\ell-1,m,n}]\ a^{u^+}_{\ell-1} + [D^{u^+,hom}_{\ell-1,m,n}]\ b^{u^+}_{\ell-1} + [E^{u^+,hom}_{\ell-1,m,n}] c^{u^+}_{\ell-1} \right] [S^{u,hom}_{\ell,m,n}]
\end{aligned}
$$

$$u = x, y, z \qquad (2.16)$$

Similarly, the differential equation 2.11 is solved for the homogeneous node (ℓ,m,n) subject to the boundary conditions

$$\phi^{u,hom}_{g_{\ell,m,n}}(u)\Big|_{u=u_\ell} = \phi^{u,hom}_{g_{\ell,m,n}}(u_\ell)$$

$$J^{u,hom}_{g_{\ell,m,n}}(u)\Big|_{u=u_\ell} = J^{u,hom}_{g_{\ell,m,n}}(u_\ell)$$

$$u = x,\ y,\ z \qquad (2.17)$$

This solution is integrated over the node width $(u_\ell\ ,\ u_{\ell+1})$ to yield an equation involving node-surface-averaged net leakages and node-volume-averaged fluxes for the homogeneous node (ℓ,m,n) in terms of the homogeneous, surface-averaged net current at u_ℓ , $J^{u,hom}_{g_{\ell,m,n}}(u_\ell)$, and the homogeneous, surface-averaged fluxes at u_ℓ , $\phi^{u,hom}_{g_{\ell,m,n}}(u_\ell)$. In matrix form, the resulting equation is

$$[\phi^{u,hom}_{\ell,m,n}(u_\ell)] = [A^{u,hom}_{\ell,m,n}]\ [J^{u,hom}_{\ell,m,n}(u_\ell)]$$

$$+[B^{u,hom}_{\ell,m,n}]\ [\bar{\bar{\Phi}}^{hom}_{\ell,m,n}]$$

$$-\left[[C^{u^-,hom}_{\ell,m,n}]\ a^{u^-}_\ell + [D^{u^-,hom}_{\ell,m,n}]\ b^{u^-}_\ell + [E^{u^-,hom}_{\ell,m,n}]\ c^{u^-}_\ell \right] [S^{u,hom}_{\ell-1,m,n}]$$

$$-\Big[[C^{u^-,hom}_{\ell,m,n}]\ (1 - a^{u^-}_\ell - a^{u^+}_\ell) + [D^{u^-,hom}_{\ell,m,n}]\ (-b^{u^-}_\ell - b^{u^+}_\ell)$$

$$+[E^{u^-,hom}_{\ell,m,n}]\ (-c^{u^-}_\ell - c^{u^+}_\ell) \Big] [S^{u,hom}_{\ell,m,n}]$$

$$-\left[[C^{u^-,hom}_{\ell,m,n}]\ a^{u^+}_\ell + [D^{u^-,hom}_{\ell,m,n}]\ b^{u^+}_\ell + [E^{u^-,hom}_{\ell,m,n}]\ c^{u^+}_\ell \right] [S^{u,hom}_{\ell+1,m,n}]$$

$$u = x,\ y,\ z. \qquad (2.18)$$

In equations 2.16 and 2.18 the G x 1 column vectors have the following definitions:

$[\bar{\bar{\phi}}^{hom}_{\ell,m,n}]$	is a column vector of homogeneous, node-volume-averaged group-fluxes for node (ℓ,m,n)
$[\phi^{u,hom}_{\ell,m,n}(u_\ell)]$	is a column vector of homogeneous, node-surface-averaged group fluxes at nodal interface u_ℓ for node (ℓ,m,n)
$[J^{u,hom}_{\ell,m,n}(u_\ell)]$	is a column vector of homogeneous, node-surface-averaged net currents for direction u, at nodal interface u_ℓ for node (ℓ,m,n)
$[S^{u,hom}_{\ell,m,n}]$	is a column vector of homogeneous, node-surface-averaged total transverse leakages for the direction u and the node (ℓ,m,n).

The G x G matrices in equations 2.16 and 2.18 are defined in Appendix 3 of Reference 16. They depend only on the homogenized nodal cross sections, homogeneous diffusion coefficients, mesh spacings and λ^{hom}. The transverse leakage expansion coefficients, $a^{u\pm}_\ell$, $b^{u\pm}_\ell$, $c^{u\pm}_\ell$, depend only on the nodal mesh spacings. They are defined in Appendix 1 of Reference 16.

An examination of the equations 2.16 and 2.18 reveals that if the homogenized net current at u_ℓ is continuous and if a relationship is found between the two homogeneous surface fluxes at u_ℓ, $\phi^{u,hom}_{g_{\ell-1,m,n}}(u_\ell)$ and $\phi^{u,hom}_{g_{\ell,m,n}}(u_\ell)$, then that relationship could be used to combine equations 2.16 and 2.18. The resulting equation would contain only the (continuous) net surface-averaged current at u_ℓ, node-surface-averaged net leakages and node-volume-averaged fluxes. Furthermore, by indexing the subscript ℓ by 1 to $\ell+1$ and repeating the process described in this section, a second equation involving only the (continuous) net surface-averaged current at $u_{\ell+1}$, node-surface-averaged net leakages and node-volume-averaged fluxes is derived. Finally, by taking the difference of these two equations and noting that the difference of the net currents at u_ℓ and $u_{\ell+1}$ is a node-surface-averaged net leakage, the spatial coupling equation for the direction u (= x,y,z) is found. As desired, this spatial coupling equation will contain only node-surface-averaged net leakages and node-volume-averaged fluxes.

For the purposes of this thesis, the Analytic Nodal Method and the QUANDRY equations have been sufficiently described. However, two problems have not been resolved. The first problem is how to calculate homogenized cross sections and diffusion coefficients for the global homogeneous problem in Figure 1.3 given the heterogeneous values of these parameters used in the global heterogeneous problem in Figure 1.2. The second problem is how to specify relationships between the homogeneous, node-surface-averaged fluxes and currents shown in Figure 2.1.

The resolution of these two problems is found in nodal equivalence theory. It is the topic of the next section.

2.3 NODAL EQUIVALENCE THEORY

The purpose of this section is to illustrate how nodal equivalence theory is implemented in QUANDRY to allow the generation of equivalent diffusion theory parameters. The discussion in this section is conducted in a formal fashion in that it is assumed that the exact, heterogeneous, global reactor solution is known. In this section, quantities that are labeled "het" with a superscript have come from such a reference heterogeneous solution. Note that no assumption has been made regarding the method used to solve the global heterogeneous problem. Indeed, the reference solution could come from collision theory techniques, diffusion theory or any other global solution method that one might desire to employ.

The goal is to establish a "nodal equivalence" between the global heterogeneous solution and the global homogeneous (QUANDRY) solution. See Figures 1.2 and 1.3 of Chapter 1. Such a nodal equivalence is established if the homogeneous global solution simultaneously preserves k_{eff}, nodal group reaction rates and group surface currents in each homogenized node as compared to the reference values of these quantities as calculated from the (assumed) known reference global heterogeneous solution.

Since the heterogeneous solution to the global reactor problem is assumed known, the following quantities are also known:

$\phi_g^{het}(x,y,z)$ is the reference heterogeneous group g flux

$J_g^{u,het}(x,y,z)$ is the reference heterogeneous current in direction u (= x, y, z) and group g

$\Sigma_{\alpha g}^{het}(x,y,z)$ is the macroscopic cross section for process α (= a, s, f, etc.) for group g.

Fundamental neutron conservation considerations indicate that the balance equation in node (i,j,k) for the heterogeneous reactor problem is

$$h_j^y \; h_k^z \; L^{x,het}_{g_{i,j,k}} + h_i^x \; h_k^z \; L^{y,het}_{g_{i,j,k}} +$$

$$h_i^x \; h_j^y \; L^{z,het}_{g_{i,j,k}} + V_{i,j,k} \; \bar{\Sigma}^{het}_{Rg_{i,j,k}} \; \bar{\bar{\phi}}^{het}_{g_{i,j,k}} =$$

$$\sum_{g'=g}^{G} V_{i,j,k} \left(\bar{\Sigma}^{het}_{gg'_{i,j,k}} + \frac{1}{\lambda^{het}} \; \overline{\chi_g \nu\Sigma}^{het}_{fg'_{i,j,k}}\right] \bar{\bar{\phi}}^{het}_{g'_{i,j,k}}$$

$$g = 1, 2, \ldots G . \qquad (2.19)$$

In equation 2.19 the heterogeneous, volume-averaged flux in group g is

$$\bar{\bar{\phi}}^{het}_{g_{i,j,k}} = \frac{1}{V_{i,j,k}} \int_{x_i}^{x_{i+1}} dx \int_{y_j}^{y_{j+1}} dy \int_{z_k}^{z_{k+1}} dz \; \phi^{het}_g(x,y,z). \tag{2.20}$$

The heterogeneous, node-surface-averaged net leakage in the direction u is

$$L^{u,het}_{g_{\ell,m,n}} = \left(J^{u,het}_{g_{\ell+1,m,n}} - J^{u,het}_{g_{\ell,m,n}} \right)$$

$$u = x, y, z \tag{2.21}$$

where the heterogeneous, node-surface-averaged net current in the direction u is

$$J^{u,het}_{g_{i,j,k}} = \frac{1}{h^v_m \, h^w_n} \int_{v_m}^{v_{m+1}} dv \int_{w_n}^{w_{n+1}} dw \; J^{u,het}_g(u_\ell, v, w)$$

$$u = x, y, z$$

$$v \neq u$$

$$w \neq u \neq v. \tag{2.22}$$

The heterogeneous, flux-weighted, node-volume-averaged cross section in equation 2.19 is

$$\bar{\Sigma}^{het}_{\alpha g_{i,j,k}} = \frac{\frac{1}{V_{i,j,k}} \int_{x_i}^{x_{i+1}} dx \int_{y_j}^{y_{j+1}} dy \int_{z_k}^{z_{k+1}} dz \; \Sigma^{het}_{\alpha g}(x,y,z) \; \phi^{het}_{g}(x,y,z)}{\frac{1}{V_{i,j,k}} \int_{x_i}^{x_{i+1}} dx \int_{y_j}^{y_{j+1}} dy \int_{z_k}^{z_{k+1}} dz \; \phi^{het}_{g}(x,y,z)}$$

$$g = 1, 2, \ldots G. \qquad (2.23)$$

Compare the nodal balance equation 2.2 for the homogeneous problem and the nodal balance equation 2.19 for the heterogeneous problem on a term-by-term basis. If the equivalent homogenized cross section for the process α in group g, $\Sigma^{hom}_{\alpha g_{i,j,k}}$, is defined as

$$\Sigma^{hom}_{\alpha g_{i,j,k}} = \bar{\Sigma}^{het}_{\alpha g_{i,j,k}} \qquad (2.24)$$

and if the QUANDRY solution method for the homogeneous

problem can guarantee that the homogeneous surface-averaged currents (or net leakages) match their heterogeneous counterparts

$$L^{u,hom}_{g_{i,j,k}} = L^{u,het}_{g_{i,j,k}} \qquad (u = x, y, z) \qquad (2.25)$$

then equations 2.2 and 2.19 imply

$$\bar{\bar{\Phi}}^{hom}_{g_{i,j,k}} = \bar{\bar{\Phi}}^{het}_{g_{i,j,k}} \qquad (2.26)$$

and

$$\lambda^{hom} = \lambda^{het} \; . \qquad (2.27)$$

Furthermore, the node (i,j,k) volume-averaged reaction rate for process α , in group g, $RR_{\alpha g_{i,j,k}}$, is preserved

since

$$RR_{\alpha g_{i,j,k}} = \frac{\int_{x_i}^{x_{i+1}} dx \int_{y_j}^{y_{j+1}} dy \int_{z_k}^{z_{k+1}} dz \; \Sigma_{\alpha g}^{het}(x,y,z) \; \phi_g^{het}(x,y,z)}{V_{i,j,k}}$$

$$= \bar{\Sigma}_{\alpha g_{i,j,k}}^{het} \; \bar{\bar{\phi}}_{g_{i,j,k}}^{het}$$

$$= \Sigma_{\alpha g_{i,j,k}}^{hom} \; \bar{\bar{\phi}}_{g_{i,j,k}}^{hom} \qquad (2.28)$$

Thus, the nodal equivalence theory goal of preserving all node-volume-averaged reaction rates can be achieved if the homogenized cross sections are defined as in equation 2.23 and if the solution to the QUANDRY equations for the homogenized problem preserves surface currents or net leakages as described in equation 2.25.

To investigate the question of surface-averaged current (or net leakage) preservation, it is necessary to examine the part of the QUANDRY solution method dealing with the formulation of the spatial coupling equations. In particular, the details of the solution of the differential equation 2.11 for the homogeneous, one-dimensional fluxes are critical to the question of surface-averaged current preservation. The details of concern are as follows:

1. How are the homogenized cross sections in the $[\Sigma^{hom}_{\ell,m,n}]$ matrix calculated from the known heterogeneous cross sections?

2. How are the homogenized diffusion coefficients in the $[D^{u,hom}_{\ell,m,n}]$ matrix calculated from the known heterogeneous diffusion coefficients?

3. What approximation is made for the shape of the transverse leakages in the column vector $[S^{u,hom}_{\ell,m,n}(u)]$?

The answer to the first question is that standard flux-weighting techniques are used. Thus, the homogenized cross sections for all QUANDRY analysis are set equal to their heterogeneous, flux-weighted counterparts as defined by equation 2.24 and 2.23.

The homogenized diffusion coefficients are also found by flux-weighting techniques. However, the inverse of D is flux-weighted. Thus, the homogenized diffusion coefficients are found from the following equation:

$$D_{g_{i,j,k}}^{u,hom} = \left(\frac{\frac{1}{V_{i,j,k}} \int_{x_i}^{x_{i+1}} dx \int_{y_j}^{y_{j+1}} dy \int_{z_k}^{z_{k+1}} dz \; \frac{\phi_g^{het}(x,y,z)}{D_g^{u,het}(x,y,z)}}{\frac{1}{V_{i,j,k}} \int_{x_i}^{x_{i+1}} dx \int_{y_j}^{y_{j+1}} dy \int_{z_k}^{z_{k+1}} dz \; \phi_g^{het}(x,y,z)} \right)^{-1}$$

$$u = x, y, z. \qquad (2.29)$$

The answer to the third question is that the transverse leakage is expanded in a quadratic polynomial. (See equation 2.12.)

Thus, once some method has been specified for approximating the right-hand side of the differential equation 2.11 and for calculating the coefficient matrices $[D_{\ell,m,n}^{u,hom}]$ and $[\Sigma_{\ell,m,n}^{hom}]$, the differential equation can be solved.

To insure that surface-averaged currents (or net leakages are preserved as in equation 2.25 by the solution of the differential equation, the heterogeneous surface currents are taken equal to the homogeneous surface currents. These currents are then imposed as the required current boundary conditions for equation 2.11 through the use of equation 2.14. Furthermore, since the heterogeneous surface currents are continuous at all nodal interfaces and since the homogeneous surface currents are equal to their known heterogeneous counterparts, it follows that the homogeneous surface currents are continuous at all nodal interfaces.

Thus, the nodal equivalence between the heterogeneous and homogeneous problems has now been assured since the QUANDRY global homogeneous solution method will preserve surface-averaged currents and net leakages as in equation 2.25. However, imposing the continuous heterogeneous surface currents on equation 2.11 has consequences in terms of the homogeneous surface-averaged fluxes that are calculated as part of the QUANDRY solution method. These consequences are now explored.

As described in the previous section, equations 2.16 and 2.18 are expressions for the homogeneous, surface-averaged fluxes at a nodal interface u_ℓ . The right-hand sides of these equations are normally calculated using information from the homogeneous problem. However, working within the nodal equivalence theory framework, the right-hand sides of equations 2.16 and 2.18 can be calculated using only information from the assumed known heterogeneous global solution. Thus, the G x G coefficient matrices in 2.16 and 2.18 are calculated using homogenized cross sections, diffusion coefficients and eigenvalues which are computed directly from the known heterogeneous solution according to equations 2.24, 2.29 and 2.27 respectively. As shown in equations 2.25 and 2.26, the homogeneous, surface-averaged net currents, net leakages and volume-averaged fluxes are calculated directly from their heterogeneous counterparts. Unfortunately, except for the special case when the heterogeneous problem is identical to the homogeneous problem and the transverse leakage in this problem is accurately described by the quadratic transverse leakage approximation in equation 2.12, it is unlikely that the calculated, homogeneous, surface-averaged fluxes from equations 2.16 and 2.18 would match their heterogeneous counterparts.

Instead, the relationship between $\phi^{u,hom}_{g_{\ell-1,m,n}}(u_\ell)$ and $\phi^{u,hom}_{g_{\ell,m,n}}(u_\ell)$ is likely to be discontinuous as shown in Figure 2.2. At the nodal interface u_ℓ, the known heterogeneous surface-averaged flux is continuous; thus,

$$\phi^{u,het}_{g_{\ell-1,m,n}}(u_\ell) = \phi^{u,het}_{g_{\ell,m,n}}(u_\ell). \tag{2.30}$$

However, for node $(\ell-1,m,n)$

$$\phi^{u,hom}_{g_{\ell-1,m,n}}(u_\ell) \neq \phi^{u,het}_{g_{\ell-1,m,n}}(u_\ell) \tag{2.31}$$

$$\neq \phi^{u,hom}_{g_{\ell,m,n}}(u_\ell). \tag{2.32}$$

Similarly, for node (ℓ,m,n)

$$\phi^{u,hom}_{g_{\ell,m,n}}(u_\ell) \neq \phi^{u,het}_{g_{\ell,m,n}}(u_\ell) \tag{2.33}$$

$$\neq \phi^{u,hom}_{g_{\ell-1,m,n}}(u_\ell). \tag{2.34}$$

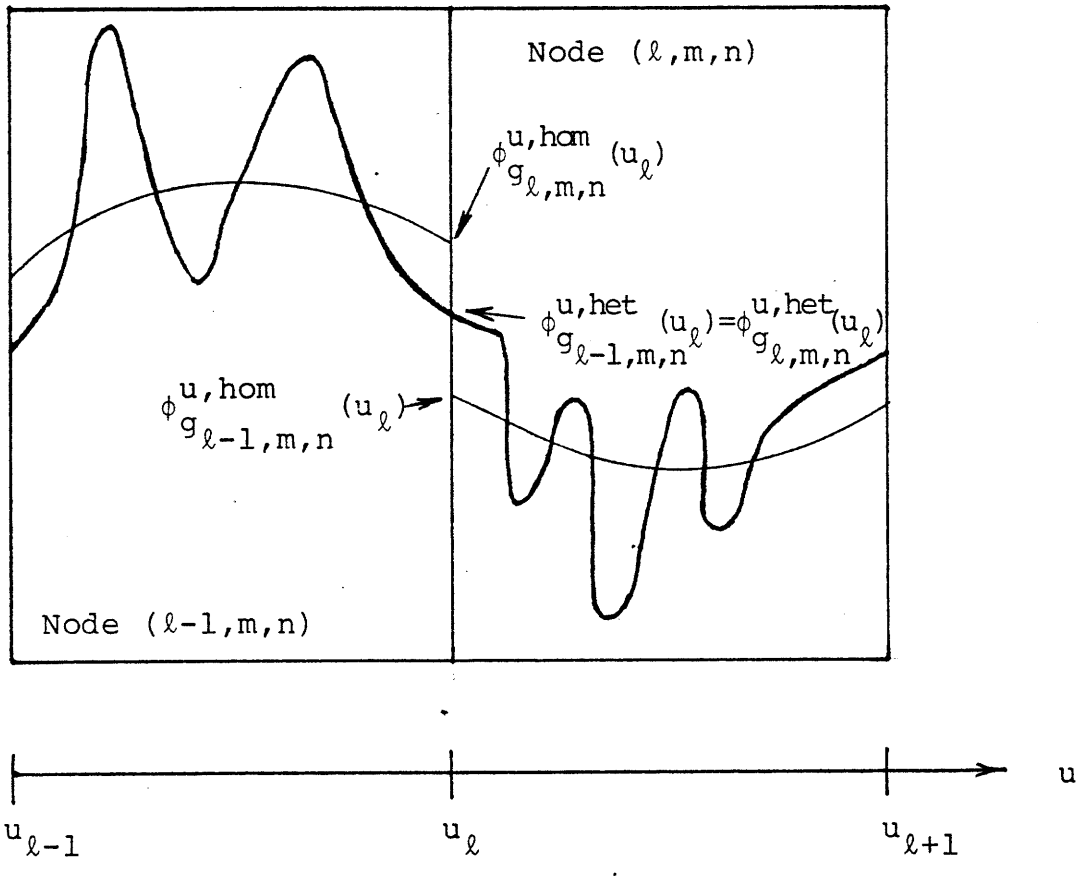

Figure 2.2 Homogeneous and Heterogeneous One-Dimensional Fluxes At a Nodal Interface

To complete the QUANDRY solution method, a relationship between the homogeneous, surface-averaged fluxes, $\phi^{u,hom}_{g_{\ell-1,m,n}}(u_\ell)$ and $\phi^{u,hom}_{g_{\ell,m,n}}(u_\ell)$ must be specified [27]. A simple way to do this is to introduce two additional homogenization parameters per direction per group. These additional parameters are called discontinuity factors. They are defined for node (ℓ,m,n) as

$$f^{u+}_{g_{\ell,m,n}} = \frac{\phi^{u,het}_{g_{\ell,m,n}}(u_{\ell+1})}{\phi^{u,hom}_{g_{\ell,m,n}}(u_{\ell+1})} \qquad (2.35)$$

and

$$f^{u-}_{g_{\ell,m,n}} = \frac{\phi^{u,het}_{g_{\ell,m,n}}(u_{\ell})}{\phi^{u,hom}_{g_{\ell,m,n}}(u_{\ell})} \qquad (2.36)$$

The discontinuity factors in equations 2.35 and 2.36 are easily calculated if the global heterogeneous solution is assumed known. Then the numerators of equations 2.35 and 2.36 are known immediately. The denominators are calculated by using information from the global heterogeneous solution on the right-hand sides of equations 2.16 and 2.18.

The desired relationship between the homogeneous node-surface-averaged group-fluxes at u_ℓ for node $(\ell-1,m,n)$ and node (ℓ,m,n) is

$$f^{u+}_{g_{\ell-1,m,n}} \phi^{u,hom}_{g_{\ell-1,m,n}}(u_\ell) = f^{u-}_{g_{\ell,m,n}} \phi^{u,hom}_{g_{\ell,m,n}}(u_\ell) \tag{2.37}$$

which is simply a statement of continuity of the heterogeneous, surface-averaged group-fluxes as expressed in equation 2.30.

To summarize, it is possible to establish a nodal equivalence between a known global heterogeneous solution and the QUANDRY homogeneous solution. The salient feature of nodal equivalence theory is the introduction of two additional homogenization parameters (discontinuity factors) which have the effect of allowing the homogeneous surface

fluxes to be discontinuous at nodal interfaces. Homogenized cross sections and diffusion coefficients are calculated from the known heterogeneous solution using the standard flux-weighting techniques described in equations 2.24 and 2.29.

In this thesis, discontinuity factors that are calculated using information from a known reference heterogeneous solution are called reference discontinuity factors (RDF's). Homogenized cross sections and diffusion coefficients calculated from equations 2.24 and 2.29 using known reference heterogeneous information are called reference homogenized cross sections (RXS). When RDF's and RXS are used in a QUANDRY run, the resulting global homogeneous solution reproduces all the node-averaged quantities found from the reference heterogeneous solution.

One large difficulty remains. In general, the global heterogeneous solution is not known and is expensive to find. Furthermore, if it were known, one would have no incentive to perform a global homogeneous calculation. Thus, to make nodal equivalence theory practical, a method from which discontinuity factors and homogenized cross sections can be calculated without reference to an expensive global heterogeneous solution is desired. Such a method is described in the next section of this chapter.

2.4 HOMOGENIZED CROSS SECTIONS AND DISCONTINUITY FACTORS BASED ON HETEROGENEOUS ASSEMBLY CALCULATIONS

2.4.1 Introduction

To make the theory presented in the last section useful for practical cases, it is necessary to find a method of calculating equivalent diffusion theory parameters without prior knowledge of the global heterogeneous flux, $\phi_g^{het}(x,y,z)$. The cell calculation method of Smith [27, Chapter 3] is used in this thesis. The basis of the cell calculation method is the use of heterogeneous "cell calculations" to derive a heterogeneous cell flux which substitutes for the reference heterogeneous flux. All of Smith's applications are for BWR's where a "cell" is usually defined as an eight-by-eight bundle of fuel rods. In this section, the cell calculation method is described as it applys to PWR analysis. Here a "cell" becomes a PWR assembly. Further use of the term "cell" in this connection will be discontinued to avoid confusion with the homogenized pin-cells described in Chapter 1 of this thesis. Instead, Smith's technique will here be called the assembly calculation method.

2.4.2 The Heterogeneous Assembly Flux

At the beginning of life (B.O.L.) most PWR cores contain a large number (roughly 200) of fuel assemblies. However, in terms of physical dimensions and compositions, many of these assemblies are identical. Thus, there is only a small number (usually less than 7) of unique types of assemblies. For each unique assembly type, a relatively inexpensive heterogeneous assembly eigenvalue calculation with zero-net-current boundary conditions yields a heterogeneous assembly flux, $A_g^{het}(x,y,z)$. In the assembly calculation method, this heterogeneous assembly flux replaces the reference global heterogeneous flux, $\phi_g^{het}(x,y,z)$, in the last section.

2.4.3 Assembly Homogenized Cross Sections and Diffusion Coefficients

Since the heterogeneous cross sections and diffusion coefficients for each assembly type are known, equations 2.23 and 2.24 are used to calculate assembly homogenized cross sections and equation 2.29 is used to calculate assembly homogenized diffusion coefficients. In these calculations, the weighting flux is the heterogeneous assembly flux, $A_g^{het}(x,y,z)$. Such assembly homogenized cross sections and diffusion coefficients are called AXS. Spatial homogenization of heterogeneous cross sections and diffusion coefficients via AXS methods is common practice in the nuclear industry.

2.4.4 Assembly Discontinuity Factors

Equations 2.35 and 2.36 are used to calculate discontinuity factors based on assembly calculations. However, heterogeneous and homogeneous assembly fluxes are again substituted for global heterogeneous and homogeneous fluxes. Thus the assembly discontinuity factors (ADF's) are

$$ADF^{u+}_{g_{\ell,m,n}} = \frac{A^{u,het}_{g_{\ell,m,n}}(u_{\ell+1})}{A^{u,hom}_{g_{\ell,m,n}}(u_{\ell+1})} \qquad (2.38)$$

and

$$ADF^{u-}_{g_{\ell,m,n}} = \frac{A^{u,het}_{g_{\ell,m,n}}(u_{\ell})}{A^{u,hom}_{g_{\ell,m,n}}(u_{\ell})} \qquad (2.39)$$

The numerators of equations 2.38 and 2.39 are found immediately by calculating the surface average of the

heterogeneous assembly flux which is

$$A^{u,het}_{g_{\ell,m,n}}(u_\ell) = \frac{1}{h^v_m h^w_n} \int_{v_m}^{v_{m+1}} dv \int_{w_n}^{w_{n+1}} dw \; A^{het}_{g_{\ell,m,n}}(u_\ell, v, w)$$

$$g = 1, 2, \ldots G. \qquad (2.40)$$

The denominators of equations 2.38 and 2.39 are easily calculated from equations 2.16 and 2.18 as applied to a homogeneous assembly calculation with zero-net-current boundary conditions. The homogeneous flux from such a calculation is spatially flat and thus

$$A^{u,hom}_{g_{\ell,m,n}}(u_\ell) = A^{u,hom}_{g_{\ell,m,n}}(u_{\ell+1}) = \bar{\bar{A}}^{hom}_{g_{\ell,m,n}} = \bar{\bar{A}}^{het}_{g_{\ell,m,n}} \qquad (2.41)$$

where $\bar{\bar{A}}^{hom}_{g_{\ell,m,n}}$ and $\bar{\bar{A}}^{het}_{g_{\ell,m,n}}$ are the assembly-volume averages of the homogeneous and heterogeneous assembly fluxes respectively. Thus, when assembly calculations are based on zero-net-current boundary conditions, the assembly discontinuity factors can also be expressed as

$$ADF^{u+}_{g_{\ell,m,n}} = \frac{A^{u,het}_{g_{\ell,m,n}}(u_{\ell+1})}{A^{het}_{g_{\ell,m,n}}} \qquad (2.42)$$

and

$$ADF^{u-}_{g_{\ell,m,n}} = \frac{A^{u,het}_{g_{\ell,m,n}}(u_{\ell})}{A^{het}_{g_{\ell,m,n}}} . \qquad (2.43)$$

2.4.5 Heterogeneous Extended Assembly Calculations

Realistic PWR cores are surrounded by a steel baffle and a light water reflector. The small core in Figure 2.3 is an example which contains 16 total nodes. Eight of the nodes are regular fueled assemblies and the others are baffle/reflector nodes. Such baffle/reflector nodes present a homogenization difficulty since an assembly eigenvalue calculation is undefined. This is because

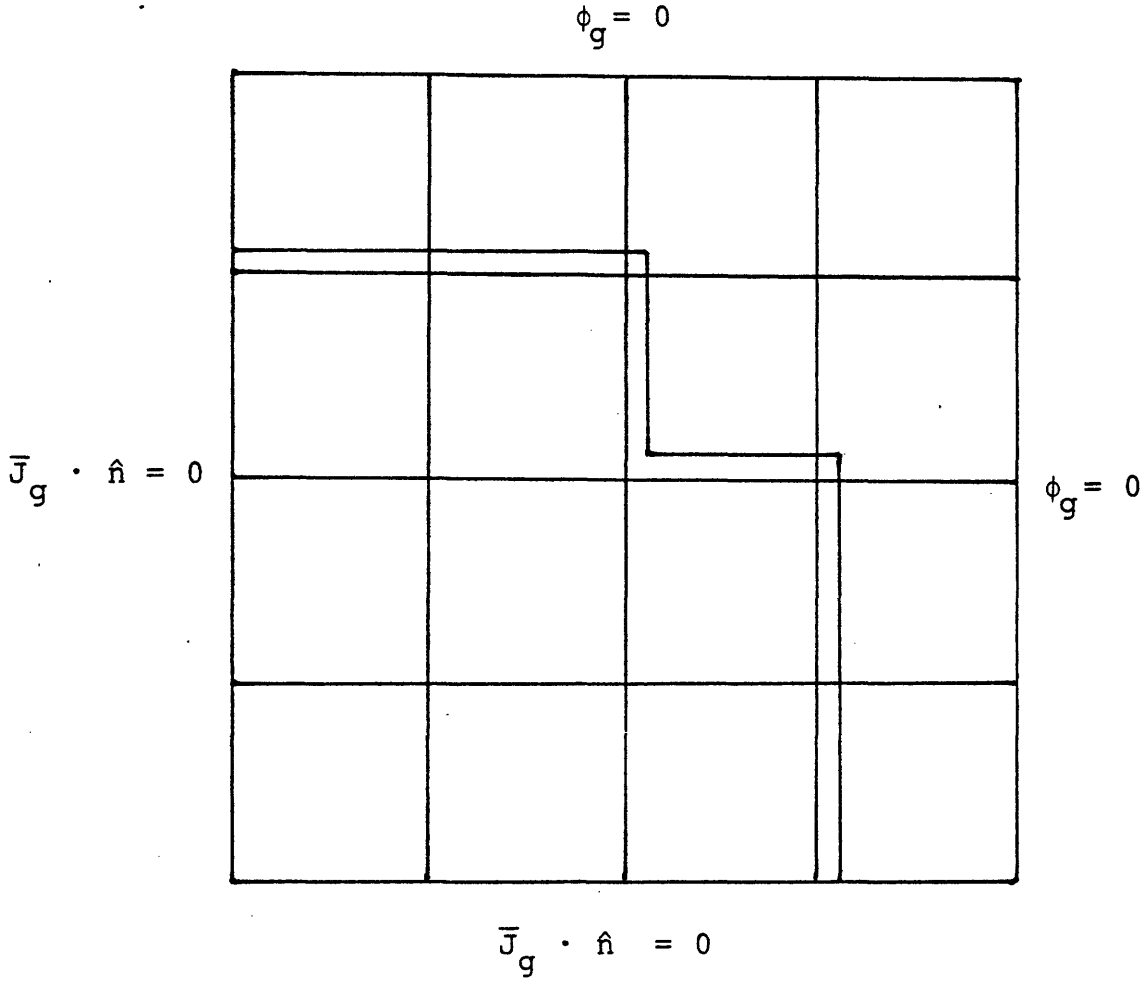

Figure 2.3: A Small PWR Core With an Explicitly Represented Steel Baffle

the fission cross section of water and steel is zero. In this thesis, this problem is circumvented by simply including one or more of the core fueled assemblies in a heterogeneous extended assembly calculation and abandoning the $\bar{J}_g \cdot \hat{n} = 0$ boundary condition for certain surfaces. The extended assembly problems and boundary conditions required for the small core in Figure 2.3 are shown in Figure 2.4.

Once the eigenvalue problems for the heterogeneous extended assembly calculations are complete, then $A_g^{het}(x,y,z)$ is again known and it can be substituted for $\phi_g^{het}(x,y,z)$. Thus assembly homogenized cross sections and diffusion coefficients can be calculated for each of the assemblies in the extended assembly calculation as described in section 2.4.3.

Assembly discontinuity factors are calculated as described in section 2.4.4. Note, however, that equations 2.42 and 2.43 cannot be used since the zero-net-current boundary conditions do not exist at the faces of each of the individual assemblies in an extended assembly calculation. Instead, equations 2.38 and 2.39 must be used. The homogeneous surface assembly fluxes in the denominator of equations 2.38 and 2.39 must be calculated by using the QUANDRY equations 2.16 and 2.18 for the homogeneous surface fluxes.

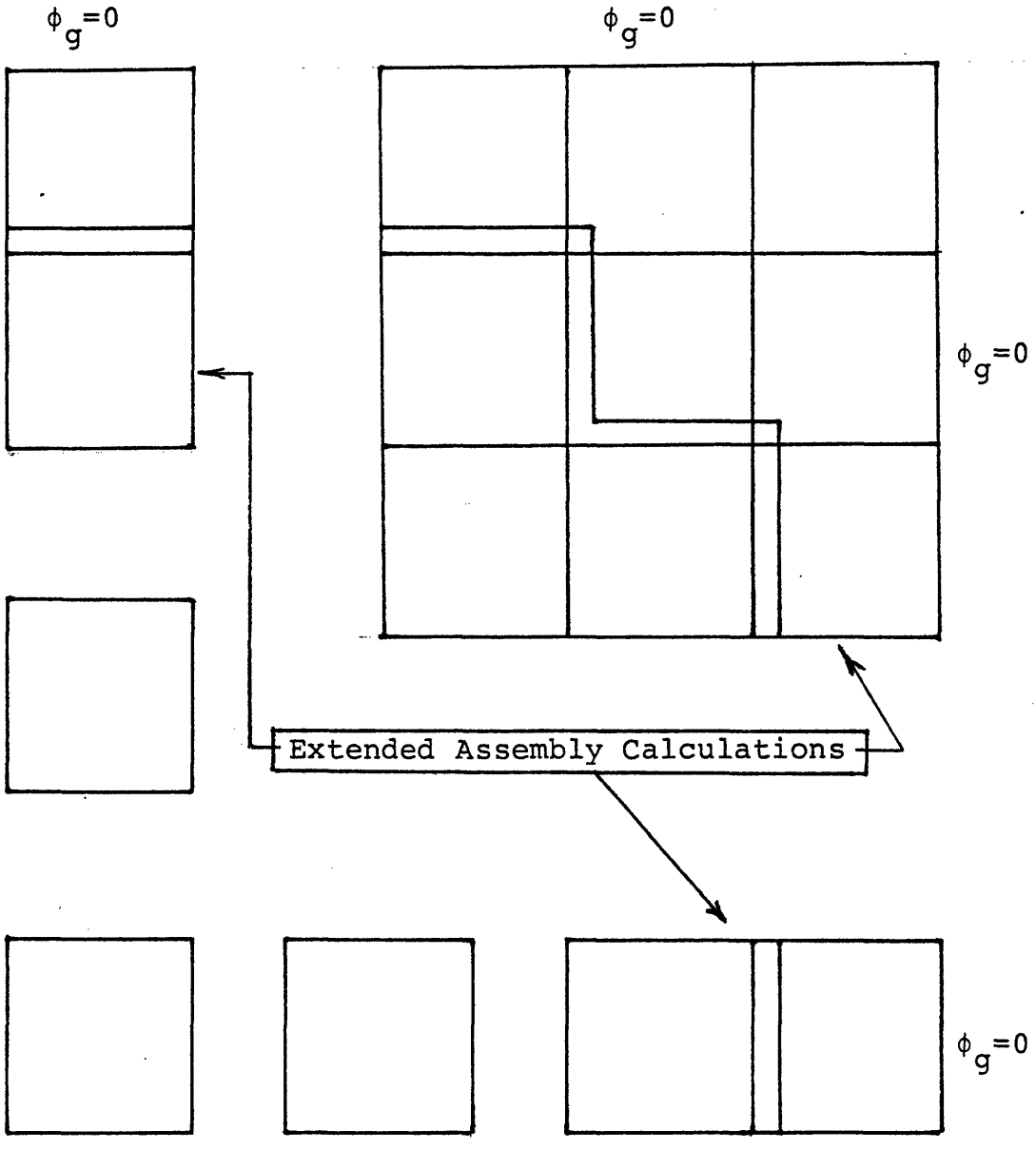

All surfaces have $\bar{J}_g \cdot \hat{n} = 0$ boundary conditions unless otherwise noted.

Figure 2.4: Extended Assembly Calculations for the Small PWR Core in Figure 2.3

Figure 2.4 shows that to analyze the small PWR core in Figure 2.3, two types of extended assembly configurations are used. The first configuration contains 2 nodes. One node is a fueled PWR assembly and the other is a baffle/reflector node. Such a configuration could be used all along the smooth edge of a PWR core. The second extended assembly configuration contains 9 nodes. Three of them are fueled assemblies and the others are baffle/reflector nodes. This configuration was chosen so that the jagged baffle at the edge of the PWR core would be modeled accurately within the extended assembly calculation.

For the small 4 by 4 node problem in Figure 2.3, running the large 3 by 3 node extended assembly problem costs a significant fraction of what it costs to run the global heterogeneous 4 by 4 problem. However, realistic, two-dimensional PWR quarter-cores contain up to 64 assemblies. For such a realistic case, the cost of a few extended assembly calculations containing 9 nodes would be a small fraction of the cost of running the heterogeneous global quarter-core problem.

2.4.6 Unity Discontinuity Factors

The interface, homogeneous, surface-averaged fluxes in QUANDRY can be made continuous through the use of unity discontinuity factors (UDF's). The use of UDF's and assembly homogenized cross sections (AXS) is identical to the common nuclear industry practice of using ordinary flux-weighted cross sections. The chief virtue of UDF's is that finding them does not require additional calculations. The main disadvantage of using UDF's is that two degrees of freedom per direction per group are lost from the QUANDRY equations. Thus the homogeneous problem can no longer rigorously match all node-averaged quantities from the heterogeneous problem. In this thesis, both UDF/AXS and ADF/AXS results will be presented for several PWR benchmark problems so that these two methods of spatial homogenization may be compared and contrasted.

2.5 SUMMARY

This chapter has presented a review of the analytic nodal method and nodal equivalence theory as implemented in the nodal code QUANDRY. Approximate methods, based on heterogeneous assembly eigenvalue calculations, were presented for finding homogenized parameters. Smith [27] developed and applied these methods to the analysis of BWR's. In the next chapter of this thesis, several PWR benchmark problems will be presented and analyzed.

Chapter 3

APPLICATION OF NODAL EQUIVALENCE THEORY TO PWR BENCHMARK PROBLEMS

3.1 INTRODUCTION

In this chapter, the nodal equivalence theory reviewed in Chapter 2 is applied to the neutronic analysis of several two-dimensional PWR benchmark problems. These benchmark problems are described in section 2 of this chapter. The calculation of the nodal equivalence theory parameters is discussed in section 3. The results of using these parameters in QUANDRY runs are presented in section 4. Section 5 provides conclusions and a summary of this chapter.

For discussion of benchmark problems, the following arbitrary node number system is employed. The nodes are numbered (starting with the upper, left-hand corner node) from left to right along rows. Counting proceeds from the top row to the bottom row. Thus, for a 3-by-3 node problem the node numbering would be as illustrated in Figure 3.1.

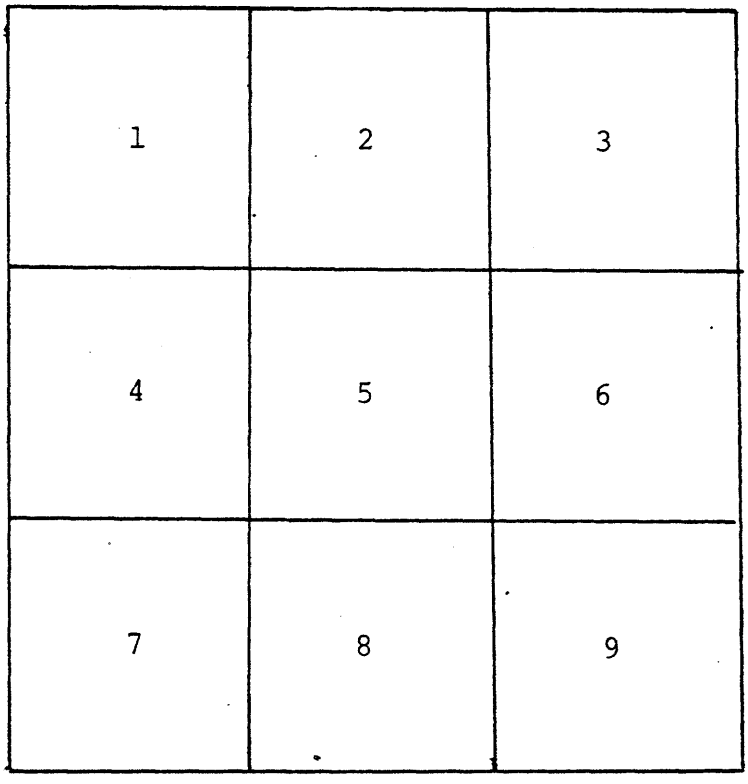

Figure 3.1: Node Numbering for a 3-by-3 Node Problem

3.2 DESCRIPTION OF PWR BENCHMARK PROBLEMS

The heterogeneous PWR benchmark problems for this thesis were constructed using information from Appendix 1. Included are heterogeneous cross section sets and descriptions of fueled PWR assemblies and non-fueled baffle/reflector nodes. The descriptions include the physical diminsions of the assemblies and the location and composition of heterogeneities within the assemblies.

Eight small PWR problems are presented in Appendix 2. Benchmark problems 7 and 8 will only be employed in later chapters on heterogeneous pointwise flux reconstruction. This leaves benchmark problems 1 through 6 which are analyzed in this chapter.

3.3 CALCULATION OF EQUIVALENCE PARAMETERS

Two-dimensional, reference solutions in this chapter are fine-mesh, two-group diffusion theory calculations from QUANDRY. Each QUANDRY node in the reference solution is a 1.4 cm-by-1.4 cm homogenized pin-cell. Such a fine-mesh calculation yields $\phi_g^{het}(x,y)$ which is used to generate reference homogenized cross sections (RXS) and reference discontinuity factors (RDFs) employing the nodal equivalence theory in Chapter 2. The RDF/RXS are then applied

in a global, homogeneous, coarse-mesh (one PWR assembly per node) QUANDRY run. This run yields reference node-integrated quantities against which the corresponding quantities from approximate solutions may be compared. These node-integrated quantities are usually nodal power densities, surface-averaged currents and fluxes, and volume-averaged fluxes.

The approximate solutions in this chapter come from coarse-mesh QUANDRY calculations. The solutions are "approximate" because the equivalence parameters used are not RDF/RXS. Instead, they are generated from heterogeneous assembly calculations as explained in section 4 of Chapter 2. The equivalence theory parameters used in the approximate solutions will include assembly discontinuity factors and assembly homogenized cross sections (ADF/AXS). The ADF/AXS for each PWR assembly type considered in this thesis are presented in Appendix 3. Approximate solutions based on unity discontinuity factors and assembly homogenized cross sections (UDF/AXS) will also be included. The UDF/AXS results are equivalent to results from conventional solution techniques employing standard flux-weighted cross sections.

For benchmark problems 1 through 4 results will also be presented in which RXS (reference homogenized cross sections) are used with ADFs and UDFs. The errors in results using ADF/RXS or UDF/RXS are due solely to the use of inaccurate discontinuity factors. This is in contrast to the ADF/AXS and UDF/AXS results where errors are due to inaccurate discontinuity factors and homogenized cross sections. Thus, by comparing ADF/AXS and ADF/RXS results or by comparing UDF/AXS and UDF/RXS results one sees roughly how much of the error is due to cross sections and how much is due to discontinuity factors.

To summarize: For a given benchmark problem, five coarse-mesh QUANDRY runs are performed. In terms of the input nodal equivalence theory parameters, the five runs may be described as follows:

1. RDF/RXS
2. ADF/AXS
3. UDF/AXS
4. ADF/RXS
5. UDF/RXS.

The RDF/RXS solution serves as a reference against which the other four solutions are compared.

3.4 RESULTS FOR SIX PWR BENCHMARK PROBLEMS

The results for k_{eff} and normalized assembly power densities for benchmark problems 1 through 6 are presented in Appendix 4. These results will now be discussed.

3.4.1 Benchmark Problem 1 Results

Benchmark problem 1 is a 3-by-3, symmetric checkerboard of unrodded PWR assemblies containing fuel types 1 and 2. Figure A4.1 in Appendix 4 presents the results for this problem. The percent errors in k_{eff} and normalized assembly power densities are small. This is true regardless of which of the four combinations of equivalence parameters (ADF/AXS, UDF/AXS, ADF/RXS, UDF/RXS) are used. The maximum percent error in normalized assembly power density using any of the four sets of equivalence theory parameters is only -0.37% and the percent error in eigenvalue is only 0.016%. The results for this benchmark problem appear to provide no incentive to use ADF/AXS instead of the conventional UDF/AXS.

There is evidence that both ADF/AXS and UDF/AXS benefit from cancellation of errors caused by using both approximate discontinuity factors and approximate cross sections. In

both cases using better cross section information (RXS instead of AXS) led to a small increase in the percent errors in k_{eff} and power density.

3.4.2. Benchmark Problem 2 Results

Benchmark problem 2 was formulated to test the effect of the presence of control rods in a PWR core. Thus it is identical to benchmark problem 1 except that control rods replace the water holes in the fresh fuel-1 assemblies in nodes 2, 4, 6 and 8. The addition of control rods does increase percent errors; however, they are still small regardless of the nodal equivalence parameters used. For example, the maximum percent error in normalized assembly power densities using ADF/AXS is only -1.49% and the percent error in eigenvalue is only -0.16%.

In this problem, the ADF/AXS run does marginally better than the UDF/AXS run in k_{eff} (-0.16% vs. -0.37%) and in maximum percent error in normalized assembly power densities (-1.49% vs. -1.60%). However, the UDF/AXS run has a slightly lower average percent error in nodal power (1.04% vs. 1.18%). On the whole, these results are again so close that there appears to be no incentive to use ADF/AXS instead of UDF/AXS.

The UDF/AXS result again appears to benefit from some cancellation of errors since when better cross sections are used in the UDF/RXS run the percent error (both average and maximum) in nodal power densities again increases. However, the global eigenvalue prediction is helped by the use of RXS instead of AXS. When ADFs are used, better cross section information reduces errors for this rodded benchmark problem.

This pattern for rodded benchmark problems is repeated in the next two benchmark problems. When UDFs are used, the introduction of RXS instead of AXS increases errors in nodal power densities. Conversely, when ADFs are used for a rodded benchmark problem, the introduction of RXS instead of AXS decreases errors in nodal power densities.

3.4.3 Benchmark Problem 3 Results

Benchmark problem 3 is identical to benchmark problem 2 except that albedo boundary conditions are added to two sides to cause a non-symmetric tilt in the global power distribution. Note that fuel 1 is still rodded. The effect of the tilt in power distribution is a further increase in maximum percent error in nodal power densities. For example, the ADF/AXS run exhibits a maximum percent error of 2.40 % and an average percent error of 1.80 %

in nodal power densities. The corresponding numbers for the symmetric benchmark problem 2 are -1.49% and 1.18%. However, the error in k_{eff} decreased from -0.16% for benchmark problem 2 to -0.09% for benchmark problem 3 when using ADF/AXS.

The UDF/AXS results are slightly better than the ADF/AXS results in power distribution but the ADF/AXS results yield smaller percent errors in eigenvalue. Again there appears to be little incentive to use ADF/AXS instead of UDF/AXS.

3.4.4 Benchmark Problem 4 Results

Benchmark problem 4 is designed to be an extreme test of QUANDRY and nodal equivalence theory as it applies to PWRs. Thus, nodes 1, 2, 5 and 8 are rodded. The third node contains water; this simulates reflector effects and causes a severe thermal flux peak in the nodes adjacent to node 3. The boundary conditions on two sides are $\phi_g = 2\ \bar{J}_g \cdot n$; this causes a severe global flux tilt. However, even for this extreme case, the maximum percent error in normalized assembly power densities is only -3.05% for ADF/AXS and 1.57% for UDF/AXS.

3.4.5 Benchmark Problem 5 Results

Benchmark problem 5 is an infinite checkerboard of two types of PWR fuel assemblies. It is designed to simulate assemblies in the center of a large, 3-batch PWR in which the fresh fuel batch is loaded on the periphery of the core and the once- and twice-burned batches are scattered in a checkerboard pattern in the interior of the PWR. Since PWRs usually operate at full power with all rods out, the assemblies in this problem were left unrodded.

Since the problem contains no rodded assemblies and no severe global flux tilts, the percent errors in Figure A4.5 are extremely small. There is almost no difference in the ADF/AXS and UDF/AXS results; they are both almost perfect. For example, the maximum percent error in the normalized assembly power densities is only -0.10% using ADF/AXS and -0.08% using UDF/AXS.

3.4.6 Benchmark Problem 6 Results

Benchmark problem 6 is a small quarter-core reactor. It contains an explicitly represented steel baffle and a light water reflector. Fresh fuel assemblies are loaded next to the baffle and once-burned assemblies are loaded in the center of the reactor.

For this benchmark problem, extended assemblies were used to generate the nodal equivalence parameters. Those parameters are presented in Appendix 3. For this problem, the ADF/AXS results are far superior to the UDF/AXS results. For example, the maximum percent error in normalized assembly power densities is only -0.16% using ADF/AXS. This is compared to an error of 5.37% when using UDF/AXS. The reason for this is the steel baffle. As an examination of Appendix 3 reveals, the discontinuity factors change from 0.9 to 0.3 across the core-baffle interface. Clearly, using unity discontinuity factors on both sides of this interface is a poor approximation.

The conventional UDF/AXS approach could be used more successfully on this problem if the steel baffle and reflector were replaced by an albedo boundary condition at the edge of the core. This approach is commonly employed in the nuclear industry [11]. The albedo boundary conditions are calculated from a fine-mesh diffusion theory calculation at B.O.L. or by experimental or approximate analytic techniques.

The reason for the success of the ADF/AXS approach on this problem is found in the relatively large amount

of calculational effort that was employed in doing the extended assembly problems. The 3-by-3 node extended assembly calculation is more expensive than assembly calculations involving a single node; however, accurate homogenized parameters (including discontinuity factors) are calculated when extended assembly calculations are used.

3.5 SUMMARY AND CONCLUSIONS

Smith [27] was able to show that for several BWR problems, the use of the conventional UDF/AXS approach to spatial homogenization led to large (>10%) errors in normalized power distributions. By the simple introduction of ADF/AXS he was able to reduce the maximum error in BWR power distributions to about 3.0%. This consistent reduction of error has not held up for PWRs.

The reason for the lack of reduction in error is not due to a failure of the ADF/AXS approach to analyze PWR cores accurately. Indeed, for the six benchmark problems just presented, the maximum percent error in normalized power distributions was only -3.05% and this occurred in the extremely difficult (and probably unrealistic) benchmark

problem 4. For unrodded PWRs an error of more than 0.5% in normalized power distributions has not been observed. Thus, the reason for the lack of reduction in error is that the conventional UDF/AXS approach appears to work equally well compared to the ADF/AXS approach on problems without an explicit baffle. Furthermore, UDF/AXS could be used in benchmark problem 6 if the baffle were replaced by an albedo condition.

Comparison of the ADF/AXS and UDF/AXS results for the unrodded benchmark problems 1 and 5 leads to the conclusion that in terms of normalized power distributions it makes little difference whether ADFs or UDFs are used in unrodded problems. This is true even though the values of the group 2 ADFs in Appendix 3 are 0.9284 for assemblies containing fuel 1 and 0.9380 for assemblies containing fuel 2 and are thus roughly 7% different from unity. The reason for this apparent insensitivity of the normalized power distributions to the values of the individual discontinuity factors is now explored.

Discontinuity factors on either side of the nodal interface u_ℓ are implemented in the QUANDRY code through equation 2.37 which is rewritten here as

$$\frac{f^{u+}_{g_{\ell-1,m,n}}}{f^{u-}_{g_{\ell,m,n}}} \quad \phi^{u,hom}_{g_{\ell-1,m,n}}(u_\ell) = \phi^{u,hom}_{g_{\ell,m,n}}(u_\ell). \qquad (3.1)$$

This statement of continuity of the heterogeneous surface flux provides the necessary relationship in QUANDRY between the homogeneous surface fluxes. One of the factors affecting the normalized power densities calculated by QUANDRY is the size of the discontinuity in the homogeneous surface fluxes. As equation 3.1 shows, it is the ratio of the discontinuity factors at an interface u_ℓ which determines the size of the discontinuity in the homogeneous surface fluxes, not the individual values of the discontinuity factors themselves.

For the unrodded benchmark problems 1 and 5, the ratio of the discontinuity factors using UDFs is

$$\frac{f^{u+}_{g_{\ell-1,m,n}}}{f^{u-}_{g_{\ell,m,n}}} = \frac{1.0}{1.0} = 1.0. \qquad (3.2)$$

The ratio of the discontinuity factors when ADFs are used is for g = 1

$$f_{1_{\ell-1,m,n}}^{u+} \Big/ f_{1_{\ell,m,n}}^{u-} = \frac{1.003}{1.003} = 1.0. \qquad (3.3)$$

The ratio of the discontinuity factors for two adjacent fuel 1 assemblies when ADFs are used and g = 2 is

$$f_{2_{\ell-1,m,n}}^{u+} \Big/ f_{2_{\ell,m,n}}^{u-} = \frac{0.9284}{0.9284} = 1.0. \qquad (3.4)$$

The ratio of the discontinuity factors for two adjacent fuel 2 assemblies when ADFs are used and g = 2 is

$$f_{2_{\ell-1,m,n}}^{u+} \Big/ f_{2_{\ell,m,n}}^{u-} = \frac{0.9380}{0.9380} = 1.0. \qquad (3.5)$$

The ratio of the discontinuity factors for a fuel 1 assembly to the left of the nodal interface u_ℓ and a fuel 2 assembly to the right when ADFs are used and g = 2 is

$$f_{2_{\ell-1,m,n}}^{u+} \Big/ f_{2_{\ell,m,n}}^{u-} = \frac{0.9284}{0.9380} = 0.9898. \qquad (3.6)$$

The ratio of the discontinuity factors for a fuel 2 assembly to the left of the nodal interface u_ℓ and a fuel 1 assembly to the right when ADFs are used and g = 2 is

$$f_{2_{\ell-1,m,n}}^{u+} \Big/ f_{2_{\ell,m,n}}^{u-} = \frac{0.9380}{0.9284} = 1.010. \qquad (3.7)$$

Thus, when UDFs are used, the ratio of the discontinuity factors at all nodal interfaces is 1.0. Similarly, for unrodded PWR problems made up of fuel 1 and fuel 2 heterogeneous assemblies, the ratio of the ADFs at a nodal interface is always close to 1.0. This is why the ADF/AXS results for benchmark problems 1 and 5 are so close to the UDF/AXS results.

The situation for the rodded benchmark problems is clearly different. For example, consider the adjacent assemblies 4 and 5 of benchmark problem 2. Assembly 4 is rodded and assembly 5 is not. The ratio of the thermal ADFs at the interface between assemblies 4 and 5 is 1.121/0.9380 = 1.195 which is far from unity. At such an interface, the homogeneous surface flux in QUANDRY would have a large discontinuity and this would certainly be expected to affect the normalized power distribution. However, as scrutiny of the benchmark problem 2 results reveals, the ADFs tend to overcorrect for the errors made in the UDF/AXS run. Thus the UDF/AXS percent errors in the normalized power densities in benchmark problem 2 are roughly of the same magnitude in each node as the ADF/AXS percent errors; however, they are of different sign.

So far, the UDF/AXS scheme has been compared to the ADF/AXS scheme through the use of normalized assembly power densities and k_{eff}. If these are the only quantities of interest, then UDFs work as well as ADFs. However, there are other node-averaged quantities that may be used in a comparison between ADFs and UDFs. These other quantities, as calculated for the infinite checkerboard of two fuel assembly types (benchmark problem 5), are now used to compare the ADF/AXS approach to the UDF/AXS approach.

Consider the maximum percent error in the volume-averaged fluxes in benchmark problem 5: ADF/AXS yields +0.20% and UDF/AXS yields +0.097%. Try the maximum percent error in the surface-averaged currents: ADF/AXS yields +3.76% and UDF/AXS yields +2.54%. Comparisons like these for the other benchmark problems show little incentive to use ADFs instead of UDFs. The values are usually quite close with ADFs doing slightly better on some problems and UDFs doing slightly better on others.

However, there is one node-averaged quantity that the ADF/AXS scheme consistently predicts more accurately than the UDF/AXS scheme. That quantity is the heterogeneous surface-averaged thermal flux. Again referring to benchmark problem 5, the maximum percent error in the heterogeneous surface-averaged thermal fluxes using ADF/AXS is-0.243%; UDF/AXS yields 7.24% error.

The fact that the UDF/AXS value of the heterogeneous surface-averaged thermal flux is about 7% in error is directly related to individual values of the thermal ADFs for unrodded PWR assemblies being about 7% different from unity. To illustrate this, the situation for benchmark problem 5 at a nodal interface u_ℓ, with fuel 2 on the left and fuel 1 on the right is sketched in Figure 3.2.

Figure 3.2 is cut in half vertically by the nodal interface u_ℓ. To the left of the interface lies node $(\ell-1,m,n)$; to the right lies node (ℓ,m,n). Only the few centimeters of the nodes near u_ℓ are depicted.

The top half of Figure 3.2 shows two sketches of one-dimensional, surface-averaged thermal fluxes. The top one of these is the homogeneous surface-averaged thermal flux found from the ADF/AXS scheme. Note the discontinuity in the flux at u_ℓ. The bottom flux in the top half of Figure 3.2 is the reference heterogeneous surface-averaged thermal flux. Note the thermal flux peaking due to water holes in the assembly. (This is not drawn to scale.)

The bottom half of Figure 3.2 shows two more sketches of one-dimensional, surface-averaged thermal fluxes. The top one of these is the homogeneous surface-averaged thermal flux found from the UDF/AXS scheme. Note that since the

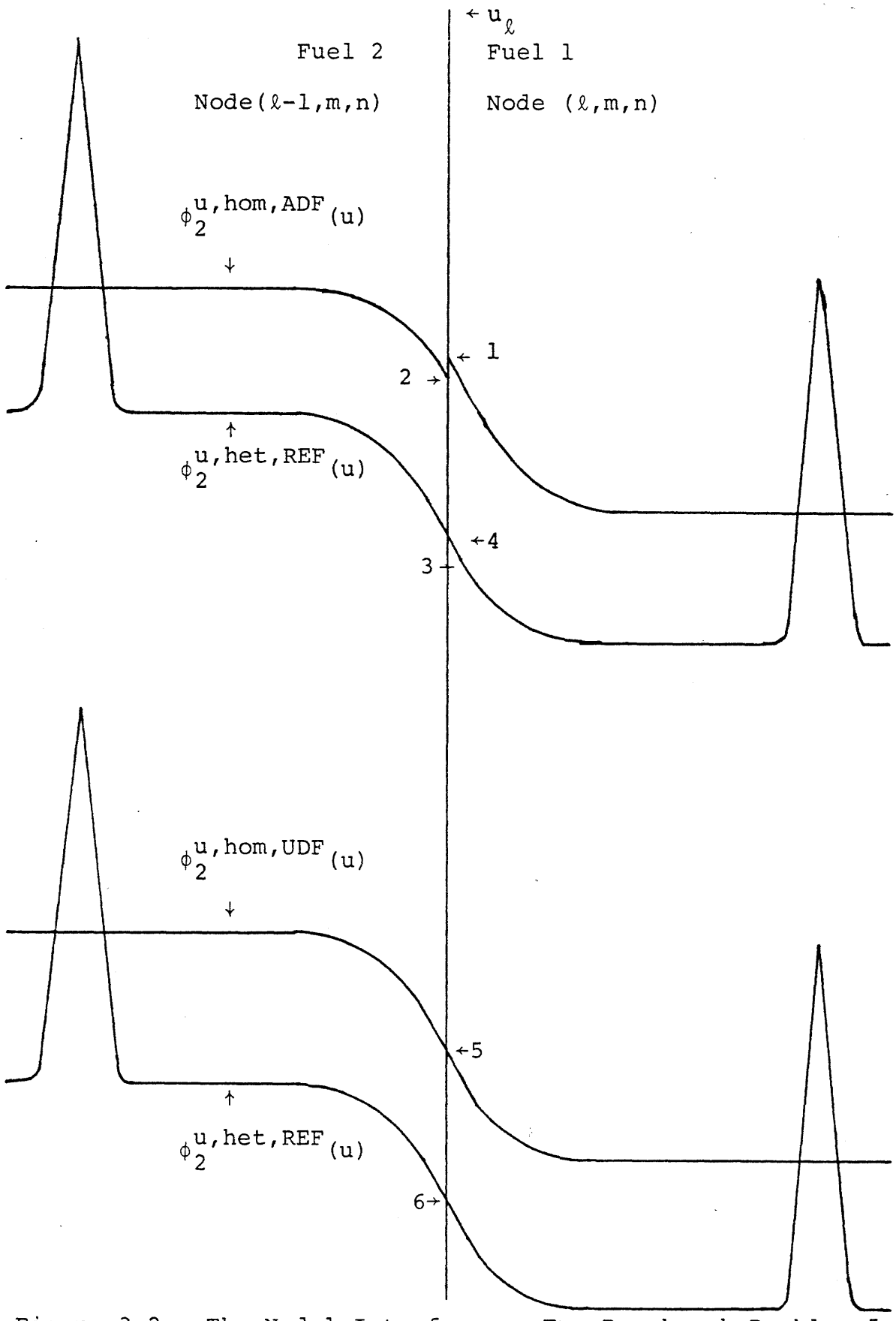

Figure 3.2: The Nodal Interface u_ℓ For Benchmark Problem 5

UDFs are 1.0, this flux is continuous at u_ℓ . The bottom flux in the bottom half of Figure 3.2 is (again) the reference heterogeneous surface-averaged thermal flux.

The reason that both the ADF and UDF homogeneous surface fluxes in Figure 3.2 lie above the smooth part of the reference heterogeneous surface flux is that these shapes should all have about the same volume integral. (In fact, if RDF/RXS were being used, equation 2.26 shows that the heterogeneous and homogeneous volume-averaged fluxes are identical.)

The six labeled points on the interface u_ℓ represent the following surface fluxes:

1. $\phi_{2_{\ell,m,n}}^{u,hom,ADF}(u_\ell)$

2. $\phi_{2_{\ell-1,m,n}}^{u,hom,ADF}(u_\ell)$

3. $\phi_{2_{\ell-1,m,n}}^{u,het,ADF}(u_\ell) = \phi_{2_{\ell,m,n}}^{u,het,ADF}(u_\ell)$

4. $\phi_{2_{\ell-1,m,n}}^{u,het,REF}(u_\ell) = \phi_{2_{\ell,m,n}}^{u,het,REF}(u_\ell)$

5. $\phi_{2_{\ell-1,m,n}}^{u,hom,UDF}(u_\ell) = \phi_{2_{\ell,m,n}}^{u,hom,UDF}(u_\ell) =$

   $\phi_{2_{\ell-1,m,n}}^{u,het,UDF}(u_\ell) = \phi_{2_{\ell,m,n}}^{u,het,UDF}(u_\ell)$

6. $\phi_{2_{\ell-1,m,n}}^{u,het,REF}(u_\ell) = \phi_{2_{\ell,m,n}}^{u,het,REF}(u_\ell)$.

Note that the ADF/AXS and UDF/AXS homogeneous flux shapes are quite similar in Figure 3.2. The only difference is the small discontinuity in the homogeneous ADF surface thermal fluxes at points 1 and 2. As has already been explained, the magnitude of this discontinuity is indicated by the ratio of the discontinuity factors at u_ℓ. As equation 3.7 shows, this ratio is close to 1.0 for this case and thus the ADF/AXS calculation of normalized power distribution is not much different than the UDF/AXS calculation.

However, Figure 3.2 shows that the individual values of the discontinuity factors (not just their ratio) are important if the heterogeneous surface fluxes are to be calculated. For the ADF case in the top half of Figure 3.2, the reference heterogeneous surface flux is at point 4. Because of the ADFs, a good approximation of this flux (-0.243% error) is found at point 3 by making either one of the following calculations involving the individual discontinuity factors:

$$\phi_{2\,\ell-1,m,n}^{u,het,ADF}(u_\ell) = \phi_{2\,\ell,m,n}^{u,het,ADF}(u_\ell) = f_{2\,\ell-1,m,n}^{u+}\,\phi_{2\,\ell-1,m,n}^{u,hom,ADF}(u_\ell)$$

$$\text{or} \quad = f_{2\,\ell,m,n}^{u-}\,\phi_{2\,\ell,m,n}^{u,hom,ADF}(u_\ell). \qquad (3.8)$$

Unfortunately, for the UDF/AXS in the bottom half of Figure 3.2, the effect of setting the individual discontinuity factors to 1.0 is that the reference heterogeneous surface flux at point 6 is not accurately calculated. Instead, when UDFs are used, the poor approximation of this flux (7.24% error) at point 5 is found from

$$\phi_{2\,\ell-1,m,n}^{u,het,UDF}(u_\ell) = \phi_{2\,\ell,m,n}^{u,het,UDF}(u_\ell) = \phi_{2\,\ell-1,m,n}^{u,hom,UDF}(u_\ell) = \phi_{2\,\ell,m,n}^{u,hom,UDF}(u_\ell) \qquad (3.9)$$

To conclude: The use of ADF/AXS instead of the conventional UDF/AXS spatial homogenization approach for PWR analysis yields no consistent improvement in the accuracy of computed normalized power distributions. However, the heterogeneous, surface-averaged thermal fluxes are determined more accurately. This latter point provides the motivation for using ADFs in the remainder of this thesis which deals with heterogeneous pointwise flux reconstruction from nodal calculations. The heterogeneous, surface-averaged fluxes are used (along with other information from the nodal calculation) in the determination of the boundary values of the pointwise flux reconstruction. Thus, the more accurate heterogeneous, surface-averaged fluxes associated with the use of ADFs may improve the accuracy of the reconstructed pointwise fluxes.

Chapter 4

INTERPOLATION OF THE HETEROGENEOUS FLUX AT ASSEMBLY CORNER POINTS

4.1 INTRODUCTION

The results of Chapter 3 show that the use of ADF/AXS equivalence parameters calculated from fine-mesh assembly calculations in a global homogeneous QUANDRY calculation (see Figure 1.3) yields good approximations of node-averaged quantities from a fine-mesh global heterogeneous problem (see Figure 1.2). Specifically, QUANDRY with ADFs yields accurate approximations of the following heterogeneous node-averaged quantities:

1. volume-averaged fluxes
2. surface-averaged fluxes
3. surface-averaged currents.

Unfortunately, QUANDRY yields absolutely no pointwise heterogeneous flux information. Such information is essential if QUANDRY is to be extended for use in PWR fuel management calculations where pin-by-pin depletions are performed and where it may be necessary to calculate the location of the hottest pin in a given assembly.

Methods of pointwise heterogeneous flux reconstruction from nodal calculations are the topic of Chapters 5 and 6 of this thesis. These methods require a knowledge of the

heterogeneous pointwise fluxes at the corners of an assembly. Thus, the topic of this chapter is how to interpolate heterogeneous corner point fluxes from the heterogeneous node-averaged fluxes and currents derived from a QUANDRY run using ADFs.

4.2 POINTWISE FLUX RECONSTRUCTION BENCHMARK PROBLEMS

Four benchmark problems are used in this study of corner point interpolation methods and pointwise flux reconstruction. The four are benchmark problems 5, 6, 7 and 8 described in Appendix 2. Benchmark problem 5 is the infinite checkerboard of two unrodded fuel assembly types. Benchmark problem 6 is the 4-by-4 quarter-core with all rods out and an explicit baffle. Benchmark problem 7 is a small 3-by-3 quarter-core. The center node 5 is an unrodded heterogeneous fuel 1 assembly. The other eight nodes are homogeneous and contain fuel 2. All flux reconstruction results for this benchmark are for the center node only. Benchmark problem 8 is designed to be an extreme test of the flux reconstruction methods. It contains rodded and unrodded assemblies and a severe flux tilt is caused by zero-flux boundary conditions on two sides. Node 3 in this problem contains water to simulate reflector effects.

4.3 REFERENCE POINTWISE FLUX CALCULATIONS

The reference heterogeneous calculations of the pointwise fluxes for benchmark problems 5, 6, 7 and 8 are from fine-mesh PDQ-7 calculations [2]. The convergence criterion for the eigenvalue is 10^{-6} and for the eigenvector (fluxes) it is 10^{-5}. A constant fine mesh of 0.7 cm (four mesh rectangles per pin-cell) is used on unrodded benchmark problems 5 and 7. For benchmark problems 6 and 8 which are rodded, a finer spatial mesh of 0.35 cm (16 mesh rectangles per pin-cell) is used. Unfortunately, any reference PDQ-7 calculation only yields an approximation of the true physical neutron flux in a reactor. This is because of several sources of error which will now be discussed.

The first source of error is due to the formulation of a mathematical model (i.e., the multidimensional, two-group diffusion equations) which fails to describe perfectly the physical problem. Thus, even if an analytic solution to the general multidimensional, two-group diffusion equations was known, the flux from that solution would not match the true physical flux due to defects in the model (for example, transport effects are not included). However, for PWR fuel management problems the multidimensional, two-group diffusion equations are accurate enough. Thus, this first source of error is deemed to be small and for the

purposes of this thesis, an exact analytic solution to the multidimensional, two-group diffusion equations could be used as a reference. Unfortunately, the diffusion equations represent a coupled set of variable coefficient differential equations for which no general multidimensional analytic solution is known.

Computers are just as helpless as humans when it comes to solving complicated sets of differential equations in a continuous spatial domain. However, the differential equations can be converted through the use of finite difference methods into a large set of coupled algebraic equations. PDQ-7 solves this set of algebraic equations to yield a solution at a finite number of discrete spatial points. This discretization process gives rise to a second source of error called spatial truncation error. The spatial truncation error in a PDQ-7 solution is a function of the spatial mesh. It is generally assumed that as the distance between mesh points shrinks to zero, the spatial truncation error vanishes. However, Hageman and Pfeifer [37] indicate that there is no rigorous mathematical verification of this assumption. Furthermore, estimating the amount of truncation error for a given problem is quite difficult. The general approach usually taken is to run problems in which truncation error may be large twice: the first run with a

standard mesh and the second run with a finer mesh. If the difference between the solutions is small, then the truncation error is assumed to be small. Again, this is an assumption; however, years of experience with the PDQ-7 code seem to indicate that it is a good assumption.

For the benchmark problems 5, 6 and 7, the spatial truncation error in the pointwise solutions is probably a maximum of $\pm$ 0.5% near areas where the spatial truncation error is expected to be large (i.e., near control rods, water holes, steel baffles, etc.) and only a few tenths of a percent in the middle of fueled regions away from heterogeneities. The error in the extremely difficult benchmark problem 8 is probably a few percent. The numerical calculations to justify these conclusions are contained in Appendix 5. For the purposes of this thesis, this accuracy is sufficient.

A third possible source of error is computer round-off error. It is due to computers using a finite number of significant digits to represent real numbers, some of which have an infinite number of significant digits. Ideally, reducing the mesh spacing in PDQ-7 should yield an improved answer since spatial truncation error is reduced with decreasing mesh spacing. Unfortunately, reduced mesh spacing tends to increase computer round-off error due to an increase in the number of arithmatic operations required

by the finer mesh problem. Also, in the finer mesh problem the fluxes are likely to differ less from point-to-point. Thus, many of the leading significant digits of the fluxes in the finite difference process cancel out, increasing the importance of the accuracy of the later digits in the fluxes. PDQ-7 is written in double precision for the IBM computer system. Thus, real floating-point operations are done with sixteen place accuracy. This fact, and the good agreement of the single precision, fine-mesh QUANDRY results with the PDQ-7 results in Appendix 5, leads to the conclusion that round-off error in the PDQ-7 benchmark calculations is very small.

The final source of error that will be discussed is called iteration error. Application of the finite difference methods in PDQ-7 to benchmark problem 6 leads to a system of algebraic equations involving 57,600 unknowns. Thus, an iterative solution strategy is employed to solve this large scale system of equations. Strictly speaking, these iterative methods require an infinite number of iterations to converge to an exact solution of the finite difference equations. Practically, the iteration is usually stopped when the first several digits of the solution fail to change from iteration to iteration. Thus, iteration

error is caused by halting the iteration process after a finite (instead of infinite) number of iterations. To reduce the iteration error in the benchmark solutions, the rather tight convergence criterion of 10^{-6} for eigenvalue and 10^{-5} for fluxes is used. The use of these values leads to solutions that are well converged iteratively. Thus, when compared to other sources of error in the benchmark problems, iteration error is probably negligible.

In summary, an exact solution to the multidimensional two-group diffusion equations is sufficient for many fuel management calculations. PDQ-7 provides a close approximation to such an exact solution. The main reason that the PDQ-7 reference solutions employed here are in error is due to spatial truncation error. Computer round-off error and iteration error are negligible. The total error in the reference benchmark problem 5, 6 and 7 solutions from PDQ-7 is probably less than $\pm$ 0.5%. This is sufficiently accurate for the purposes of this thesis since the approximations made in interpolating corner point fluxes and in reconstructing pointwise fluxes are expected to cause errors on the order of several percent.

4.4 INTERPOLATION METHOD 1 - CHIME

This section contains a discussion of a method of interpolating approximate heterogeneous fluxes at the corners of assemblies. The technique described here is a slight extension of the method suggested by Koebke and Wagner [31]. For brevity the interpolation technique described in this section is call CHIME. (Corner point Heterogeneous flux Interpolation MEthod). A computer code named CHIME has been written which automates the theory in this section.

To aid in the discussion of CHIME, start by placing four heterogeneous PWR assemblies together as shown in Figure 4.1. Note that an (x,y) coordinate system is placed at the central corner point where the four assemblies meet. The assemblies are assumed to be square and have dimensions h x h. The object is to use the flux and current information from an inexpensive QUANDRY calculation employing ADF/AXS equivalence parameters to find the interpolated heterogeneous flux at the central corner point (0,0).

In each of the four assemblies (n=1,2,3,4) it is assumed that the heterogeneous flux may be represented by the product of the assembly flux, $A_g^n(x,y)$, and an eight-term bi-quadratic form function $Q_g^n(x,y)$. The form of the

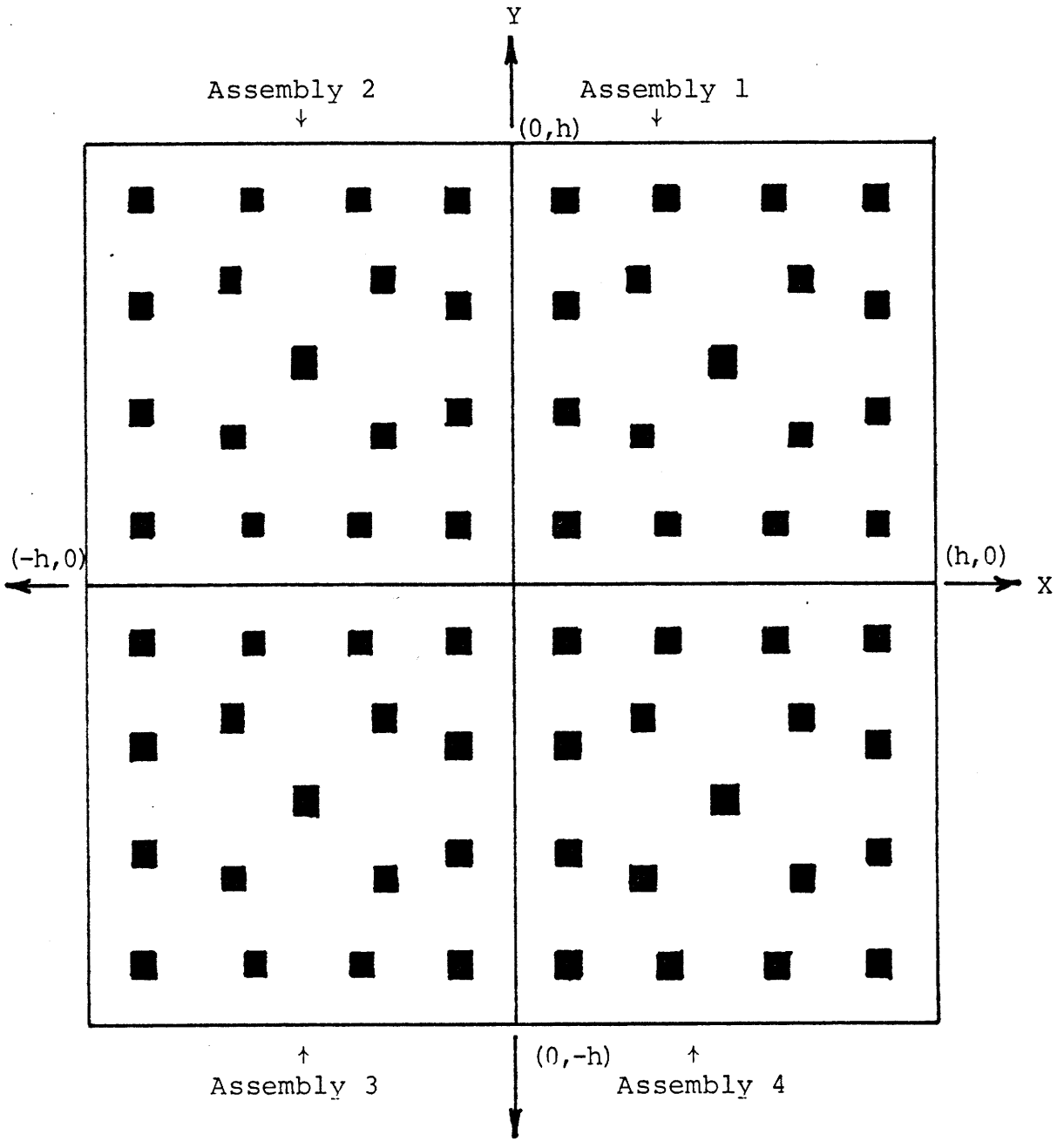

Figure 4.1: Four Assembly Configuration for CHIME Interpolation of a Corner Point Flux

bi-quadratic is given in Appendix 6. The $A_g^n(x,y)$ are calculated independently during the generation of the ADF/AXS equivalence parameters for QUANDRY. Thus the $A_g^n(x,y)$ are assumed known. Therefore in each assembly the eight coefficients of the $Q_g^n(x,y)$ become the only unknowns. Since there are four assemblies, there are 4 x 8 = 32 unknowns. To determine these unknowns, 32 conditions are imposed on the products, $A_g^n(x,y) \cdot Q_g^n(x,y)$, n = 1, 2, 3, 4. The 32 conditions are summarized in Table A6.0.1 of Appendix 6.

The result of imposing the 32 conditions on the products, $A_g^n(x,y) \cdot Q_g^n(x,y)$, is a system of 32 equations in 32 unknowns. This system is presented and solved algebraically in Appendix 6. Thus, given the appropriate values of surface fluxes and currents, volume fluxes, diffusion coefficients and assembly dimensions, the solution in Appendix 6 can be used to find the 32 unknown coefficients. Once this is done, the functions $Q_g^n(x,y)$ are known and the interpolated corner point flux is found from

$$\phi_g(0,0) = A_g^n(0,0) \cdot Q_g^n(0,0); \quad n = 1, 2, 3, 4. \tag{4.1}$$

Note that for n = 1, equation 4.1 becomes

$$\phi_g(0,0) = A_g^1(0,0)\ a_1 \qquad (4.2)$$

since $Q_g^1(0,0) = a_1$. Thus if only the heterogeneous corner point flux is desired, Appendix 6 can be used to solve for a_1 only. However, some of the polynomial flux reconstruction schemes which are described in Chapter 5 require estimates of the point x- and y-directed currents at assembly corners. These can be found if all the a_i are known. CHIME solves for all 32 of the a_i.

For the discussion of heterogeneous corner point interpolation, the following scheme is used to identify a given corner of a given assembly in a benchmark problem. First the node numbering scheme in Figure 3.1 of Chapter 3 is used to identify the assembly. For a given assembly, if a Cartesian coordinate system were placed at the center of the assembly then the corner points of the assembly are labeled according to what quadrant they are in. See Figure A6.0.2 in Appendix 6.

CHIME was tested by using it to interpolate the heterogeneous corner point fluxes for the center node (node 5) of benchmark problems 5, 7 and 8. These results will now be discussed.

Benchmark problem 5 is the infinite checkerboard of two fuel assembly types. The assembly environment in this problem is representative of the center of a large PWR. Because of the 90-degree rotational symmetry, all corner point fluxes have the same numerical value. Thus, the interpolation of any one corner point flux for this problem is sufficient.

Table 4.1 presents the CHIME results for benchmark problem 5. The input fluxes and currents for the CHIME run came from a coarse-mesh QUANDRY run employing ADF/AXS equivalence parameters. The results are excellent. There was practically no error in the fast group corner point interpolation and only -0.243% error in the thermal group.

Benchmark problem 7 is a small 3 x 3 quarter-core. The central node (node 5) is an unrodded fuel 1 assembly. The other eight nodes are homogeneous fuel 2. Because of the $\phi = 0$ boundary conditions on two sides of the problem, there is a severe flux tilt across the center assembly.

Table 4.2 displays the CHIME results for benchmark problem 7. A coarse-mesh QUANDRY run employing ADF/AXS equivalence parameters provided the input fluxes and currents for CHIME. The CHIME results are again very good. A maximum error of -0.672% is exhibited in the group 2, corner point 2 interpolation.

Legend

1.	Reference PDQ-7 Corner Point Flux, 0.7 cm mesh
2.	QUANDRY-ADF/AXS/CHIME Corner Point Flux
3.	Percent Error

	1.	2.2784×10^{12}
group 1	2.	2.2784×10^{12}
	3.	0.00%

	1.	2.8458×10^{11}
group 2	2.	2.8389×10^{11}
	3.	-0.243%

Table 4.1: CHIME Corner Point Flux Interpolation Results for Benchmark Problem 5

Legend

1. Reference PDQ-7 Corner Point Flux, 0.7 cm mesh
2. QUANDRY-ADF/AXS/CHIME Corner Point Flux
3. Percent Error

1. 2.8234×10^{12}	1. 1.7058×10^{12}
2. 2.8191×10^{12}	2. 1.7037×10^{12}
3. -0.152%	3. -0.123%

Node 5 group 1

1. 4.7321×10^{12}	1. 2.8234×10^{12}
2. 4.7152×10^{12}	2. 2.8191×10^{12}
3. -0.357%	3. -0.152%

1. 3.5990×10^{11}	1. 2.1687×10^{11}
2. 3.5748×10^{11}	2. 2.1738×10^{11}
3. -0.672%	3. +0.235%

Node 5 group 2

1. 6.0475×10^{11}	1. 3.5990×10^{11}
2. 6.0130×10^{11}	2. 3.5748×10^{11}
3. -0.570 %	3. -0.672%

Table 4.2: CHIME Corner Point Flux Interpolation Results for Benchmark Problem 7

Benchmark problem 8 is a difficult problem to analyze. It is a 3-by-3 quarter core. Some of the assemblies are rodded and node 3 contains water to simulate reflector effects. Corner point fluxes are interpolated for the central node 5 which contains fuel 2 and is rodded.

Table 4.3 shows the CHIME results for benchmark problem 8. Again input surface fluxes and currents were from a QUANDRY run using ADF/AXS. For this problem the CHIME results are not as good. The maximum percent error of -7.0% occurs in group 2 at corner point 1 of node 5 adjacent to the water reflector. Three pertinent comments apply to this result:

1. The -7.0% error at corner point 1 has a rather large uncertainty associated with it since the reference corner point 1 flux in group 2 is perhaps 3.0% in error (see Appendix 5).

2. For this difficult problem the input (into CHIME from QUANDRY) surface fluxes were up to 1.7% in error and the surface currents were up to 18% in error.

3. The reference thermal flux (see Figure A12.28 of Appendix 12) and the reference thermal form function (see Figure A15.14 of Appendix 15) rise sharply in magnitude as one proceeds from the center of node 5 toward corner point 1 near the reflector. The eight-term, bi-quadratic form functions employed in CHIME can not match this behavior very well. Specifically, they fail to curve upward sharply enough near corner point 1. Thus the interpolated corner point 1 flux is 7% low.

Legend

1. Reference PDQ-7 Corner Point Flux, 0.35 cm mesh
2. QUANDRY-ADF/AXS/CHIME Corner Point Flux
3. Percent Error

1. 1.7019×10^{12}	1. 4.6946×10^{11}
2. 1.7008×10^{12}	2. 4.6619×10^{11}
3. -0.0646%	3. -0.697%

Node 5 group 1

1. 4.2451×10^{12}	1. 1.1401×10^{12}
2. 4.2551×10^{12}	2. 1.1766×10^{12}
3. +0.236%	3. +3.20%

1. 2.0412×10^{11}	1. 7.9947×10^{10}
2. 2.1500×10^{11}	2. 7.4349×10^{10}
3. +5.33%	3. -7.00%

Node 5 group 2

1. 5.3104×10^{11}	1. 1.3544×10^{11}
2. 5.4241×10^{11}	2. 1.3721×10^{11}
3. +2.14%	3. +1.31%

Table 4.3: CHIME Corner Point Flux Interpolation Results for Benchmark Problem 8

4.5 INTERPOLATION METHOD 2 - CARILLON

In the previous section, the CHIME interpolation scheme was introduced. It works well on realistic PWR problems; however, it is somewhat tedious to implement in that a system of 32 equations in 32 unknowns has to be solved at each assembly corner point (and in each group) in a PWR core. Thus in this section a scheme called CARILLON is introduced as an alternate method of corner point interpolation. It has the advantage that all the corner point fluxes in a PWR core (in a given energy group) are interpolated at once. A computer code named CARILLON (Corner points ARe InterpoLated via Linkage Of Neighbors) has been written which automates the theory in this section.

Another advantage of CARILLON over CHIME is that the assumptions upon which CARILLON is based are somewhat milder than those upon which CHIME is based. Specifically, CARILLON employs only two assumptions:

1. The flux shape along an assembly face may be well represented by a quadratic fit to the average flux along the face and the two corner point fluxes at each end of the face.

2. Each assembly corner point in the PWR core is source free (see Appendix 6, equation A6.0.10).

The first assumption was inspired by plotting the fast and

thermal flux shapes along the surfaces of assemblies. For many PWR problems the quadratic approximation for the shape of the flux on the assembly surface is a good one. See in Appendix 12, for example, Figures A12.1 and A12.2 for benchmark problem 5 and see Figures A12.25 and A12.26 for benchmark problem 7. The source free assumption is expected to be true on physical grounds.

The CARILLON method starts by expressing the flux along the surface of the PWR assemblies as a quadratic. The quadratic for each assembly face is chosen such that it matches the (unknown) corner point fluxes at each end of the face and it yields the correct (known) surface-averaged flux when integrated over the face. The source free condition at a corner point is used to link four of these quadratics together. The result of applying the source free condition is a 5-point difference equation linking the unknown flux at corner point (i,j) to the four nearest unknown corner point fluxes at (i+1,j), (i-1,j), (i,j+1) and (i,j-1). A similar 5-point difference equation is written for each of the N assembly corner points in the PWR core. The resulting system of N equations in N unknown corner point fluxes is solved numerically using a Gauss-Seidel iterative method. The details of this entire procedure are given in Appendix 7.

CARILLON was tested by using it to interpolate the heterogeneous corner point fluxes of benchmark problems 5, 6, 7 and 8. These results will now be discussed.

Benchmark problem 5 is the infinite checkerboard of two fuel assembly types. Table 4.4 shows the CARILLON results. The input surface fluxes for CARILLON came from a QUANDRY-ADF-AXS run. The results are very good. The error in the interpolated thermal corner point flux is a little over 1.0%. The fast flux error is only +0.0132%. The fast flux error is less than the thermal flux error for this problem (and for most other problems) because the fast flux is smoother and is thus easier to fit with a quadratic polynomial.

Benchmark problem 7 is the small 3-by-3 quarter-core with an unrodded fuel 1 assembly as the center node 5. Table 4.5 presents the CARILLON results for this problem. The results are very good. The maximum percent error of +0.475% occurs in the group 1, corner point 1 flux.

Thus on benchmark problem 5 and 7 either CHIME or CARILLON can interpolate corner point fluxes to within about 1% accuracy. Since CARILLON is easier to implement and faster running, it is the choice so far. However, to really test CARILLON, it was used to interpolate the fluxes for the center node of the difficult benchmark problem 8. The CARILLON results are displayed in Table 4.6.

Legend

1.	Reference PDQ-7 Corner Point Flux, 0.7 cm mesh
2.	QUANDRY-ADF-AXS/CARILLON Corner Point Flux
3.	Percent Error

	1.	2.2784×10^{12}
group 1	2.	2.2787×10^{12}
	3.	+0.0132 %

	1.	2.8458×10^{11}
group 2	2.	2.8764×10^{11}
	3.	+1.07%

Table 4.4: CARILLON Corner Point Flux Interpolation Results for Benchmark Problem 5

Legend

1. Reference PDQ-7 Corner Point Flux, 0.7 cm mesh
2. QUANDRY-ADF-AXS/CARILLON Corner Point Flux
3. Percent Error

1. 2.8234×10^{12}	1. 1.7058×10^{12}
2. 2.8266×10^{12}	2. 1.7139×10^{12}
3. +0.113%	3. +0.475%

group 1
node 5

1. 4.7321×10^{12}	1. 2.8234×10^{12}
2. 4.7227×10^{12}	2. 2.8266×10^{12}
3. -0.199%	3. +0.113%

1. 3.5990×10^{11}	1. 2.1687×10^{11}
2. 3.5859×10^{11}	2. 2.1608×10^{11}
3. -0.364%	3. -0.364%

group 2
node 5

1. 6.0475×10^{11}	1. 3.5990×10^{11}
2. 6.0465×10^{11}	2. 3.5859×10^{11}
3. -0.0165%	3. -0.364%

Table 4.5: CARILLON Corner Point Flux Interpolation Results for Benchmark Problem 7

Legend

1. Reference PDQ-7 Corner Point Flux, 0.35 cm mesh
2. QUANDRY-ADF-AXS/CARILLON Corner Point Flux
3. Percent Error

1. 1.7019×10^{12}	1. 4.6946×10^{11}
2. 1.7060×10^{12}	2. 4.7145×10^{11}
3. +0.241%	3. +0.424%

group 1
node 5

1. 4.2451×10^{12}	1. 1.1401×10^{12}
2. 4.2416×10^{12}	2. 1.1251×10^{12}
3. -0.0824%	3. -1.32%

1. 2.0412×10^{11}	1. 7.9947×10^{10}
2. 2.0642×10^{11}	2. 7.6251×10^{10}
3. +1.13%	3. -4.62%

group 2
node 5

1. 5.3104×10^{11}	1. 1.3544×10^{11}
2. 5.3277×10^{11}	2. 1.2802×10^{11}
3. +0.326%	3. -5.48%

Table 4.6: CARILLON Corner Point Flux Interpolation Results for Benchmark Problem 8

The CARILLON results for benchmark problem 8 are not so good. The maximum error is -5.48% in the thermal flux at corner point 4 of node 5. The three comments made in the section on the CHIME results for benchmark problem 8 also apply here. An examination of the thermal flux along the surface of this node show that it will not be well fit by a quadratic (see Appendix 12, Figure A12.28). The sharp upward curl of the thermal flux at corner point 1 is particularly hard to model with a quadratic shape.

The sharp upward curl in the thermal flux at corner point 1 of node 5 in benchmark problem 8 is caused by the water reflector in node 3. However, in real PWRs there is a steel baffle at the edge of the core. The neutron absorption in the baffle holds down the thermal flux peaking in the area. Since benchmark problem 6 explicitly models the baffle, it is a more realistic test problem. Thus CARILLON was employed to interpolate the corner point fluxes for benchmark problem 6. The results are shown in Table 4.7. The input data for this CARILLON run came from a QUANDRY-ADF-AXS calculation in which extended assemblies were used to generate the equivalence parameters.

Legend

1.	Reference PDQ-7 Corner Point Flux, 0.35 cm mesh ($x10^{11}$)
2.	QUANDRY-ADF-AXS/CARILLON Corner Point Flux ($x10^{11}$)
3.	Percent Error

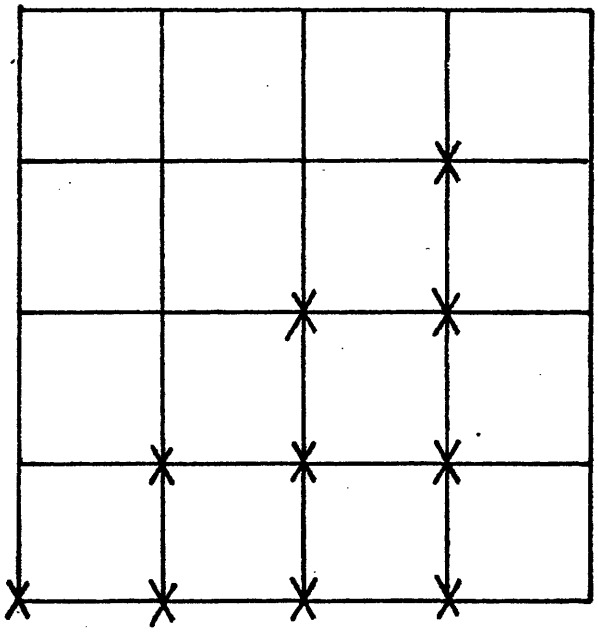

						1.	0.27510
						2.	0.052956
						3.	-80.75%
				1.	14.322	1.	3.2374
				2.	14.533	2.	3.3783
				3.	+1.47%	3.	+4.35%
		1.	31.993	1.	23.872	1.	8.0193
		2.	31.954	2.	23.725	2.	8.4253
		3.	-0.12%	3.	-0.62%	3.	+5.06%
1.	36.546	1.	33.872	1.	25.930	1.	9.2469
2.	36.547	2.	33.755	2.	25.852	2.	9.6705
3.	+0.0027%	3.	-0.35%	3.	-0.30%	3.	+4.58%

These are the fast flux results at the assembly corner points indicated by an x in the above diagram. Note the diagonal symmetry of the problem.

Table 4.7: CARILLON Corner Point Flux Interpolation Results for Benchmark Problem 6

Legend

1.	Reference PDQ-7 Corner Point Flux, 0.35 cm mesh ($x10^{11}$)
2.	QUANDRY-ADF-AXS/CARILLON Corner Point Flux ($x10^{11}$)
3.	Percent Error

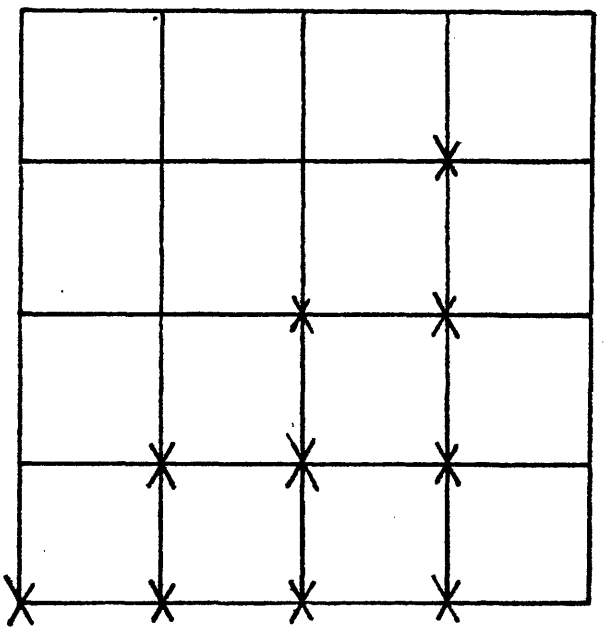

						1.	0.22355
						2.	0.33141
						3.	+48.25%
				1.	1.3633	1.	0.26713
				2.	1.4463	2.	0.44815
				3.	+6.09%	3.	+67.76%
		1.	4.1855	1.	2.8474	1.	0.70936
		2.	4.2709	2.	2.8858	2.	0.96998
		3.	+2.04%	3.	+1.35%	3.	+36.74%
1.	5.0107	1.	4.6439	1.	3.2446	1.	0.81849
2.	5.0724	2.	4.7738	2.	3.3189	2.	1.1045
3.	+1.23%	3.	+2.80%	3.	+2.29%	3.	+34.94%

These are the thermal flux results at the assembly corner points indicated by an x in the above diagram. Note the diagonal symmetry of the problem.

Table 4.7 (cont.): CARILLON Corner Point Flux Interpolation Results for Benchmark Problem 6

A review of the results in Table 4.7 shows that CARILLON does a reasonable job of interpolating the flux at assembly corner points that are far from the steel baffle. However, for corner points adjacent to the steel baffle, the interpolated thermal corner point flux may be 68% in error. The reason for this is that the flux along the surface of assemblies adjacent to the baffle is not quadratic. This may be seen by examining the reference flux plots for benchmark problem 6 in section A12.2 of Appendix 12. Because of the large thermal absorption cross section in the steel baffle, the thermal flux falls drastically near the baffle. The quadratic cannot match this behavior.

The inability of the quadratic shape to match the behavior of the flux near a steel baffle is an important and disappointing result for CARILLON. Since most realistic PWR cores are surrounded by a steel baffle, CARILLON will have trouble interpolating corner point fluxes near the baffles of these cores. In the next section, a third corner point interpolation method is introduced which can handle PWR cores with explicitly represented steel baffles.

4.6 INTERPOLATION METHOD 3 - CAMPANA

In the last section it was shown that CARILLON has difficulty interpolating accurate heterogeneous corner point fluxes near a steel baffle because the flux shapes there are not well fit by a quadratic. However, a review of the form function shapes (i.e., $\phi_g(x,y)/A_g(x,y)$) in Appendix 16 shows that these shapes are smooth along assembly surfaces and could probably be fit by a quadratic.

In this section a corner point interpolation method is introduced which was developed jointly by H. Khalil, P. Finck and the author. The scheme is similar to CARILLON; however, instead of assuming that the global heterogeneous flux, $\phi_g^{u-}(u)$, (u=x,y) is quadratic along an assembly surface, the new scheme assumes that the ratio, $\phi_g^{u-}(u) \; / \; A_g^{u-}(u)$, (u=x,y) (i.e., the ratio of the global heterogeneous flux to an average assembly flux shape) is quadratic. At any nodal interface, there are usually two assembly shapes that could be used. For example, for a vertical interface one could use the surface assembly flux shape from the node on the left or the node on the right. The approach employed here is to normalize the two assembly flux shapes at a surface to unity average and then take a simple arithmetical average to obtain $A_g^{u-}(u)$ (u=x,y). Thus this new scheme takes shape information from the assembly

calculations and factors it into the corner point interpolation. The new scheme is here called CAMPANA (CArillon Method Plus Assembly iNformAtion). Appendix 8 contains the algebra for implementing this new scheme. A computer code named CAMPANA has been written which automates the corner point interpolation process.

Table 4.8 displays the CAMPANA corner point interpolation results for the PWR benchmark problem 6 with the explicit steel baffle. The results are much improved over the CARILLON results. The maximum percent error of 5.5% occurs at the baffle-fuel interface . (Note that the corner point flux with 11% error is greater than 20 cm out in the reflector away from the fueled PWR core and is thus of little concern here.) CAMPANA results for interior corner point fluxes away from the steel baffle are excellent with a maximum error of only slightly more than 1%.

4.7 SUMMARY

In this chapter three methods have been presented for interpolating the value of the heterogeneous flux at the corners of PWR assemblies. The only input required by these methods is information from an inexpensive QUANDRY-ADF-AXS calculation and information from assembly calculations. In general, the first method, CHIME, is somewhat

Legend

1. Reference PDQ-7 Corner Point Flux, 0.35 cm mesh ($x10^{11}$)
2. QUANDRY-ADF-AXS/CAMPANA Corner Point Flux (x 10^{11})
3. Percent Error

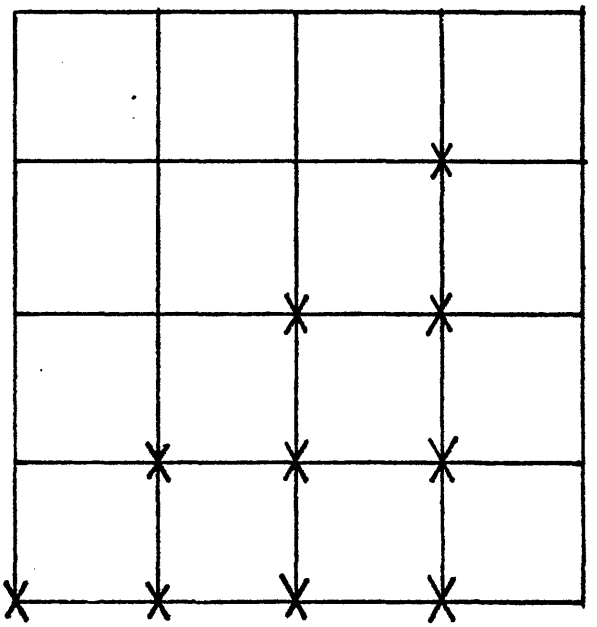

						1.	0.27510
						2.	0.30619
						3.	+11.30%
				1.	14.322	1.	3.2374
				2.	14.235	2.	3.3426
				3.	-0.61%	3.	+3.25%
		1.	31.993	1.	23.872	1.	8.0193
		2.	32.042	2.	23.869	2.	8.3025
		3.	+0.15%	3.	-0.01%	3.	+3.53%
1.	36.546	1.	33.872	1.	25.930	1.	9.2469
2.	36.598	2.	33.765	2.	25.963	2.	9.4852
3.	+0.14%	3.	-0.32%	3.	+0.13%	3.	+2.58%

These are the fast flux results at the assembly corner points indicated by an x in the above diagram. Note the diagonal symmetry of the problem.

Table 4.8: CAMPANA Corner Point Flux Interpolation Results for Benchmark Problem 6

Legend

1.	Reference PDQ-7 Corner Point Flux, 0.35 cm mesh ($x10^{11}$)
2.	QUANDRY-ADF-AXS/CAMPANA Corner Point Flux (x 10^{11})
3.	Percent Error

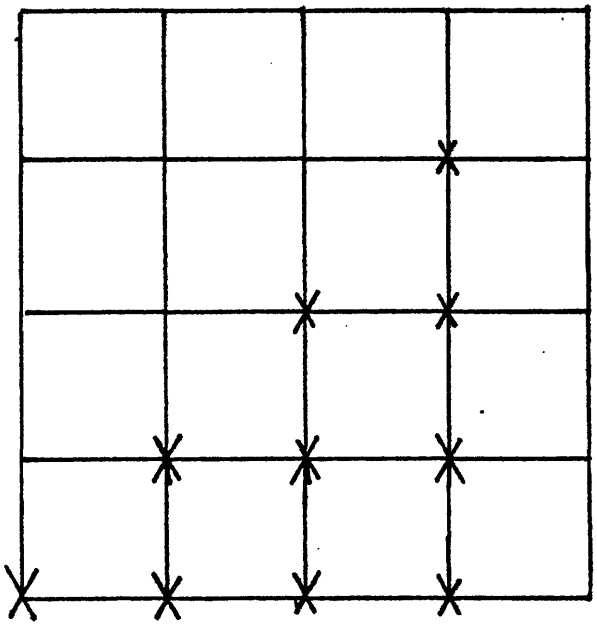

						1.	0.22355
						2.	0.24924
						3.	+11.49%
				1.	1.3633	1.	0.26713
				2.	1.3370	2.	0.28181
				3.	-1.93%	3.	+5.50%
		1.	4.1855	1.	2.8474	1.	0.70936
		2.	4.2202	2.	2.8280	2.	0.74712
		3.	+0.83%	3.	-0.68%	3.	+5.32%
1.	5.0107	1.	4.6439	1.	3.2446	1.	0.81849
2.	4.9960	2.	4.6924	2.	3.2821	2.	0.84387
3.	-0.29%	3.	+1.04%	3.	+1.16%	3.	+3.10%

These are the thermal flux results at the assembly corner points indicated by an x in the above diagram. Note the diagonal symmetry of the problem.

Table 4.8 (cont.): CAMPANA Corner Point Flux Interpolation Results for Benchmark Problem 6

cumbersome since a system of 32 equations in 32 unknowns must be solved at each corner point just to interpolate one corner point flux. For this reason, methods like CARILLON and CAMPANA were introduced in which all the corner point fluxes in a PWR core are interpolated at once.

Benchmark problem 5 models the interior of a large checkerboard-loaded PWR. It appears that any of the three methods of corner point flux interpolation work satisfactorily on this problem (maximum errors in the interpolated flux of about 1%) since the flux and form function shapes are fairly smooth. Similarly, in benchmark problem 6 (which is the 4-by-4 quarter core with the explicitly represented baffle) the interpolation methods appear to work well (about 1% error) on interior assemblies away from the steel baffle. Next to the steel baffle, the best results were obtained by using CAMPANA. Here the errors are larger, the maximum error being 5.5% in the thermal group flux. For the purpose of this thesis this accuracy is sufficient although further work to reduce the error in the interpolated corner point fluxes near the baffle would be helpful.

In the next chapter, a method will be presented which uses the heterogeneous surface fluxes and currents and volume fluxes from a QUANDRY-ADF-AXS run as well as the interpolated heterogeneous corner point fluxes from this chapter to reconstruct the detailed heterogeneous flux at each point within a PWR assembly.

Chaper 5

APPLICATION OF POLYNOMIAL FORM FUNCTIONS TO THE RECONSTRUCTION OF HETEROGENEOUS POINTWISE FLUXES

5.1 INTRODUCTION

In Chapter 1 the form function method was introduced as a flux reconstruction technique. Its essence is to find an analytic form function, $F_g^R(x,y)$, which can be multiplied into a heterogeneous assembly flux shape, $A_g(x,y)$, to yield the reconstructed heterogeneous flux, $\phi_g^R(x,y)$, as

$$\phi_g^R(x,y) = A_g(x,y) * F_g^R(x,y) \qquad (5.1)$$

In this chapter, quadratic and quartic polynomials in x and y are tested as reconstructed form functions.

In general, the coefficients of the polynomial form functions could be determined by forcing the product in equation 5.1 $[A_g(x,y)*F_g^R(x,y)]$ to match heterogeneous flux information derived from one of the two following inexpensive sources:

1. Approximations of the heterogeneous node-averaged fluxes and currents from a QUANDRY calculation employing assembly homogenized parameters (ADF-AXS)
2. Approximations of heterogeneous flux and derivatives of the flux at assembly corner points from the corner point interpolation schemes; CHIME, CARILLON, or CAMPANA (see Chapter 4).

However, the goal of this chapter is to see if polynomial functions are appropriate representatives of $F_g^R(x,y)$. For this reason, reference information from the global heterogeneous reference solution is used in the chapter to calculate the coefficients of the polynomial form functions.

For this chapter only, the heterogeneous assembly fluxes, $A_g(x,y)$, are all from single assembly criticality calculations with zero-current boundary conditions (i.e., extended assembly calculations are not used.) Appendix 13 contains plots of the assembly flux shapes employed in this chapter.

5.2 A FLUX RECONSTRUCTION METHOD BASED ON A 9-TERM, BI-QUADRATIC FORM FUNCTION

The first method of heterogeneous flux reconstruction which will be investigated is a technique based on a 9-term, bi-quadratic form function. For brevity the scheme is called the bi-quadratic method. The reconstructed flux, $\phi_g^R(x,y)$, is given by equation 5.1 as

$$\phi_g^R(x,y) = A_g(x,y) * F_g^R(x,y)$$

where $A_g(x,y)$ is the known assembly flux and $F_g^R(x,y)$ is a 9-term, bi-quadratic expressed as

$$F_g^R(x,y) = a_1 + a_2\left[\frac{x}{h_x}\right] + a_3\left[\frac{x^2}{h_x^2}\right] + a_4\left[\frac{y}{h_y}\right] +$$

$$a_5\left[\frac{y^2}{h_y^2}\right] + a_6\left[\frac{xy}{h_x h_y}\right] + a_7\left[\frac{x^2 y}{h_x^2 h_y}\right] +$$

$$a_8\left[\frac{x y^2}{h_x h_y^2}\right] + a_9\left[\frac{x^2 y^2}{h_x^2 h_y^2}\right]. \qquad (5.2)$$

The h_x and h_y are the PWR assembly dimensions. The coefficients, a_1 through a_9, are determined by forcing the $\phi_g^R(x,y)$ in equation 5.1 to match the four corner point fluxes from the reference global solution and to match approximately the volume- and surface-averaged fluxes from the reference global solution. The reference volume- and surface-averaged fluxes will be matched exactly only when $A_g(x,y)$ is spatially flat. The algebraic details of the bi-quadratic method are given in Appendix 9.

Benchmark problem 7 is a small, 3-by-3 node quarter core. The center node 5 is an unrodded fuel 1 assembly and the other eight nodes are homogeneous fuel 2. The bi-quadratic method was tested by employing it to reconstruct a 31-by-31 array of the detailed pointwise fluxes in the center node 5 of benchmark problem 7. The reference calculation was a 0.7 cm mesh PDQ-7 calculation. The results of the flux reconstruction are contained in Table 5.1.

	Average Percent Error in the Reconstructed Pointwise Flux	Maximum Percent Error in the Reconstructed Pointwise Flux	Location (row,column) of Maximum Error in the Reconstructed Pointwise Flux
Fast Flux	0.21	0.72	(11,21)
Thermal Flux	1.49	4.31	(28,4)

Note:

$$\text{Pointwise percent error at } (i,j) = E_{i,j} = \frac{\phi^{R}_{i,j} - \phi_{i,j}}{\phi_{i,j}} * 100$$

$$\text{Maximum percent error} = \max_{i,j} (E_{i,j})$$

$$\text{Average Percent Error} = \frac{\sum_{i,j} \left| E_{i,j} \right|}{\text{total number of points}}$$

Table 5.1: Bi-Quadratic Method Flux Reconstruction Results for Benchmark Problem 7

The bi-quadratic flux reconstruction results for benchmark problem 7 are good in the fast group. The maximum percent error in the fast reconstructed flux is only 0.72%. This is because the reference fast form function for this problem (see Figure A15.11 in Appendix 15) is smooth and easily fit by a bi-quadratic. Since the fast assembly flux (see Figure A13.1 in Appendix 13) is almost spatially flat, the reconstructed fast bi-quadratic form function has a shape very close to the smooth fast flux itself (see Figure A12.25 in Appendix 12). Figure A17.1 displays a plot of the pointwise percent error in the fast flux reconstruction.

In the thermal group the bi-quadratic flux reconstruction for benchmark problem 7 is not as accurate. The maximum percent error is 4.31% even though the reference solution was used to provide the information for determining the 9 coefficients of the bi-quadratic. Figure A15.12 shows the reference thermal form function. It is encouraging that the reference form function is smooth and shows no fine structure due to local heterogeneities (water holes). However, the 4.31% error indicates that this smooth shape is not particularly well fit by the bi-quadratic in equation 5.2. To further emphasize this point, Figure A17.2 presents a plot of the pointwise error in the reconstructed flux. A close examination of this figure reveals that the

bi-quadratic flux reconstruction method could be improved if information on the derivative of the flux could be incorporated. For example, the percent error at a corner point in this figure is zero; however, because of the lack of flux derivative information, the flux reconstruction is more than one percent in error just one mesh point away from the corner along the diagonal of the assembly.

If the assumption is made that QUANDRY-ADF-AXS could yield accurate information on the surface-averaged derivative of the flux (i.e., via the surface-averaged currents and the diffusion coefficient along the surface), and that CHIME could yield accurate information about the derivative of the flux at assembly corner points, then how could this information be incorporated into a flux reconstruction method? This question is answered in the next section where a 25-term, bi-quartic polynomial in x and y is employed as a form function. The bi-quartic function has enough degrees of freedom to incorporate 25-9=16 pieces of flux derivative information which the 9-term, bi-quadratic cannot incorporate.

5.3 A FLUX RECONSTRUCTION METHOD BASED ON A 25-TERM, BI-QUARTIC FORM FUNCTION

In this section, the reconstructed flux, $\phi_g^R(x,y)$, is again given by equation 5.1 as

$$\phi_g^R(x,y) = A_g(x,y) * F_g^R(x,y).$$

However, this time the form function is a 25-term, bi-quartic polynomial. This polynomial is presented in Appendix 10. The 25 coefficients of the polynomial are determined by forcing the $\phi_g^R(x,y)$ in equation 5.1 to match exactly the following 16 heterogeneous quantities from the reference solution:

1. the four corner point fluxes
2. the x-component of the net current at each of the four assembly corner points
3. the y-component of the net current at each of the four assembly corner points
4. the cross derivative of the flux, $\frac{\partial^2 \phi}{\partial x \, \partial y}$, at each of the four assembly corner points

and by forcing $\phi_g^R(x,y)$ to match approximately the following 9 heterogeneous quantities from the reference solution:

1. the volume-averaged flux
2. the four surface-averaged fluxes
3. the four surface-averaged currents.

The latter 9 quantities will be matched exactly for the case of a spatially flat $A_g(x,y)$ and spatially flat diffusion

coefficients along the surfaces of the PWR assembly. More of the algebraic details of the bi-quartic method are given in Appendix 10.

The bi-quartic method was tested by reconstructing the flux in the center node 5 of benchmark problems 5, 7 and 8. See Appendix 2 for a description of these benchmark problems. The results of the bi-quartic reconstruction are shown in Table 5.2.

The results in Table 5.2 are disappointing. In the thermal reconstruction the maximum error in the pointwise reconstructed flux is still roughly 5 percent or more. It is especially disappointing that for benchmark problem 7 the maximum error in the thermal reconstruction actually increased from +4.31% (when the bi-quadratic method was used) to -5.51% (when the bi-quartic method was employed).

An examination of the error plots in Appendix 18 (especially Figure A18.2 for benchmark problem 7) reveals why the bi-quartic method failed to improve the flux reconstruction results. Again the error plots exhibit an undulating character, just as they did in Appendix 17 for the bi-quadratic method. The addition of flux derivative information at the edges of the assembly reduced the errors near the edges of the assembly. Unfortunately, there are no points of support for the reconstructed flux in the interior of the assembly and thus the polynomial form

	Average Percent Error in the Reconstructed Pointwise Flux	Maximum Percent Error in the Reconstructed Pointwise Flux	Location (row,column) of Maximum Error in the Reconstructed Pointwise Flux
Fast Flux			
Benchmark Problem 5	0.18	-0.63	(16,19)
Benchmark Problem 7	0.13	-0.55	(15,17)
Benchmark Problem 8	1.21	-5.16	(7,25)
Thermal Flux			
Benchmark Problem 5	1.75	-4.73	(26,26)
Benchmark Problem 7	1.58	-5.51	(25, 7)
Benchmark Problem 8	3.42	19.45	(5,26)

Table 5.2: Bi-Quartic Method Flux Reconstruction Results for Benchmark Problems 5, 7 and 8

functions are free to undulate about the imposed volume-averaged flux value. These undulations still allow errors in the reconstructed flux of roughly 5%.

5.4 SUMMARY AND CONCLUSIONS

In this chapter bi-quadratic and bi-quartic polynomials were employed to approximate the shapes of some of the reference form functions displayed in Appendix 15. Reference information from the global heterogeneous solution was used to find the values of the coefficients of the polynomials.

It is concluded that the reference fast form functions in Appendix 15 can be fit fairly well by polynomials. However, the reference thermal form functions are not well fit by the bi-quadratic or bi-quartic polynomials. Specifically, the reconstructed thermal fluxes for unrodded benchmark problems 5 and 7 were roughly a maximum of 5% in error.

In the next chapter, non-polynomial form functions are explored in an attempt to reduce the errors in the pointwise thermal flux reconstructions.

Chapter 6

APPLICATION OF NON-POLYNOMIAL FORM FUNCTIONS TO THE RECONSTRUCTION OF HETEROGENEOUS POINTWISE FLUXES

6.1 INTRODUCTION

The essence of the form function method for heterogeneous flux reconstruction is to search for a form function, $F_g(x,y)$, that multiplicatively corrects the assembly flux, $A_g(x,y)$, such that the product, $A_g(x,y)*F_g(x,y)$, reconstructs the global heterogeneous flux, $\phi_g(x,y)$, within the assembly. Thus, the form function is defined by the equation

$$\phi_g(x,y) = A_g(x,y)*F_g(x,y). \qquad (6.1)$$

Since the heterogeneous structure of the assembly is reflected in the shapes of both $\phi_g(x,y)$ and $A_g(x,y)$, the form function, $F_g(x,y)$, is expected to be smooth. A quick review of the reference form functions plotted in Appendix 15 (for single assembly criticality calculations with zero-net-current boundary conditions) and Appendix 16 (for extended assembly calculations) reveals that the form functions are indeed smooth. However, the results from Chapter 5 show that these smooth shapes are not well fit by low order polynomials.

In this chapter, the group diffusion equations are employed to derive a coupled set of differential equations for the reference form functions, $F_g(x,y)$, g= 1,2. A solution technique is employed to solve the coupled set of equations in an approximate fashion. The resulting solution yields a non-polynomial analytic form function, $F_g^R(x,y)$, which when multiplied into the assembly flux, $A_g(x,y)$, yields the approximate reconstructed global flux, $\phi_g^R(x,y)$. Thus, the reconstructed flux in the assembly is

$$\phi_g^R(x,y) = A_g(x,y) * F_g^R(x,y). \qquad (6.2)$$

A computer code has been written which automates the process of evaluating the reconstructed form function. It is called FORTE (FORm funcTion Evaluation). For brevity the flux reconstruction technique using the non-polynomial form function is called the FORTE method.

The reconstructed form function, $F_g^R(x,y)$, contains coefficients whose magnitudes are determined by matching known values of $F_g^R(x,y)$. Specifically, the following values of F_g^R are required:

1. four corner point values
2. four surface-averaged values
3. one volume-averaged value.

To test only the ability of the non-polynomial form function to duplicate the shape of the reference form function, reference information can be used to find the exact values of the coefficients of the reconstructed form function. This approach will be employed for certain nodes in benchmark problems 5, 6 and 7 as an academic exercise to test the accuracy of the non-polynomial fit to the reference form function. Such reconstructions are referred to as flux reconstructions using reference information for determination of the coefficients of the form function.

The practical case, in which reference pointwise information from a global solution is not known, is also examined in this chapter. For such cases, the coefficients of the reconstructed form function are determined approximately by using information from the following three inexpensive sources:

1. Approximations of the global heterogeneous node-averaged fluxes come from a QUANDRY-ADF-AXS solution.
2. Approximations of the heterogeneous flux at assembly corner points come from the corner point interpolation schemes; CHIME, CARILLON, and CAMPANA from Chapter 4.

3. The known heterogeneous assembly flux shapes, $A_g(x,y)$, come from assembly calculations. In this chapter, some of the assembly calculations are from extended assembly calculations.

Complete pointwise flux reconstructions for the practical case just described are included for the center node 5 of benchmark problems 5 and 7 and for all of the fueled nodes in benchmark problem 6.

6.2 FORTE THEORY

To find a coupled set of differential equations for the reference form functions, $F_g(x,y)$, the following procedure is used. Equation 6.1 is substituted into the two-group diffusion equations for the global heterogeneous flux, $\phi_g(x,y)$. From that result, substract the analogous two-group diffusion equations for the assembly flux, $A_g(x,y)$, multiplied by the form function $F_g(x,y)$. With some rearrangement the result is

$$-\nabla\cdot D_1\nabla F_1 + \{\left(\frac{1}{\lambda_A} - \frac{1}{\lambda_\phi}\right)\nu\Sigma_{f1}\}F_1 + \frac{1}{r}\nu\Sigma_{f2}\left(\frac{F_1}{\lambda_A} - \frac{F_2}{\lambda_\phi}\right) = \frac{2D_1}{A_1}\nabla F_1\cdot\nabla A_1 \tag{6.3}$$

$$-\nabla\cdot D_2\nabla F_2 + r\,\Sigma_{21}(F_2 - F_1) = \frac{2D_2}{A_2}\nabla F_2\cdot\nabla A_2 \tag{6.4}$$

where

$$r = \frac{A_1(x,y)}{A_2(x,y)} \qquad (6.5)$$

and λ_A is the eigenvalue for the assembly problem and λ_ϕ is the eigenvalue for the global problem.

Suppose the reference shape of the global heterogeneous flux on each surface of a PWR assembly is known. This shape could be divided by the known assembly flux shape to yield the reference boundary value shape of the form function. This boundary value shape of F_g could then be employed in an exact numerical solution of equations 6.3 and 6.4 for the reference $F_g(x,y)$.

Unfortunately, the reference global flux shape on the surfaces of PWR assemblies is not generally known. However, a practical implementation of the above scheme has been performed at M.I.T. by Taiwo [42]. For example, for the center node 5 of benchmark problem 7 Taiwo followed this practical procedure to reconstruct the flux. From a QUANDRY-ADF-AXS calculation and CHIME calculation, good approximations of the heterogeneous corner point fluxes and surface-averaged fluxes were derived. Along each face

of the center node, the heterogeneous flux shape was assumed to be well fit by

$$\phi(u) = c_1 \cos(c_2 u + c_3) \; ; \quad u = x, \; y \qquad (6.6)$$

where the constants c_1 , c_2 and c_3 were determined by requiring $\phi(u)$ to match the two corner point fluxes and the surface-averaged flux along the face. Taiwo then divided the assembly flux shape on the surface into $\phi(u)$. This yielded the boundary value of the reconstructed form function. Taiwo then numerically solved an approximate form of equations 6.3 and 6.4 (Specifically, the product of gradients term on the right-hand side of equations 6.3 and 6.4 was neglected and constant values of r and group parameters appropriate to the perimeter of the assembly were employed). He found that using this procedure he could reconstruct the pointwise flux to 1.38% in the center node of benchmark problem 5.

Taiwo's scheme has two disadvantages. The first is that the flux shape on the surfaces of PWR assemblies is not always well fit by the form in equation 6.6. The second is that the numerical solution of equations 6.3 and 6.4 is somewhat expensive (although it is much

less expensive than finding the reference fine mesh solution, $\phi_g(x,y)$). To avoid the expense of a numerical solution, an approximate analytic solution for equations 6.3 and 6.4 will be developed here.

Equations 6.3 and 6.4 are the starting point for developing an approximate analytic solution for the form functions. Unfortunately, these equations represent a coupled set of differential equations with variable coefficients for which a general solution is unknown. Thus, to make these equations more tractable, simplifying approximations are made. The objective is to find a set of approximations which allow the resulting simplified set of equations to be solved analytically; however, the approximations must also be mild enough to allow the approximate analytic solution to be a close approximation of the reference form function, F_g.

The first approximation for simplifying the equations 6.3 and 6.4 is to neglect the source-like terms containing $\nabla F_g \cdot \nabla A_g$ on the right-hand side of the equations. It is argued that $\nabla F_g \cdot \nabla A_g$ is small compared to other terms in equations 6.3 and 6.4. Evidence for this can be seen by examining the smooth reference form function plots in Appendix 15 and Appendix 16.

Consider first the case when A_g is from an assembly calculation with zero-net-current boundary conditions. Since the gradient of A_g is only expected to be large near the water holes in the interior of the assembly, one would expect the effect of the source-like terms $\nabla F_g \cdot \nabla A_g$ to be a localized one which would result in fine structure in the form function plots. Since the plots contain little evidence of structure, it is likely that the $\nabla F_g \cdot \nabla A_g$ term is indeed small. The reason for this is that even though the ∇A_g is large in the vicinity of the water holes in the interior of the assembly, ∇F_g is small there so that the dot product, $\nabla F_g \cdot \nabla A_g$, is also small.

At the edges of the assembly, the situation is often reversed. If the neighboring assembly has a different average enrichment (i.e., if it is from a different batch) then ∇F_g tends to be large near the edge of the assembly reflecting the fact that the $A_g(x,y)$ will need a lot of correcting near such an edge since the zero current boundary condition is likely to be a poor approximation in this case. However, if the assembly calculation is based on zero-net-current boundary conditions, then ∇A_g is zero at the assembly surface and $\nabla F_g \cdot \nabla A_g$ is again small.

For extended assembly calculations, the gradient of A_g is not necessarily zero at edges of the PWR assemblies in the interior of such extended assembly calculations. However, since the environment is explicitly modeled in the vicinity of such edges, the $A_g(x,y)$ needs less correcting and thus ∇F_g is not expected to be large near such edges. Thus $\nabla F_g \cdot \nabla A_g$ is again small.

Taiwo's good numerical results (in which the $\nabla F_g \cdot \nabla A_g$ terms were ignored) are further proof that neglecting this dot product of gradients is a good approximation.

Even if the terms involving $\nabla F_g \cdot \nabla A_g$ in equations 6.3 and 6.4 are neglected, the resulting simplified set of equations is still hard to solve analytically because of its multidimensional character and variable coefficients. Thus, further simplifying approximations are required. However, before these approximations can be discussed, the assembly geometry for the two-dimensional FORTE flux reconstruction must be presented.

Figure 6.1 illustrates the assembly geometry for the FORTE flux reconstructions. An x-y Cartesian coordinate system is placed at the center of the assembly which has dimensions h-by-h. The corner points of the assembly are labeled according to which quadrant they are in. The diagonal lines, x = y and x = -y divide the assembly into

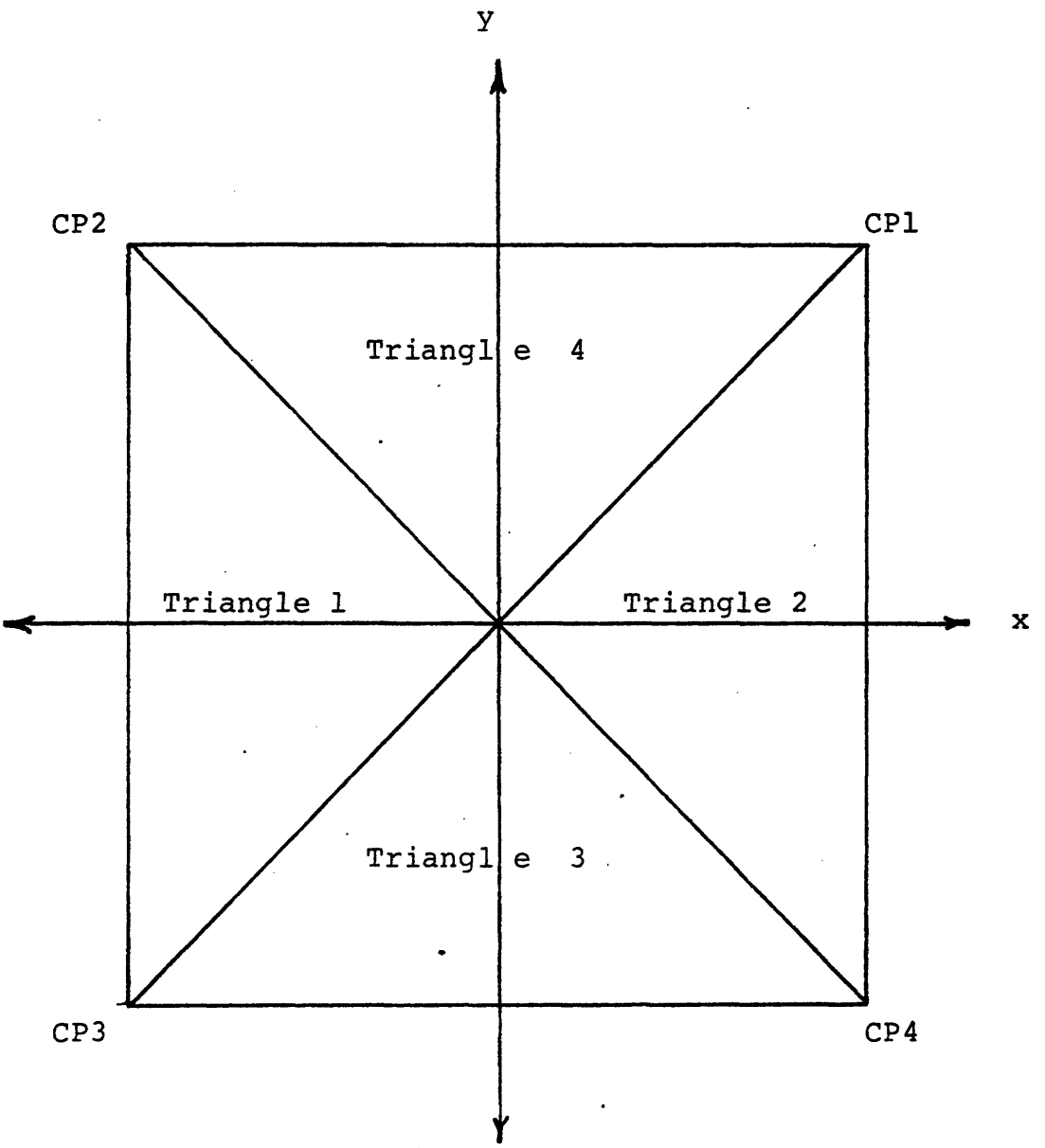

Figure 6.1: FORTE Flux Reconstruction Geometry

four triangles. The triangles are labeled 1, 2, 3 and 4 and each triangle contains one of the faces of the assembly, x-, x+, y- and y+ respectively.

In the FORTE method, a different analytic reconstructed form function is found in each of the four triangles in Figure 6.1. In the following, the solution for triangle 1 is presented. The solutions for the other triangles are similar to it.

To find a solution for triangle 1, consider equations 6.3 and 6.4 with the product of gradients term neglected. The additional assumption is now made that r and the group parameters are constant throughout the triangle 1. The values of these constants are taken as those appropriate to the x- face of the assembly.

A motivation for this approximation can be found by examining Figure A15.2 of Appendix 15. This is the reference form function for the center node of the infinite checkerboard (benchmark problem 5). One can see that the hardest part of this shape to reconstruct is the "lip" at the edge of the PWR assembly. Thus, if only one representative value of r and the group parameters is to be chosen, one might choose a value of r and the group parameters that is accurate near the PWR assembly edge.

At beginning of life (B.O.L.) most PWR fuel assemblies are composed of identical fuel pins. Thus, the assumption of constant group parameters in triangle 1 which are appropriate to the surface of the assembly is a fair one for most of the fueled homogenized pin cells. The situation with respect to $r = A_1(x,y)/A_2(x,y)$ is less clear. Because of thermal flux peaking in the vicinity of water holes, r is far from spatially constant in the interior of triangle 1.

The compelling reason for choosing r as a value that is accurate near the edge of the assembly and perhaps less accurate in the interior of triangle 1 can be seen by examining the terms in which r appears in equations 6.3 and 6.4. The r divides $\left(\frac{1}{\lambda_A} F_1 - \frac{1}{\lambda_\phi} F_2 \right)$ in equation 6.3 and r multiplies (F_2-F_1) in equation 6.4. It will be shown that the asymptotic fast-to-slow form function ratio ($F_1/F_2 = s$) is close to unity in the interior of a PWR assembly. Thus, if λ_A is not very different from λ_ϕ, then the differences $\left(\frac{1}{\lambda_A} F_1 - \frac{1}{\lambda_\phi} F_2 \right)$ and (F_2-F_1) will be small in the interior of a PWR assembly and thus errors in the chosen value of r are mitigated by this fact. However, near the edge of triangle 1 the differences $\left(\frac{1}{\lambda_A} F_1 - \frac{1}{\lambda_\phi} F_2 \right)$ and $(F_2 - F_1)$ become large and accuracy of r becomes quite important.

Thus, for triangle 1, r is approximated by

$$r \simeq \frac{\bar{A}_1^{x-}}{\bar{A}_2^{x-}} \tag{6.7}$$

where $\bar{A}_g^{x-}$ is the surface-average of the group-g assembly flux on the x- surface of the assembly.

With these approximations, the simplified form of equations 6.3 and 6.4 becomes

$$-D_1 \nabla^2 F_1 + \{(\frac{1}{\lambda_A} - \frac{1}{\lambda_\phi}) \nu\Sigma_{f1}\} F_1 + \frac{1}{r} \nu\Sigma_{f2} (\frac{F_1}{\lambda_A} - \frac{F_2}{\lambda_\phi}) = 0 \tag{6.8}$$

$$-D_2 \nabla^2 F_2 + r\Sigma_{21} (F_2 - F_1) = 0. \tag{6.9}$$

Equations 6.8 and 6.9 have the same form as the two-group diffusion equations in reactor physics for a homogeneous medium. Thus, to find solutions for these two equations, standard methods are employed [1].

One searches for solutions of 6.8 and 6.9 which are also solutions of the buckling equation

$$\nabla^2 F_g(x,y) = B^2 F_g(x,y). \tag{6.10}$$

Substitution of equation 6.10 into equations 6.8 and 6.9 yields a coupled set of algebraic equations which have non-trivial solutions if and only if the determinant of the system of equations is zero. Setting the determinant of the system of equations to zero yields the following quadratic equation in B^2

$$[B^2]^2 \{ D_1 D_2 \} +$$

$$[B^2] \{-D_1 r \Sigma_{21} - D_2 (\frac{1}{\lambda_A} - \frac{1}{\lambda_\phi})\nu\Sigma_{f1} - D_2 \frac{1}{\lambda_A} \frac{1}{r} \nu\Sigma_{f2} \} +$$

$$\{ (\frac{1}{\lambda_A} - \frac{1}{\lambda_\phi}) \Sigma_{21} (r\nu\Sigma_{f1} + \nu\Sigma_{f2}) \} = 0 \quad (6.11)$$

For practical cases, the quadratic equation for B^2 will have two real solutions. The fundamental value of B^2 is called B_1^2 and is zero or very near zero. (Note that if $\lambda_\phi = \lambda_A$ the B_1^2 is zero.) The harmonic value of B^2 is called B_2^2 and is generally much larger than B_1^2. Values of B^2 for the center node of benchmark problem 5 yield typical bucklings as $B_1^2 = -0.000473$ and $B_2^2 = +0.449$. Note that B_2^2 is a positive number for all practical cases.

The term containing $\nabla^2 F_2$ in equation 6.9 can be eliminated by using the buckling equation 6.10. The resulting equation can be solved to yield the fast-to-slow form function ratio, F_1 / F_2 as a function of the buckling and group parameters for triangle 1. When the fundamental buckling, B_1^2 is used, the fundamental fast-to-slow form function ratio, s, results as

$$s = 1.0 + \frac{-D_2 \quad B_1^2}{r \quad \Sigma_{21}} . \qquad (6.12)$$

As mentioned earlier, s is usually very close to unity since B_1^2 is usually a very small number.
When the harmonic buckling, B_2^2 is used, the harmonic fast-to-slow form function ratio, t results as

$$t = 1.0 + \frac{-D_2 \quad B_2^2}{r \quad \Sigma_{21}} . \qquad (6.13)$$

The following analytic functions for the reconstructed form function, $F_g^{R(1)}$, are solutions of the simplified set of equations 6.8 and 6.9 in triangle 1. These solutions were strongly motivated by studying the shape of the reference form functions for the center node of benchmark problem 5. See Appendix 15, Figures A15.1 and A15.2. Especially suggestive is the behavior of the $F_2(x,y)$ function

along the negative x-axis. Starting at the center of the assembly, the function $F_2(x,y)$ has a smooth interior and then as x approaches -h/2, F_2 rises in a sudden "lip". The asymptotic part of the solution in triangle 1 models the smooth interior part of the F_2 function and the harmonic part reproduces the "lip".

The two-dimensional buckling equation is difficult to solve for the general case. Thus it was decided to simply "stitch together" solutions for each of the four triangles. Within each triangle, $F_g^R(x,y)$ is represented as the sum of a fundamental or asymptotic term and a harmonic term. Each of the terms is separable in the multiplicative sense

$$F(x,y) = X(x) * Y(y). \qquad (6.14)$$

The separation of variables represented in equation 6.14 allows fundamental and harmonic solutions of the two-dimensional buckling equation to easily be found. These solutions are also solutions of the coupled set of simplified equations 6.8 and 6.9.

The reconstructed form function for triangle 1 is

$$F_g^{R(1)}(x,y) =$$

$$C_1 \; s_g^{(1)} \left[\cos\mu_x^{(1)}x + \frac{C_x^{(1)}}{\mu_x^{(1)}} \sin\mu_x^{(1)}x\right] \left[\cos\mu_y^{(1)}y + \frac{C_y^{(1)}}{\mu_y^{(1)}} \sin\mu_y^{(1)}y\right] +$$

$$\left[\left(\frac{1}{2} + \frac{y}{h} \right) a_2^{(1)} + \left(\frac{1}{2} - \frac{y}{h} \right) a_3^{(1)} \right] t_g^{(1)} \exp\left[-B_2^{(1)} \left(\frac{h}{2} + x \right)\right]$$

where $[\mu_x^{(1)}]^2 + [\mu_y^{(1)}]^2 = -[B_1^{(1)}]^2$ and (6.15)

where for $g = 1$, $s_g^{(1)} = s$; $t_g^{(1)} = t$ and

where for $g = 2$, $s_g^{(1)} = 1$; $t_g^{(1)} = 1$. Note that the superscript 1 refers to triangle 1. Analogous expressions may be written for triangles 2, 3 and 4. See Appendix 11 for details.

The coefficients $a_2^{(1)}$ and $a_3^{(1)}$ are interpreted as the amount of harmonic present at corner points 2 and 3 for triangle 1. These coefficients are not group dependent. They can be calculated if the corner point values of the form function are known in both groups. See Appendix 11 for details.

The coefficients $\mu_x^{(1)}$, $\mu_y^{(1)}$, $C_x^{(1)}$ and $C_y^{(1)}$ are calculated by forcing the reconstructed form function $F_g^R(x,y)$ in equation 6.15 to match known corner point 2 and 3 values of the form function and the surface average of the form function for triangle 1. This information (3 F_g^R - related values for triangle 1) plus the condition $[\mu_x^{(1)}]^2 + [\mu_y^{(1)}]^2 = -[B_1^{(1)}]^2$ determines the four coefficients $\mu_x^{(1)}$, $\mu_y^{(1)}$, $C_x^{(1)}$ and $C_y^{(1)}$.

The coefficient C_1 is calculated by forcing the sum of the volume integrals of the four triangular reconstructed form functions to match the known volume-average of the form function.

The 5 coefficients $\mu_x^{(1)}$, $\mu_y^{(1)}$, $C_x^{(1)}$, $C_y^{(1)}$ and C_1 are all actually group dependent in the general case. However, to avoid further notational complexity, a subscript g is not added to these quantities. The quantities are group dependent because differing values of these parameters

are calculated depending on whether, for example, C_1 is calculated by matching the fast or the thermal volume-average of the form function. In general, fast group information is used to determine these 5 parameters when the fast form function is being reconstructed and thermal group information is used to calculate the 5 parameters when the thermal form function is being reconstructed.

Further information about how FORTE calculates the coefficients in the equation 6.15 is contained in Appendix 11.

Because FORTE reconstructs the form function in a PWR assembly as four triangles, there may be discontinuities in the $F_g^R(x,y)$ along the diagonal lines $x = y$ and $x = -y$. FORTE eliminates the discontinuity by taking an average of the discontinuous values of the F_g^R along the diagonal. Several FORTE reconstructed form functions are presented in Appendix 20.

One final point regarding the FORTE theory requires discussion. In general, $[\mu_x^{(1)}]^2$ or $[\mu_y^{(1)}]^2$ may be calculated to be a negative real number. If this happens then the value of the $\mu_x^{(1)}$ or $\mu_y^{(1)}$ will be a pure imaginary number. This is dealt with in FORTE through the use of hyperbolic trigonometric functions instead of the normal sines and cosines in equation 6.15. If $\mu^2 = -\alpha^2$ where α is a positive real number, then $\cos \mu x = \cosh \alpha x$ and $\frac{1}{\mu} \sin \mu x = \frac{1}{\alpha} \sinh \alpha x$.

6.3 FORTE HETEROGENEOUS FLUX RECONSTRUCTION RESULTS

To test how well the non-polynomial form functions match the shapes of the reference form functions, FORTE was employed with reference corner point, surface-averaged and volume-averaged form function values used to determine the coefficients of the reconstructed form function. The thermal flux in the center node 5 of benchmark problems 5 and 7 was reconstructed. The maximum error in the pointwise flux for benchmark problem 5 (the infinite checkerboard) was 1.6%. The maximum error in the reconstructed flux for benchmark problem 7 (the small, unrodded 3-by-3 node quarter core) was 2.7%.

These results were encouraging enough that a full practical implementation of the heterogeneous flux reconstruction scheme was tried for benchmark problems 5 and 7. Thus, a QUANDRY-ADF-AXS run yielded approximate fluxes and currents for the center nodes of these problems. These node-averaged fluxes and currents were used in CHIME runs to determine the heterogeneous corner point fluxes (See Chapter 4). Then 9 F_g^R values for FORTE were approximated as follows:

1. At the four corners of the assembly, n = 1,2,3,4

$$F_g^{R(n)} \simeq \frac{\phi_g^{\text{interpolated}(n)}}{A_g^{(n)}}$$

2. For the four surfaces of the assembly

$$\bar{F}^{R}_{g_{u^{\pm}}} \simeq \frac{\bar{\phi}^{\text{QUANDRY-ADF-AXS}}_{g_{u^{\pm}}}}{\bar{A}_{g_{u^{\pm}}}} \quad ; \; u = x,y$$

3. For the volume of the assembly

$$\bar{\bar{F}}^{R}_{g} \simeq \frac{\bar{\bar{\phi}}^{\text{QUANDRY-ADF-AXS}}_{g}}{\bar{\bar{A}}_{g}}$$

where A_g is the flux from an inexpensive assembly calculation.

Note that in approximating the surface and volume averages of F^R_g, the additional approximation has been made that the integral of the quotient ϕ_g/A_g is approximately equal to the quotient of the integrals of ϕ_g and A_g.

The results of the practical FORTE heterogeneous flux reconstructions for benchmark problems 5 and 7 are contained in Table 6.1.

Benchmark Problem 5: Infinite Checkerboard of Two Batches of Fuel; in Fuel 1

Group 1: 0.50%

Group 2: 1.56%

Benchmark Problem 7: Central Node of a 3-by-3 Array of assemblies; in Fuel 1

Group 1: 0.43%

Group 2: 3.20%

Table 6.1: The Maximum Percent Error in the FORTE Heterogeneous Flux Reconstructions for Benchmark Problems 5 and 7.

Sections 1 and 2 of Appendix 19 contain the error plots for the FORTE flux reconstructions for benchmark problems 5 and 7 respectively. Sections 1 and 2 of Appendix 20 contain plots of the FORTE reconstructed form functions. Evidence of the triangular nature of the reconstructed form functions is clearly exhibited in some of these plots, especially in Figures A19.4 and A20.4 for the thermal reconstruction of the flux in the center node of benchmark problem 7.

FORTE was next employed to reconstruct the heterogeneous flux in the fueled assemblies of benchmark problem 6. This is the symmetric, 4-by-4 node, unrodded quarter core with the explicitly represented steel baffle. Heterogeneous node-averaged fluxes were derived from a QUANDRY-ADF-AXS calculation. Extended assembly calculations were employed to find the equivalence parameters for QUANDRY. The node-averaged fluxes from QUANDRY were input into CAMPANA to interpolate heterogeneous corner point values. Then 9 F_g^R values for FORTE were approximated in the same fashion that they were for benchmark problems 5 and 7 (i.e., as ratios of global flux quantities to assembly flux quantities). The FORTE average and maximum percent errors in the reconstructed flux for benchmark problem 6 are presented in Figure 6.2.

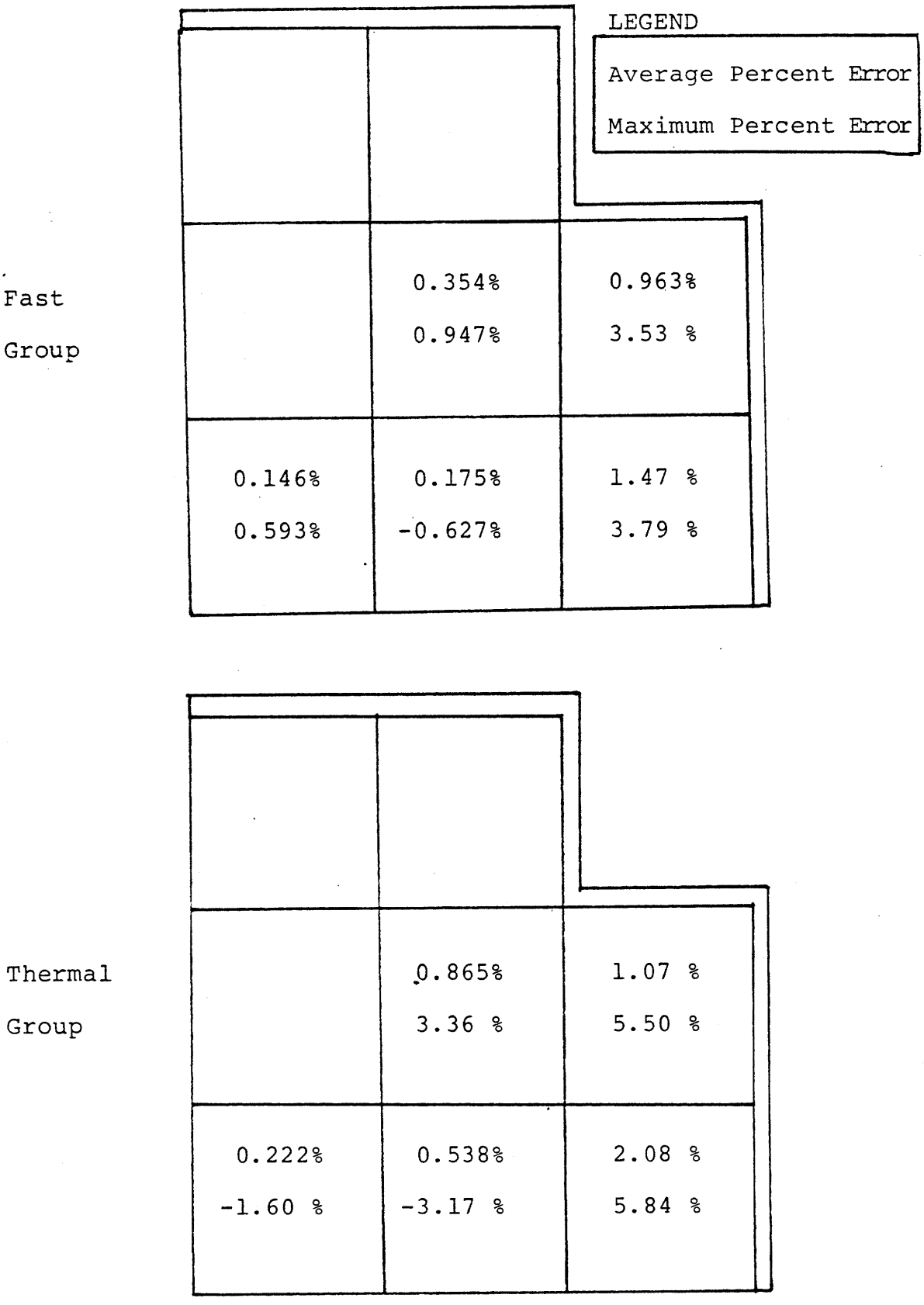

Figure 6.2: FORTE Heterogeneous Flux Reconstruction Results for Benchmark Problem 6

For interior PWR assemblies, the results from benchmark problems 5, 6 and 7 show that FORTE heterogeneous flux reconstructions are a maximum of about 3.5 % in error. For PWR assemblies adjacent to the steel baffle at the edge of the core, the FORTE flux reconstructions are up to 5.9% in error.

There are at least two reasons for the poor results near the baffle. The first is that the approximate heterogeneous corner point fluxes from CAMPANA were already up to 5.5% in error along the baffle-fuel interface. Thus, better corner point interpolation procedures need to be developed if better results are desired.

The second reason for the poor results is that the non-polynomial shapes employed by FORTE cannot always accurately match the reference form function shapes. The most serious shortcoming of FORTE in this regard is the shape it allows for form functions on the surface of an assembly. The allowed shape is a combination of sine and cosine terms from the fundamental part of the solution and a linear function for the harmonic part of the solution. Unfortunately, for certain combinations of assemblies (for example, along the y- face of assembly 15 in benchmark problem 6) the reference form function shape along the surface of the assembly has an exponential

character which the non-polynomial form functions in FORTE cannot duplicate. (Note that the exponential functions in the harmonic terms of the forte reconstructions do not apply to the shape of the form function along the surface of an assembly.) Some initial efforts at M.I.T. are under way to develop non-polynomial form functions which can deal with an exponential shape of the form function on the surfaces of assemblies [43].

Section 3 of Appendix 19 contains the error plots for the FORTE flux reconstructions for benchmark problem 6. Section 3 of Appendix 20 contains plots of the FORTE reconstructed form functions.

The purpose of the heterogeneous flux reconstruction is to be able to calculate pin powers. In general, the maximum pointwise error in the thermal reconstructed flux is a conservative indicator of the maximum error in the pin power at B. O. L. This is because the B. O. L. heterogeneous cross sections are constant within a fuel assembly and are known. Thus, cross section information does not contribute to pin power error. Any error in the pin power is because of errors in the fast and thermal reconstructed fluxes. Since about 85% of a fuel pin's power is generated in the thermal group, and since errors in the reconstructed fast flux are generally smaller than

errors in the reconstructed thermal flux, it follows that the maximum pointwise error in the thermal reconstructed flux is a conservative indicator of the maximum error in the pin power.

This hypothesis has been tested by calculating the percent error in power of the coldest pin in node 11 of benchmark problem 6. The maximum percent error in the thermal reconstructed flux occurred in this pin and was 5.5%. However, the percent error in the pin power is only 3.91%. Thus, by using the FORTE flux reconstruction method described here, the pin power in benchmark problem 6 can be reconstructed to within about 4% maximum error.

Figure 6.2 shows errors in the thermal FORTE flux reconstruction of 5.5% for node 11 and 5.84 % for node 15. In an effort to sort out the sources of error in this reconstruction, reference corner point, surface-averaged and volume-averaged form function data for FORTE was calculated directly from the reference form functions in Appendix 16 (i.e., these reference form functions are based on extended assembly calculations). By inputting this reference data into FORTE one is testing only the ability of the FORTE form functions to match the reference form functions. The results for nodes 11 and 15 are displayed in Figure 6.3.

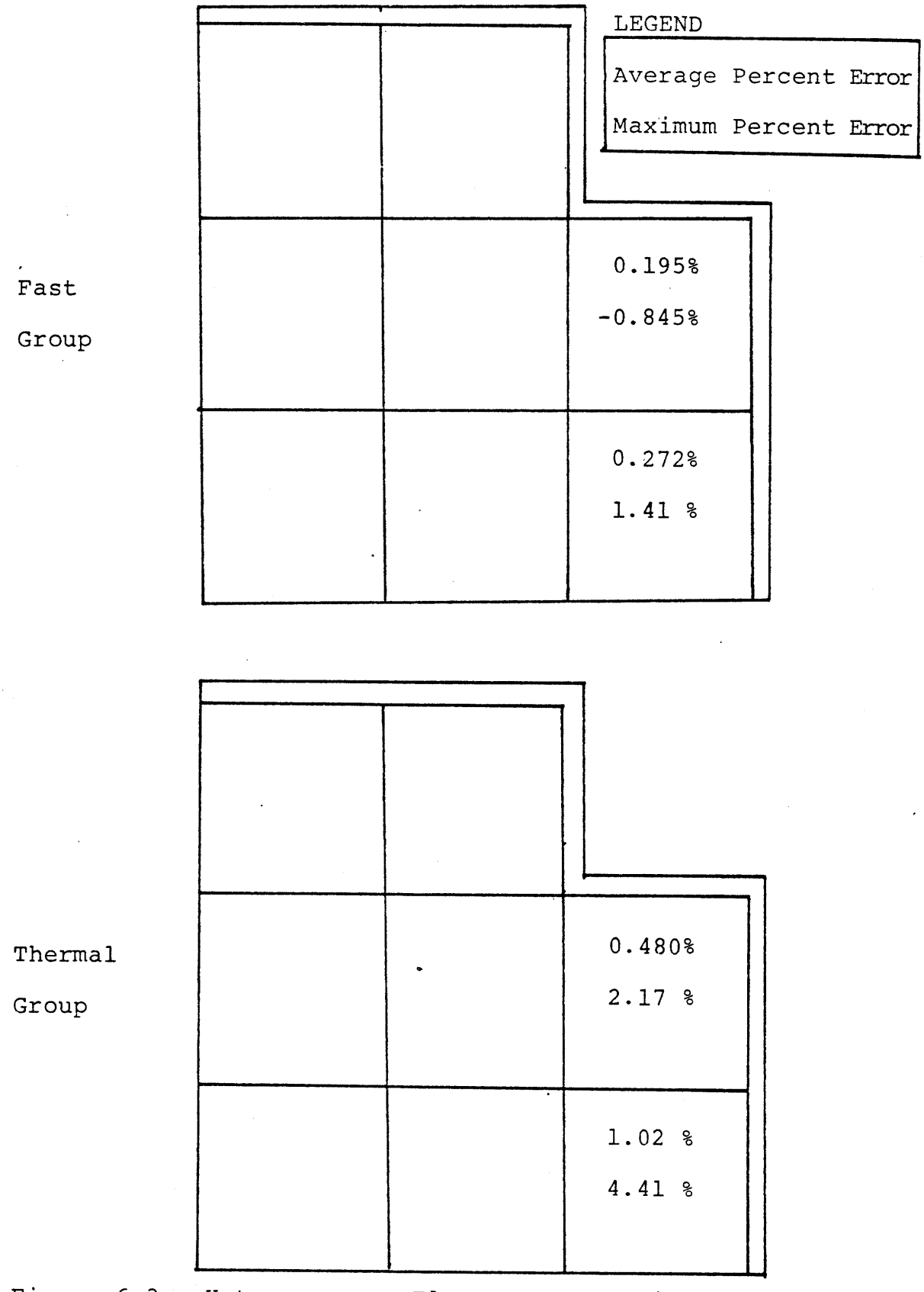

Figure 6.3: Heterogeneous Flux Reconstruction Results for Benchmark Problem 6 Using Reference Form Function Data for FORTE from Appendix 16

The result for node 15 in the thermal group from Figure 6.3 is somewhat disappointing. It shows that even when reference data is input into FORTE, the flux reconstruction is still a maximum of 4.41 % in error. As mentioned earlier, this is mostly because of the inablilty of FORTE to reconstruct form functions with an exponential shape along a surface of the assembly.

Section 4 of Appendix 19 contains the error plots for the FORTE flux reconstructions using reference form function data from Appendix 16 for benchmark problem 6. Figure A19.18 displays large percent errors along the surface of node 15. This is a graphical presentation of the inability of the FORTE form functions to match the reference exponential shape of the reference form function along the surfaces of the assembly. Section 4 of Appendix 20 contains the actual plots of the FORTE reconstructed form functions for nodes 11 and 15 of benchmark problem 6. These can be compared with the reference form function plots in Appendix 16.

A review of the reference form function shapes for node 11 of benchmark problem 6 in Appendix 15 (these form functions are <u>not</u> based on extended assembly calculations) reveals that these shapes are probably even harder to model than the ones in Appendix 16 (which are based on extended assembly calculations). This is

because for PWR assemblies at the edge of the core next to the steel baffle, the flux reconstruction is made much more difficult because of the severe flux depression that takes place near the baffle. An assembly flux shape based on zero-net-current boundary conditions at the edge of the assembly does not reflect this severe flux depression. Thus if the global flux shape is to be matched by the product $A_g * F_g^R$, then the form function, F_g^R, will also have to drop precipitously near the baffle. The non-polynomial functions for F_g^R in FORTE do not fit this behavior well. To show this, reference form factor data from Appendix 15 was input into FORTE for node 11 of benchmark problem 6. Even with this reference data, the maximum percent error in the fast and thermal flux reconstructions was 7.83 % and 14.1% respectively.

Section 5 of Appendix 19 contains the error plots for the FORTE flux reconstructions using reference form function data from Appendix 15 for benchmark problem 6. Section 5 of Appendix 20 contains the actual plots of the FORTE reconstructed form functions for node 11 of benchmark problem 6.

Chapter 7

SUMMARY AND CONCLUSIONS

7.1 OVERVIEW OF THE INVESTIGATION

The objective of this research effort was to apply the analytic nodal method and nodal equivalence theory as embodied in the nodal code, QUANDRY, to the neutronic anaysis of pressurized water reactors (PWRs). This included applying QUANDRY to the calculation of normalized assembly power distributions for PWRs and devising, implementing and testing a heterogeneous PWR flux reconstruction scheme for QUANDRY.

The motivation for much of this research is the desire to develop more efficient and faster methods for obtaining detailed spatial power distributions in PWRs. Currently, fine-mesh finite difference calculations are used for this purpose in the American utility industry. However, these methods are very expensive and thus more inexpensive methods are desired.

Chapter 2 of this thesis contains a review of the analytic nodal method and nodal equivalence theory as embodied in the nodal code, QUANDRY. The concepts found in this chapter are not new; however, an understanding of them is essential for comprehending the ideas and results in the rest of this thesis. This chapter also presents the

inexpensive methods which were used to generate assembly equivalence parameters from fine-mesh heterogeneous assembly calculations.

In Chapter 3, nodal equivalence theory based on assembly calculations was applied to several rodded and unrodded PWR benchmark problems. The disappointing conclusion was reached that the consistent reduction in the error of normalized assembly power densities that Smith [27] found for BWRs does not hold up for PWRs. It was found that both conventional homogenization techniques (based soley on flux-weighted assembly homogenized cross sections) and Smith's nodal equivalence theory (based on assembly homogenized cross sections and assembly discontinuity factors) yielded maximum errors in normalized assembly power densities of less than 2% for unrodded PWR cores.

However, it was found that the conventional homogenization techniques yielded rather poor (about 7% error) estimates of the heterogeneous assembly surface-averaged fluxes. When such fluxes were found using nodal equivalence parameters based on assembly calculations for PWRs, the maximum error in these surface fluxes was less than 2%. This was an encouraging result because such heterogeneous surface fluxes are input into schemes for reconstructing the detailed heterogeneous pointwise flux within a node.

In Chapter 4, three methods (CHIME, CARILLON and CAMPANA) were introduced for interpolation of the heterogeneous flux at assembly corner points. These methods use the node-averaged fluxes and currents from QUANDRY calculations to find approximate values of the heterogeneous flux at the corners of PWR assemblies. Such corner point flux information is required by the pointwise flux reconstruction methods introduced in Chapters 5 and 6.

The corner point flux interpolation methods introduced in Chapter 4 were shown to be able to interpolate the corner point fluxes for assemblies in the interior of a large PWR to within a few percent accuracy. For assemblies at the edge of a PWR core next to a steel baffle, the interpolated fluxes were found to within 5.5% accuracy.

In Chapters 5 and 6, the form function method was introduced as a method of heterogeneous flux reconstruction. This method consists of finding analytic form functions which can be multiplied into an inexpensive heterogeneous assembly flux shape to yield the global flux shape within a PWR assembly.

In Chapter 5 bi-quadratic and bi-quartic polynomials were tested as form functions. It was found that the

shapes of the reference form functions (defined as the global reference flux divided by the assembly flux) were not well fit by the bi-quadratic or bi-quartic polynomial functions. Thus, even when reference boundary value fluxes and currents were used to determine the coefficients of the polynomials, the reconstructed pointwise fluxes in the interior of an assembly were up to 5.5% in error.

In Chapter 6, the group diffusion equations were employed to derive a coupled set of differential equations for the reference form functions. A solution technique was then used to solve the coupled set of equations in an approximate fashion. The resulting solution yielded a non-polynomial, approximate analytic form function. A computer code called FORTE was written which automates the calculation of this non-polynomial form function.

Use of the FORTE method on realistic PWR cores was shown to yield maximum errors in the pointwise reconstructed flux of 3.5% for assemblies in the interior of a PWR core. For assemblies near the steel baffle at the edge of the core, extended assembly criticality calculations were employed in which the baffle and water reflector were included. FORTE calculations based on such extended assembly calculations were shown to yield flux reconstructions with a maximum error of 5.9% for points in the fuel near the

baffle. Pin powers calculated on the basis of FORTE results were shown to be within 4.0% maximum error.

7.2 RECOMMENDATIONS FOR FUTURE RESEARCH

During the course of this investigation, many items of potential interest have been left unresolved. Many of these items warrant additional investigation, and this section contains a description of the potential research areas.

7.2.1 Improved Methods of Heterogeneous Corner Point Interpolation

The methods of corner point interpolation presented in Chapter 4 are all based on the assumption of a quadratic flux or form factor for the surfaces of PWR assemblies. During the course of this research it was found that flux and form factor shapes on the surfaces of assemblies often have an exponential character to them. Thus further research implementing functions which can model these exponentials into the corner point interpolation schemes would be desirable.

7.2.2 Elimination of Extended Assembly Calculations

Many conventional PWR analysis methods use albedo boundary conditions to eliminate the core baffle and reflector. These albedo boundary conditions are usually calculated from a fine-mesh diffusion theory calculation at B.O.L. Since the objective of this research was to eliminate the need for such fine-mesh calculations, this procedure was not employed. Further research into alternate, inexpensive methods of obtaining albedo boundary conditions for PWRs would be helpful. Response matrix methods for representing the baffle and reflector may be useful here.

If such albedo conditions could be found in an inexpensive manner, then QUANDRY could be run without using equivalence parameters from extended assembly calculations. However, it was shown in Chapter 6 that the extended assembly flux shape was required to perform reasonably accurate pointwise flux reconstructions. If the albedo boundary conditions were known, it is possible that the extended assembly flux shapes could be replaced by a single assembly flux shape calculated on the basis of the albedo boundary conditions.

7.2.3 Application of Flux Reconstruction Methods to PWR Depletion Calculations

All of the flux reconstructions performed in this thesis were for PWR benchmark problems at B.O.L. The effect of fuel depletion on these flux reconstruction methods should be investigated. Such research is already being pursued by H. Khalil at M.I.T.

7.2.4 Improved Flux Reconstruction Methods

In Chapter 6 a coupled set of differential equations were presented for the reference form functions. Many alternate numerical and analytic solution techniques could be developed for solving these equations or a simplified form of them.

REFERENCES

1. A. F. Henry, Nuclear Reactor Analysis, M.I.T. Press, Cambridge, MA, 1975.

2. W. R. Cadwell, "PDQ-7 Reference Manual," WAPD-TM-678, Bettis Atomic Power Laboratory, 1967.

3. H. C. Honeck, "Simulation of a Parallel Processor on a Serial Processor: The Neutron Diffusion Equation," Proceedings of the International Topical Meeting on 'Advances in Mathematical Methods for the Solution of Nuclear Engineering Problems,' Munich, W. Germany, Vol. 2, April 1981. pgs. 529-548.

4. W. M. Stacey, Jr., Variational Methods in Nuclear Reactor Physics, Academic Press, New York, NY, 1974.

5. F. A. R. Schmidt, "Finite Element Application to Global Reactor Analysis," Proceedings of the International Topical Meeting on 'Advances in Mathematical Methods for the Solution of Nuclear Engineering Problems,' Munich, W. Germany, Vol. 1, April 1981. pgs. 315-334.

6. Z. Weiss, S. O. Lindahl, "High-Order Response Matrix Equations in Two-Dimensional Geometry," Nuclear Science and Engineering, Vol. 58, No. 2, 1975. pgs. 166-181.

7. J. J. Dorning, "Modern Coarse-Mesh Methods - A Development of the 70's," ANS Proceedings of the Topical Meeting on 'Computational Methods in Nuclear Engineering', Williamsburg, Virginia, April 1979. pgs. 3-1 -- 3-32.

8. R. Frohlich, "Summary Discussion and State of the Art Review for Coarse-Mesh Computational Methods," Atomkernenergie (ATKE) , Bd. 30, Lfg. 2, 1977. pgs. 152-158.

9. D. L. Delp, D. L. Fischer, J. M. Harriman, M. J. Stedwell, "FLARE, A Three-Dimensional Boiling Water Reactor Simulator," GEAP-4598, General Electric Company, July 1964.

10. Nuclear Associates International Corporation, "Advanced Recycle Methodology Program, Computer Code Manuals," EPRI-CCM-3, 1977.

11. B. A. Zolotar, "Nodal Methods for Utility Applications," Proceedings of the Specialist Meeting on Calculation of 3-Dimensional Rating Distributions in Operating Reactors," Paris, France, Nov. 1979.

12. R. A. Shober, A. F. Henry, "Nonlinear Methods for Solving the Diffusion Equation," MITNE-196, Department of Nuclear Engineering, M.I.T., November 1976.

13. H. D. Fischer, H. Finnemann, "The Nodal Integration Method - A Diverse Solver for Neutron Diffusion Problems," Atomkernenergie (ATKE), Bd. 39, Lfg. 4, 1981.

14. G. Greenman, K. Smith, A. F. Henry, "Recent Advances in an Analytic Nodal Method for Static and Transient Reactor Analysis," ANS Proceedings of the Topical Meeting on 'Computational Methods in Nuclear Engineering,' Williamsburg, Virginia, Vol. 1, pgs. 3-49 -- 3-72, April 1979.

15. G. Greenman, "Derivation of an Analytic Nodal Method Employing the Quadratic Transverse Leakage Approximation," Special Problem in Nuclear Engineering for Professor A. F. Henry, M.I.T., August 1977.

16. K. S. Smith, "An Analytic Nodal Method for Solving the Two-Group, Multidimensional, Static and Transient Neutron Diffusion Equation," N. E. Thesis, Department of Nuclear Engineering, M.I.T., Cambridge, MA, March 1979.

17. F. Bennewitz, H. Finnemann, M. R. Wagner, "Higher Order Corrections in Nodal Reactor Calculations," ANS Transactions, Vol. 22, 1975. pgs. 250-252.

18. Argonne Code Center: Benchmark Problem Book, ANL-7416, Supplement 2, 1977.

19. W. H. Werner, H. Finnemann, S. Langenbuch, Two- and Three-Dimensional BWR Kinetics Benchmark Problem," ANS Transactions, Vol. 23, June 1976. pgs. 215-216.

20. S. Langenbuch, W. Maurer and W. Werner, "Coarse-Mesh Nodal Diffusion Method for the Analysis of Space-Time Effects in Large Light Water Reactors," Nuclear Science and Engineering, Vol. 63, 1977. pgs. 437-456.

21. A. Jonnson, J. R. Rec, U. N. Singh, "Verification of a Fuel Assembly Spectrum Code Based on Integral Transport Theory," ANS Transactions, Vol. 28, pgs. 778-779, 1978.

22. G. Pierini, "A Consistent Homogenization Procedure to Obtain Few-Group Cell Parameters," Atomkernenergie (ATKE), Bd. 34, Lfg. 4, 1979. pgs. 269-274.

23. A. F. Henry, B. A. Worley, and A. A. Morshed, "Spatial Homogenization of Diffusion Theory Parameters," Paper presented at the IAEA Technical Committee Meeting on Homogenization Methods in Reactor Physics, Lugano, Switzerland , Nov. 1978.

24. B. A. Worley, A. F. Henry, "Spatial Homogenization of Diffusion Theory Parameters," MITNE-210, Department of Nuclear Engineering, M.I.T., 1977.

25. R. A. Bonalumi, "Rigorous Homogenized Diffusion Theory Parameters for Neutrons," Nuclear Science and Engineering, Vol. 77, 1981. pgs. 219-229.

26. K. Koebke, "A New Approach to Homogenization and Group Condensation," Paper presented at the IAEA Technical Committee Meeting on Homogenization Methods in Reactor Physics, Lugano, Switzerland, Nov. 1978.

27. K. S. Smith, "Spatial Homogenization Methods for Light Water Reactor Analysis," Ph.D. Thesis, Department of Nuclear Engineering, M.I.T., Cambridge, MA, June 1980.

28. K. S. Smith, A. F. Henry, R. A. Loretz, "The Determination of Homogenized Diffusion Theory Parameters for Coarse Mesh Nodal Analysis," Proceedings of the Conference '1980 Advances in Reactor Physics and Shielding', September, 1980, pgs. 294-308.

29. A. Y. Cheng, A. F. Henry, C. L. Hoxie, "A Method for Determining Equivalent Homogenized Parameters," Proceedings of the International Topical Meeting on 'Advances in Mathematical Methods for the Solution of Nuclear Engineering Problems', April, 1981, Vol. 2, pgs. 3-22.

30. D. J. Denver, E. E. Pilat, R. J. Cacciapouti, "Application of Yankee's Reactor Physics Methods to Maine Yankee," YAEC-1115, October 1976.

31. K. Koebke, M. R. Wagner, "The Determination of the Pin Power Distribution in a Reactor Core on the Basis of Nodal Coarse Mesh Calculations," Atomkernenergie (ATKE) , Bd. 30, Lfg. 2, pgs. 136-142, 1977.

32. A. Jonsson, S. Grill, J. R. Rec, "Nodal Imbedded Calculation for the Retrieval of Local Power Peaking from Coarse Mesh Reactor Analysis," Proceedings of the International Topical Meeting on 'Advances in Mathematical Methods for the Solution of Nuclear Engineering Problems', Munich, W. Germany, Vol. 2, pgs 23-41, April 1981.

33. C. L. Hoxie, A. F. Henry, "Reconstruction of Heterogeneous PWR Flux Shapes from Nodal Calculations," ANS Tranactions, Vol 39, Dec. 1981, pgs. 905-906.

34. D. K. Parsons, " Application of Response Matrix Methods to PWR Analysis," Masters Thesis, Department of Nuclear Engineering, M.I.T., Cambridge, MA, June 1982.

35. P. J. Finck, C. L. Hoxie, H. S. Khalil, D. K. Parsons, A. F. Henry, "The Application of Nodal Methods to Light Water Reactors," ANS Topical Meeting on 'Advances in Reactor Physics and Core Thermal Hydraulics, Kiamesha Lake, NY, September, 1982.

36. K. S. Smith, "Homogenization and Space-Dependent Neutronics Within the Context of an Analytic Nodal Method," Special Problem in Nuclear Engineering for Professor A. F. Henry, M.I.T., May 1979.

37. L. A. Hageman, C. J. Pfeifer, "The Utilization of the Neutron Diffusion Program PDQ-5," WAPD-TM-395, Bettis Atomic Power Laboratory, 1965.

38. R. A. Loretz, "The Determination of Equivalent Diffusion Theory Parameters by Local Implementation Of the Koebke Method," Master of Science Thesis, Department of Nuclear Engineering, M.I.T., Cambridge, MA, August 1980.

39. J. H. Wilkinson, The Algebraic Eigenvalue Problem, Clarendon Press, Oxford, England, 1965.

40. R. S. Varga, Matrix Iterative Analysis, Prentice-Hall, Inc., Englewood Cliffs, N.J., 1962.

41. S. Nakamura, Computational Methods in Engineering and Science With Applications to Fluid Dynamics and Nuclear Systems, John Wiley and Sons, New York, N.Y., 1977.

42. T. A. Taiwo, "Determination of Form Functions by Numerical Solution of Two-Group Equations," A Special Problem in Nuclear Engineering Submitted to Professor A. F. Henry, M.I.T., Cambridge, MA May 1982.

43. M. H. Chang, "Study on the Heterogeneous Flux Reconstruction Method Using the Form Functions in a Heterogeneous Assembly," A Special Problem in Nuclear Engineering Submitted to Professor A. F. Henry, M.I.T., Cambridge, MA May 1982.

Appendix 1

INFORMATION FOR CONSTRUCTING HETEROGENEOUS PWR BENCHMARKS

A1.1 Pin-Cell Homogenized Cross Section Sets

Table A1.1 contains the pin-cell homogenized cross section sets used in this thesis to construct heterogeneous PWR benchmark problems. The fuel 1, fuel 2 and water cross sections were supplied by Dr. Robert Lee who was formerly the Project Manager for EPRI contract RP 1936 under which this research was performed. The control rod cross sections were derived from the LSH benchmark problem described in Loretz's Master of Science Thesis [38]. The steel baffle cross sections are rounded-off values fo the baffle cross section set for the Zion 1 reactor in Smith's Nuclear Engineer Thesis [16].

A1.1 Pin-Cell Homogenized Cross Section Sets

	Fuel 1	Fuel 2	Water	Control Rod 1 (CR1)	Control Rod 2 (CR2)	Steel Baffle
D_1	1.5	1.5	1.7	1.1133	1.1133	1.02
D_2	0.4	0.4	0.35	0.18401	0.18401	0.335
Σ_{21}	0.02	0.02	0.035	0.037529	0.0037529	0.0
Σ_{a1}	0.013	0.01	0.001	0.049890	0.0836661	0.00322
Σ_{a2}	0.18	0.15	0.05	0.96726	0.96726	0.146
$\nu\Sigma_{f1}$	0.0065	0.005	0.00	0.00	0.00	0.00
$\nu\Sigma_{f2}$	0.24	0.18	0.00	0.00	0.00	0.00
Σ_{f1}	0.0026	0.002	0.00	0.00	0.00	0.00
Σ_{f2}	0.096	0.072	0.00	0.00	0.00	0.00

Table A1.1: Pin-Cell Homogenized Cross Section Sets

A1.1 Pin-Cell Homogenized Cross Section Set (cont.)

	Fuel 1	Fuel 2	Water	Control Rod 1 (CR1)	Control Rod 2 (CR2)	Steel Baffle
$\kappa\Sigma_{f1}$	8.580 $\times 10^{-14}$	6.600 $\times 10^{-14}$	0.0	0.0	0.0	0.0
$\kappa\Sigma_{f2}$	3.168 $\times 10^{-12}$	2.376 $\times 10^{-12}$	0.0	0.0	0.0	0.0
Σ_{a1} + Σ_{21}	0.033	0.03	0.36	0.087419	0.087419	0.00322

Table A1.1 (cont.): Pin-Cell Homogenized Cross Section Sets

A1.2 Description of Heterogeneous Fueled Assemblies

All PWR benchmark problems in this thesis use heterogeneous, fueled assemblies similar to the one illustrated in Figure A1.2.1. The assemblies contain 15 homogenized pin-cells by 15 homogenized pin-cells for a total of 225 pin-cells. Possible control rod locations are indicated by black pin-cells. If the assembly is rodded, then the pin-cell contains control rod material. If the assembly is unrodded, then the pin-cell contains water.

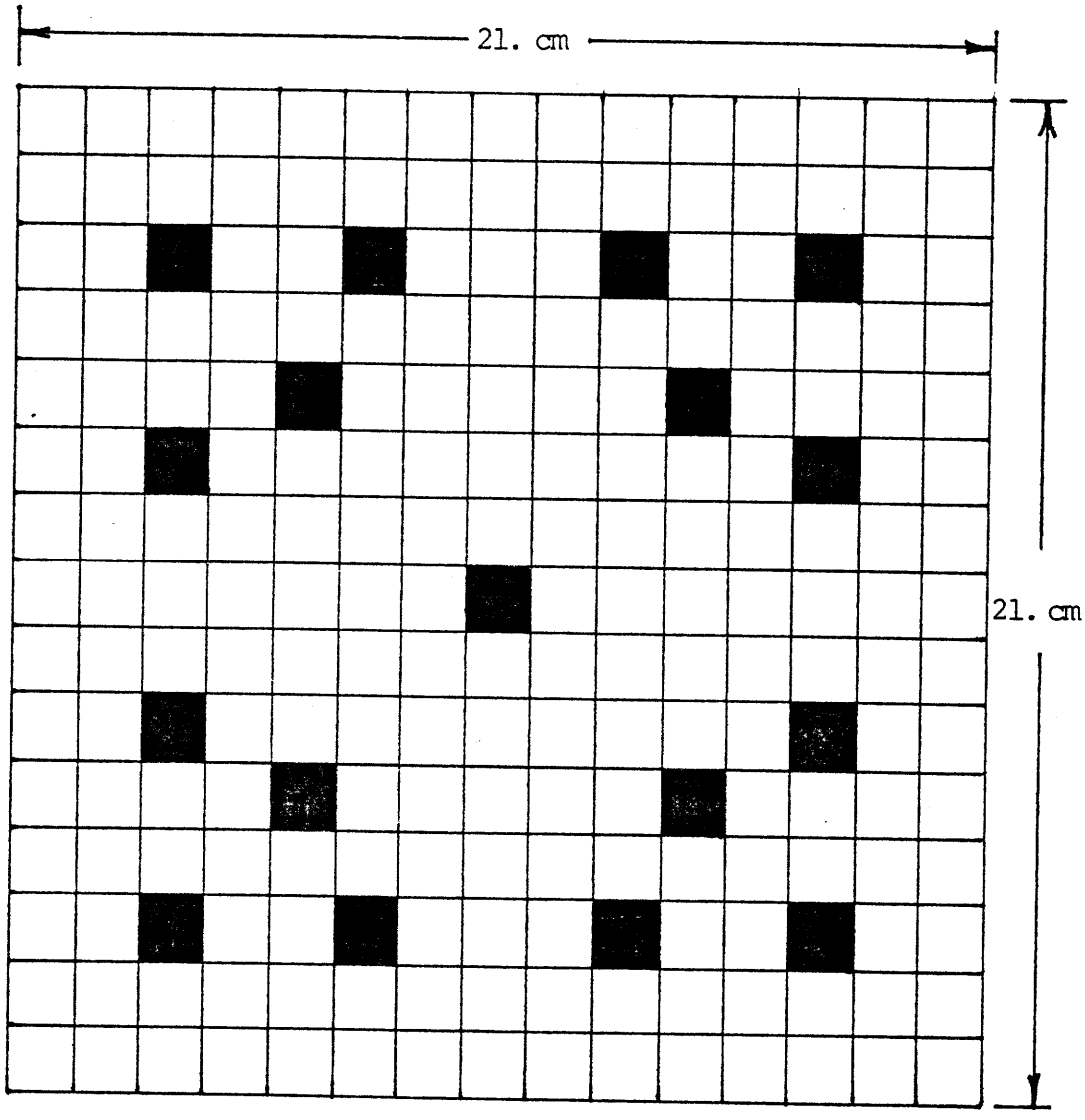

Legend

Homogenized pin-cell containing fuel
(1.4 cm by 1.4 cm)

Homogenized pin-cell containing:
a) control rod if assembly is rodded
b) water if the assembly is unrodded
(1.4 cm by 1.4 cm)

Figure A1.2.1: Heterogeneous, Fueled PWR Assembly

A1.3 Description of Heterogeneous Water-Baffle Nodes

All PWR benchmark problems in this thesis which have explicit steel baffles in the global heterogeneous problem use heterogeneous water-baffle nodes similar to those illustrated in Figure A1.3.1. The nodes are made up of 2.8 cm thick steel baffle material and water. Outer dimensions of all nodes 21 cm by 21 cm.

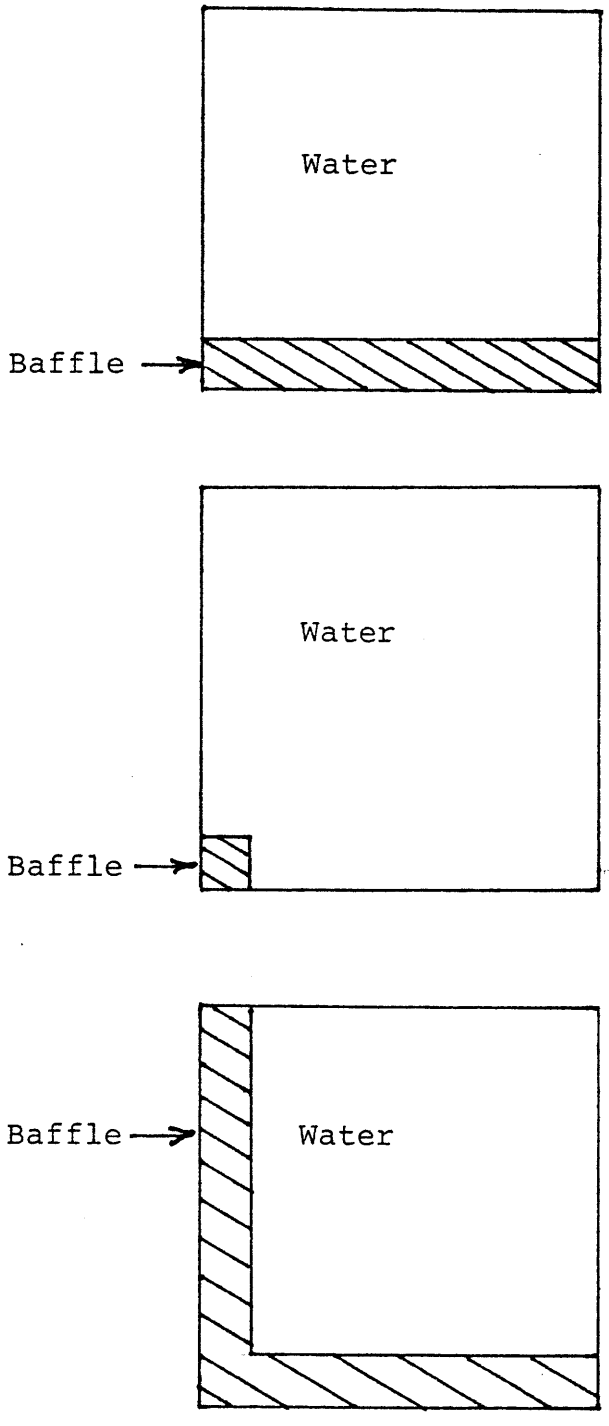

Figure A1.3.1: Heterogeneous Water-Baffle Nodes

Appendix 2

DESCRIPTIONS OF PWR BENCHMARK PROBLEMS

A2.0 Introduction

A2.1 Benchmark Problem 1;
3 x 3, Symmetric Checkerboard, Unrodded

A2.2 Benchmark Problem 2;
3 x 3, Symmetric Checkerboard, Rodded Fuel 1

A2.3 Benchmark Problem 3;
3 x 3, Asymmetric Checkerboard, Rodded Fuel 1

A2.4 Benchmark Problem 4;
3 x 3, Quarter-Core, Some Assemblies Rodded

A2.5 Benchmark Problem 5;
True infinite Checkerboard, Unrodded

A2.6 Benchmark Problem 6;
4 x 4, Quarter-Core, Unrodded, Explicit Baffle

A2.7 Benchmark Problem 7;
3 x 3, Center Node Heterogeneous, Unrodded

A2.8 Benchmark Problem 8;
3 x 3, Quarter-Core, Some Assemblies Rodded,
phi = 0 boundary conditions on two sides

A2.0 Introduction

This appendix contains a description of the arrangement of the assemblies in the PWR benchmark problems used in this thesis. The cross section information and a description of the heterogeneous assemblies for use in these problems is contained in Appendix 1. Cross sections for each assembly (node) are specified on two lines. The first line indicates the cross section set of the most abundant material in the assembly. This will be fuel 1 or fuel 2 for fueled assemblies and water for baffle/reflector nodes. The second line indicates the cross section set for heterogeneities in the assembly. The following abbreviations are used:

W	= heterogeneities are water holes
CR1	= heterogeneities are control rod material 1
CR2	= heterogeneities are control rod material 2
HOMOG.	= assembly is homogeneous.

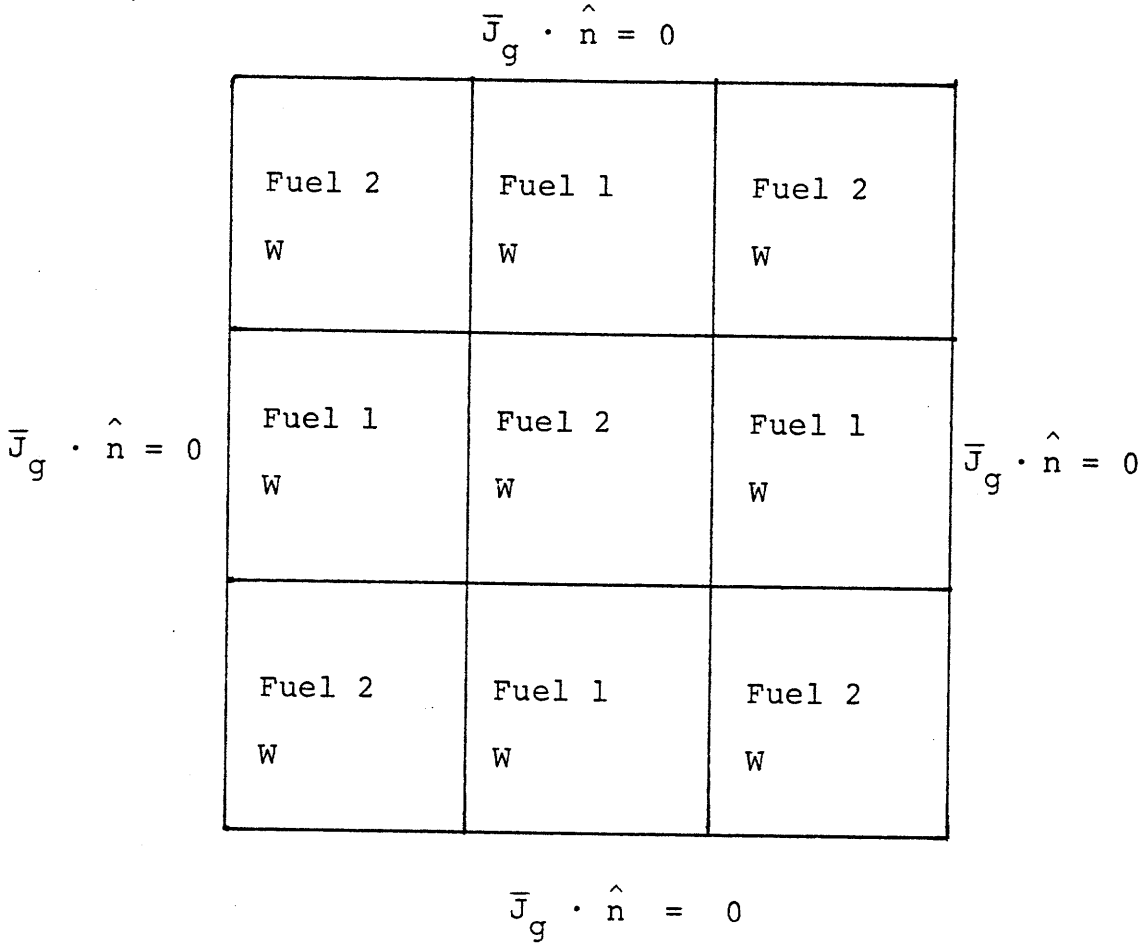

Figure A2.1: Benchmark Problem 1

3 x 3, Symmetric Checkerboard, Unrodded

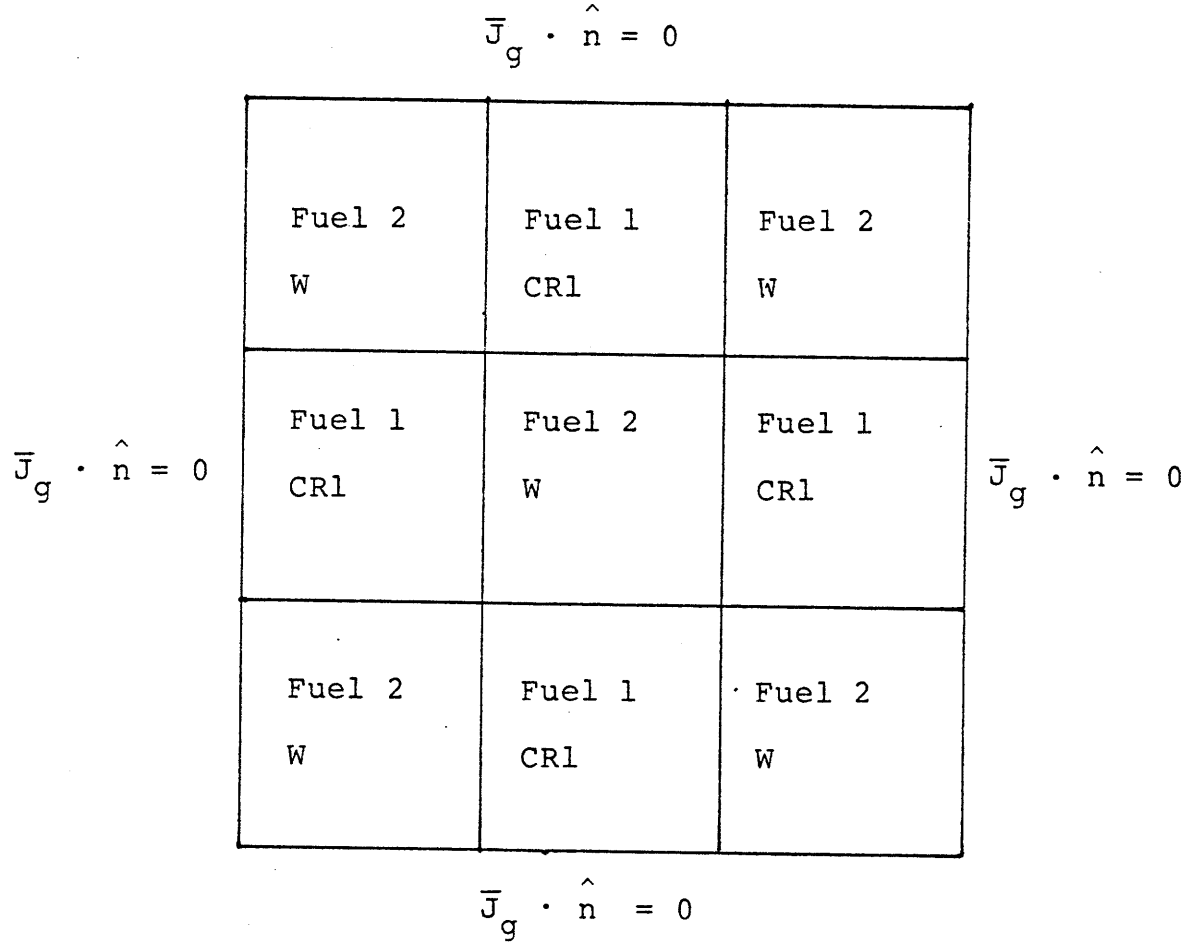

Figure A2.2: Benchmark Problem 2

3 x 3, Symmetric Checkerboard, Rodded Fuel 1

$$\phi_1 = -170\ J_{y1}$$

$$\phi_2 = -640\ J_{y2}$$

$\bar{J}_g \cdot \hat{n} = 0$

Fuel 2 W	Fuel 1 CR1	Fuel 2 W
Fuel 1 CR1	Fuel 2 W	Fuel 1 CR1
Fuel 2 W	Fuel 1 CR1	Fuel 2 W

$\phi_1 = 85\ J_{x1}$

$\phi_2 = 320\ J_{x2}$

$$\bar{J}_g \cdot \hat{n} = 0$$

Figure A2.3: Benchmark Problem 3

3 x 3, Asymmetric Checkerboard, Rodded Fuel 1

$$\phi_g = 2\,\bar{J}_g \cdot \hat{n}$$

$\bar{J}_g \cdot \hat{n} = 0$

Fuel 1 CR1	Fuel 1 CR1	Water Homog.
Fuel 2 W	Fuel 2 CR1	Fuel 1 W
Fuel 1 W	Fuel 2 CR1	Fuel 1 W

$\phi_g = 2\,\bar{J}_g \cdot \hat{n}$

$$\bar{J}_g \cdot \hat{n} = 0$$

Figure A2.4: Benchmark Problem 4

3 x 3, Quarter-Core, Some Assemblies Rodded

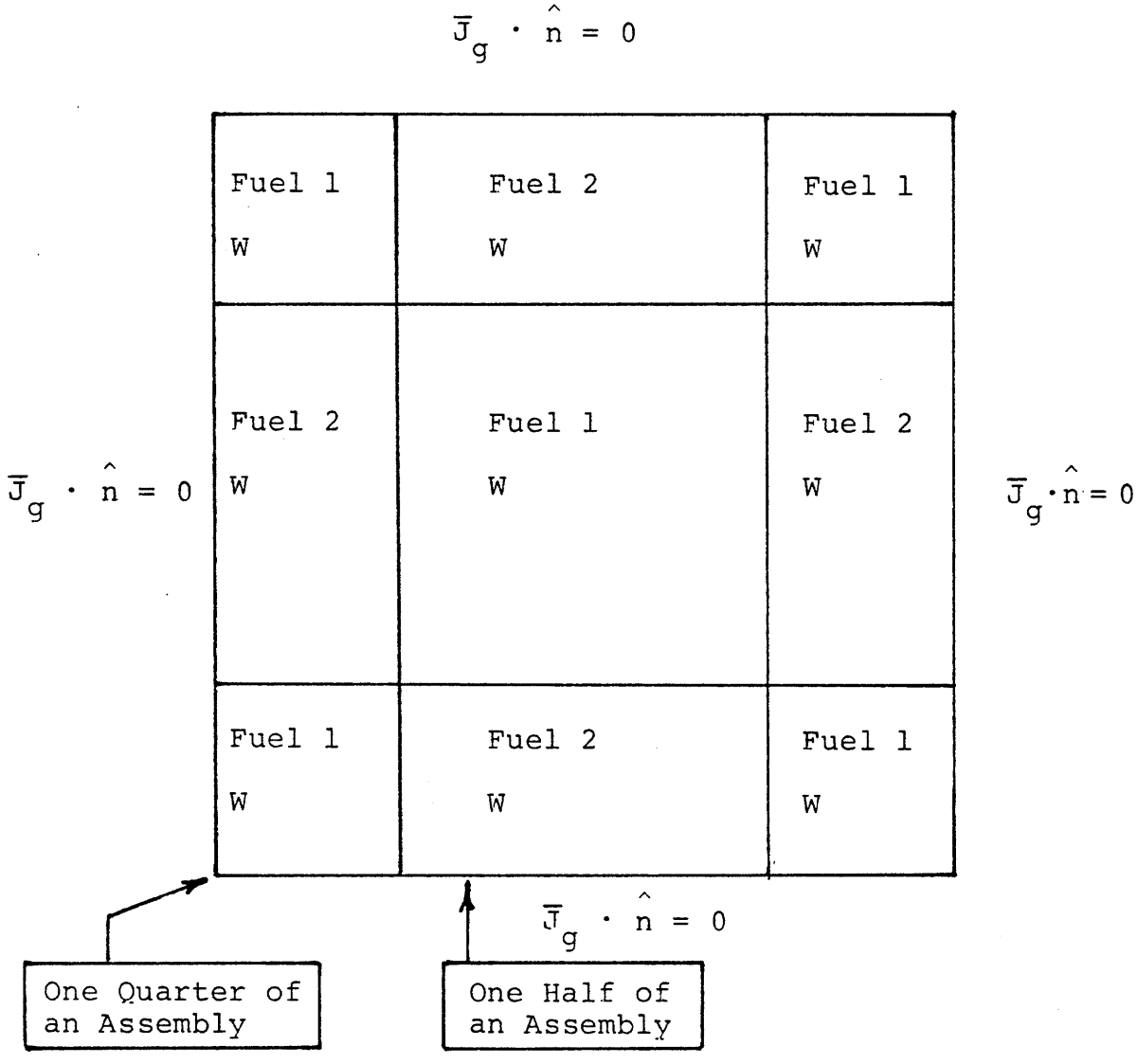

Figure A2.5: Benchmark Problem 5

True Infinite Checkerboard, Unrodded

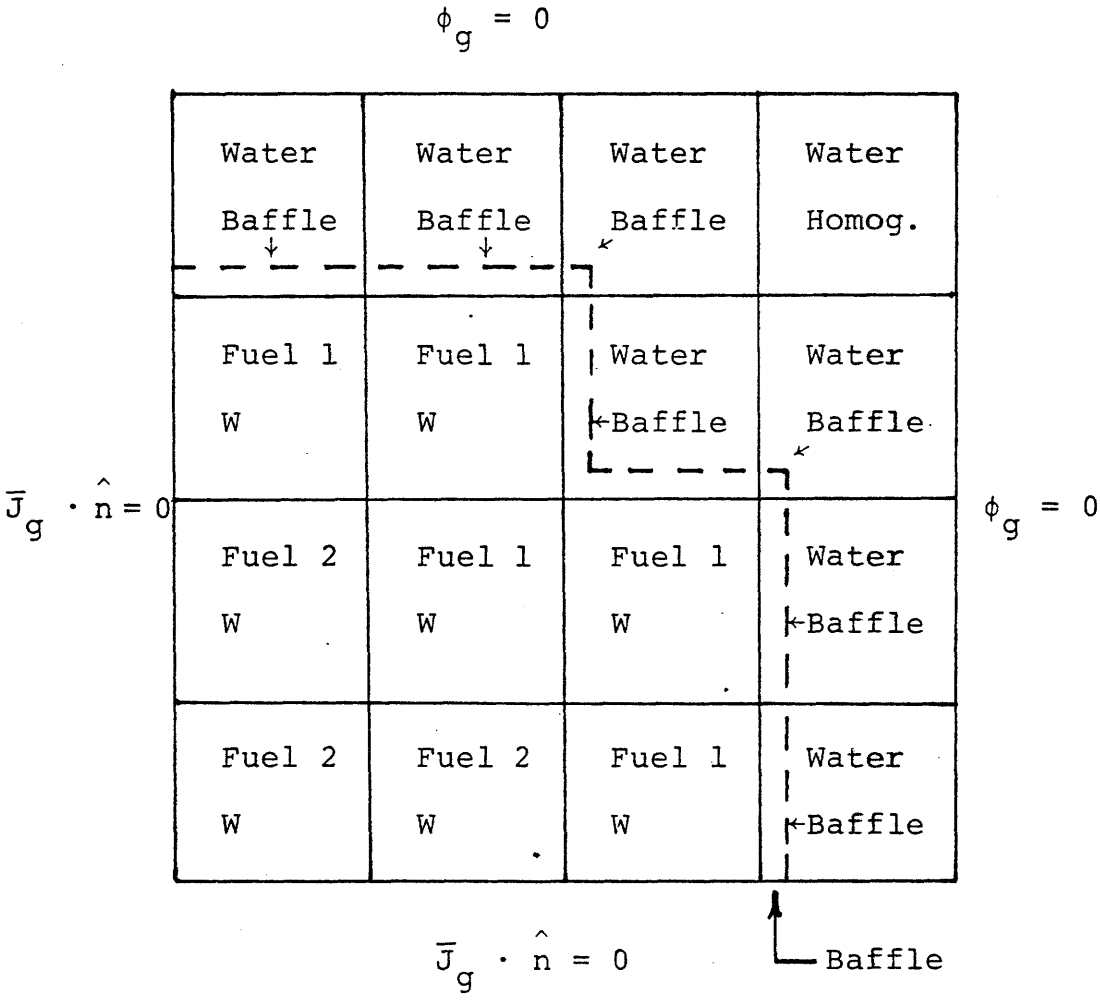

Figure A2.6: Benchmark Problem 6

4 x 4, Quarter-Core, Unrodded, Explicit Baffle

$\phi_g = 0$

$\bar{J}_g \cdot \hat{n} = 0$

Fuel 2 Homog.	Fuel 2 Homog.	Fuel 2 Homog.
Fuel 2 Homog.	Fuel 1 W	Fuel 2 Homog.
Fuel 2 Homog.	Fuel 2 Homog.	Fuel 2 Homog.

$\phi_g = 0$

$\bar{J}_g \cdot \hat{n} = 0$

Figure A2.7: Benchmark Problem 7

3 x 3, Center Node Heterogeneous, Unrodded

$\phi_g = 0$

$\bar{J}_g \cdot \hat{n} = 0$

Fuel 1 CR2	Fuel 1 CR2	Water Homog.
Fuel 2 W	Fuel 2 CR2	Fuel 1 W
Fuel 1 W	Fuel 2 CR2	Fuel 1 W

$\phi_g = 0$

$\bar{J}_g \cdot \hat{n} = 0$

Figure A2.8: Benchmark Problem 8

3 x 3, Quarter-Core, Some Assemblies Rodded

Phi = 0 Boundary Conditions on 2 Sides

Appendix 3

ASSEMBLY HOMOGENIZED CROSS SECTIONS AND ASSEMBLY DISCONTINUITY FACTORS FOR PWRS

A3.0 Introduction

This appendix contains the assembly homogenized cross sections and assembly discontinuity factors used to analyze the PWR benchmark problems in this thesis. The assembly calculations for this appendix were performed using a fine-mesh (one node per pin-cell) heterogeneous QUANDRY calculation.

The notation of Appendix 2 is used to specify the heterogeneous cross section sets for each node. Thus, the cross sections for each assembly are specified on two lines. The first line indicates the cross section set for the most abundant material in the heterogeneous node. The second line indicates the cross section set for heterogeneities in the node.

The notation for discontinuity factors is $f_g^{u\pm}$ where u = x,y and g = 1,2. The assembly surface orientations are

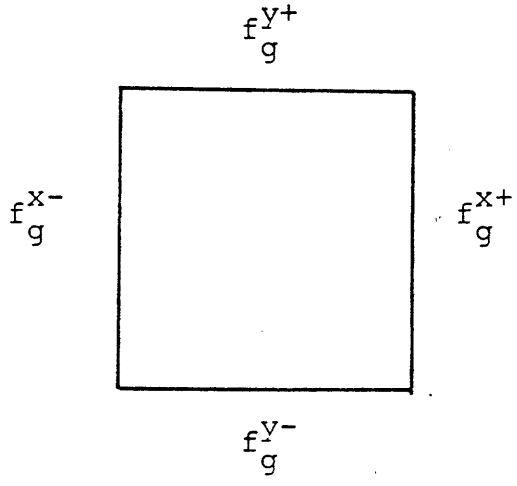

A3.1 ADF/AXS for Unrodded PWR Fuel Assemblies

Table A3.1 contains assembly discontinuity factors (ADF's) and assembly homogenized cross sections (AXS) for the the following two heterogeneous PWR fuel assemblies:

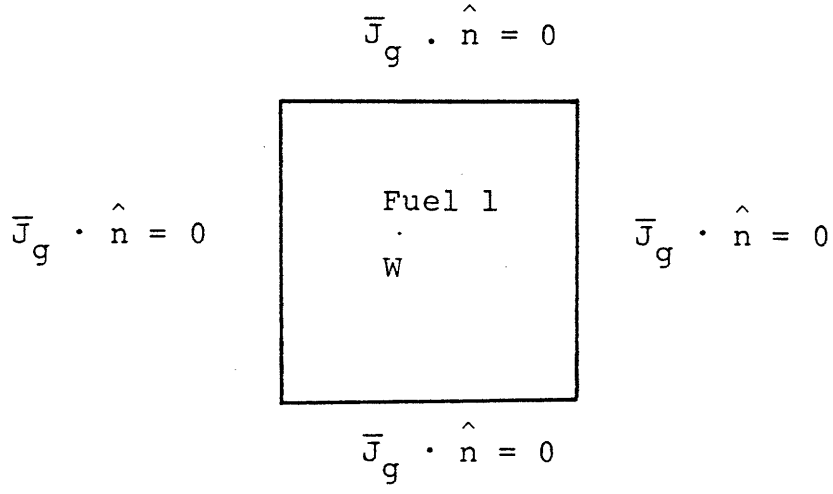

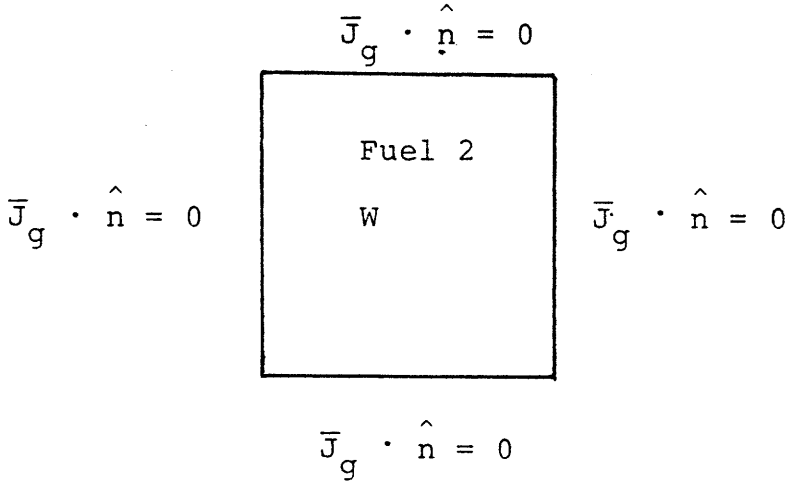

	Fuel 1 W	Fuel 2 W
D_1	1.513	1.513
$\Sigma_{a1} + \Sigma_{21}$	0.03323	0.03045
Σ_{21}	0.02113	0.02113
$\nu\Sigma_{f1}$	0.006012	0.004625
Σ_{f1}	0.002405	0.001850
D_2	0.3950	0.3951
Σ_{a2}	0.1684	0.1414
$\nu\Sigma_{f2}$	0.2186	0.1645
Σ_{f2}	0.08745	0.06580
f_1^{x-}	1.003	1.003
f_2^{x-}	0.9284	0.9380
f_1^{x+}	1.003	1.003
f_2^{x+}	0.9284	0.9380
f_1^{y-}	1.003	1.003
f_2^{y-}	0.9284	0.9380
f_1^{y+}	1.003	1.003
f_2^{y+}	0.9284	0.9380

Table A3.1: ADF/AXS for Unrodded PWR Fuel Assemblies

A3.2 ADF/AXS for Rodded (CR1) PWR Fuel Assemblies

Table A3.2 contains assembly discontinuity factors (ADF's) and assembly homogenized cross sections (AXS) for the following two heterogeneous assemblies:

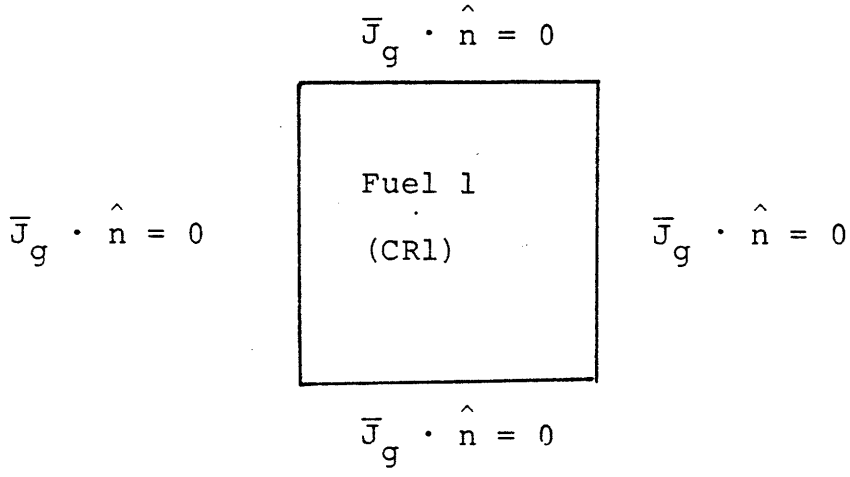

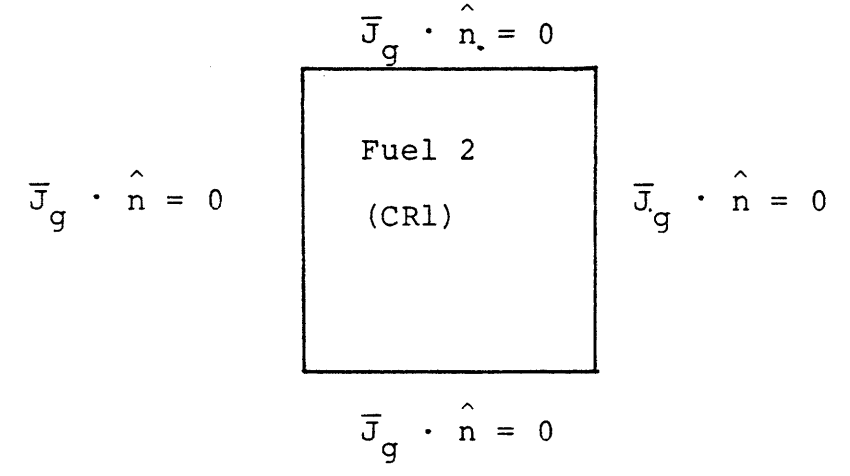

	Fuel 1 CR1	Fuel 2 CR1
D_1	1.463	1.463
$\Sigma_{a1} + \Sigma_{21}$	0.03700	0.03422
Σ_{21}	0.02129	0.02129
$\nu\Sigma_{f1}$	0.006022	0.004633
Σ_{f1}	0.002409	0.001853
D_2	0.3763	0.3772
Σ_{a2}	0.2223	0.1921
$\nu\Sigma_{f2}$	0.2271	0.1707
Σ_{f2}	0.09084	0.06829
f_1^{x-}	1.024	1.025
f_2^{x-}	1.121	1.139
f_1^{x+}	1.024	1.025
f_2^{x+}	1.121	1.139
f_1^{y-}	1.024	1.025
f_2^{y-}	1.121	1.139
f_1^{y+}	1.024	1.025
f_2^{y+}	1.121	1.139

Table A3.2: ADF/AXS for Rodded (CR1) PWR Fuel Assemblies

A3.3 ADF/AXS for Rodded (CR2) PWR Fuel Assemblies

Table A3.3 contains the assembly discontinuity factors (ADF's) and assembly homogenized cross sections (AXS) for the following two heterogeneous assemblies:

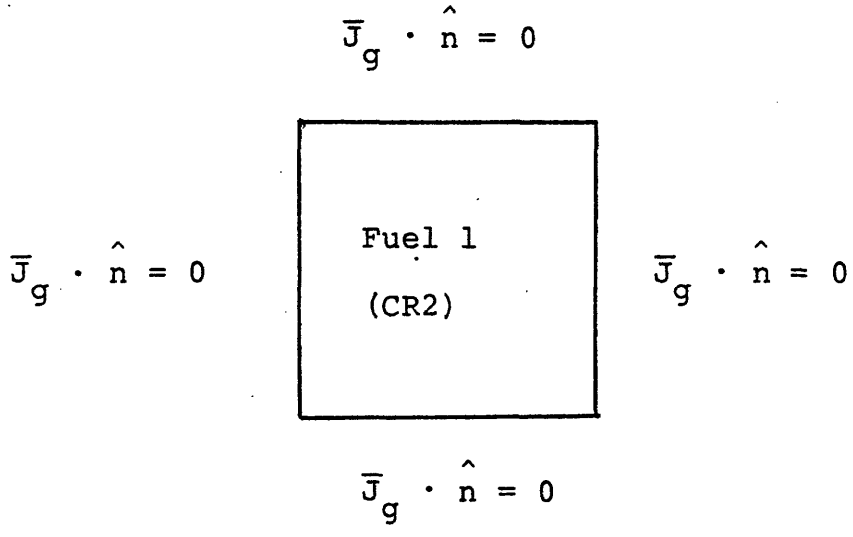

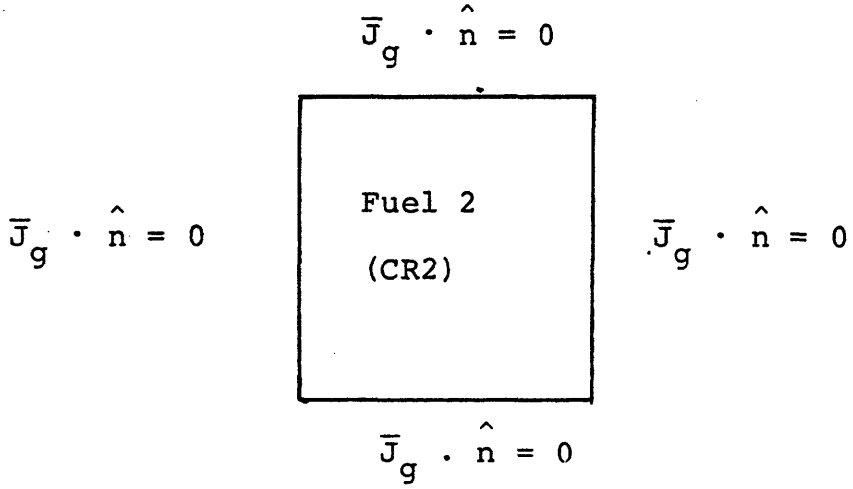

	Fuel 1 CR2	Fuel 2 CR2
D_1	1.463	1.463
$\Sigma_{a1} + \Sigma_{21}$	0.03699	0.03421
Σ_{21}	0.01881	0.01881
$\nu\Sigma_{f1}$	0.006023	0.004633
Σ_{f1}	0.002409	0.001853
D_2	0.3815	0.3818
Σ_{a2}	0.2125	0.1832
$\nu\Sigma_{f2}$	0.2301	0.1727
Σ_{f2}	0.9204	0.06908
f_1^{x-}	1.027	1.028
f_2^{x-}	1.186	1.199
f_1^{x+}	1.027	1.028
f_2^{x+}	1.186	1.199
f_1^{y-}	1.027	1.028
f_2^{y-}	1.186	1.199
f_1^{y+}	1.027	1.028
f_2^{y+}	1.186	1.199

Table A3.3: ADF/AXS for Rodded (CR2) PWR Fuel Assemblies

A3.4 ADF/AXS Using an Extended Assembly Calculation for an Unrodded Fuel 1 Assembly and a Baffle/Water Node

Table A3.4 contains assembly discontinuity factors (ADF's) and assembly homogenized cross sections calculated on the basis of an extended assembly calculation for the following two heterogeneous nodes:

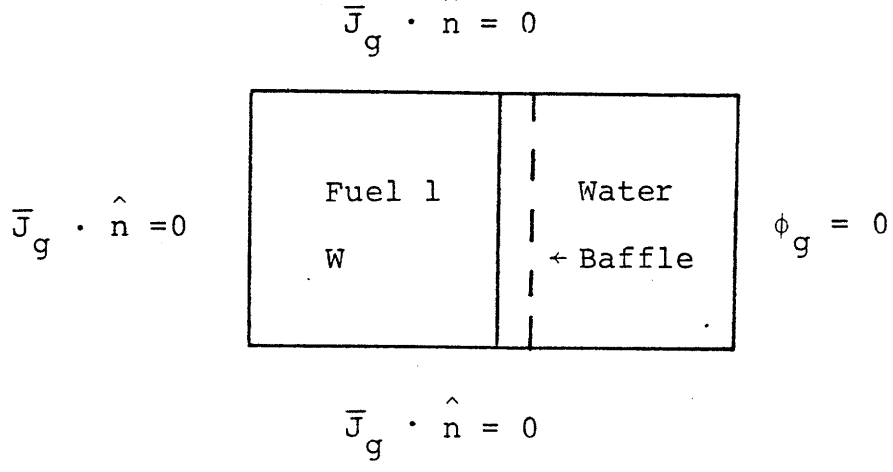

	Extended Assembly, Fuel 1 W	Extended Assembly, Water/ Baffle
D_1	1.513	1.351
$\Sigma_{a1} + \Sigma_{21}$	0.03323	0.02333
Σ_{21}	0.02114	0.02143
$\nu\Sigma_{f1}$	0.006007	0.0
Σ_{f1}	0.002403	0.0
D_2	0.3949	0.3483
Σ_{a2}	0.1683	0.06046
$\nu\Sigma_{f2}$	0.2185	0.0
Σ_{f2}	0.08739	0.0
f_1^{x-}	1.003	1.162
f_2^{x-}	0.9270	0.2866
f_1^{x+}	1.002	0.0
f_2^{x+}	0.9166	0.0
f_1^{y-}	1.003	0.0
f_2^{y-}	0.9279	0.9992
f_1^{y+}	1.003	0.9994
f_2^{y+}	0.9281	0.9987

Table A3.4: ADF/AXS Using an Extended Assembly Calculation For an Unrodded Fuel 1 Assembly and a Baffle/ Water Node

A3.5 ADF/AXS Using An Extended Assembly Calculation for Nodes Near a Jagged Baffle, Nodes 1-6

Tables A3.5.1 through A3.5.3 contain assembly discontinuity factors (ADF's) and assembly homogenized cross sections calculated on the basis of an extended assembly calculation for the following nine nodes:

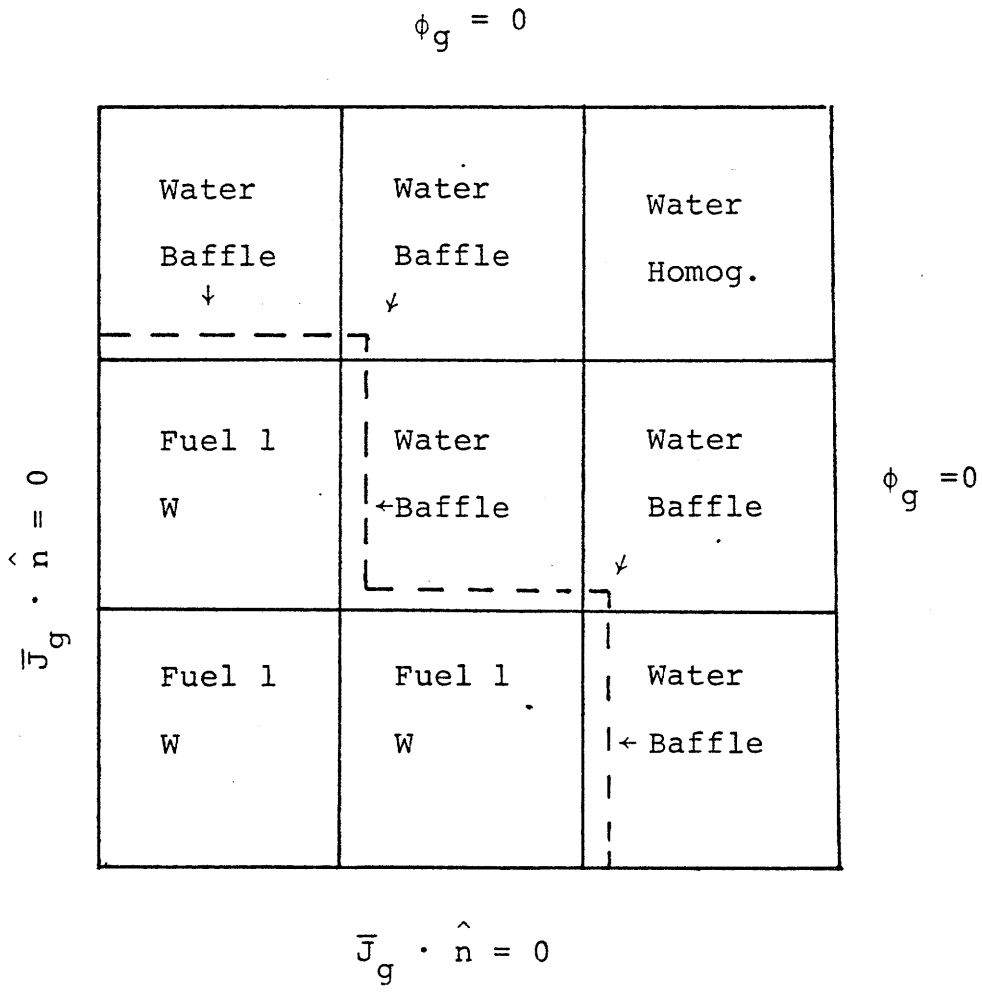

	Node 1 Water/ Baffle	Node 2 Water/ Baffle
D_1	1.343	1.590
$\Sigma_{a1} + \Sigma_{21}$	0.02299	0.03261
Σ_{21}	0.02103	0.03138
$\nu\Sigma_{f1}$	0.0	0.0
Σ_{f1}	0.0	0.0
D_2	0.3482	0.3496
Σ_{a2}	0.06090	0.05254
$\nu\Sigma_{f2}$	0.0	0.0
Σ_{f2}	0.0	0.0
f_1^{x-}	1.026	1.043
f_2^{x-}	1.025	0.7284
f_1^{x+}	0.9492	1.233
f_2^{x+}	0.9485	1.520
f_1^{y-}	1.166	1.034
f_2^{y-}	0.2970	0.8079
f_1^{y+}	0.0	0.0
f_2^{y+}	0.0	0.0

Table A3.5.1: ADF/AXS Using an Extended Assembly Calculation for Nodes Near A Jagged Baffle, Nodes 1 and 2

	Node 3 Water Homog.	Node 4 Fuel 1 W
D_1	1.700	1.513
$\Sigma_{a1} + \Sigma_{21}$	0.03600	0.03323
Σ_{21}	0.03500	0.02113
$\nu\Sigma_{f1}$	0.0	0.006008
Σ_{f1}	0.0	0.002403
D_2	0.3500	0.3949
Σ_{a2}	0.05000	0.1683
$\nu\Sigma_{f2}$	0.0	0.2184
Σ_{f2}	0.0	0.08735
f_1^{x-}	0.8975	0.9928
f_2^{x-}	0.9284	0.9177
f_1^{x+}	0.0	1.025
f_2^{x+}	0.0	0.9494
f_1^{y-}	0.8975	0.9951
f_2^{y-}	0.9284	0.9139
f_1^{y+}	0.0	1.043
f_2^{y+}	0.0	0.9856

Table A3.5.2: ADF/AXS Using an Extended Assembly Calculation for Nodes Near a Jagged Baffle, Nodes 3 and 4

	Node 5 Water/ Baffle	Node6 Fuel 1 W
D_1	1.283	1.513
$\Sigma_{a1} + \Sigma_{21}$	0.02004	0.03323
$\nu\Sigma_{f1}$	0.0	0.02114
Σ_{f1}	0.0	0.006008
D_2	0.3475	0.3950
Σ_{a2}	0.06535	0.1684
$\nu\Sigma_{f2}$	0.0	0.2186
Σ_{f2}	0.0	0.08744
f_1^{x-}	1.151	1.004
f_2^{x-}	0.3192	0.9283
f_1^{x+}	0.8298	1.001
f_2^{x+}	1.258	0.9251
f_1^{y-}	1.151	1.004
f_2^{y-}	0.3192	0.9283
f_1^{y+}	0.8298	1.001
f_2^{y+}	1.258	0.9251

Table A3.5.3: ADF/AXS Using an Extended Assembly Calculation for Nodes Near a Jagged Baffle, Nodes 5 and 6

Appendix 4

RESULTS FOR K_{EFF} AND NORMALIZED POWER DENSITIES FOR BENCHMARK PROBLEMS 1-6

A4.0 Introduction

Figure A4.1: Results for k_{eff} and Normalized Power Densities for Benchmark Problem 1

Figure A4.2: Results for k_{eff} and Normalized Power Densities for Benchmark Problem 2

Figure A4.3: Results for k_{eff} and Normalized Power Densities for Benchmark Problem 3

Figure A4.4: Results for k_{eff} and Normalized Power Densities for Benchmark Problem 4

Figure A4.5: Results for k_{eff} and Normalized Power Densities for Benchmark Problem 5

Figure A4.6: Results for k_{eff} and Normalized Power Densities for Benchmark Problem 6

A4.0 Introduction

This appendix contains the QUANDRY results for normalized power distributions and k_{eff} for six benchmark problems. The global reference calculation for this appendix is a fine-mesh (one node per pin-cell) QUANDRY run. Such a calculation provides reference discontinuity factors (RDF's) and reference homogenized cross sections (RXS) which are used in a coarse-mesh (one node per PWR assembly) QUANDRY run to yield the reference node-averaged quantities and k_{eff}. The assembly discontinuity factors (ADF's) presented in Appendix 3 are used in this appendix. Results are also presented for unity discontinuity factors (UDF's) and assembly homogenized cross sections.

Legend

Reference
% Error with ADF's and Assembly Homogenized Cross Sections
% Error with UDF's and Assembly Homogenized Cross Sections
% Error with ADF's and Reference Homogenized Cross Sections
% Error with UDF's and Reference Homogenized Cross Sections

Normalized Assembly Power Densities

0.9039 -0.07 0.02 -0.13 -0.04	1.1156 0.05 -0.05 0.14 0.04	0.9039 -0.07 0.02 -0.13 -0.04
1.1156 0.05 -0.05 0.14 0.04	0.9220 -0.24 -0.10 -0.37 -0.24	1.1156 0.05 -0.05 0.14 0.04
0.9039 -0.07 0.02 -0.13 -0.04	1.1156 0.05 -0.05 0.14 0.04	0.9039 -0.07 0.02 -0.13 -0.04

k_{eff}	Maximum % Error in Nodal Power	Average % Error in Nodal Power
0.98233 0.010 0.005 0.016 0.012	0.0 -0.24 -0.10 -0.37 -0.24	0.0 0.08 0.04 0.16 0.06

Figure A4.1: Results for k_{eff} and Normalized Power Densities for Benchmark Problem 1

Legend

Reference
% Error with ADF's and Assembly Homogenized Cross Sections
% Error with UDF's and Assembly Homogenized Cross Sections
% Error with ADF's and Reference Homogenized Cross Sections
% Error with UDF's and Reference Homogenized Cross Sections

Normalized Assembly Power Densities

1.1286 0.88 -0.70 0.22 -1.37	0.8877 -1.49 1.25 -0.64 2.12	1.1286 0.88 -0.70 0.22 -1.37
0.8877 -1.49 1.25 -0.64 2.12	0.9346 1.20 -1.60 1.15 -1.65	0.8877 -1.49 1.25 -0.64 2.12
1.1286 0.88 -0.70 0.22 -1.37	0.8877 -1.49 1.25 -0.64 2.12	1.1286 0.88 -0.70 0.22 -1.37

k_{eff}	Maximum % Error in Nodal Power	Average % Error in Nodal Power
0.86824 -0.16 -0.37 0.08 -0.12	0.0 -1.49 -1.60 1.15 2.12	0.0 1.18 1.04 0.51 1.73

Figure A4.2: Results for k_{eff} and Normalized Power Densities for Benchmark Problem 2

Legend

Reference
% Error with ADF's and Assembly Homogenized Cross Sections
% Error with UDF's and Assembly Homogenized Cross Sections
% Error with ADF's and Reference Homogenized Cross Sections
% Error with UDF's and Reference Homogenized Cross Sections

Normalized Assembly Power Densities

1.3244 1.71 0.11 0.82 -0.80	0.9556 -1.89 0.82 -1.10 1.63	1.0657 2.36 0.91 1.70 0.23
0.9591 -2.28 0.36 -1.50 1.16	0.9410 2.40 -0.44 2.32 -0.53	0.7896 -2.33 0.50 -1.37 1.49
1.1675 -0.11 -1.74 -0.73 -2.37	0.8537 -2.36 0.33 -1.40 1.32	0.9435 0.79 -0.71 0.37 -1.14

k_{eff}	Maximum % Error in Nodal Power	Average % Error in Nodal Power
0.86648 -0.09 -0.29 0.15 -0.05	0.0 2.40 -1.74 2.32 -2.37	0.0 1.80 0.66 1.26 1.18

Figure A.4.3: Results for k_{eff} and Normalized Power Densities for Benchmark Problem 3

Legend

Reference
% Error with ADF's and Assembly Homogenized Cross Sections
% Error with UDF's and Assembly Homogenized Cross Sections
% Error with ADF's and Reference Homogenized Cross Sections
% Error with UDF's and Reference Homogenized Cross Sections

Normalized Assembly Power Densities

0.4467 -3.05 -1.00 -2.02 0.07	0.2112 -0.80 1.32 1.59 3.79	0.0 0.0 0.0 0.0 0.0
1.7105 -0.27 -1.53 -0.63 -1.89	0.5496 -1.08 1.57 -0.11 2.58	0.2880 0.69 -0.75 1.77 0.32
3.4673 0.89 0.29 0.36 -0.26	0.8793 -1.23 1.51 -0.76 1.99	0.4474 0.85 -0.45 1.41 0.11

k_{eff}	Maximum % Error in Nodal Power	Average % Error in Nodal Power
0.87086 -0.04 -0.27 0.001 -0.22	0.0 -3.05 1.57 -2.02 3.79	0.0 1.11 1.05 1.08 1.38

Figure A4.4: Results for k_{eff} and Normalized Power Densities for Benchmark Problem 4

Legend

Reference % Error with ADF's and Assembly Homogenized Cross Sections % Error with UDF's and Assembly Homogenized Cross Sections

Normalized Assembly Power Densities

1.0860 0.10 -0.08	0.8926 -0.10 0.06	1.0860 0.10 -0.08
0.8926 -0.10 0.06	1.0860 0.10 -0.08	0.8926 -0.10 0.06
1.0860 0.10 -0.08	0.8926 -0.10 0.06	1.0860 0.10 -0.08

k_{eff}	Maximum % Error in Nodal Power	Average % Error in Nodal Power
0.98512 0.007 0.001	0.0 -0.10 -0.08	0.0 0.10 0.07

Figure A4.5: Results for k_{eff} and Normalized Power Densities for Benchmark Problem 5

Legend

Reference % Error with ADF's and Assembly Homogenized Cross Sections % Error with UDF's and Assembly Homogenized Cross Sections

Normalized Assembly Power Densities

0.0 0.0 0.0	0.0 0.0 0.0	0.0 0.0 0.0	0.0 0.0 0.0
0.8482 0.01 2.17	0.6097 -0.16 5.37	0.0 0.0 0.0	0.0 0.0 0.0
1.2173 0.03 -2.01	1.2062 0.02 -1.00	0.6097 -0.16 5.37	0.0 0.0 0.0
1.4435 0.05 -2.86	1.2173 0.03 -2.01	0.8482 0.01 2.17	0.0 0.0 0.0

k_{eff}	Maximum % Error in Nodal Power	Average % Error in Nodal Power
0.92748 0.008 0.178	0.0 -0.16 +5.37	0.0 0.06 2.87

Figure A4.6: Results for k_{eff} and Normalized Power Densities for Benchmark Problem 6

Appendix 5

TESTING FOR SPATIAL TRUNCATION ERROR IN THE REFERENCE PDQ-7 POINTWISE FLUX CALCULATIONS

A5.0 Introduction

The main source of error in the PDQ-7 reference solutions for benchmark problems 5, 6, 7 and 8 is probably spatial truncation error. Following the suggestion of Hageman and Pfeifer [37], the magnitude of the spatial truncation error is roughly estimated by running a 0.35 cm mesh solution and a 0.7 cm mesh solution and then computing the relative % error using the finer mesh solution as a reference. This approach is used directly for benchmark problems 6 and 8. For the unrodded benchmark problems 5 and 7 a heterogeneous unrodded fuel 1 assembly calculation with $\overline{J} \cdot \hat{n} = 0$ boundary conditions acts as a proxy to the global solutions. This approach is taken because 0.35 cm mesh solutions are not available for benchmark problems 5 and 7.

Fine-mesh (1.4 cm mesh or equivalently one node per pin-cell) global QUANDRY solutions are also available for benchmark problems 5, 6, 7 and 8. At a given assembly corner point, the fine-mesh QUANDRY solution yields no flux information. However, for the four pin-cells surrounding the corner point, the QUANDRY solutions yields surface-averaged fluxes and currents and volume-averaged

fluxes. This information is used in a CHIME run (see Chapter 4) for the four homogeneous pin-cells to interpolate an approximate value of the reference flux at the assembly corner point. This value is expected to be in reasonable agreement with the reference PDQ-7 corner point flux.

A5.1 Benchmark Problem 5 Results

Benchmark problem 5 is the infinite checkerboard of two unrodded fuel assembly types. The locations in and around water holes are the places where spatial truncation error is likely to be the largest since the magnitude of the thermal flux changes rapidly at these places. Furthermore, the magnitude of the thermal flux peaking is only slightly dependent on whether the assembly contains fuel 1 or fuel 2. Thus some idea of the spatial truncation error in benchmark problems 5 and 7 can be obtained by investigating a $\bar{J} \cdot \hat{n} = 0$ assembly calculation for fuel 1 with water holes. The results of such a calculation are shown in Table A5.1.1.

FOR A POINT AT THE EDGE OF THE CENTER WATER HOLE

PDQ Mesh	Location (Row,Column)	Thermal Flux (10^{+11})	Percent Error
61 x 61	(32,32)	2.8618	-------
31 x 31	(16,16)	2.8522	-0.34%
15 x 15	(8, 8)	2.8250	-1.29%

FOR A POINT AT THE CORNER OF THE ASSEMBLY

PDQ Mesh	Location (Row, Column)	Thermal Flux (10^{+11})	Percent Error
61 x 61	(1,61)	2.4727	-------
31 x 31	(1,31)	2.4709	-0.07%
15 x 15	(1,15)	2.4662	-0.26%

Table A5.1.1: Estimate of Spatial Truncation Error For An Unrodded Fuel-1 Assembly Calculation

The 61 x 61, 0.35 cm mesh solution in Table A5.1.1 is treated as a reference solution. Thus, relative percent errors for the 31 x 31 and 15 x 15 solutions are calculated with reference to the 61 x 61 solution. The agreement between solutions is worse near water holes. However, if a 31 x 31 mesh is used, the percent error near the center water hole is only -0.34%. Away from water holes the agreement is excellent. For example, at a corner point of the assembly the relative percent error between the 61 x 61 and 31 x 31 solutions is only -0.07%.

For benchmark problem 5, the fine-mesh QUANDRY/CHIME reference heterogeneous corner point values are compared to the reference heterogeneous corner point values from the reference PDQ-7 global calculation using a 0.7 cm mesh in Table A5.1.2. Note that because of symmetry in benchmark problem 5, there is one unique value of the corner point flux in each group. Table A5.1.2 shows excellent agreement (less that 0.1% error) between the reference 0.7 cm mesh PDQ and reference 1.4 cm mesh QUANDRY/CHIME calculations.

Legend

1. Reference QUANDRY/CHIME Corner Point Flux
   For Benchmark Problem 5
   1.4 cm fine mesh

2. Reference PDQ-7 Corner Point Flux
   For Benchmark Problem 5
   0.7 cm mesh

3. Percentage Difference between #1 and #2 =

   {[#1 - #2]*100.0}/ #2

group 1	1.	2.280×10^{12}
	2.	2.278×10^{12}
	3.	+0.064%
group 2	1.	$2.\dot{8}466 \times 10^{11}$
	2.	2.8458×10^{11}
	3.	+0.028%

Table A5.1.2: A Comparison of the Reference QUANDRY/CHIME Corner Point Fluxes vs. the Reference PDQ-7 Corner Point Fluxes For Benchmark Problem 5

A5.2 Benchmark Problem 6 Results

Benchmark problem 6 is the unrodded quarter-core with an explicit baffle. For this problem, the reference calculation is a 0.35 cm mesh PDQ-7 calculation. However, a 0.70 cm mesh solution is also available. Thus, the percentage difference between these two solutions can be calculated at mesh points that the solutions have in common. For the purposes here, the corner points of assembly 6 (adjacent to the jag in the baffle) are compared. See Table A5.2.1. As this table shows, the agreement between the 0.7 cm mesh and 0.35 cm mesh solutions is good. The maximum percentage difference in the table is -0.24%.

AT CORNER POINT 1 OF NODE 6 IN BENCHMARK PROBLEM 6

Group	PDQ Mesh	Location (Row,Column)	Group Flux	Percent Difference
1	240 x 240	(60,120)	3.2374×10^{11}	------
1	120 x 120	(30, 60)	3.2296×10^{11}	-0.24%
2	240 x 240	(60,120)	2.6713×10^{10}	------
2	120 x 120	(30, 60)	2.6669×10^{10}	-0.16%

AT CORNER POINT 2 OF NODE 6 IN BENCHMARK PROBLEM 6

Group	PDQ Mesh	Location (Row,Column)	Group Flux	Percent Difference
1	240 x 240	(60, 60)	8.0193×10^{11}	------
1	120 x 120	(30, 30)	8.0052×10^{11}	-0.18%
2	240 x 240	(60, 60)	7.0936×10^{10}	------
2	120 x 120	(30, 30)	7.0773×10^{10}	-0.23%

AT CORNER POINT 3 OF NODE 6 IN BENCHMARK PROBLEM 6

Group	PDQ Mesh	Location (Row,Column)	Group Flux	Percent Difference
1	240 x 240	(120, 60)	2.3872×10^{12}	------
1	120 x 120	(60, 30)	2.3863×10^{12}	-0.04%
2	240 x 240	(120, 60)	2.8474×10^{11}	------
2	120 x 120	(60, 30)	2.8452×10^{11}	-0.08%

AT CORNER POINT 4 OF NODE 6 IN BENCHMARK PROBLEM 6

Group	PDQ Mesh	Location (Row, Column)	Group Flux	Percent Difference
1	240 x 240	(120,120)	1.4322×10^{12}	------
1	120 x 120	(60, 60)	1.4301×10^{12}	-0.15%
2	240 x 240	(120,120)	1.3633×10^{11}	------
2	120 x 120	(60, 60)	1.3604×10^{11}	-0.21%

Table A5.2.1: Estimate of Spatial Truncation Error For Benchmark Problem 6

A5.3 Benchmark Problem 7 Results

Benchmark problem 7 is a small, unrodded, 3-by-3 quarter-core. Node 5 contains fuel 1 and water holes and the other nodes are homogeneous fuel 2. Since no 0.35 cm mesh solution for this problem is available, a direct comparison between PDQ-7 solutions is not possible. However, for flux reconstructions and corner point interpolations dealing with node 5, Table A5.1.1 of this appendix probably yields a rough estimate of the spatial truncation error that might be encountered using the 31 x 31, 0.37 cm mesh solution.

For benchmark problem 7, the fine-mesh QUANDRY/CHIME heterogeneous corner point values are compared to the heterogeneous corner point values from the reference PDQ-7 global calculation using a 0.7 cm mesh in Table A5.3.1. The agreement between the PDQ-7 and QUANDRY/CHIME solutions is excellent. The maximum error is -0.1049%.

Legend

1. Reference QUANDRY/CHIME Corner Point Flux For Benchmark Problem 7, 1.4 cm fine mesh
2. Reference PDQ-7 Corner Point Flux For Benchmark Problem 7, 0.7 cm fine mesh
3. Percentage Difference Between #1 and #2 = {[#1 - #2]* 100.0} / #2

1. 2.82354×10^{12}	1. 1.70401×10^{12}
2. 2.82340×10^{12}	2. 1.70580×10^{12}
3. +0.00487%	3. -0.1049%
Node 5 Group 1	
1. 4.73336×10^{12}	1. 2.82354×10^{12}
2. 4.73210×10^{12}	2. 2.82340×10^{12}
3. +0.02667 %	3. +0.00487%

1. 3.59919×10^{11}	1. 2.16764×10^{11}
2. 3.59900×10^{11}	2. 2.16870×10^{11}
3. +0.00518 %	3. -0.0488%
Node 5 Group 2	
1. 6.05028×10^{11}	1. 3.59919×10^{11}
2. 6.04750×10^{11}	2. 3.59900×10^{11}
3. +0.0459%	3. +0.00518%

Table A5.3.1: A Comparison of the Reference QUANDRY/CHIME Corner Point Fluxes vs. the Reference PDQ-7 Corner Point Fluxes For Benchmark Problem 7

A5.4 Benchmark Problem 8 Results

Benchmark problem 8 is an extremely difficult, 3-by-3 quarter-core containing rodded and unrodded nodes. Node 3 contains water to simulate reflector effects. For this problem, the reference calculation is a 0.35 cm mesh PDQ-7 calculation. However, a 0.70 cm mesh solution is also available. Thus, the percentage difference between these two solutions can be calculated at mesh points that these two solutions have in common. For the purposes here, the corner points of assembly 5 (the rodded fuel 2 central node) are compared. See Table A5.4.1. As this table shows, the agreement between the 0.7 cm mesh and 0.35 cm mesh solutions is no so good. The maximum error is in the thermal flux at corner point 1 next to the water reflector. The magnitude of the maximum error is -3.047%.

Table A5.4.1 also presents the fine-mesh (1.4 cm) QUANDRY/CHIME heterogeneous corner point values for this problem. The QUANDRY/CHIME fluxes are compared to the 0.35 cm PDQ-7 reference solution. Again the maximum error of +1.719 is relatively large. Thus, an examination of Table A5.4.1 leads to the conclusion that benchmark problem 8 is indeed a difficult problem. The reference pointwise fluxes for this problem are only known to within a few percent.

Legend

1. Reference PDQ-7 Corner Point Fluxes for Node 5 of Benchmark Problem 8, 0.35 cm mesh

2. PDQ-7 Corner Point Fluxes for Node 5 of Benchmark Problem 8, 0.70 cm mesh

3. Percentage Difference Between #2 and #1 =

   {[#2 - #1]*100.0} / #1

4. Reference QUANDRY/CHIME Corner Point Flux for Node 5 of Benchmark Problem 8, 1.4 cm mesh

5. Percentage Difference Between #4 and #1 =

   {[#4 - #1]*100.0} / #1

1. 1.7019×10^{12}	1. 4.6946×10^{11}
2. 1.6895×10^{12}	2. 4.5723×10^{11}
3. -0.730%	3. -2.605%
4. 1.7089×10^{12}	4. 4.7662×10^{11}
5. +0.413%	5. +1.53%

Group 1
Node 5

1. 4.2451×10^{12}	1. 1.1401×10^{12}
2. 4.2564×10^{12}	2. 1.1146×10^{12}
3. +0.265%	3. -2.23%
4. 4.2399×10^{12}	4. 1.1548×10^{12}
5. -0.123%	5. +1.29%

Table A5.4.1: A Comparison of Reference Corner Points For Node 5 of Benchmark Problem 8

1. 2.0412×10^{11}	1. 7.9947×10^{10}
2. 2.0214×10^{11}	2. 7.7511×10^{10}
3. -0.970%	3. -3.047%
4. 2.0535×10^{11}	4. 8.1321×10^{10}
5. +0.603%	5. +1.719%

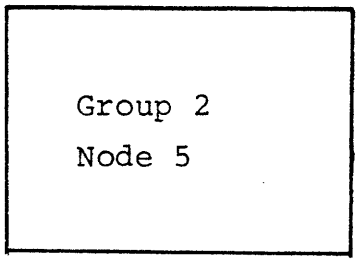

1. 5.3104×10^{11}	1. 1.3544×10^{11}
2. 5.3155×10^{11}	2. 1.3208×10^{11}
3. +0.0968%	3. -2.478%
4. 5.3086×10^{11}	4. 1.3746×10^{11}
5. -0.0339%	5. +1.494%

Table A5.4.1 (continued): A Comparison of Reference Corner Points For Node 5 of Benchmark Problem 8

Appendix 6

CHIME

A6.0 Introduction

The purpose of this appendix is to present a scheme for interpolation of the heterogeneous flux at the corners of assemblies in a PWR core. This scheme is called CHIME. It is an extension of a corner point interpolation method proposed by Koebke and Wagner [31].

The geometry for a CHIME interpolation is shown in Figure A6.0.1. When four heterogeneous nodes are placed together, they meet at a central corner point at (0,0). Note that the node-numbering (n = 1, 2, 3, 4) is by quadrants in a Cartesian coordinate system. The object is to use the node-averaged fluxes and currents from QUANDRY to interpolate a heterogeneous corner point flux at (0,0). To simplify the notation in this appendix, the superscript "het" will be omitted from node-averaged fluxes and currents and from diffusion coefficients. However, it is understood that heterogeneous node-averaged quantities should be input since the desired output from the interpolation is the heterogeneous corner point flux. Since corner points are interpolated one group at a time, the group index g is also suppressed in this appendix.

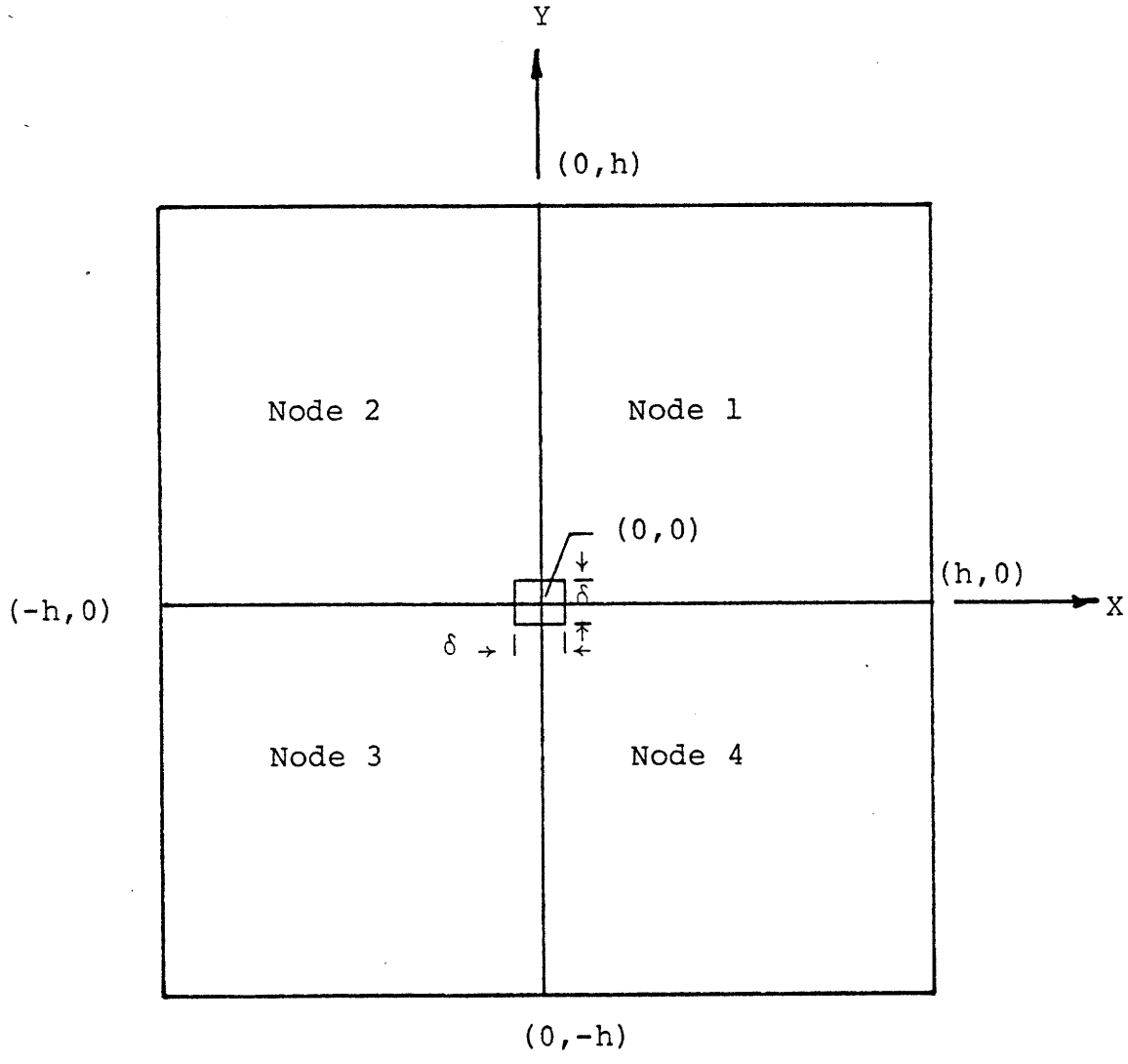

Figure A6.0.1: Geometry for a CHIME Interpolation

Single digit superscripts refer to the node number, n. Thus, $\phi^1(x,y)$ is the pointwise heterogeneous flux in node 1. A single bar over a quantity indicates that the quantity has been spatially averaged over a node surface. A two digit superscript in parentheses refers to a node surface shared by two nodes. Thus $\bar{\phi}_x^{(12)}$ is the x-directed, surface-averaged flux where the averaging has been done transverse to the direction x and along the interface between nodes 1 and 2. Three bars over a quantity indicate volume averaging. Thus $\bar{\bar{\bar{\phi}}}^1$ is the heterogeneous volume-averaged flux in node 1.

It is assumed that the heterogeneous assembly flux, $A^n(x,y)$ (n = 1, 2, 3, 4) is available for each of the four assemblies. Furthermore, it is expected that the assembly calculations were performed with $\bar{J} \cdot \hat{n} = 0$ boundary conditions. Since $A^n(x,y)$ is known, the following quantities are known also:

1. Corner point assembly fluxes for node n;

$$A^n_{CP1} \quad , \quad A^n_{CP2} \quad , \quad A^n_{CP3} \quad , \quad A^n_{CP4}$$

2. Surface-averaged Assembly fluxes for node n;

$$\bar{A}^n_{x-} \quad , \quad \bar{A}^n_{x+} \quad , \quad \bar{A}^n_{y-} \quad , \quad \bar{A}^n_{y+}$$

3. Volume-Averaged Assembly flux in node n; $\bar{\bar{\bar{A}}}^n$.

The surface and cornerpoint labeling for node n is given in Figure A6.0.2.

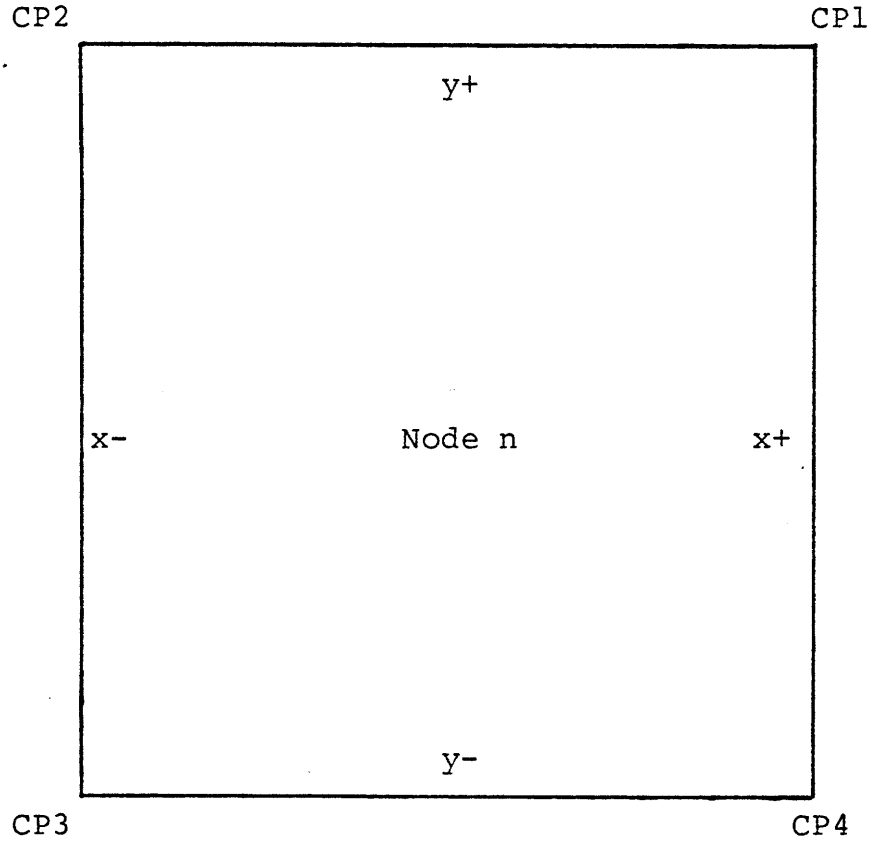

Figure A6.0.2: Surface and Corner Point Labeling of a Node n = 1, 2, 3, 4

The basic approximation made in CHIME is that the heterogeneous flux in node n (=1, 2, 3, 4), $\phi^n(x,y)$, can be expanded as the product of the heterogeneous assembly flux, $A^n(x,y)$, and an eight-term, bi-quadratic form function, $Q^n(x,y)$. Thus the flux in each node n becomes

$$\phi^n(x,y) = A^n(x,y) \cdot Q^n(x,y); \quad n = 1, 2, 3, 4. \tag{A6.0.1}$$

Since the $A^n(x,y)$ are known, the eight coefficients of the bi-quadratic in each node become the only unknowns. There are four assemblies involved in the interpolation and thus there are 4 x 8 = 32 unknown coefficients. To determine these coefficients, a total of 32 conditions are imposed on the products, $A^n(x,y) \cdot Q^n(x,y)$. The 32 conditions are summarized in Table A6.0.1. Once the resulting system of 32 equations in 32 unknowns has been solved algebraically, then the heterogeneous corner point is found from

$$\phi^1(0,0) = A^1(0,0) \cdot Q^1(0,0). \tag{A6.0.2}$$

To illustrate how the conditions in Table A6.0.1 are implemented, a few examples for node 1 are now presented. For node 1 the heterogeneous flux is represented by

$$\phi^1(x,y) = A^1(x,y) \cdot Q^1(x,y) \tag{A6.0.3}$$

1.	$\bar{\bar{\phi}}^1$	in node 1	17.	$J_y^{(14)}$	in node 1
2.	$\bar{\bar{\phi}}^2$	in node 2	18.	$J_y^{(23)}$	in node 2
3.	$\bar{\bar{\phi}}^3$	in node 3	19.	$J_y^{(23)}$	in node 3
4.	$\bar{\bar{\phi}}^4$	in node 4	20.	$J_y^{(14)}$	in node 4
5.	$\bar{\phi}_x^{(12)}$	in node 1	21.	Pointwise continuity of flux at (0,0) in nodes 1 and 2	
6.	$\bar{\phi}_x^{(12)}$	in node 2	22.	Pointwise continuity of flux at (0,0) in nodes 2 and 3	
7.	$\bar{\phi}_x^{(34)}$	in node 3	23.	Pointwise continuity of flux at (0,0) in nodes 3 and 4	
8.	$\bar{\phi}_x^{(34)}$	in node 4	24.	Pointwise continuity of flux at (0,h) in nodes 1 and 2	
9.	$\bar{\phi}_y^{(14)}$	in node 1	25.	Pointwise continuity of flux at (h,0) in nodes 1 and 4	
10.	$\bar{\phi}_y^{(23)}$	in node 2	26.	Pointwise continuity of flux at (0,-h) in nodes 3 and 4	
11.	$\bar{\phi}_y^{(23)}$	in node 3	27.	Pointwise continuity of flux at (-h,0) in nodes 2 and 3	
12.	$\bar{\phi}_y^{(14)}$	in node 4	28.	Pointwise continuity of current at (0,h) in nodes 1 and 2	
13.	$J_x^{(12)}$	in node 1	29.	Pointwise continuity of current at (h,0) in nodes 1 and 4	
14.	$J_x^{(12)}$	in node 2	30.	Pointwise continuity of current at (0,-h) in nodes 3 and 4	
15.	$J_x^{(34)}$	in node 3	31.	Pointwise continuity of current at (-h,0)in nodes 2 and 3	
16.	$J_x^{(34)}$	in node 4	32.	Source-free at the origin	

Table A6.0.1: Thirty-Two Conditions on the Products

$$A^n(x,y) \cdot Q^n(x,y);\ n = 1,\ 2,\ 3,\ 4$$

where $A^1(x,y)$ is the known heterogeneous assembly flux and $Q^1(x,y)$ is the eight-term, bi-quadratic,

$$Q^1(x,y) = a_1 + \left[\frac{x}{h}\right] a_2 + \left[\frac{x}{h}\right]^2 a_3 + \left[\frac{y}{h}\right] a_4 + \left[\frac{y}{h}\right]^2 a_5 + \left[\frac{xy}{h^2}\right] a_6 + \left[\frac{x^2 y}{h^3}\right] a_7 + \left[\frac{x y^2}{h^3}\right] a_8 \qquad \text{(A6.0.4)}$$

To implement condition 1 in Table A6.0.1, the volume integral of the product $A^1(x,y) \cdot Q^1(x,y)$ is set equal to $\bar{\bar{\phi}}^1$. Doing this yields

$$\bar{\bar{\phi}}^1 = \frac{1}{h^2} \int_0^h dx \int_0^h dy \; A^1(x,y) \cdot Q^1(x,y) \qquad \text{(A6.0.5)}$$

Unfortunately, an analytic form of $A^1(x,y)$ is not known. Instead, pointwise values of $A^1(x,y)$ are known. Thus a numerical integration procedure could be employed to implement the condition in equation A6.0.5. However, a simpler approach is taken here. The additional approximation is made that $A^1(x,y)$ is spatially constant and equal to the known volume integral of the assembly flux $\bar{\bar{A}}^1$. Accordingly, the condition A6.0.5 is replaced by

$$\frac{\bar{\bar{\phi}}^1}{\bar{\bar{A}}^1} = \frac{1}{h^2} \int dx \int dy \; Q^1(x,y). \qquad \text{(A6.0.6)}$$

The advantage of taking $A^1(x,y) \simeq \bar{\bar{A}}^1$ in equation A6.0.5 is that the integral on the right-hand side of equation A6.0.6 can be done algebraically and the left-hand side is a known number.

For a heterogeneous PWR assembly the $A^1(x,y)$ in the thermal group is usually not spatially flat. The consequence of this is that the $Q^1(x,y)$ found employing equation A6.0.6 as one of the conditions (on the coefficients of $Q^1(x,y)$) is such that the $\phi^1(x,y)$ (found from $\phi^1(x,y) = A^1(x,y) \cdot Q^1(x,y)$) will not return the input heterogeneous volume-averaged flux when it is numerically volume integrated. However, it is only desired that $A^1(0,0) \cdot Q^1(0,0)$ yield an accurate approximation of the corner point heterogeneous flux. Thus the fact that $A^1(x,y) \cdot Q^1(x,y)$ fails to match perfectly the volume flux when it is integrated is not necessarily a serious defect.

A similar procedure is used when the condition from Table A6.0.1 is a surface-averaged flux. The difference is that the assembly flux is only approximated as spatially flat along the surface of the assembly. This is often a good approximation

The implementation of a condition from Table A6.0.1 involving a surface-averaged current is more complicated. For example, condition 13 for the x- face of node 1 is implemented as

$$J_x^{(12)} = \frac{-1}{h} \int_0^h dy \left[D^1(x=0,y) \cdot \frac{\partial}{\partial x} \{ A^1(x,y) \cdot Q^1(x,y) \} \Big|_{x=0} \right] \tag{A6.0.7}$$

An analytic form of $A^1(x,y)$ and $D^1(x=0,y)$ is not known. Since the $D^1(x=0,y)$ dependence on y is usually weak for PWR assemblies (even after depletion), a surface-averaged value is used. Doing this and noting that $\frac{\partial}{\partial x} A^1 = 0$ at the assembly surface yields

$$\frac{-J_x^{(12)} \; h}{\bar{D}^1_{x-}} = \int_0^h dy \left[A^1(0,y) \cdot \left[\frac{1}{h} a_2 + \frac{y}{h^2} a_6 + \frac{y^2}{h^3} a_8 \right] \right] \tag{A6.0.8}$$

The $A^1(0,y)$ is approximated as $\bar{A}^1_{x-}$ which is the surface-averaged flux from the assembly calculation for node 1 on the x- face of the node. Thus, condition 13 in Table A6.0.1 is actually put into effect as

$$\frac{-J_x^{(12)} \; h}{\bar{D}^1_{x-} \quad \bar{A}^1_{x-}} = a_2 + \frac{1}{2} a_6 + \frac{1}{3} a_8 \, . \tag{A6.0.9}$$

Again the advantage of neglecting the spatial dependence of the diffusion coefficient and assembly flux along the node face is that the integral in equation A6.0.7 can be done analytically.

The source-free condition at the origin (see Table A6.0.1, condition 32) is based on the physical principle that if a small box of dimension δ is constructed around the origin and if the volume of the box shrinks to zero, then the point at the origin should not be a net source or sink of neutrons. This can be expressed mathematically as

$$\lim_{\delta \to o} \int_{V_{box}} \nabla \cdot \vec{J} \; dV = \lim_{\delta \to o} \int_{S_{box}} \vec{J} \cdot \hat{n} \; dS = 0 \qquad \text{(A6.0.10)}$$

where V_{box} and S_{box} refer to the volume and surface of the box in Figure A6.0.1. The result of applying equation A6.0.10 is presented in section A6.2 of this appendix.

The next section of this appendix presents the eight-term, bi-quadratics which are used in each of the four nodes. A system of 32 equations in 32 unknowns is developed after that. The final section of this appendix contains the solution to the system of equations.

A 6.1 The Eight-Term Bi-Quadratic Form Functions

For node 1:

$$\frac{\phi^1(x,y)}{A^1(x,y)} = a_1 + a_2\left[\frac{x}{h}\right] + a_3\left[\frac{x}{h}\right]^2 + a_4\left[\frac{y}{h}\right] + a_5\left[\frac{y}{h}\right]^2 + a_6\left[\frac{xy}{h^2}\right] + a_7\left[\frac{x^2y}{h^3}\right] + a_8\left[\frac{xy^2}{h^3}\right] \quad \text{(A6.1.1)}$$

For node 2:

$$\frac{\phi^2(x,y)}{A^2(x,y)} = a_9 + a_{10}\left[\frac{x}{h}\right] + a_{11}\left[\frac{x}{h}\right]^2 + a_{12}\left[\frac{y}{h}\right] + a_{13}\left[\frac{y}{h}\right]^2 + a_{14}\left[\frac{xy}{h^2}\right] + a_{15}\left[\frac{x^2y}{h^3}\right] + a_{16}\left[\frac{xy^2}{h^3}\right] \quad \text{(A6.1.2)}$$

For node 3:

$$\frac{\phi^3(x,y)}{A^3(x,y)} = a_{17} + a_{18}\left[\frac{x}{h}\right] + a_{19}\left[\frac{x}{h}\right]^2 + a_{20}\left[\frac{y}{h}\right] + a_{21}\left[\frac{y}{h}\right]^2 + a_{22}\left[\frac{xy}{h^2}\right] + a_{23}\left[\frac{x^2y}{h^3}\right] + a_{24}\left[\frac{xy^2}{h^3}\right] \quad \text{(A6.1.3)}$$

For node 4:

$$\frac{\phi^4(x,y)}{A^4(x,y)} = a_{25} + a_{26}\left[\frac{x}{h}\right] + a_{27}\left[\frac{x}{h}\right]^2 + a_{28}\left[\frac{y}{h}\right] +$$

$$a_{29}\left[\frac{y}{h}\right]^2 + a_{30}\left[\frac{xy}{h^2}\right] + a_{31}\left[\frac{x^2 y}{h^3}\right] + a_{32}\left[\frac{x y^2}{h^3}\right]$$

(A6.1.4)

A6.2 Thirty-Two Equations in Thirty-Two Unknowns

Volume Integral, Node 1:

$$\frac{\bar{\bar{\Phi}}^1}{\bar{\bar{A}}^1} = \beta_1 = a_1 + \frac{1}{2}a_2 + \frac{1}{3}a_3 + \frac{1}{2}a_4 + \frac{1}{3}a_5 + \frac{1}{4}a_6 + \frac{1}{6}a_7 + \frac{1}{6}a_8 \qquad \text{(A6.2.1)}$$

Volume Integral, Node 2:

$$\frac{\bar{\bar{\Phi}}^2}{\bar{\bar{A}}^2} = \beta_2 = a_9 - \frac{1}{2}a_{10} + \frac{1}{3}a_{11} + \frac{1}{2}a_{12} + \frac{1}{3}a_{13} - \frac{1}{4}a_{14} + \frac{1}{6}a_{15} - \frac{1}{6}a_{16} \qquad \text{(A6.2.2)}$$

Volume Integral, Node 3:

$$\frac{\bar{\bar{\Phi}}^3}{\bar{\bar{A}}^3} = \beta_3 = a_{17} - \frac{1}{2}a_{18} + \frac{1}{3}a_{19} - \frac{1}{2}a_{20} + \frac{1}{3}a_{21} + \frac{1}{4}a_{22} - \frac{1}{6}a_{23} - \frac{1}{6}a_{24} \qquad \text{(A6.2.3)}$$

Volume Integral, Node 4:

$$\frac{\bar{\bar{\Phi}}^4}{\bar{\bar{A}}^4} = \beta_4 = a_{25} + \frac{1}{2}a_{26} + \frac{1}{3}a_{27} - \frac{1}{2}a_{28} + \frac{1}{3}a_{29} - \frac{1}{4}a_{30} - \frac{1}{6}a_{31} + \frac{1}{6}a_{32} \qquad \text{(A6.2.4)}$$

x-Directed, Surface-Flux, Node 1:

$$\frac{\bar{\Phi}_x^{(12)}}{\bar{A}_{x-}^1} = \beta_5 = a_1 + \frac{1}{2}a_4 + \frac{1}{3}a_5 \qquad \text{(A6.2.5)}$$

x-Directed, Surface Flux, Node 2:

$$\frac{\bar{\phi}_x^{(12)}}{\bar{A}_{x+}^{2}} = \beta_6 = a_9 + \frac{1}{2} a_{12} + \frac{1}{3} a_{13} \qquad \text{(A6.2.6)}$$

x-Directed, Surface Flux, Node 3:

$$\frac{\bar{\phi}_x^{(34)}}{\bar{A}_{x+}^{3}} = \beta_7 = a_{17} - \frac{1}{2} a_{20} + \frac{1}{3} a_{21} \qquad \text{(A6.2.7)}$$

x-Directed, Surface Flux, Node 4:

$$\frac{\bar{\phi}_x^{(34)}}{\bar{A}_{x-}^{4}} = \beta_8 = a_{25} - \frac{1}{2} a_{28} + \frac{1}{3} a_{29} \qquad \text{(A6.2.8)}$$

y-Directed, Surface Flux, Node 1:

$$\frac{\bar{\phi}_y^{(14)}}{\bar{A}_{y-}^{1}} = \beta_9 = a_1 + \frac{1}{2} a_2 + \frac{1}{3} a_3 \qquad \text{(A6.2.9)}$$

y-Directed, Surface Flux, Node 2:

$$\frac{\bar{\phi}_y^{(23)}}{\bar{A}_{y-}^{2}} = \beta_{10} = a_9 - \frac{1}{2} a_{10} + \frac{1}{3} a_{11} \qquad \text{(A6.2.10)}$$

y - Directed, Surface Flux, Node 3:

$$\frac{\bar{\phi}_y^{(23)}}{\bar{A}_{y+}^3} = \beta_{11} = a_{17} - \frac{1}{2} a_{18} + \frac{1}{3} a_{19} \qquad \text{(A6.2.11)}$$

y - Directed, Surface Flux, Node 4:

$$\frac{\bar{\phi}_y^{(14)}}{\bar{A}_{y+}^4} = \beta_{12} = a_{25} + \frac{1}{2} a_{26} + \frac{1}{3} a_{27} \qquad \text{(A6.2.12)}$$

x - Directed, Surface Current, Node 1:

$$\frac{-J_x^{(12)} \; h}{\bar{D}_{x-}^1 \quad \bar{A}_{x-}^1} = \beta_{13} = a_2 + \frac{1}{2} a_6 + \frac{1}{3} a_8 \qquad \text{(A6.2.13)}$$

x - Directed, Surface Current, Node 2:

$$\frac{-J_x^{(12)} \; h}{\bar{D}_{x+}^2 \quad \bar{A}_{x+}^2} = \beta_{14} = a_{10} + \frac{1}{2} a_{14} + \frac{1}{3} a_{16} \qquad \text{(A6.2.14)}$$

x - Directed, Surface Current, Node 3:

$$\frac{-J_x^{(34)}\ h}{\bar{D}^3_{x+}\quad \bar{A}^3_{x+}} = \beta_{15} = a_{18} - \frac{1}{2}a_{22} + \frac{1}{3}a_{24} \qquad \text{(A6.2.15)}$$

x - Directed, Surface Current, Node 4:

$$\frac{-J_x^{(34)}\ h}{\bar{D}^4_{x-}\quad \bar{A}^4_{x-}} = \beta_{16} = a_{26} - \frac{1}{2}a_{30} + \frac{1}{3}a_{32} \qquad \text{(A6.2.16)}$$

y - Directed, Surface Current, Node 1:

$$\frac{-J_y^{(14)}\ h}{\bar{D}^1_{y-}\quad \bar{A}^1_{y-}} = \beta_{17} = a_4 + \frac{1}{2}a_6 + \frac{1}{3}a_7 \qquad \text{(A6.2.17)}$$

y - Directed, Surface Current, Node 2:

$$\frac{-J_y^{(23)}\ h}{\bar{D}^2_{y-}\quad \bar{A}^2_{y-}} = \beta_{18} = a_{12} - \frac{1}{2}a_{14} + \frac{1}{3}a_{15} \qquad \text{(A6.2.18)}$$

y - Directed, Surface Current, Node 3:

$$\frac{-J_y^{(23)}\ h}{\bar{D}_{y+}^{3}\ \bar{A}_{y+}^{3}} = \beta_{19} = a_{20} - \frac{1}{2}a_{22} + \frac{1}{3}a_{23} \qquad \text{(A6.2.19)}$$

y - Directed, Surface Current, Node 4:

$$\frac{-J_y^{(14)}\ h}{\bar{D}_{y+}^{4}\ \bar{A}_{y+}^{4}} = \beta_{20} = a_{28} + \frac{1}{2}a_{30} + \frac{1}{3}a_{31} \qquad \text{(A6.2.20)}$$

Continuity of Flux at the origin, Nodes 1 and 2:

$$A_{CP3}^{1}\ a_1 - A_{CP4}^{2}\ a_9 = 0 \qquad \text{(A6.2.21)}$$

Continuity of Flux at the origin, Nodes 2 and 3:

$$A_{CP4}^{2}\ a_9 - A_{CP1}^{3}\ a_{17} = 0 \qquad \text{(A6.2.22)}$$

Continuity of Flux at the origin, Nodes 3 and 4:

$$A_{CP1}^{3}\ a_{17} - A_{CP2}^{4}\ a_{25} = 0 \qquad \text{(A6.2.23)}$$

Continuity of Flux at (0,h), Nodes 1 and 2:

$$A^1_{CP2}\ a_1 + A^1_{CP2}\ a_4 + A^1_{CP2}\ a_5 +$$

$$-A^2_{CP1}\ a_9 - A^2_{CP1}\ a_{12} - A^2_{CP1}\ a_{13} = 0 \qquad \text{(A6.2.24)}$$

Continuity of Flux at (h,0), Nodes 1 and 4:

$$A^1_{CP4}\ a_1 + A^1_{CP4}\ a_2 + A^1_{CP4}\ a_3 +$$

$$-A^4_{CP1}\ a_{25} - A^4_{CP1}\ a_{26} - A^4_{CP1}\ a_{27} = 0 \qquad \text{(A6.2.25)}$$

Continuity of Flux at (0,-h), Nodes 3 and 4:

$$A^3_{CP4}\ a_{17} - A^3_{CP4}\ a_{20} + A^3_{CP4}\ a_{21} +$$

$$-A^4_{CP3}\ a_{25} + A^4_{CP3}\ a_{28} - A^4_{CP3}\ a_{29} = 0 \qquad \text{(A6.2.26)}$$

Continuity of Flux at (-h,0), Nodes 2 and 3:

$$-A^2_{CP3}\ a_9 + A^2_{CP3}\ a_{10} - A^2_{CP3}\ a_{11} +$$

$$A^3_{CP2}\ a_{17} - A^3_{CP2}\ a_{18} + A^3_{CP2}\ a_{19} = 0 \qquad \text{(A6.2.27)}$$

Continuity of Current at (0,h), Nodes 1 and 2:

$$D^1_{CP2}\ A^1_{CP2}\ a_2 + D^1_{CP2}\ A^1_{CP2}\ a_6 + D^1_{CP2}\ A^1_{CP2}\ a_8 +$$
$$-D^2_{CP1}\ A^2_{CP1}\ a_{10} - D^2_{CP1}\ A^2_{CP1}\ a_{14} - D^2_{CP1}\ A^2_{CP1}\ a_{16} = 0$$

(A6.2.28)

Continuity of Current at (h,0), Nodes 1 and 4:

$$D^1_{CP4}\ A^1_{CP4}\ a_4 + D^1_{CP4}\ A^1_{CP4}\ a_6 + D^1_{CP4}\ A^1_{CP4}\ a_7 +$$
$$-D^4_{CP1}\ A^4_{CP1}\ a_{28} - D^4_{CP1}\ A^4_{CP1}\ a_{30} - D^4_{CP1}\ A^4_{CP1}\ a_{32} = 0$$

(A6.2.29)

Continuity of Current at (0,-h), Nodes 3 and 4:

$$D^3_{CP4}\ A^3_{CP4}\ a_{18} - D^3_{CP4}\ A^3_{CP4}\ a_{22} + D^3_{CP4}\ A^3_{CP4}\ a_{24} +$$
$$-D^4_{CP3}\ A^4_{CP3}\ a_{26} + D^4_{CP3}\ A^4_{CP3}\ a_{30} - D^4_{CP3}\ A^4_{CP3}\ a_{32} = 0$$

(A6.2.30)

Continuity of Current at (-h,0), Nodes 2 and 3:

$$-D^2_{CP3}\ A^2_{CP3}\ a_{12} + D^2_{CP3}\ A^2_{CP3}\ a_{14} - D^2_{CP3}\ A^2_{CP3}\ a_{15} +$$
$$D^3_{CP2}\ A^3_{CP2}\ a_{20} - D^3_{CP2}\ A^3_{CP2}\ a_{22} + D^3_{CP2}\ A^3_{CP2}\ a_{23} = 0$$

(A6.2.31)

Source Free Condition at the Origin, Nodes 1, 2, 3, 4:

$$D^1_{CP3}\ A^1_{CP3}\ a_2 + D^1_{CP3}\ A^1_{CP3}\ a_4 +$$

$$-D^2_{CP4}\ A^2_{CP4}\ a_{10} + D^2_{CP4}\ A^2_{CP4}\ a_{12} +$$

$$-D^3_{CP1}\ A^3_{CP1}\ a_{18} - D^3_{CP1}\ A^3_{CP1}\ a_{20} +$$

$$D^4_{CP2}\ A^4_{CP2}\ a_{26} - D^4_{CP2}\ A^4_{CP2}\ a_{28} = 0 \qquad \text{(A6.2.32)}$$

A6.3 The Algebraic Solution

A6.3.0 Introduction

The 32 equations in 32 unknowns are now solved by algebraic substitution. A defining equation for each of the unknown a_i (i = 1 through 32) is presented. However, 30 of the defining equations for the a_i contain other $a_{i'}$ $(i' \neq i)$. Only the last two defining equations A6.3.93 for a_1 and A6.3.94 for a_4 are in terms of parameters which can be calculated from the node-averaged surface fluxes and currents, node geometry and assembly flux information only. Thus to implement the solution for all 32 a_i, start at the end of the solution and work toward the front. This is the method used by the CHIME code and it solves for all 32 unknown a_i. Note that if all that is desired is the value of the heterogeneous corner point flux, then knowledge of a_1 suffices since

$$\phi^1_{CP3} = A^1_{CP3} \quad a_1 \cdot \qquad \text{(A6.3.0)}$$

A6.3.1 Reduction to 16 Equations in 16 Unknowns

Solve equation A6.2.9 for a_3 in terms of a_1 and a_2. This yields the defining equation for a_3 as

$$a_3 = 3\beta_9 - 3a_1 - \frac{3}{2} a_2 . \qquad \text{(A6.3.1)}$$

Solve equation A6.2.5 for a_5 in terms of a_1 and a_4. This yields the defining equation for a_5 as

$$a_5 = 3\beta_5 - 3a_1 - \frac{3}{2} a_4 . \qquad \text{(A6.3.2)}$$

Solve equation A6.2.17 for a_7 in terms of a_4 and a_6. This yields the defining equation for a_7 as

$$a_7 = 3\beta_{17} - 3a_4 - \frac{3}{2} a_6 . \qquad \text{(A6.3.3)}$$

Solve equation A6.2.13 for a_8 in terms of a_2 and a_6. This yields the defining equation for a_8 as

$$a_8 = 3\beta_{13} - 3a_2 - \frac{3}{2} a_6 . \qquad \text{(A6.3.4)}$$

Solve equation A6.2.10 for a_{11} in terms of a_9 and a_{10}. This yields the defining equation for a_{11} as

$$a_{11} = 3\beta_{10} - 3a_9 + \frac{3}{2}a_{10}. \qquad \text{(A6.3.5)}$$

Solve equation A6.2.6 for a_{13} in terms of a_9 and a_{12}. This yields the defining equation for a_{13} as

$$a_{13} = 3\beta_6 - 3a_9 - \frac{3}{2}a_{12}. \qquad \text{(A6.3.6)}$$

Solve equation A6.2.18 for a_{15} in terms of a_{12} and a_{14}. This yields the defining equation for a_{15} as

$$a_{15} = 3\beta_{18} - 3a_{12} + \frac{3}{2}a_{14}. \qquad \text{(A6.3.7)}$$

Solve equation A6.2.14 for a_{16} in terms of a_{10} and a_{14}. This yields the defining equation for a_{16} as

$$a_{16} = 3\beta_{14} - 3a_{10} - \frac{3}{2}a_{14}. \qquad \text{(A6.3.8)}$$

Solve equation A6.2.11 for a_{19} in terms of a_{17} and a_{18}. This yields the defining equation for a_{19} as

$$a_{19} = 3\,\beta_{11} - 3\,a_{17} + \frac{3}{2}\,a_{18}\,. \qquad \text{(A6.3.9)}$$

Solve equation A6.2.7 for a_{21} in terms of a_{17} and a_{20}. This yields the defining equation for a_{21} as

$$a_{21} = 3\,\beta_{7} - 3\,a_{17} + \frac{3}{2}\,a_{20}\,. \qquad \text{(A6.3.10)}$$

Solve equation A6.2.19 for a_{23} in terms of a_{20} and a_{22}. This yields the defining equation for a_{23} as

$$a_{23} = 3\,\beta_{19} - 3a_{20} + \frac{3}{2}\,a_{22}. \qquad \text{(A6.3.11)}$$

Solve equation A6.2.15 for a_{24} in terms of a_{18} and a_{22}. This yields the defining equation for a_{24} as

$$a_{24} = 3\,\beta_{15} - 3\,a_{18} + \frac{3}{2}\,a_{22}. \qquad \text{(A6.3.12)}$$

Solve equation A6.2.12 for a_{27} in terms of a_{25} and a_{26}. This yields the defining equation for a_{27} as

$$a_{27} = 3\beta_{12} - 3\, a_{25} - \frac{3}{2}\, a_{26}\,. \qquad \text{(A6.3.13)}$$

Solve equation A6.2.8 for a_{29} in terms of a_{25} and a_{28}. This yields the defining equation for a_{29} as

$$a_{29} = 3\,\beta_{8} - 3\, a_{25} + \frac{3}{2}\, a_{28}. \qquad \text{(A6.3.14)}$$

Solve equation A6.2.20 for a_{31} in terms of a_{28} and a_{30}. This yields the defining equation for a_{31} as

$$a_{31} = 3\,\beta_{20} - 3\, a_{28} - \frac{3}{2}\, a_{30}. \qquad \text{(A6.3.15)}$$

Solve equation A6.2.16 for a_{32} in terms of a_{26} and a_{30}. This yields the defining equation for a_{32} as

$$a_{32} = 3\,\beta_{16} - 3\, a_{26} + \frac{3}{2}\, a_{30}. \qquad \text{(A6.3.16)}$$

Thus, 16 of the 32 equations in section A6.2 of this appendix have been used to solve for 16 of the unknowns. Table A6.3.1 summarizes the 16 equations which have been used to define 16 of the unknowns. This leaves 16 equations which have not been employed in this section. The next task is to write these 16 (so far unused) equations in terms of the 16 unknowns which were not defined in equations A6.3.1 through A6.3.16.

Defining Equation	Unknown Defined	Sixteen Unknowns Left	Defining Equation	Unknown Defined	Sixteen Unknowns Left
A6.2.5	a_5	a_1	A6.2.13	a_8	a_{17}
A6.2.6	a_{13}	a_2	A6.2.14	a_{16}	a_{18}
A6.2.7	a_{21}	a_4	A6.2.15	a_{24}	a_{20}
A6.2.8	a_{29}	a_6	A6.2.16	a_{32}	a_{22}
A6.2.9	a_3	a_9	A6.2.17	a_7	a_{25}
A6.2.10	a_{11}	a_{10}	A6.2.18	a_{15}	a_{26}
A6.2.11	a_{19}	a_{12}	A6.2.19	a_{23}	a_{28}
A6.2.12	a_{27}	a_{14}	A6.2.20	a_{31}	a_{30}

Table A6.3.1: Defining Equations for Sixteen Unknowns

To simplify the notation, the following definitions are introduced:

$$N = A^1_{CP2} \,/\, A^2_{CP1} \tag{A6.3.17}$$

$$n = D^1_{CP2} \,/\, D^2_{CP1} \tag{A6.3.18}$$

$$S = A^3_{CP4} \,/\, A^4_{CP3} \tag{A6.3.19}$$

$$s = D^3_{CP4} \,/\, D^4_{CP3} \tag{A6.3.20}$$

$$E = A^1_{CP4} \,/\, A^4_{CP1} \tag{A6.3.21}$$

$$e = D^1_{CP4} \,/\, D^4_{CP1} \tag{A6.3.22}$$

$$W = A^2_{CP3} \,/\, A^3_{CP2} \tag{A6.3.23}$$

$$w = D^2_{CP3} \,/\, D^3_{CP2}. \tag{A6.3.24}$$

These definitions are now employed as the remaining 16 equations are written in terms of the remaining 16 unknowns.

Equation A6.2.1 becomes

$$a_1 + \tfrac{1}{2} a_2 + \tfrac{1}{2} a_4 + \tfrac{1}{4} a_6 = \xi_1 \tag{A6.3.25}$$

$$= -\beta_1 + \beta_5 + \beta_9 + \tfrac{1}{2} \beta_{13} + \tfrac{1}{2} \beta_{17}$$

Equation A6.2.2 becomes

$$a_9 - \tfrac{1}{2} a_{10} + \tfrac{1}{2} a_{12} - \tfrac{1}{4} a_{14} = \xi_2 \tag{A6.3.26}$$

$$= -\beta_2 + \beta_6 + \beta_{10} - \tfrac{1}{2} \beta_{14} + \tfrac{1}{2} \beta_{18}$$

Equation A6.2.3 becomes

$$a_{17} - \frac{1}{2} a_{18} - \frac{1}{2} a_{20} + \frac{1}{4} a_{22} = \xi_3 \qquad \text{(A6.3.27)}$$

$$= -\beta_3 + \beta_7 + \beta_{11} - \frac{1}{2} \beta_{15} - \frac{1}{2}\beta_{19}.$$

Equation A6.2.4 becomes

$$a_{25} + \frac{1}{2} a_{26} - \frac{1}{2} a_{28} - \frac{1}{4} a_{30} = \xi_4 \qquad \text{(A6.3.28)}$$

$$= -\beta_4 + \beta_8 + \beta_{12} - \frac{1}{2} \beta_{20} + \frac{1}{2} \beta_{16}.$$

Equation A6.2.21 becomes

$$A^1_{CP3} \; a_1 - A^2_{CP4} \; a_9 = 0 = \xi_5. \qquad \text{(A6.3.29)}$$

Equation A6.2.22 becomes

$$A^2_{CP4} \; a_9 - A^3_{CP1} \; a_{17} = 0 = \xi_6. \qquad \text{(A6.3.30)}$$

Equation A6.2.23 becomes

$$A^3_{CP1} \; a_{17} - A^4_{CP2} \; a_{25} = 0 = \xi_7. \qquad \text{(A6.3.31)}$$

Equation A6.2.24 becomes

$$2N \; a_1 + \frac{1}{2} N \; a_4 - 2 \; a_9 - \frac{1}{2} \; a_{12} = \xi_8 \qquad \text{(A6.3.32)}$$

$$= 3N \; \beta_5 - 3\beta_6.$$

Equation A6.2.25 becomes

$$2E\ a_1 + \frac{1}{2}\ E\ a_2 - 2\ a_{25} - \frac{1}{2}\ a_{26} = \xi_9 \qquad \text{(A6.3.33)}$$

$$= 3E\beta_9 - 3\ \beta_{12}.$$

Equation A6.2.26 becomes

$$2S\ a_{17} - \frac{1}{2}\ S\ a_{20} - 2\ a_{25} + \frac{1}{2}\ a_{28} = \xi_{10} \qquad \text{(A6.3.34)}$$

$$= 3S\beta_7 - 3\ \beta_8.$$

Equation A6.2.27 becomes

$$2W\ a_9 - \frac{1}{2}\ W\ a_{10} - 2\ a_{17} + \frac{1}{2}\ a_{18} = \xi_{11} \qquad \text{(A6.3.35)}$$

$$= 3W\beta_{10} - 3\beta_{11}.$$

Equation A6.2.28 becomes

$$2Nn\ a_2 + \frac{1}{2}\ Nn\ a_6 - 2\ a_{10} - \frac{1}{2}\ a_{14} = \xi_{12} \qquad \text{(A6.3.36)}$$

$$= 3Nn\ \beta_{13} - 3\ \beta_{14}.$$

Equation A6.2.29 becomes

$$2Ee\ a_4 + \frac{1}{2}\ Ee\ a_6 - 2\ a_{28} - \frac{1}{2}\ a_{30} = \xi_{13} \qquad \text{(A6.3.37)}$$

$$= 3Ee\ \beta_{17} - 3\ \beta_{20}.$$

Equation A6.2.30 becomes

$$2Ss\ a_{18} - \frac{1}{2}\ Ss\ a_{22} - 2\ a_{26} + \frac{1}{2}\ a_{30} = \xi_{14} \qquad (A6.3.38)$$

$$= 3Ss\ \beta_{15} - 3\ \beta_{16}.$$

Equation A6.2.31 becomes

$$2Ww\ a_{12} - \frac{1}{2}\ Ww\ a_{14} - 2\ a_{20} + \frac{1}{2}\ a_{22} = \xi_{15} \qquad (A6.3.39)$$

$$= 3Ww\ \beta_{18} - 3\ \beta_{19}.$$

Equation A6.2.32 becomes

$$D^1_{CP3}\ A^1_{CP3}\ a_2 + D^1_{CP3}\ A^1_{CP3}\ a_4 +$$

$$-D^2_{CP4}\ A^2_{CP4}\ a_{10} + D^2_{CP4}\ A^2_{CP4}\ a_{12} +$$

$$-D^3_{CP1}\ A^3_{CP1}\ a_{18} - D^3_{CP1}\ A^3_{CP1}\ a_{20} +$$

$$D^4_{CP2}\ A^4_{CP2}\ a_{26} - D^4_{CP2}\ A^4_{CP2}\ a_{28} = 0. \qquad (A6.3.40)$$

A6.3.2 Reduction to 12 Equations in 12 Unknowns

Solve equation A6.3.25 for a_6 in terms of a_1 , a_2 and a_4. This yields the defining equation for a_6 as

$$a_6 = 4\ \xi_1 - 4\ a_1 - 2\ a_2 - 2\ a_4\ . \qquad \text{(A6.3.41)}$$

Solve equation A6.3.26 for a_{14} in terms of a_9 , a_{10} and a_{12}. This yields the defining equation for a_{14} as

$$a_{14} = -4\xi_2 + 4a_9 - 2\ a_{10} + 2\ a_{12}. \qquad \text{(A6.3.42)}$$

Solve equation A6.3.27 for a_{22} in terms of a_{17}, a_{18} and a_{20}. This yields the defining equation for a_{22} as

$$a_{22} = 4\ \xi_3 - 4\ a_{17} + 2\ a_{18} + 2\ a_{20} \qquad \text{(A6.3.43)}$$

Solve equation A6.3.28 for a_{30} in terms of a_{25} , a_{26} and a_{28}. This yields the defining equation for a_{30} as

$$a_{30} = -4\ \xi_4 + 4\ a_{25} + 2\ a_{26} - 2\ a_{28} \qquad \text{(A6.3.44)}$$

Thus, 4 of the 16 equations A6.3.25 through A6.3.40 have been used to solve for 4 of the unknowns. This leaves 12 equations which have not been employed in this section. The next task is to write these 12 equations in terms of the 12 unknowns which were not defined in equations A6.3.41 through A6.3.44.

Equation A6.3.29 becomes

$$A^1_{CP3}\, a_1 - A^2_{CP4}\, a_9 = \xi_5. \qquad \text{(A6.3.45)}$$

Equation A6.3.30 becomes

$$A^2_{CP4}\, a_9 - A^3_{CP1}\, a_{17} = \xi_6. \qquad \text{(A6.3.46)}$$

Equation A6.3.31 becomes

$$A^3_{CP1}\, a_{17} - A^4_{CP2}\, a_{25} = \xi_7. \qquad \text{(A6.3.47)}$$

Equation A6.3.32 becomes

$$2\,N\,a_1 + \tfrac{1}{2}\,N\,a_4 - 2\,a_9 - \tfrac{1}{2}\,a_{12} = \xi_8. \qquad \text{(A6.3.48)}$$

Equation A6.3.33 becomes

$$2\,E\,a_1 + \tfrac{1}{2}\,E\,a_2 - 2\,a_{25} - \tfrac{1}{2}\,a_{26} = \xi_9. \qquad \text{(A6.3.49)}$$

Equation A6.3.34 becomes

$$2\ S\ a_{17} - \frac{1}{2}\ S\ a_{20} - 2\ a_{25} + \frac{1}{2}\ a_{28} = \xi_{10}. \qquad \text{(A6.3.50)}$$

Equation A6.3.35 becomes

$$2\ W\ a_{9} - \frac{1}{2}\ W\ a_{10} - 2\ a_{17} + \frac{1}{2}\ a_{18} = \xi_{11}. \qquad \text{(A6.3.51)}$$

Equation A6.3.36 becomes

$$2\ Nn\ a_1 - Nn\ a_2 + Nn\ a_4 + 2\ a_9 + a_{10} + a_{12} =$$

$$2\ Nn\ \xi_1 + 2\ \xi_2 - \xi_{12}. \qquad \text{(A6.3.52)}$$

Equation A6.3.37 becomes

$$2\ Ee\ a_1 + Ee\ a_2 - Ee\ a_4 + 2\ a_{25} + a_{26} + a_{28} =$$

$$2\ Ee\ \xi_1 + 2\ \xi_4 - \xi_{13}. \qquad \text{(A6.3.53)}$$

Equation A6.3.38 becomes

$$2\ Ss\ a_{17} + Ss\ a_{18} - Ss\ a_{20} + 2\ a_{25} - a_{26} - a_{28} =$$

$$2\ Ss\ \xi_3 + 2\ \xi_4 + \xi_{14}. \qquad \text{(A6.3.54)}$$

Equation A6.3.39 becomes

$$2\,Ww\,a_9 - Ww\,a_{10} - Ww\,a_{12} + 2a_{17} - a_{18} + a_{20} = 2\,Ww\,\xi_2 + 2\,\xi_3 - \xi_{15}. \quad \text{(A6.3.55)}$$

Equation A6.3.40 becomes

$$\begin{aligned} & D^1_{CP3}\ A^1_{CP3}\ a_2 + D^1_{CP3}\ A^1_{CP3}\ a_4 + \\ & -D^2_{CP4}\ A^2_{CP4}\ a_{10} + D^2_{CP4}\ A^2_{CP4}\ a_{12} + \\ & -D^3_{CP1}\ A^3_{CP1}\ a_{18} - D^3_{CP1}\ A^3_{CP1}\ a_{20} + \\ & D^4_{CP2}\ A^4_{CP2}\ a_{26} - D^4_{CP2}\ A^4_{CP2}\ a_{28} = 0 \end{aligned} \quad \text{(A6.3.56)}$$

A6.3.3 Reduction to 9 Equations in 9 Unknowns

Solve equation A6.3.45 for a_9 in terms of a_1. This yields the defining equation for a_9 as

$$a_9 = \frac{A^1_{CP3}}{A^2_{CP4}} a_1 = C_2 a_1. \qquad \text{(A6.3.57)}$$

Solve equation A6.3.46 for a_{17} in terms of a_1. This yields the defining equation for a_{17} as

$$a_{17} = \frac{A^1_{CP3}}{A^3_{CP1}} a_1 = C_3 a_1. \qquad \text{(A6.3.58)}$$

Solve equation A6.3.47 for a_{25} in terms of a_1. This yields the defining equation for a_{25} as

$$a_{25} = \frac{A^1_{CP3}}{A^4_{CP2}} a_1 = C_4 a_1. \qquad \text{(A6.3.59)}$$

Thus, 3 of the 12 equations A6.3.45 through A6.3.56 have been used to solve for 3 of the unknowns. This leaves 9 equations which have not been employed in this section. The next task is to write these 9 equations in terms of the 9 unknowns which were not defined in equations A6.3.57 through A6.3.59.

Equation A6.3.48 becomes

$$[2N - 2C_2]\, a_1 + \frac{1}{2} N\, a_4 - \frac{1}{2} a_{12} = \xi_8. \qquad \text{(A6.3.60)}$$

Equation A6.3.49 becomes

$$[2E - 2C_4]\, a_1 + \frac{1}{2} E\, a_2 - \frac{1}{2} a_{26} = \xi_9. \qquad \text{(A6.3.61)}$$

Equation A6.3.50 becomes

$$[2SC_3 - 2C_4]\, a_1 - \frac{1}{2} S\, a_{20} + \frac{1}{2} a_{28} = \xi_{10}. \qquad \text{(A6.3.62)}$$

Equation A6.3.51 becomes

$$[2WC_2 - 2C_3]\, a_1 - \frac{1}{2} W\, a_{10} + \frac{1}{2} a_{18} = \xi_{11}. \qquad \text{(A6.3.63)}$$

Equation A6.3.52 becomes

$$[2\,Nn + 2C_2]\, a_1 - Nn\, a_2 + Nn\, a_4 + a_{10} + a_{12} = 2\,Nn\,\xi_1 + 2\,\xi_2 - \xi_{12}. \qquad \text{(A6.3.64)}$$

Equation A6.3.53 becomes

$$[2\ Ee + 2C_4]\ a_1 + Ee\ a_2 - Ee\ a_4 + a_{26} + a_{28} =$$

$$2\ Ee\ \xi_1 + 2\ \xi_4 - \xi_{13}. \quad \text{(A6.3.65)}$$

Equation A6.3.54 becomes

$$[2\ Ss\ C_3 + 2\ C_4]\ a_1 + Ss\ a_{18} - Ss\ a_{20} - a_{26} - a_{28} =$$

$$2\ Ss\ \xi_3 + 2\ \xi_4 + \xi_{14}. \quad \text{(A6.3.66)}$$

Equation A6.3.55 becomes

$$[2\ Ww\ C_2 + 2\ C_3]\ a_1 - Ww\ a_{10} - Ww\ a_{12} - a_{18} + a_{20} =$$

$$2\ Ww\ \xi_2 + 2\ \xi_3 - \xi_{15}. \quad \text{(A6.3.67)}$$

Equation A6.3.56 becomes

$$D^1_{CP3}\ A^1_{CP3}\ a_2 + D^1_{CP3}\ A^1_{CP3}\ a_4 +$$

$$-D^2_{CP4}\ A^2_{CP4}\ a_{10} + D^2_{CP4}\ A^2_{CP4}\ a_{12} +$$

$$-D^3_{CP1}\ A^3_{CP1}\ a_{18} - D^3_{CP1}\ A^3_{CP1}\ a_{20} +$$

$$D^4_{CP2}\ A^4_{CP2}\ a_{26} - D^4_{CP2}\ A^4_{CP2}\ a_{28} = 0. \quad \text{(A6.3.68)}$$

A6.3.4 Reduction to 5 Equations in 5 Unknowns

Solve equation A6.3.60 for a_{12} in terms of a_1 and a_4. This yields the defining equation for a_{12} as

$$a_{12} = -2\,\xi_8 + 4(N - C_2)\,a_1 + N\,a_4. \qquad \text{(A6.3.69)}$$

Solve equation A6.3.61 for a_{26} in terms of a_1 and a_2. This yields the defining equation for a_{26} as

$$a_{26} = -2\,\xi_9 + 4(E - C_4)\,a_1 + E\,a_2. \qquad \text{(A6.3.70)}$$

Solve equation A6.3.62 for a_{28} in terms of a_1 and a_{20}. This yields the defining equation for a_{28} as

$$a_{28} = 2\,\xi_{10} - 4(SC_3 - C_4)\,a_1 + S\,a_{20}. \qquad \text{(A6.3.71)}$$

Solve equation A6.3.63 for a_{18} in terms of a_1 and a_{10}. This yields the defining equation for a_{18} as

$$a_{18} = 2\,\xi_{11} - 4(WC_2 - C_3)\,a_1 + W\,a_{10}. \qquad \text{(A6.3.72)}$$

Thus, 4 of the 9 equations A6.3.60 through A6.3.68 have been used to solve for 4 of the unknowns. This leaves 5 equations which have not been employed in this section. The next task is to write these 5 equations in terms of the 5 unknowns which were not defined in equations A6.3.69 through A6.3.72.

To simplify the notation, the following definitions are introduced:

$$c_2 = D^1_{CP3} / D^2_{CP4} \qquad \text{(A6.3.73)}$$

$$c_3 = D^1_{CP3} / D^3_{CP1} \qquad \text{(A6.3.74)}$$

$$c_4 = D^1_{CP3} / D^4_{CP2} \, . \qquad \text{(A6.3.75)}$$

These definitions are now used as the remaining 5 equations are written in terms of the remaining 5 unknowns.

Equation A6.3.64 becomes

$$[4N + 2Nn - 2C_2]\, a_1 - Nn\, a_2 + (Nn + N)\, a_4 + a_{10} =$$

$$2Nn\, \xi_1 + 2\, \xi_2 + 2\, \xi_8 - \xi_{12} = \zeta_1 . \qquad \text{(A6.3.76)}$$

Equation A6.3.65 becomes

$$[2Ee + 4E + 2C_4 - 4\, S\, C_3]\, a_1 + [Ee + E]\, a_2 - Ee\, a_4 + S\, a_{20} =$$

$$2\, Ee\, \xi_1 + 2\, \xi_4 + 2\, \xi_9 - 2\, \xi_{10} - \xi_{13} = \zeta_2 . \qquad \text{(A6.3.77)}$$

Equation A6.3.66 becomes

$$[2\ Ss\ C_3 + 2\ C_4 - 4\ Ss\ W\ C_2 + 4\ Ss\ C_3 - 4E + 4\ S\ C_3]\ a_1 +$$

$$- E\ a_2 + Ss\ W\ a_{10} - [Ss + S]\ a_{20} =$$

$$2\ Ss\ \xi_3 + 2\ \xi_4 - 2\ \xi_9 + 2\ \xi_{10} - 2\ Ss\ \xi_{11} + \xi_{14} = \zeta_3. \qquad \text{(A6.3.78)}$$

Equation A6.3.67 becomes

$$[6\ Ww\ C_2 - 2\ C_3 - 4\ Ww\ N + 4\ W\ C_2]\ a_1 +$$

$$- Ww\ N\ a_4 - (Ww + W)\ a_{10} + a_{20} =$$

$$2\ Ww\ \xi_2 + 2\ \xi_3 - 2\ Ww\ \xi_8 + 2\ \xi_{11} - \xi_{15} = \zeta_4. \qquad \text{(A6.3.79)}$$

Equation A6.3.68 becomes

$$\left(\frac{4N}{C_2\ c_2} - \frac{4}{c_2} + \frac{4\ W\ C_2}{C_3\ c_3} - \frac{4}{c_3} + \frac{4\ E}{C_4\ c_4} - \frac{4}{c_4} + \frac{2\ S\ C_3}{C_4\ c_4} - \frac{4}{c_4} \right) a_1 +$$

$$\left[1 + \frac{E}{C_4\ c_4} \right] a_2 + \left[1 + \frac{N}{C_2\ c_2} \right] a_4 - \left[\frac{1}{C_2\ c_2} + \frac{W}{C_3\ c_3} \right] a_{10} +$$

$$- \left[\frac{1}{C_3\ c_3} + \frac{S}{C_4\ c_4} \right] a_{20} =$$

$$\left(\frac{2\ \xi_8}{C_2\ c_2} + \frac{2\ \xi_9}{C_4\ c_4} + \frac{2\ \xi_{10}}{C_4\ c_4} + \frac{2\ \xi_{11}}{C_3\ c_3} \right) = \zeta_5. \qquad \text{(A6.3.80)}$$

A6.3.5 Reduction to 4 Equations in 4 Unknowns

Solve equation A6.3.76 for a_{10} in terms of a_1, a_2 and a_4. This yields the defining equation for a_{10} as

$$a_{10} = \zeta_1 - [4N + 2Nn - 2C_2]\, a_1 + Nn\, a_2 - [Nn+N]\, a_4 \qquad \text{(A6.3.81)}$$

Thus, 1 of the 5 equations A6.3.76 through A6.3.80 has been used to solve for 1 of the unknowns. This leaves 4 equations which have not been employed in this section. The next task is to write these 4 equations in terms of the 4 unknowns which were not defined in equation A6.3.81.

Equation A6.3.77 becomes

$$[2\,Ee + 4E + 2C_4 - 4\,S\,C_3]\, a_1 + [Ee + E]\, a_2 - Ee\, a_4 + S\, a_{20} = \zeta_2. \qquad \text{(A6.3.82)}$$

Equation A6.3.78 becomes

$$[6SsC_3 + 2C_4 - 2SsWC_2 - 4E + 4SC_3 - 4NSsW - 2NnSsW]\, a_1 + [Nn\,Ss\,W - E]\, a_2 - [(Nn + N)SsW]\, a_4 - [Ss+S]\, a_{20} = \zeta_3 - Ss\,W\,\zeta_1. \qquad \text{(A6.3.83)}$$

Equation A6.3.79 becomes

$$[4WwC_2 + 2WC_2 - 2C_3 + 4NW + 2Nn(Ww+W)]\ a_1 +$$

$$-[Nn(Ww+W)]\ a_2 + [Nn(Ww+W) + WN]\ a_4 + a_{20} =$$

$$\zeta_4 + (Ww+W)\ \zeta_1. \qquad \text{(A6.3.84)}$$

Equation A6.3.80 becomes

$$\left(\frac{8N}{C_2\ c_2} + \frac{2\ N\ n}{C_2\ c_2} + \frac{4\ W\ C_2}{C_3\ c_3} + \frac{4\ N\ W}{C_3\ c_3} + \frac{2\ Nn\ W}{C_3\ c_3} + \frac{4\ S\ C_3}{C_4\ c_4} + \right.$$

$$\left. + \frac{4E}{C_4\ c_4} - \frac{2\ W}{c_3} - \frac{6}{c_2} - \frac{4}{c_3} - \frac{8}{c_4} \right) a_1 +$$

$$\left[1 - \frac{Nn}{C_2\ c_2} - \frac{Nn\ W}{C_3\ c_3} + \frac{E}{C_4\ c_4} \right]\ a_2 +$$

$$\left[1 + \frac{2N}{C_2\ c_2} + \frac{Nn}{C_2\ c_2} + \frac{Nn\ W}{C_3\ c_3} + \frac{NW}{C_3\ c_3} \right]\ a_4 +$$

$$-\left[\frac{1}{C_3\ c_3} + \frac{S}{C_4\ c_4} \right]\ a_{20} =$$

$$\left[\frac{1}{C_2\ c_2} + \frac{W}{C_3\ c_3} \right]\ \zeta_1 + \zeta_5. \qquad \text{(A6.3.85)}$$

A6.3.6 Reduction to 3 Equations in 3 Unknowns

Solve equation A6.3.84 for a_{20} in terms of a_1, a_2 and a_4. This yields the defining equation for a_{20} as

$$a_{20} = (Ww + W)\,\zeta_1 + \zeta_4 +$$
$$[-4Ww\,C_2 - 2W\,C_2 + 2\,C_3 - 4\,NW - 2Nn(Ww+W)]\,a_1 +$$
$$[Nn\,(Ww+W)]\,a_2 +$$
$$-[Nn\,(Ww+W) + WN]\,a_4. \qquad \text{(A6.3.86)}$$

Thus, 1 equation of the 4 equations A6.3.82 through A6.3.85 has been used to solve for 1 of the unknowns. This leaves 3 equations which have not been employed in this section. The next task is to write these 3 equations in terms of the 3 unknowns; a_1, a_2 and a_4.

Equation A6.3.83 becomes

$$[6\,Ss\,C_3 + 2\,C_4 - 2\,Ss\,W\,C_2 - 4E + 4\,S\,C_3 - 4NSs\,W +$$
$$-2NnSsW + 4Ww(Ss+S)\,C_2 + 2W(Ss+S)C_2 - 2(Ss+S)\,C_3 +$$
$$+4NW(Ss+S)+2Nn(Ss+S)(Ww+W)]\quad a_1 +$$
$$[NnSsW - Nn(Ss+S)(Ww+W) - E]\quad a_2 +$$
$$[Nn(Ss+S)(Ww+W) + NW(Ss+S) - SsW(Nn+N)]\,a_4 =$$
$$[(Ss+S)(Ww+W) - SsW]\,\zeta_1 + \zeta_3 + [Ss+S]\,\zeta_4. \qquad \text{(A6.3.87)}$$

Equation A6.3.82 becomes

$$[2Ee + 4E + 2\,C_4 - 2S\,C_3 - 4SWw\,C_2 - 2SW\,C_2 - 4NSW$$

$$- 2\,NnS(Ww+W)\,]\quad a_1\ +$$

$$[(Ee+E) + NnS(Ww+W)]\quad a_2\ +$$

$$[-NSW - NnS(Ww+W) - Ee]\ a_4\ =$$

$$[\,-S(Ww+W)]\ \zeta_1\ +\ \zeta_2\ -\ S\,\zeta_4. \qquad \text{(A6.3.88)}$$

Equation A6.3.85 becomes

$$\left(\frac{8\,N}{C_2\ c_2} + \frac{2\,N\,n}{C_2\ c_2} - \frac{6}{c_2} + \frac{4\ (Ww+W)\ C_2}{C_3\ c_3} + \frac{8NW}{C_3\ c_3}\ +\right.$$

$$+ \frac{2NnW}{C_3\ c_3} + \frac{2\ W\ C_2}{C_3\ c_3} - \frac{6}{c_3} + \frac{2\ Nn(Ww+W)}{C_3\ c_3}\ +$$

$$- \frac{2\ W}{c_3} + \frac{4\ E}{C_4\ c_4} + \frac{4\ S\ Ww\ C_2}{C_4\ c_4} + \frac{2\ S\ W\ C_2}{C_4\ c_4}\ +$$

$$- \frac{2\ S\ C_3}{C_4\ c_4} + \frac{4\ S\ C_2}{C_4\ c_4} + \frac{4\ NSW}{C_4\ c_4}\ +$$

$$\left.+ \frac{2\ Nn\ S\ (Ww+W)}{C_4\ c_4} - \frac{8}{C_4}\right)\ a_1\ +\ \text{(Equation continued on next page)}$$

$$\left(1 - \frac{Nn}{C_2\ c_2} - \frac{Nn\ W}{C_3\ c_3} - \frac{Nn\ (Ww+W)}{C_3\ c_3} + \frac{E}{C_4\ c_4} + \right.$$

$$\left. - \frac{Nn\ S\ (Ww+W)}{C_4\ c_4} \right) a_2 +$$

$$\left(1 + \frac{2N}{C_2\ c_2} + \frac{Nn}{C_2\ c_2} + \frac{Nn\ W}{C_3\ c_3} + \frac{2NW}{C_3\ c_3} + \frac{Nn\,(Ww+W)}{C_3\ c_3} + \right.$$

$$\left. + \frac{Nn\ S\ (Ww+W)}{C_4\ c_4} + \frac{NSW}{C_4\ c_4} \right) a_4 =$$

$$\left(\frac{1}{C_2\ c_2} + \frac{2W}{C_3\ c_3} + \frac{Ww}{C_3\ c_3} + \frac{S\ (Ww+W)}{C_4\ c_4} \right) \zeta_1 +$$

$$\left(\frac{1}{C_3\ c_3} + \frac{S}{C_4\ c_4} \right) \zeta_4 + \zeta_5. \qquad \text{(A6.3.89)}$$

A6.3.7 Reduction to 2 Equations in 2 Unknowns

Solve equation A6.3.88 for a_2 in terms of a_1 and a_4. This yields the defining equation for a_2 as

$$a_2 =$$

$$\frac{[-2Ee - 4E - 2C_4 + 2SC_3 + 4SWwC_2 + 2SWC_2 + 4NSW + 2NnS(Ww+W)]\ a_1}{[(Ee+E) + NnS(Ww+W)]} +$$

$$\frac{[NSW + Ee + NnS(Ww+W)]\ a_4}{[(Ee+E) + NnS(Ww+W)]} +$$

$$\frac{[\ -S(Ww+W)\ \zeta_1 + \zeta_2 - S\ \zeta_4\ ]}{[(Ee+E) + NnS(Ww+W)]} \quad . \qquad \text{(A6.3.90)}$$

This 1 equation for a_2 is used to eliminate a_2 from equations A6.3.87 and A6.3.89. When this is done equation A6.3.87 can be expressed as

$$B_{11}\ a_1 + B_{12}\ a_4 = \theta_1 \qquad \text{(A6.3.91)}$$

and equation A6.3.89 can be expressed as

$$B_{21}\ a_1 + B_{22}\ a_4 = \theta_2. \qquad \text{(A6.3.92)}$$

The meanings of B_{11} , B_{12} , θ_1 , B_{21} , B_{22} and θ_2 are given momentarily. However, first the coupled set of equations A6.3.91 and A6.3.92 is solved to yield the defining equations for a_1 as

$$a_1 = \frac{[\theta_1 B_{22} - \theta_2 B_{12}]}{[B_{11} B_{22} - B_{21} B_{12}]} \qquad \text{(A6.3.93)}$$

and

$$a_2 = \frac{[\theta_2 B_{11} - \theta_1 B_{21}]}{[B_{11} B_{22} - B_{21} B_{12}]} . \qquad \text{(A6.3.94)}$$

The equation for B_{11} is

$$B_{11} = \left\{ [6Ss\,C_3 + 2C_4 - 2SsWC_2 - 4E + 4SC_3 - 4NSsW - 2NnSsW + \right.$$

$$\left. + 4Ww(Ss+S)C_2 + 2W(Ss+S)\,C_2 - 2(Ss+S)\,C_3 + 4NW(Ss+S) + \right.$$

$$\left. + 2\,Nn\,(Ss+S)\,(Ww+W)\,] \right\} + \left\{ [NnSsW - Nn(Ss+S)(Ww+W) - E\,] * \right.$$

$$\left. \frac{[-2Ee - 4E - 2C_4 + 2SC_3 + 4SWwC_2 + 2SWC_2 + 4NSW + 2NnS(Ww+W)]}{[\,(Ee+E) + NnS(Ww+W)\,]} \right\} \qquad \text{(A6.3.95)}$$

The equation for B_{12} is

$$B_{12} =$$

$$[Nn(Ss+S)(Ww+W) + NW(Ss+S) - Ss\ W(Nn+N)] +$$

$$\frac{[NnSsW - Nn(Ss+S)(Ww+W) - E]\ [\ NSW + Ee + NnS(Ww+W)]}{[\ (Ee+E) + NnS(Ww+W)\ ]} .$$

(A6.3.96)

The equation for θ_1 is

$$\theta_1 =$$

$$\left([(Ss+S)(Ww+W) - SsW] + \frac{[S(Ww+W)][NnSsW - Nn(Ss+S)(Ww+W) - E]}{[(Ee+E) + NnS(Ww+W)\ ]} \right) \zeta_1 +$$

$$\left(\frac{[\ E - NnSsW + Nn(Ss+S)(Ww+W)\ ]}{[(Ee+E) + NnS\ (Ww+W)\ ]} \right) \zeta_2 + \zeta_3 +$$

$$\left([Ss+S] + \frac{S[NnSsW - Nn(Ss+S)(Ww+W) - E\ ]}{[(Ee+E) + Nn\ S\ (Ww+W)\ ]} \right) \zeta_4$$

(A6.3.97)

The following quantity is useful in the definitions of B_{21} , B_{22} and θ_2 :

$$T = \left(\frac{\left[1 - \frac{Nn}{C_2\ c_2} - \frac{Nn\ W}{C_3\ c_3} - \frac{Nn(Ww+W)}{C_3\ c_3} + \frac{E}{C_4\ c_4} - \frac{NnS(Ww+W)}{C_4\ c_4}\right.}{\left.[(Ee+E) + NnS(Ww+W)\ ]\right.} \right).$$

(A6.3.98)

The equation for B_{21} is

$$B_{21} =$$

$$\left(\frac{8N}{C_2\ c_2} + \frac{2\ Nn}{C_2\ c_2} - \frac{6}{c_2} + \frac{4(Ww+W)\ C_2}{C_3\ c_3} + \frac{8NW}{C_3\ c_3} + \frac{2NnW}{C_3\ c_3} + \right.$$

$$+ \frac{2WC_2}{C_3\ c_3} - \frac{6}{c_3} + \frac{2Nn(Ww+W)}{C_3\ c_3} - \frac{2W}{C_3} + \frac{4E}{C_4\ c_4} +$$

$$+ \frac{4SWw\ C_2}{C_4\ c_4} + \frac{2\ SW\ C_2}{C_4\ c_4} - \frac{2\ S\ C_3}{C_4\ c_4} + \frac{4S\ C_2}{C_4\ c_4} + \frac{4NSW}{C_4\ c_4} +$$

$$\left. + \frac{2NnS(Ww+W)}{C_4\ c_4} - \frac{8}{c_4} \right) +$$

$$T\ [\ -2Ee - 4E - 2\ C_4 + 2S\ C_3 + 4SWw\ C_2 + 2SW\ C_2 + 4NSW + 2NnS(Ww+W)]$$

(A6.3.99)

The equation for B_{22} is

$$B_{22} =$$

$$\left[1 + \frac{2N}{C_2\ c_2} + \frac{Nn}{C_2\ c_2} + \frac{NnW}{C_3\ c_3} + \frac{2NW}{C_3\ c_3} + \frac{Nn(Ww+W)}{C_3\ c_3} + \right.$$

$$\left. + \frac{NnS(Ww+W)}{C_4\ c_4} + \frac{NSW}{C_4\ c_4} \right] + T[NSW + Ee + NnS(Ww+W)]$$

(A6.3.100)

The equation for θ_2 is

$$\theta_2 =$$

$$\left(\left[\frac{1}{C_2\ c_2} + \frac{2W}{C_3\ c_3} + \frac{Ww}{C_3\ c_3} + \frac{S(Ww+W)}{C_4\ c_4} \right] + T[S(Ww+W)] \right) \zeta_1 +$$

$$- T\ \zeta_2$$

$$\left(\left[\frac{1}{C_3\ c_3} + \frac{S}{C_4\ c_4} + TS \right) \zeta_4 + \zeta_5 . \right. \qquad \text{(A6.3.101)}$$

APPLICATION OF NODAL EQUIVALENCE THEORY TO THE NEUTRONIC ANALYSIS OF PWRS

(Vol. II)

by

Christopher Lloyd Hoxie

B. S., University of Florida (1975)

M. E., University of Florida (1978)

SUBMITTED IN PARTIAL FULFILLMENT

OF THE REQUIREMENTS FOR THE

DEGREE OF

DOCTOR OF PHILOSOPHY

AT THE

MASSACHUSETTS INSTITUTE OF TECHNOLOGY

JUNE 1982

Signature of Author . . . . . .
Department of Nuclear Engineering
June 1982

Certified by . . . . . .
Allan F. Henry
Thesis Supervisor

Accepted by . . . . . .
Allan F. Henry
Chairman, Department Graduate Committee

Appendix 7

CARILLON

The purpose of this appendix is to describe the CARILLON method for interpolating the heterogeneous fluxes at the corners of PWR assemblies. This method is based upon two assumptions:

1. The heterogeneous flux shape along an assembly face may be well represented by a quadratic function fit to the average flux along the face and the two corner point fluxes at each end of the face.

2. Each corner point in the PWR core is source free.

For a discussion of the CARILLON method, start by viewing Figure A7.1. This figure shows four PWR assembly interfaces which meet at a central point (i,j). The four nearest neighboring corner points are at points (i+1,j), (i-1,j), (i,j+1) and (i,j-1). The fluxes at these five corner points are unknown. However the diffusion coefficients and the four surface-averaged fluxes, $\bar{\phi}_{i+\frac{1}{2},j}$, $\bar{\phi}_{i-\frac{1}{2},j}$, $\bar{\phi}_{i,j+\frac{1}{2}}$ and $\bar{\phi}_{i,j-\frac{1}{2}}$ are known. For convenience an (x,y) Cartesian coordinate system is placed with its origin at (i,j).

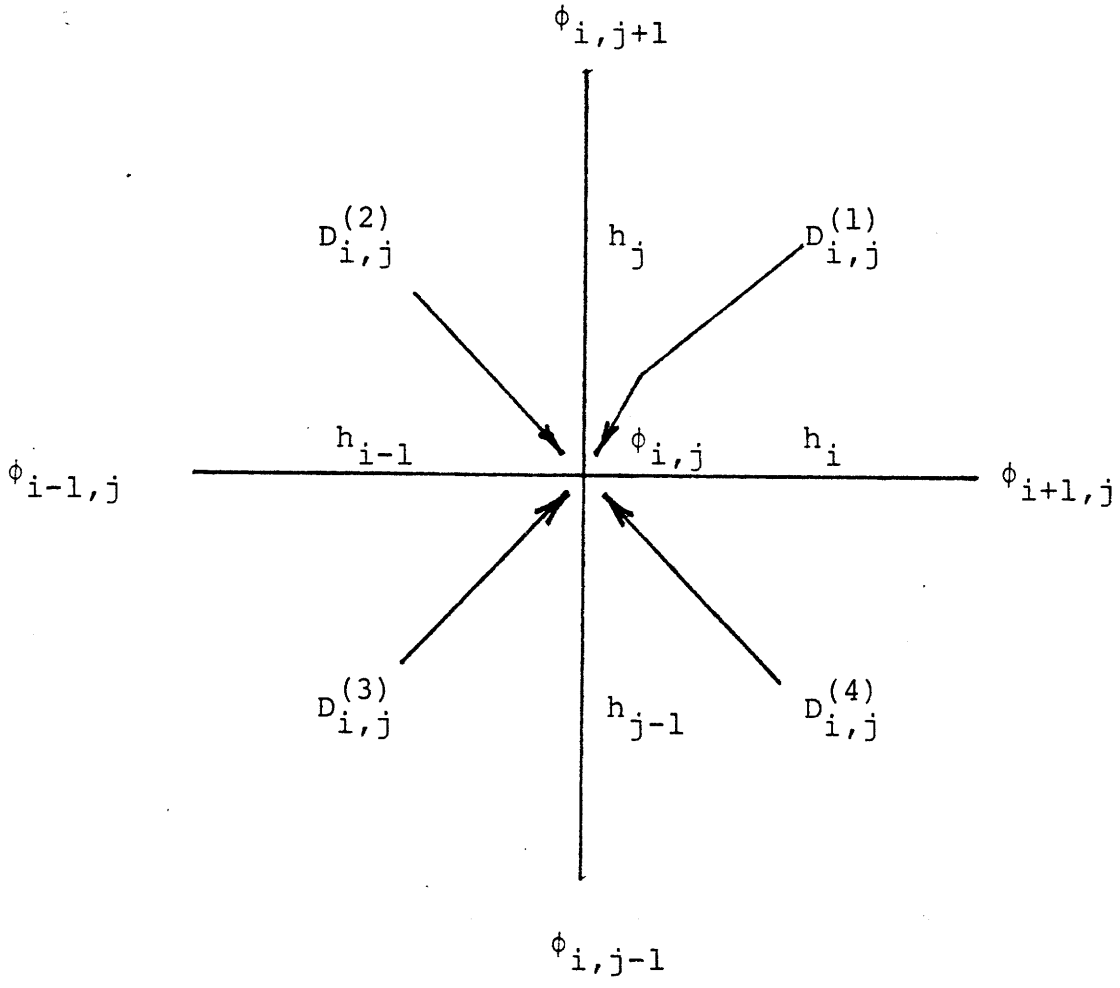

Figure A7.1: CARILLON Geometry

The first step in the CARILLON derivation is to use assumption 1 to express the heterogeneous flux shapes along the four assembly surfaces as quadratics which preserve the known surface-averaged heterogeneous fluxes and the unknown heterogeneous corner point fluxes. Along the x+ axis this yields

$$\phi^{+}(x) = \left[3\phi_{i+1,j} + 3\phi_{i,j} - 6\,\bar{\phi}_{i+\frac{1}{2},j}\right]\left(\frac{x}{h_i}\right)^2 + \left[-2\phi_{i+1,j} - 4\phi_{i,j} + 6\,\bar{\phi}_{i+\frac{1}{2},j}\right]\left(\frac{x}{h_i}\right) + \phi_{i,j} \cdot \qquad \text{(A7.1)}$$

Along the x- axis the following quadratic is used:

$$\phi^{-}(x) = \left[3\phi_{i-1,j} + 3\phi_{i,j} - 6\bar{\phi}_{i-\frac{1}{2},j}\right]\left(\frac{x}{h_{i-1}}\right)^2 + \left[2\phi_{i-1,j} + 4\phi_{i,j} - 6\bar{\phi}_{i-\frac{1}{2},j}\right]\left(\frac{x}{h_{i-1}}\right) + \phi_{i,j} \qquad \text{(A7.2)}$$

Along the y+ axis the following quadratic is used:

$$\phi^{+}(y) = \left[\, 3\phi_{i,j+1} + 3\phi_{i,j} - 6\bar{\phi}_{i,j+\frac{1}{2}} \,\right] \left(\frac{y}{h_j}\right)^2 +$$

$$\left[-2\phi_{i,j+1} - 4\phi_{i,j} + 6\bar{\phi}_{i,j+\frac{1}{2}} \,\right] \left(\frac{y}{h_j}\right) +$$

$$\phi_{i,j} \; . \qquad \text{(A7.3)}$$

Along the y- axis the following quadratic is used:

$$\phi^{-}(y) = \left[\, 3\phi_{i,j-1} + 3\phi_{i,j} - 6\,\bar{\phi}_{i,j-\frac{1}{2}} \,\right] \left(\frac{y}{h_{j-1}}\right)^2 +$$

$$\left[\, 2\phi_{i,j-1} + 4\phi_{i,j} - 6\,\bar{\phi}_{i,j-\frac{1}{2}} \,\right] \left(\frac{y}{h_{j-1}}\right) +$$

$$\phi_{i,j} \; . \qquad \text{(A7.4)}$$

These four quadratic flux expressions A7.1 through A7.4 are related by requiring the point (i,j) to be source free. A small box of dimension δ-by-δ is constructed about the point (i,j). The source free condition is then expressed as

$$\lim_{\delta \to o} \int_{V_{box}} \nabla \cdot \vec{J} \; dV = \lim_{\delta \to o} \int_{S_{box}} \vec{J} \cdot \hat{n} \; dS = 0 \qquad \text{(A7.5)}$$

where V_{box} refers to the volume of the small box and S_{box} refers to the surface of the small box. By using the source free condition and Fick's law, the following 5-point difference equation is derived:

$$a^N \phi_{i,j+1} + a^E \phi_{i+1,j} + a^S \phi_{i,j-1} + a^W \phi_{i-1,j} + a^C \phi_{i,j} =$$

$$3[\, a^N \overline{\phi}_{i,j+\frac{1}{2}} + a^E \overline{\phi}_{i+\frac{1}{2},j} + a^S \overline{\phi}_{i,j-\frac{1}{2}} + a^W \overline{\phi}_{i-\frac{1}{2},j}] \qquad \text{(A7.6)}$$

where

$$a^N = \frac{D^{(1)}_{i,j} + D^{(2)}_{i,j}}{2\,h_j} \qquad \text{(A7.7)}$$

$$a^E = \frac{D^{(1)}_{i,j} + D^{(4)}_{i,j}}{2\,h_i} \qquad \text{(A7.8)}$$

$$a^S = \frac{D^{(3)}_{i,j} + D^{(4)}_{i,j}}{2\,h_{j-1}} \qquad \text{(A7.9)}$$

$$a^W = \frac{D^{(2)}_{i,j} + D^{(3)}_{i,j}}{2\,h_{i-1}} \qquad \text{(A7.10)}$$

$$a^C = 2\,[\,a^N + a^E + a^S + a^W\,]. \qquad \text{(A7.11)}$$

Thus equation A7.6 shows that each corner point is coupled to its four nearest neighbors.

Suppose a PWR core has N corner points. Then an equation of the form presented in equation A7.6 may be written for each of the N points resulting in a large linear system of N equations in N unknown corner point fluxes. By solving this system of equations, all N corner point fluxes are "interpolated" at once.

The system of N equations in N unknowns may be cast in matrix form as

$$\underline{\underline{A}}\ \underline{\phi} = \underline{S} \qquad \text{(A7.12)}$$

where $\underline{\underline{A}}$ is an N-by-N matrix with 5 stripes, and $\underline{\phi}$ is and N-by-1 column vector of corner point fluxes and $\underline{S}$ is a known N-by-1 column vector.

For the special case where the diffusion coefficients at the corners of any given PWR assembly are identical, the matrix $\underline{\underline{A}}$ is symmetric. It may also be shown that $\underline{\underline{A}}$ is positive definite and a non-iterative method of solution called Cholesky decomposition [39] is available. However, for the more general case when the diffusion coefficients at each corner of a PWR assembly are allowed to be different, $\underline{\underline{A}}$ is not symmetric and Cholesky decomposition may not be employed.

For the general case of differing diffusion coefficients at each corner of a PWR assembly, the matrix $\underline{\underline{A}}$ is still strictly diagonally dominant. Therefore, a point Gauss-Seidel iterative method is guaranteed to converge [40, pg. 73]. Thus this is the method which was chosen for solving the matrix equation A7.12.

In CARILLON the point Gauss-Seidel method is implemented in the following manner. The spatial grid is set up with the point (i=1,j=1) in the upper right-hand corner of the reactor core. Sweeping of the mesh starts at the top left and continues row-by-row until the point at the bottom right-hand corner of the reactor is reached. A consistent line ordering [41] of the elements in the $\underline{\phi}$ vector is used. For this type of mesh sweeping, the point Gauss-Seidel iterative method may be written as

$$\phi_{i,j}^{(t)} = \frac{1}{a^C} \left[S_{i,j} - a^W \phi_{i-1,j}^{(t)} - a^N \phi_{i,j+1}^{(t)} + \right.$$

$$\left. -a^E \phi_{i+1,j}^{(t-1)} - a^S \phi_{i,j-1}^{(t-1)} \right] \qquad \text{(A7.13)}$$

where the superscript t is the iteration number or index.

Appendix 8

CAMPANA

The purpose of this appendix is to describe the CAMPANA method for interpolating the heterogeneous fluxes at the corners of PWR assemblies. This method is based on two assumptions:

1. The form function along the surfaces of a PWR assembly may be well represented by a quadratic function.

2. Each corner point in a PWR core is source free. (See Appendix 7 for a description of this condition.)

For a discussion of the CAMPANA method, start by viewing Figure A8.1. This figure shows four PWR assembly interfaces which meet at a central point (i,j). The four nearest neighboring corner points are at the points (i+1,j), (i-1,j), (i,j+1) and (i,j-1). The fluxes at these five corner points are unknown. However, the diffusion coefficients and the four surface-averaged fluxes, $\bar{\phi}_{i+\frac{1}{2},j}$, $\bar{\phi}_{i-\frac{1}{2},j}$, $\bar{\phi}_{i,j+1}$ and $\bar{\phi}_{i,j-\frac{1}{2}}$ are known. For convenience an (x,y) Cartesian coordinate system is

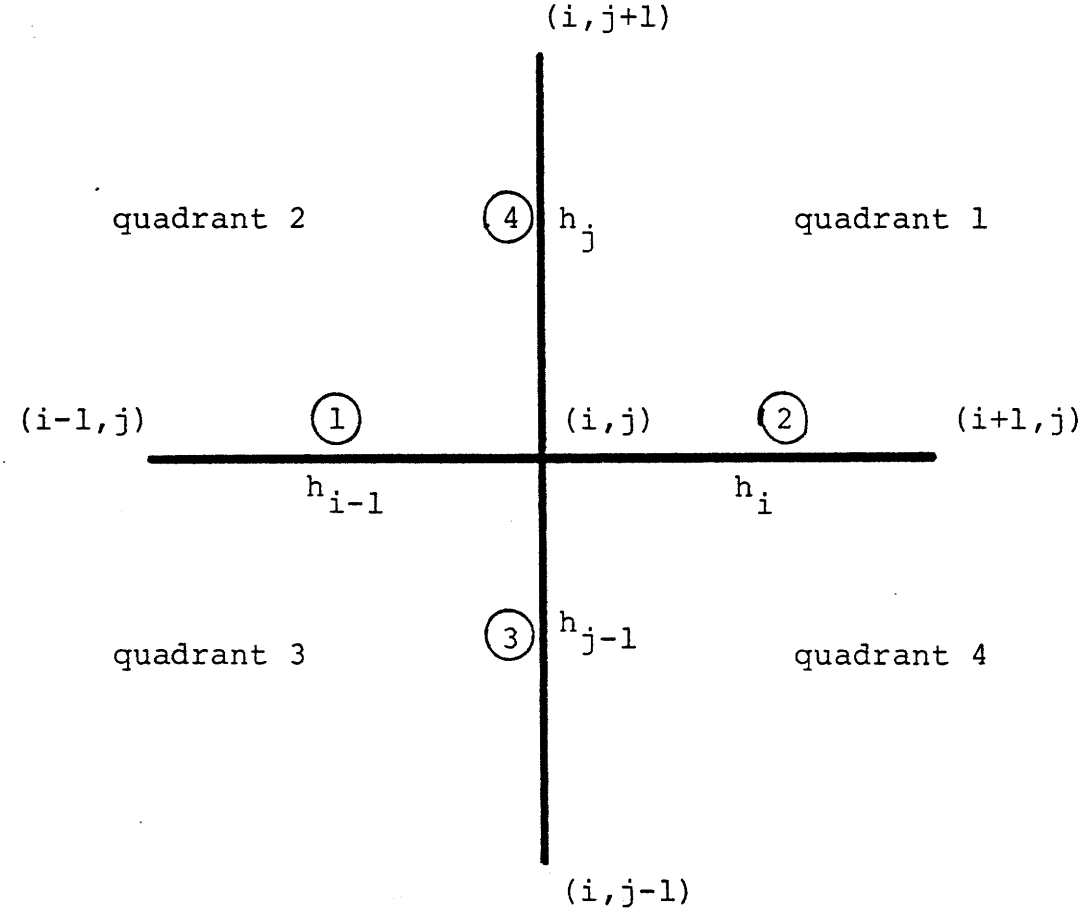

Figure A8.1 CAMPANA Geometry

placed with its origin at (i,j). Note that the x-, x+ , y- and y+ portions of the assembly faces are labeled 1, 2, 3 and 4 respectively.

The heterogeneous assembly flux shape is assumed known for each of the assemblies. From these assembly flux shapes, four average assembly flux shapes along the x-, x+, y- and y+ portions of the assembly faces are found as follows:

$$1.\quad A^{x-}(x) = \tfrac{1}{2}\left(A^{q2}(x) + A^{q3}(x)\right) \qquad \text{(A8.1)}$$

$$2.\quad A^{x+}(x) = \tfrac{1}{2}\left(A^{q1}(x) + A^{q4}(x)\right) \qquad \text{(A8.2)}$$

$$3.\quad A^{y-}(y) = \tfrac{1}{2}\left(A^{q3}(y) + A^{q4}(y)\right) \qquad \text{(A8.3)}$$

$$4.\quad A^{y+}(y) = \tfrac{1}{2}\left(A^{q1}(y) + A^{q2}(y)\right). \qquad \text{(A8.4)}$$

In the above equations, $A^{q1}(x)$; for example, is found from the known assembly flux shape for the quadrant 1 assembly, $A^{q1}(x,y)$. $A^{q1}(x)$ is found by normalizing the shape $A^{q1}(x, y=0)$ along the x+ axis to unity average.

From the equations A8.1 through A8.4, the corner point values of the average assembly flux shape are:

$$A^{x-}_{i,j} = A^{x-}(0) \qquad A^{x-}_{i-1,j} = A^{x-}(-h_{i-1})$$

$$A^{x+}_{i,j} = A^{x+}(0) \qquad A^{x+}_{i+1,j} = A^{x+}(+h_i)$$

$$A^{y-}_{i,j} = A^{y-}(0) \qquad A^{y-}_{i,j-1} = A^{y-}(-h_{j-1})$$

$$A^{y+}_{i,y} = A^{y+}(0) \qquad A^{y+}_{i,j+1} = A^{y+}(+h_j).$$

Along the x+ axis require:

$$\phi^{x+}(x) = F^{x+}(x) \quad A^{x+}(x) \tag{A8.5}$$

$$F^{x+}(x) = a_2 \left[\frac{x}{h_i} \right]^2 + a_1 \left[\frac{x}{h_i} \right] + a_0 . \tag{A8.6}$$

Along the x- axis require:

$$\phi^{x-}(x) = F^{x-}(x) \quad A^{x-}(x) \tag{A8.7}$$

$$F^{x-}(x) = b_2 \left[\frac{x}{h_{i-1}} \right]^2 + b_1 \left[\frac{x}{h_{i-1}} \right] + b_0. \tag{A8.8}$$

Along the y+ axis require:

$$\phi^{y+}(y) = F^{y+}(y) \quad A^{y+}(y) \tag{A8.9}$$

$$F^{y+}(y) = c_2 \left[\frac{y}{h_j} \right]^2 + c_1 \left[\frac{y}{h_j} \right] + c_0. \tag{A8.10}$$

Along the y- axis require:

$$\phi^{y-}(y) = F^{y-}(y) \quad A^{y-}(y) \tag{A8.11}$$

$$F^{y-}(y) = d_2 \left[\frac{y}{h_{j-1}} \right]^2 + d_1 \left[\frac{y}{h_{j-1}} \right] + d_0. \tag{A8.12}$$

Solve for the 12 unknowns a_2 , a_1, a_0, b_2 , b_1 , b_0, c_2 , c_1 , c_0 , d_2 , d_1 and d_0. Express these in terms of the corner point fluxes and the surface-averaged fluxes.

Continuity of flux at (i,j) immediately yields

$$a_0 = \phi_{i,j} \; / \; A^{x+}_{i,j} \qquad \text{(A8.13)}$$

$$b_0 = \phi_{i,j} \; / \; A^{x-}_{i,j} \qquad \text{(A8.14)}$$

$$c_0 = \phi_{i,j} \; / \; A^{y+}_{i,j} \qquad \text{(A8.15)}$$

$$d_0 = \phi_{i,j} \; / \; A^{y-}_{i,j}. \qquad \text{(A8.16)}$$

The other 8 unknowns are solved for by matching the four known surface averaged fluxes and the four neighboring corner point fluxes to the point (i,j).

To match the surface-averaged flux, $\overline{\phi}_{i+\frac{1}{2}}$, along the x+ axis impose

$$\overline{\phi}_{i+\frac{1}{2},j} \; h_i = \int_0^{h_i} A^{x+}(x) \; F^{x+}(x) \; dx. \qquad \text{(A8.17)}$$

In general, the condition in equation A8.17 is imposed numerically since $A^{x+}(x)$ is known in a piecewise fashion.

On the x+ face, $A^{x+}(x)$ is known from two averaged PDQ-7 calculations and is piecewise flat. Assume that the PDQ mesh points are labeled as

This means one has NXP - 1 intervals for which appropriate values of A^{x+} are calculated.

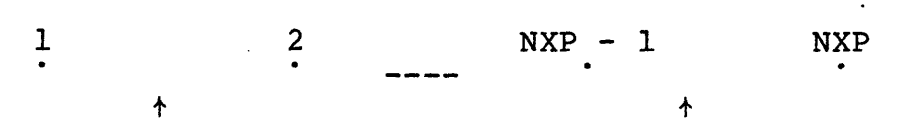

Then the condition A8.17 becomes

$$\bar{\phi}_{i+\frac{1}{2},j}\ h_i = \sum_{n=1}^{NXP-1} A^{x+}(n) \int_{x2(n)}^{x2(n+1)} F^{x+}(x)\ dx. \quad (A8.18)$$

Substituting equation A8.10 into A8.18 yields an equation of the following form after the integral is performed:

$$\bar{\phi}_{i+\frac{1}{2},j} = a_2\ \alpha^{x+} + a_1\ \beta^{x+} + a_0\ \gamma^{x+}. \quad (A8.19)$$

where

$$\alpha^{x+} = \frac{1}{h_i^3} \sum_{n=1}^{NXP-1} A^{x+}(n) \ \frac{1}{3} \left[(x2(n+1))^3 - (x2(n))^3 \right] \quad \text{(A8.20)}$$

$$\beta^{x+} = \frac{1}{h_i^2} \sum_{n=1}^{NXP-1} A^{x+}(n) \ \frac{1}{2} \left[(x2(n+1))^2 - (x2(n))^2 \right] \quad \text{(A8.21)}$$

$$\gamma^{x+} = \frac{1}{h_i} \sum_{n=1}^{NXP-1} A^{x+}(n) \ \left[(x2(n+1)) - (x2(n)) \right]. \quad \text{(A8.22)}$$

Matching the surface-averaged flux on the x- face yields

$$\overline{\phi}_{i-\frac{1}{2},j} = b_2 \ \alpha^{x-} + b_1 \ \beta^{x-} + b_0 \ \gamma^{x-} \quad \text{(A8.23)}$$

where

$$\alpha^{x-} = \frac{1}{h_{i-1}^3} \sum_{n=1}^{NXM-1} A^{x-}(n) \ \frac{1}{3} \left[(x1(n+1))^3 - (x1(n))^3 \right] \quad \text{(A8.24)}$$

$$\beta^{x-} = \frac{1}{h_{i-1}^2} \sum_{n=1}^{NXM-1} A^{x-}(n) \ \frac{1}{2} \left[(x1(n+1))^2 - (x1(n))^2 \right] \quad \text{(A8.25)}$$

$$\gamma^{x-} = \frac{1}{h_{i-1}} \sum_{n=1}^{NXM-1} A^{x-}(n) \ \left[(x1(n+1)) - (x1(n)) \right]. \quad \text{(A8.26)}$$

Matching the surface-averaged flux on the y+ face yields

$$\bar{\phi}_{i,j+\frac{1}{2}} = c_2 \alpha^{y+} + c_1 \beta^{y+} + c_0 \gamma^{y+} \qquad \text{(A8.27)}$$

where

$$\alpha^{y+} = \frac{1}{h_j^3} \sum_{n=1}^{NYP-1} A^{y+}(n) \frac{1}{3} [(y4(n+1))^3 - (y4(n))^3] \qquad \text{(A8.28)}$$

$$\beta^{y+} = \frac{1}{h_j^2} \sum_{n=1}^{NYP-1} A^{y+}(n) \frac{1}{2} [(y4(n+1))^2 - (y4(n))^2] \qquad \text{(A8.29)}$$

$$\gamma^{y+} = \frac{1}{h_j} \sum_{n=1}^{NYP-1} A^{y+}(n) [(y4(n+1)) - (y4(n))]. \qquad \text{(A8.30)}$$

Matching the surface-averaged flux on the y- face yields

$$\bar{\phi}_{i,j-\frac{1}{2}} = d_2 \alpha^{y-} + d_1 \beta^{y-} + d_0 \gamma^{y-} \qquad \text{(A8.31)}$$

where

$$\alpha^{y-} = \frac{1}{h_{j-1}^3} \sum_{n=1}^{NYM-1} A^{y-}(n) \frac{1}{3} [(y3(n+1))^3 - (y3(n))^3] \qquad \text{(A8.32)}$$

$$\beta^{y-} = \frac{1}{h_{j-1}^2} \sum_{n=1}^{NYM-1} A^{y-}(n) \frac{1}{2} [(y3(n+1))^2 - (y3(n))^2] \qquad \text{(A8.33)}$$

$$\gamma^{y-} = \frac{1}{h_{j-1}} \sum_{n=1}^{NYM-1} A^{y-}(n) [(y3(n+1)) - (y3(n))]. \qquad \text{(A8.34)}$$

Matching the flux at (i+1,j) yields

$$\phi_{i+1,j} / A^{x+}_{i+1,j} = a_2 + a_1 + a_0 . \qquad \text{(A8.35)}$$

Matching the flux at (i-1,j) yields

$$\phi_{i-1,j} / A^{x-}_{i-1,j} = b_2 - b_1 + b_0. \qquad \text{(A8.36)}$$

Matching the flux at (i,j+1) yields

$$\phi_{i,j+1} / A^{y+}_{i,j+1} = c_2 + c_1 + c_0. \qquad \text{(A8.37)}$$

Matching the flux at (i,j-1) yields

$$\phi_{i,j-1} / A^{y-}_{i,j-1} = d_2 - d_1 + d_0. \qquad \text{(A8.38)}$$

The eight equations A8.19, A8.23, A8.27, A8.31, A8.35 A8.36, A8.37, and A8.38 can be solved for the eight unknowns a_2, a_1, b_2, b_1, c_2, c_1, d_2 and d_1.

The result is

$$a_1 = \phi_{i,j} \frac{(\gamma^{x+} - \alpha^{x+})}{A_{i,j}^{x+} (\alpha^{x+} - \beta^{x+})} +$$

$$\phi_{i+1,j} \frac{\alpha^{x+}}{A_{i+1,j}^{x+} (\alpha^{x+} - \beta^{x+})} +$$

$$\overline{\phi}_{i+\frac{1}{2},j} \frac{-1}{(\alpha^{x+} - \beta^{x+})} \qquad \text{(A8.39)}$$

$$a_2 = \phi_{i,j} \frac{(\beta^{x+} - \gamma^{x+})}{A_{i,j}^{x+} (\alpha^{x+} - \beta^{x+})} +$$

$$\phi_{i+1,j} \frac{(-\beta^{x+})}{A_{i+1,j}^{x+} (\alpha^{x+} - \beta^{x+})} +$$

$$\overline{\phi}_{i+\frac{1}{2},j} \frac{(+1)}{(\alpha^{x+} - \beta^{x+})} \qquad \text{(A8.40)}$$

$$b_1 = \phi_{i,j} \frac{(\alpha^{x-} - \gamma^{x-})}{A^{x-}_{i,j}(\alpha^{x-} + \beta^{x-})} + \phi_{i-1,j} \frac{(-\alpha^{x-})}{A^{x-}_{i-1,j}(\alpha^{x-} + \beta^{x-})} + \overline{\phi}_{i-\frac{1}{2},j} \frac{(+1)}{(\alpha^{x-} + \beta^{x-})} \quad \text{(A8.41)}$$

$$b_2 = \phi_{i,j} \frac{(-\beta^{x-} - \gamma^{x-})}{A^{x-}_{i,j}(\alpha^{x-} + \beta^{x-})} + \phi_{i-1,j} \frac{(+\beta^{x-})}{A^{x-}_{i-1,j}(\alpha^{x-} + \beta^{x-})} + \overline{\phi}_{i-\frac{1}{2},j} \frac{(+1)}{(\alpha^{x-} + \beta^{x-})} \quad \text{(A8.42)}$$

$$c_1 = \phi_{i,j} \frac{\left(\gamma^{y+} - \alpha^{y+} \right)}{A^{y+}_{i,j} \left(\alpha^{y+} - \beta^{y+} \right)} +$$

$$\phi_{i,j+1} \frac{\left(+\alpha^{y+} \right)}{A^{y+}_{i,j+1} \left(\alpha^{y+} - \beta^{y+} \right)} +$$

$$\overline{\phi}_{i,j+\frac{1}{2}} \frac{\left(-1 \right)}{\left(\alpha^{y+} - \beta^{y+} \right)} \qquad \text{(A8.43)}$$

$$c_2 = \phi_{i,j} \frac{\left(\beta^{y+} - \gamma^{y+} \right)}{A^{y+}_{i,j} \left(\alpha^{y+} - \beta^{y+} \right)} +$$

$$\phi_{i,j+1} \frac{\left(-\beta^{y+} \right)}{A^{y+}_{i,j+1} \left(\alpha^{y+} - \beta^{y+} \right)} +$$

$$\overline{\phi}_{i,j+\frac{1}{2}} \frac{\left(+1 \right)}{\left(\alpha^{y+} - \beta^{y+} \right)} \qquad \text{(A8.44)}$$

$$d_1 = \phi_{i,j} \frac{(\alpha^{Y-} - \gamma^{Y-})}{A^{Y-}_{i,j} (\alpha^{Y-} + \beta^{Y-})} +$$

$$\phi_{i,j-1} \frac{(-\alpha^{Y-})}{A^{Y-}_{i,j-1} (\alpha^{Y-} + \beta^{Y-})} +$$

$$\bar{\phi}_{i,j-\frac{1}{2}} \frac{(+1)}{(\alpha^{Y-} + \beta^{Y-})} \qquad \text{(A8.45)}$$

$$d_2 = \phi_{i,j} \frac{(-\beta^{Y-} - \gamma^{Y-})}{A^{Y-}_{i,j} (\alpha^{Y-} + \beta^{Y-})} +$$

$$\phi_{i,j-1} \frac{(+\beta^{Y-})}{A^{Y-}_{i,j-1} (\alpha^{Y-} + \beta^{Y-})} +$$

$$\bar{\phi}_{i,j-\frac{1}{2}} \frac{(+1)}{(\alpha^{Y-} + \beta^{Y-})} \qquad \text{(A8.46)}$$

Application of the source-free condition to the fluxes in equations A8.5, A8.7, A8.9 and A8.11 yields the following five-point difference equation:

$$\phi_{i,j} \left(\{D^1_{i,j} + D^4_{i,j}\} \frac{1}{h_i} \{\frac{(\gamma^{x+} - \alpha^{x+})}{(\alpha^{x+} - \beta^{x+})}\} + \right.$$

$$\{D^2_{i,j} + D^3_{i,j}\} \frac{1}{h_{i-1}} \{\frac{(\gamma^{x-} - \alpha^{x-})}{(\alpha^{x-} + \beta^{x-})}\} +$$

$$\{D^1_{i,j} + D^2_{i,j}\} \frac{1}{h_j} \{\frac{(\gamma^{y+} - \alpha^{y+})}{(\alpha^{y+} - \beta^{y+})}\} +$$

$$\{D^3_{i,j} + D^4_{i,j}\} \frac{1}{h_{j-1}} \{\frac{(\gamma^{y-} - \alpha^{y-})}{(\alpha^{y-} + \beta^{y-})}\} +$$

$$\{D^1_{i,j} + D^4_{i,j}\} \frac{A'^{x+}_{i,j}}{A^{x+}_{i,j}} - \{D^2_{i,j} + D^3_{i,j}\} \frac{A'^{x-}_{i,j}}{A^{x-}_{i,j}} +$$

$$\left. \{D_{i,j} + D_{i,j}\} \frac{A'^{y+}_{i,j}}{A^{y+}_{i,j}} - \{D_{i,j} + D_{i,j}\} \frac{A'^{y-}_{i,j}}{A^{y-}_{i,j}} \right) +$$

(Equation Continued On Next Page)

$$\phi_{i+1,j}\left[\{D^1_{i,j}+D^4_{i,j}\}A^{x+}_{i,j}\frac{1}{h_i}\left\{\frac{\left(\alpha^{x+}\right)}{A^{x+}_{i+1,j}\left(\alpha^{x+}-\beta^{x+}\right)}\right\}\right]+$$

$$\phi_{i-1,j}\left[\{D^2_{i,j}+D^3_{i,j}\}A^{x-}_{i,j}\frac{1}{h_{i-1}}\left\{\frac{\left(\alpha^{x-}\right)}{A^{x-}_{i-1,j}\left(\alpha^{x-}+\beta^{x-}\right)}\right\}\right]+$$

$$\phi_{i,j+1}\left[\{D^1_{i,j}+D^2_{i,j}\}A^{y+}_{i,j}\frac{1}{h_j}\left\{\frac{\left(\alpha^{y+}\right)}{A^{y+}_{i,j+1}\left(\alpha^{y+}-\beta^{y+}\right)}\right\}\right]+$$

$$\phi_{i,j-1}\left[\{D^3_{i,j}+D^4_{i,j}\}A^{y-}_{i,j}\frac{1}{h_{j-1}}\left\{\frac{\left(\alpha^{y-}\right)}{A^{y-}_{i,j-1}\left(\alpha^{y-}+\beta^{y-}\right)}\right\}\right]+$$

$$\overline{\phi}_{i+\frac{1}{2},j}\left[\{D^1_{i,j}+D^4_{i,j}\}A^{x+}_{i,j}\frac{1}{h_i}\left\{\frac{-1}{\alpha^{x+}-\beta^{x+}}\right\}\right]$$

$$\overline{\phi}_{i-\frac{1}{2},j}\left[\{D^2_{i,j}+D^3_{i,j}\}A^{x-}_{i,j}\frac{1}{h_{i-1}}\left\{\frac{-1}{\alpha^{x-}+\beta^{x-}}\right\}\right]$$

$$\overline{\phi}_{i,j+\frac{1}{2}}\left[\{D^1_{i,j}+D^2_{i,j}\}A^{y+}_{i,j}\frac{1}{h_j}\left\{\frac{-1}{\alpha^{y+}-\beta^{y+}}\right\}\right]$$

$$\overline{\phi}_{i,j-\frac{1}{2}}\left[\{D^3_{i,j}+D^4_{i,j}\}A^{y-}_{i,j}\frac{1}{h_{j-1}}\left\{\frac{-1}{\alpha^{y-}+\beta^{y-}}\right\}\right]=0$$

(A8.47)

In equation A8.47, the following notation has been used

$$\frac{d}{dx} A^{x-}(x) \Big|_{(0,0)} = A'^{x-}_{i,j}. \qquad \text{(A8.48)}$$

Such terms involving the derivative of the assembly flux are identically zero when the assembly calculation was performed on the basis of zero-net-current boundary conditions.

The rest of the CAMPANA solution technique is identical to the CARILLON solution method in Appendix 7.

Appendix 9

A FLUX RECONSTRUCTION METHOD BASED ON A 9-TERM BI-QUADRATIC FORM FUNCTION

The purpose of this appendix is to give the algebraic details of the bi-quadratic form function method of flux reconstruction. Start by placing an x-y Cartesian coordinate system at the center of a PWR assembly of dimensions h_x by h_y. The corner points of the assembly are labeled according to the quadrant they are in. The left and right faces of the assembly are the x- and x+ faces respectively. Similarly, the bottom and top faces are the y- and y+ faces respectively. A single bar over a quantity indicates surface averaging. Thus, $\bar{\phi}_{x-}$ is the surface-averaged flux on the left face of the assembly. A double bar indicates volume averaging. Thus $\bar{\bar{A}}$ is the volume average of the heterogeneous assembly flux. The group index, g, is suppressed in this appendix since the flux reconstruction is performed one group at a time. Finally, ϕ_1 , ϕ_2 , ϕ_3 and ϕ_4 are the fluxes at corner points 1, 2, 3 and 4.

The reconstructed flux in an assembly is

$$\phi^R(x,y) = A(x,y) * F^R(x,y) \qquad \text{(A9.1)}$$

where A(x,y) is the heterogeneous flux from an assembly

criticality calculation. The bi-quadratic form function is

$$F^R(x,y) = a_1 + a_2\left[\frac{x}{h_x}\right] + a_3\left[\frac{x^2}{h_x^2}\right] + a_4\left[\frac{y}{h_y}\right] + a_5\left[\frac{y^2}{h_y^2}\right] + a_6\left[\frac{xy}{h_x\ h_y}\right] + a_7\left[\frac{x^2\ y}{h_x^2\ h_y}\right] + a_8\left[\frac{x\ y^2}{h_x\ h_y^2}\right] + a_9\left[\frac{x^2\ y^2}{h_x^2\ h_y^2}\right]. \qquad \text{(A9.2)}$$

The coefficients a_1 through a_9 are determined by forcing the product, $A(x,y)*F^R(x,y)$, to match exactly the four corner point fluxes and to match approximately the four surface-averaged fluxes and the volume-averaged flux. The surface- and volume-averaged fluxes will be matched exactly if the $A(x,y)$ is spatially flat so that it can be taken outside of the surface and volume integrals.

Forcing $A(x,y)*F^R(x,y)$ to match the volume-averaged flux, $\overline{\overline{\phi}}$, yields

$$\overline{\overline{\phi}} = \frac{1}{h_x\ h_y} \int_{-\frac{1}{2}h_y}^{+\frac{1}{2}h_y} dy \int_{-\frac{1}{2}h_x}^{+\frac{1}{2}h_x} dx\ A(x,y)*F^R(x,y) \qquad \text{(A9.3)}$$

Forcing $A(x,y)*F^R(x,y)$ to match the surface-averaged flux on the x- face of the assembly, $\bar{\phi}_{x-}$, yields

$$\bar{\phi}_{x-} = \frac{1}{h_y} \int_{-\frac{1}{2}h_y}^{+\frac{1}{2}h_y} dy \; A(-\tfrac{1}{2}h_x,y) \; F^R(-\tfrac{1}{2}h_x,y). \qquad \text{(A9.4)}$$

Forcing $A(x,y)*F^R(x,y)$ to match the surface-averaged flux on the x+ face of the assembly, $\bar{\phi}_{x+}$, yields

$$\bar{\phi}_{x+} = \frac{1}{h_y} \int_{-\frac{1}{2}h_y}^{+\frac{1}{2}h_y} dy \; A(\tfrac{1}{2}h_x,y) \; F^R(\tfrac{1}{2}h_x,y). \qquad \text{(A9.5)}$$

Forcing $A(x,y)* F^R(x,y)$ to match the surface-averaged flux on the y- face of the assembly, $\bar{\phi}_{y-}$, yields

$$\bar{\phi}_{y-} = \frac{1}{h_x} \int_{-\frac{1}{2}h_x}^{+\frac{1}{2}h_x} dx \; A(x,-\tfrac{1}{2}h_y) \; F^R(x,-\tfrac{1}{2}h_y). \qquad \text{(A9.6)}$$

Forcing $A(x,y) * F^R(x,y)$ to match the surface-averaged flux on the y+ face of the assembly, $\bar{\phi}_{y+}$, yields

$$\bar{\phi}_{y+} = \frac{1}{h_x} \int_{-\frac{1}{2}h_x}^{+\frac{1}{2}h_x} dx \; A(x,\tfrac{1}{2}h_y) \; F^R(x,\tfrac{1}{2}h_y). \qquad \text{(A9.7)}$$

Forcing $A(x,y) * F^R(x,y)$ to match the corner point 1 flux, ϕ_1 , yields

$$\phi_1 = A_1 \; F^R(\tfrac{1}{2}h_x \; , \; \tfrac{1}{2}h_y). \qquad \text{(A9.8)}$$

Forcing $A(x,y) * F^R(x,y)$ to match the corner point 2 flux, ϕ_2 , yields

$$\phi_2 = A_2 \; F^R(-\tfrac{1}{2}h_x, \tfrac{1}{2}h_y). \qquad \text{(A9.9)}$$

Forcing $A(x,y) * F^R(x,y)$ to match the corner point 3 flux, ϕ_3 , yields

$$\phi_3 = A_3 \; F^R(-\tfrac{1}{2}h_x, \; -\tfrac{1}{2}h_y). \qquad \text{(A9.10)}$$

Forcing $A(x,y) * F^R(x,y)$ to match the corner point 4 flux, ϕ_4 , yields

$$\beta_3 = \frac{\bar{\phi}_{x+}}{\bar{A}_{x+}} = a_1 + \tfrac{1}{2} a_2 + \tfrac{1}{4} a_3 + \frac{1}{12} a_5 + \frac{1}{24} a_8 + \frac{1}{48} a_9.$$

(A9.14)

The integral in equation A9.6 can be completed algebraically if the approximation is made that $A(x,-\tfrac{1}{2}h_y)$ is spatially flat and can be replaced by its surface average, $\bar{A}_{y-}$. Doing this and completing the integral yields

$$\beta_4 = \frac{\bar{\phi}_{y-}}{\bar{A}_{y-}} = a_1 + \frac{1}{12} a_3 - \tfrac{1}{2} a_4 + \tfrac{1}{4} a_5 - \frac{1}{24} a_7 + \frac{1}{48} a_9.$$

(A9.15)

The integral in equation A9.7 can be completed algebraically if the approximation is made that $A(x,\tfrac{1}{2}h_y)$ is spatially flat and can be replace by its surface average, $\bar{A}_{y+}$. Doing this and completing the integral yields

$$\beta_5 = \frac{\bar{\phi}_{y+}}{\bar{A}_{y+}} = a_1 + \frac{1}{12} a_3 + \tfrac{1}{2} a_4 + \tfrac{1}{4} a_5 + \frac{1}{24} a_7 + \frac{1}{48} a_9.$$

(A9.16)

$$\phi_4 = A_4 \; F^R(\tfrac{1}{2}h_x, -\tfrac{1}{2}h_y). \qquad \text{(A9.11)}$$

The integral in equation A9.3 can be completed algebraically if the approximation is made that A(x,y) is spatially flat and can be replaced by its average, $\bar{\bar{A}}$. Doing this and completing the integral yields

$$\beta_1 = \frac{\bar{\bar{\phi}}}{\bar{\bar{A}}} = a_1 + \frac{1}{12} a_3 + \frac{1}{12} a_5 + \frac{1}{144} a_9 . \qquad \text{(A9.12)}$$

The integral in equation A9.4 can be completed algebraically if the approximation is made that $A(-\tfrac{1}{2}h_x, y)$ is spatially flat and can be replaced by its surface average, $\bar{A}_{x-}$. Doing this and completing the integral yields

$$\beta_2 = \frac{\bar{\phi}_{x-}}{\bar{A}_{x-}} = a_1 - \tfrac{1}{2} a_2 + \tfrac{1}{4} a_3 + \frac{1}{12} a_5 - \frac{1}{24} a_8 + \frac{1}{48} a_9 .$$

(A9.13)

The integral in equation A9.5 can be completed algebraically if the approximation is made that $A(\tfrac{1}{2}h_x, y)$ is spatially flat and can be replaced by its surface average, $\bar{A}_{x+}$. Doing this and completing the integral yields

Equation A9.8 is written as

$$\beta_6 = \frac{\phi_1}{A_1} = a_1 + \tfrac{1}{2} a_2 + \tfrac{1}{4} a_3 + \tfrac{1}{2} a_4 + \tfrac{1}{4} a_5 + \tfrac{1}{4} a_6 + \frac{1}{8} a_7 + \frac{1}{8} a_8 + \frac{1}{16} a_9. \quad \text{(A9.17)}$$

Equation A9.9 is written as

$$\beta_7 = \frac{\phi_2}{A_2} = a_1 - \tfrac{1}{2} a_2 + \tfrac{1}{4} a_3 + \tfrac{1}{2} a_4 + \tfrac{1}{4} a_5 - \tfrac{1}{4} a_6 + \frac{1}{8} a_7 - \frac{1}{8} a_8 + \frac{1}{16} a_9 . \quad \text{(A9.18)}$$

Equation A9.10 is written as

$$\beta_8 = \frac{\phi_3}{A_3} = a_1 - \tfrac{1}{2} a_2 + \tfrac{1}{4} a_3 - \tfrac{1}{2} a_4 + \tfrac{1}{4} a_5 + \tfrac{1}{4} a_6 - \frac{1}{8} a_7 - \frac{1}{8} a_8 + \frac{1}{16} a_9 . \quad \text{(A9.19)}$$

Equation A9.11 is written as

$$\beta_9 = \frac{\phi_4}{A_4} = a_1 + \tfrac{1}{2} a_2 + \tfrac{1}{4} a_3 - \tfrac{1}{2} a_4 + \tfrac{1}{4} a_5 - \tfrac{1}{4} a_6 - \frac{1}{8} a_7 + \frac{1}{8} a_8 + \frac{1}{16} a_9. \quad \text{(A9.20)}$$

Equations A9.12 through A9.20 constitute a system of 9 equations in 9 unknowns (a_1 through a_9). The solution of this system of equations is

$$a_1 = \frac{9}{4}\beta_1 - \frac{3}{8}\beta_2 - \frac{3}{8}\beta_3 - \frac{3}{8}\beta_4 - \frac{3}{8}\beta_5 + \\ + \frac{1}{16}\beta_6 + \frac{1}{16}\beta_7 + \frac{1}{16}\beta_8 + \frac{1}{16}\beta_9. \quad \text{(A9.21)}$$

$$a_2 = -\frac{3}{2}\beta_2 + \frac{3}{2}\beta_3 - \frac{1}{4}\beta_6 + \frac{1}{4}\beta_7 + \frac{1}{4}\beta_8 - \frac{1}{4}\beta_9. \quad \text{(A9.22)}$$

$$a_3 = -9\beta_1 + \frac{9}{2}\beta_2 + \frac{9}{2}\beta_3 + \frac{3}{2}\beta_4 + \frac{3}{2}\beta_5 - \frac{3}{4}\beta_6 + \\ - \frac{3}{4}\beta_7 - \frac{3}{4}\beta_8 - \frac{3}{4}\beta_9. \quad \text{(A9.23)}$$

$$a_4 = -\frac{3}{2}\beta_4 + \frac{3}{2}\beta_5 - \frac{1}{4}\beta_6 - \frac{1}{4}\beta_7 + \frac{1}{4}\beta_8 + \frac{1}{4}\beta_9. \quad \text{(A9.24)}$$

$$a_5 = -9\,\beta_1 + \frac{3}{2}\,\beta_2 + \frac{3}{2}\,\beta_3 + \frac{9}{2}\,\beta_4 + \frac{9}{2}\,\beta_5 - \frac{3}{4}\,\beta_6$$

$$- \frac{3}{4}\,\beta_7 - \frac{3}{4}\,\beta_8 - \frac{3}{4}\,\beta_9. \qquad \text{(A9.25)}$$

$$a_6 = \beta_6 - \beta_7 + \beta_8 - \beta_9. \qquad \text{(A9.26)}$$

$$a_7 = 6\,\beta_4 - 6\,\beta_5 + 3\,\beta_6 + 3\,\beta_7 - 3\,\beta_8 - 3\,\beta_9. \qquad \text{(A9.27)}$$

$$a_8 = 6\,\beta_2 - 6\,\beta_3 + 3\,\beta_6 - 3\,\beta_7 - 3\,\beta_8 + 3\,\beta_9. \qquad \text{(A9.28)}$$

$$a_9 = 36\beta_1 - 18\,\beta_2 - 18\,\beta_3 - 18\,\beta_4 - 18\,\beta_5 +$$

$$+ 9\beta_6 + 9\beta_7 + 9\beta_8 + 9\beta_9. \qquad \text{(A9.29)}$$

Appendix 10

A FLUX RECONSTRUCTION METHOD BASED ON A 25-TERM BI-QUARTIC FORM FUNCTION

The purpose of this appendix is to give the algebraic details of the bi-quartic form function method of flux reconstruction. Start by placing an x-y Cartesian coordinate system at the center of a PWR assembly of dimensions h_x by h_y. The corner points of the assembly are labeled according to the quadrant they are in. The left and right faces of the assembly are the x- and x+ faces respectively. Similarly, the bottom and top faces are the y- and y+ faces respectively. A single bar over a quantity indicates surface averaging. Thus, $\bar{\phi}_{x-}$ is the surface-averaged flux on the left face of the assembly. A double bar indicates volume averaging. Thus $\bar{\bar{A}}$ is the volume average of the heterogeneous assembly flux from an assembly criticality calculation with zero-net-current boundary conditions. The group index, g, is suppressed in this appendix since the flux reconstruction is performed one group at a time. Finally, ϕ_1 , ϕ_2 , ϕ_3 and ϕ_4 are the fluxes at corner points 1, 2, 3 and 4.

Consider the following one-dimensional quartic

$$f(x) = a_0 + a_1\left(\frac{2x}{h_x}\right) + a_2\left(\frac{2x}{h_x}\right)^2 + a_3\left(\frac{2x}{h_x}\right)^3 + a_4\left(\frac{2x}{h_x}\right)^4 \qquad \text{(A10.1)}$$

To determine the 5 unknowns a_0 through a_4 impose 5 general conditions

1. $f(\frac{1}{2} h_x) = f^+$ (A10.2)

2. $f(-\frac{1}{2} h_x) = f^-$ (A10.3)

3. $h_x \left.\frac{df}{dx}\right|_{x=\frac{1}{2}h_x} = f'^+$ (A10.4)

4. $h_x \left.\frac{df}{dx}\right|_{x=-\frac{1}{2}h_x} = f'^-$ (A10.5)

5. $\frac{1}{h_x} \int_{-\frac{1}{2}h_x}^{+\frac{1}{2}h_x} dx \; f(x) = \bar{f}.$ (A10.6)

The solution to the resulting system of 5 equations in 5 unknowns is

$$a_0 = \frac{-7}{16}\left[f^+ + f^-\right] + \frac{1}{32}\left[f'^+ - f'^-\right] + \frac{15}{8}\bar{f} \qquad \text{(A10.7)}$$

$$a_1 = \frac{3}{4}\left[f^+ - f^- \right] - \frac{1}{8}\left[f'^+ + f'^- \right] \qquad \text{(A10.8)}$$

$$a_2 = \frac{15}{8}\left[f^+ + f^- \right] - \frac{3}{16}\left[f'^+ - f'^- \right] - \frac{15}{4}\bar{f} \qquad \text{(A10.9)}$$

$$a_3 = \frac{-1}{4}\left[f^+ - f^- \right] + \frac{1}{8}\left[f'^+ + f'^- \right] \qquad \text{(A10.10)}$$

$$a_4 = \frac{-15}{16}\left[f^+ + f^- \right] + \frac{5}{32}\left[f'^+ - f'^- \right] + \frac{15}{8}\bar{f} \,. \qquad \text{(A10.11)}$$

Thus, if f^+, f^-, f'^+, f'^- and $\bar{f}$ are specified, then a_0 through a_4 may be found and equation A10.1 defines a particular one-dimensional quartic.

The f^+, f^-, f'^+, f'^- and $\bar{f}$ are now chosen 5 different ways such that the 5 different one-dimensional quartics; Q_x^+, Q_x^-, $Q_x'^+$, $Q_x'^-$ and $\bar{Q}_x$ are defined as follows:

1. Definition of $Q_x^+(x)$

   Let $f^+ = 1$, $f^- = 0$, $f'^+ = 0$, $f'^- = 0$ and $\bar{f} = 0$. Then equation A10.1 yields the quartic

$$Q_x^+(x) = \frac{-7}{16} + \frac{3}{4}\left(\frac{2x}{h_x}\right) + \frac{15}{8}\left(\frac{2x}{h_x}\right)^2 - \frac{1}{4}\left(\frac{2x}{h_x}\right)^3 - \frac{15}{16}\left(\frac{2x}{h_x}\right)^4 . \qquad \text{(A10.12)}$$

2. Definition of $Q_x^-(x)$

Let $f^+ = 0$, $f^- = 1$, $f'^+ = 0$, $f'^- = 0$ and $\bar{f} = 0$.
Then equation A10.1 yields the quartic

$$Q_x^-(x) = \frac{-7}{16} - \frac{3}{4}\left(\frac{2x}{h_x}\right) + \frac{15}{8}\left(\frac{2x}{h_x}\right)^2 + \frac{1}{4}\left(\frac{2x}{h_x}\right)^3 - \frac{15}{16}\left(\frac{2x}{h_x}\right)^4. \qquad \text{(A10.13)}$$

3. Definition of $Q_x'^+(x)$

Let $f^+ = 0$, $f^- = 0$, $f'^+ = 1$, $f'^- = 0$ and $\bar{f} = 0$.
Then equation A10.1 yields the quartic

$$Q_x'^+(x) = h_x\left\{\frac{1}{32} - \frac{1}{8}\left(\frac{2x}{h_x}\right) - \frac{3}{16}\left(\frac{2x}{h_x}\right)^2 + \frac{1}{8}\left(\frac{2x}{h_x}\right)^3 + \frac{5}{32}\left(\frac{2x}{h_x}\right)^4\right\}. \qquad \text{(A10.14)}$$

4. Definition of $Q_x'^-(x)$

Let $f^+ = 0$, $f^- = 0$, $f'^+ = 0$, $f'^- = 1$ and $\bar{f} = 0$.
Then equation A10.1 yields the quartic

$$Q_x'^-(x) = h_x\left\{\frac{-1}{32} - \frac{1}{8}\left(\frac{2x}{h_x}\right) + \frac{3}{16}\left(\frac{2x}{h_x}\right)^2 + \frac{1}{8}\left(\frac{2x}{h_x}\right)^3 - \frac{5}{32}\left(\frac{2x}{h_x}\right)^4\right\}. \qquad \text{(A10.15)}$$

5. Definition of $\bar{Q}_x(x)$

Let $f^+ = 0$, $f^- = 0$, $f'^+ = 0$, $f'^- = 0$ and $\bar{f} = 1$.
Then equation A10.1 yields the quartic

$$\bar{Q}_x(x) = \frac{15}{8} - \frac{15}{4}\left(\frac{2x}{h_x}\right)^2 + \frac{15}{8}\left(\frac{2x}{h_x}\right)^4 \qquad \text{(A10.16)}$$

Note that $dQ_x^+/dx \neq Q_x^{'+}$, i.e., the meaning of the prime is not shorthand for d/dx. Here the prime is a mnemonic device which means that $dQ_x^{'+}/dx$ evaluated at $x = \frac{1}{2}h_x$ equals 1.

Five more quartics for the y dimension; Q_y^+ , Q_y^- , $Q_y^{'+}$, $Q_y^{'-}$ and $\bar{Q}_y$, are defined by interchanging y for x in equations A10.12 through A10.16.

Thus, by using the 10 quartic functions

1. Q_x^+
2. Q_x^-
3. $Q_x^{'+}$
4. $Q_x^{'-}$
5. $\bar{Q}_x$
6. Q_y^+
7. Q_y^-
8. $Q_y^{'+}$
9. $Q_y^{'-}$
10. $\bar{Q}_y$

and the heterogeneous assembly flux A(x,y) from an assembly calculation with zero-net-current boundary conditions a 25-term, bi-quartic reconstruction method may be written as

$$\phi^R(x,y) = A(x,y) * \{ \quad \beta_1 \ \bar{Q}_x \ \bar{Q}_y +$$

$$+ \beta_2 \ Q_x^- \ \bar{Q}_y + \beta_3 \ Q_x^+ \ \bar{Q}_y + \beta_4 \ \bar{Q}_x \ Q_y^- + \beta_5 \ \bar{Q}_x \ Q_y^+ +$$

$$+ \beta_6 \ Q_x^{'-} \ \bar{Q}_y + \beta_7 \ Q_x^{'+} \ \bar{Q}_y + \beta_8 \ \bar{Q}_x \ Q_y^{'-} + \beta_9 \ \bar{Q}_x \ Q_y^{'+} +$$

$$+ \beta_{10} \ Q_x^+ \ Q_y^+ + \beta_{11} \ Q_x^- \ Q_y^+ + \beta_{12} \ Q_x^- \ Q_y^- + \beta_{13} \ Q_x^+ \ Q_y^- +$$

$$+ \beta_{14} \ Q_x^{'+} \ Q_y^+ + \beta_{15} \ Q_x^{'-} \ Q_y^+ + \beta_{16} \ Q_x^{'-} \ Q_y^- + \beta_{17} \ Q_x^{'+} \ Q_y^- +$$

$$+ \beta_{18} \ Q_x^+ \ Q_y^{'+} + \beta_{19} \ Q_x^- \ Q_y^{'+} + \beta_{20} \ Q_x^- \ Q_y^{'-} + \beta_{21} \ Q_x^+ \ Q_y^{'-} +$$

$$+ \beta_{22} \ Q_x^{'+} \ Q_y^{'+} + \beta_{23} \ Q_x^{'-} \ Q_y^{'+} + \beta_{24} \ Q_x^{'-} \ Q_y^{'-} + \beta_{25} \ Q_x^{'+} \ Q_y^{'-} \ \}.$$

(A10.17)

To find the β_i , i = 1, 2, ... 25, twenty-five conditions are imposed on the reconstructed flux in equation A10.17. Let $\phi(x,y)$ be the two-dimensional flux from the reference global heterogeneous problem. In general, $\phi(x,y)$ will not be known. However, if reference discontinuity factors and cross sections are known (or some approximation of them such as ADF-AXS) then QUANDRY yields one volume-averaged flux, four surface-averaged fluxes and four surface-averaged currents in each group and for each assembly in the PWR. Sixteen "point" quantities may be interpolated using CHIME. Thus, a total of 25 $\phi(x,y)$-related quantities can be approximated (without having done the expensive global heterogeneous problem) and these 25 quantities are employed to find the β_i. The 25 quantities are now enumerated:

1. The volume-averaged flux, $\bar{\bar{\phi}}$,

$$\bar{\bar{\phi}} = \frac{1}{h_x h_y} \int_{-\frac{1}{2}h_y}^{+\frac{1}{2}h_y} dy \int_{-\frac{1}{2}h_x}^{+\frac{1}{2}h_x} dx \quad \phi(x,y) \qquad \text{(A10.18)}$$

2,3. The x-directed, surface-averaged fluxes, $\bar{\phi}_{x\pm}$

$$\bar{\phi}_{x\pm} = \frac{1}{h_y} \int_{-\frac{1}{2}h_y}^{+\frac{1}{2}h_y} \phi\left(\frac{\pm h_x}{2}, y \right) \, dy \qquad \text{(A10.19)}$$

4,5. The y-directed, surface-averaged fluxes, $\bar{\phi}_{y\pm}$

$$\bar{\phi}_{y\pm} = \frac{1}{h_x} \int_{-\frac{1}{2}h_x}^{+\frac{1}{2}h_x} \phi\left(x, \frac{\pm h_y}{2} \right) \, dx \qquad \text{(A10.20)}$$

6,7. The x-directed, surface-averaged currents, $\bar{J}_{x\pm}$

$$\bar{J}_{x\pm} = \frac{-1}{h_y} \int_{-\frac{1}{2}h_y}^{+\frac{1}{2}h_y} D\left(\frac{\pm h_x}{2}, y \right) \frac{\partial}{\partial x} [\phi(x,y)] \Big|_{x=\frac{\pm h_x}{2}} \, dy \qquad \text{(A10.21)}$$

8,9. The y-directed, surface-averaged currents, $\bar{J}_{y\pm}$

$$\bar{J}_{y\pm} = \frac{-1}{h_x} \int_{-\frac{1}{2}h_x}^{+\frac{1}{2}h_x} D\left(x, \frac{\pm h_y}{2} \right) \frac{\partial}{\partial y} [\phi(x,y)] \Big|_{y=\frac{\pm h_y}{2}} \, dx \qquad \text{(A10.22)}$$

10. The flux at corner point 1

$$\phi_1 = \phi(\tfrac{1}{2} h_x , \tfrac{1}{2} h_y) \qquad \text{(A10.23)}$$

11. The flux at corner point 2

$$\phi_2 = \phi(-\tfrac{1}{2} h_x , \tfrac{1}{2} h_y) \qquad \text{(A10.24)}$$

12. The flux at corner point 3

$$\phi_3 = \phi(-\tfrac{1}{2} h_x ,-\tfrac{1}{2} h_y) \qquad \text{(A10.25)}$$

13. The flux at corner point 4

$$\phi_4 = \phi(\tfrac{1}{2} h_x, -\tfrac{1}{2} h_y) \qquad \text{(A10.26)}$$

14. The x-component of the current at corner point 1, $J_{x,1}$

$$J_{x,1} = J_x(\tfrac{1}{2}h_x, \tfrac{1}{2}h_y) = - D(\tfrac{1}{2} h_x , \tfrac{1}{2} h_y) \frac{\partial}{\partial x}[\phi(x,y)] \Big|_{\substack{x=\frac{1}{2}h_x \\ y=\frac{1}{2}h_y}} \qquad \text{(A10.27)}$$

15. The x-component of the current at corner point 2, $J_{x,2}$

$$J_{x,2} = J_x(-\tfrac{1}{2}h_x\ ,\ \tfrac{1}{2}h_y) = -D(-\tfrac{1}{2}h_x,\tfrac{1}{2}h_y)\ \frac{\partial}{\partial x}[\phi(x,y)]\ \Big|_{\substack{x=-\frac{1}{2}h_x \\ y=\ \frac{1}{2}h_y}}$$

(A10.28)

16. The x-component of the current at corner point 3, $J_{x,3}$

$$J_{x,3} = J_x(-\tfrac{1}{2}h_x,-\tfrac{1}{2}h_y) = -D(-\tfrac{1}{2}h_x,-\tfrac{1}{2}h_y)\frac{\partial}{\partial x}[\phi(x,y)]\ \Big|_{\substack{x=-\frac{1}{2}h_x \\ y=-\frac{1}{2}h_y}}$$

(A10.29)

17. The x-component of the current at corner point 4, $J_{x,4}$

$$J_{x,4} = J_x(\tfrac{1}{2}h_x,-\tfrac{1}{2}h_y) = -D(\tfrac{1}{2}h_x,-\tfrac{1}{2}h_y)\cdot\frac{\partial}{\partial x}[\phi(x,y)]\ \Big|_{\substack{x=\ \frac{1}{2}h_x \\ y=-\frac{1}{2}h_y}}$$

(A10.30)

18. The y-component of the current at corner point 1, $J_{y,1}$

$$J_{y,1} = J_y(\tfrac{1}{2}h_x,\tfrac{1}{2}h_y) = -D(\tfrac{1}{2}h_x,\tfrac{1}{2}h_y)\ \frac{\partial}{\partial y}[\phi(x,y)]\ \Big|_{\substack{x=\ \frac{1}{2}h_x \\ y=\ \frac{1}{2}h_y}}$$

(A10.31)

19. The y-component of the current at corner point 2, $J_{y,2}$

$$J_{y,2} = J_y(-\tfrac{1}{2}h_x, \tfrac{1}{2}h_y) = -D(-\tfrac{1}{2}h_x, \tfrac{1}{2}h_y) \frac{\partial}{\partial y}[\phi(x,y)] \Big|_{\substack{x=-\frac{1}{2}h_x \\ y=\frac{1}{2}h_y}} \quad \text{(A10.32)}$$

20. The y-component of the current at corner point 3, $J_{y,3}$

$$J_{y,3} = J_y(-\tfrac{1}{2}h_x, -\tfrac{1}{2}h_y) = -D(-\tfrac{1}{2}h_x, -\tfrac{1}{2}h_y) \frac{\partial}{\partial y}[\phi(x,y)] \Big|_{\substack{x=-\frac{1}{2}h_x \\ y=-\frac{1}{2}h_y}} \quad \text{(A10.33)}$$

21. The y-component of the current at corner point 4, $J_{y,4}$

$$J_{y,4} = J_y(\tfrac{1}{2}h_x, -\tfrac{1}{2}h_y) = -D(\tfrac{1}{2}h_x, -\tfrac{1}{2}h_y) \frac{\partial}{\partial y}[\phi(x,y)] \Big|_{\substack{x=\frac{1}{2}h_x \\ y=-\frac{1}{2}h_y}} \quad \text{(A10.34)}$$

22. The cross derivative term at corner point 1, $\phi_{xy,1}$

$$\phi_{xy,1} = \frac{\partial^2}{\partial x \, \partial y}[\phi(x,y)] \Big|_{\substack{x=\frac{1}{2}h_x \\ y=\frac{1}{2}h_y}} \quad \text{(A10.35)}$$

23. The cross derivative term at corner point 2, $\phi_{xy,2}$

$$\phi_{xy,2} = \frac{\partial^2}{\partial x \partial y}[\phi(x,y)] \Bigg|_{\substack{x=-\frac{1}{2}h_x \\ y=\frac{1}{2}h_y}} \qquad \text{(A10.36)}$$

24. The cross derivative term at corner point 3, $\phi_{xy,3}$

$$\phi_{xy,3} = \frac{\partial^2}{\partial x \partial y}[\phi(x,y)] \Bigg|_{\substack{x=-\frac{1}{2}h_x \\ y=-\frac{1}{2}h_y}} \qquad \text{(A10.37)}$$

25. The cross derivative term at corner point 4, $\phi_{xy,4}$

$$\phi_{xy,4} = \frac{\partial^2}{\partial x \partial y}[\phi(x,y)] \Bigg|_{\substack{x=\frac{1}{2}h_x \\ y=-\frac{1}{2}h_y}} \qquad \text{(A10.38)}$$

The β_i , i = 1, 2, ... 25, are easy to find if the following additional approximations are made:

1. The assembly flux, A(x,y), is assumed spatially flat and is replaced by its volume average in equation A10.18.
2. The assembly flux, $A(-\frac{1}{2}h_x,y)$ on the x-minus face of the assembly is assumed spatially flat and is replaced by its surface average in equations A10.19 and A10.21 for the x- face of the assembly.

3,4,5. A similar approximation is made about the assembly surface flux shape on the x+, y- and y+ faces of the assembly.

6. The diffusion coefficient, $D(-\frac{1}{2}h_x,y)$ on the x-minus face of the assembly is assumed spatially flat and is replace by its surface average, D_{x-} , in equation A10.21 for the x-face of the assembly.

7,8,9. A similar approximation is made about the spatial dependence of the diffusion coefficient along the various surfaces of the assembly (i.e., the x+, y- and y+ faces).

Also, the assembly flux is assumed to have come from a single assembly criticality calculation with zero-net-current boundary conditions.

Thus, the 25-term, bi-quartic method becomes

$$\phi^R(x,y) = A(x,y) * \{ \quad \frac{\bar{\bar{\phi}}}{\bar{\bar{A}}} \; \bar{Q}_x \; \bar{Q}_y +$$

$$\frac{\bar{\phi}_{x-}}{\bar{A}_{x-}} \; Q_x^- \; \bar{Q}_y + \frac{\bar{\phi}_{x+}}{\bar{A}_{x+}} \; Q_x^+ \; \bar{Q}_y + \frac{\bar{\phi}_{y-}}{\bar{A}_{y-}} \; \bar{Q}_x \; Q_y^- + \frac{\bar{\phi}_{y+}}{\bar{A}_{y+}} \; \bar{Q}_x \; Q_y^+ +$$

$$\frac{-\bar{J}_{x-}}{D_{x-}\bar{A}_{x-}} \; Q_x'^- \; \bar{Q}_y + \frac{-\bar{J}_{x+}}{D_{x+}\bar{A}_{x+}} \; Q_x'^+ \; \bar{Q}_y + \frac{-\bar{J}_{y-}}{D_{y-}\bar{A}_{y-}} \; \bar{Q}_x \; Q_y'^- + \frac{-\bar{J}_{y+}}{D_{y+}\bar{A}_{y+}} \; \bar{Q}_x \; Q_y'^+ +$$

$$\frac{\phi_1}{A_1} \; Q_x^+ \; Q_y^+ + \frac{\phi_2}{A_2} \; Q_x^- \; Q_y^+ + \frac{\phi_3}{A_3} \; Q_x^- \; Q_y^- + \frac{\phi_4}{A_4} \; Q_x^+ \; Q_y^- +$$

$$\frac{-J_{x,1}}{D_1 \; A_1} \; Q_x'^+ \; Q_y^+ + \frac{-J_{x,2}}{D_2 \; A_2} Q_x'^- \; Q_y^+ + \frac{-J_{x,3}}{D_3 \; A_3} Q_x'^- \; Q_y^- + \frac{-J_{x,4}}{D_4 \; A_4} Q_x'^+ \; Q_y^- +$$

$$\frac{-J_{y,1}}{D_1 \; A_1} \; Q_x^+ \; Q_y'^+ + \frac{-J_{y,2}}{D_2 \; A_2} Q_x^- \; Q_y'^+ + \frac{-J_{y,3}}{D_3 \; A_3} Q_x^- \; Q_y'^- + \frac{-J_{y,4}}{D_4 \; A_4} Q_x^+ \; Q_y'^- +$$

$$\frac{\phi_{xy,1}}{A_1} \; Q_x'^+ \; Q_y'^+ + \frac{\phi_{xy,2}}{A_2} Q_x'^- \; Q_y'^+ + \frac{\phi_{xy,3}}{A_3} Q_x'^- \; Q_y'^- + \frac{\phi_{xy,4}}{A_4} Q_x'^+ \; Q_y'^- \}.$$

Appendix 11

FORTE

A11.0 INTRODUCTION

The purpose of this appendix is to supplement the FORTE theory presented in Chapter 6. Specifically, the expressions for the form functions in all four of the triangle in Figure 6.1 of Chapter 6 are given. Also, the methods which are employed to calculate the coefficients of the non-polynomial form functions are presented.

The following useful notation for corner point values of the form function is used:

1. $F_g(\ \frac{1}{2}h,\ \frac{1}{2}h) = F_g\ (1)$
2. $F_g(-\frac{1}{2}h,\ \frac{1}{2}h) = F_g\ (2)$
3. $F_g(-\frac{1}{2}h, -\frac{1}{2}h) = F_g\ (3)$
4. $F_g(\ \frac{1}{2}h, -\frac{1}{2}h) = F_g\ (4)$.

The surface-averaged form function values of the x-, x+ y- and y+ faces of the PWR assembly are represented by

1. $\overline{F}_{g,x-}$
2. $\overline{F}_{g,x+}$
3. $\overline{F}_{g,y-}$
4. $\overline{F}_{g,y+}$

The volume-averaged form function is $\overline{\overline{F}}_g$.

All 9 of these form function quantities are assumed known.

A11.1 NON-POLYNOMIAL FORM FUNCTIONS FOR TRIANGLES 1,2,3 and 4

For triangle 1

$$F_g^{(1)}(x,y) =$$

$$C_1\, s_g^{(1)} \left[\cos\mu_x^{(1)} x + \frac{C_x^{(1)}}{\mu_x^{(1)}} \sin\mu_x^{(1)} x\right] \left[\cos\mu_y^{(1)} y + \frac{C_y^{(1)}}{\mu_y^{(1)}} \sin\mu_y^{(1)} y\right] +$$

$$\left[\left(\frac{1}{2} + \frac{y}{h} \right) a_2^{(1)} + \left(\frac{1}{2} - \frac{y}{h} \right) a_3^{(1)} \right] t_g^{(1)} \exp\left[-B_2^{(1)} \left(\frac{h}{2} + x\right)\right]$$

(A11.1)

For triangle 2

$$F_g^{(2)}(x,y) =$$

$$C_1\, s_g^{(2)} \left[\cos\mu_x^{(2)} x + \frac{C_x^{(2)}}{\mu_x^{(2)}} \sin\mu_x^{(2)} x\right] \left[\cos\mu_y^{(2)} y + \frac{C_y^{(2)}}{\mu_y^{(2)}} \sin\mu_y^{(2)} y\right] +$$

$$\left[\left(\frac{1}{2} + \frac{y}{h} \right) a_1^{(2)} + \left(\frac{1}{2} - \frac{y}{h} \right) a_4^{(2)} \right] t_g^{(2)} \exp\left[-B_2^{(2)} \left(\frac{h}{2} - x\right)\right]$$

(A11.2)

For triangle 3

$$F_g^{(3)}(x,y) =$$

$$C_1 \; s_g^{(3)} \left[\cos\mu_x^{(3)}x + \frac{C_x^{(3)}}{\mu_x^{(3)}} \sin\mu_x^{(3)}x\right]\left[\cos\mu_y^{(3)}y + \frac{C_y^{(3)}}{\mu_y^{(3)}}\sin\mu_y^{(3)}y\right] +$$

$$\left[\left(\frac{1}{2} + \frac{x}{h}\right) a_4^{(3)} + \left(\frac{1}{2} - \frac{x}{h}\right) a_3^{(3)}\right] t_g^{(3)} \exp\left[-B_2^{(3)}\left(\frac{h}{2} + y\right)\right]$$

(A11.3)

For triangle 4

$$F_g^{(4)}(x,y) =$$

$$C_1 \; s_g^{(4)} \left[\cos\mu_x^{(4)}x + \frac{C_x^{(4)}}{\mu_x^{(4)}}\sin\mu_x^{(4)}x\right]\left[\cos\mu_y^{(4)}y + \frac{C_y^{(4)}}{\mu_y^{(4)}}\sin\mu_y^{(4)}y\right] +$$

$$\left[\left(\frac{1}{2} + \frac{x}{h}\right) a_1^{(4)} + \left(\frac{1}{2} - \frac{x}{h}\right) a_2^{(4)}\right] t_g^{(4)} \exp\left[-B_2^{(4)}\left(\frac{h}{2} - y\right)\right]$$

(A11.4)

A11.2 CALCULATION OF THE AMOUNT OF HARMONIC AT THE CORNER POINTS OF A PWR ASSEMBLY

For a given triangle "tri" (=1,2,3,4), write the fast form function equation at one of the corner points "cp" (= two of the following four numbers; 1,2,3,4). Then subtract $s^{(tri)}$ times the thermal form function equation from the fast form function equation at the corner point. This yields the amount of harmonic at a corner point for a given triangle as

$$a_{cp}^{(tri)} = \frac{F_1(cp) - s^{(tri)} F_2(cp)}{t^{(tri)} - s^{(tri)}} . \qquad (A11.5)$$

The $s^{(tri)}$ and the $t^{(tri)}$ are the fast-to-slow form function ratios for a given triangle. They are calculated from equations like 6.12 and 6.13 (using the proper values of the buckings and the r for the triangle under consideration). The $F_1(cp)$ and $F_2(cp)$ are the group 1 and group 2 corner point values of the form function which are assumed known.

Note that once $a_{cp}^{(tri)}$ has been calculated, then the entire harmonic terms of the form functions are known.

A11.3 CALCULATION OF THE COEFFICIENTS IN THE FUNDAMENTAL TERMS OF THE NON-POLYNOMIAL FORM FUNCTIONS

Since the corner point, surface-averaged and volume-averaged values of the form function are known, and since the entire harmonic term of the reconstructed form function is known, it is possible to find corner point, surface-averaged and volume-averaged values of the fundamental term of the reconstructed form function. This fundamental term information is used to calculate the remaining unknown coefficients:

$$\mu_x^{(tri)} \quad , \quad \mu_y^{(tri)} \quad , \quad C_x^{(tri)} \quad , \quad C_y^{(tri)} \quad \text{and}$$

$$C_1 \quad \text{where tri is the triangle number (1,2,3 or 4).}$$

The coefficients $\mu_x^{(tri)}$, $\mu_y^{(tri)}$, $C_x^{(tri)}$ and $C_y^{(tri)}$ are calculated by forcing the reconstructed form function $F_g^R(x,y)$ to match known corner point values of the form function and the surface average of the form function for triangle tri. These three pieces of information [plus the condition $[\mu_x^{(tri)}]^2 + [\mu_y^{(tri)}]^2 = -[B_1^{(tri)}]^2$] determine the four coefficients $\mu_x^{(tri)}$, $\mu_y^{(tri)}$, $C_x^{(tri)}$ and $C_y^{(tri)}$.

The coefficient C_1 is calculated by forcing the sum of the volume integrals of the four triangular reconstructed form functions to match the known volume-average of the form function.

These calculations are now illustrated for triangle 1. The known amount of fundamental mode at corner point 2 for triangle 1 is

$$G_g^{(1)}(2) = F_g^{(1)}(2) - t_g^{(1)} \quad a_2^{(1)} \cdot \qquad \text{(A11.6)}$$

The known amount of fundamental mode at corner point 3 for triangle 1 is

$$G_g^{(1)}(3) = F_g^{(1)}(3) - t_g^{(1)} \quad a_3^{(1)} \cdot \qquad \text{(A11.7)}$$

The known surface-average of the fundamental mode along the x- face of the node is

$$\bar{G}_{g,x-}^{(1)} = \bar{F}_{g,x-}^{(1)} - \frac{1}{2} \; t_g^{(1)} [a_2^{(1)} + a_3^{(1)}]. \qquad \text{(A11.8)}$$

Forcing the fundamental part of equation A11.1 to match the above three pieces of fundamental information yields the following equations:

$$\frac{2\ \bar{G}^{(1)}_{g,x-}}{\left[\ G^{(1)}_g(2) + G^{(1)}_g(3)\ \right]} = \frac{1}{\frac{h}{2}\ \mu^{(1)}_{y_g}} \tan \frac{h}{2}\ \mu^{(1)}_{y_g} \qquad \text{(A11.9)}$$

This equation is solved iteratively for $\mu^{(1)}_{y_g}$ using Newton's method [43]. Then $\mu^{(1)}_{x_g}$ is

$$\mu^{(1)}_{x_g} = \left\{ -[B^{(1)}_1]^2 - [\mu^{(1)}_{y_g}]^2 \right\}^{\frac{1}{2}} \qquad \text{(A11.10)}$$

The equation for $C^{(1)}_{y_g}$ is

$$C^{(1)}_{y_g} = \frac{[\ G^{(1)}_g(2) - G^{(1)}_g(3)]}{h\ \bar{G}^{(1)}_{g,x-}} \qquad \text{(A11.11)}$$

Also, for triangle 1, an equation is found of the form

$$a_{51_g}\ C^{(1)}_{x_g}\ C_{1_g} + a_{55_g}\ C_{1_g} = S_{5_g} \qquad \text{(A11.12)}$$

where

$$a_{51_g} = [\ - s^{(1)}_g \frac{1}{\mu^{(1)}_{x_g}} \sin \mu^{(1)}_{x_g} \frac{h}{2}\ ] \qquad \text{(A11.13)}$$

$$a_{55_g} = [\, s_g^{(1)} \cos \mu_{x_g}^{(1)} \frac{h}{2} \,] \qquad \text{(A11.14)}$$

$$S_{5_g} = \frac{[\, G_g^{(1)}(2) + G_g^{(1)}(3) \,]}{2 \cos \mu_{y_g}^{(1)} \frac{h}{2}} . \qquad \text{(A11.15)}$$

Integration of equation A11.1 over the volume of triangle 1 yields an equation of the form

$$a_{11_g} C_{1_g} C_{x_g}^{(1)} + a_{15_g}^{(1)} C_{1_g} = S_{1_g}^{(1)} \qquad \text{(A11.16)}$$

This completes the calculations for triangle 1.

Similar calculations for triangle 2 yield values of $\mu_{y_g}^{(2)}$, $\mu_{x_g}^{(2)}$ and $C_{y_g}^{(2)}$. Also, an equation analogous to equation A11.12 is found for triangle 2 as

$$a_{42_g} C_{x_g}^{(2)} C_{1_g} + a_{45_g} C_{1_g} = S_{4_g} \qquad \text{(A11.17)}$$

Integration of equation A11.2 over the volume of triangle 2 yields an equation of the form

$$a_{12_g} \; C_{x_g}^{(1)} \; C_{1_g} + a_{15_g}^{(2)} \; C_{1_g} = S_{1_g}^{(2)} . \qquad \text{(A11.18)}$$

Similar calculations for triangle 3 yield values of $\mu_{x_g}^{(3)}$, $\mu_{y_g}^{(3)}$ and $C_{x_g}^{(3)}$. Also, an equation analogous to equation A11.12 is found for triangle 3 as

$$a_{33_g} \; C_{y_g}^{(3)} \; C_{1_g} + a_{35_g} \; C_{1_g} = S_{3_g} . \qquad \text{(A11.19)}$$

Integration of equation A11.3 over the volume of triangle 3 yields an equation of the form

$$a_{13_g} \; C_{y_g}^{(3)} \; C_{1_g} + a_{15_g}^{(3)} \; C_{1_g} = S_{1_g}^{(3)} . \qquad \text{(A11.20)}$$

Similar calculations for triangle 4 yield values of $\mu_{x_g}^{(4)}$, $\mu_{y_g}^{(4)}$ and $C_{x_g}^{(4)}$. Also, an equation analogous to equation A11.12 is found for triangle 4 as

$$a_{24_g} \; C_{y_g}^{(4)} \; C_{1_g} + a_{25_g} \; C_{1_g} = S_{4_g} . \qquad \text{(A11.21)}$$

Integration of equation A11.4 over the volume of triangle 4 yields an equation of the form

$$a_{14_g} \; C^{(4)}_{y_g} \; C_{1_g} + a^{(4)}_{15_g} \; C_{1_g} = S^{(4)}_{1_g} . \qquad \text{(A11.22)}$$

Equations A11.16, A11.18, A11.20 and A11.22 are summed to yield a single equation for the volume-average of the reconstructed form function for the total PWR assembly. This single volume equation, plus the four equations A11.12, A11.17, A11.19 and A11.21 are easily solved for the remaining five unknowns C_{1_g}, $C^{(1)}_{x_g}$, $C^{(2)}_{x_g}$, $C^{(3)}_{y_g}$ and $C^{(4)}_{y_g}$.

Define

$$a_{15_g} = a^{(1)}_{15_g} + a^{(2)}_{15_g} + a^{(3)}_{15_g} + a^{(4)}_{15_g} \qquad \text{(A11.23)}$$

and

$$S_{1_g} = S^{(1)}_{1_g} + S^{(2)}_{1_g} + S^{(3)}_{1_g} + S^{(4)}_{1_g} . \qquad \text{(A11.24)}$$

The solution for the five remaining unknowns is

$$C_{1_g} = \frac{\left(a_{15_g} - \frac{a_{14_g}\, a_{25_g}}{a_{24_g}} - \frac{a_{13_g}\, a_{35_g}}{a_{33_g}} - \frac{a_{12_g}\, a_{45_g}}{a_{42_g}} - \frac{a_{11_g}\, a_{55_g}}{a_{51_g}} \right)}{\left(S_{1_g} - \frac{a_{14_g}\, S_{2_g}}{a_{24_g}} - \frac{a_{13_g}\, S_{3_g}}{a_{33_g}} - \frac{a_{12_g}\, S_{4_g}}{a_{42_g}} - \frac{a_{11_g}\, S_{5_g}}{a_{51_g}} \right)} \qquad \text{(A11.25)}$$

$$C_{x_g}^{(1)} = [\, S_{5_g} - a_{55_g}\, C_{1_g}] \,/\, a_{51_g}\, C_{1_g} \qquad \text{(A11.26)}$$

$$C_{x_g}^{(2)} = [\, S_{4_g} - a_{45_g}\, C_{1_g}] \,/\, a_{42_g}\, C_{1_g} \qquad \text{(A11.27)}$$

$$C_{y_g}^{(3)} = [\, S_{3_g} - a_{35_g}\, C_{1_g}] \,/\, a_{33_g}\, C_{1_g} \qquad \text{(A11.28)}$$

$$C_{y_g}^{(4)} = [\, S_{4_g} - a_{25_g}\, C_{1_g}] \,/\, a_{24_g}\, C_{1_g} \qquad \text{(A11.29)}$$

Appendix 12

REFERENCE PDQ-7 POINTWISE FLUX PLOTS

A12.0 Introduction

This appendix contains the reference heterogeneous PDQ-7 flux plots for benchmark problems 5, 6, 7 and 8. See Appendix 2 for a detailed description of these benchmark problems. The plots in this appendix are arranged according to the following system:

1. By benchmark problem number

   Section A12.1 - Benchmark Problem 5
   Section A12.2 - Benchmark Problem 6
   Section A12.3 - Benchmark Problem 7
   Section A12.4 - Benchmark Problem 8

   A brief description of each benchmark problem is given at the beginning of each section.

2. By node (PWR assembly) number

   The node numbering for each benchmark problem is given at the beginning of that benchmark problem's section.

3. By energy group

The title of each figure tells what quantity is plotted and gives the above three pieces of information.

A single example is sufficient for explaining how the plots are oriented with respect to a drawing of the benchmark problem since all the plots in this thesis have the same orientation. Figure A12.0 shows the reference

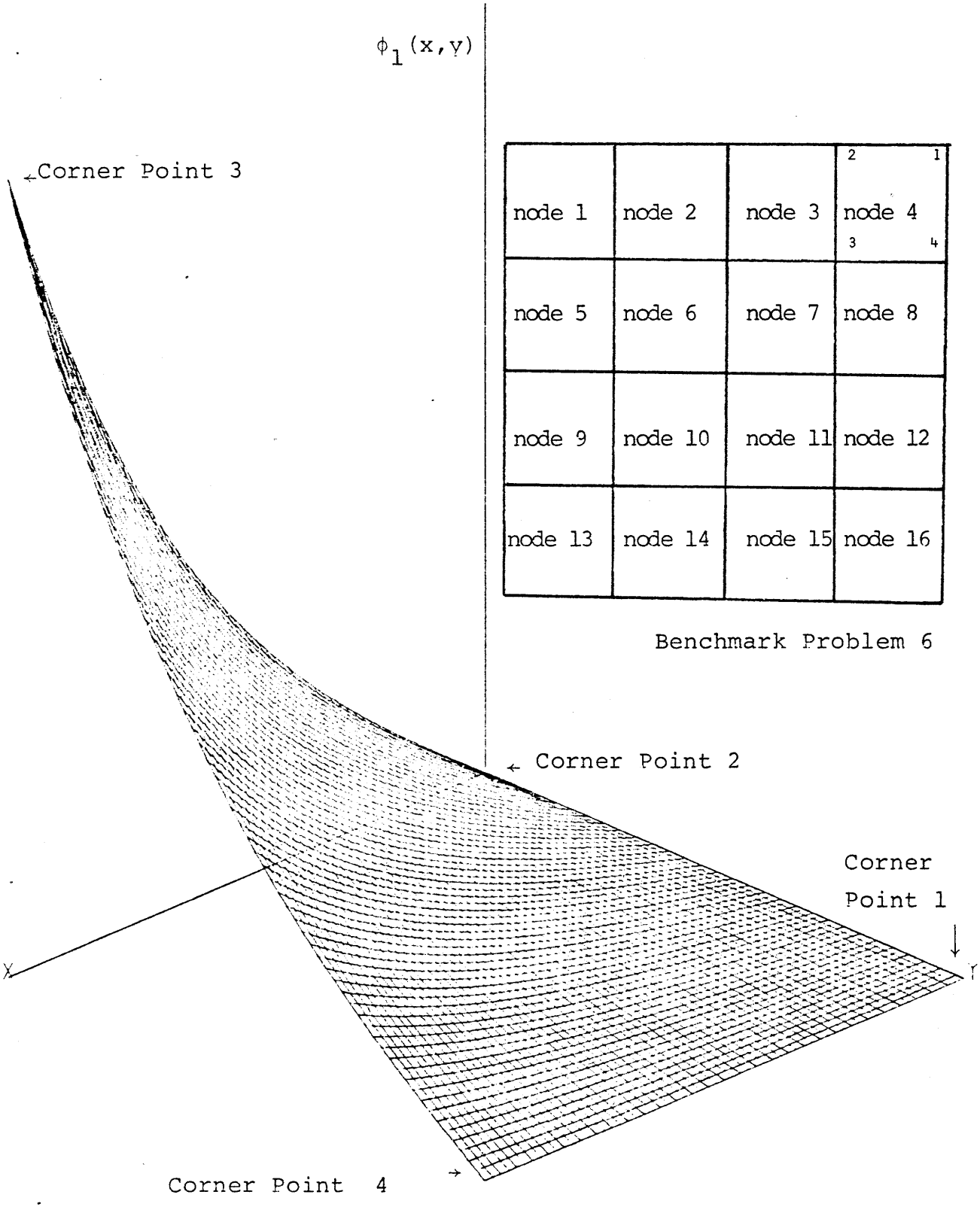

node 1	node 2	node 3	2 1 node 4 3 4
node 5	node 6	node 7	node 8
node 9	node 10	node 11	node 12
node 13	node 14	node 15	node 16

Benchmark Problem 6

Figure A12.0: Plot Orientation Example: The Reference Fast Flux in Node 4 of Benchmark Problem 6

fast flux in node 4 of benchmark problem 6. It also illustrates the node numbering scheme for benchmark problem 6. Find node 4. The corner points in node 4 are labeled according to the standard corner point numbering scheme in this thesis. See Figure A6.0.2 in Appendix 6. The orientation of the plot is revealed by labeling the corner points of the plotted flux.

A12.1 Benchmark Problem 5

Benchmark problem 5 is an infinite checkerboard of unrodded fuel 1 assemblies and unrodded fuel 2 assemblies. The sketch below gives the node numbering for this benchmark problem.

$\bar{J}_g \cdot \hat{n} = 0$

Node 1	Node 2	Node 3
Node 4	Node 5	Node 6
Node 7	Node 8	Node 9

$\bar{J}_g \cdot \hat{n} = 0$ (left)

$\bar{J}_g \cdot \hat{n} = 0$ (right)

$\bar{J}_g \cdot \hat{n} = 0$

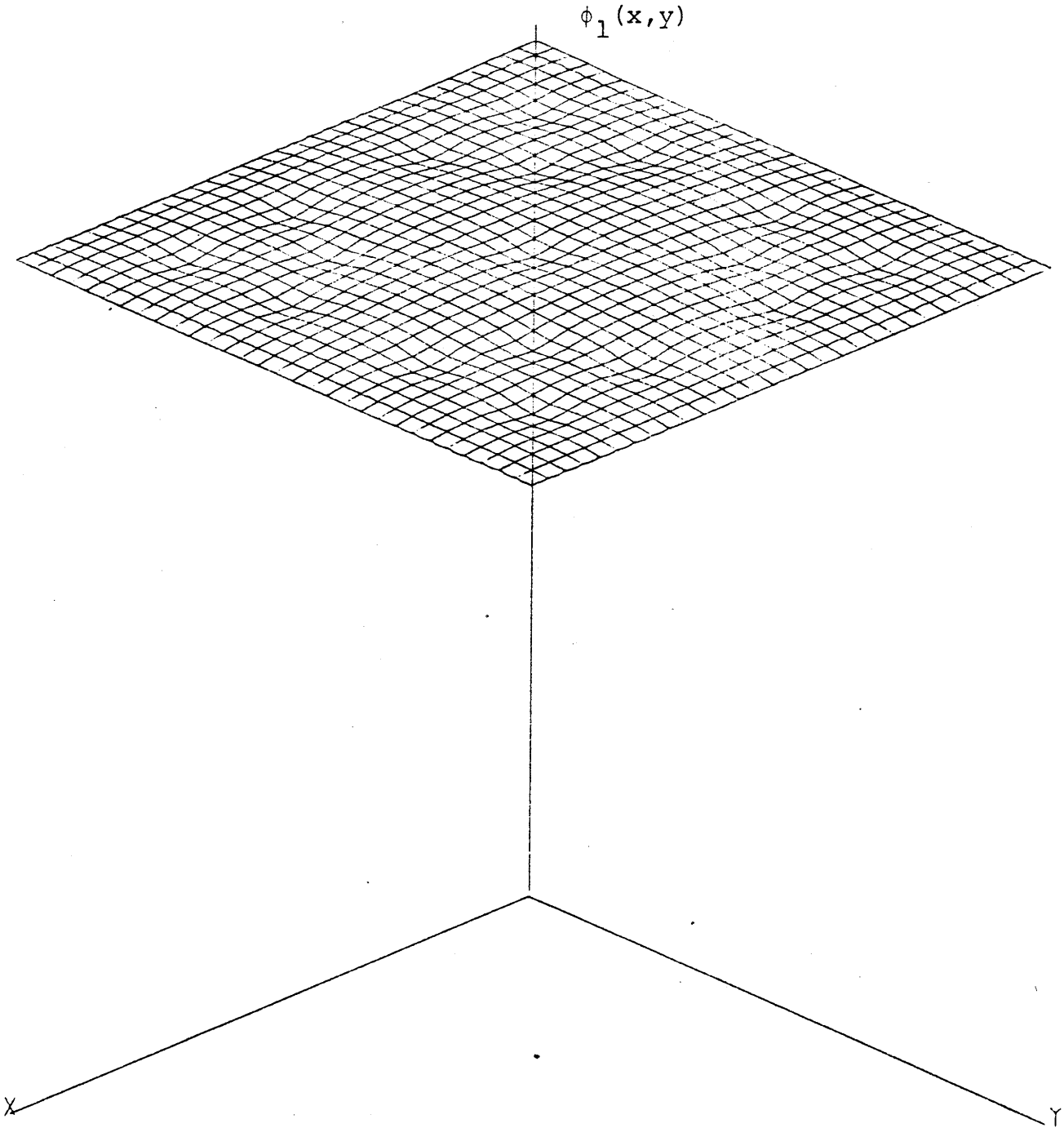

Figure A12.1: Reference Fast Flux for Node 5 of Benchmark Problem 5

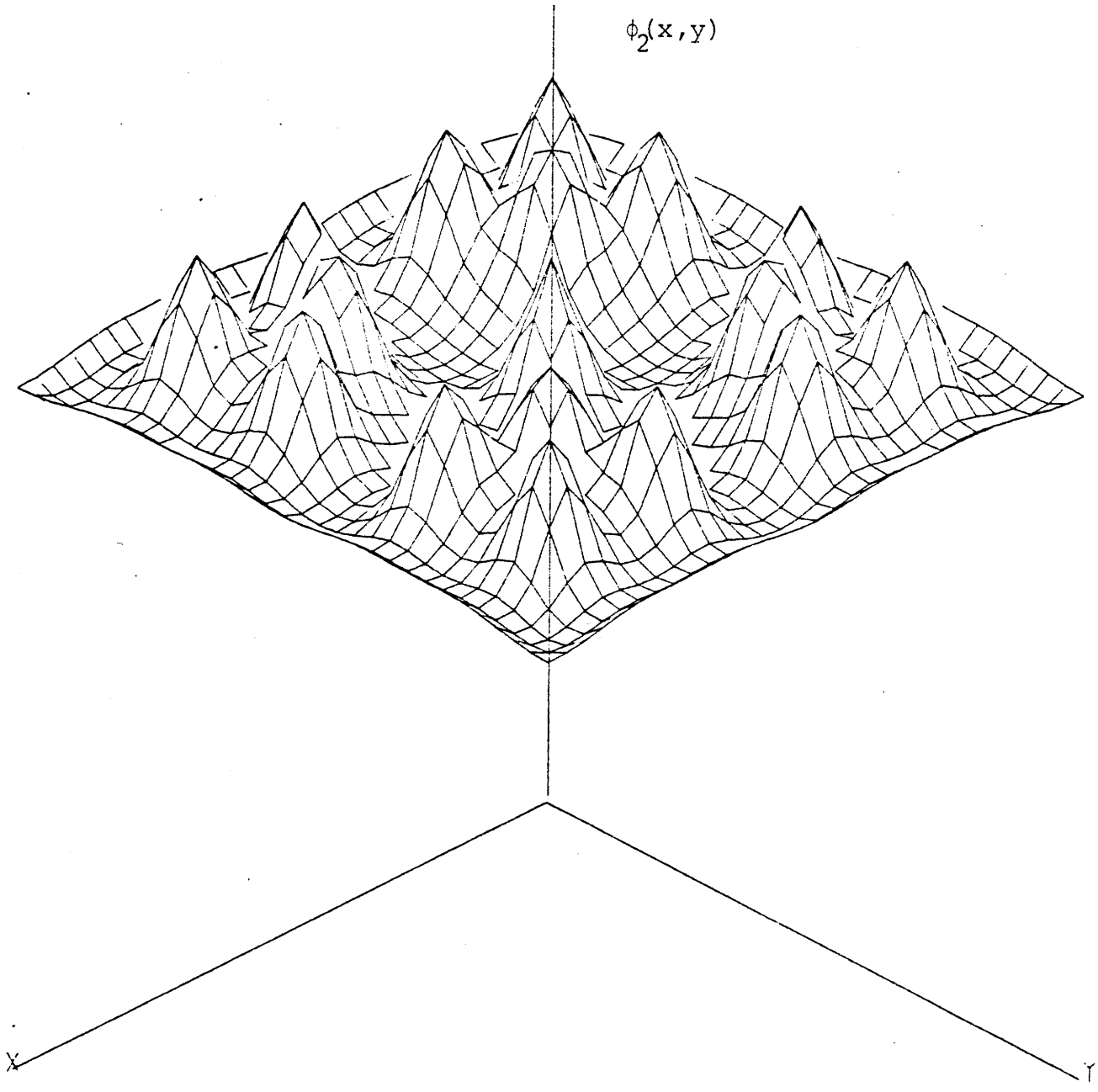

Figure A12.2: Reference Thermal Flux for Node 5 of Benchmark Problem 5

A12.2 Benchmark Problem 6

Benchmark problem 6 is a 4-by-4 node quarter core reactor with an explicitly represented baffle. All assemblies are unrodded. The sketch below gives the node numbering for this problem.

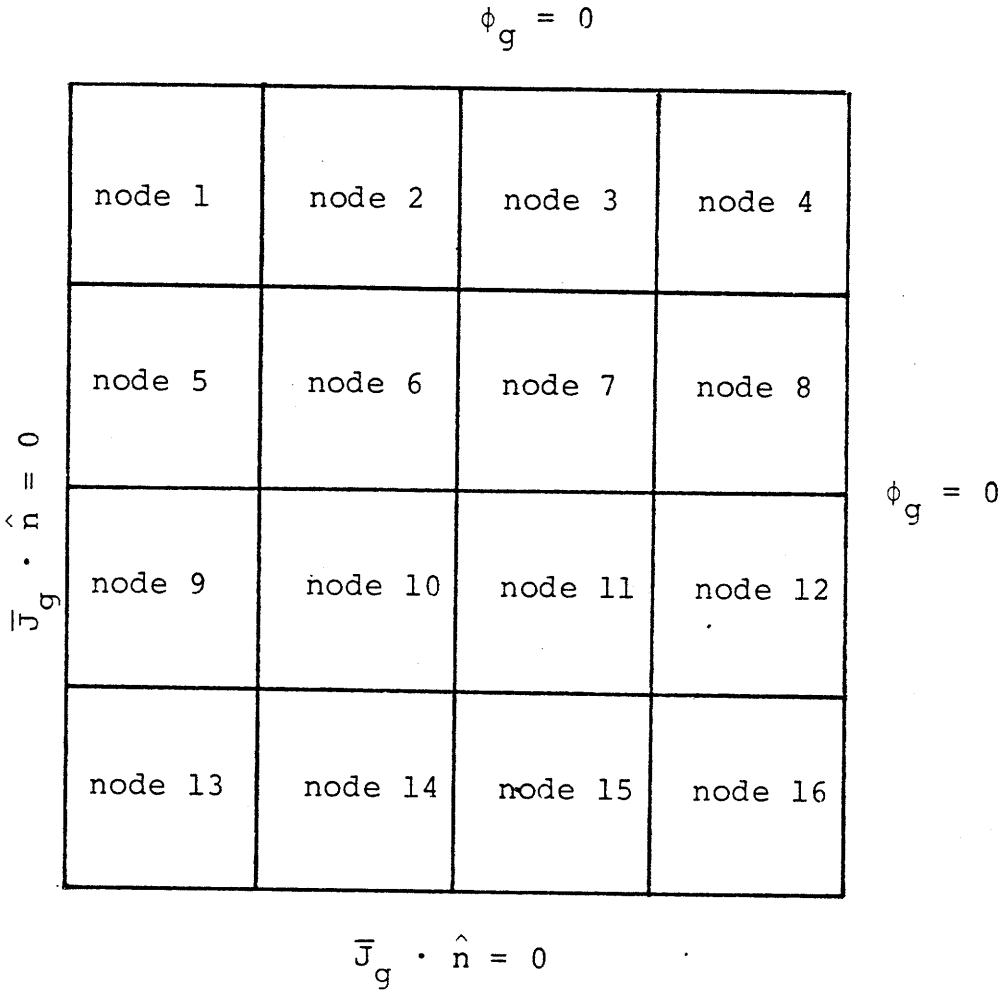

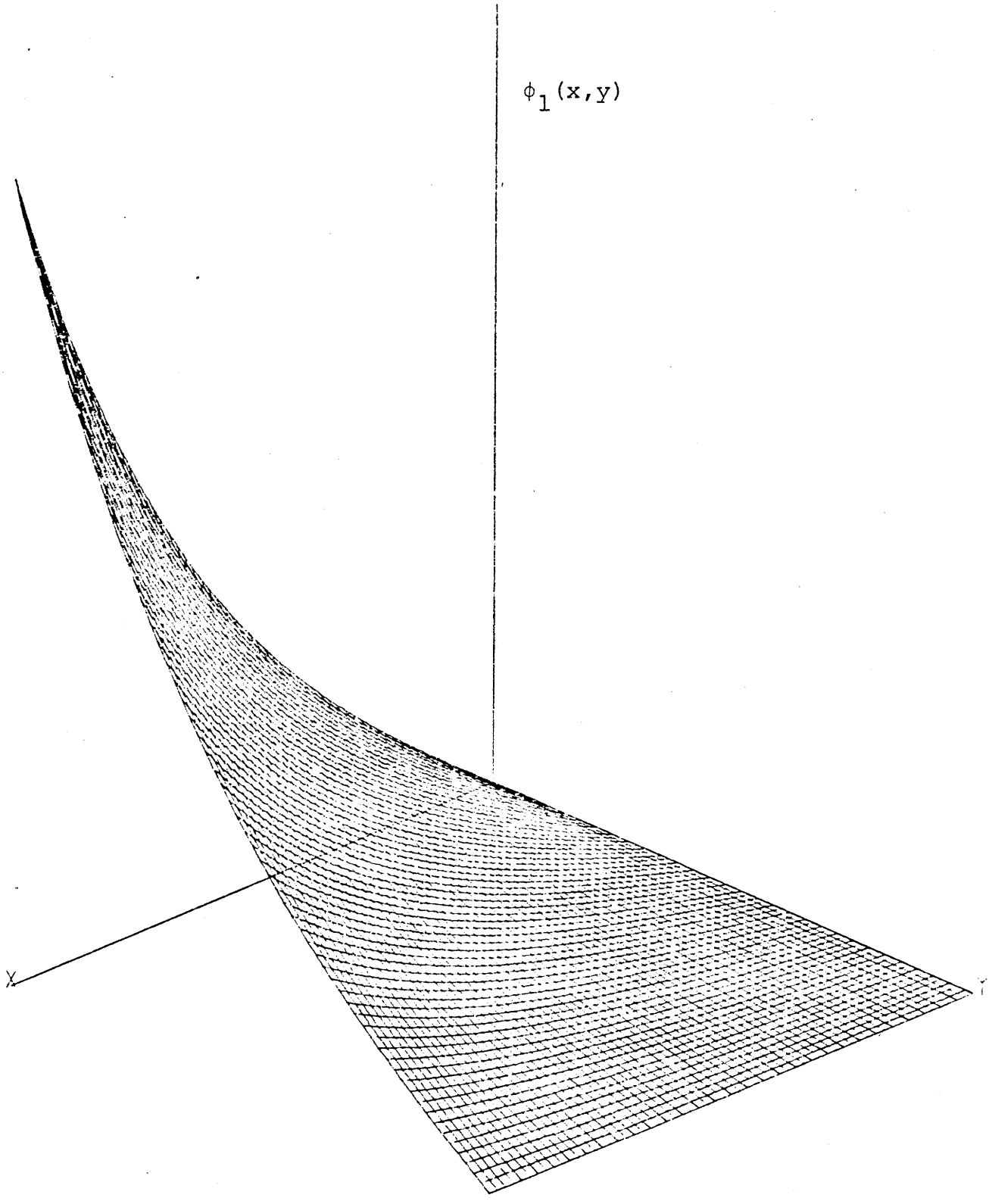

Figure A12.3: Reference Fast Flux for Node 4 of Benchmark Problem 6

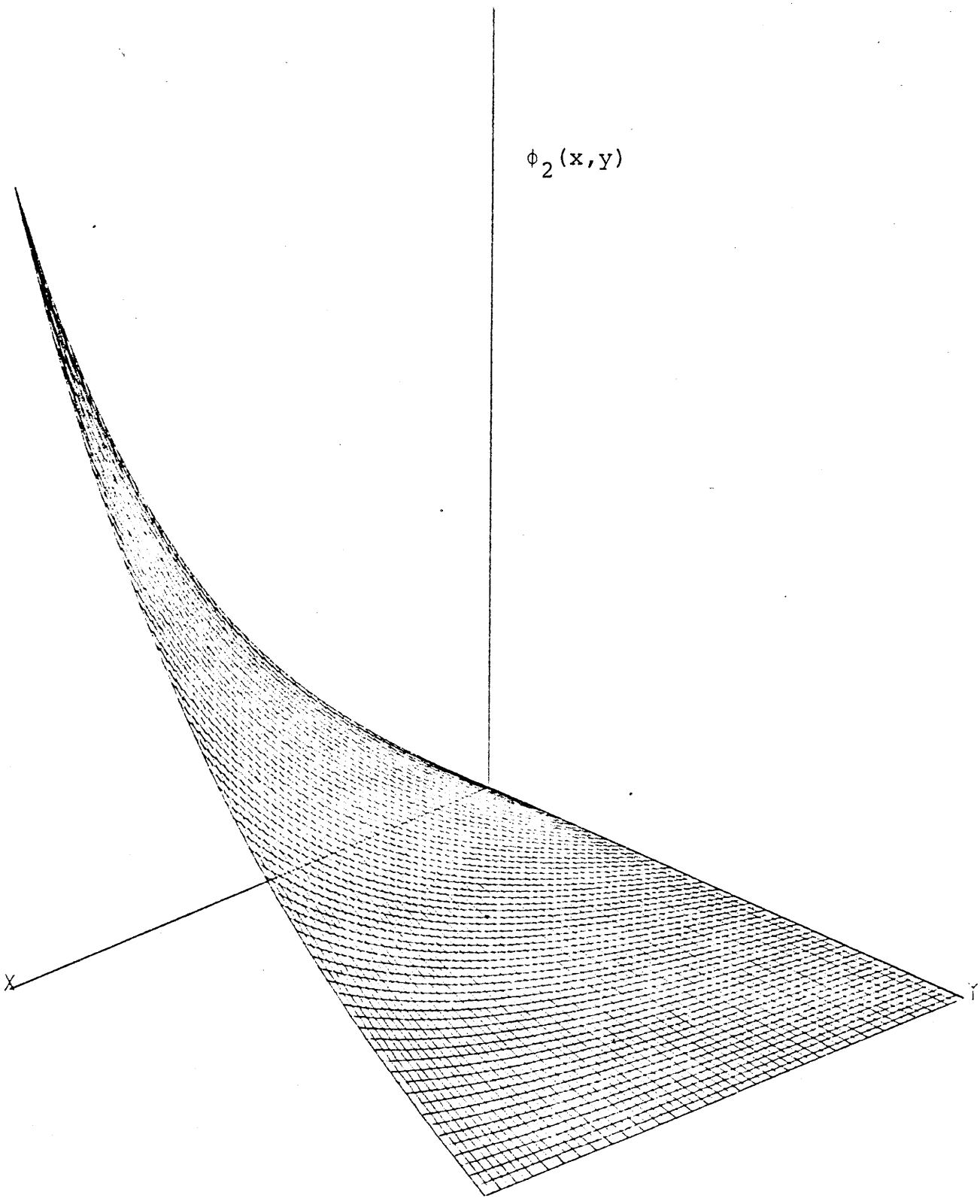

Figure A12.4: Reference Thermal Flux for Node 4 of Benchmark Problem 6

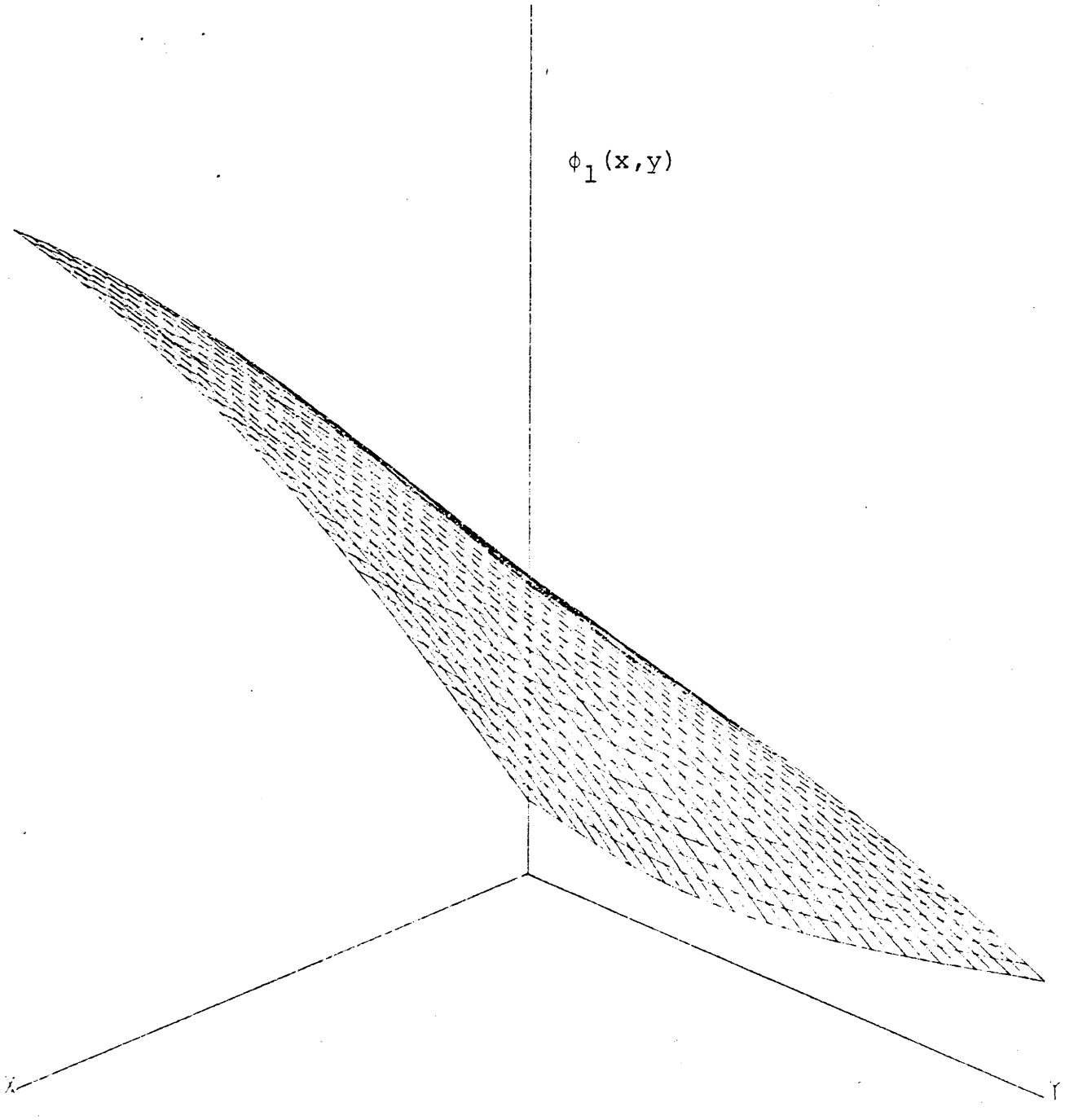

Figure A12.5: Reference Fast Flux for Node 6 of Benchmark Problem 6

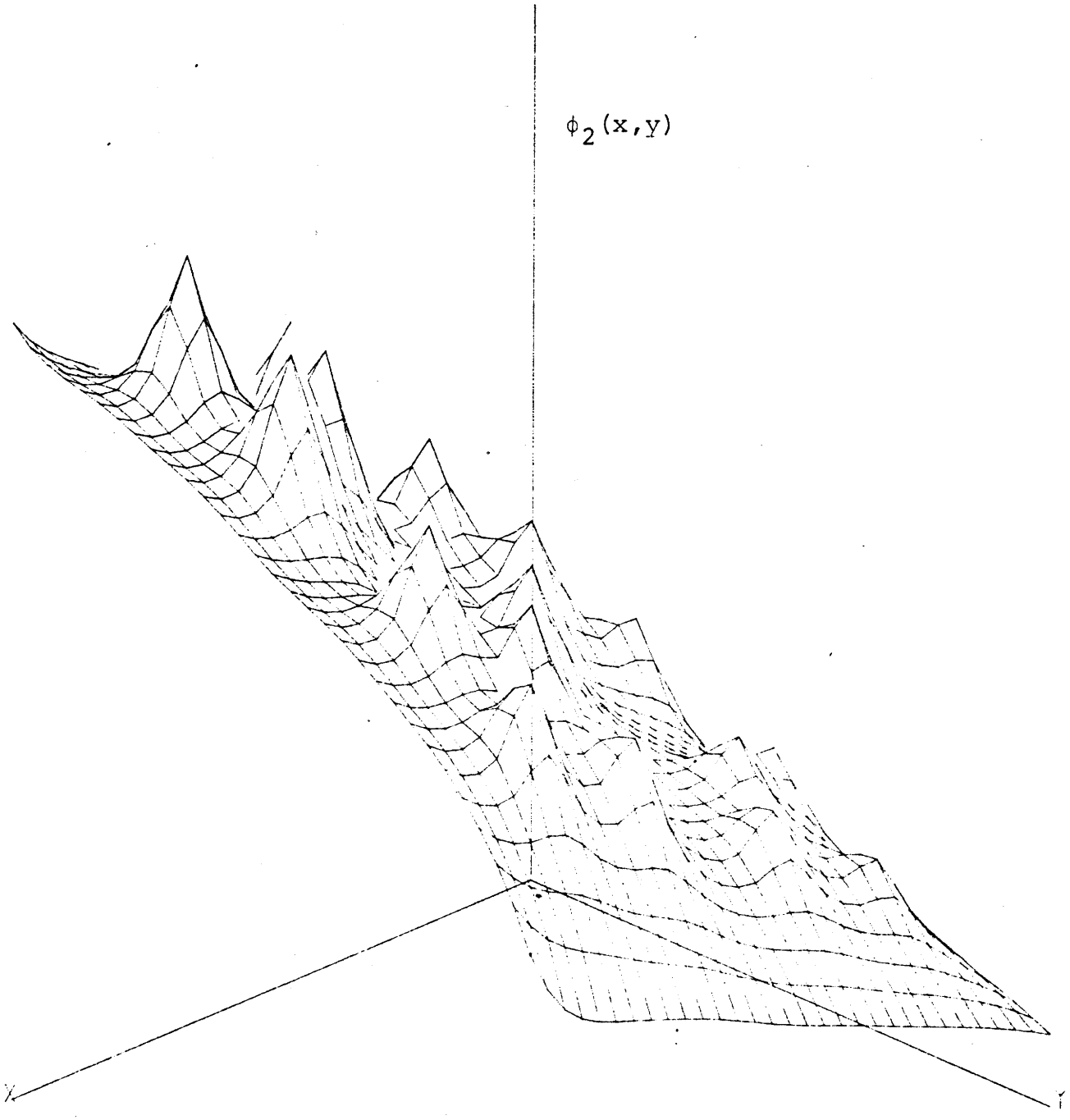

Figure A12.6: Reference Thermal Flux for Node 6 of Benchmark Problem 6

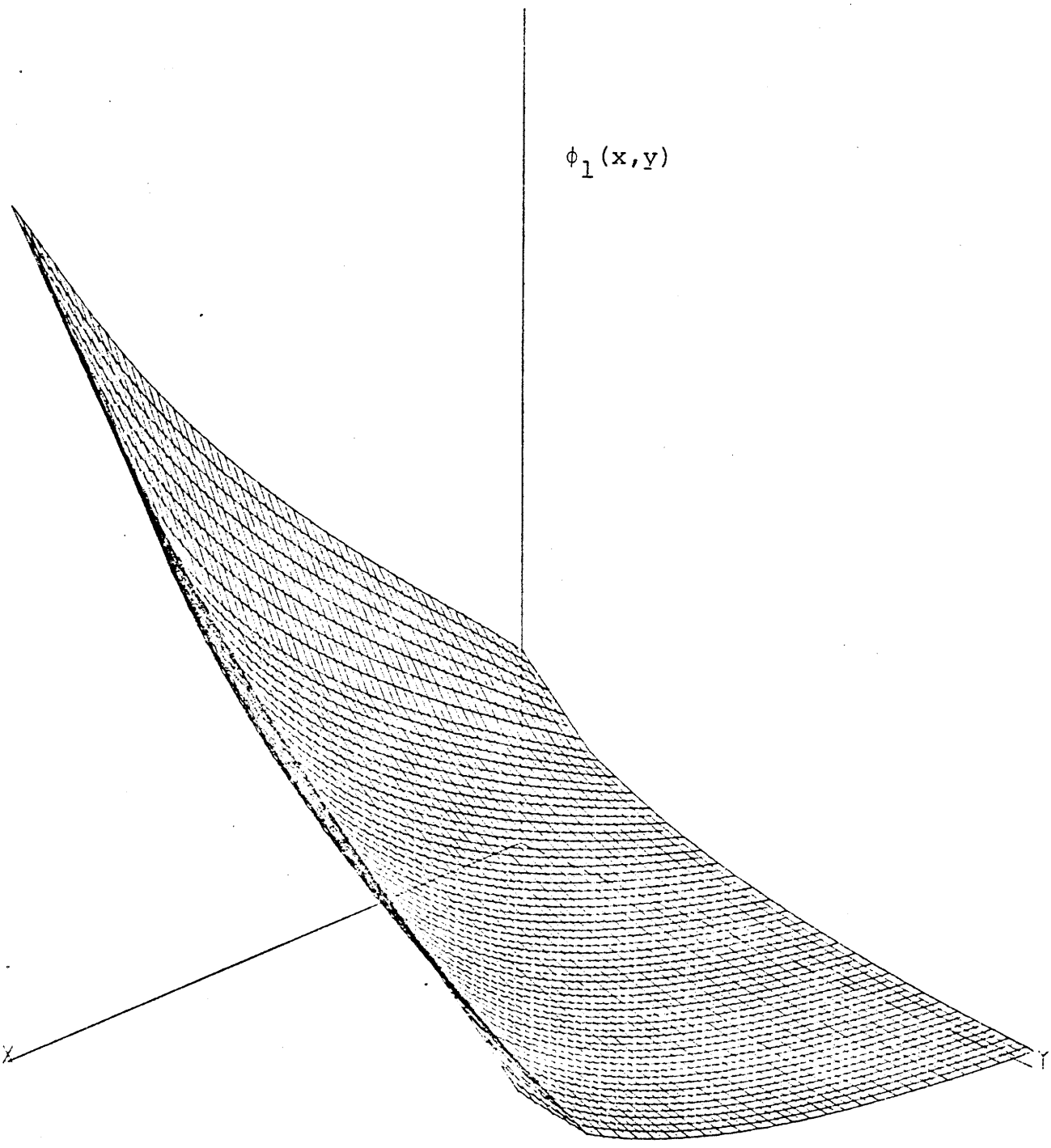

Figure A12.7: Reference Fast Flux for Node 7 of Benchmark Problem 6

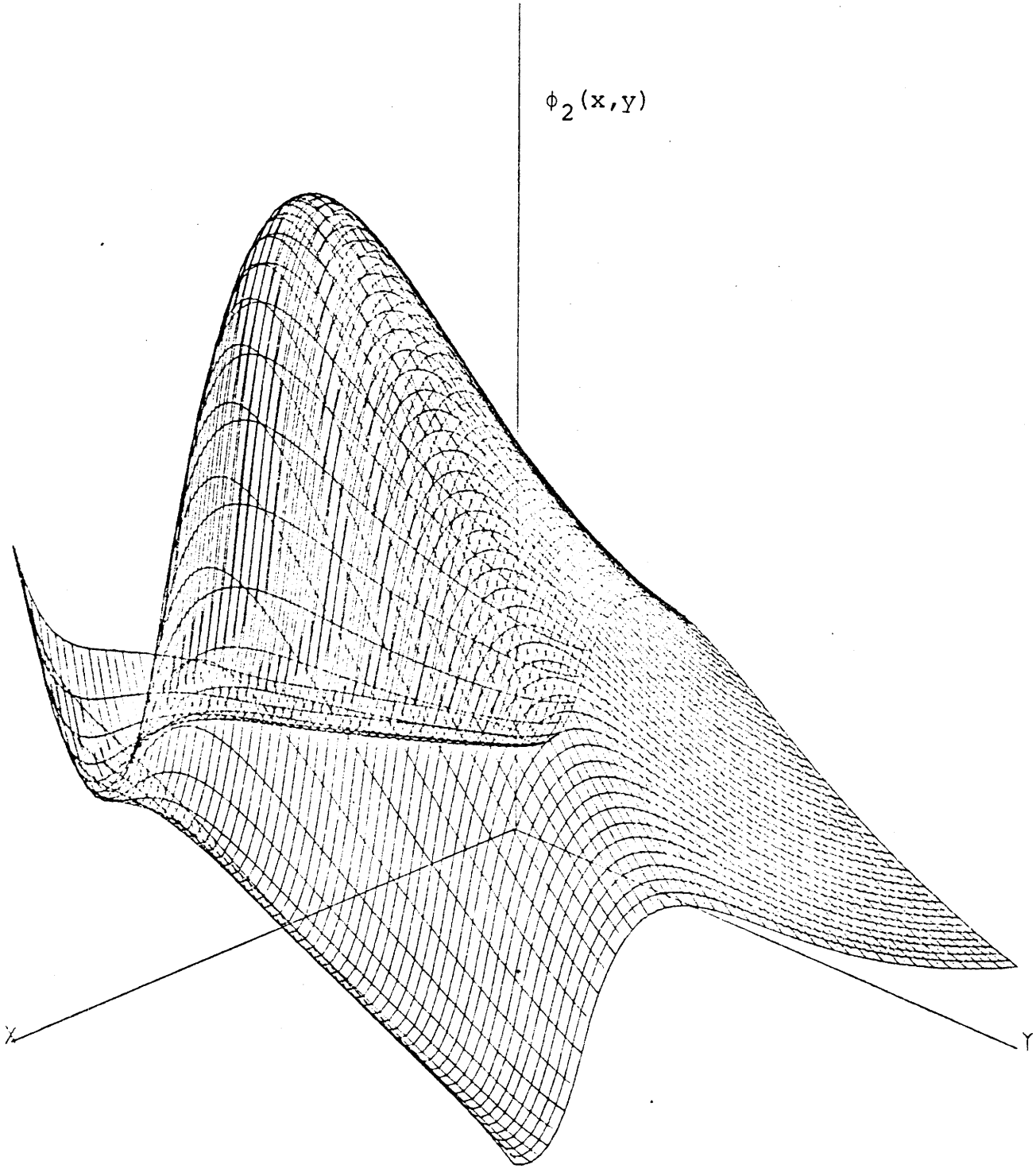

Figure A12.8: Reference Thermal Flux for Node 7 of Benchmark Problem 6

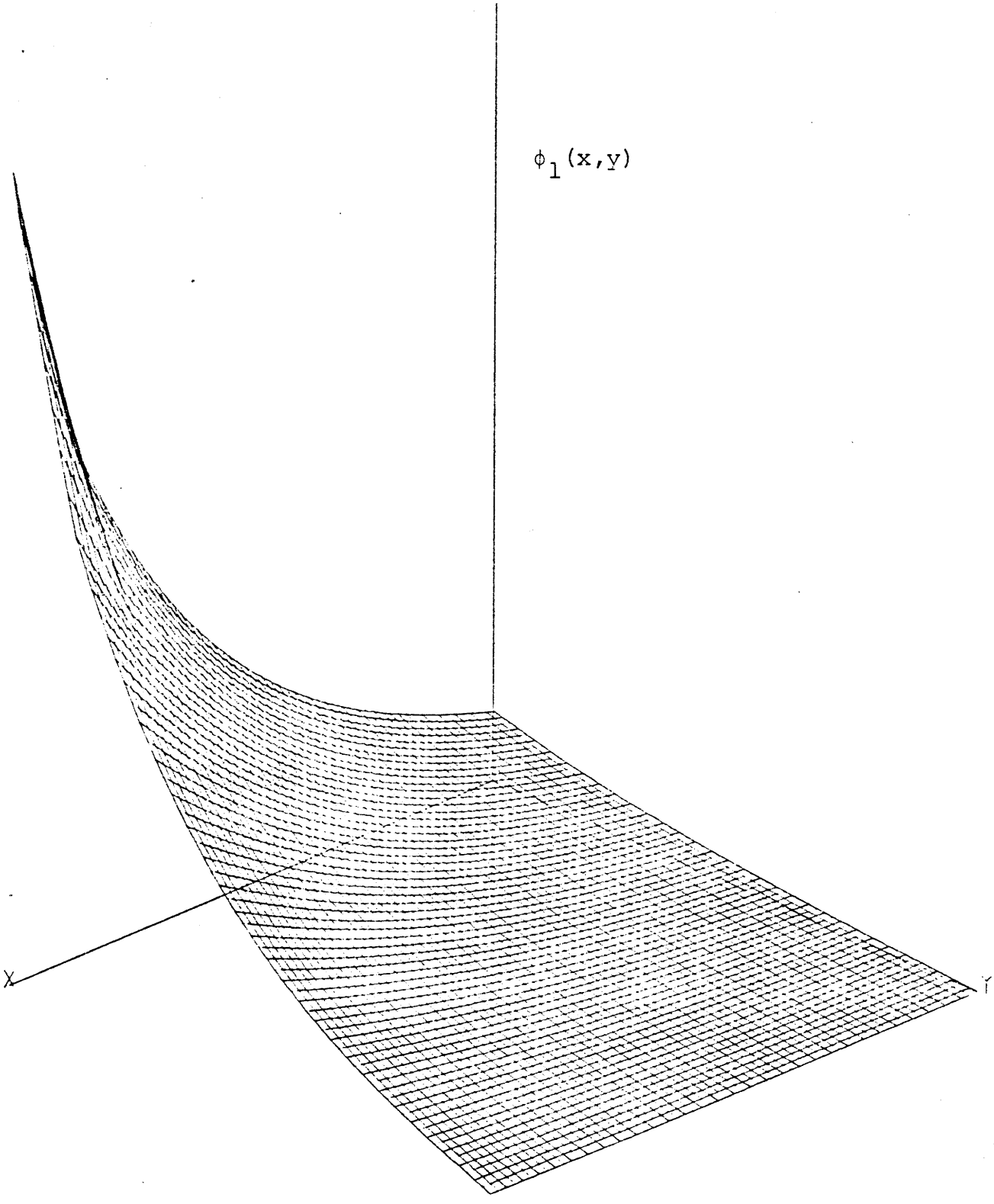

Figure A12.9: Reference Fast Flux for Node 8 of Benchmark Problem 6

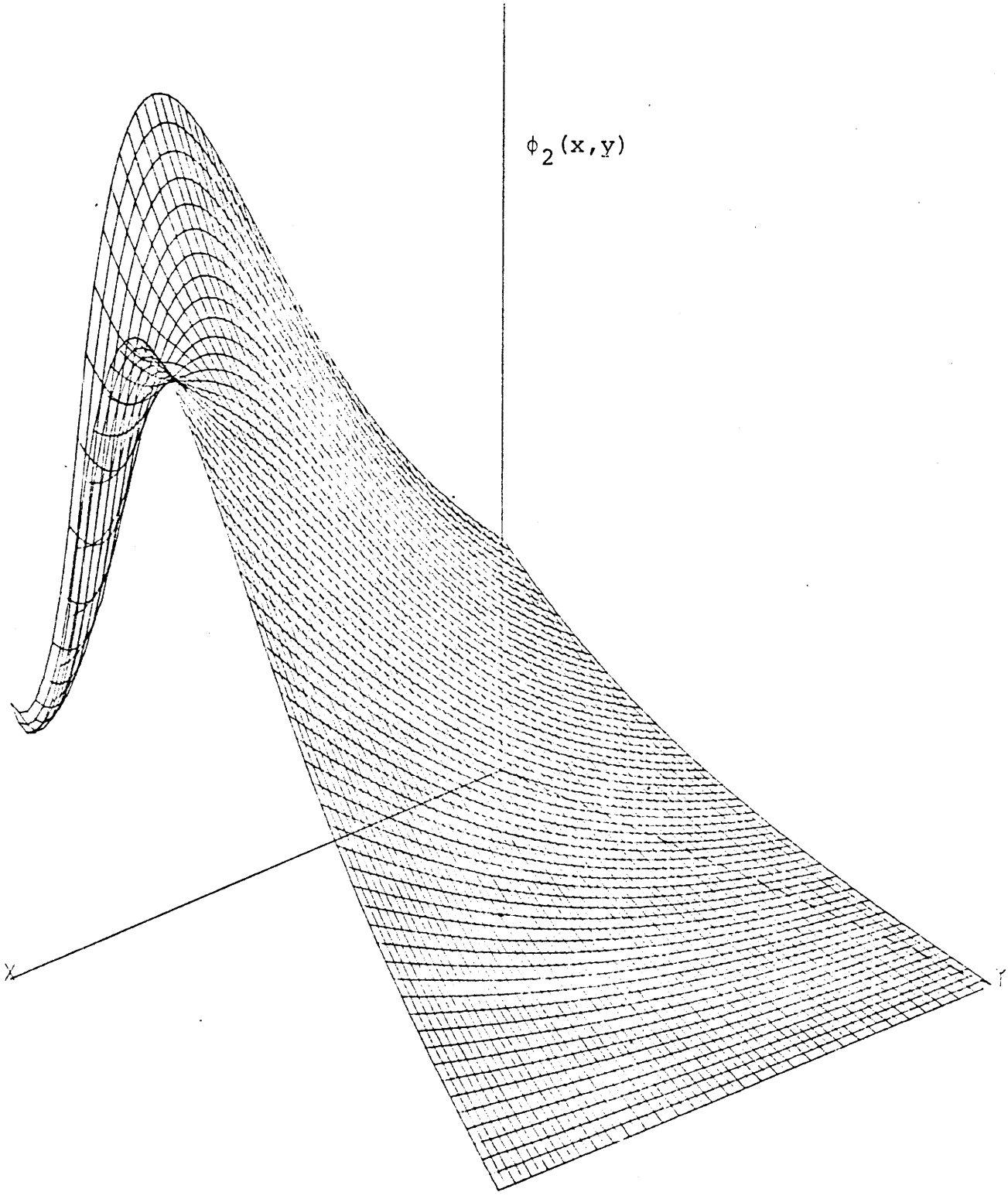

Figure A12.10: Reference Thermal Flux for Node 8 of Benchmark Problem 6

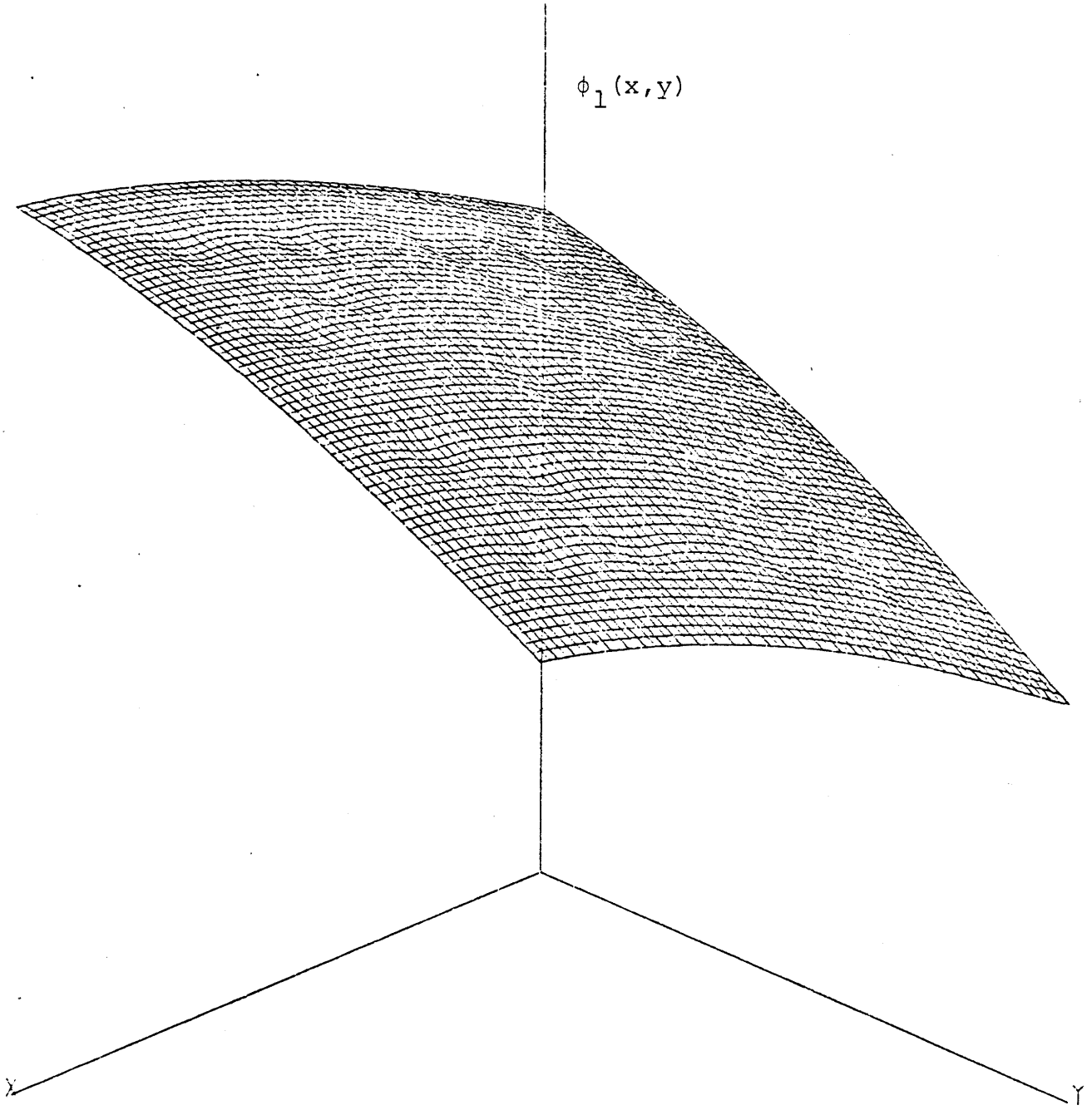

Figure A12.11: Reference Fast Flux for Node 10 of Benchmark Problem 6

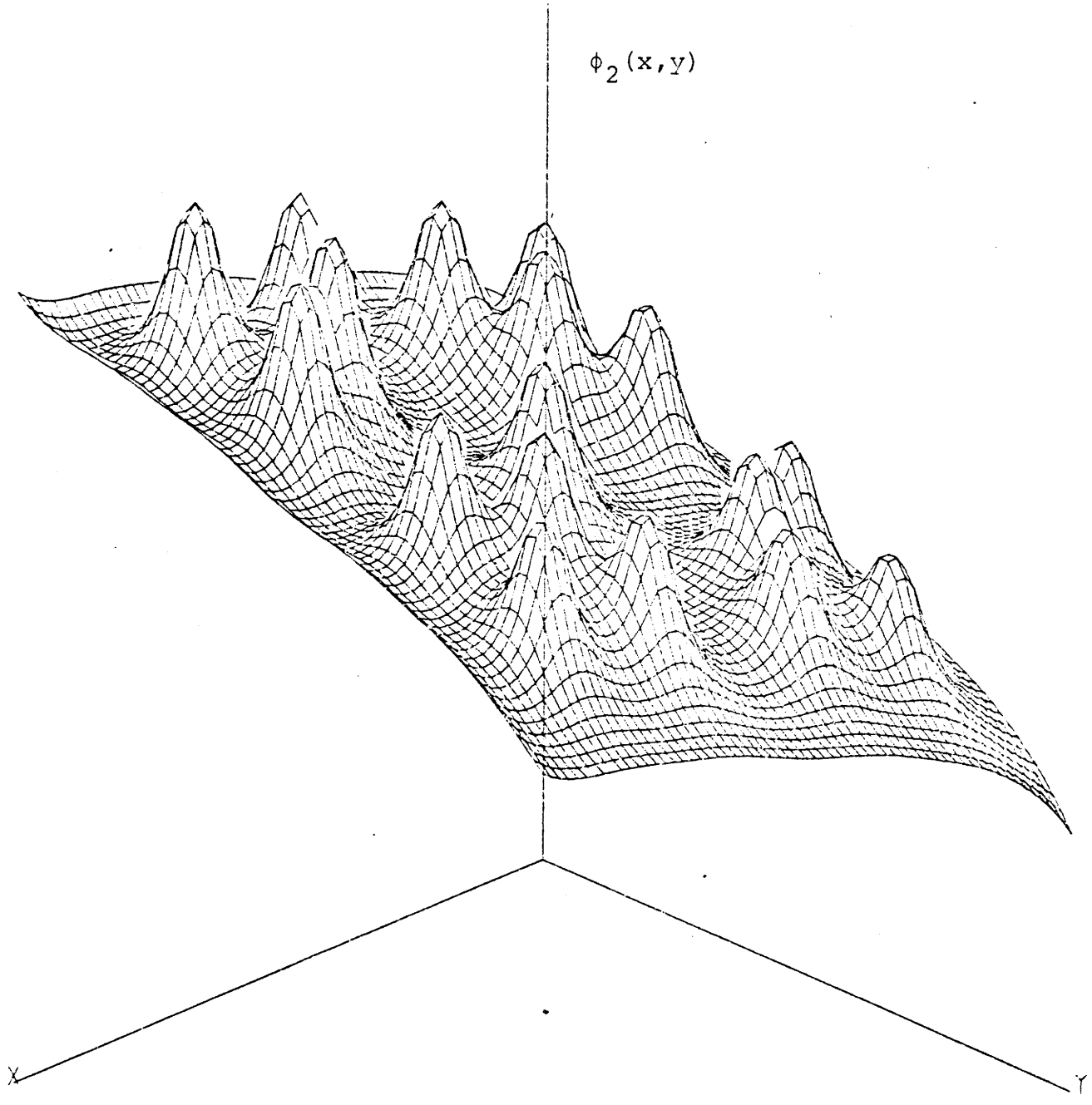

Figure A12.12: Reference Thermal Flux for Node 10 of Benchmark Problem 6

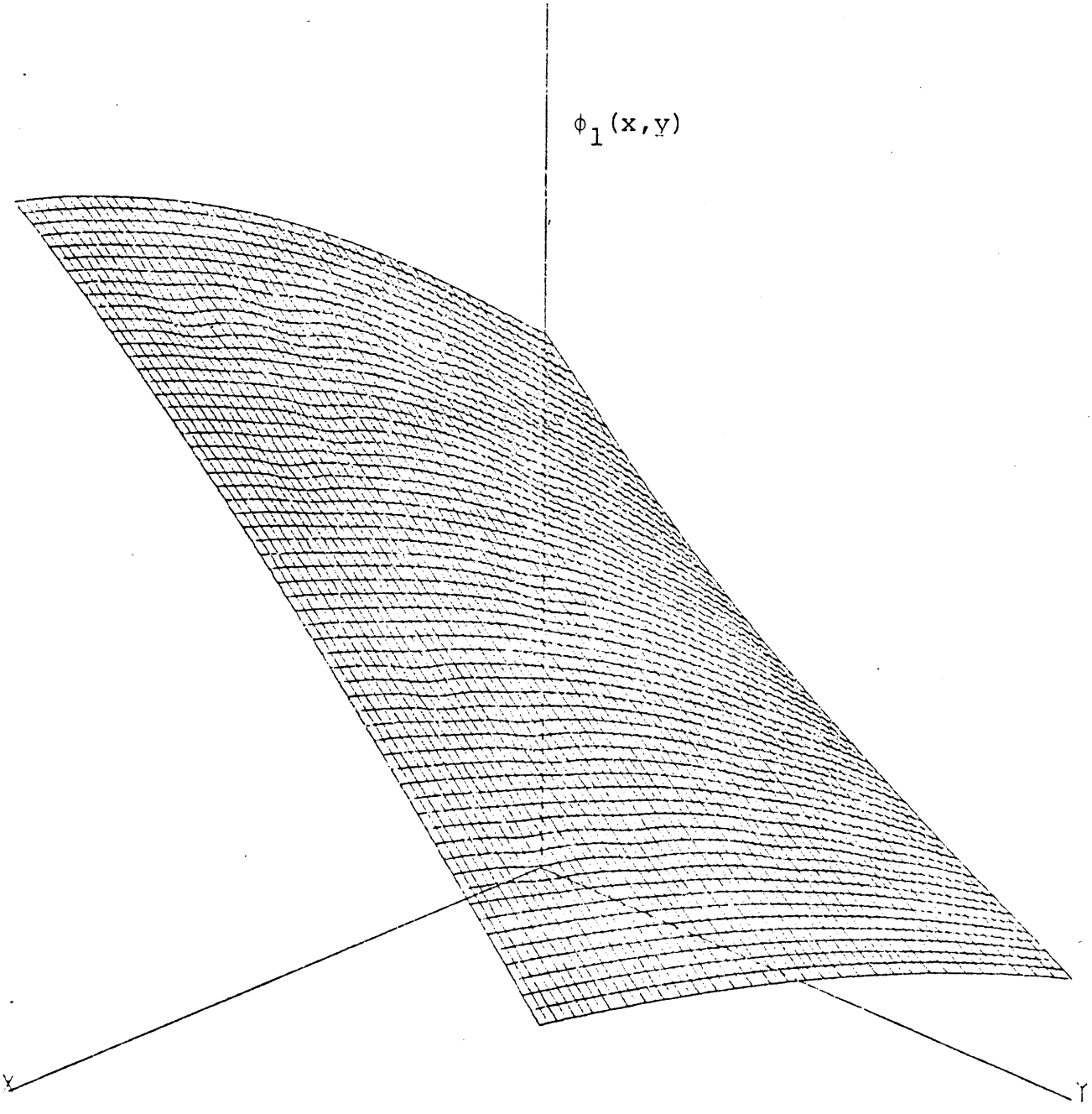

Figure A12.13: Reference Fast Flux for Node 11 of Benchmark Problem 6

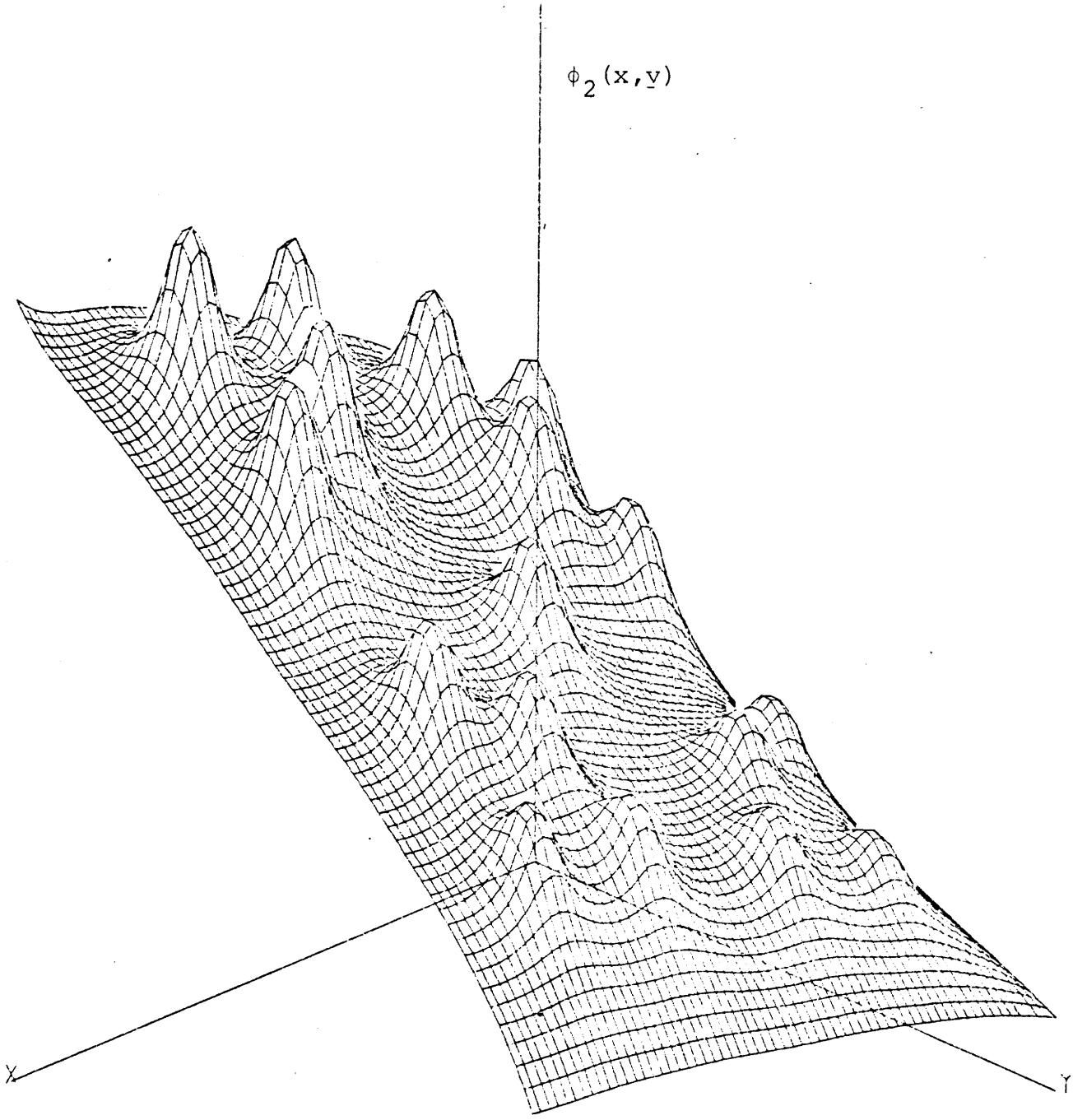

Figure A12.14: Reference Thermal Flux for Node 11 of Benchmark Problem 6

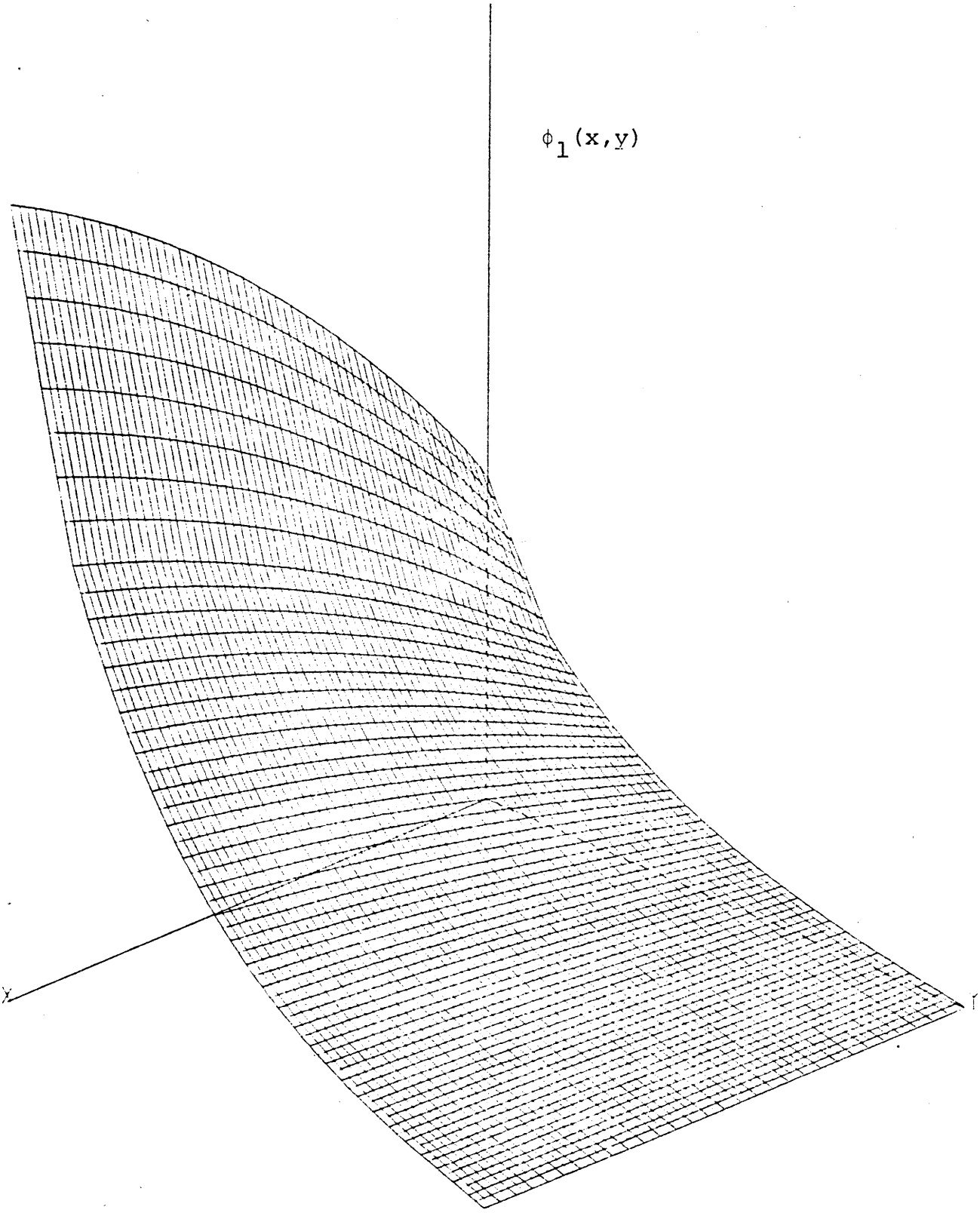

Figure A12.15: Reference Fast Flux for Node 12 of Benchmark Problem 6

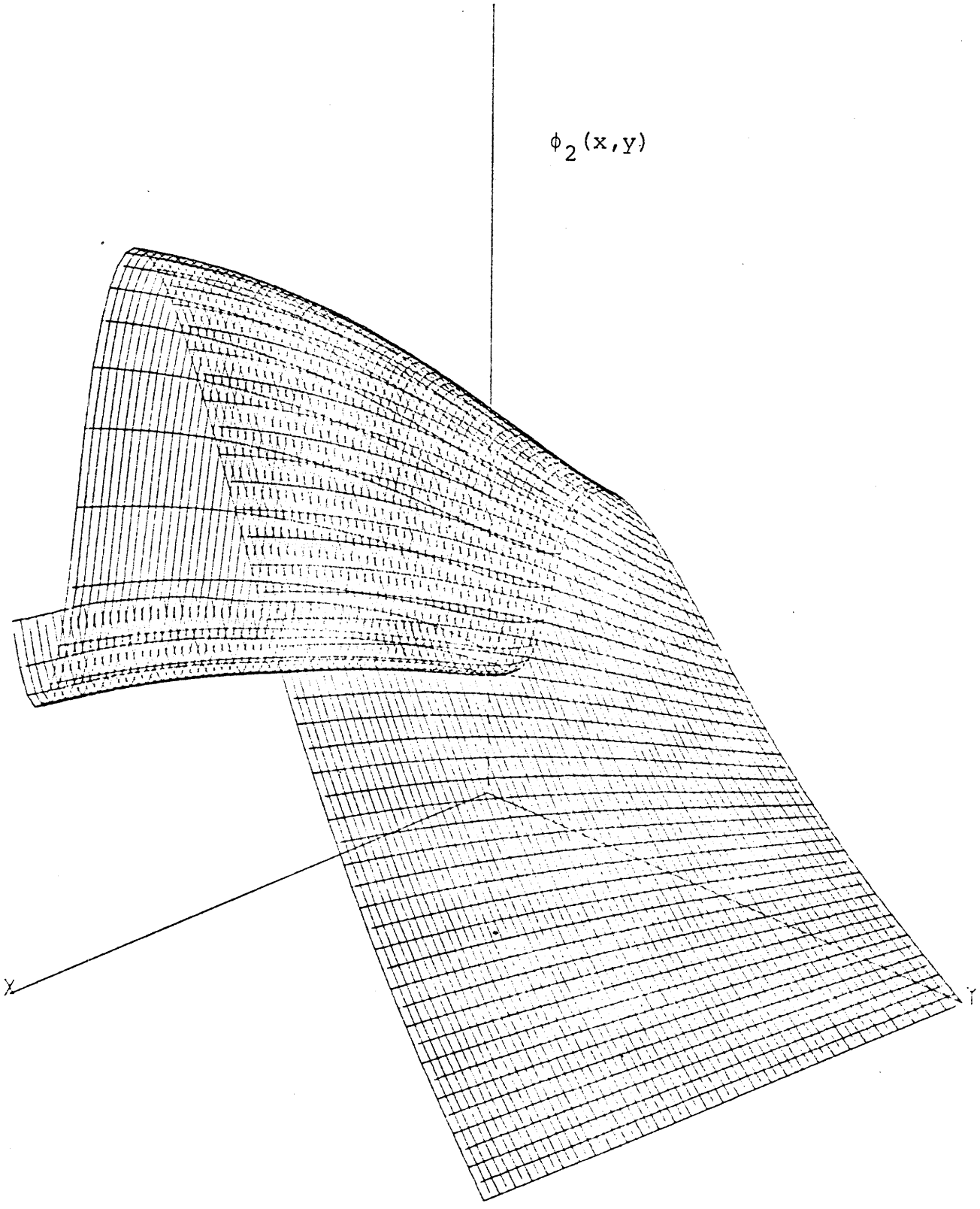

Figure A12.16: Reference Thermal Flux for Node 12 of Benchmark Problem 6

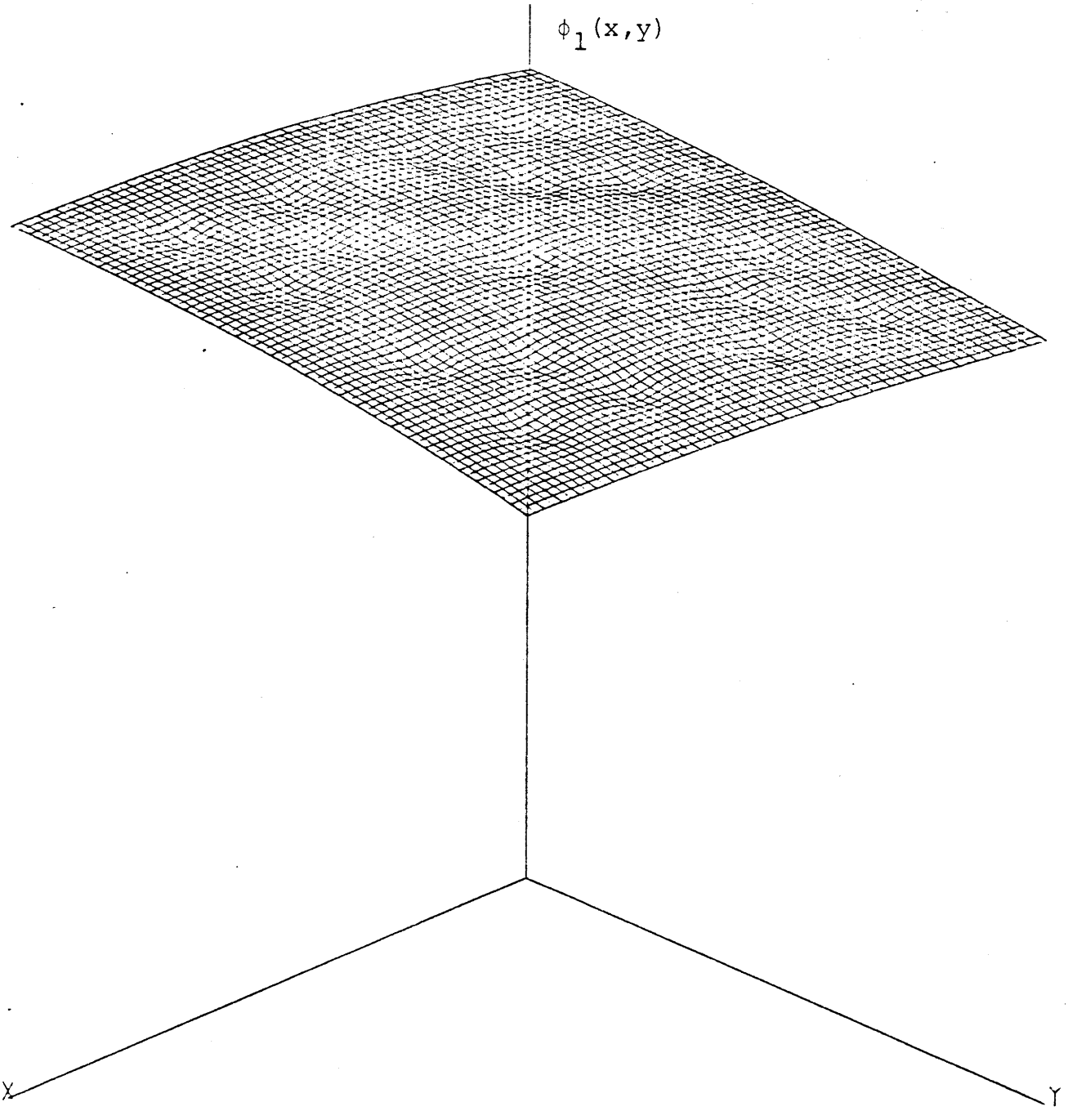

Figure A12.17: Reference Fast Flux for Node 13 of Benchmark Problem 6

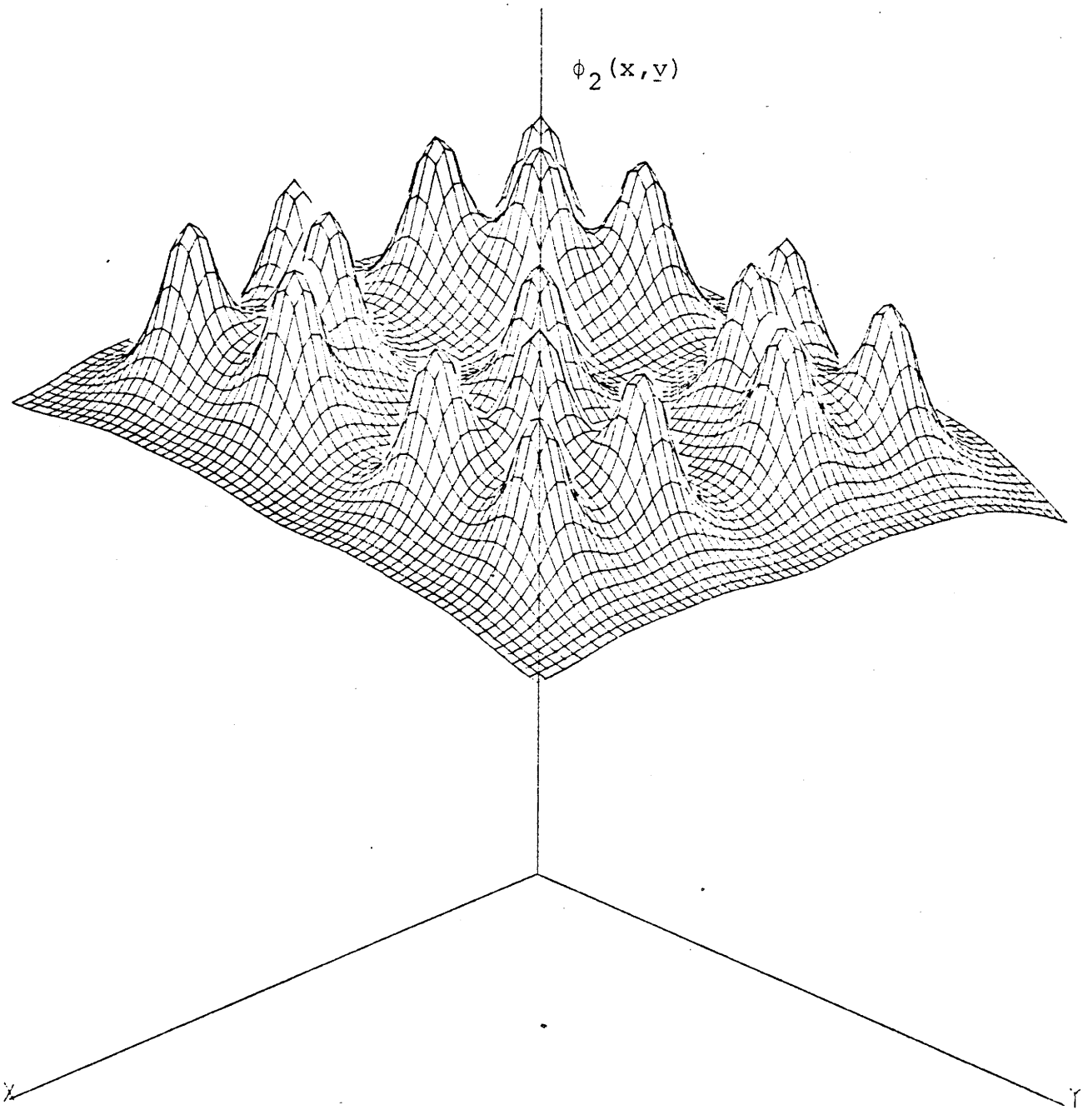

Figure A12.18: Reference Thermal Flux for Node 13 of Benchmark Problem 6

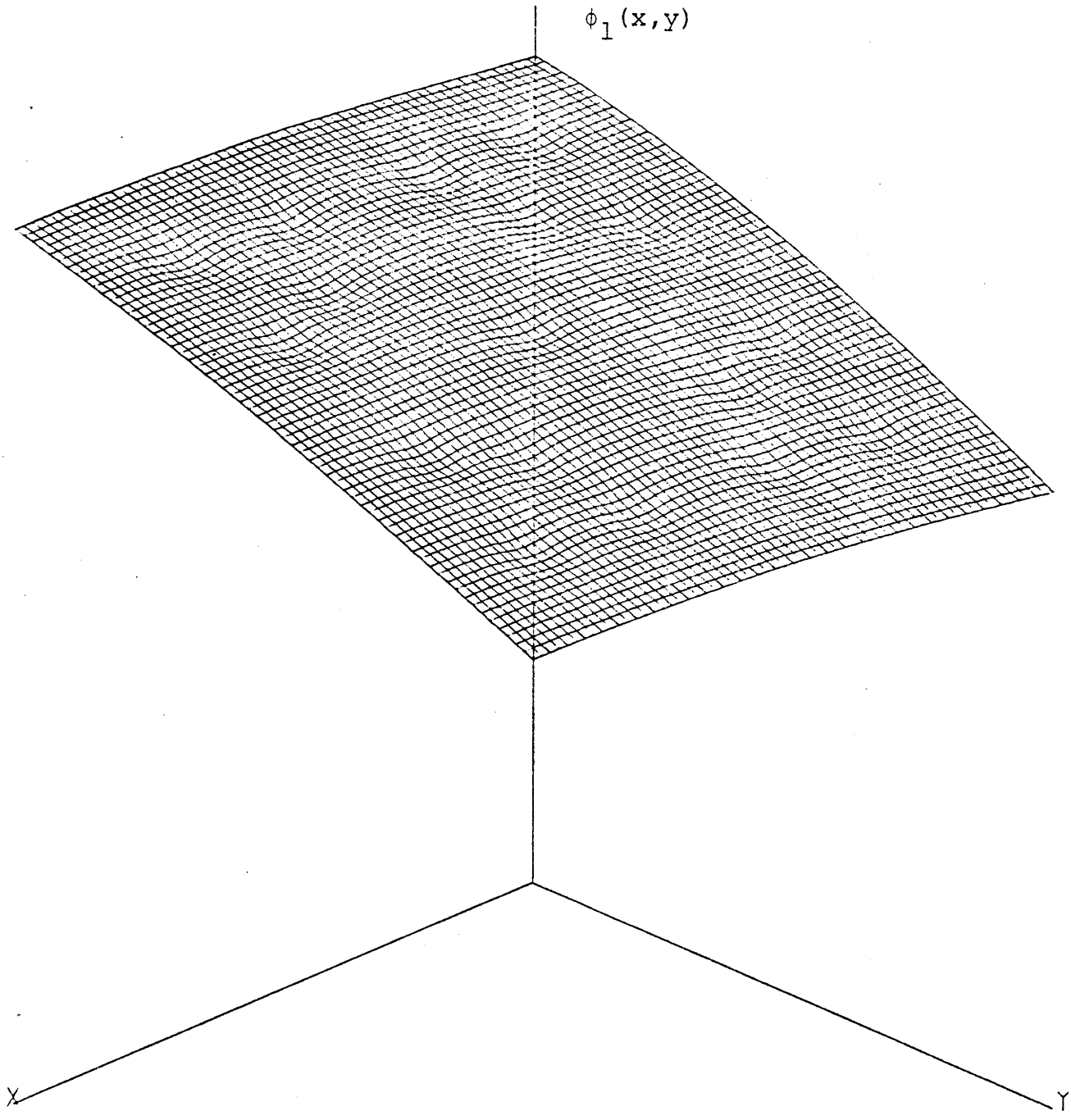

Figure A12.19: Reference Fast Flux for Node 14 of Benchmark Problem 6

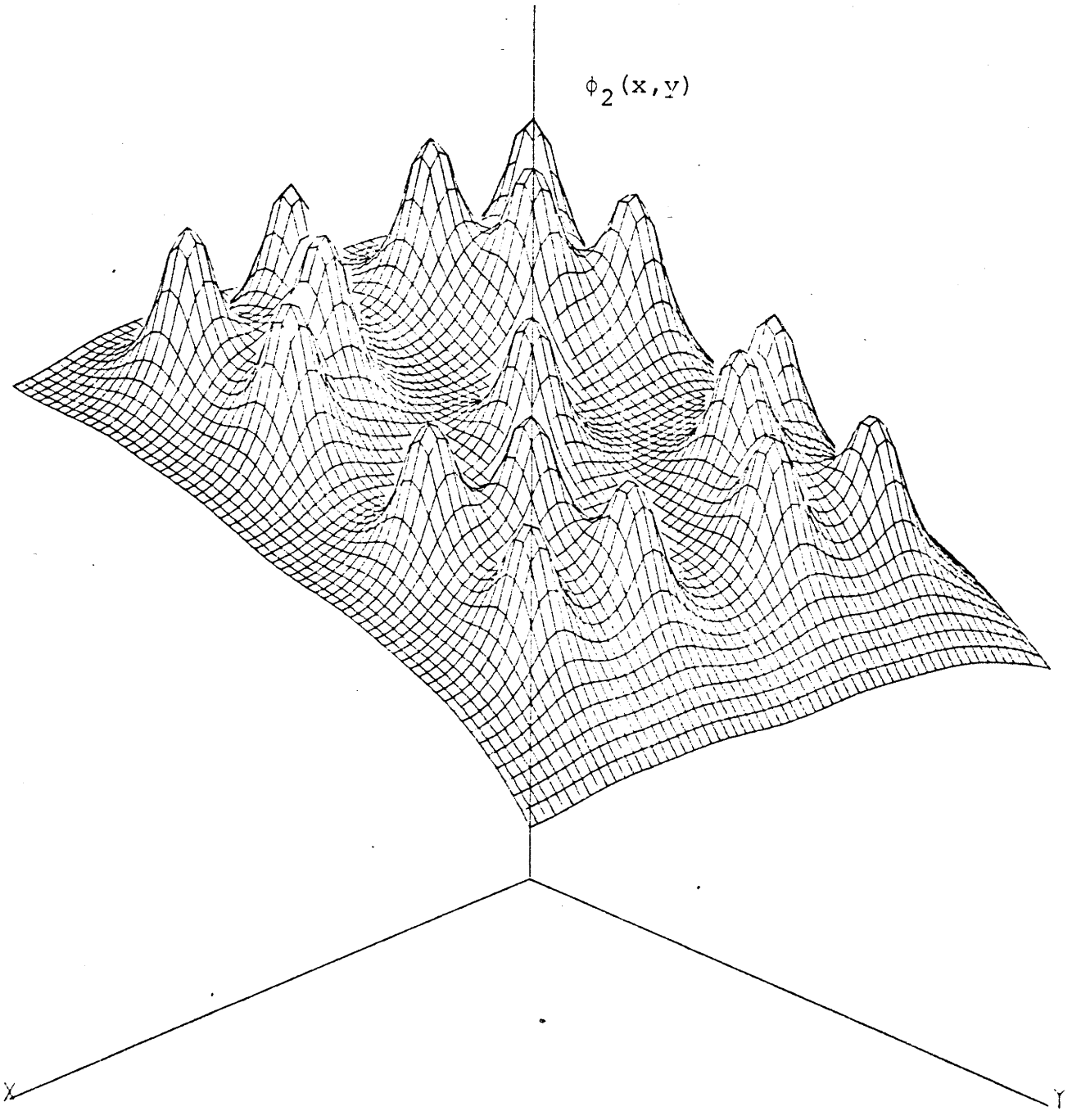

Figure A12.20: Reference Thermal Flux for Node 14 of Benchmark Problem 6

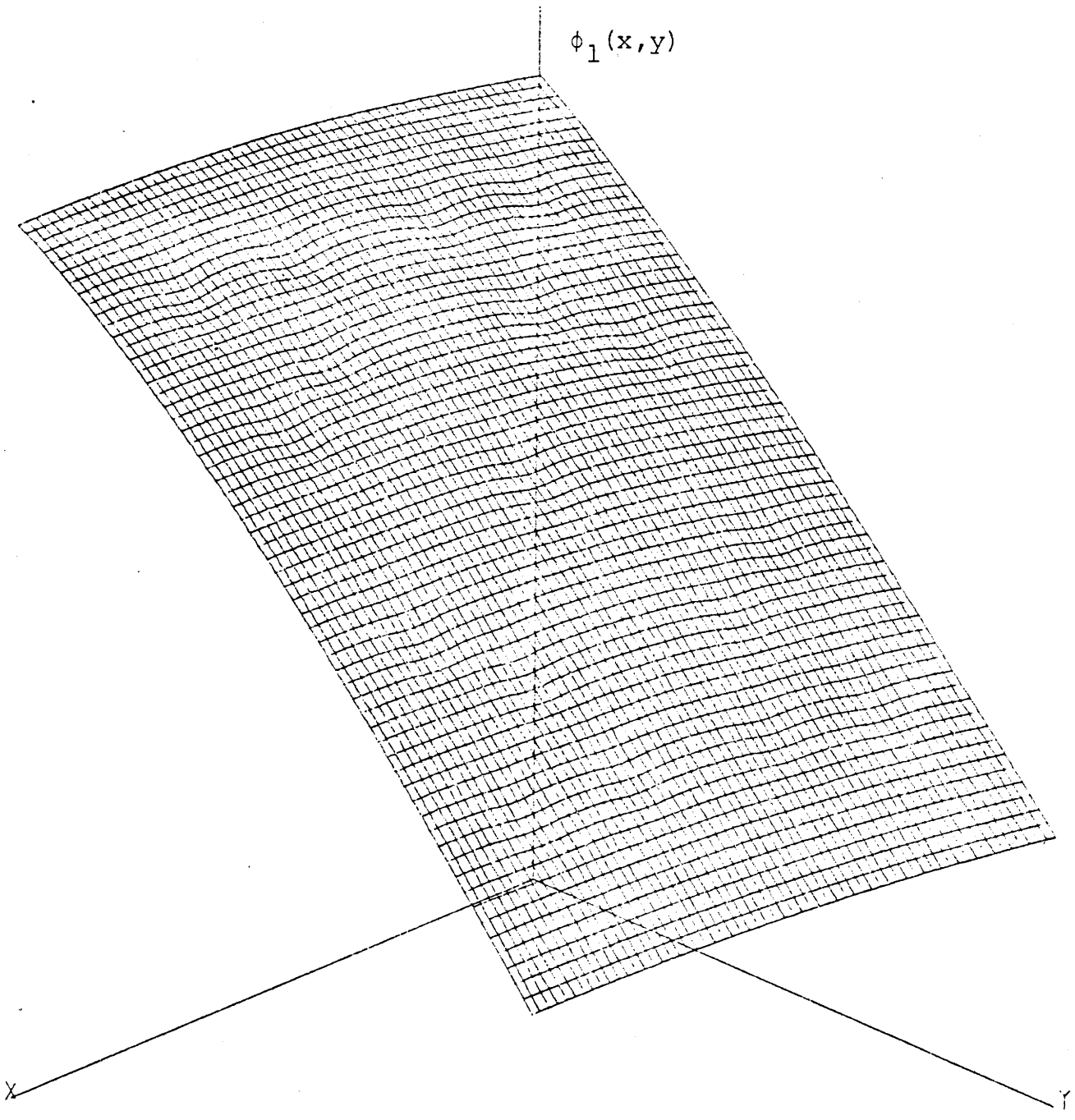

Figure A12.21: Reference Fast Flux for Node 15 of Benchmark Problem 6

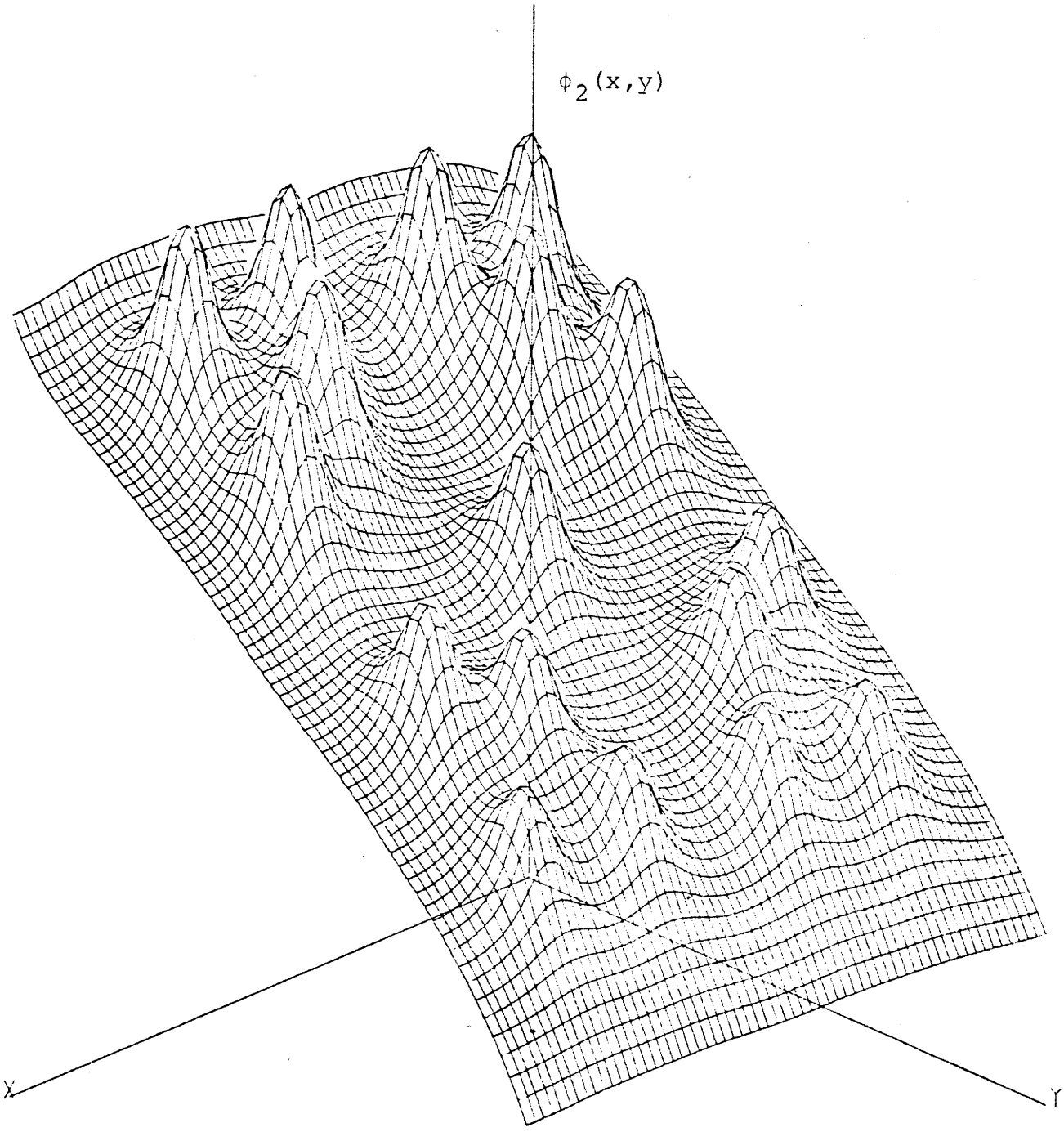

Figure A12.22: Reference Thermal Flux for Node 15 of Benchmark Problem 6

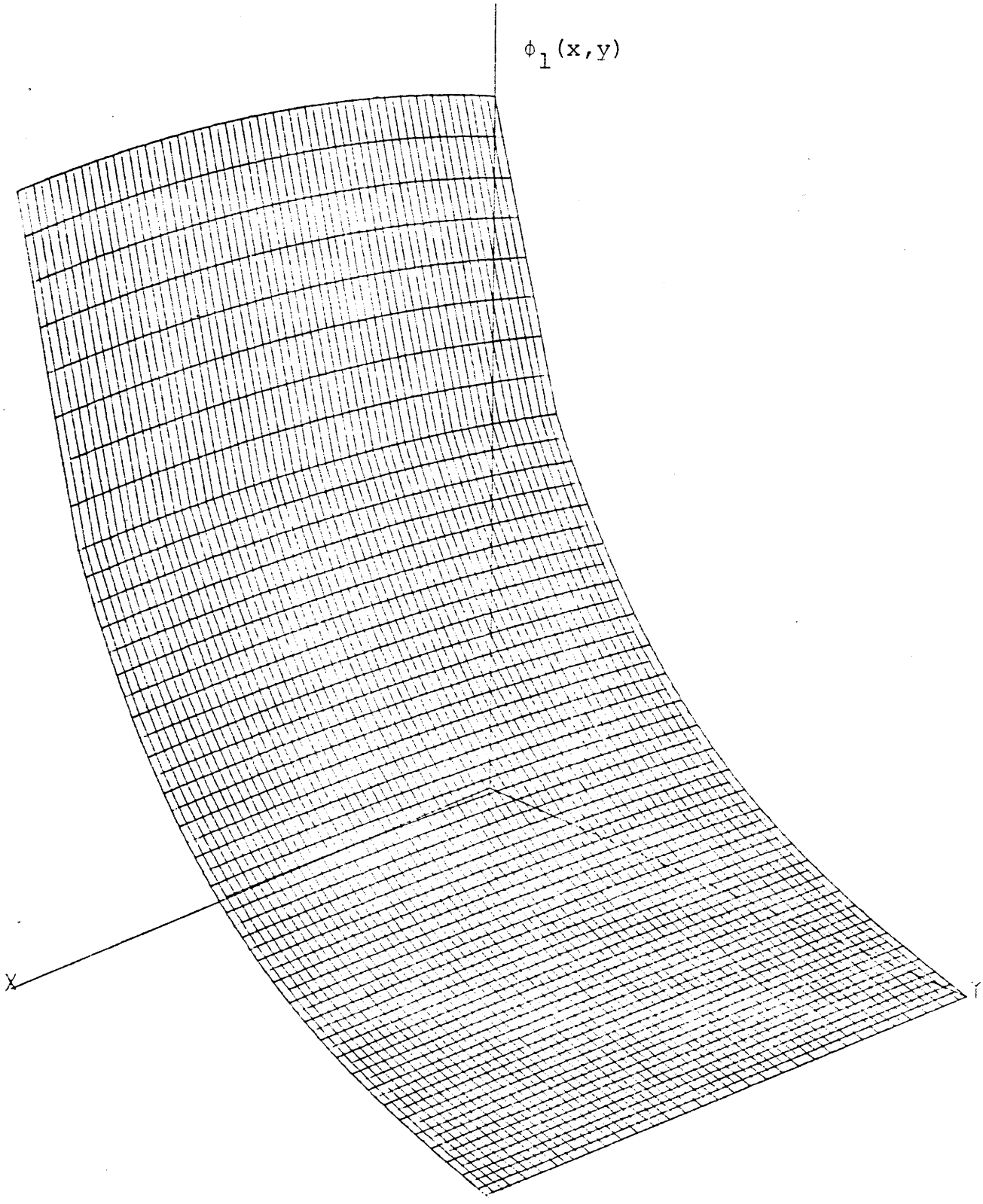

Figure A12.23: Reference Fast Flux for Node 16 of Benchmark Problem 6

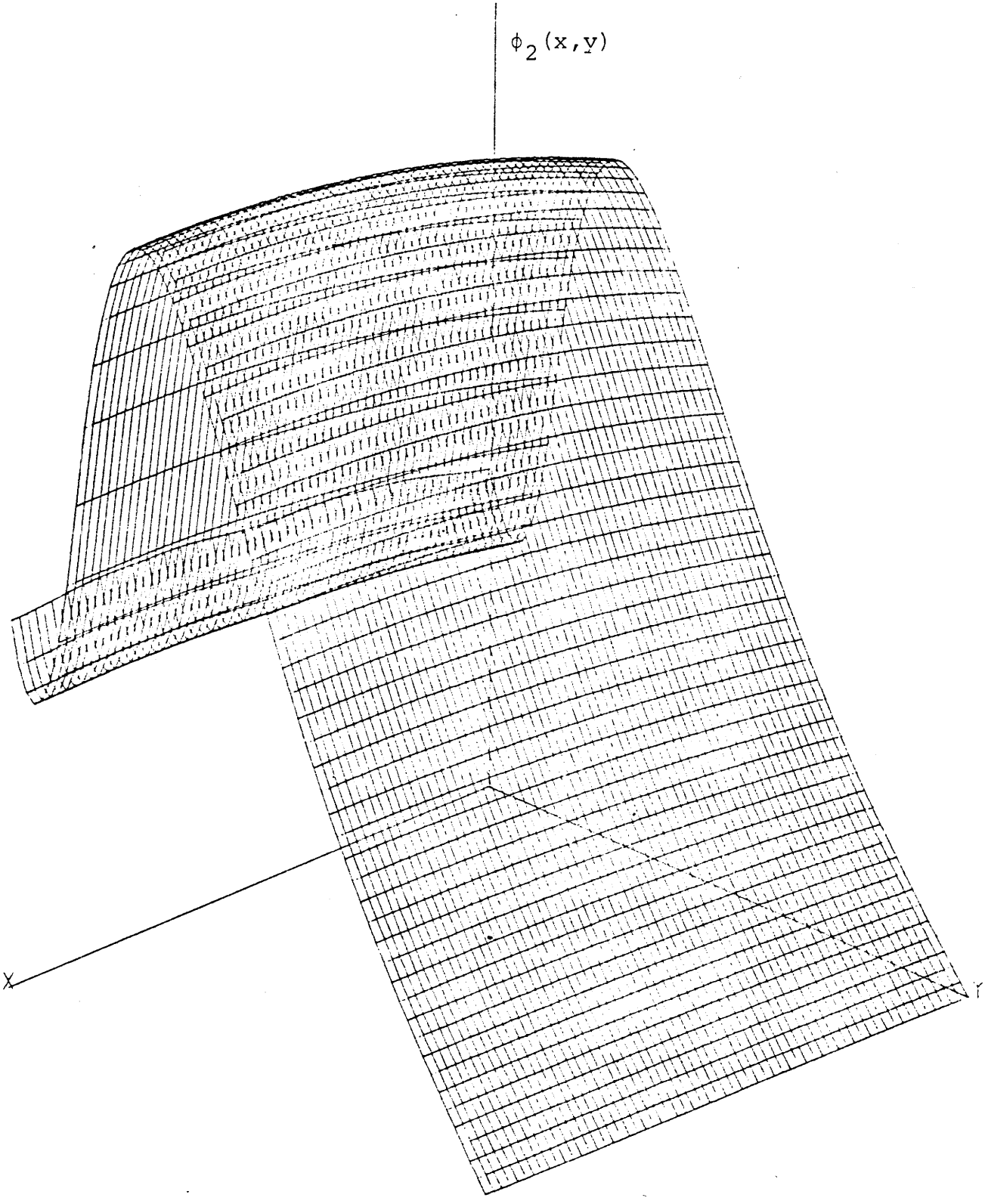

Figure A12.24: Reference Thermal Flux for Node 16 of Benchmark Problem 6

A12.3 Benchmark Problem 7

Benchmark problem 7 is a small, unrodded, 3-by-3 node problem. The center node 5 contains fuel 1 and 17 water holes. The other nodes are homogeneous fuel 2. A severe flux tilt is caused in this problem due to $\phi_g = 0$ boundary conditions. The sketch below gives the node numbering for this problem.

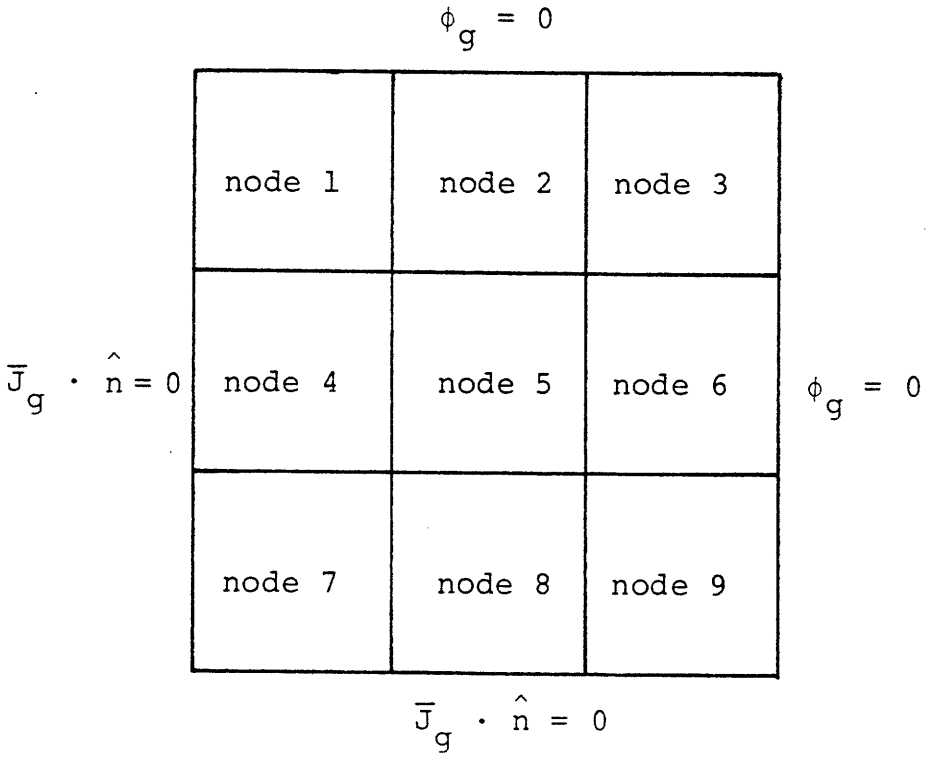

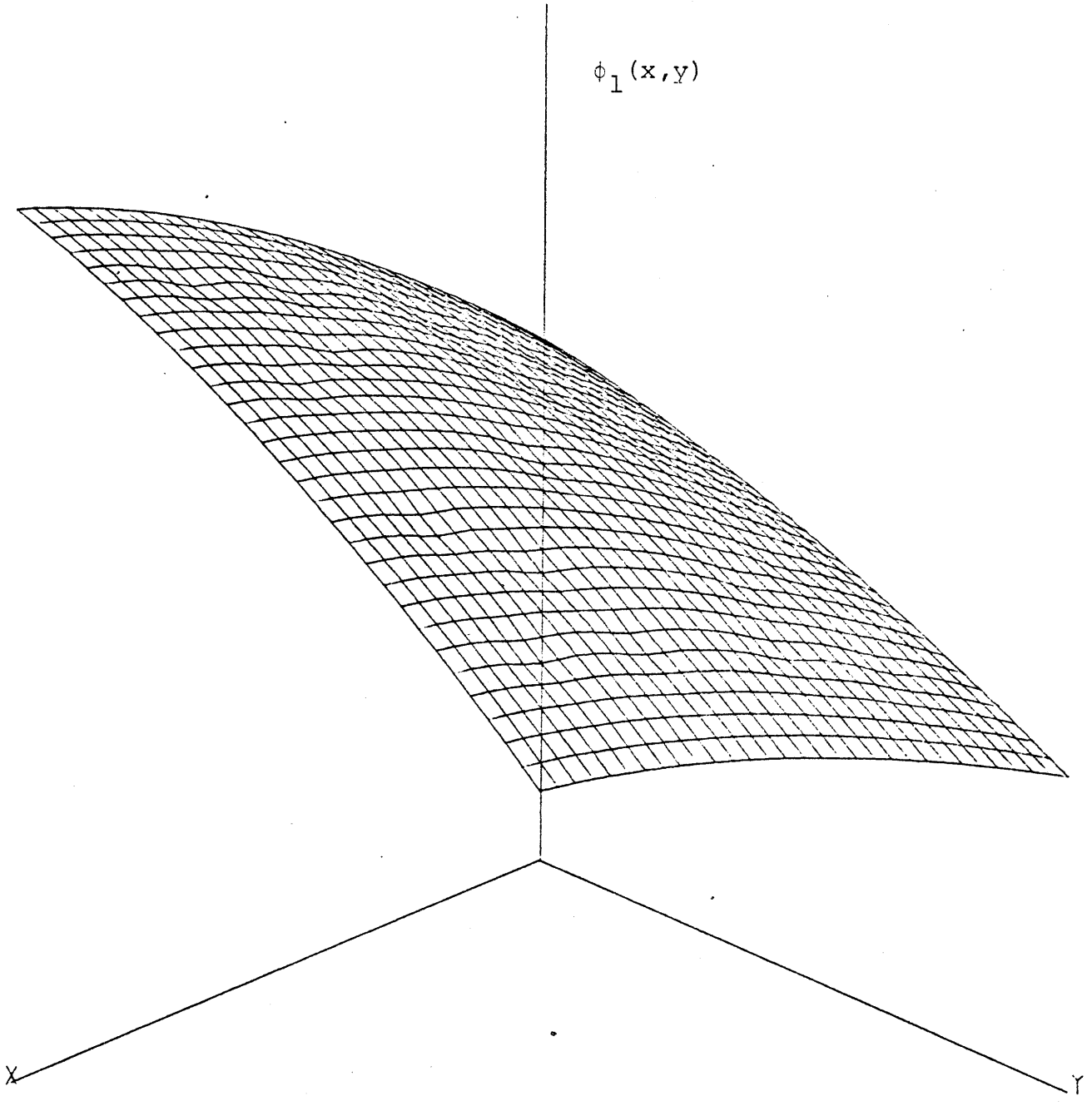

Figure A12.25: Reference Fast Flux for Node 5 of Benchmark Problem 7

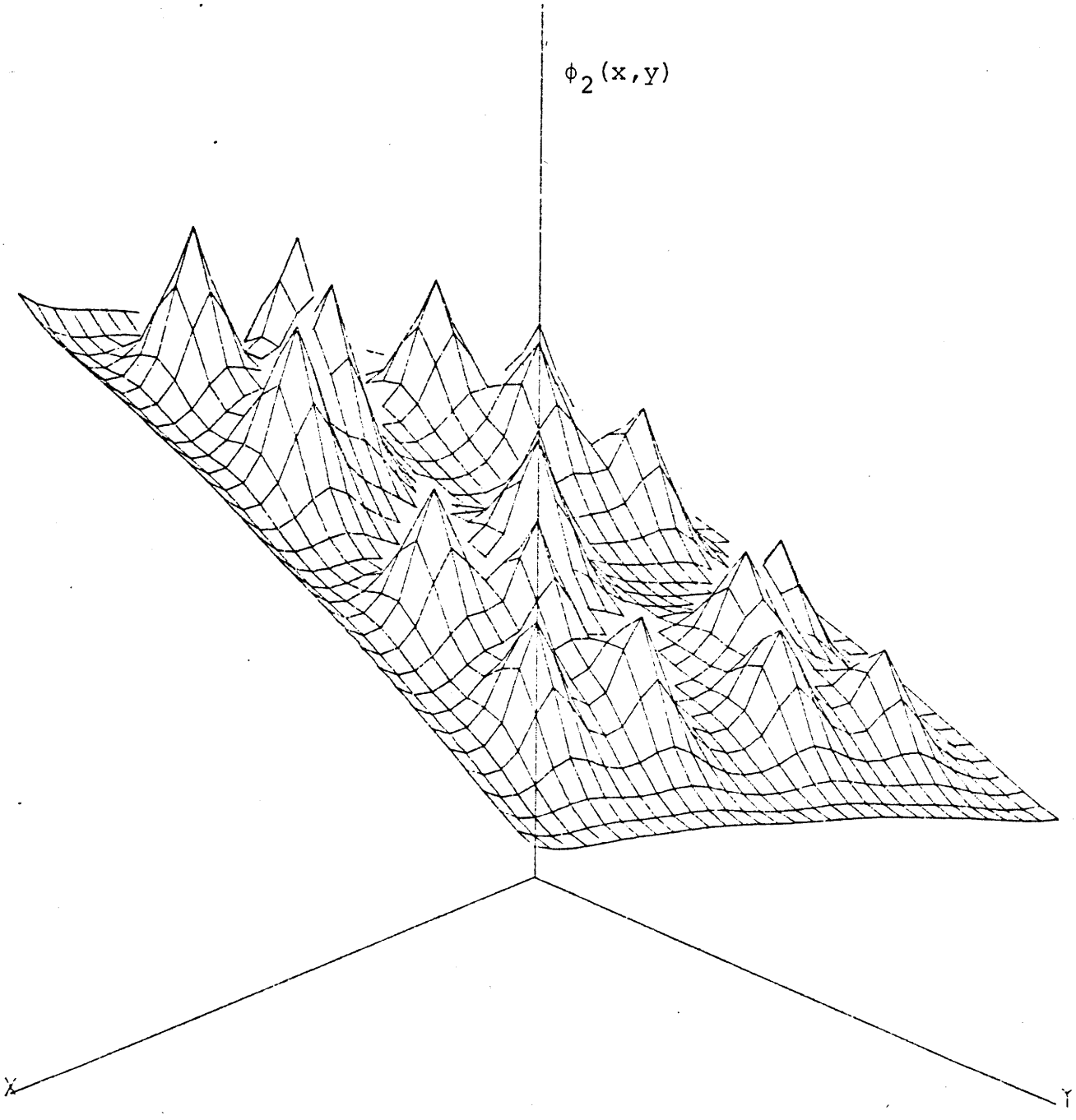

Figure A12.26: Reference Thermal Flux for Node 5 of Benchmark Problem 7

A12.4 Benchmark Problem 8

Benchmark problem 8 is a small 3-by-3 node problem. Some of the nodes are rodded and node 3 contains water to simulate reflector effects. Reconstruction of the flux was attempted in node 5 which contains fuel type 2 and control rods. The sketch below gives the node numbering for this problem.

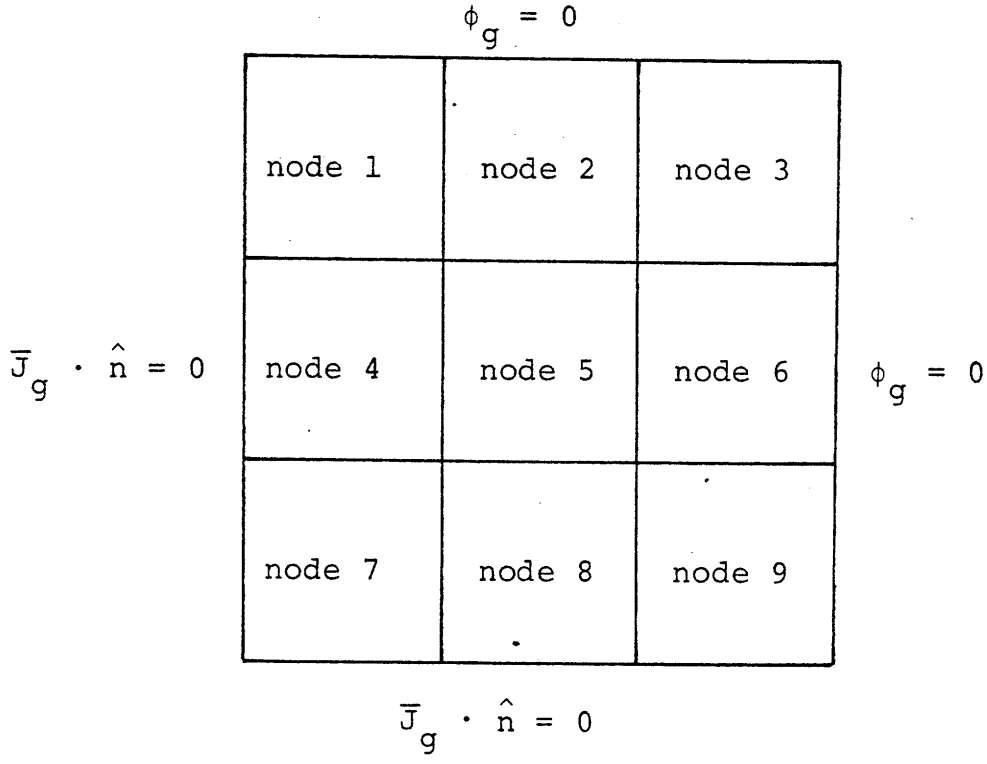

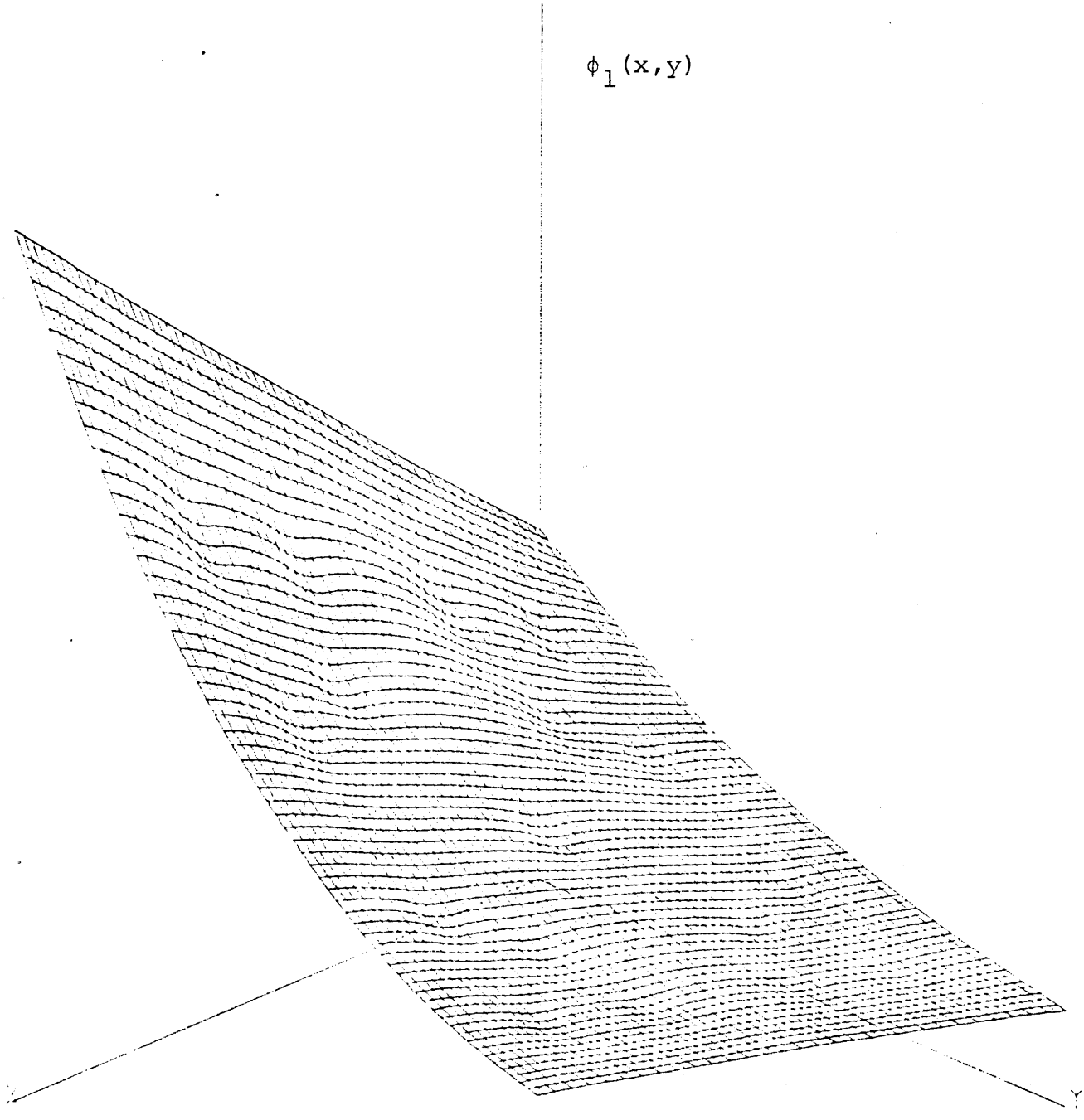

Figure A12.27: Reference Fast Flux for Node 5 of Benchmark Problem 8

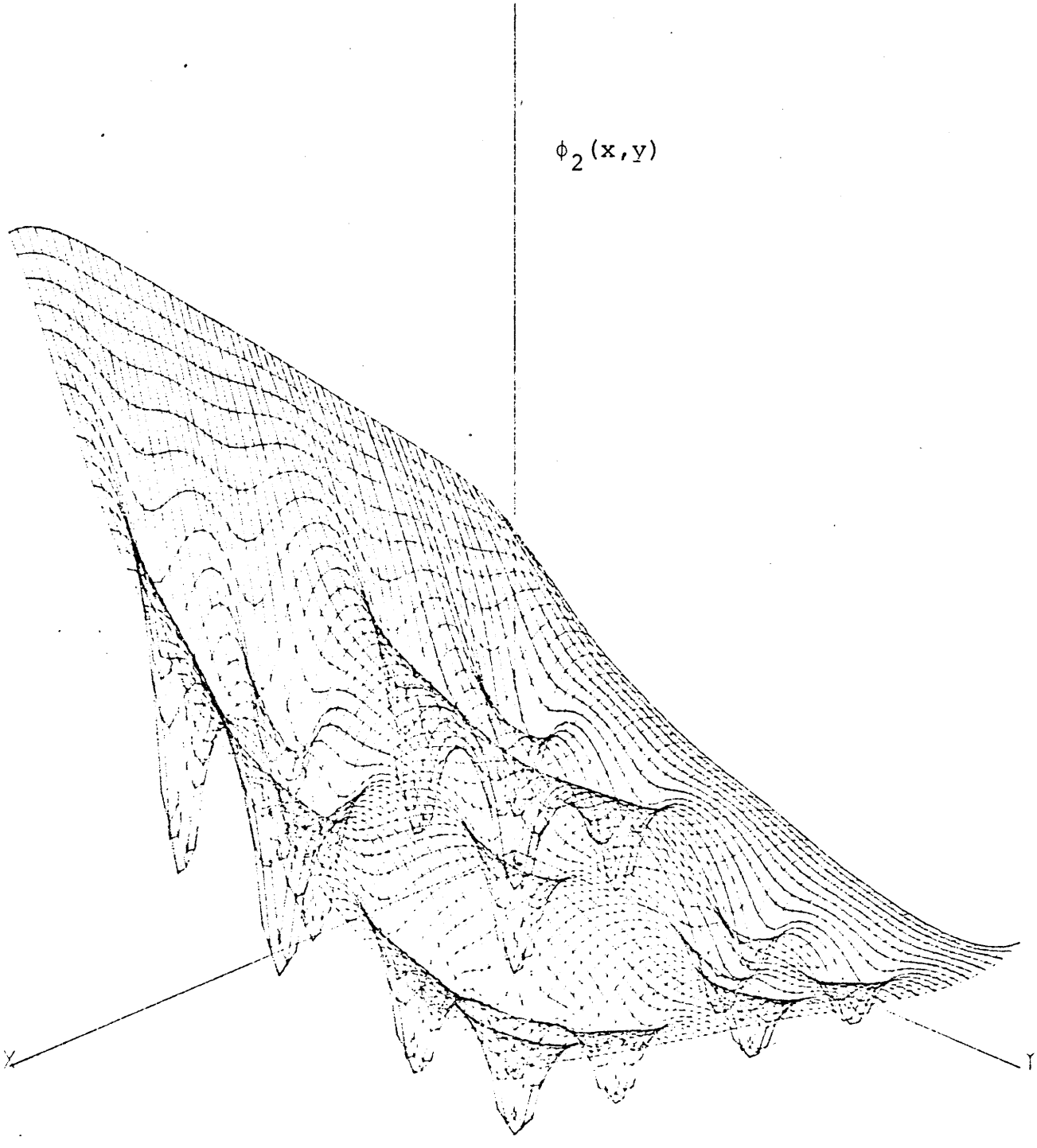

Figure A12.28: Reference Thermal Flux for Node 5 of Benchmark Problem 8

Appendix 13

ASSEMBLY FLUX PLOTS FROM ASSEMBLY CALCULATIONS EMPLOYING ZERO-CURRENT BOUNDARY CONDITIONS

A13.0 Introduction

Figure A13.1: Fast Assembly Flux for an Unrodded Fuel 1 Assembly

Figure A13.2: Thermal Assembly Flux for an Unrodded Fuel 1 Assembly

Figure A13.3: Fast Assembly Flux for a Rodded Fuel 1 Assembly

Figure A13.4: Thermal Assembly Flux for a Rodded Fuel 1 Assembly

Figure A13.5: Fast Assembly Flux for an Unrodded Fuel 2 Assembly

Figure A13.6: Thermal Assembly Flux for an Unrodded Fuel 2 Assembly

Figure A13.7: Fast Assembly Flux for a Rodded Fuel 2 Assembly

Figure A13.8: Thermal Assembly Flux for a Rodded Fuel 2 Assembly

A13.0 Introduction

This appendix contains the assembly flux plots from PDQ-7 assembly calculations employing zero-current boundary conditions. Included are fast and thermal flux plots for each of the following four types of assemblies:

1. Fuel 1 -- Unrodded
2. Fuel 1 -- Rodded
3. Fuel 2 -- Unrodded
4. Fuel 2 -- Rodded.

A description of these assemblies is contained in Appendix 1.

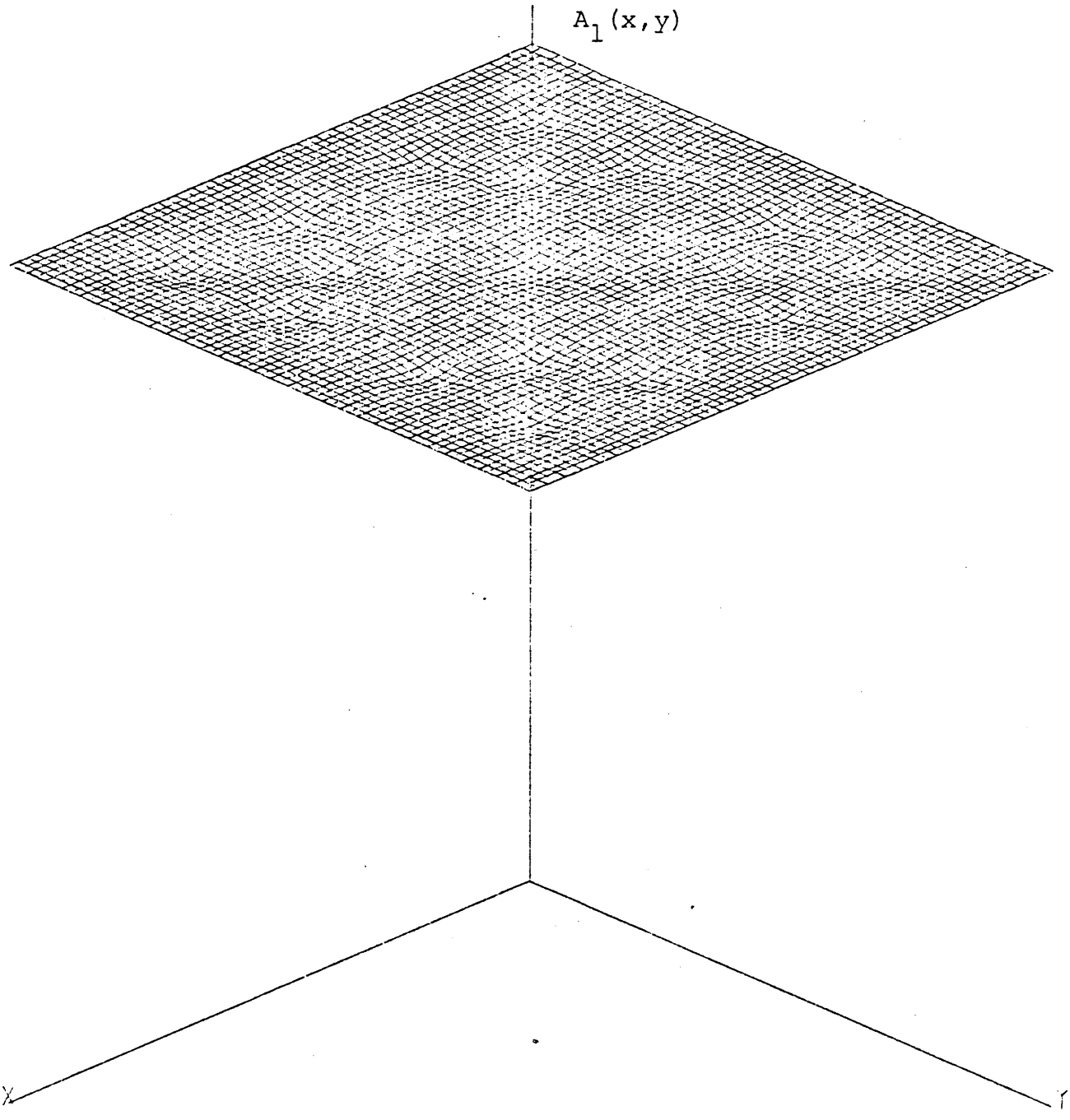

Figure A13.1: Fast Assembly Flux for an Unrodded Fuel 1 Assembly

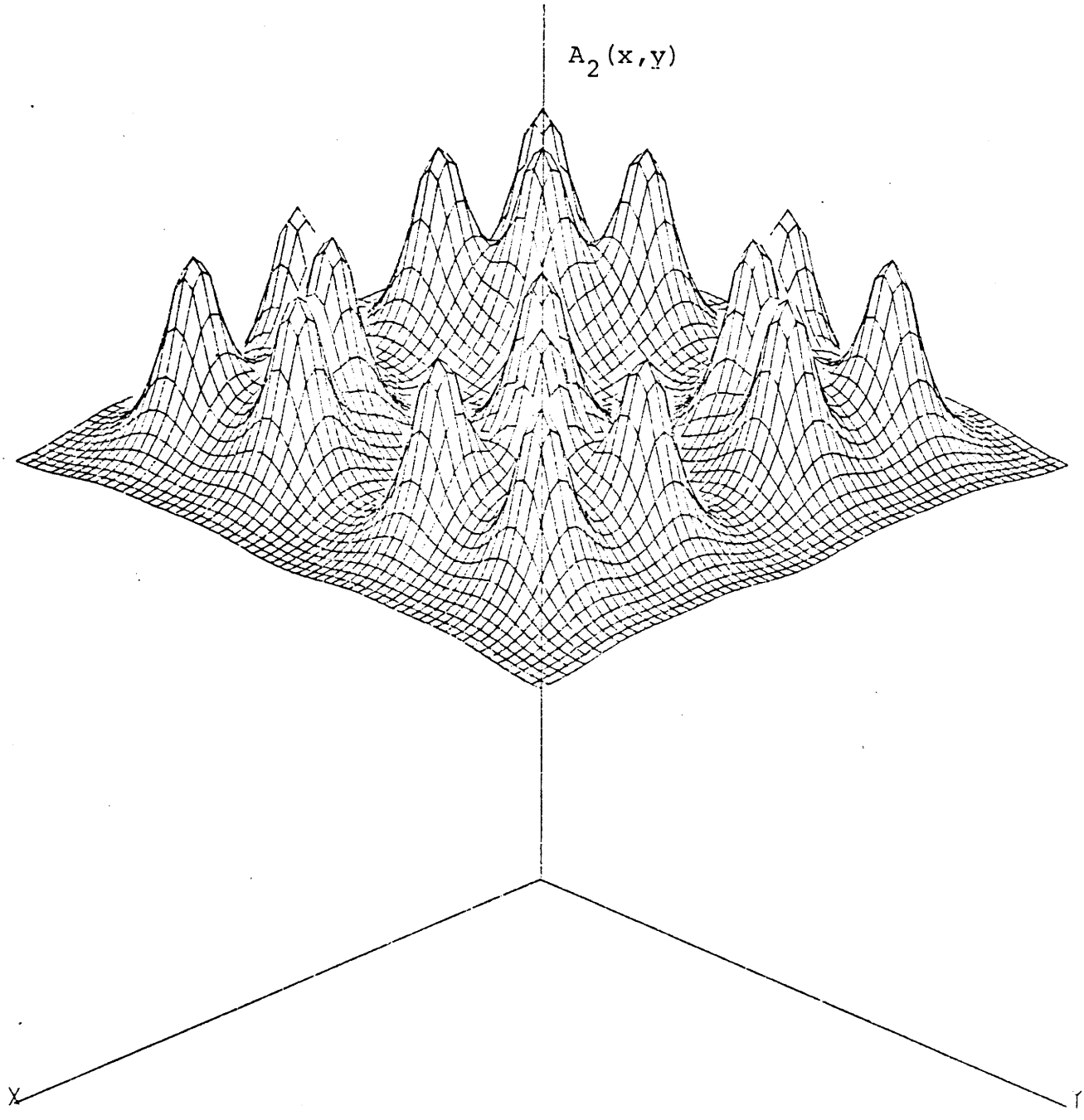

Figure A13.2: Thermal Assembly Flux for an Unrodded Fuel 1 Assembly

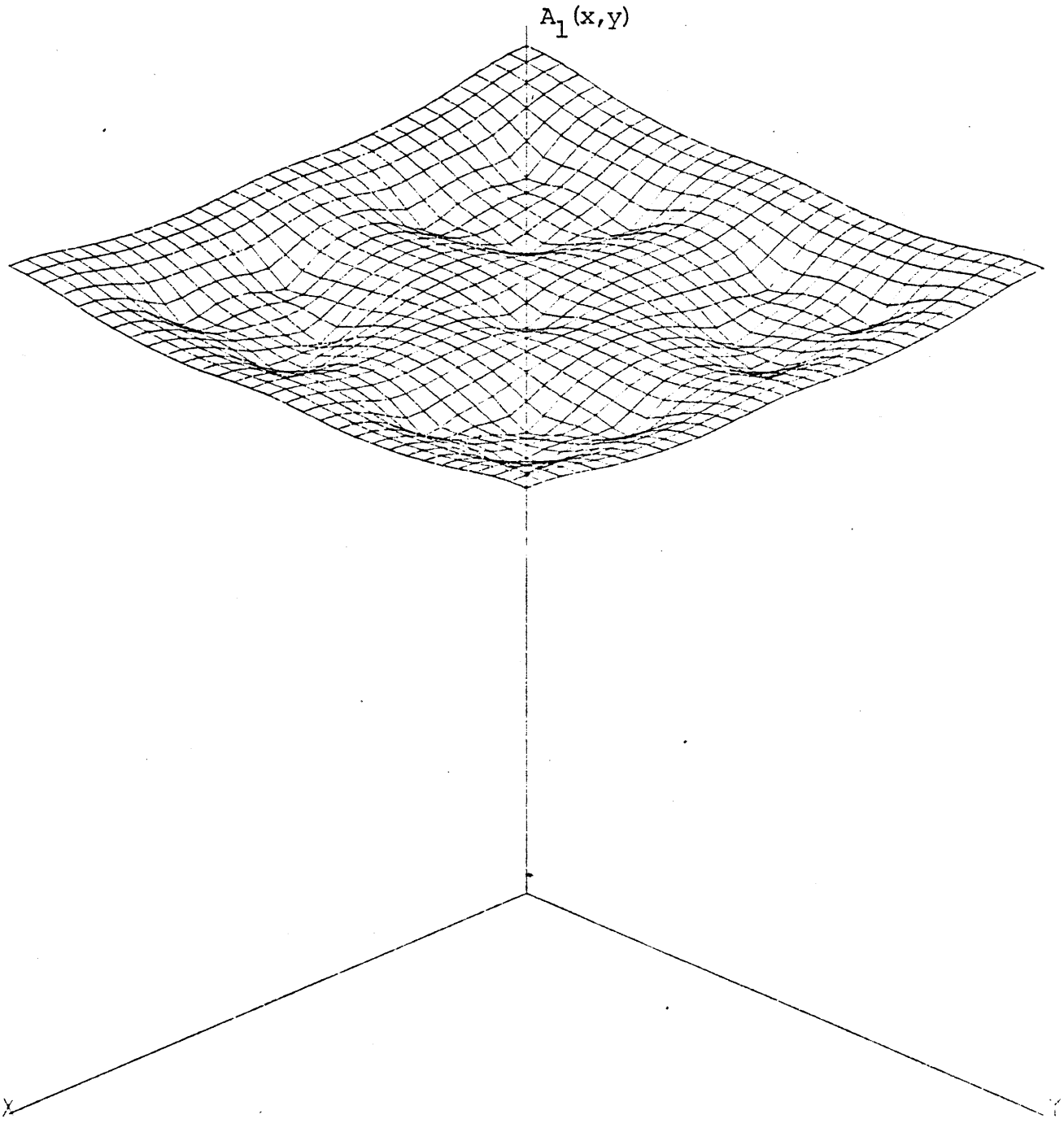

Figure A13.3: Fast Assembly Flux for a Rodded Fuel 1 Assembly

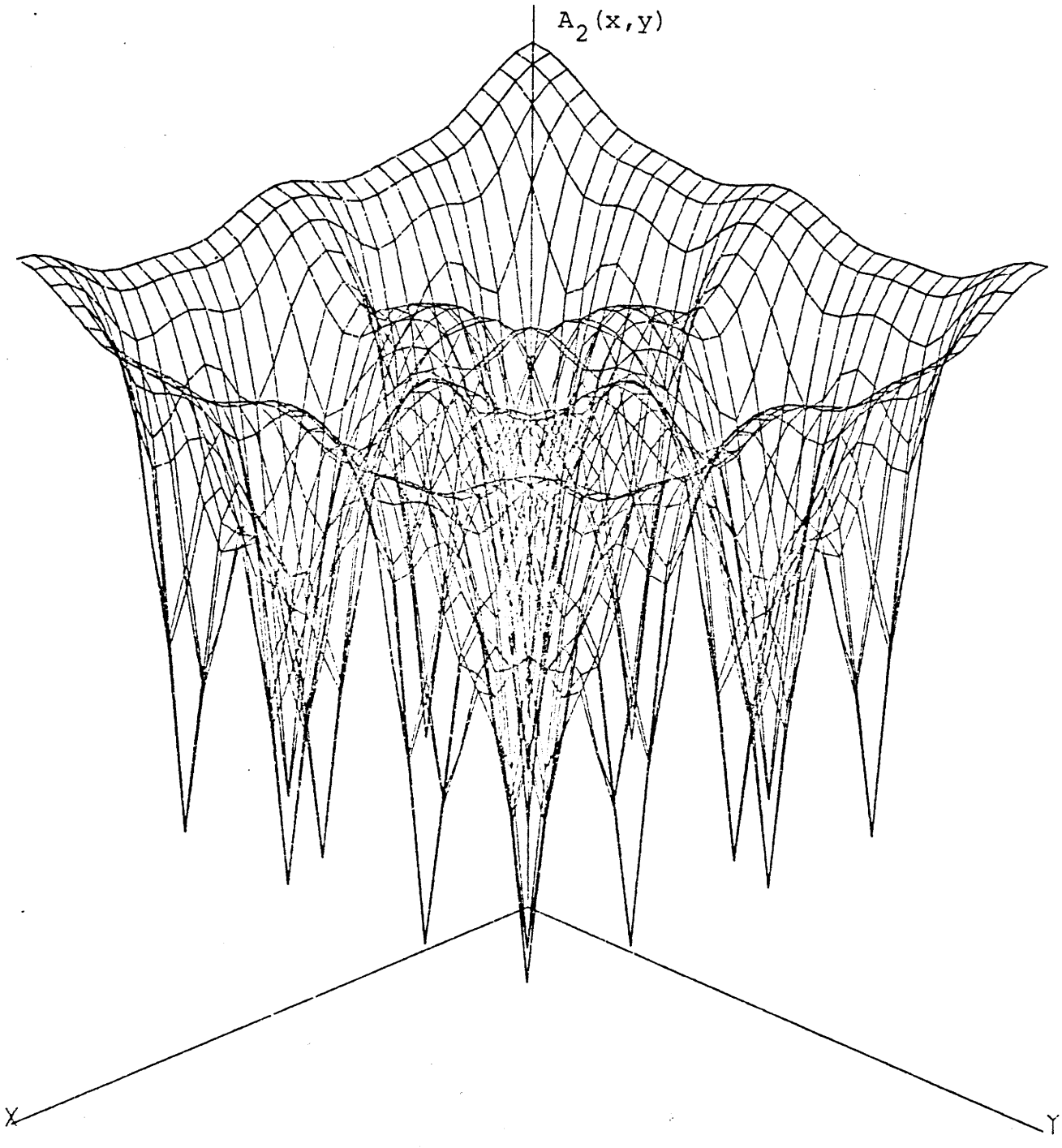

Figure A13.4: Thermal Assembly Flux for a Rodded Fuel 1 Assembly

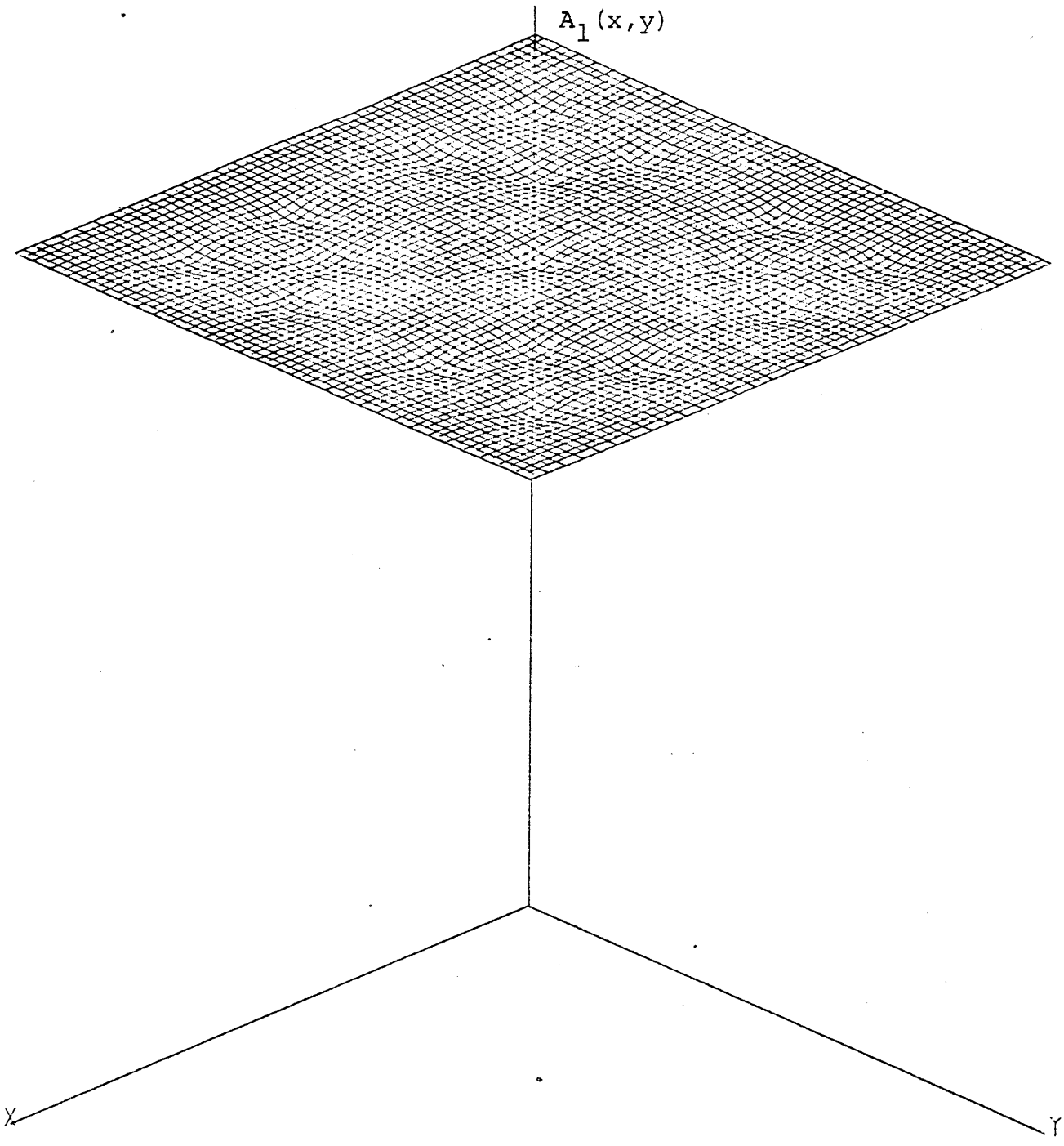

Figure A13.5: Fast Assembly Flux for an Unrodded Fuel 2 Assembly

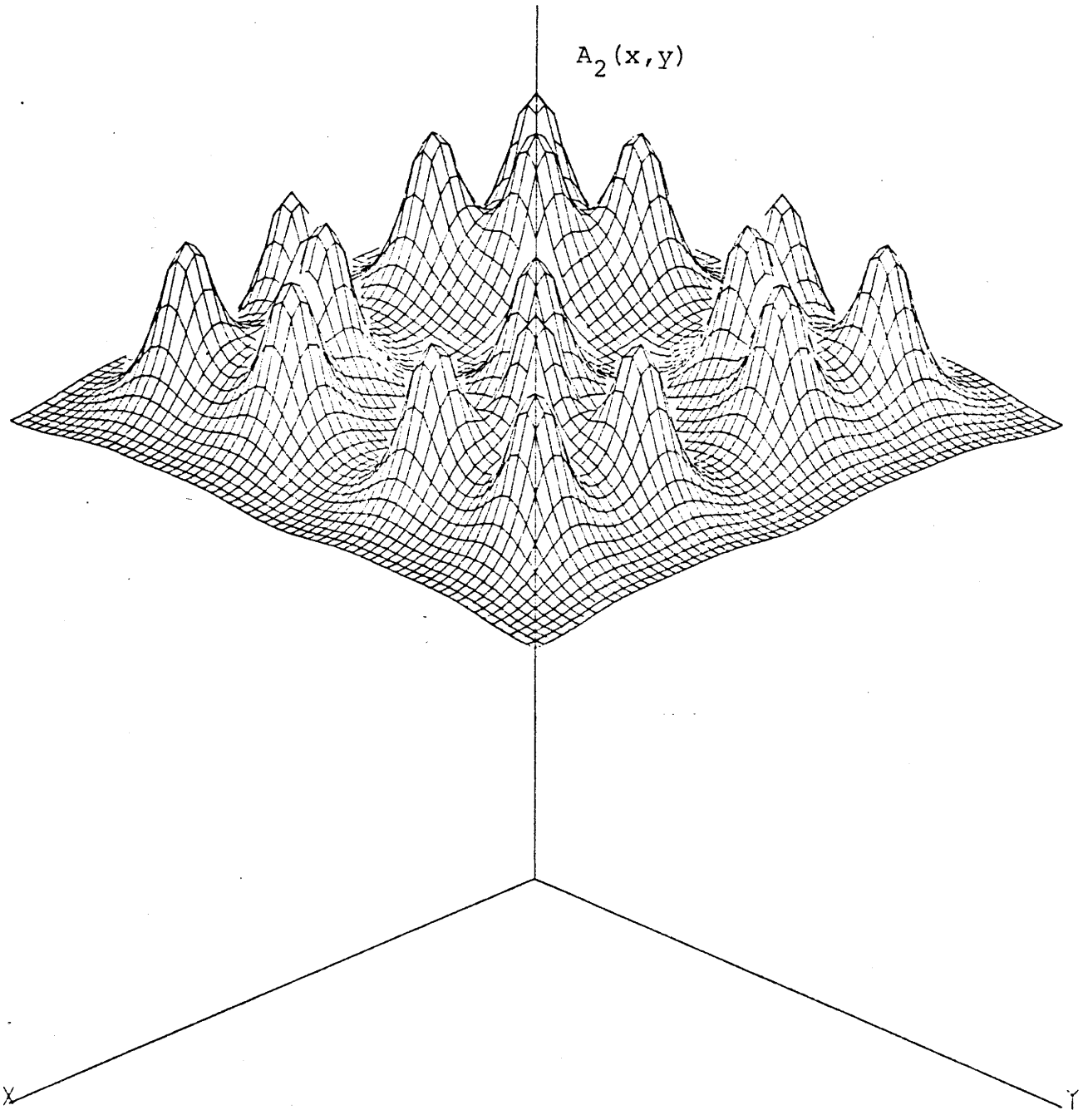

Figure A13.6: Thermal Assembly Flux for an Unrodded Fuel 2 Assembly

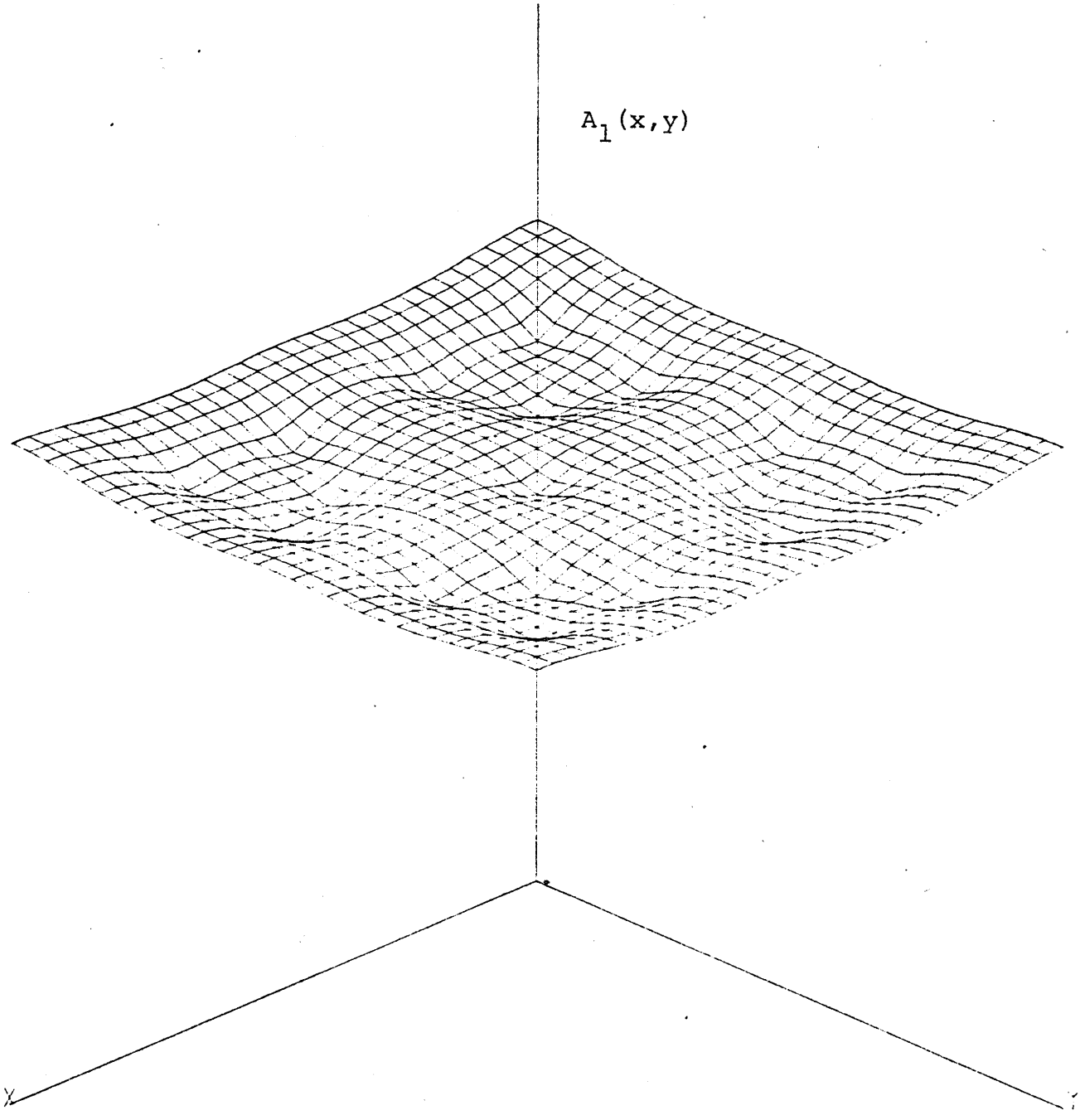

Figure A13.7: Fast Assembly Flux for a Rodded Fuel 2 Assembly

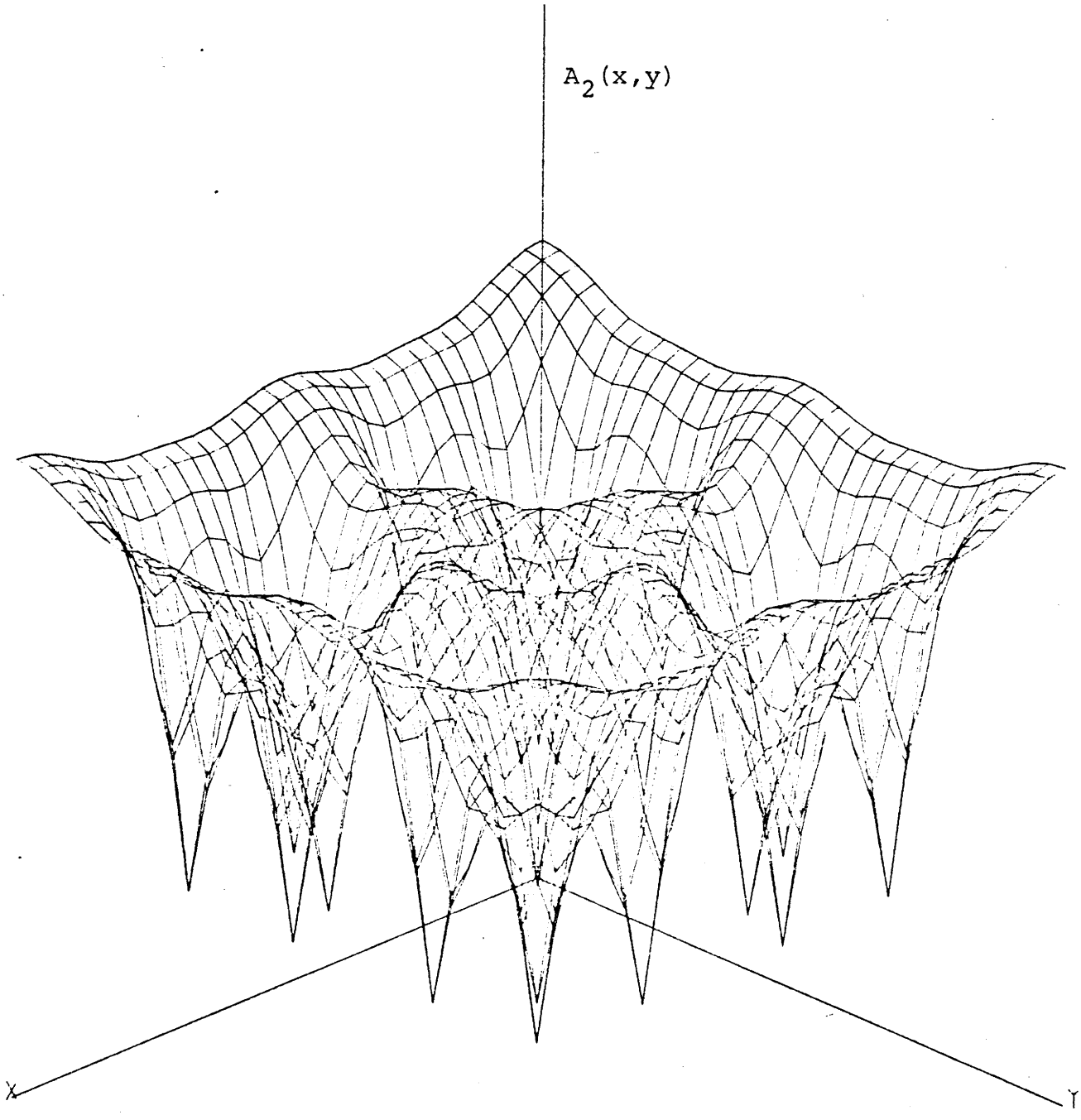

Figure A13.8: Thermal Assembly Flux for a Rodded Fuel 2 Assembly

Appendix 14

ASSEMBLY FLUX PLOTS FROM EXTENDED ASSEMBLY CALCULATIONS

A14.0 Introduction

Figure A14.1: Fast Extended-Assembly Flux for Node 4 of Benchmark Problem 6

Figure A14.2: Thermal Extended-Assembly Flux for Node 4 of Benchmark Problem 6

Figure A14.3: Fast Extended-Assembly Flux for Node 7 of Benchmark Problem 6

Figure A14.4: Thermal Extended-Assembly Flux for Node 7 of Benchmark Problem 6

Figure A14.5: Fast Extended-Assembly Flux for Node 8 of Benchmark Problem 6.

Figure A14.6: Thermal Extended-Assembly Flux for Node 8 of Benchmark Problem 6

Figure A14.7: Fast Extended-Assembly Flux for Node 10 of Benchmark Problem 6

Figure A14.8: Thermal Extended-Assembly Flux for Node 10 of Benchmark Problem 6

14.0 Introduction

This appendix contains assembly flux plots from extended assembly calculations for benchmark problem 6. The assembly flux plots for nodes 4, 7, 8, 10, 11 and 12 are from a 3-by-3 node extended assembly calculation. The plots for nodes 15 and 16 are from a 1-by-2 node extended assembly calculation. See Figure 2.4 of Chapter 2. For reference, the sketch below gives the node numbering for benchmark problem 6.

$\phi_g = 0$

node 1	node 2	node 3	node 4
node 5	node 6	node 7	node 8
node 9	node 10	node 11	node 12
node 13	node 14	node 15	node 16

$\bar{J}_g \cdot \hat{n} = 0$ (left)

$\phi_g = 0$ (right)

$\bar{J}_g \cdot \hat{n} = 0$ (bottom)

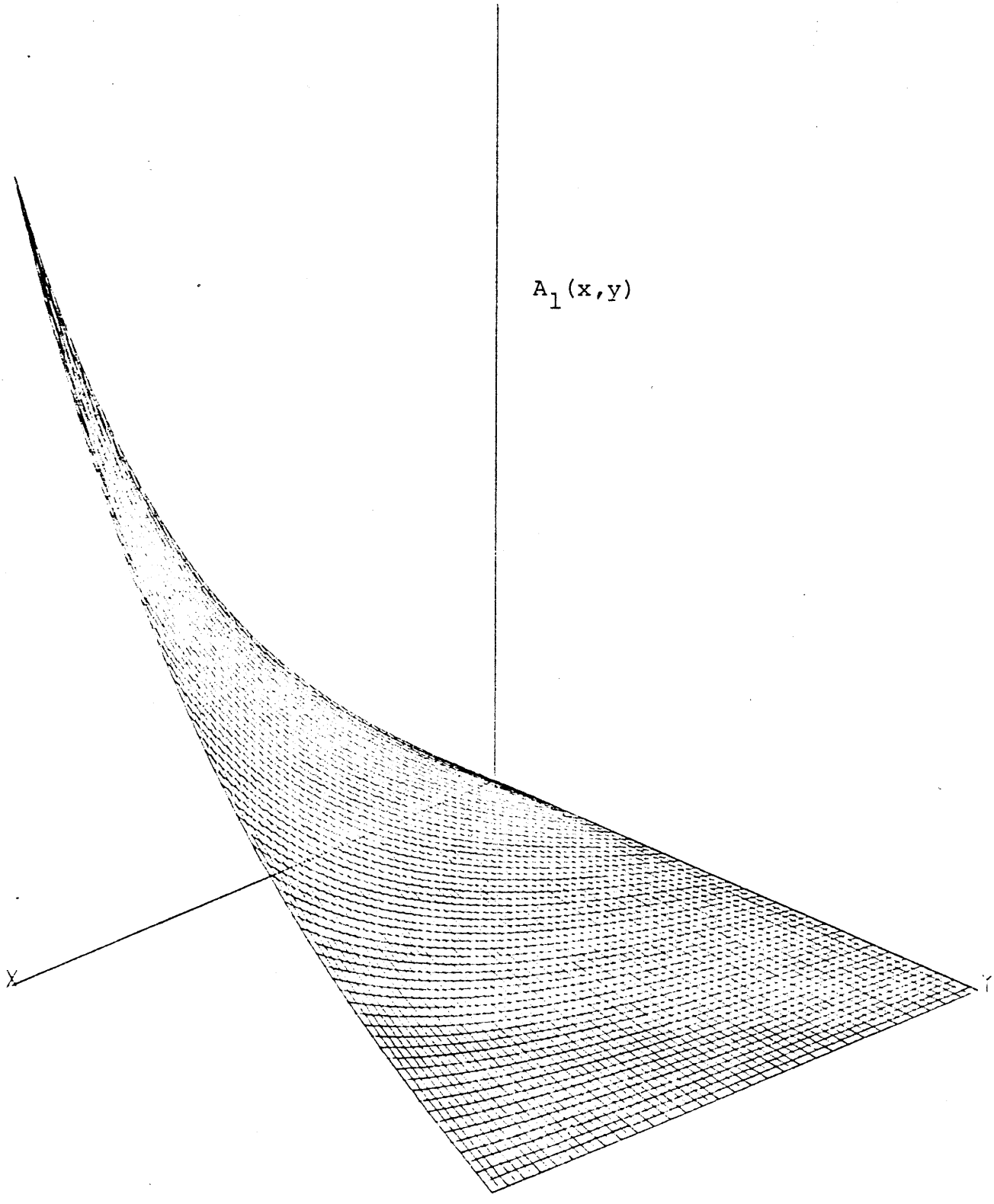

Figure A14.1: Fast Extended-Assembly Flux for Node 4 of Benchmark Problem 6

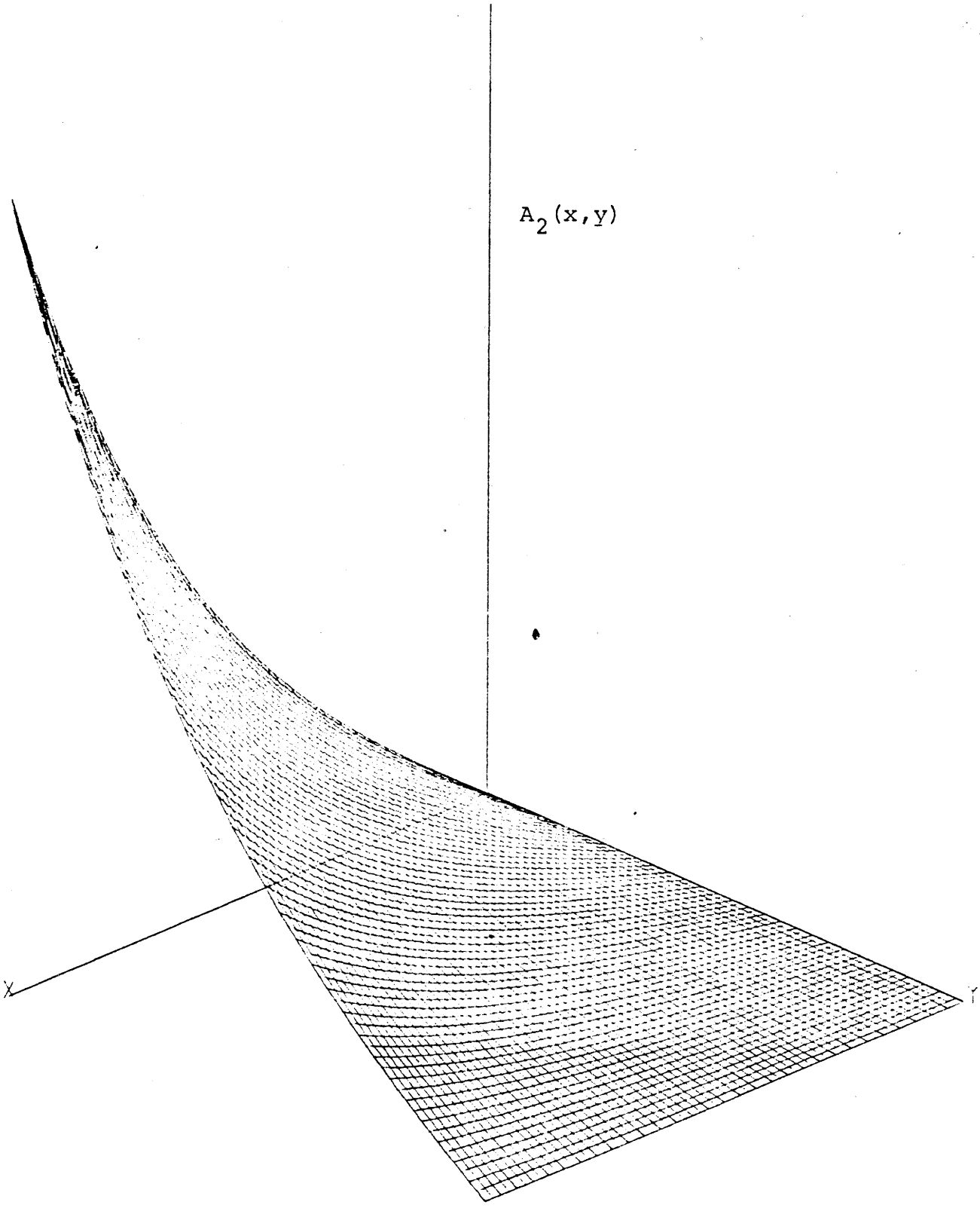

Figure A14.2: Thermal Extended-Assembly Flux for Node 4 of Benchmark Problem 6

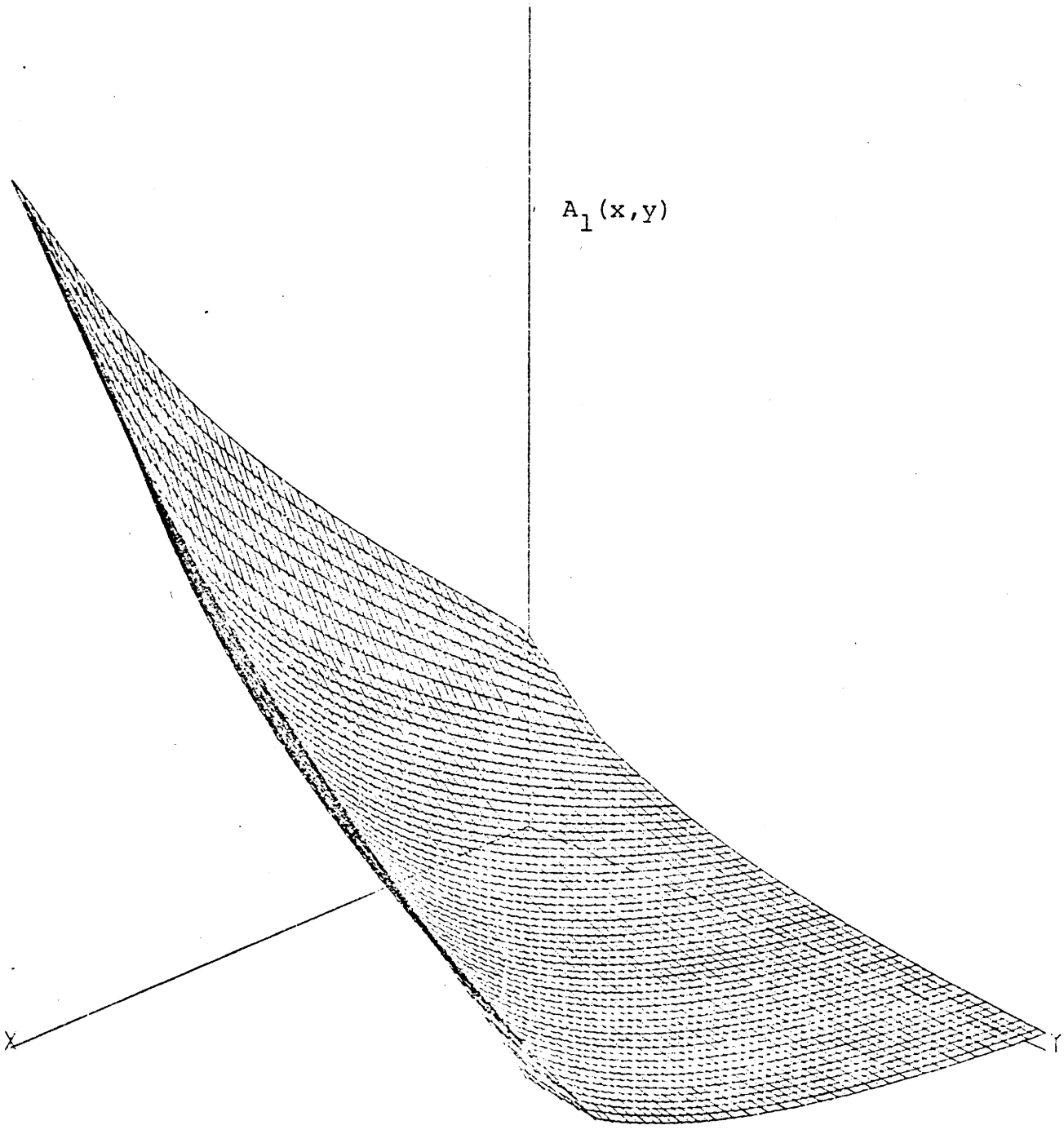

Figure A14.3: Fast Extended-Assembly Flux for Node 7 of Benchmark Problem 6

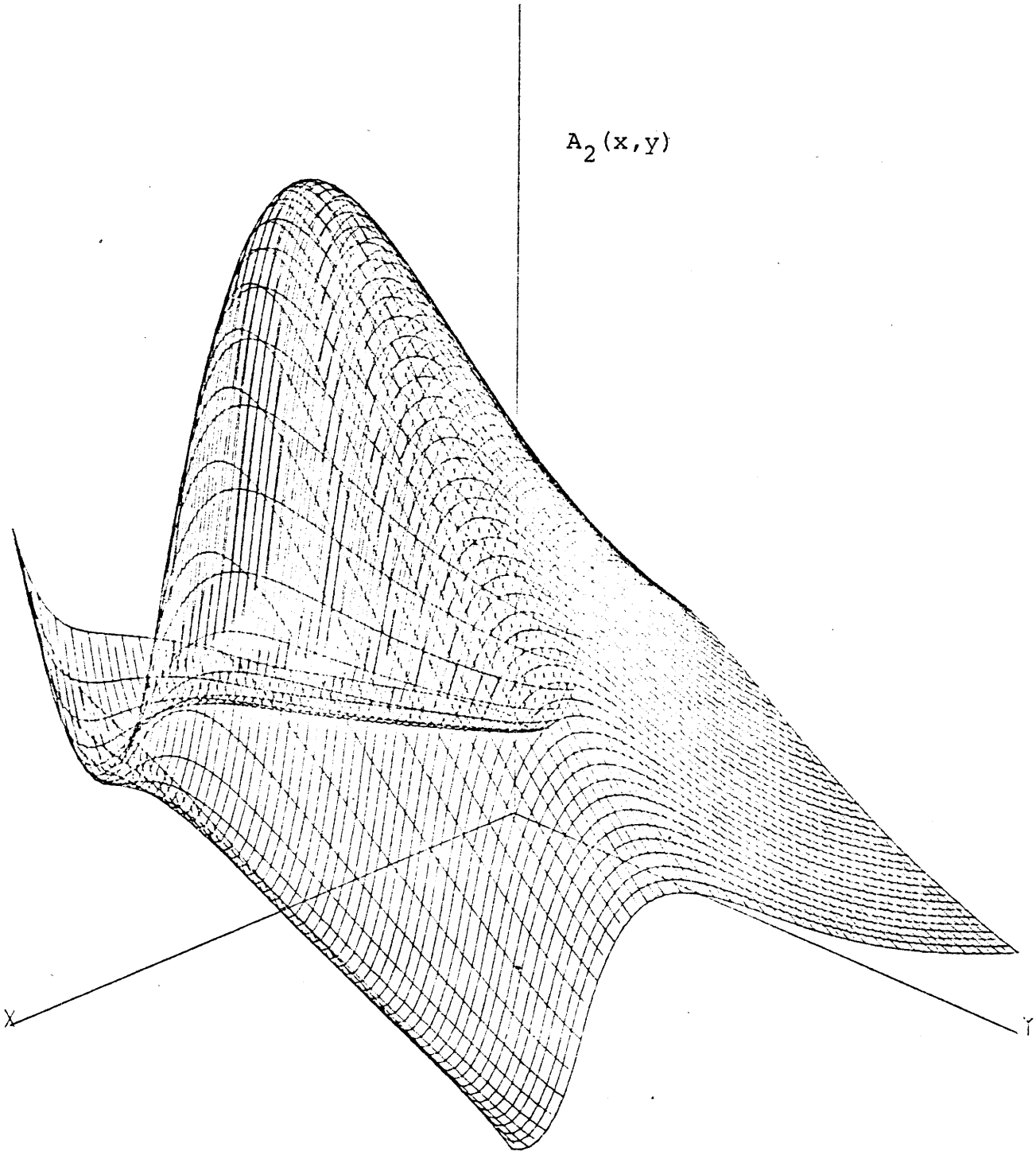

Figure A14.4: Thermal Extended-Assembly Flux for Node 7 of Benchmark Problem 6

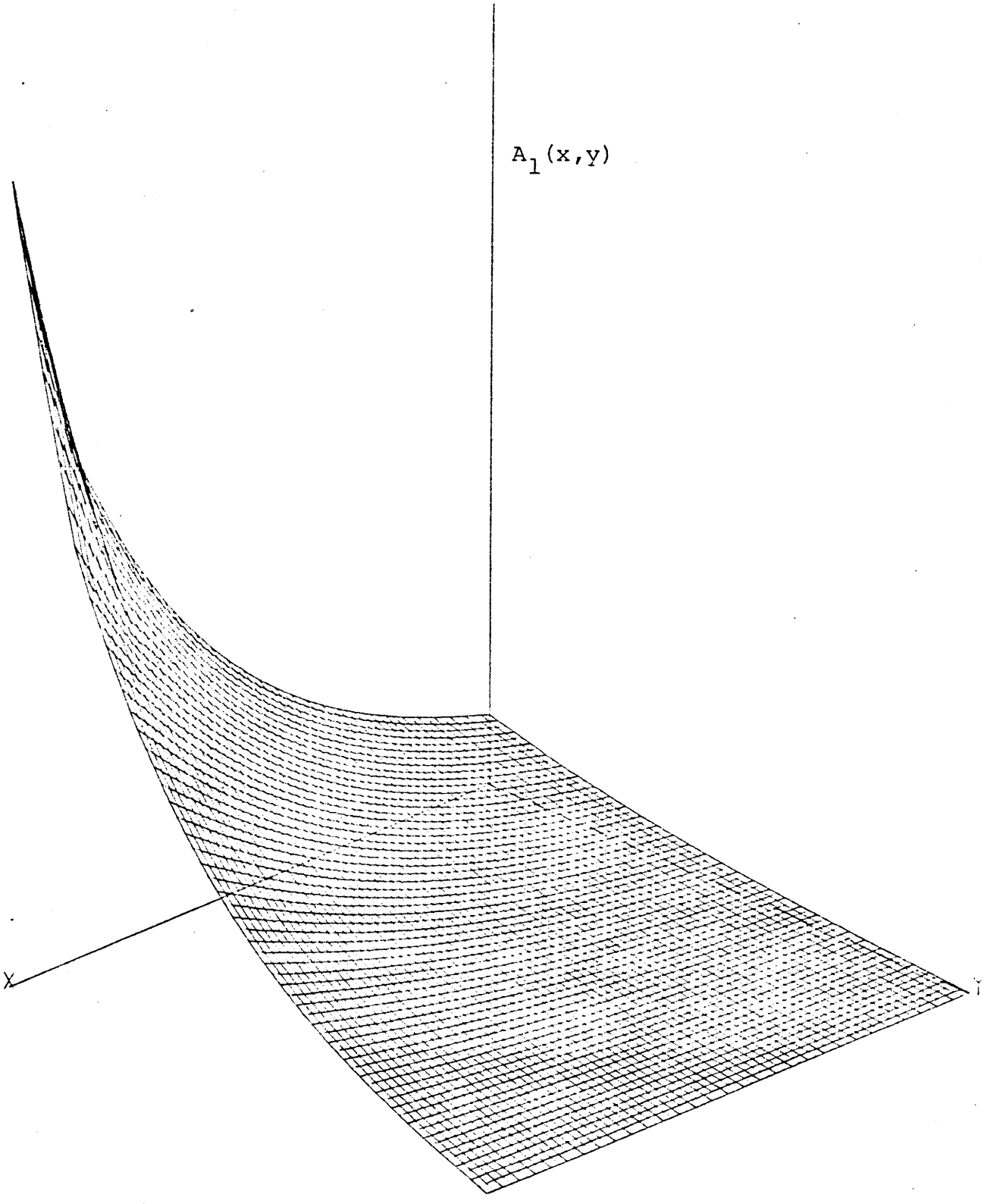

Figure A14.5: Fast Extended-Assembly Flux for Node 8 of Benchmark Problem 6

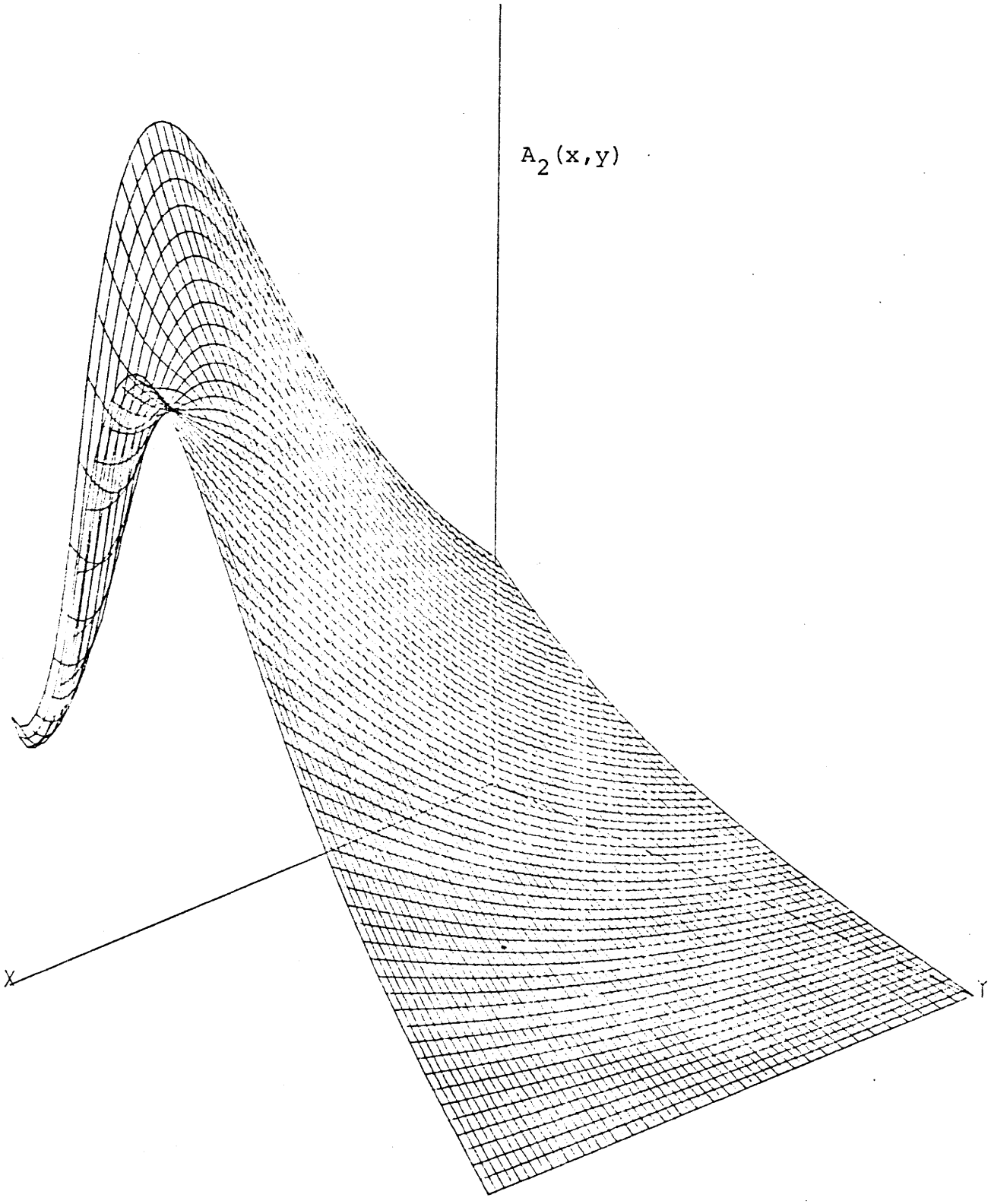

Figure A14.6: Thermal Extended-Assembly Flux for Node 8 of Benchmark Problem 6

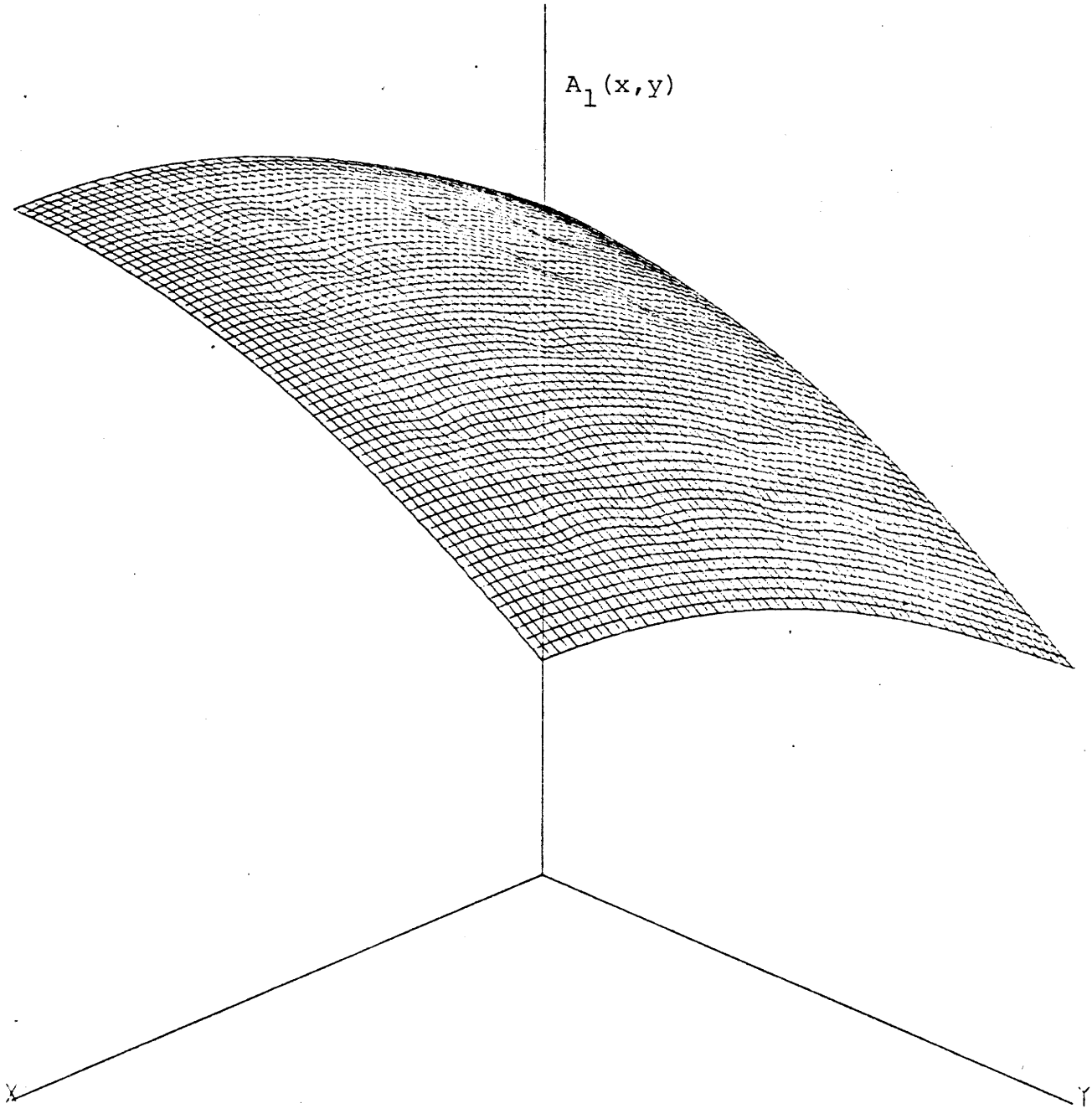

Figure A14.7: Fast Extended-Assembly Flux for Node 10 of Benchmark Problem 6

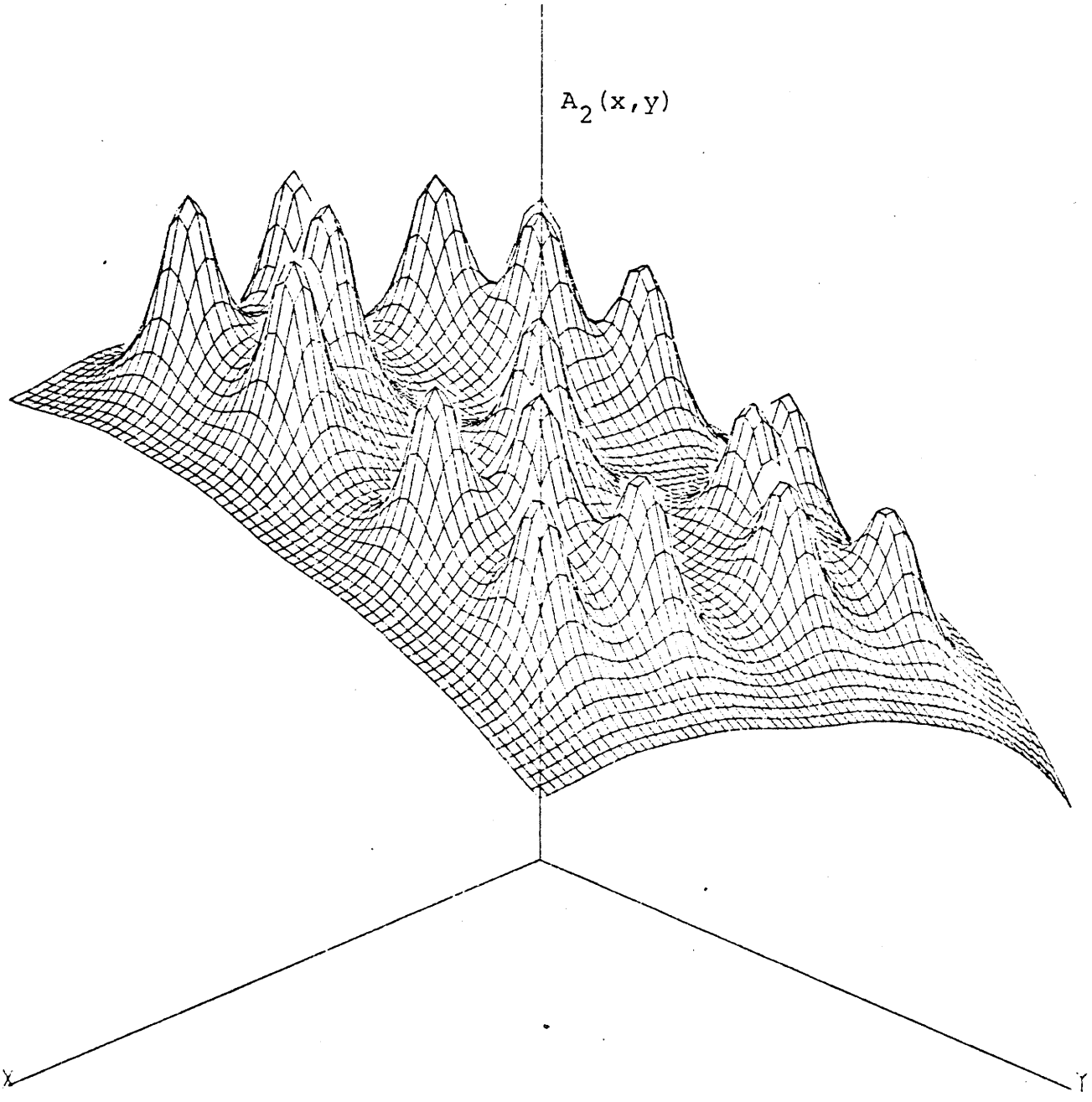

Figure A14.8: Thermal Extended-Assembly Flux for Node 10 of Benchmark Problem 6

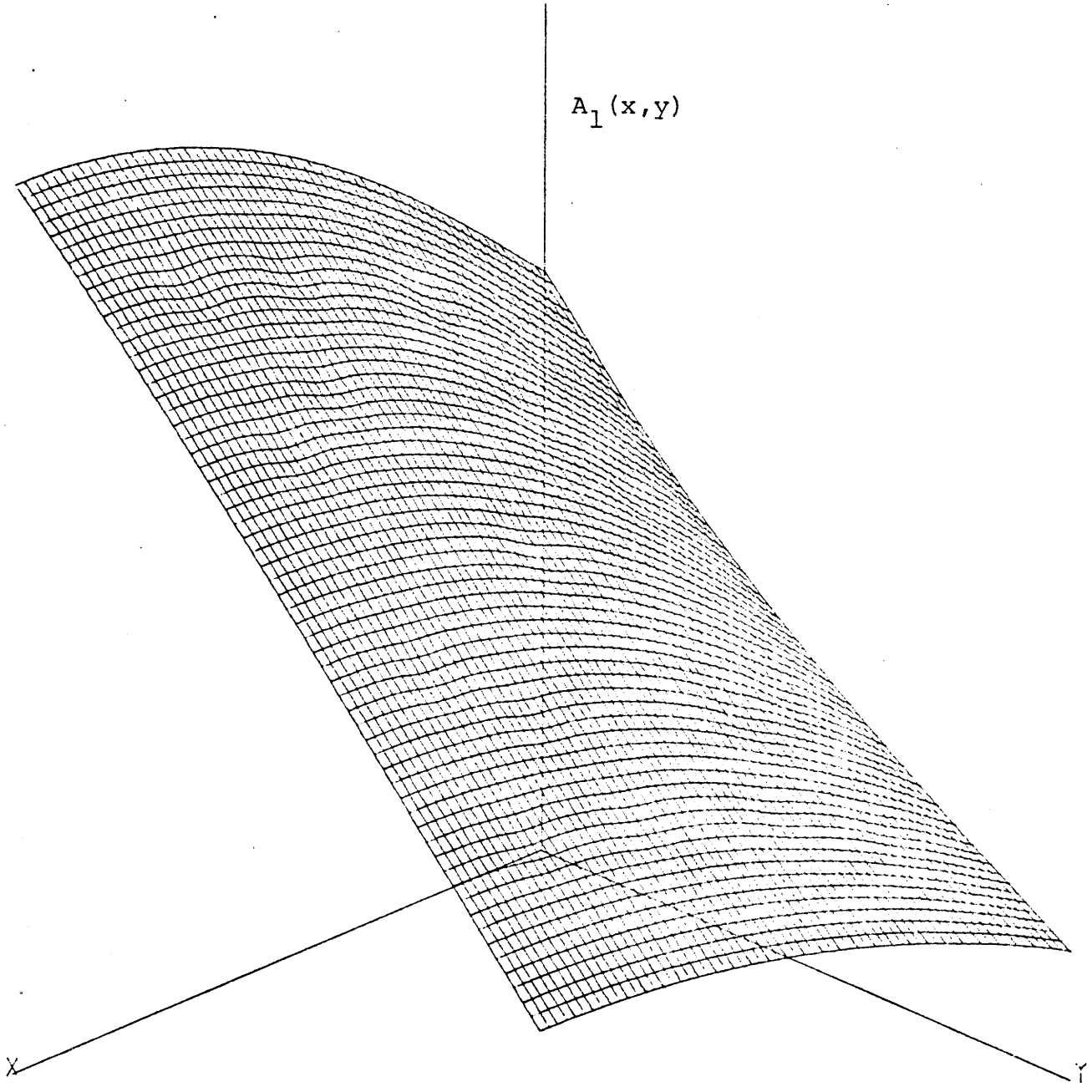

Figure A14.9: Fast Extended-Assembly Flux for Node 11 of Benchmark Problem 6

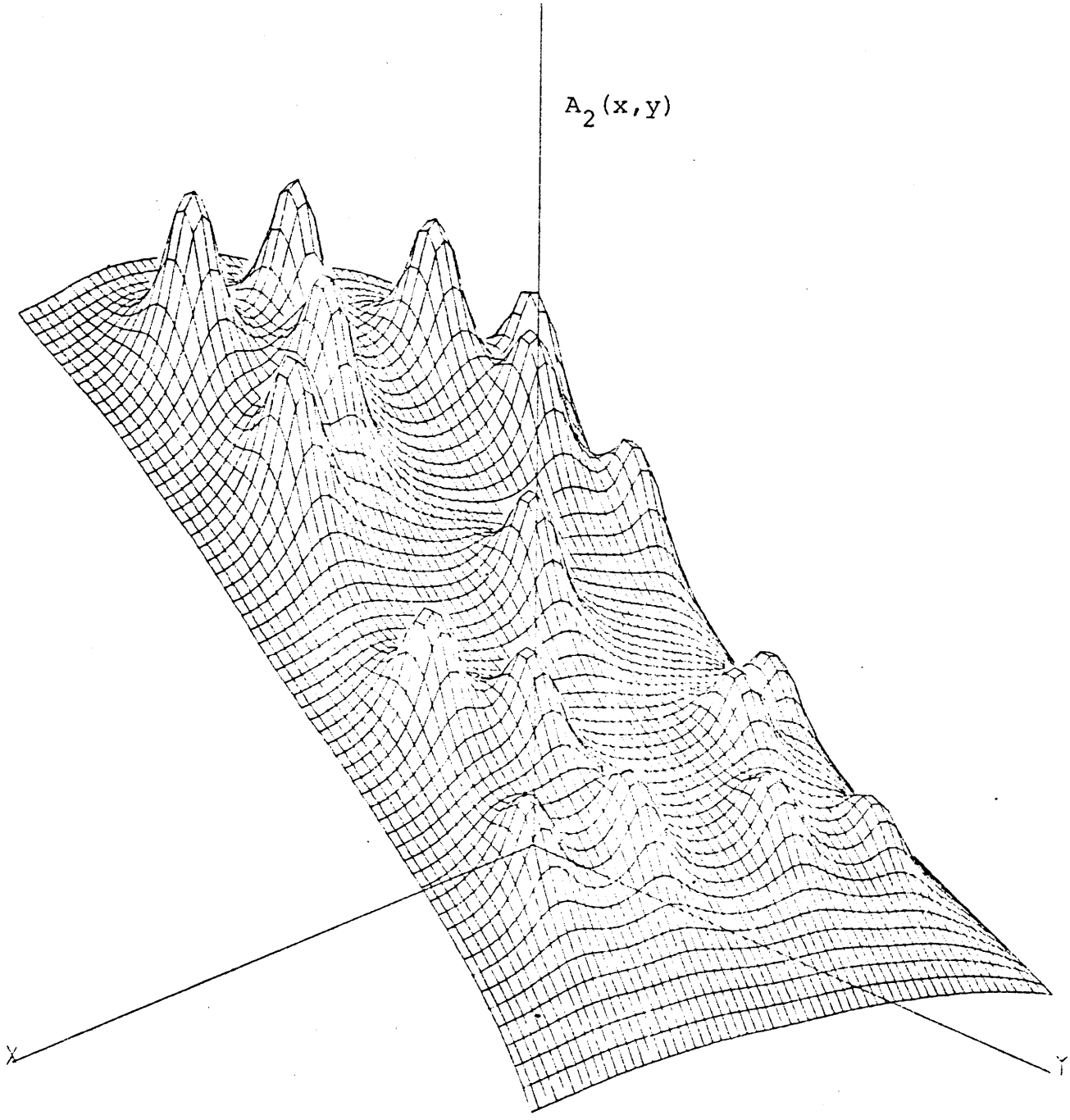

Figure A14.10: Thermal Extended-Assembly Flux for Node 11 of Benchmark Problem 6

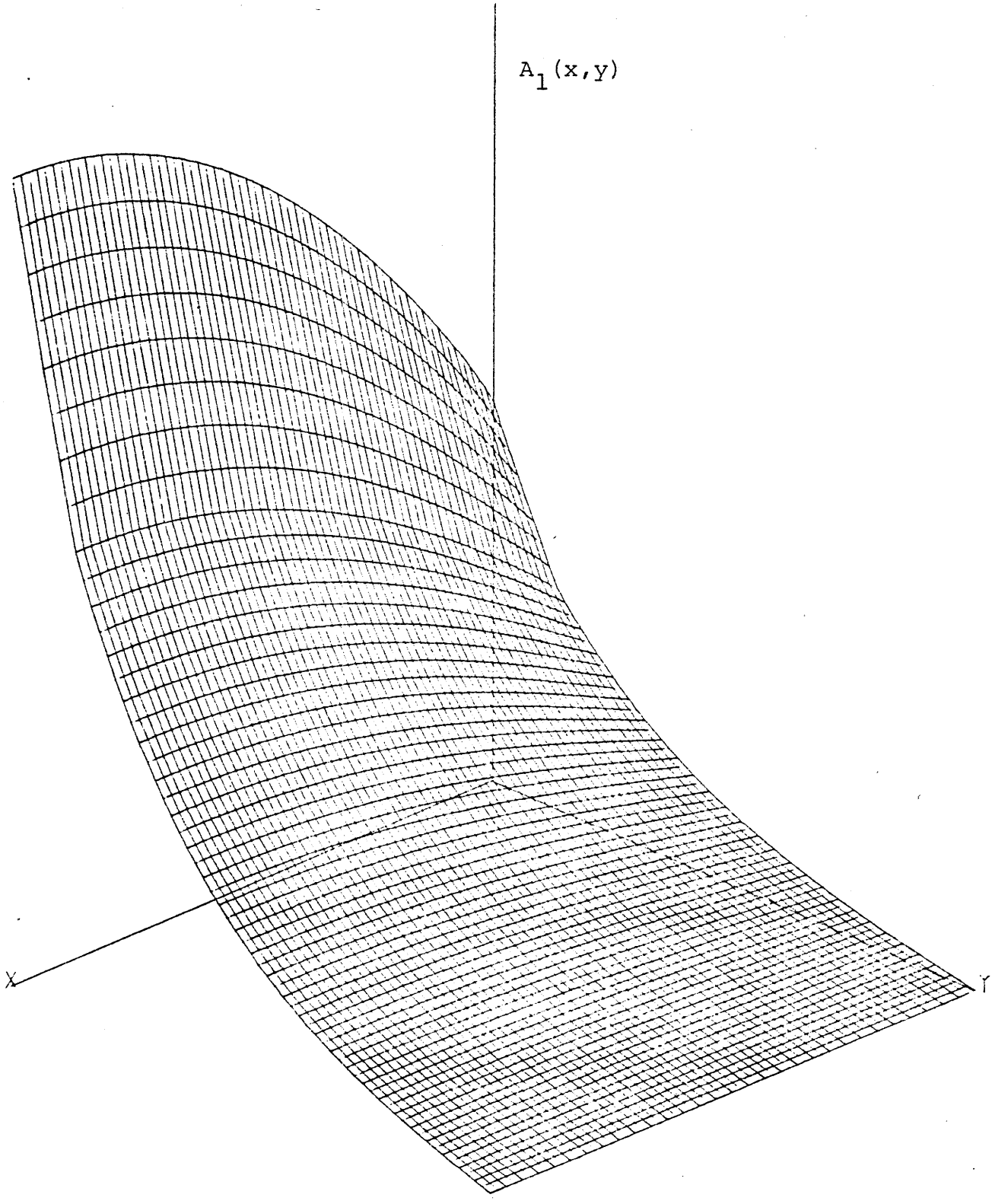

Figure A14.11: Fast Extended-Assembly Flux for Node 12 of Benchmark Problem 6

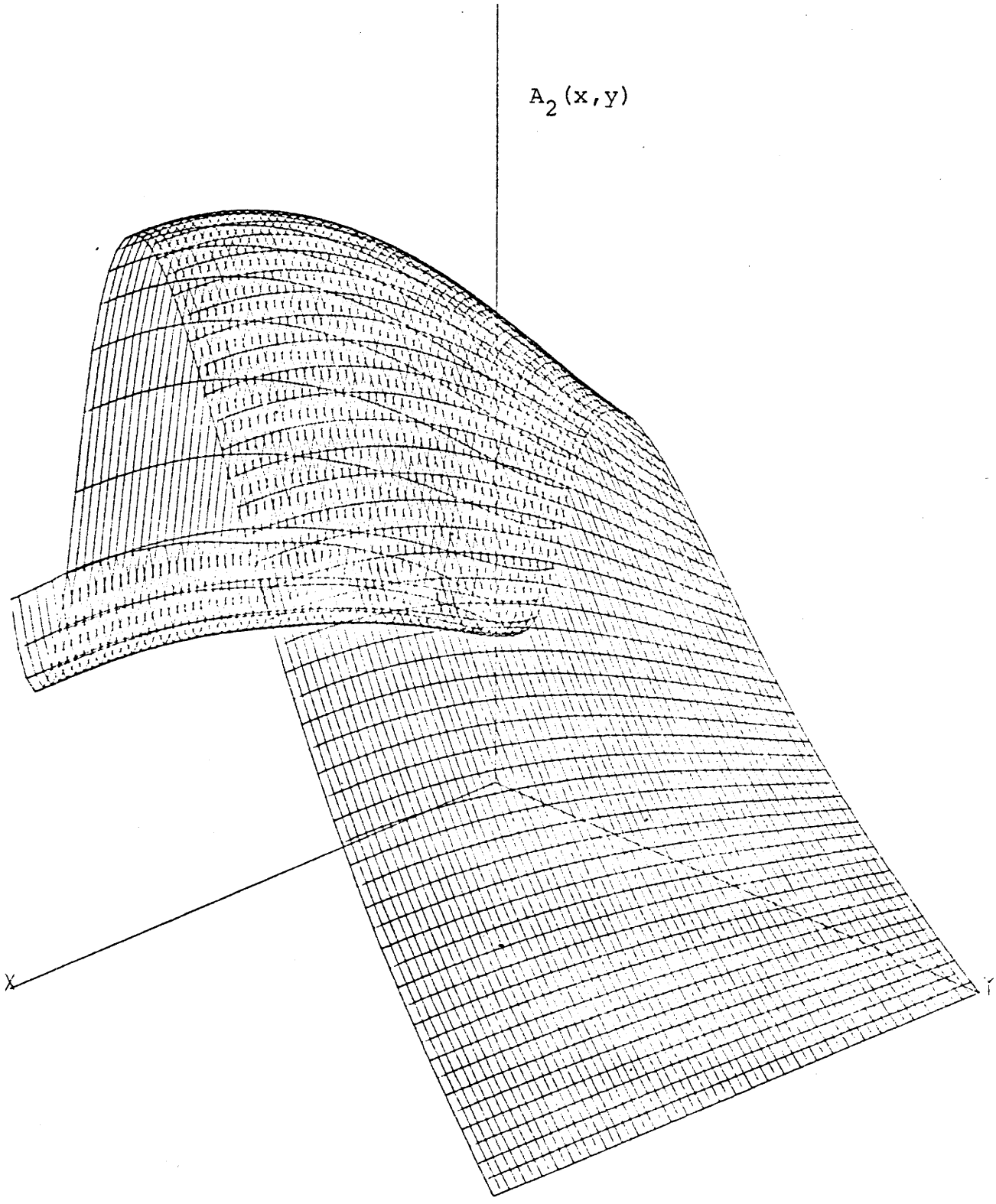

Figure A14.12: Thermal Extended-Assembly Flux for Node 12 of Benchmark Problem 6

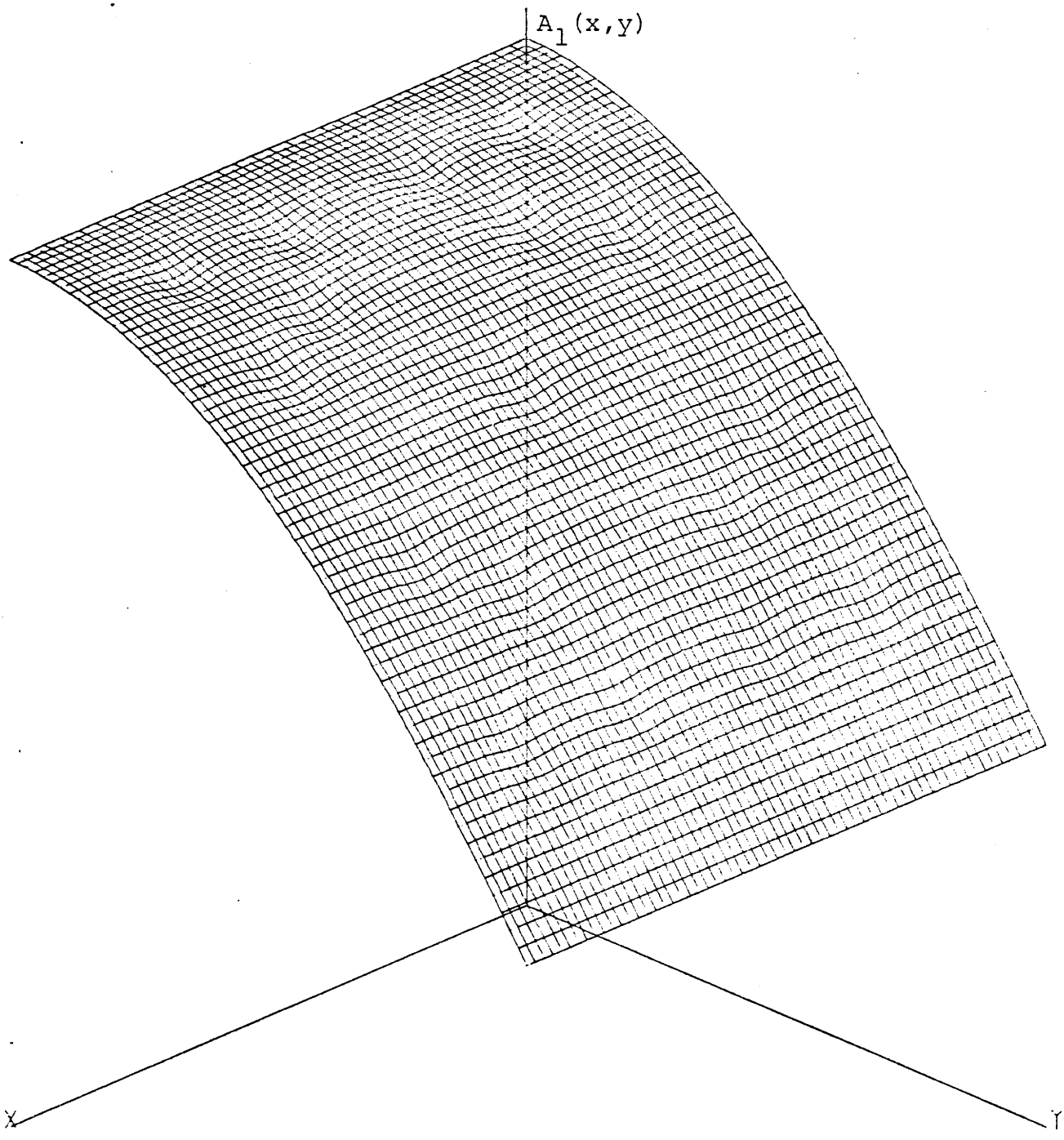

Figure A14.13: Fast Extended-Assembly Flux for Node 15 of Benchmark Problem 6

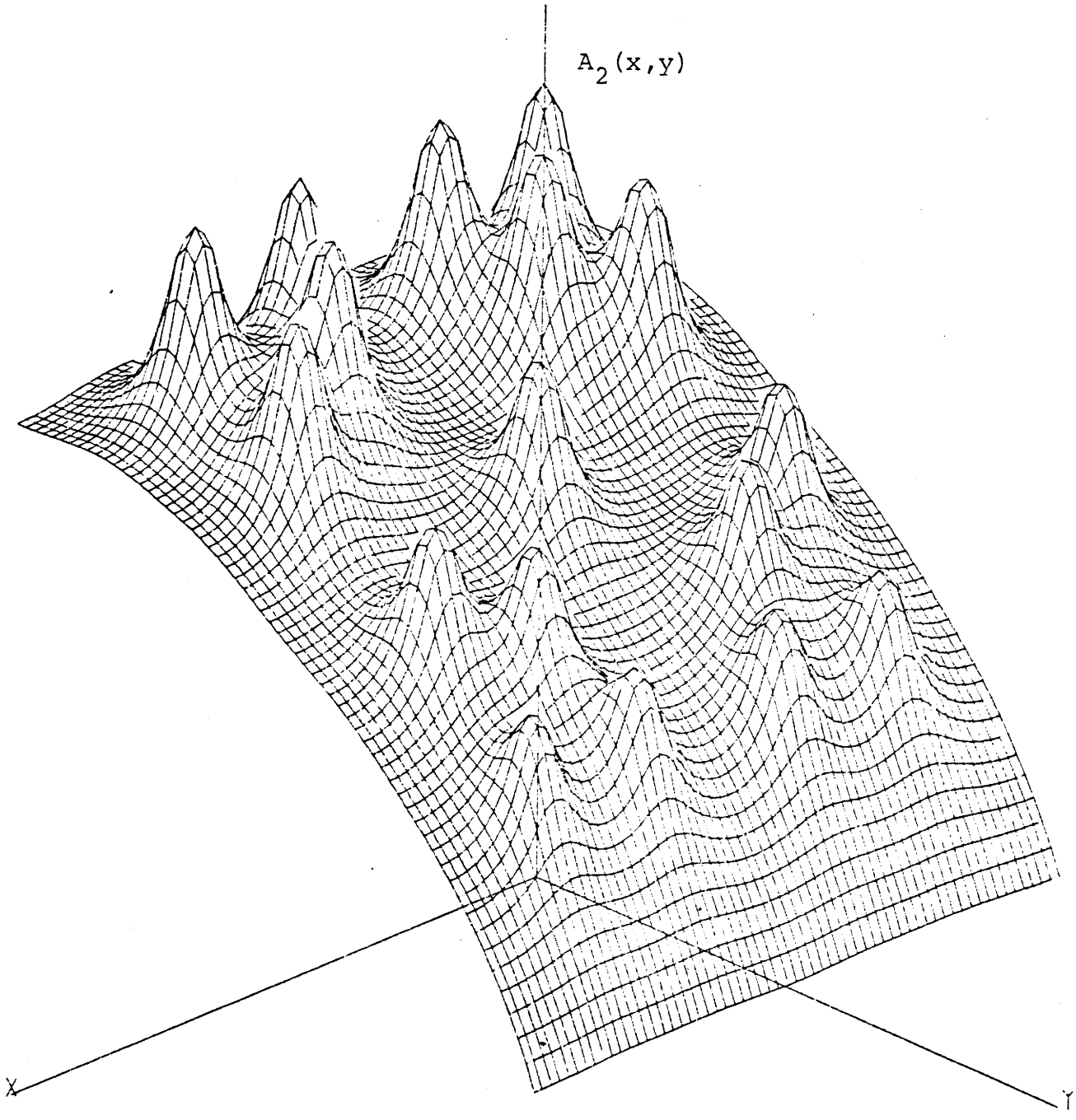

Figure A14.14: Thermal Extended-Assembly Flux for Node 15 of Benchmark Problem 6

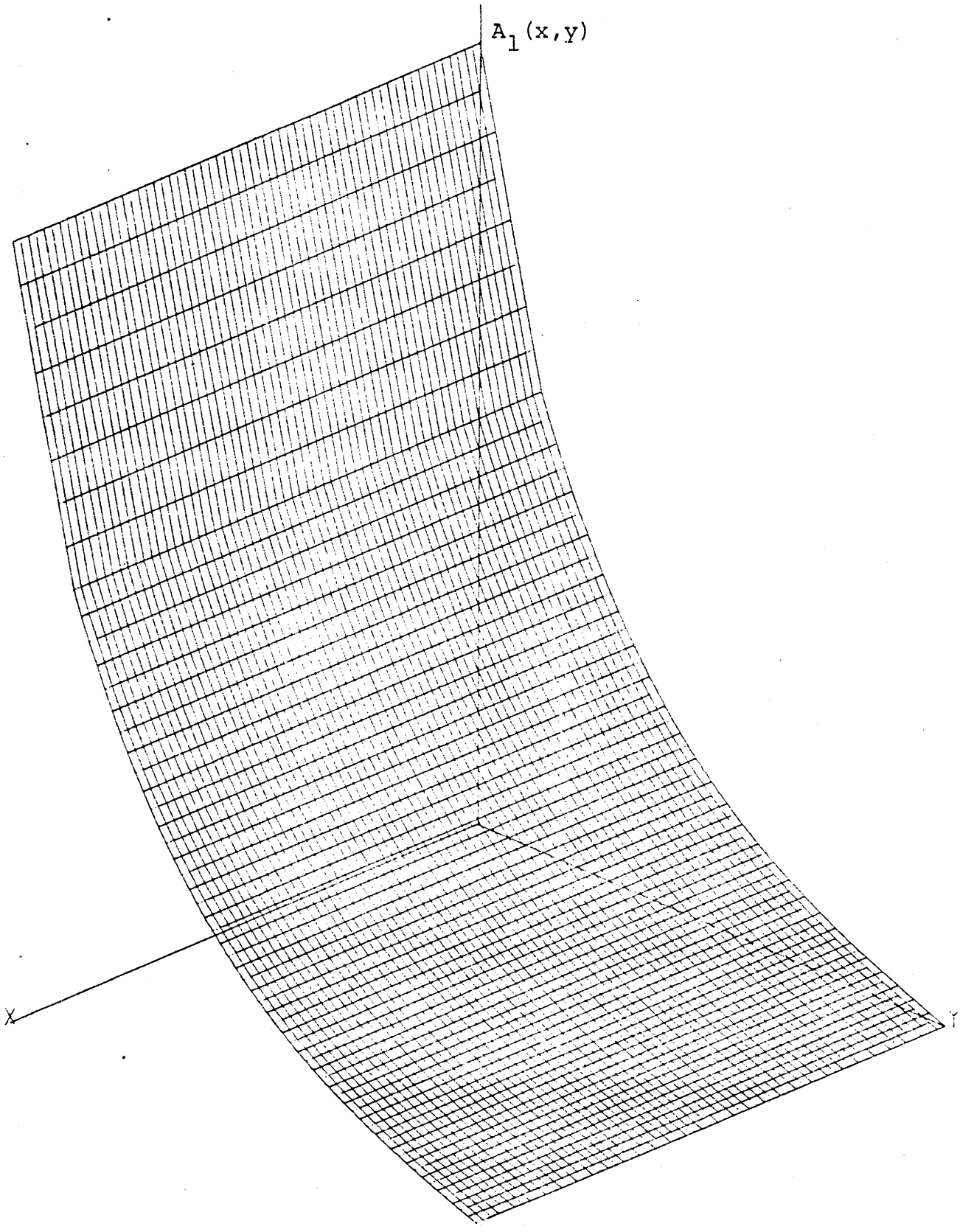

Figure A14.15: Fast Extended-Assembly Flux for Node 16 of Benchmark Problem 6

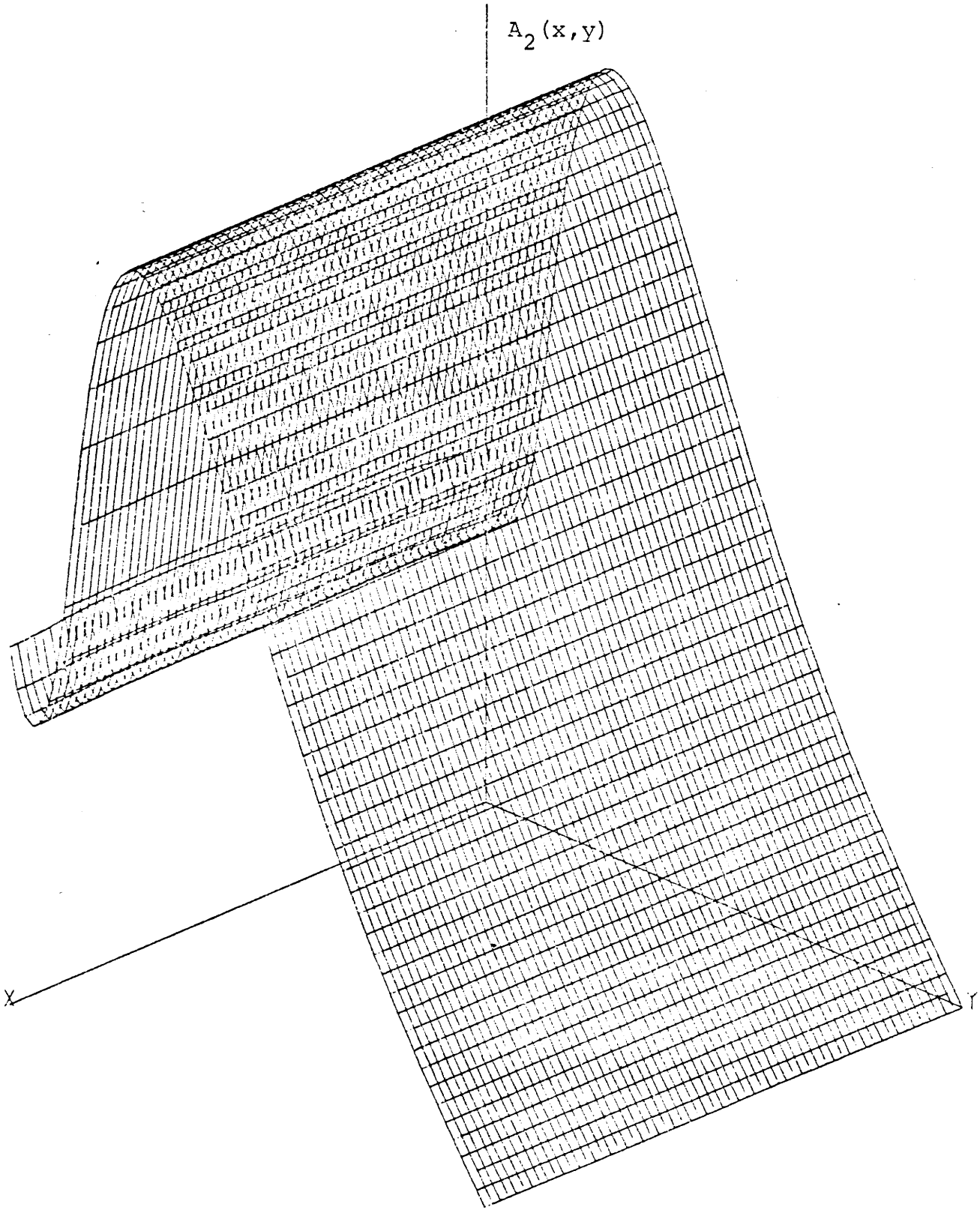

Figure A14.16: Thermal Extended-Assembly Flux for Node 16 of Benchmark Problem 6

Appendix 15

REFERENCE FORM FUNCTIONS BASED ON ASSEMBLY CALCULATIONS WITH ZERO-CURRENT BOUNDARY CONDITIONS

A15.0 Introduction

The reference form function, $F_g(x,y)$, is equal to the ratio of the global heterogeneous flux, $\phi_g(x,y)$, to the assembly heterogeneous flux, $A_g(x,y)$. This appendix presents plots of the reference form function for cases where the calculation of $A_g(x,y)$ was performed for a single PWR assembly with $\bar{J}_g \cdot \hat{n} = 0$ boundary conditions.

Plots are displayed for the center node 5 of benchmark problems 5, 7 and 8. For benchmark problem 6 (which has the explicit steel baffle) plots are shown for nodes 6, 11, 13 and 14. A brief description of each benchmark problem is given at the beginning of each section.

A15.1 Benchmark Problem 5 Reference Form Functions

Benchmark problem 5 is an infinite checkerboard of unrodded fuel 1 assemblies and unrodded fuel 2 assemblies. The sketch below gives the node numbering and boundary conditions for this problem.

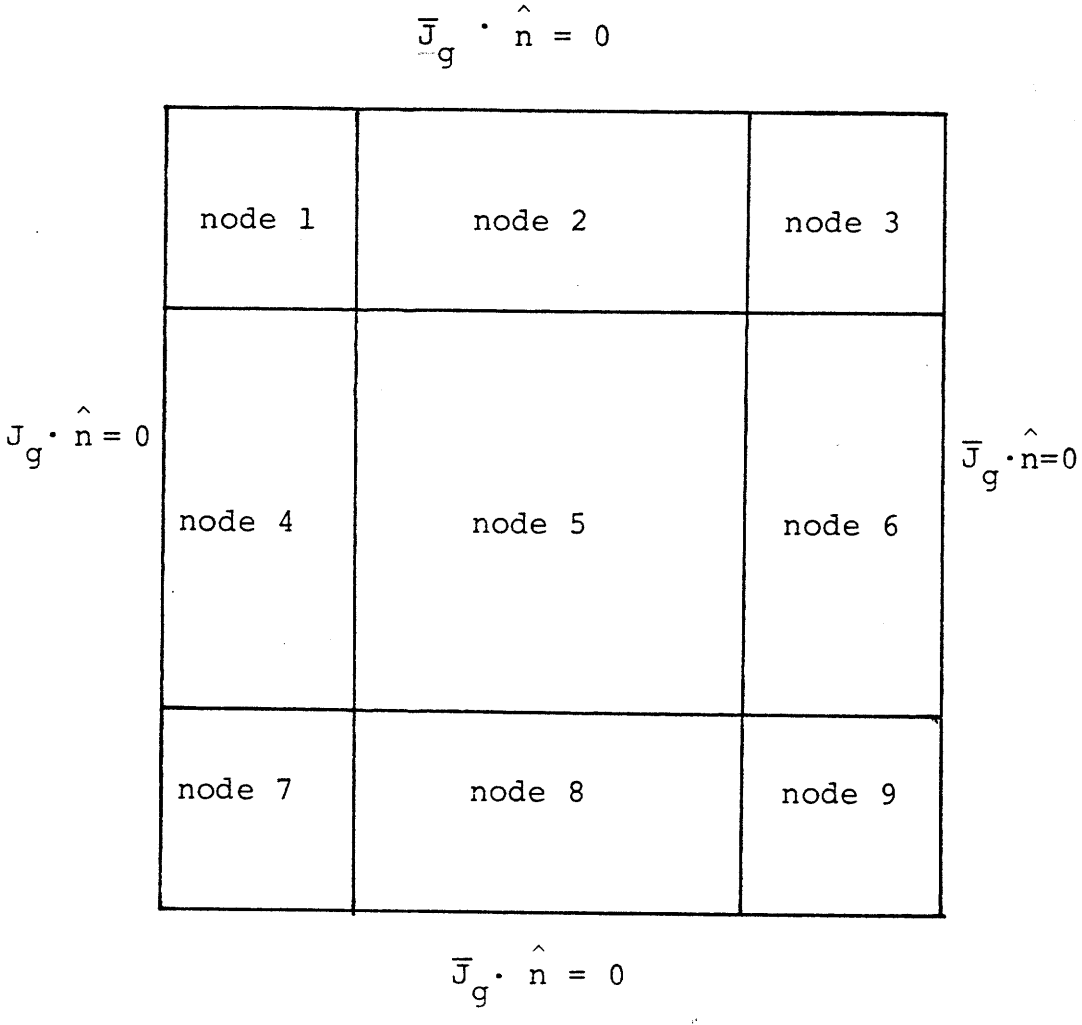

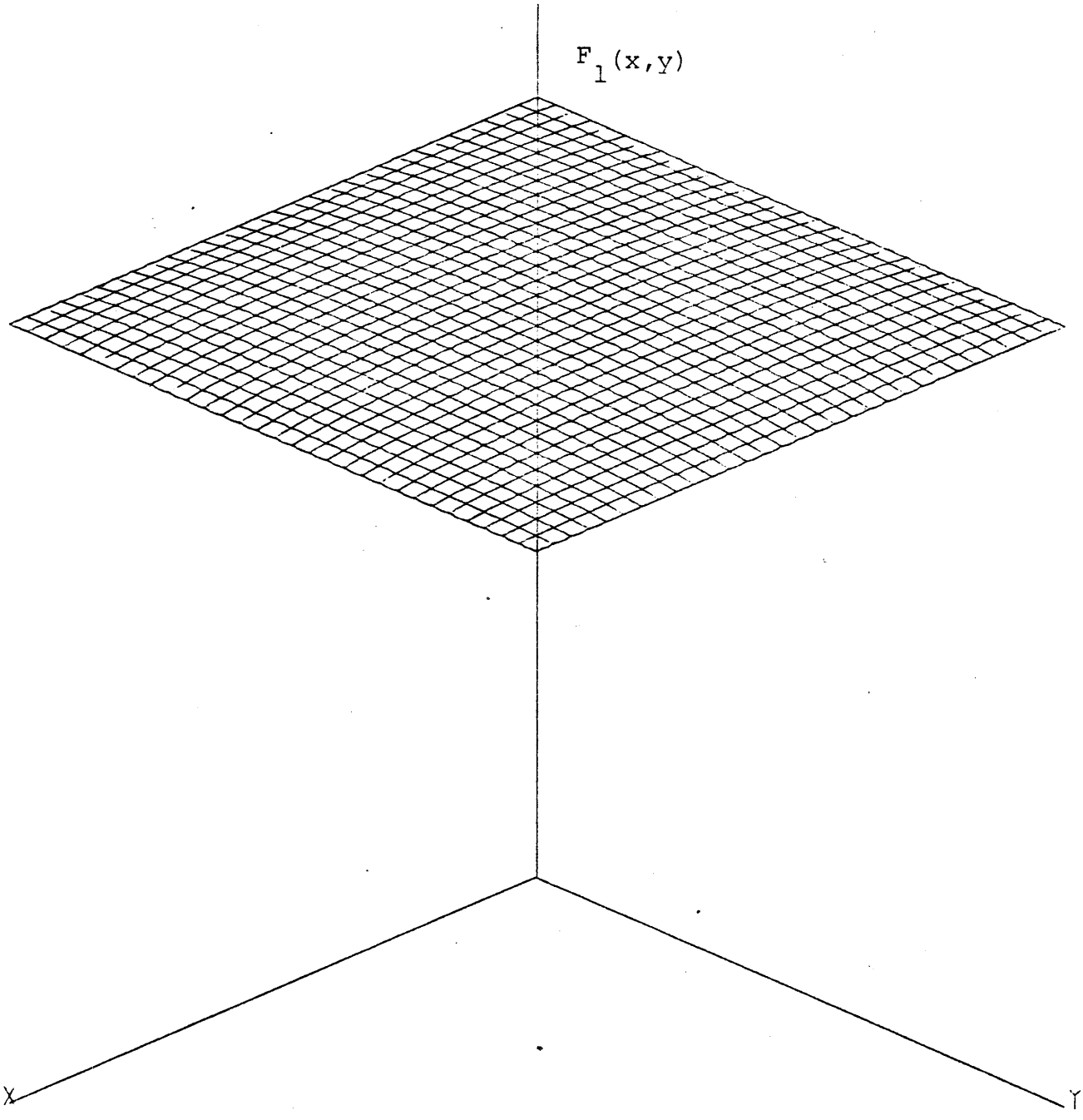

Figure A15.1: Reference Fast Form Function for Node 5 of Benchmark Problem 5

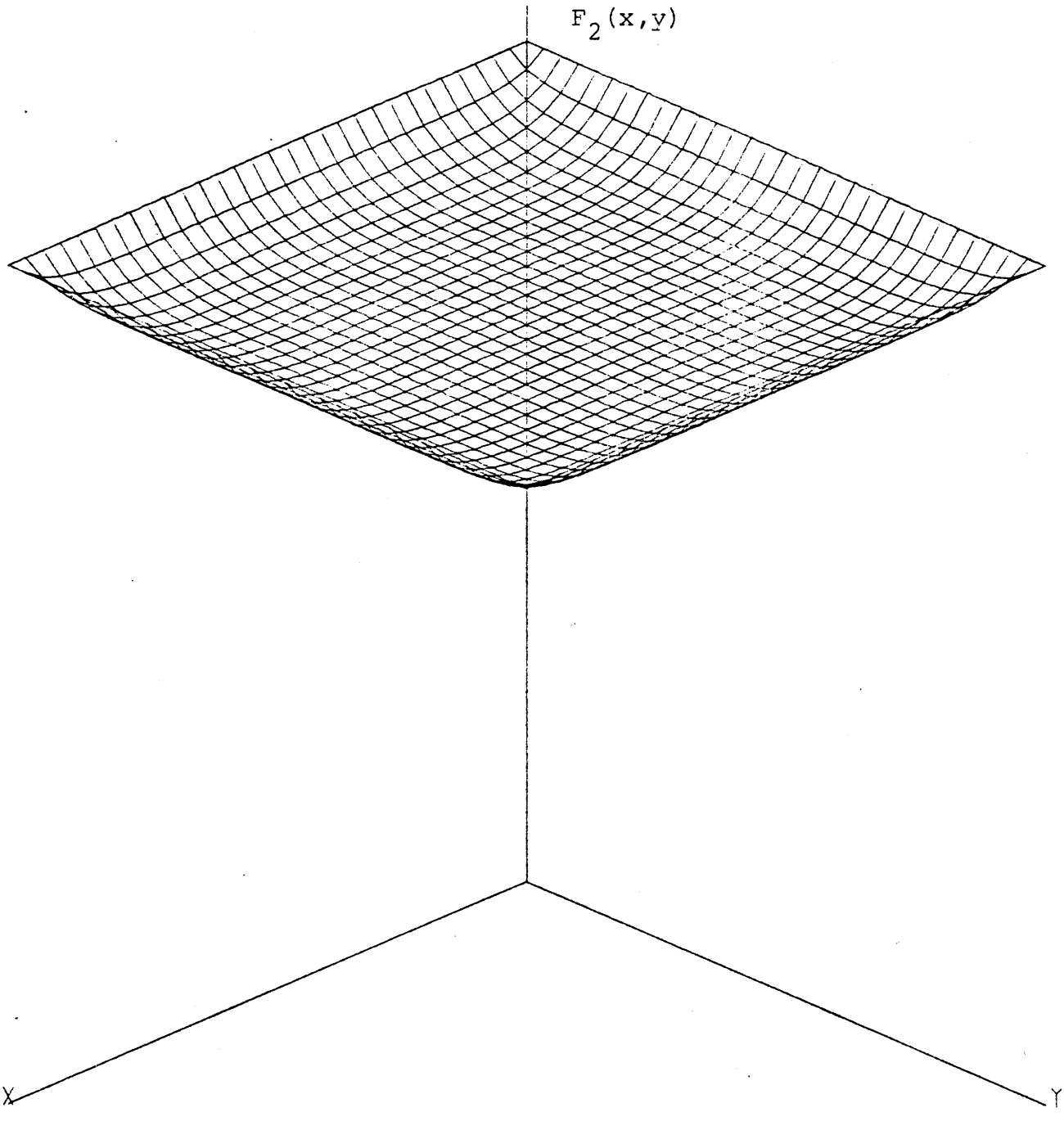

Figure A15.2: Reference Thermal Form Function for Node 5 of Benchmark Problem 5

A15.2 Benchmark Problem 6 Reference Form Functions

Benchmark problem 6 is a 4-by-4 node quarter core reactor with an explicitly represented baffle. All assemblies are unrodded. The sketch below gives the node numbering for this problem. Reference form functions are plotted for nodes 6, 11, 13 and 14.

$\phi_g = 0$

$\bar{J}_g \cdot \hat{n} = 0$

node 1	node 2	node 3	node 4
node 5	node 6	node 7	node 8
node 9	node 10	node 11	node 12
node 13	node 14	node 15	node 16

$\phi_g = 0$

$\bar{J}_g \cdot \hat{n} = 0$

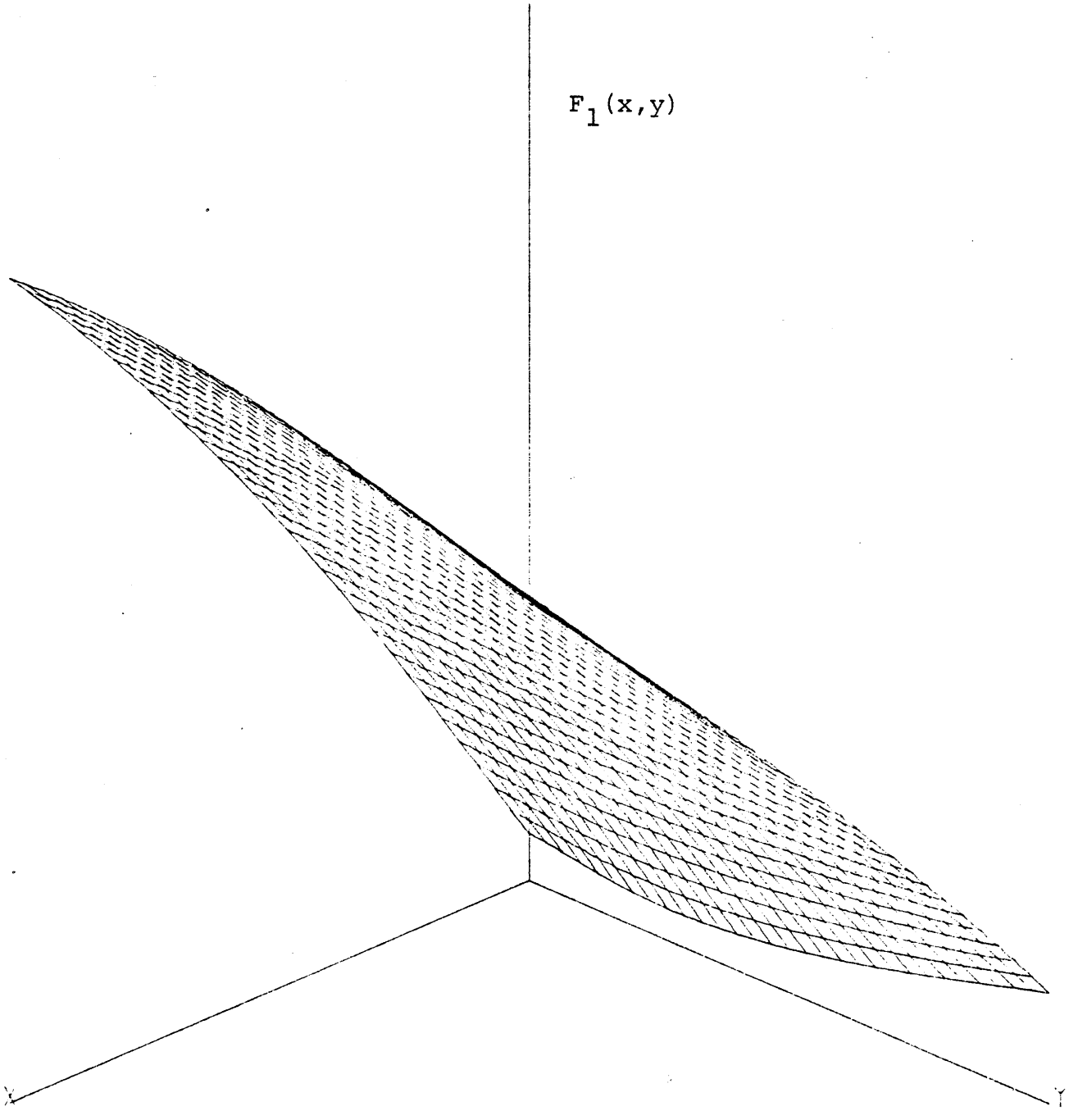

Figure A15.3: Reference Fast Form Function for Node 6 of Benchmark Problem 6

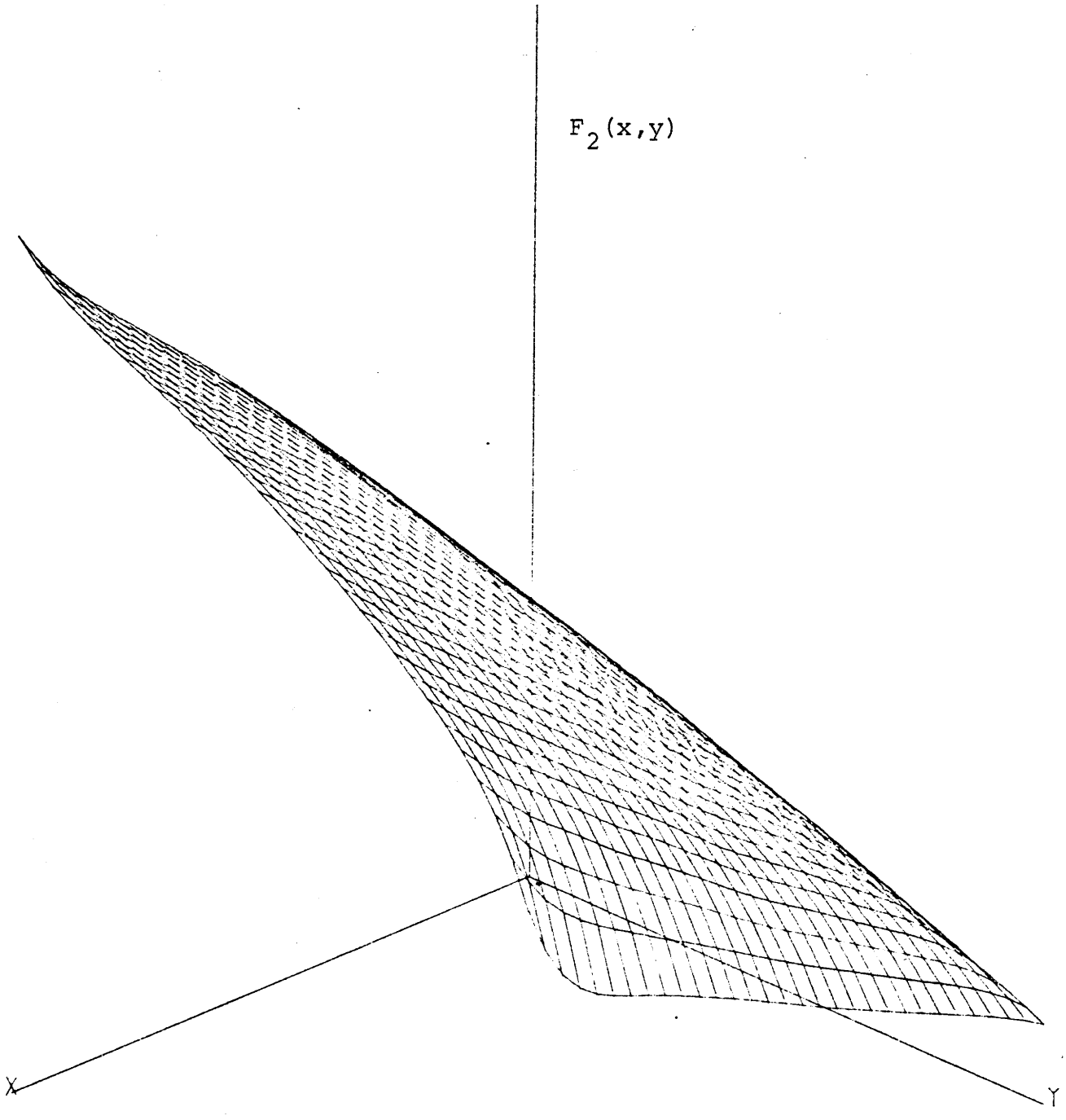

Figure A15.4: Reference Thermal Form Function for Node 6 of Benchmark Problem 6

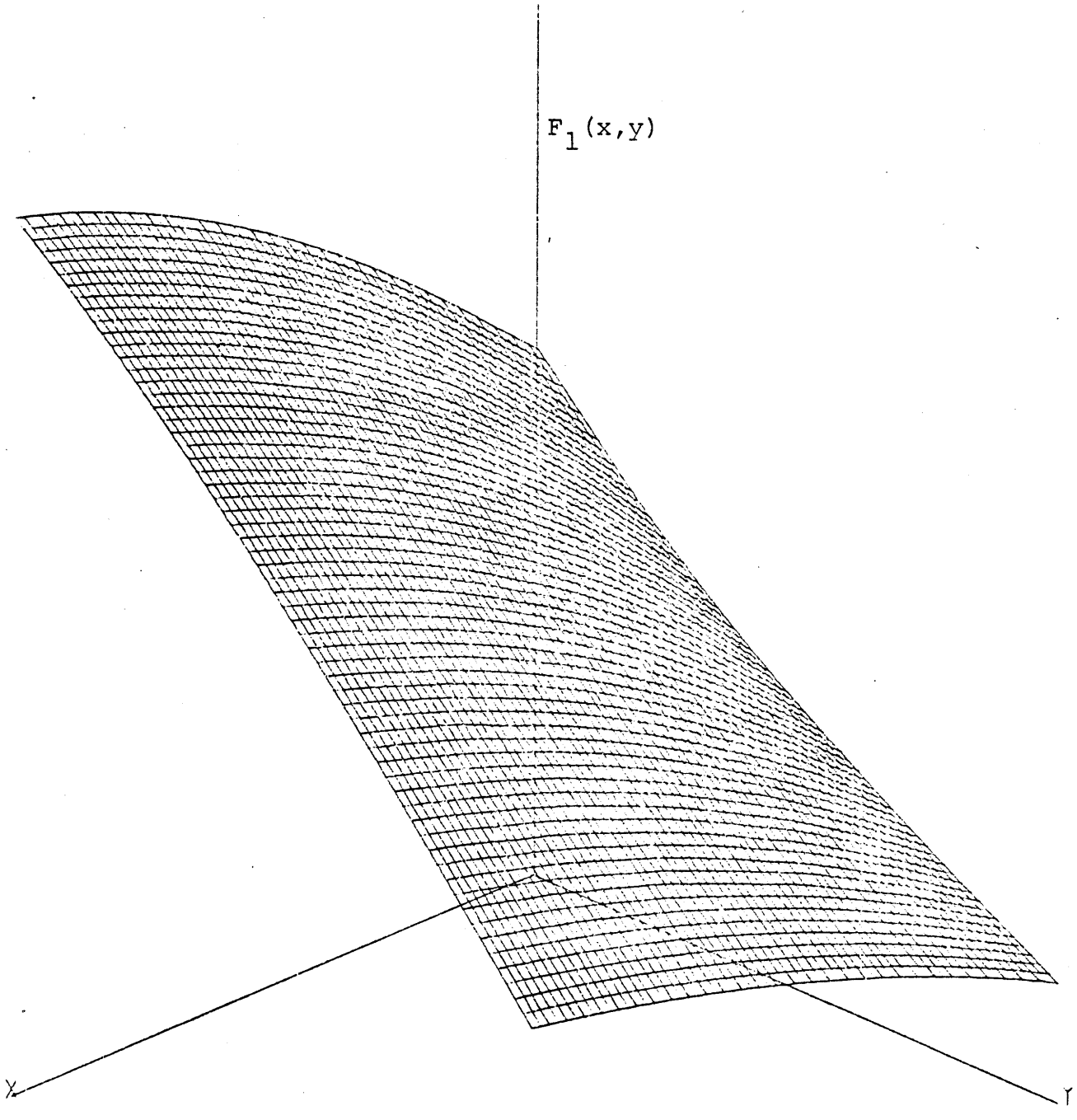

Figure A15.5: Reference Fast Form Function for Node 11 of Benchmark Problem 6

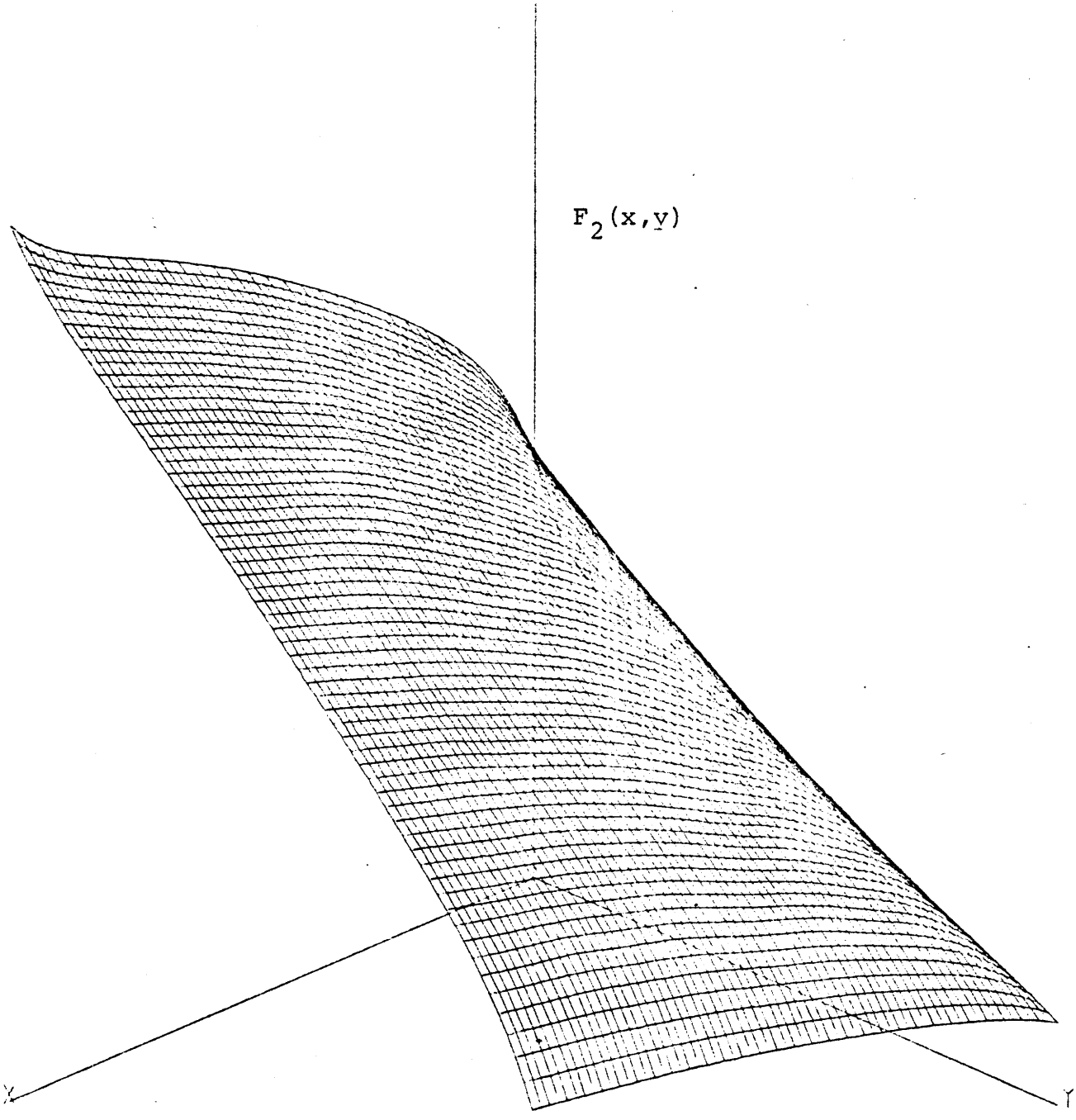

Figure A15.6: Reference Thermal Form Function for Node 11 of Benchmark Problem 6

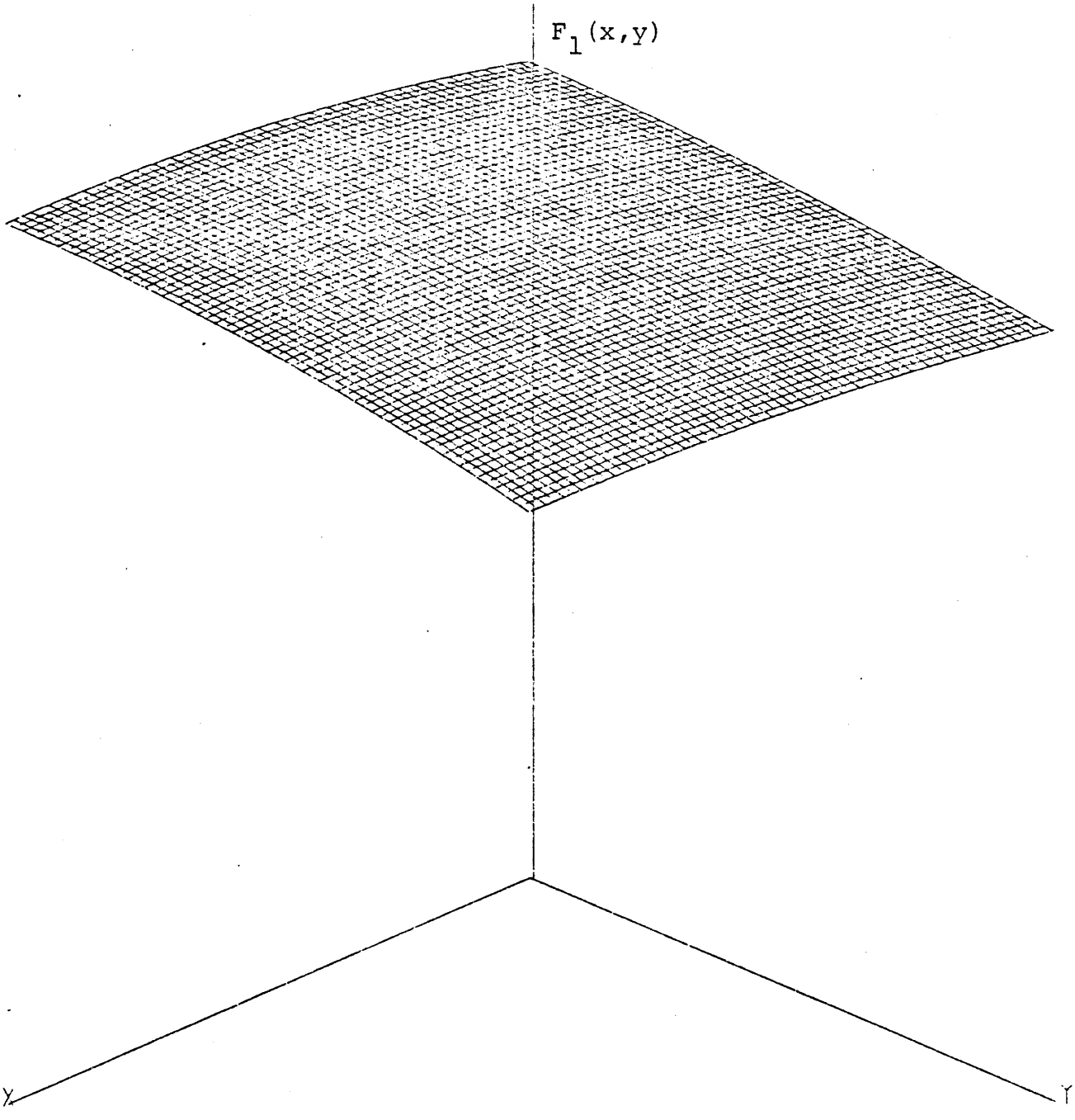

Figure A15.7: Reference Fast Form Function for Node 13 of Benchmark Problem 6

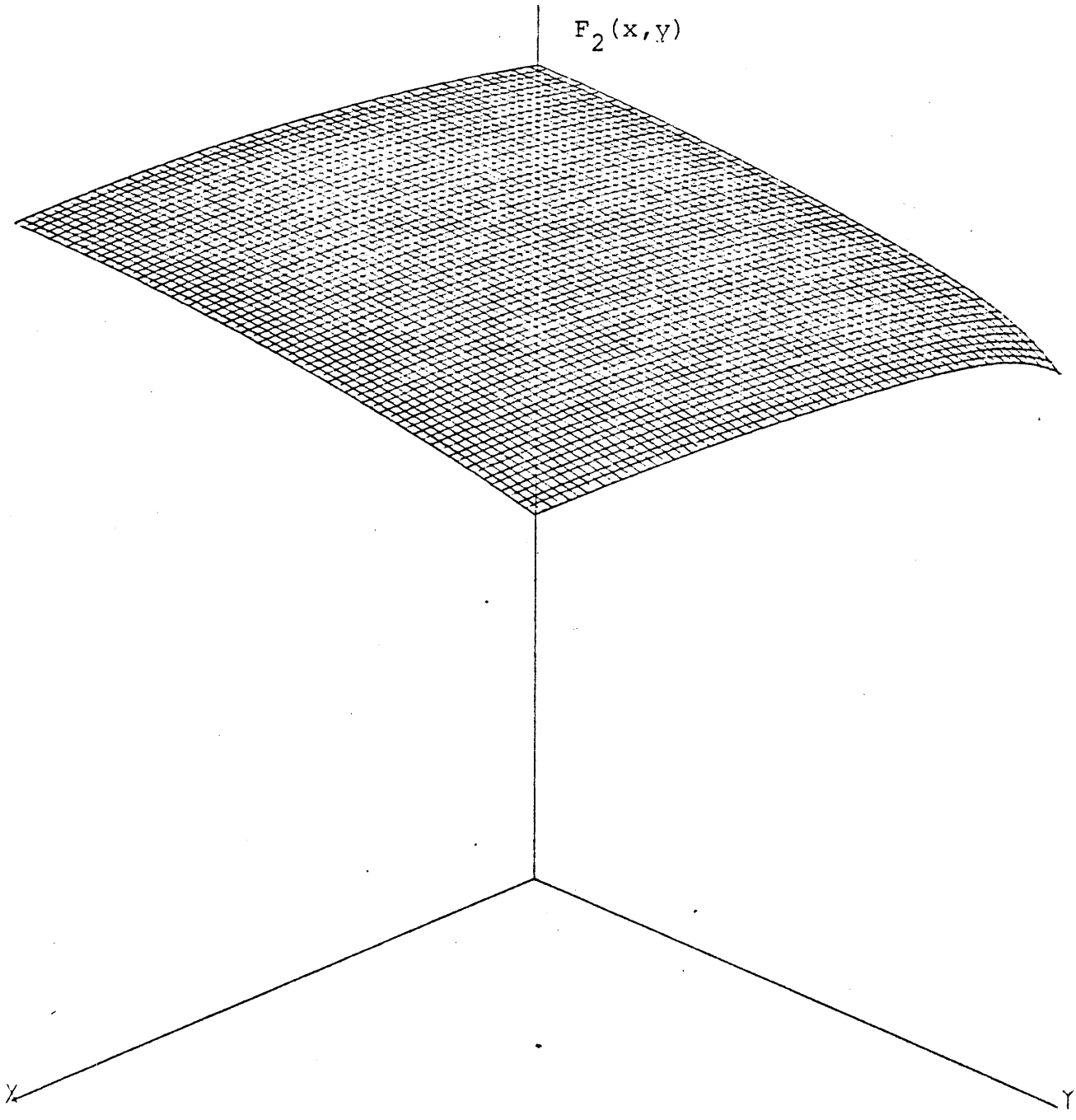

Figure A15.8: Reference Thermal Form Function for Node 13 of Benchmark Problem 6

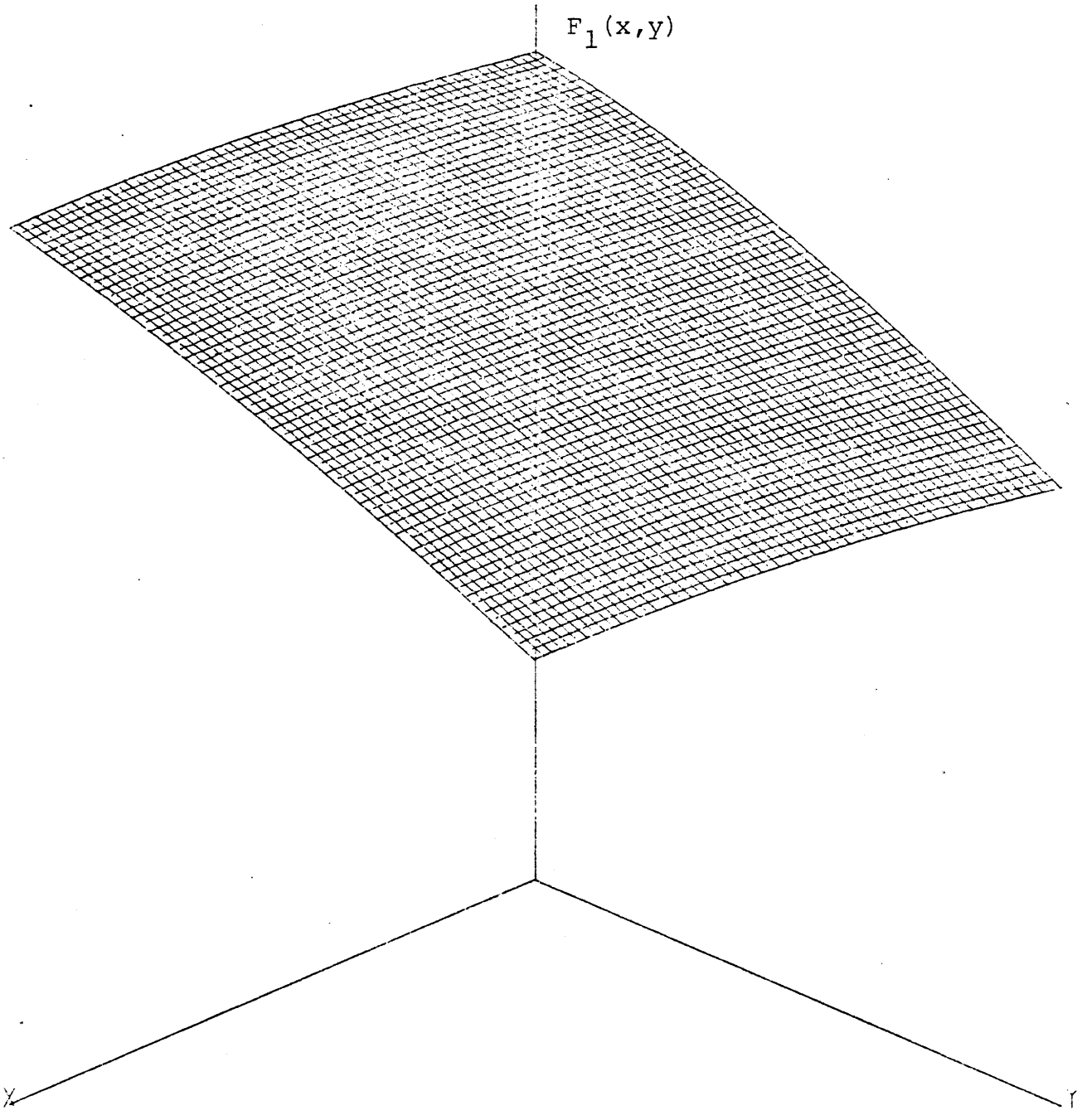

Figure A15.9: Reference Fast Form Function for Node 14 of Benchmark Problem 6

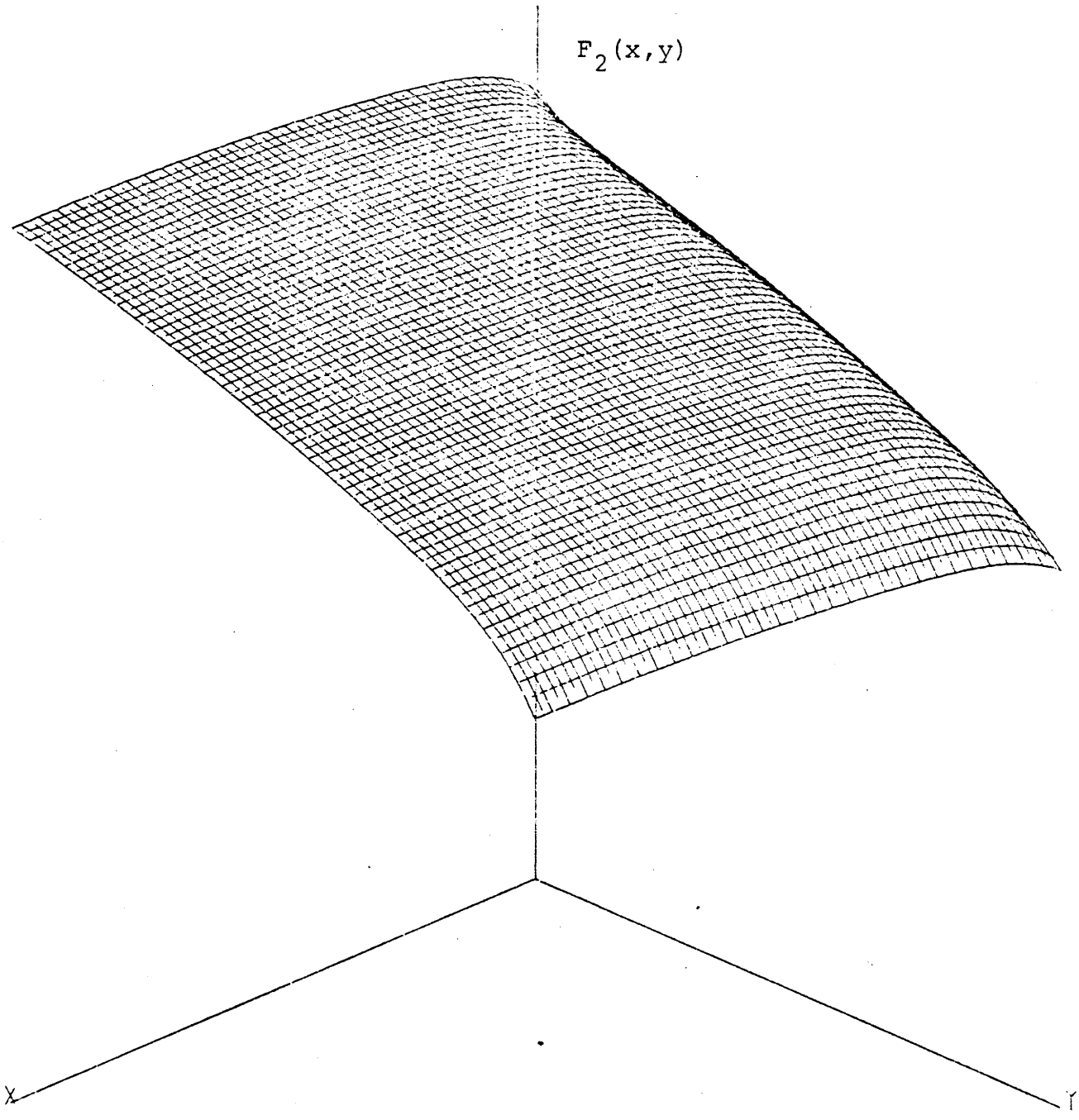

Figure A15.10: Reference Thermal Form Function for Node 14 of Benchmark Problem 6

A15.3: Benchmark Problem 7 Reference Form Functions

Benchmark Problem 7 is a small, unrodded, 3-by-3 node problem. The center node 5 contains fuel 1 and 17 water holes. The other eight nodes are homogeneous fuel 2. The sketch below gives the node numbering for this problem. All plots are for node 5.

$\phi_g = 0$

$\bar{J}_g \cdot \hat{n} = 0$

node 1	node 2	node 3
node 4	node 5	node 6
node 7	node 8	node 9

$\phi_g = 0$

$\bar{J}_g \cdot \hat{n} = 0$

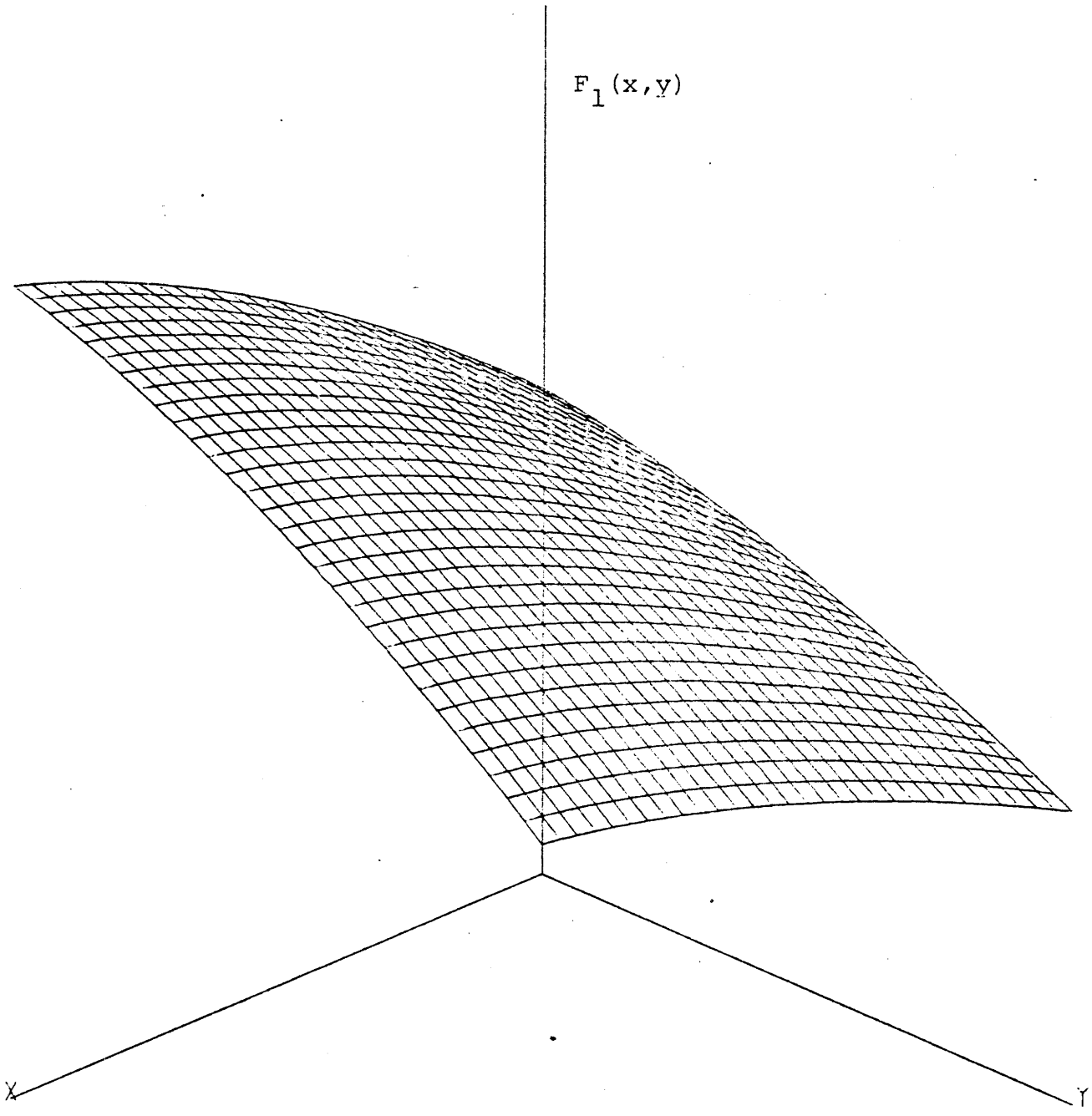

Figure A15.11: Reference Fast Form Function for Node 5 of Benchmark Problem 7

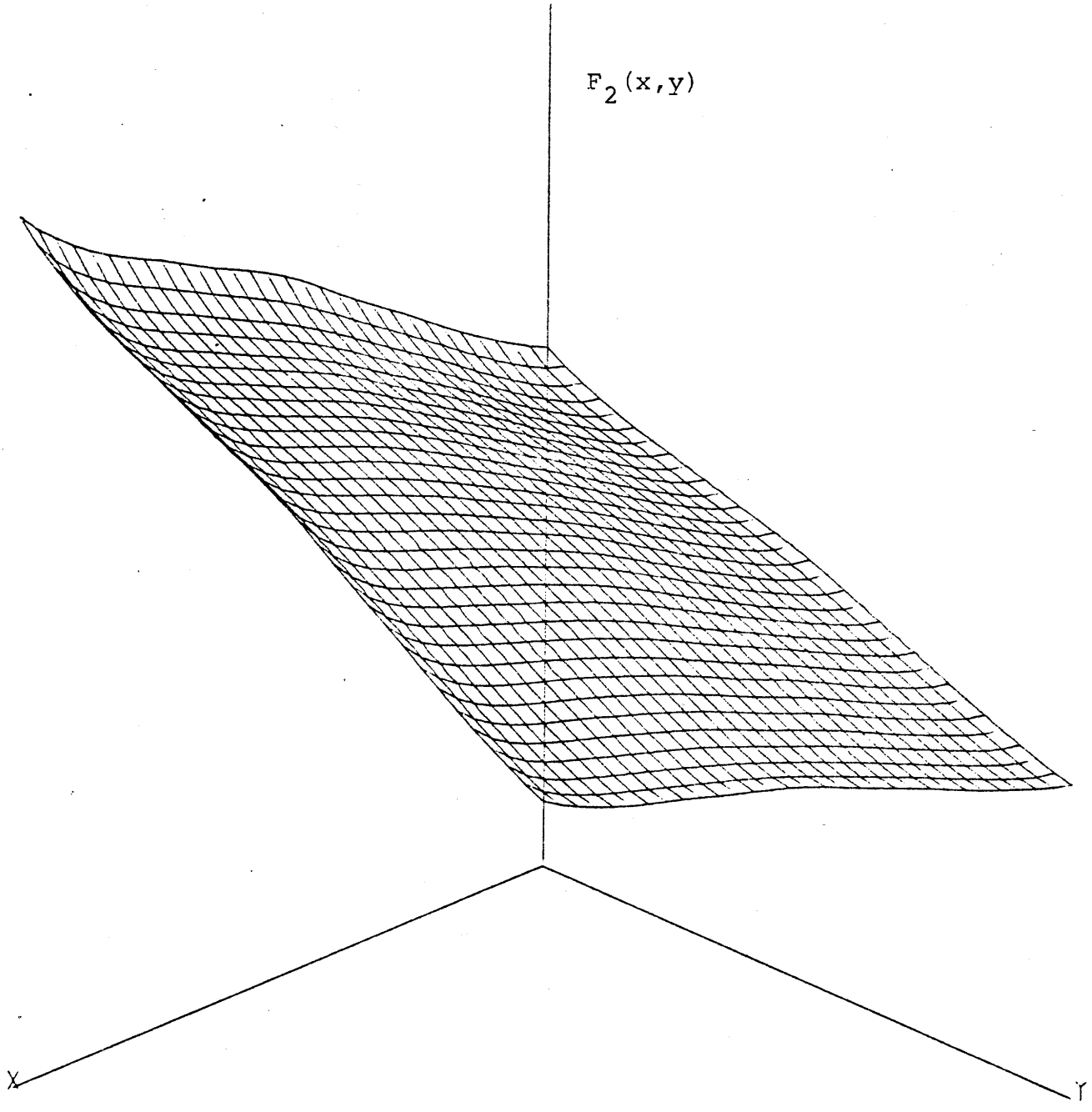

Figure A15.12: Reference Thermal Form Function for Node 5 of Benchmark Problem 7

A15.4: Benchmark Problem 8 Reference Form Functions

Benchmark problem 8 is a small 3-by-3 node problem. Some of the nodes are rodded and node 3 contains water to simulate reflector effects. All plots are for node 5 of this problem. The sketch below gives the node numbering for benchmark problem 8.

$\phi_g = 0$

$\bar{J}_g \cdot \hat{n} = 0$

node 1	node 2	node 3
node 4	node 5	node 6
node 7	node 8	node 9

$\phi_g = 0$

$\bar{J}_g \cdot \hat{n} = 0$

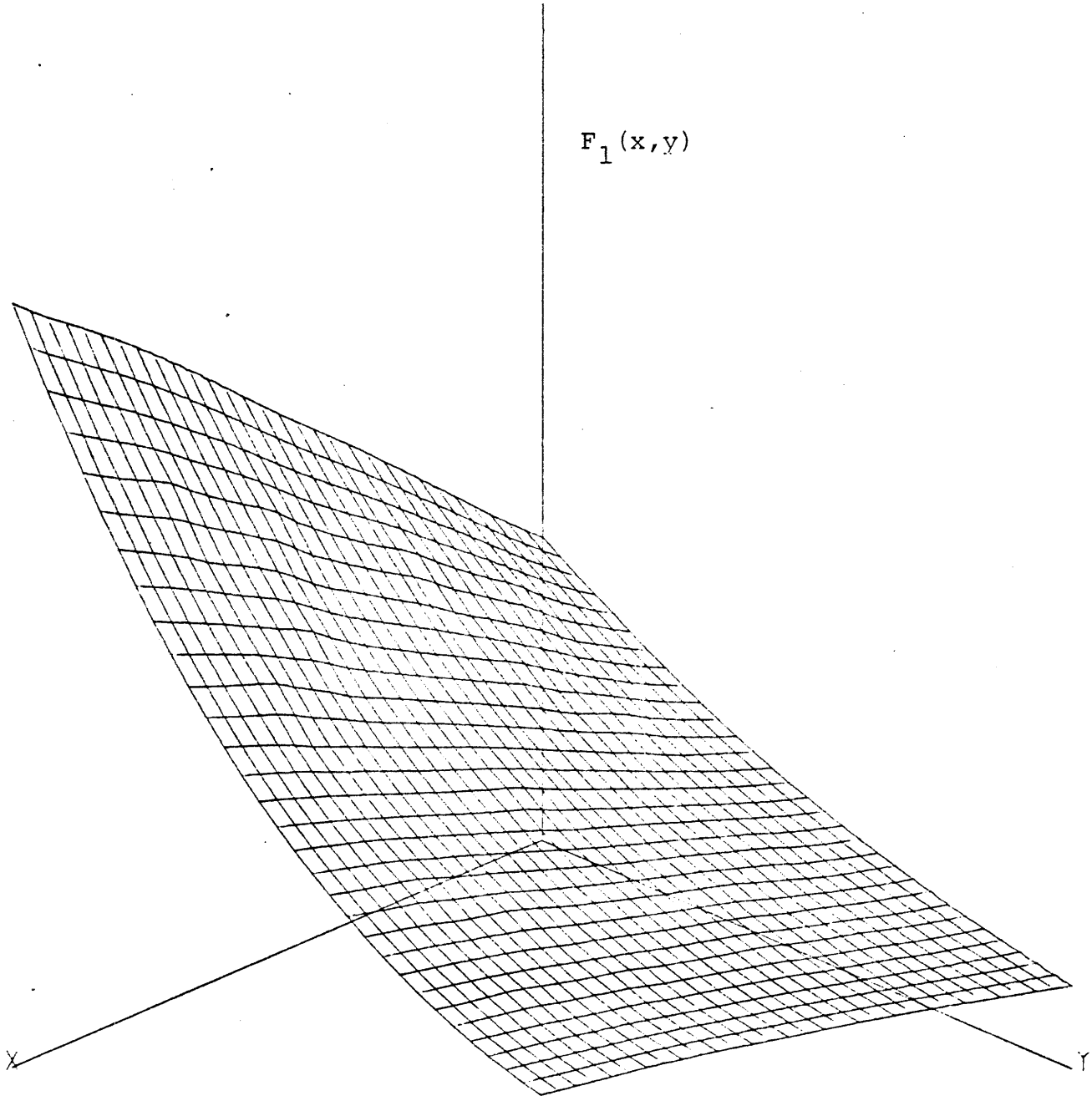

Figure A15.13: Reference Fast Form Function for Node 5 of Benchmark Problem 8

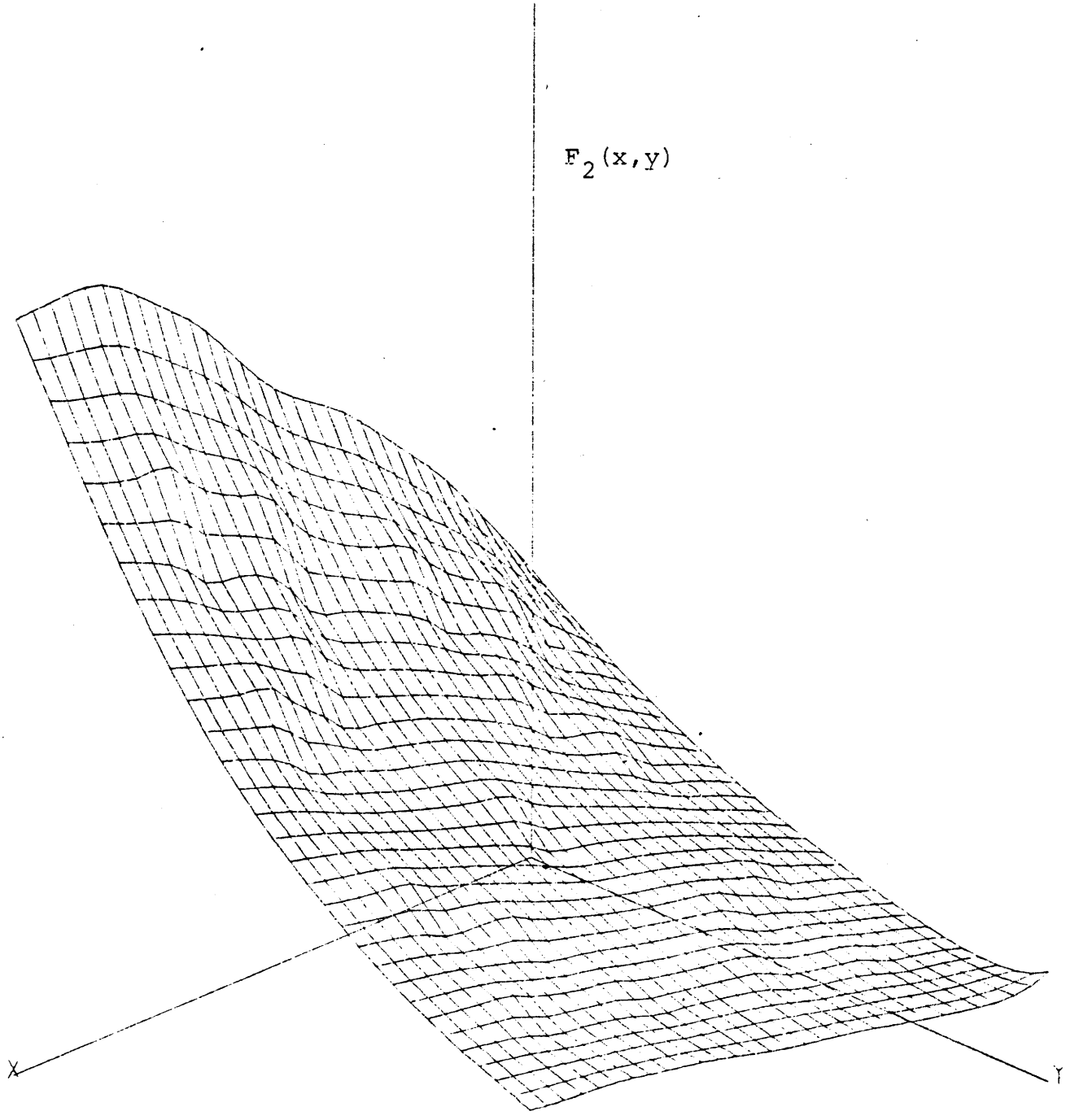

Figure A15.14: Reference Thermal Form Function for Node 5 of Benchmark Problem 8

Appendix 16

REFERENCE FORM FUNCTIONS BASED ON EXTENDED ASSEMBLY CALCULATIONS

A16.0 Introduction

Figure A16.1: Reference Fast Form Function Based on an Extended Assembly Calculation for Node 7 of Benchmark Problem 6

Figure A16.2: Reference Thermal Form Function Based on an Extended Assembly Calculation for Node 7 of Benchmark Problem 6

Figure A16.3: Reference Fast Form Function Based on an Extended Assembly Calculation for Node 10 of Benchmark Problem 6

Figure A16.4: Reference Thermal Form Function Based on an Extended Assembly Calculation for Node 10 of Benchmark Problem 6

Figure A16.5: Reference Fast Form Function Based on an Extended Assembly Calculation for Node 11 of Benchmark Problem 6

Figure A16.6: Reference Thermal Form Function Based on an Extended Assembly Calculation for Node 11 of Benchmark Problem 6

Figure A16.7: Reference Fast Form Function Based on an Extended Assembly Calculation for Node 15 of Benchmark Problem 6

Figure A16.8: Reference Thermal Form Function Based on an Extended Assembly Calculation for Node 15 of Benchmark Problem 6

A16.0 Introduction

The reference form function, $F_g(x,y)$, is equal to the ratio of the global heterogeneous flux, $\phi_g(x,y)$, to the assembly heterogeneous flux, $A_g(x,y)$. This appendix presents plots of the reference form functions for some of the nodes of benchmark problem 6 where the assembly flux, $A_g(x,y)$, was calculated from an extended assembly calculation.

See Figure 2.4 of Chapter 2. This figure shows a 3-by-3 node configuration and a 2-by-1 node configuration. The plots for nodes 7, 10, and 11 utilize the $A_g(x,y)$ from the 3-by-3 node calculation. The plot for node 15 employs the $A_g(x,y)$ from the 2-by-1 node calculation. The sketch below illustrates the node numbering for benchmark problem 6.

$\phi_g = 0$

node 1	node 2	node 3	node 4
node 5	node 6	node 7	node 8
node 9	node 10	node 11	node 12
node 13	node 14	node 15	node 16

$\bar{J}_g \cdot \hat{n} = 0$ (left) $\phi_g = 0$ (right)

$\bar{J}_g \cdot \hat{n} = 0$

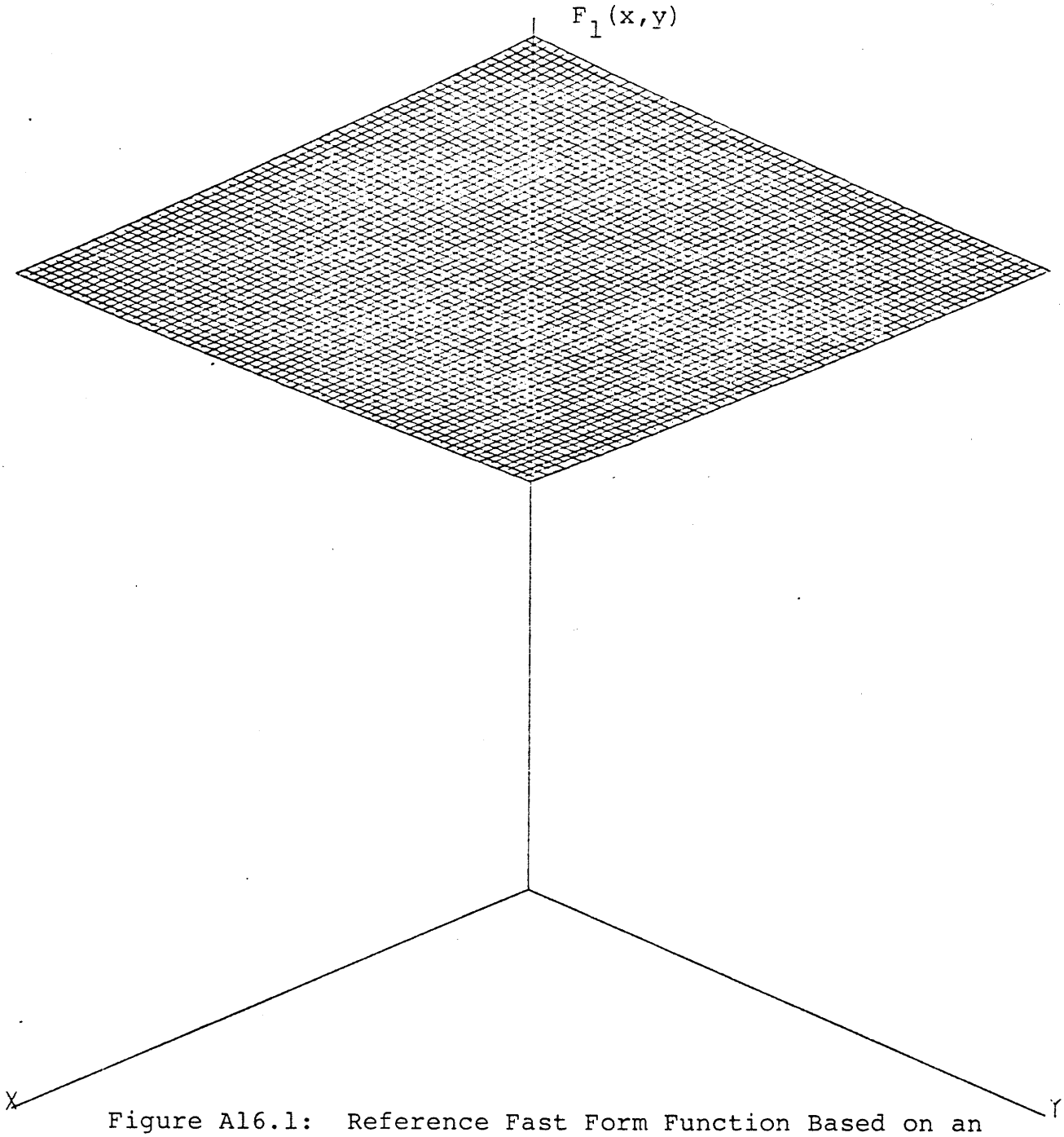

Figure A16.1: Reference Fast Form Function Based on an Extended Assembly Calculation for Node 7 of Benchmark Problem 6

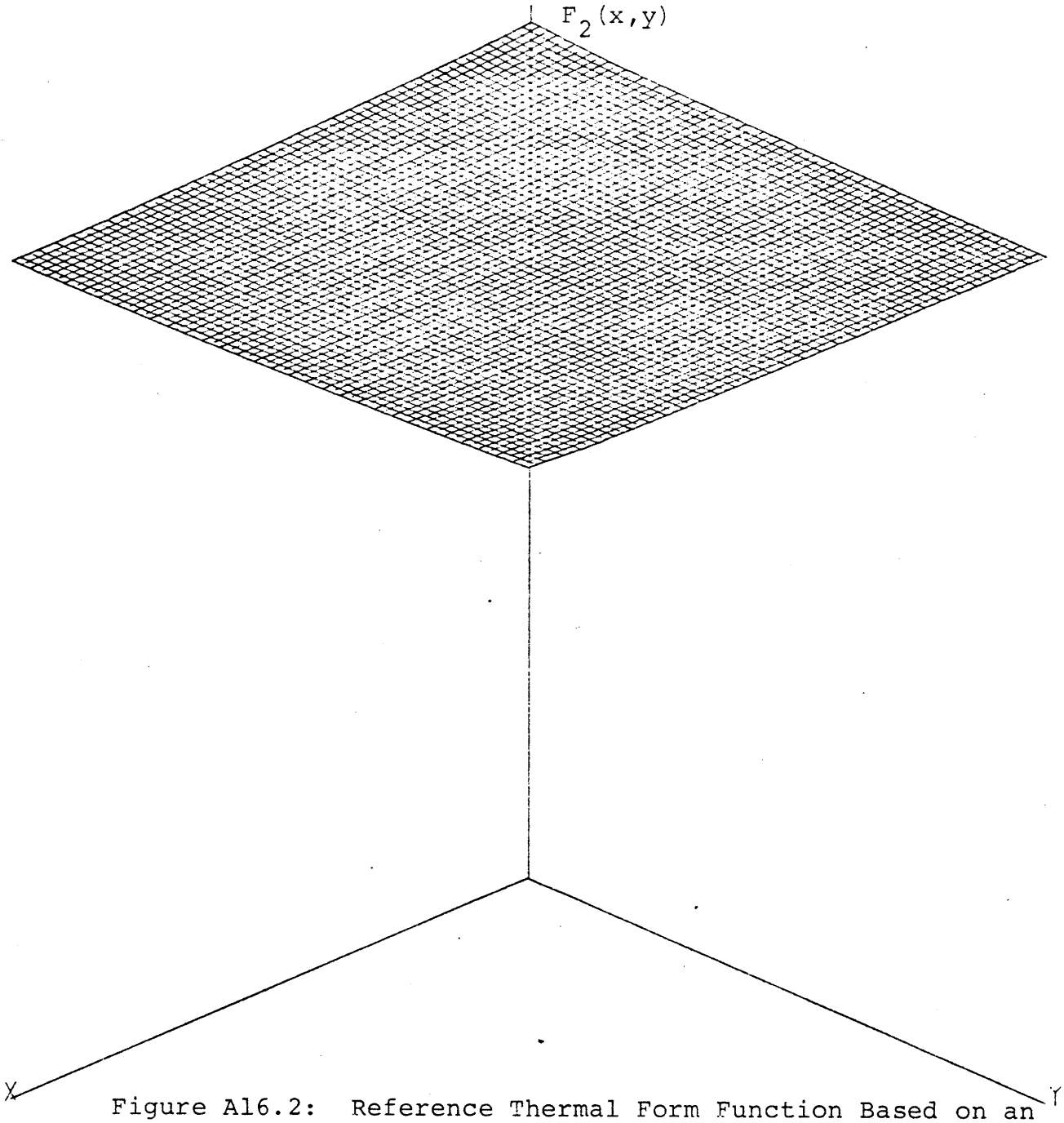

Figure A16.2: Reference Thermal Form Function Based on an Extended Assembly Calculation for Node 7 of Benchmark Problem 6

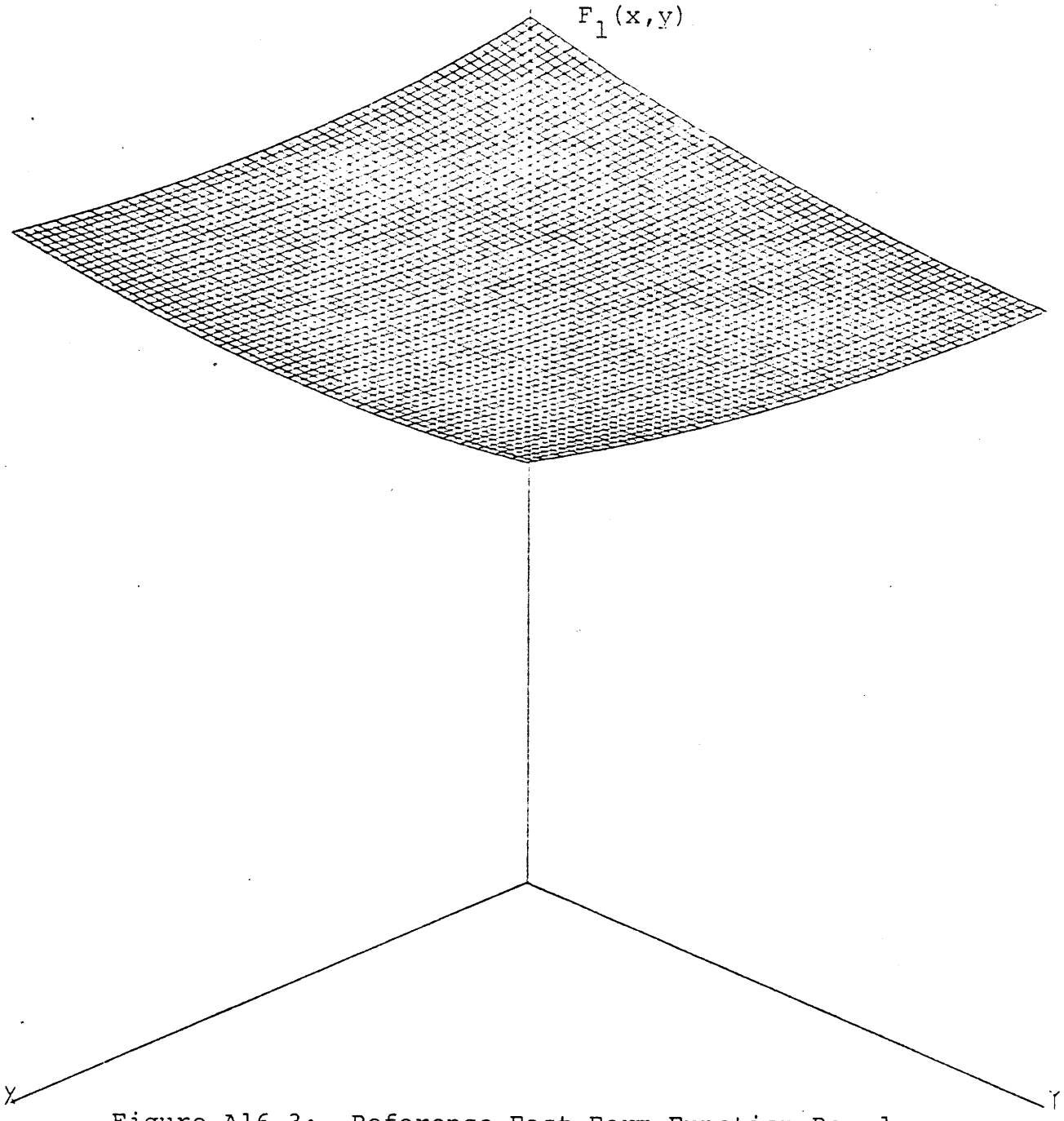

Figure A16.3: Reference Fast Form Function Based on an Extended Assembly Calculation for Node 10 of Benchmark Problem 6

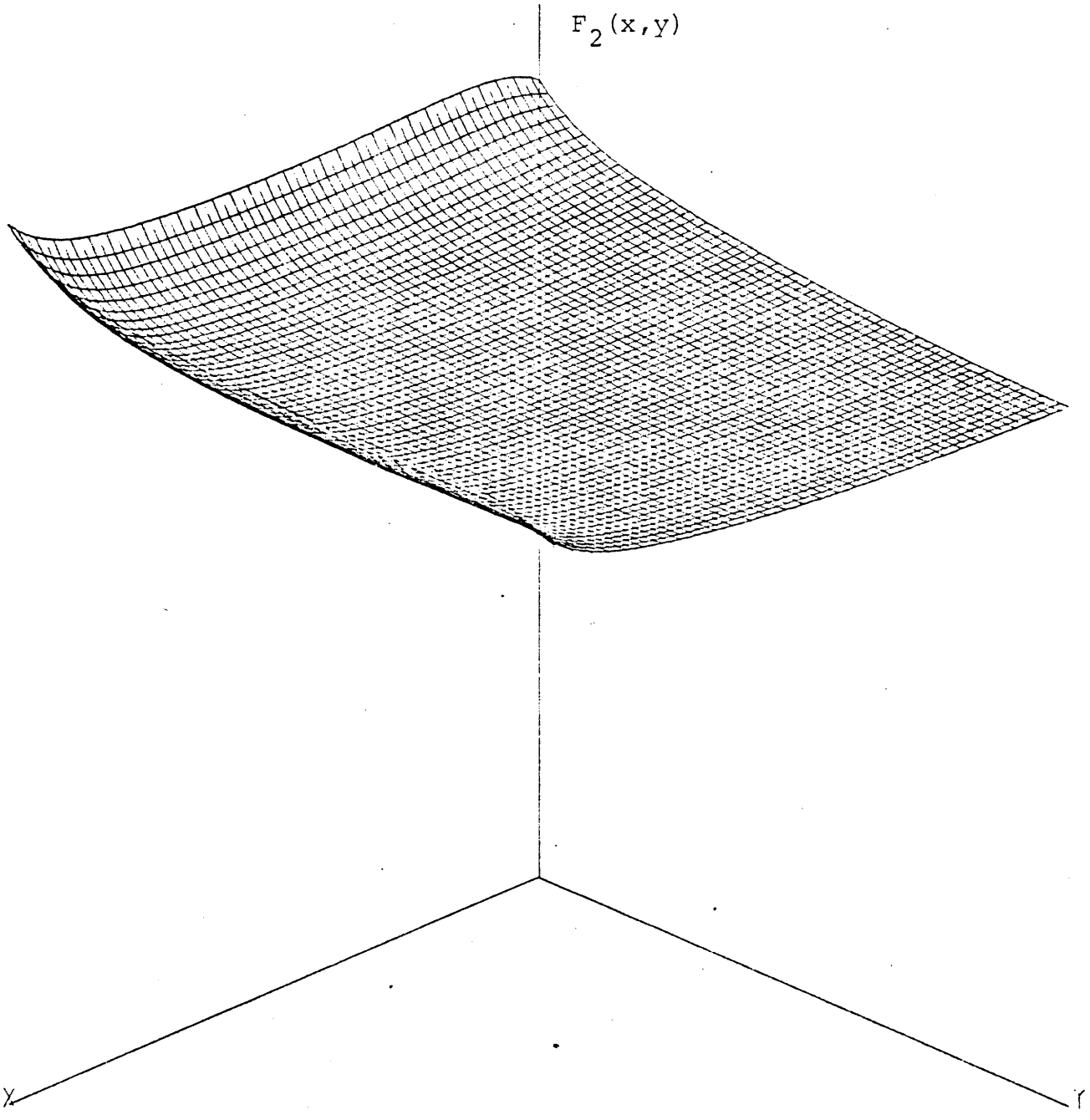

Figure A16.4: Reference Thermal Form Function Based on an Extended Assembly Calculation for Node 10 of Benchmark Problem 6

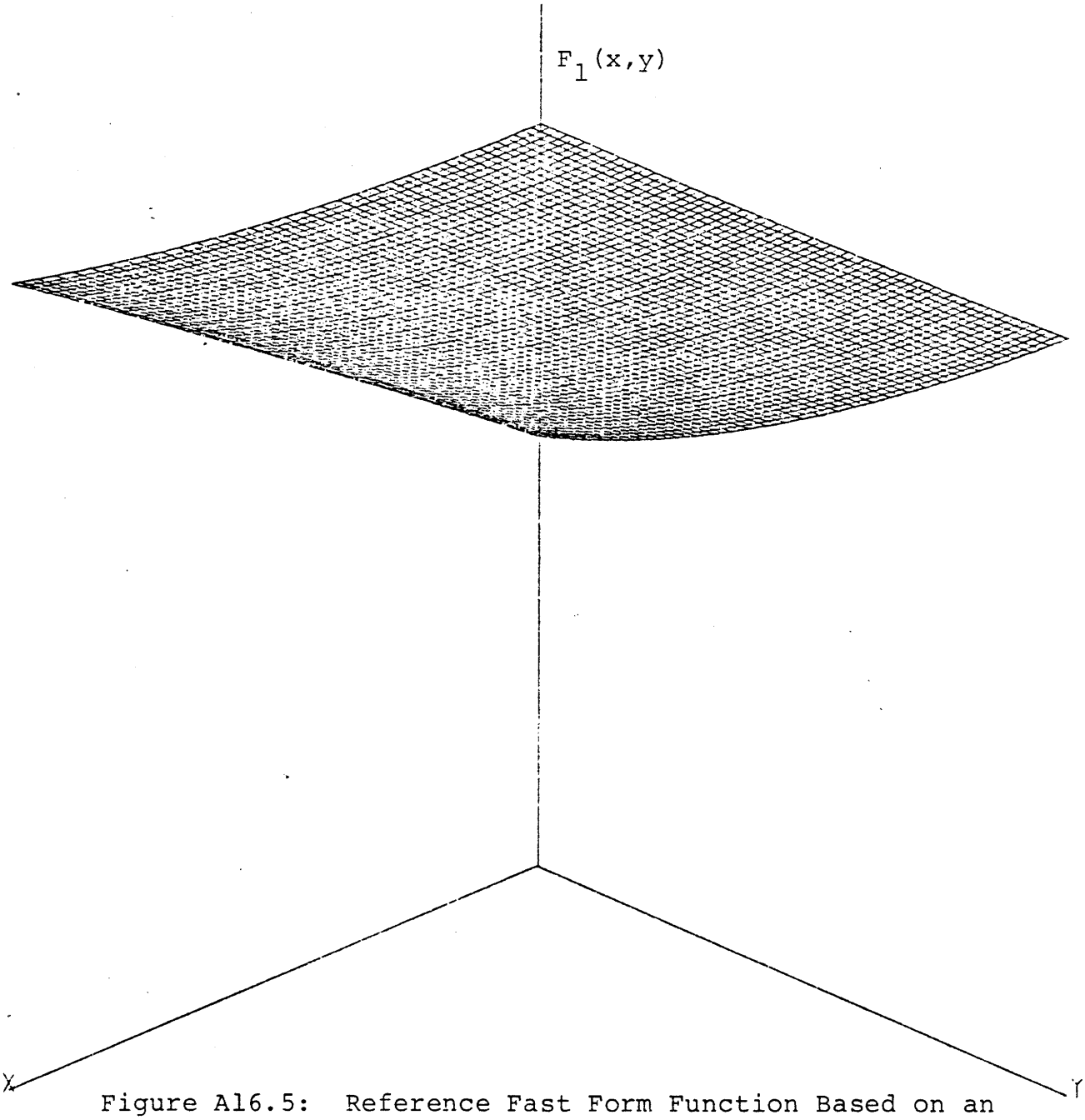

Figure A16.5: Reference Fast Form Function Based on an Extended Assembly Calculation for Node 11 of Benchmark Problem 6

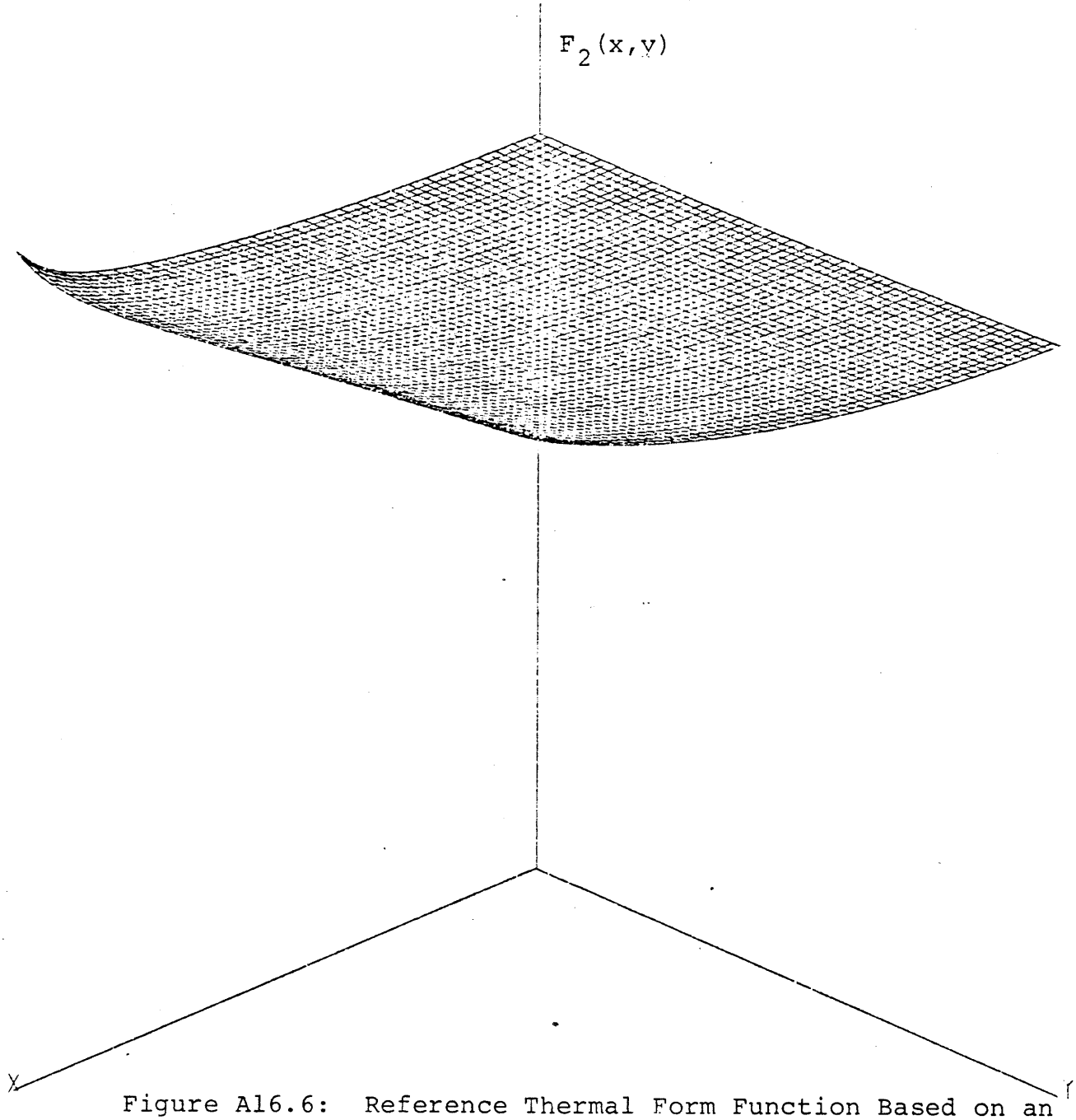

Figure A16.6: Reference Thermal Form Function Based on an Extended Assembly Calculation for Node 11 of Benchmark Problem 6

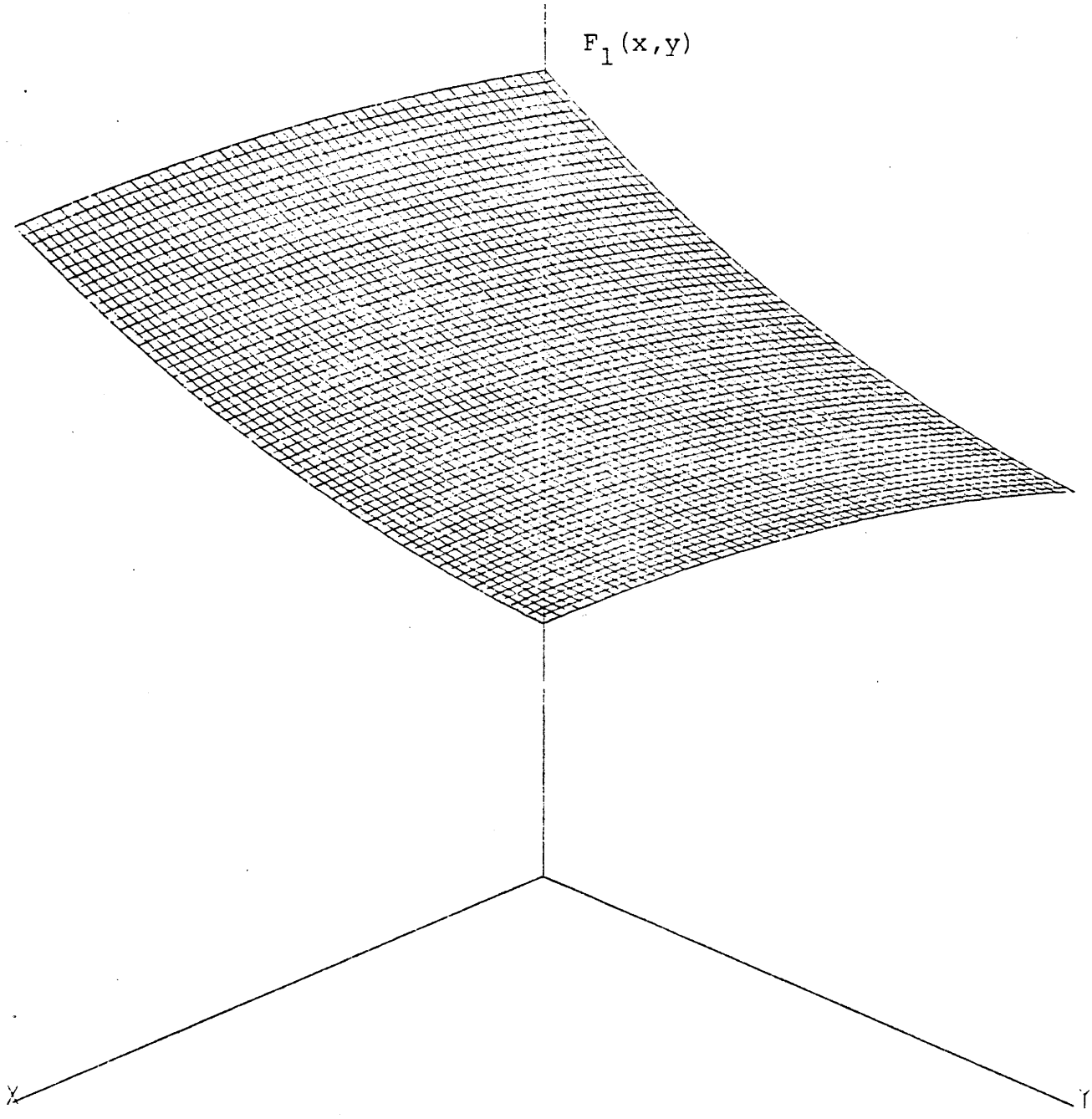

Figure A16.7: Reference Fast Form Function Based on an Extended Assembly Calculation for Node 15 of Benchmark Problem 6

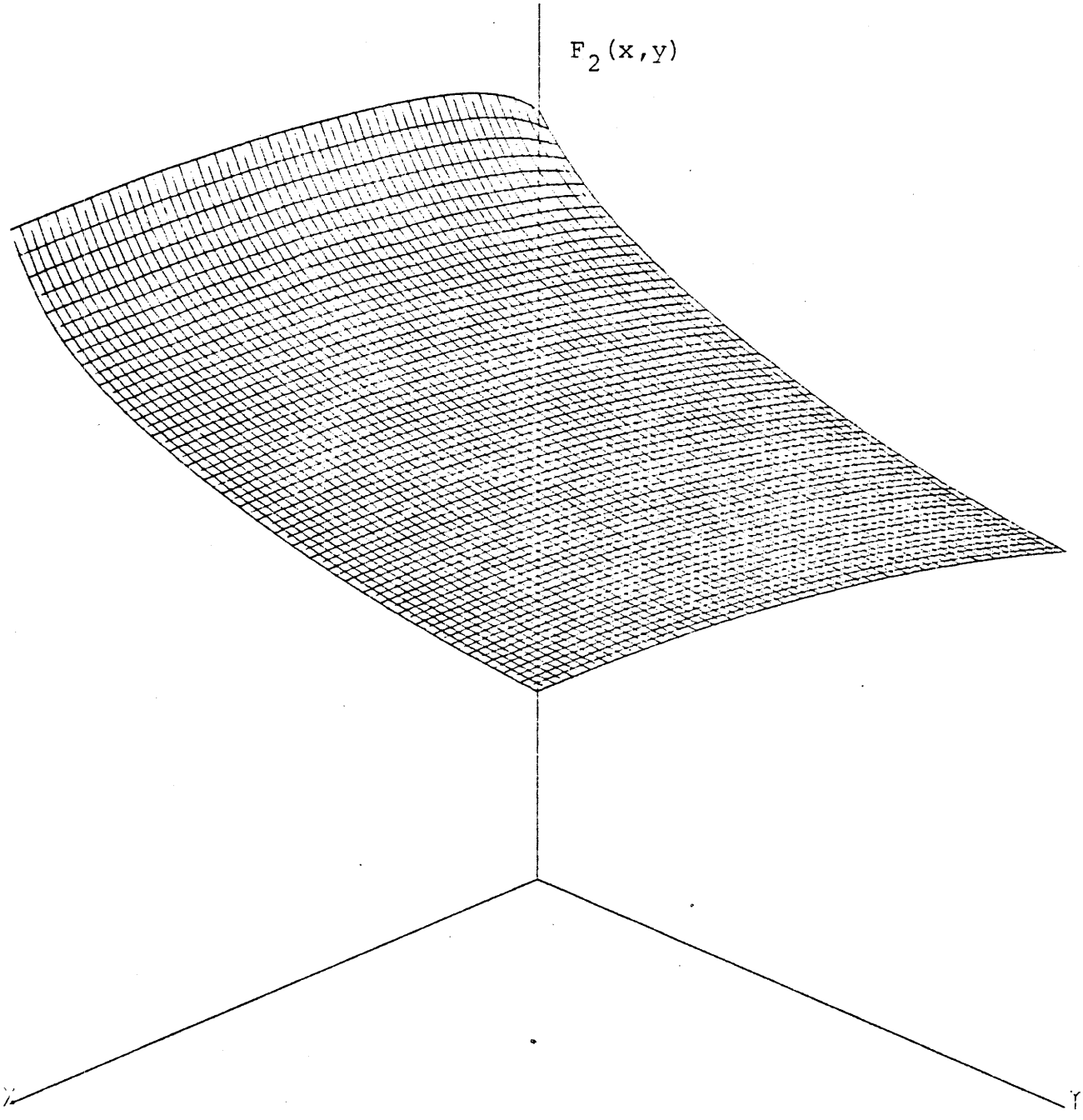

Figure A16.8: Reference Thermal Form Function Based on an Extended Assembly Calculation for Node 15 of Benchmark Problem 6

Appendix 17

ERROR PLOTS FOR A FLUX RECONSTRUCTION METHOD BASED ON A 9-TERM, BI-QUADRATIC FORM FUNCTION

A17.0 Introduction

Figure A17.1: Percent Error in the Fast Reconstructed Flux Based on a 9-Term, Bi-Quadratic Form Function for Node 5 of Benchmark Problem 7

Figure A17.2: Percent Error in the Thermal Reconstructed Flux Based on a 9-Term, Bi-Quadratic Form Function for Node 5 of Benchmark Problem 7

A17.0 Introduction

Benchmark problem 7 is the small 3-by-3 quarter core which has an unrodded fuel 1 center assembly (node 5) and homogeneous fuel 2 assemblies for the balance of the quarter core. The flux reconstruction method described in Appendix 9 was employed for node 5 of this problem. This reconstruction method is based on a 9-term, bi-quadratic form function.

This appendix presents plots of the relative percent error in the reconstructed flux. If $\phi(x,y)$ is the reference flux and $\phi^R(x,y)$ is the reconstructed flux, then the relative percent error in the reconstructed flux is given by

$$\{ [\phi^R(x,y) - \phi(x,y)] * 100.0 \} / \phi(x,y) \qquad \text{(A17.1)}$$

Division of the numerator and denominator of equation A17.1 by $A_g(x,y)$ yields the relative percent error in the reconstructed form function. Hence, the plots in this appendix are also illustrations of the percent error in the reconstructed form functions.

Percent Error in the

Fast Reconstructed Flux =

$$\frac{\phi_1^R(x,y) - \phi_1(x,y)}{\phi_1(x,y)} * 100.0$$

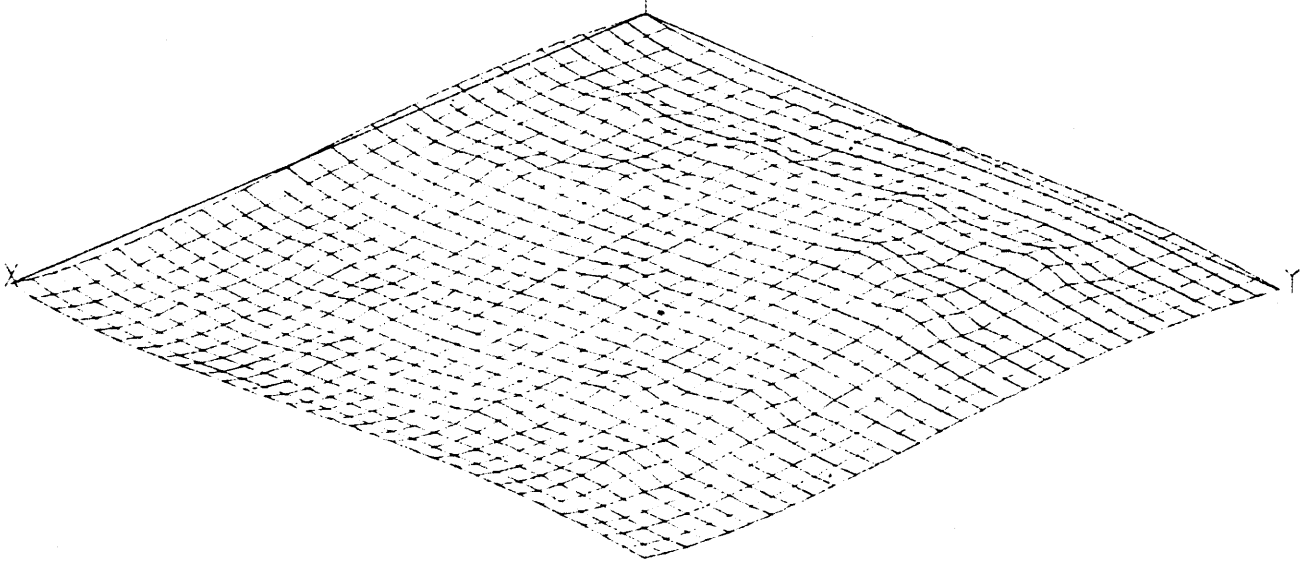

Figure A17.1: Percent Error in the Fast Reconstructed Flux Based on a 9-Term, Bi-Quadratic Form Function for Node 5 of Benchmark Problem 7

Percent Error in the

Reconstructed Thermal Flux =

$$\frac{\phi_2^R(x,y) - \phi_2(x,y)}{\phi_2(x,y)} * 100.0$$

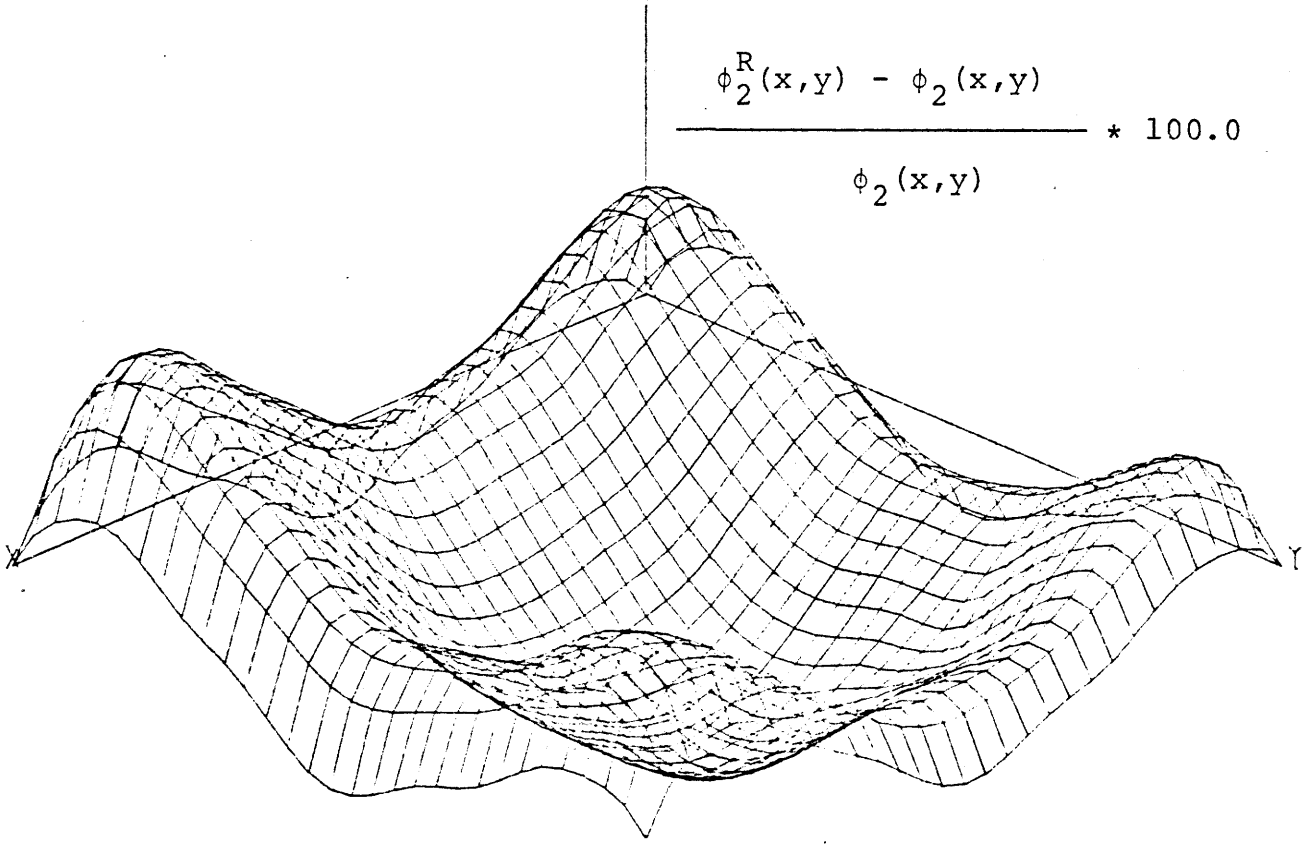

Figure A17.2: Percent Error in the Thermal Reconstructed Flux Based on a 9-Term, Bi-Quadratic Form Function for Node 5 of Benchmark Problem 7

Appendix 18

ERROR PLOTS FOR A FLUX RECONSTRUCTION METHOD BASED ON A 25-TERM, BI-QUARTIC FORM FUNCTION

A18.0 Introduction

Figure A18.1: Percent Error in the Fast Reconstructed Flux Based on a 25-Term, Bi-Quartic Form Function for Node 5 of Benchmark Problem 7

Figure A18.2: Percent Error in the Thermal Reconstructed Flux Based on a 25-Term, Bi-Quartic Form Function for Node 5 of Benchmark Problem 7

Figure A18.3: Percent Error in the Fast Reconstructed Flux Based on a 25-Term, Bi-Quartic Form Function for Node 5 of Benchmark Problem 8

Figure A18.4: Percent Error in the Thermal Reconstructed Flux Based on a 25-Term, Bi-Quartic Form Function for Node 5 of Benchmark Problem 8

A18.0 Introduction

This appendix presents plots for benchmark problems 7 and 8. Benchmark problem 7 is a 3-by-3 quarter core. The center node 5 is unrodded and contains fuel 1. The other 8 nodes are homogeneous and contain fuel 2. Benchmark problem 8 is a 3-by-3 quarter core. Some assemblies are rodded and node 3 contains water to simulate reflector effects. See Appendix 2 for more details of these problems. Flux reconstruction was performed in the center node 5 of benchmark problems 7 and 8.

The plots in this appendix illustrate the relative percent error in the reconstructed flux based on the 25-term, bi-quartic form function. As discussed in Appendix 17, these plots also show the relative percent error in the reconstructed form function.

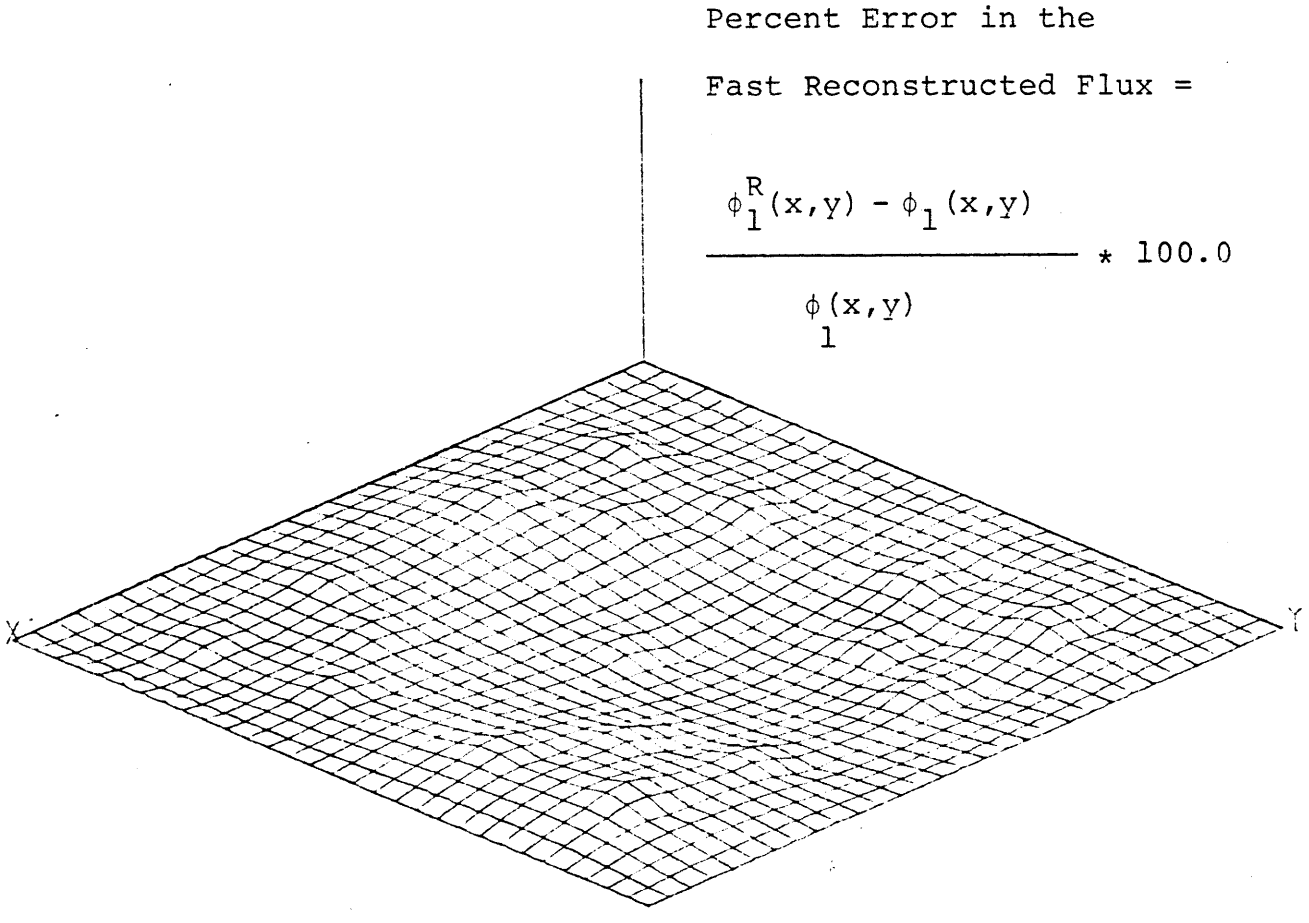

Figure A18.1: Percent Error in the Fast Reconstructed Flux Based on a 25-Term, Bi-Quartic Form Function for Node 5 of Benchmark Problem 7

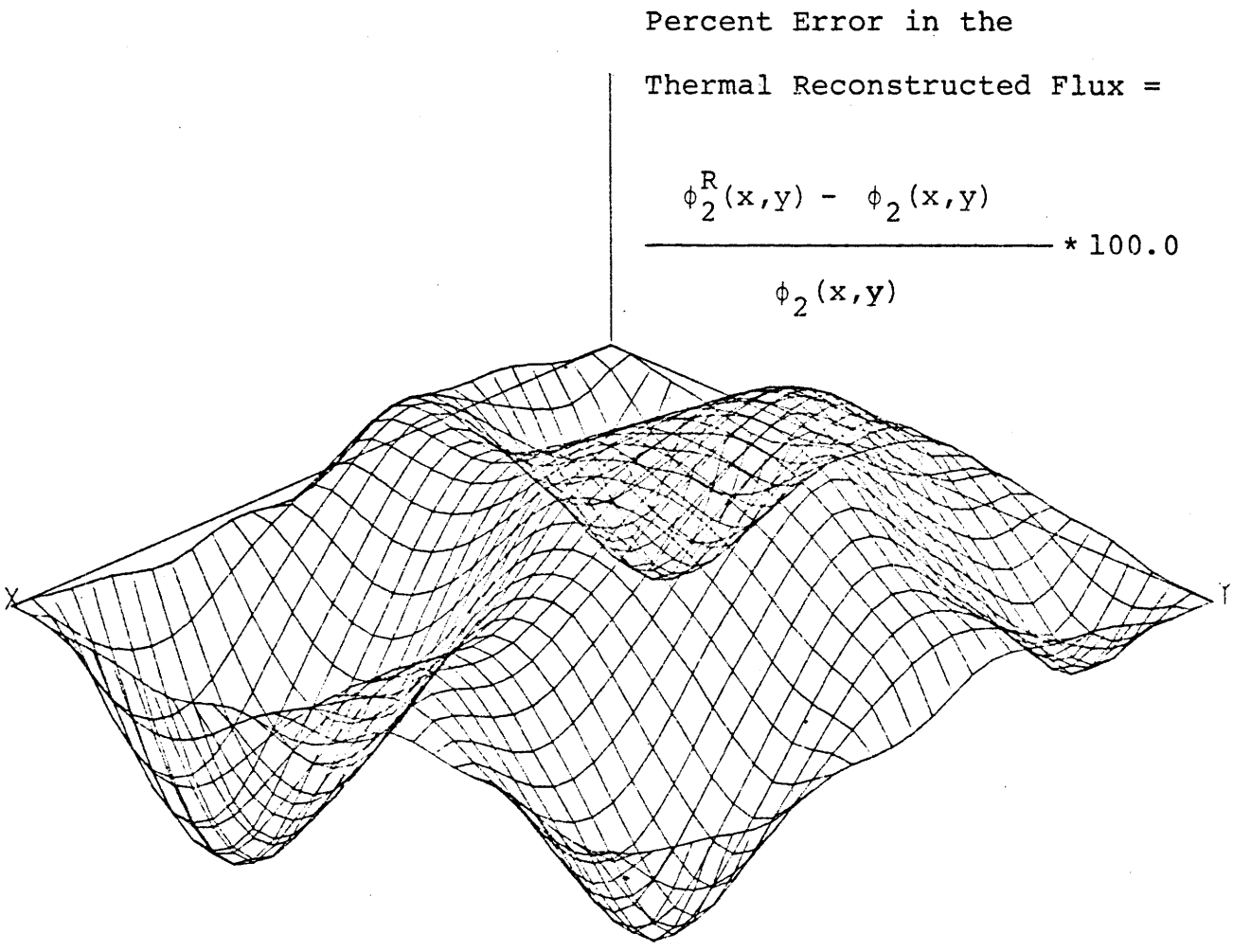

Figure A18.2: Percent Error in the Thermal Reconstructed Flux Based on a 25-Term, Bi-Quartic Form Function for Node 5 of Benchmark Problem 7

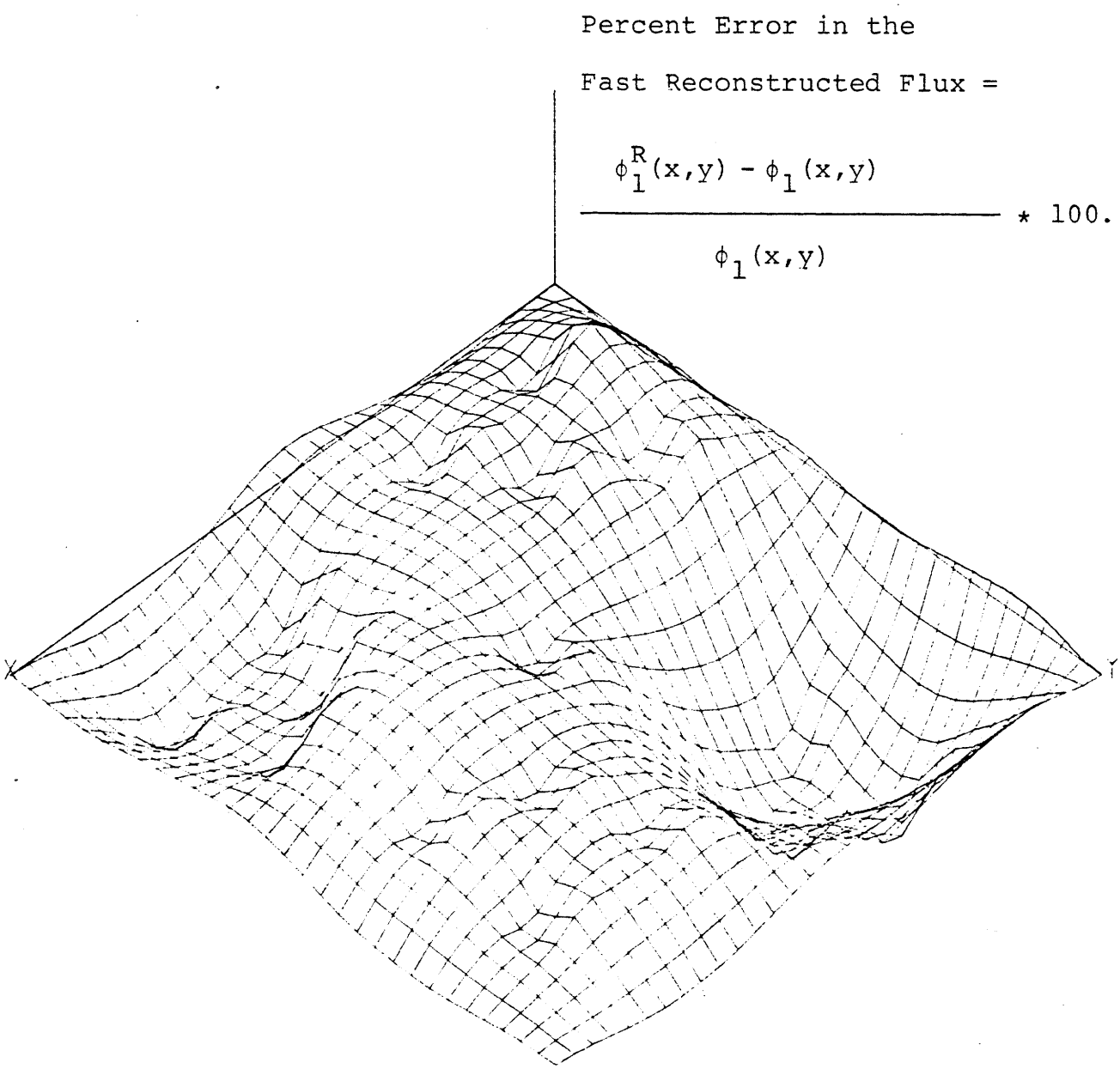

Figure A18.3: Percent Error in the Fast Reconstructed Flux Based on a 25-Term, Bi-Quartic Form Function for Node 5 of Benchmark problem 8

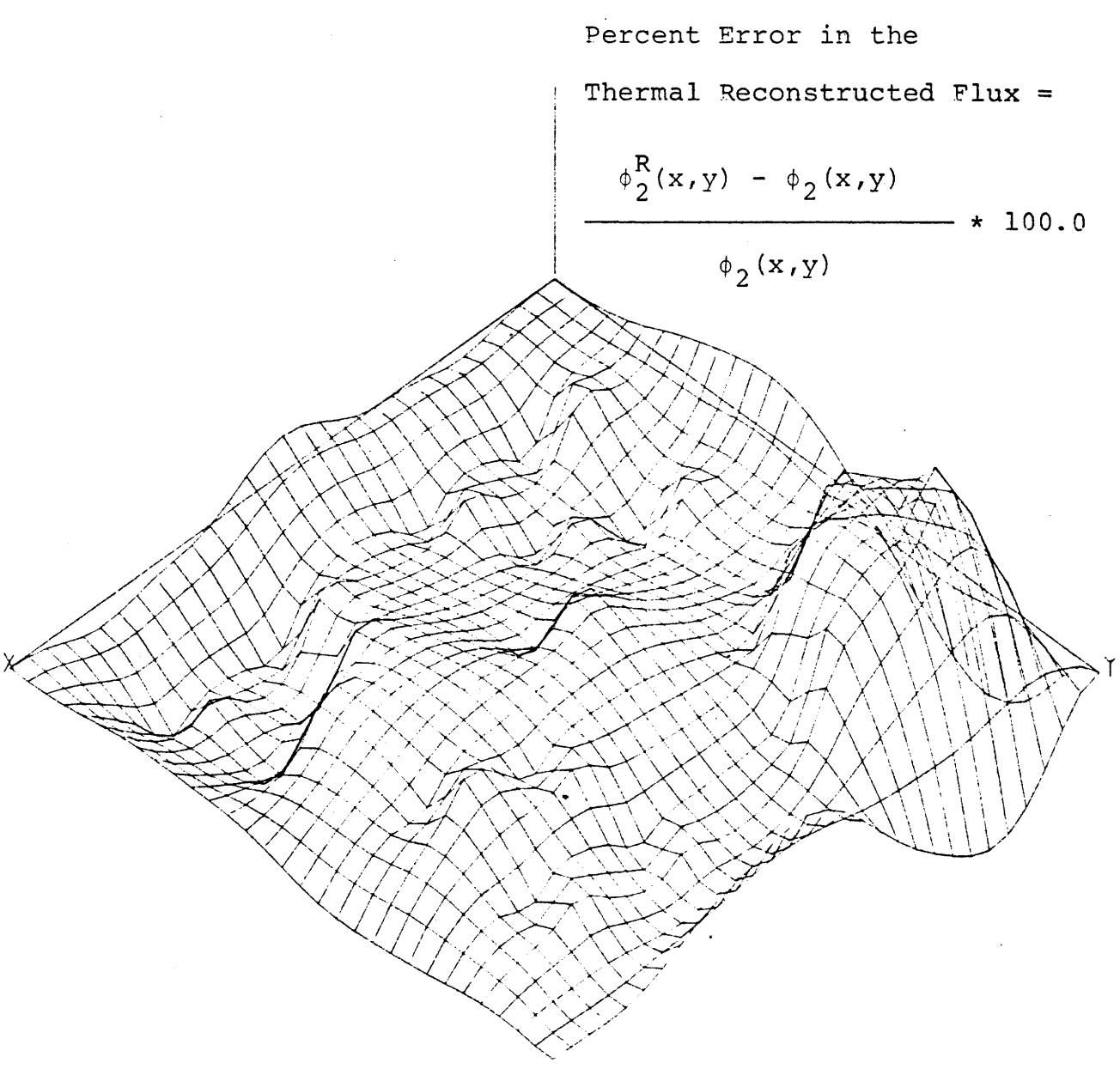

Figure A18.4: Percent Error in the Thermal Reconstructed Flux Based on a 25-Term, Bi-Quartic Form Function for Node 5 of Benchmark Problem 8

Appendix 19

ERROR PLOTS FOR THE FORTE FLUX RECONSTRUCTION METHOD

A19.0 Introduction

A19.1 Benchmark Problem 5 Error Plots
(QUANDRY-ADF-AXS/CHIME input data for FORTE)

A19.2 Benchmark Problem 7 Error Plots
(QUANDRY-ADF-AXS/CHIME input data for FORTE)

A19.3 Benchmark Problem 6 Error Plots I
(QUANDRY-ADF-AXS(from extended assembly calculations)/
CAMPANA input data for FORTE)

A19.4 Benchmark Problem 6 Error Plots II
(Reference corner point, surface-averaged and volume-averaged form function data for FORTE calculated directly from the reference form functions in Appendix 16, i.e., these reference form functions are based on extended assembly calculations.)

A19.5 Benchmark Problem 6 Error Plots III
(Reference corner point, surface-averaged and volume-averaged form function data for FORTE calculated directly from the reference form functions in Appendix 15, i.e., these reference form functions are based on assembly fluxes derived from assembly calculations employing zero-current boundary conditions.)

A19.0 Introduction

This appendix contains plots of the relative percent error in flux reconstructions (or equivalently in form function reconstructions) from the FORTE computer code. If $\phi_g^R(x,y)$ is the reconstructed flux and $\phi_g(x,y)$ is the reference flux, then the relative percent error in the flux is

$$\frac{\phi_g^R(x,y) - \phi_g(x,y)}{\phi_g(x,y)} * 100.0 . \qquad \text{(A19.1)}$$

Error plots are presented for FORTE reconstructions for some of the assemblies in benchmark problems 5, 6 and 7.

In general, the FORTE reconstruction for a problem depends on the data input into FORTE. Specifically, for each energy group FORTE requires:

1. Four corner point values of the form function
2. Four surface-averaged values of the form function
3. One volume-averaged value of the form function.

In sections 19.1, 19.2 and 19.3 of this appendix these values (see 1, 2 and 3 above) of the form function are found in an inexpensive and approximate manner (and without information from the reference global solution, $\phi_g(x,y)$).

In sections 19.1, 19.2 and 19.3 the surface-averaged values of the form function are approximated as the ratio of the surface-averaged fluxes from a QUANDRY-ADF-AXS calculation divided by the surface-averaged flux from the heterogeneous assembly calculation. The volume-averaged value of the form function is found in a similar manner. The corner point values of the form function are the ratio of the interpolated (using CHIME or CAMPANA runs based on information from the QUANDRY-ADF-AXS calculation) corner point heterogeneous flux to the corner point assembly flux.

In section 19.4 the corner point, surface-averaged and volume-averaged values of the form function are derived directly from the reference form functions in Appendix 16. These reference form functions are based on expensive global heterogeneous flux calculations and on extended assembly calculations. Thus the results in this section are the best possible FORTE reconstructions based on extended assembly calculations for nodes 11 and 15 of benchmark problem 6.

In section 19.5, the corner point, surface-averaged and volume-averaged values of the form function are calculated directly from the reference form functions in Appendix 15. These reference form functions are based on assembly fluxes derived from assembly calculations employing zero-net-current boundary conditions. Thus the results in this section are the best possible FORTE reconstructions based on assembly calculations utilizing zero-net-current boundary conditions.

A19.1 Benchmark Problem 5 Error Plots (QUANDRY-ADF-AXS/CHIME input data for FORTE)

Benchmark problem 5 is the infinite checkerboard of unrodded fuel type 1 and fuel type 2 assemblies. The sketch below gives the boundary conditions and node numbering for the problem. FORTE was used to reconstruct the fast and thermal flux in node 5 of this problem. As discussed in section A19.0 of this appendix, the input form factor data for these FORTE runs was derived from a QUANDRY-ADF-AXS global calculation and a CHIME corner point interpolation.

$\bar{J}_g \cdot \hat{n} = 0$

	node 1	node 2	node 3	
$\bar{J}_g \cdot \hat{n}=0$	node 4	node 5	node 6	$\bar{J}_g \cdot \hat{n}=0$
	node 7	node 8	node 9	

$\bar{J}_g \cdot \hat{n} = 0$

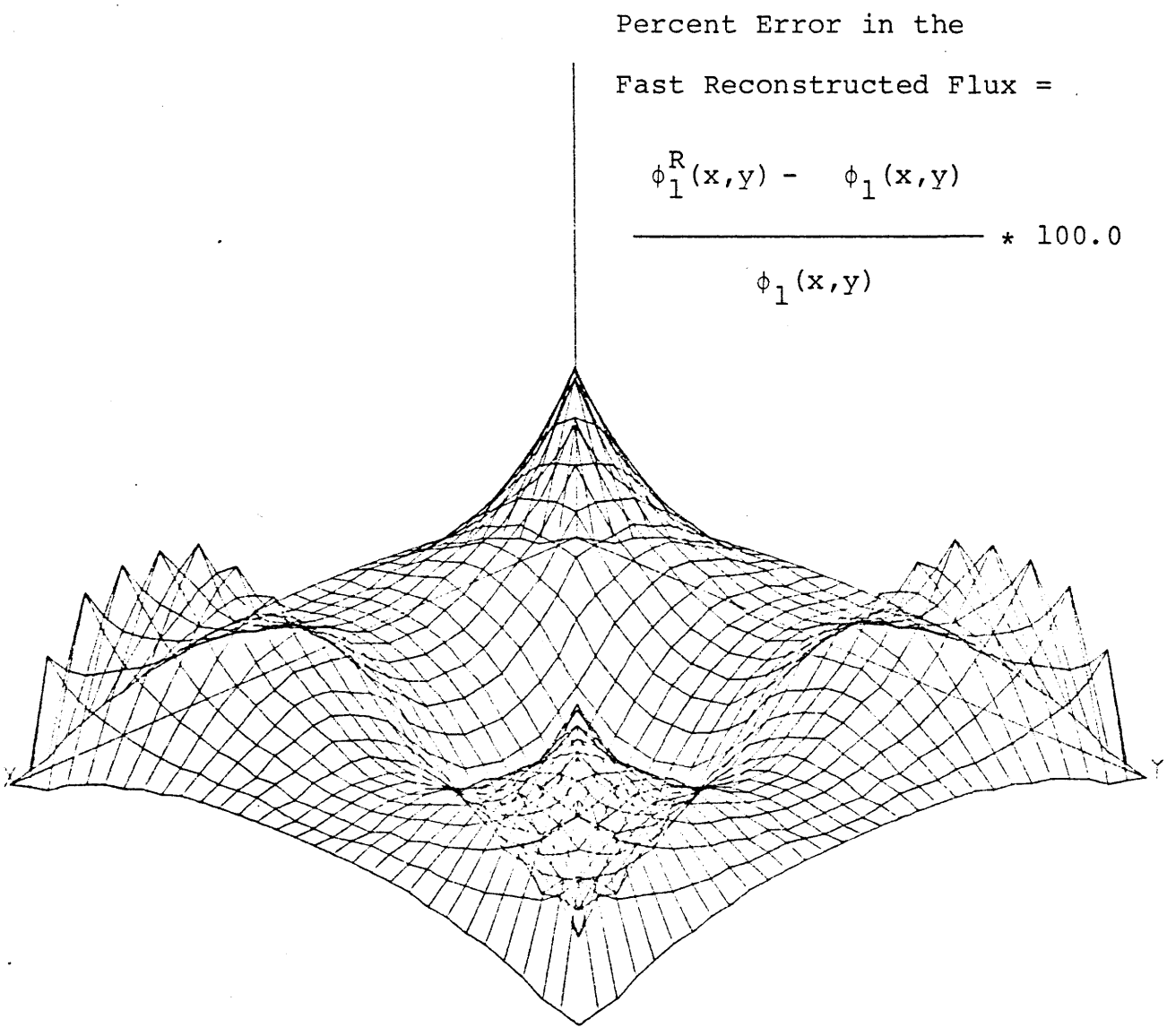

Figure A19.1: Percent Error in the Fast Reconstructed Flux from FORTE for Node 5 of Benchmark Problem 5 (FORTE input data from QUANDRY-ADF-AXS/CHIME)

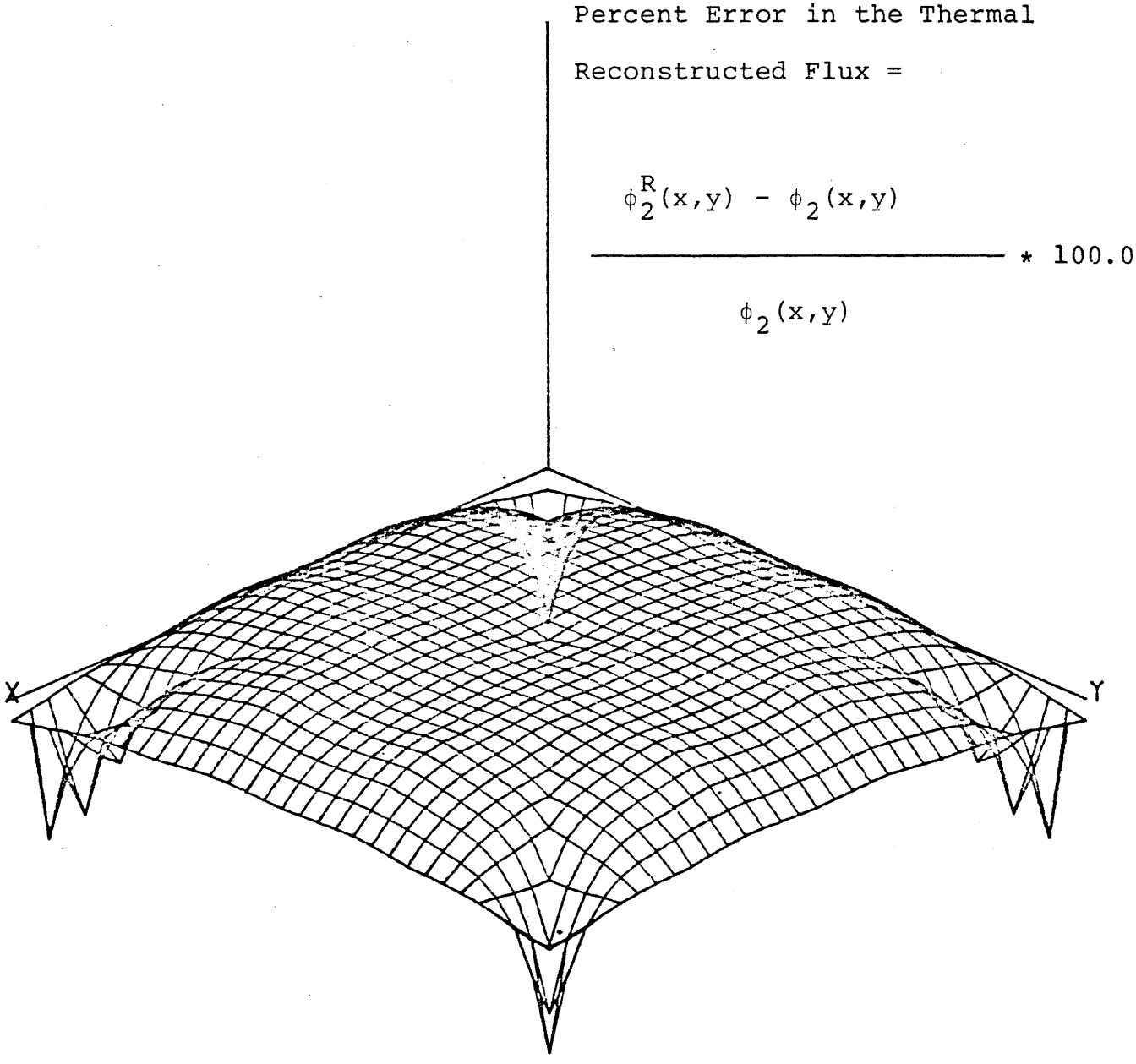

Figure A19.2: Percent Error in the Thermal Reconstructed Flux from FORTE for Node 5 of Benchmark Problem 5 (FORTE input data from QUANDRY-ADF-AXS/CHIME)

A19.2 Benchmark Problem 7 Error Plots (QUANDRY-ADF-AXS/CHIME input data for FORTE)

Benchmark problem 7 is a 3-by-3 node problem. The center node 5 is an unrodded fuel 1 assembly. The other nodes are homogeneous fuel 2. The sketch below gives the boundary conditions and node numbering for the problem. FORTE was used to reconstruct the fast and thermal flux in node 5 of this problem. As discussed in section A19.0 of this appendix, the input form function data for these FORTE runs was derived from a QUANDRY-ADF-AXS global calculation and a CHIME corner point interpolation.

$\phi_g = 0$

$\bar{J}_g \cdot \hat{n} = 0$

node 1	node 2	node 3
node 4	node 5	node 6
node 7	node 8	node 9

$\phi_g = 0$

$\bar{J}_g \cdot \hat{n} = 0$

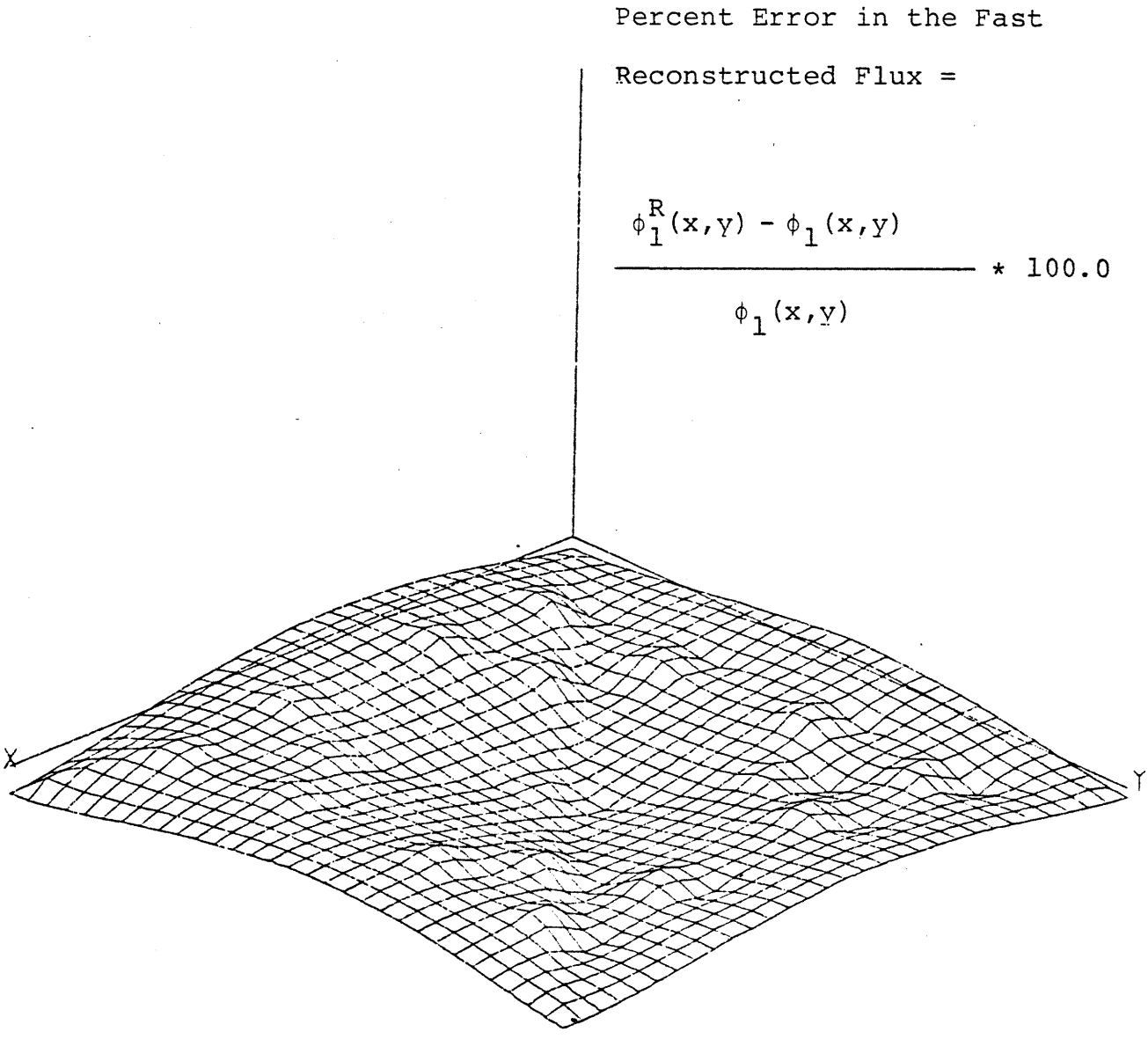

Figure A19.3: Percent Error in the Fast Reconstructed Flux from FORTE for Node 5 of Benchmark Problem 7 (FORTE input data from QUANDRY-ADF-AXS/CHIME)

Percent Error in the Thermal Reconstructed Flux =

$$\frac{\phi_2^R(x,y) - \phi_2(x,y)}{\phi_2(x,y)} * 100.0$$

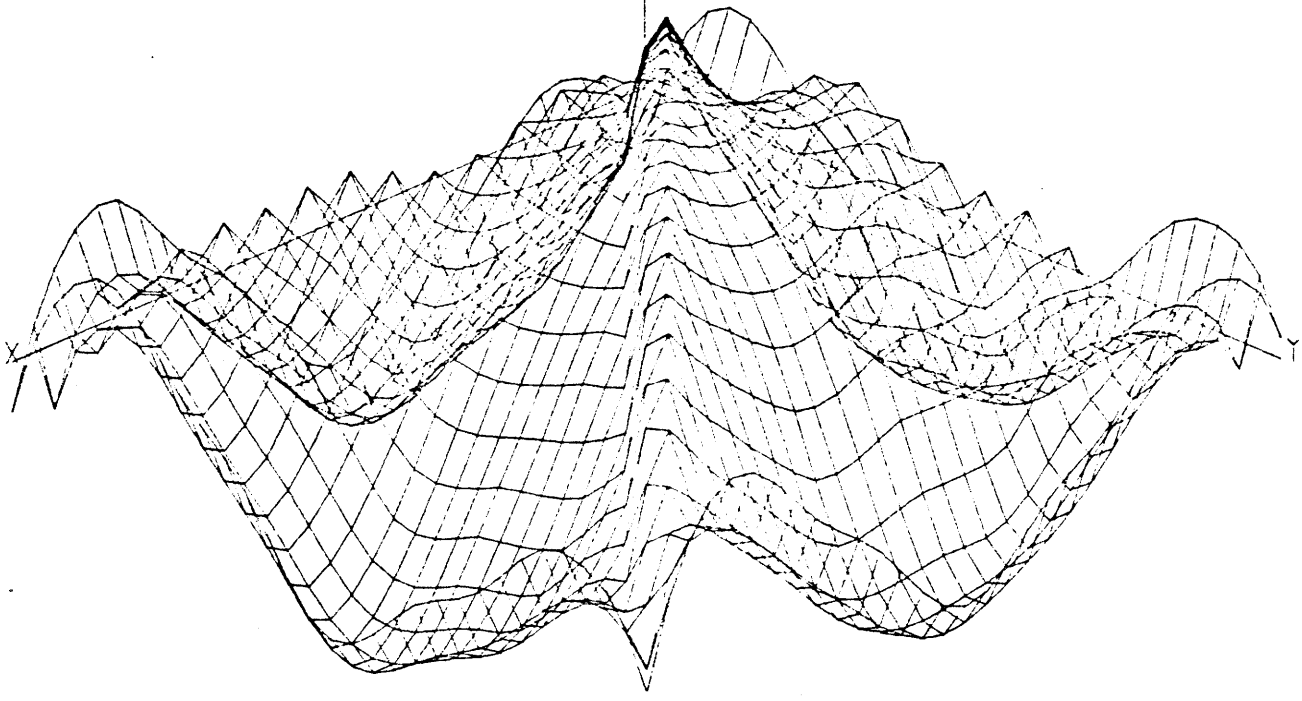

Figure A19.4: Percent Error in the Thermal Reconstructed Flux from FORTE for Node 5 of Benchmark Problem 7 (FORTE input data from QUANDRY-ADF-AXS/CHIME)

A19.3 Benchmark Problem 6 Error Plots I
(QUANDRY-ADF-AXS(from extended assembly calculations)/
CAMPANA input data for FORTE)

Benchmark problem 6 is the 4-by-4 quarter core with an explicitly represented steel baffle. The sketch below gives the boundary conditions and node numbering for the problem. FORTE was used to reconstruct the fast and thermal flux in nodes 10, 11, 13, 14 and 15 of this problem. The form function data for these FORTE runs was derived from a QUANDRY-ADF-AXS global calculation and a CAMPANA corner point interpolation.

$\phi_g = 0$

	node 1	node 2	node 3	node 4	
	node 5	node 6	node 7	node 8	
$\bar{J}_g \cdot \hat{n} = 0$	node 9	node 10	node 11	node 12	$\phi_g = 0$
	node 13	node 14	node 15	node 16	

$\bar{J}_g \cdot \hat{n} = 0$

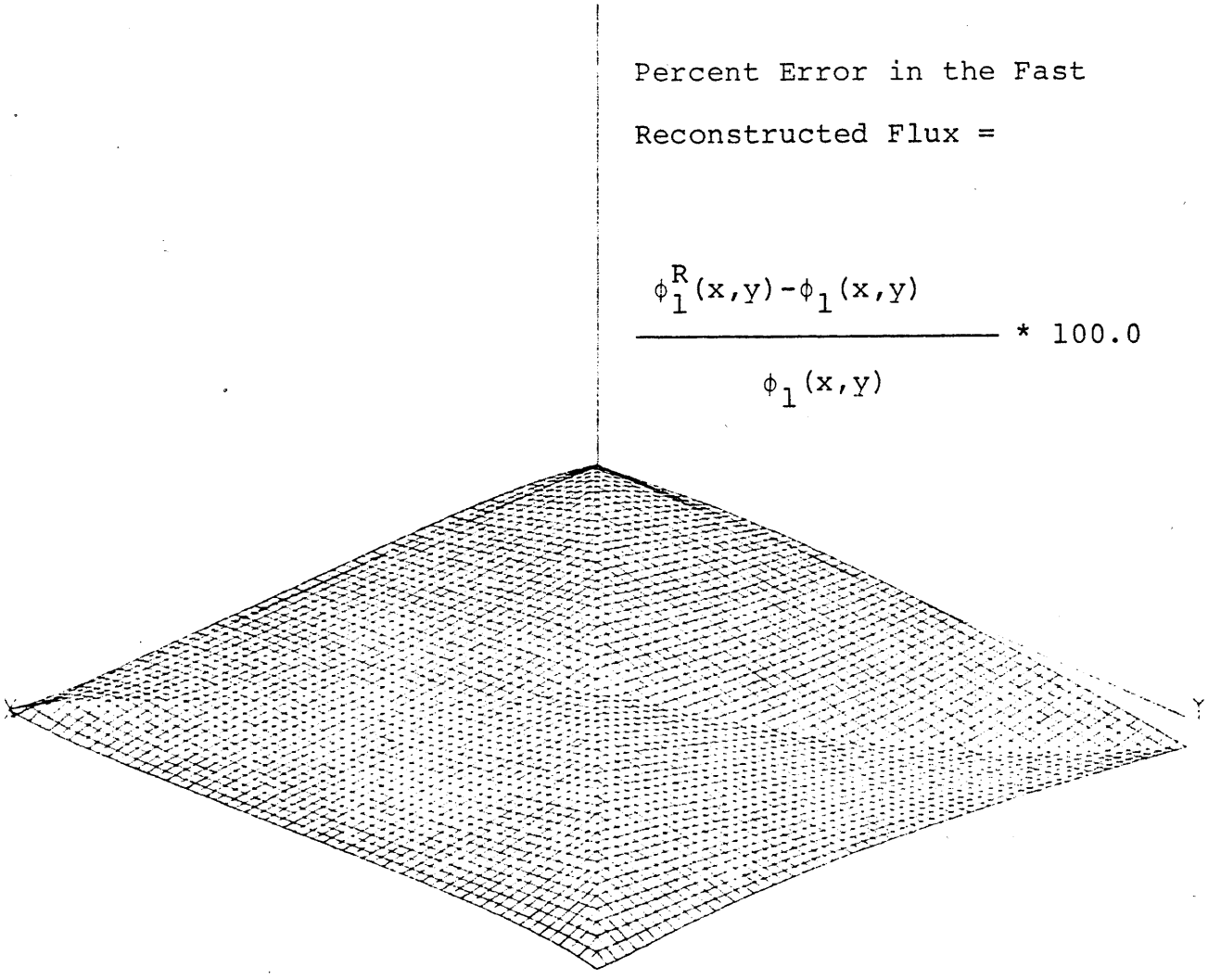

Figure A19.5: Percent Error in the Fast Reconstructed Flux from FORTE for Node 10 of Benchmark Problem 6 (FORTE input data from QUANDRY-ADF-AXS/ CAMPANA)

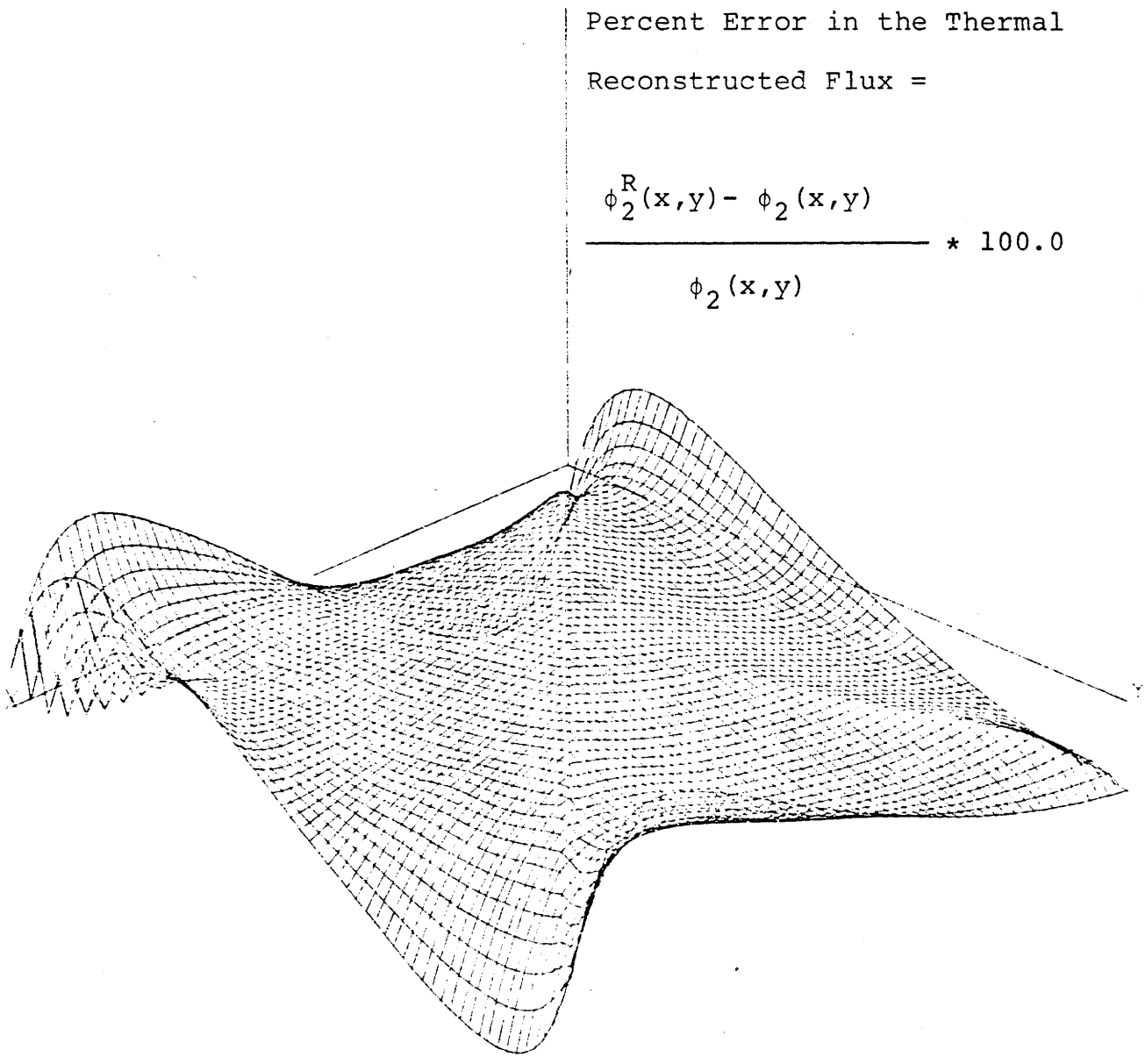

Figure A19.6: Percent Error in the Thermal Reconstructed Flux from FORTE for Node 10 of Benchmark Problem 6 (FORTE input data from QUANDRY-ADF-AXS/CAMPANA)

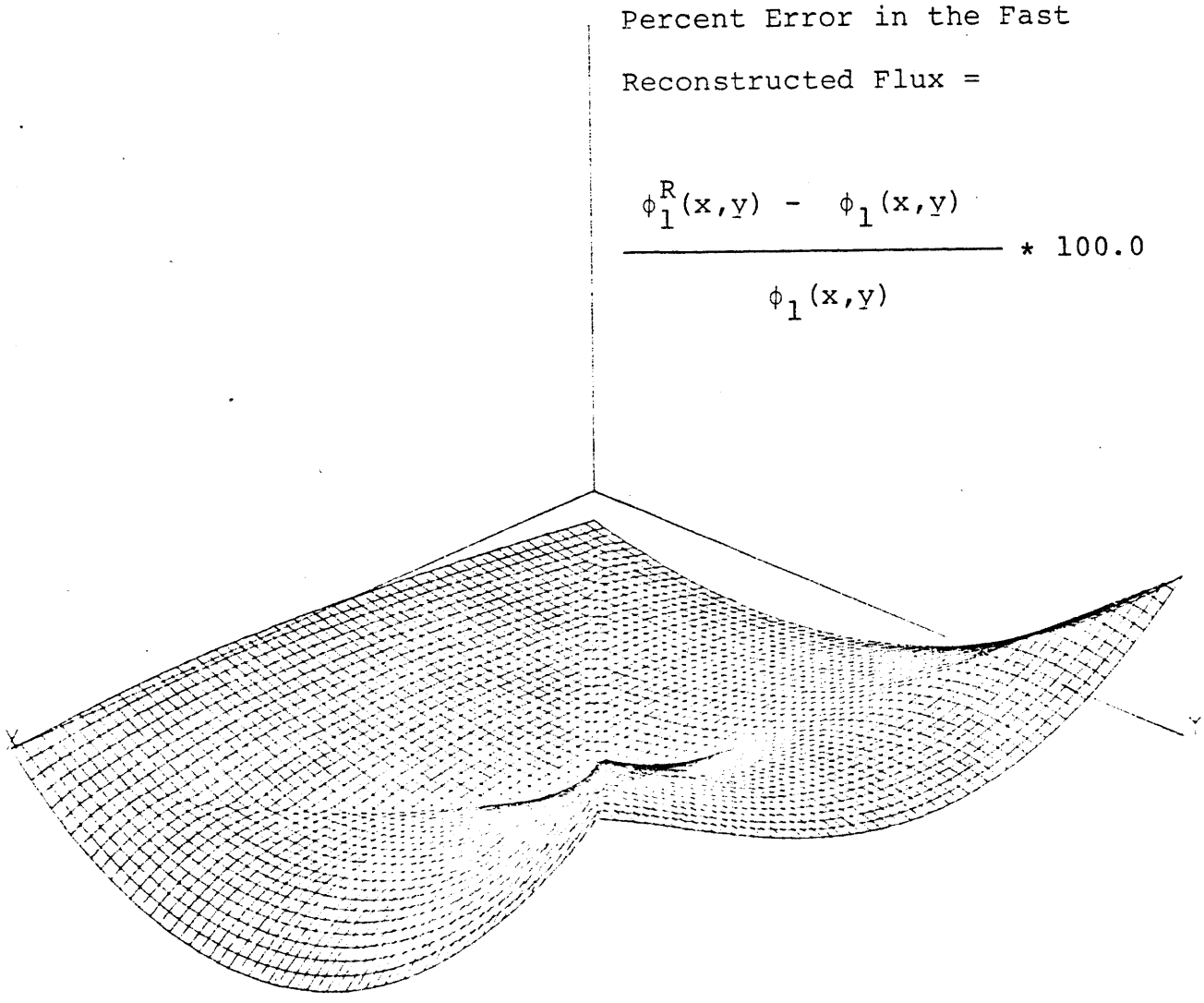

Figure A19.7: Percent Error in the Fast Reconstructed Flux from FORTE for Node 11 of Benchmark Problem 6 (FORTE input data from QUANDRY-ADF-AXS/ CAMPANA)

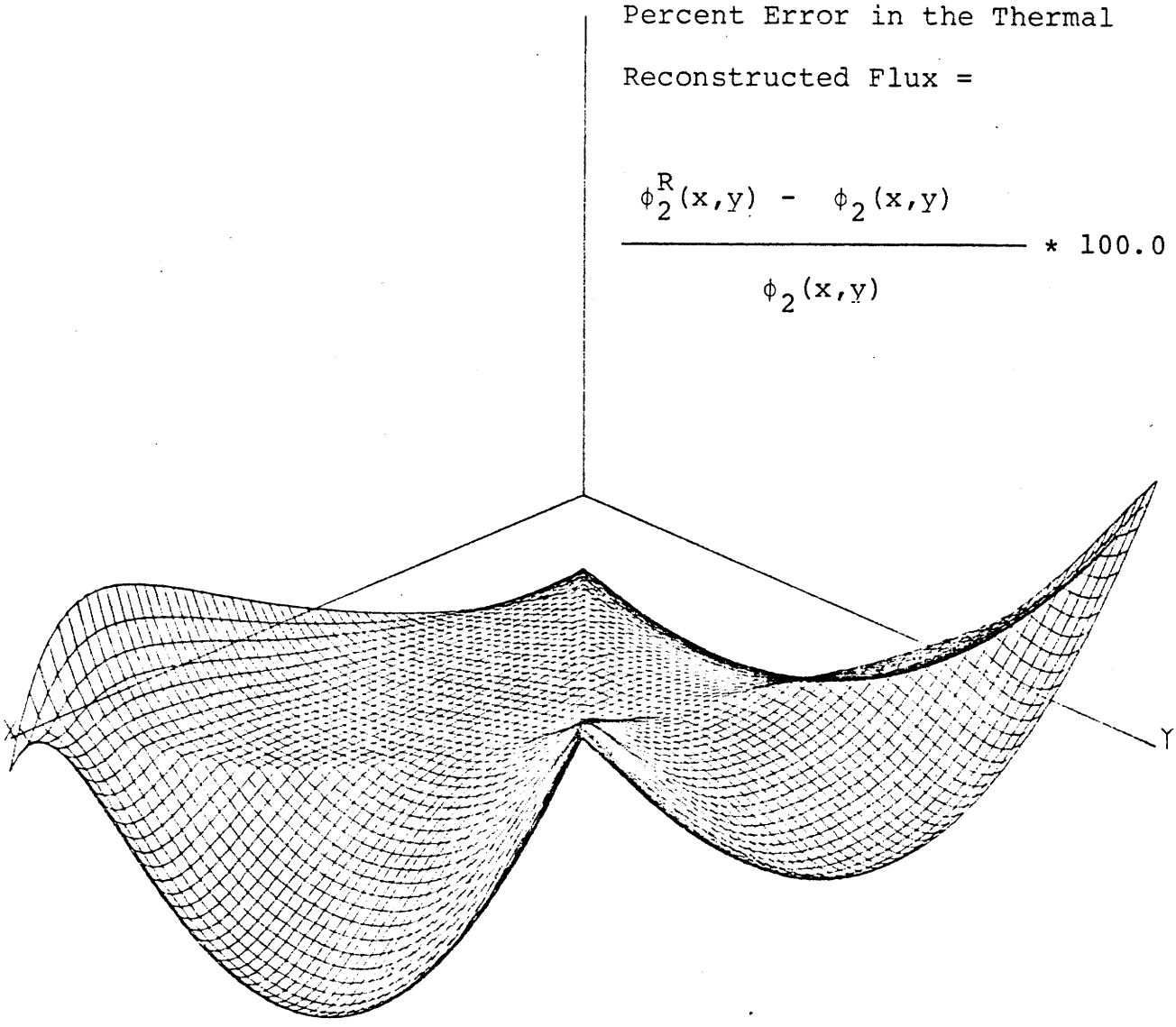

Figure A19.8: Percent Error in the Thermal Reconstructed Flux from FORTE for Node 11 of Benchmark Problem 6 (FORTE input data from QUANDRY-ADF-AXS/CAMPANA)

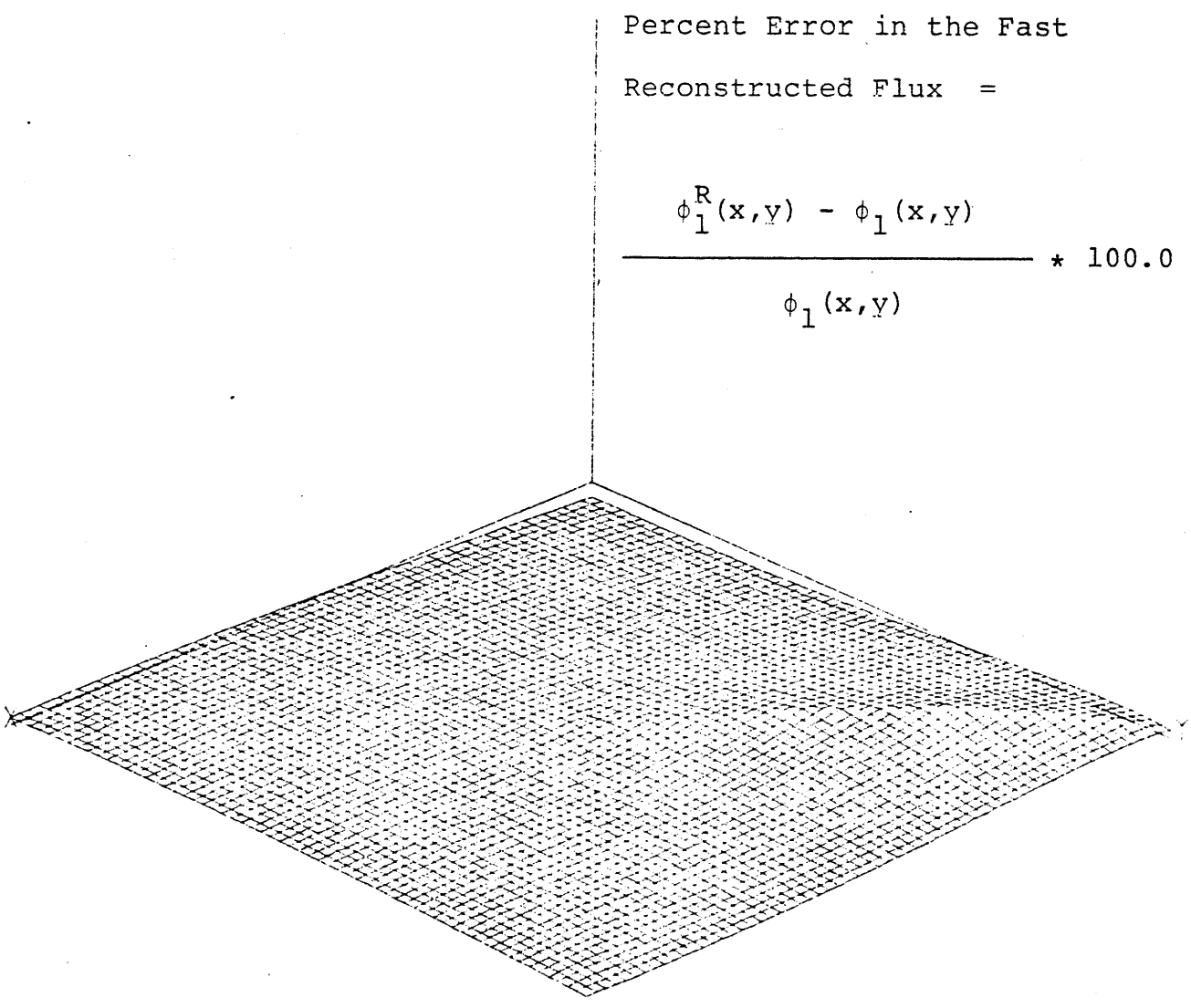

Figure A19.9: Percent Error in the Fast Reconstructed Flux from FORTE for Node 13 of Benchmark Problem 6 (FORTE input data from QUANDRY-ADF-AXS/ CAMPANA)

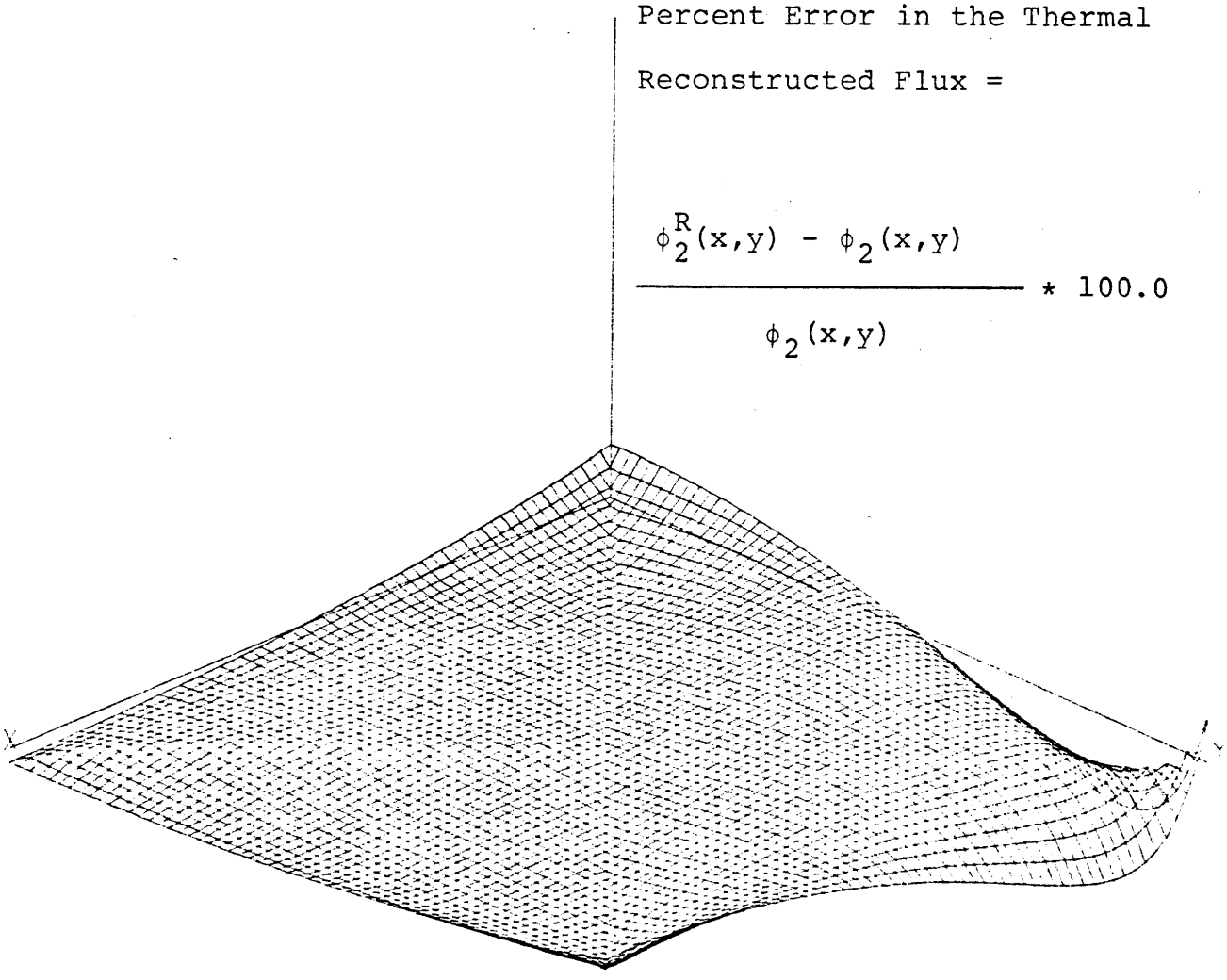

Figure A19.10: Percent Error in the Thermal Reconstructed Flux from FORTE for Node 13 of Benchmark Problem 6 (FORTE input data from QUANDRY-ADF-AXS/CAMPANA)

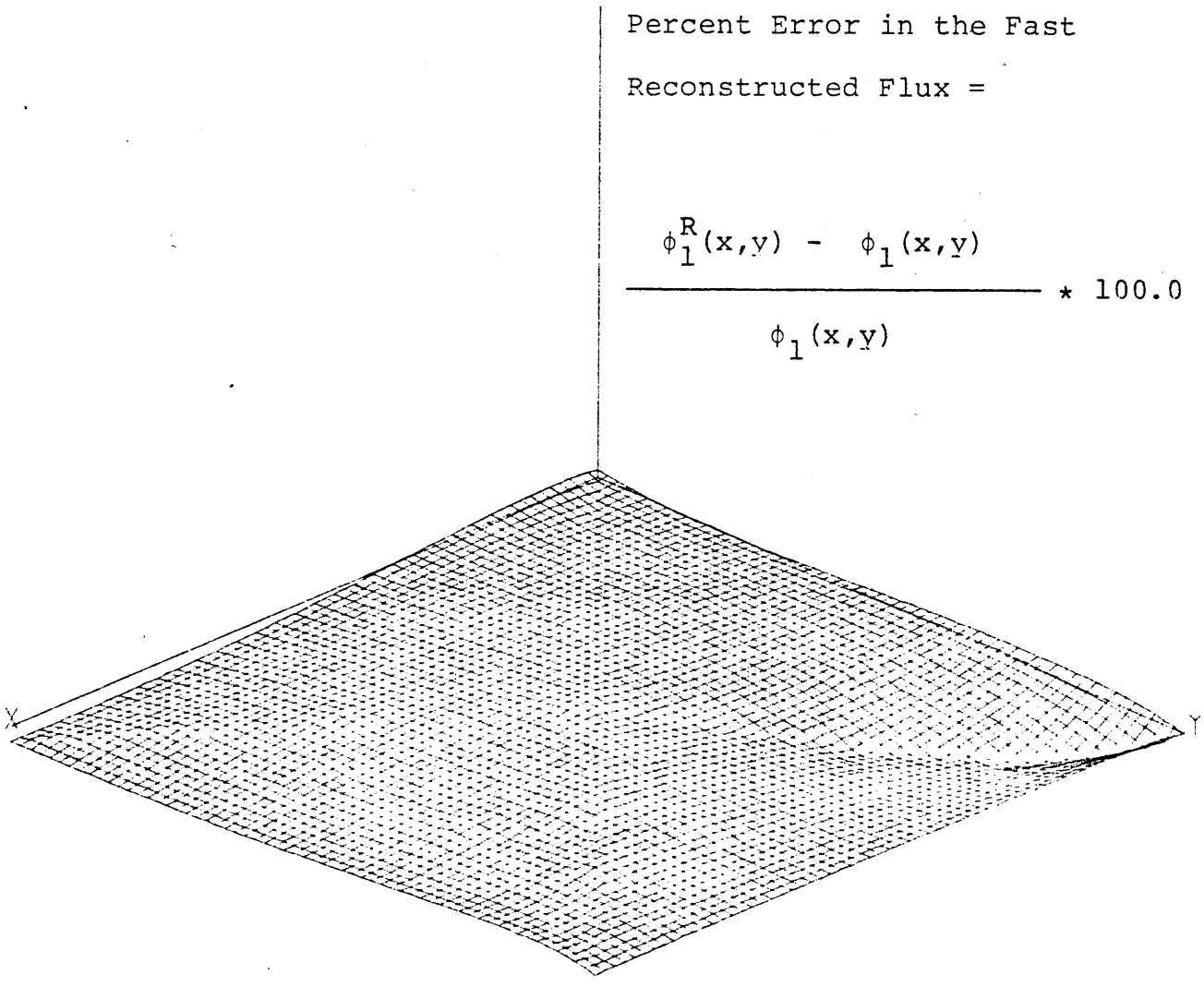

Figure A19.11: Percent Error in the Fast Reconstructed Flux from FORTE for Node 14 of Benchmark Problem 6 (FORTE input data from QUANDRY-ADF-AXS/ CAMPANA)

Percent Error in the Thermal Reconstructed Flux =

$$\frac{\phi_2^R(x,y) - \phi_2(x,y)}{\phi_2(x,y)} * 100.0$$

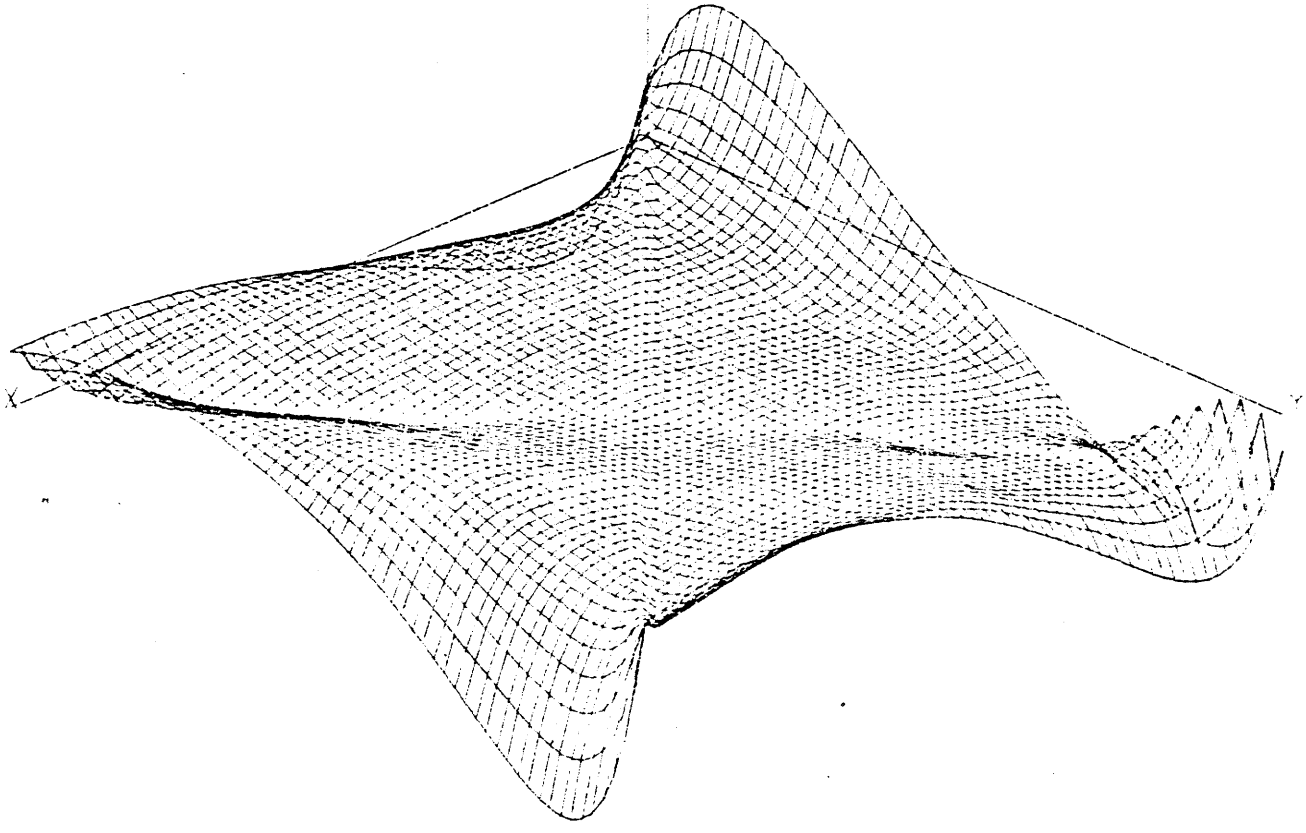

Figure A19.12: Percent Error in the Thermal Reconstructed Flux from FORTE for Node 14 of Benchmark Problem 6 (FORTE input data from QUANDRY-ADF-AXS/CAMPANA)

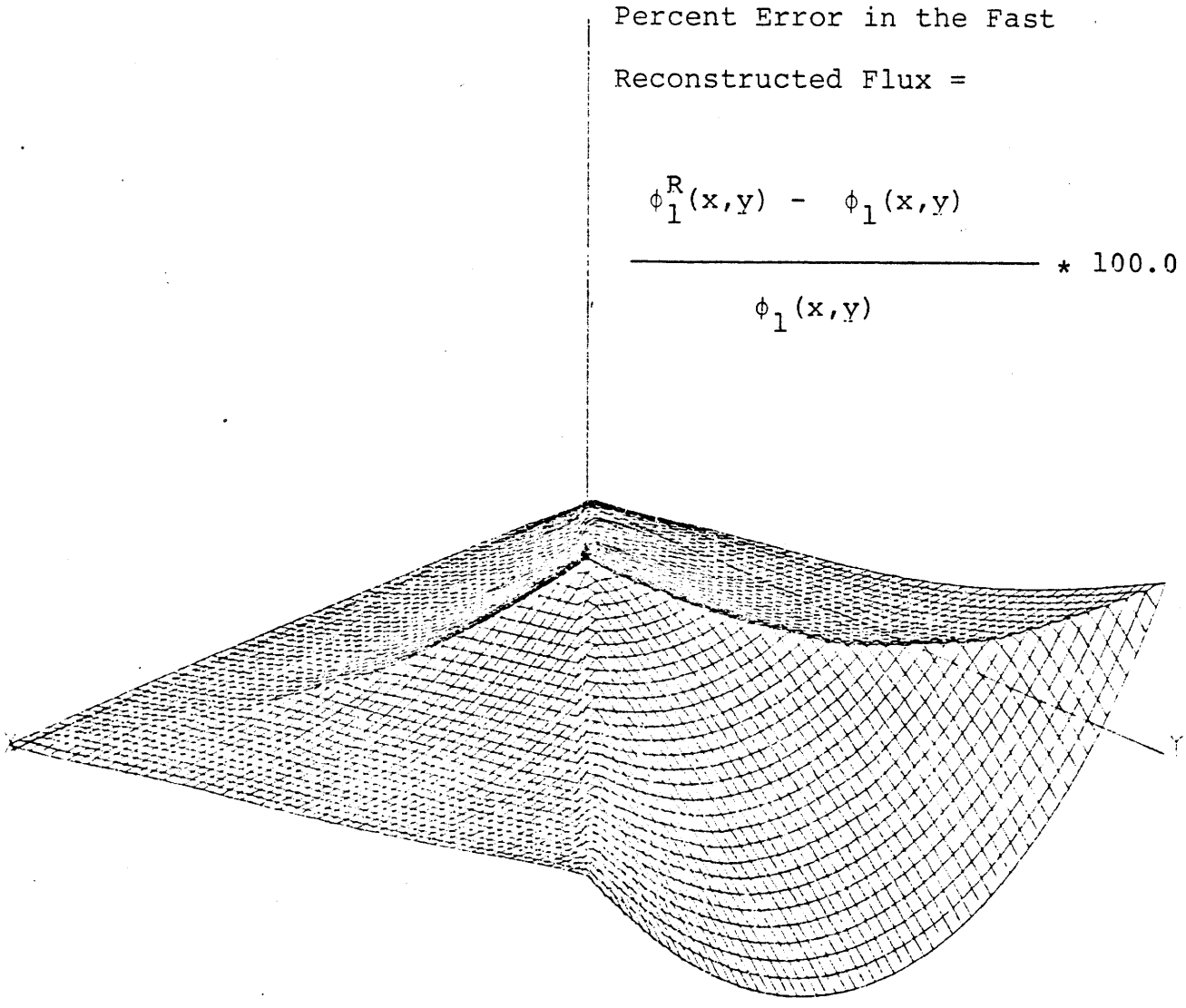

Figure A19.13: Percent Error in the Fast Reconstructed Flux from FORTE for Node 15 of Benchmark Problem 6 (FORTE input data from QUANDRY-ADF-AXS/ CAMPANA)

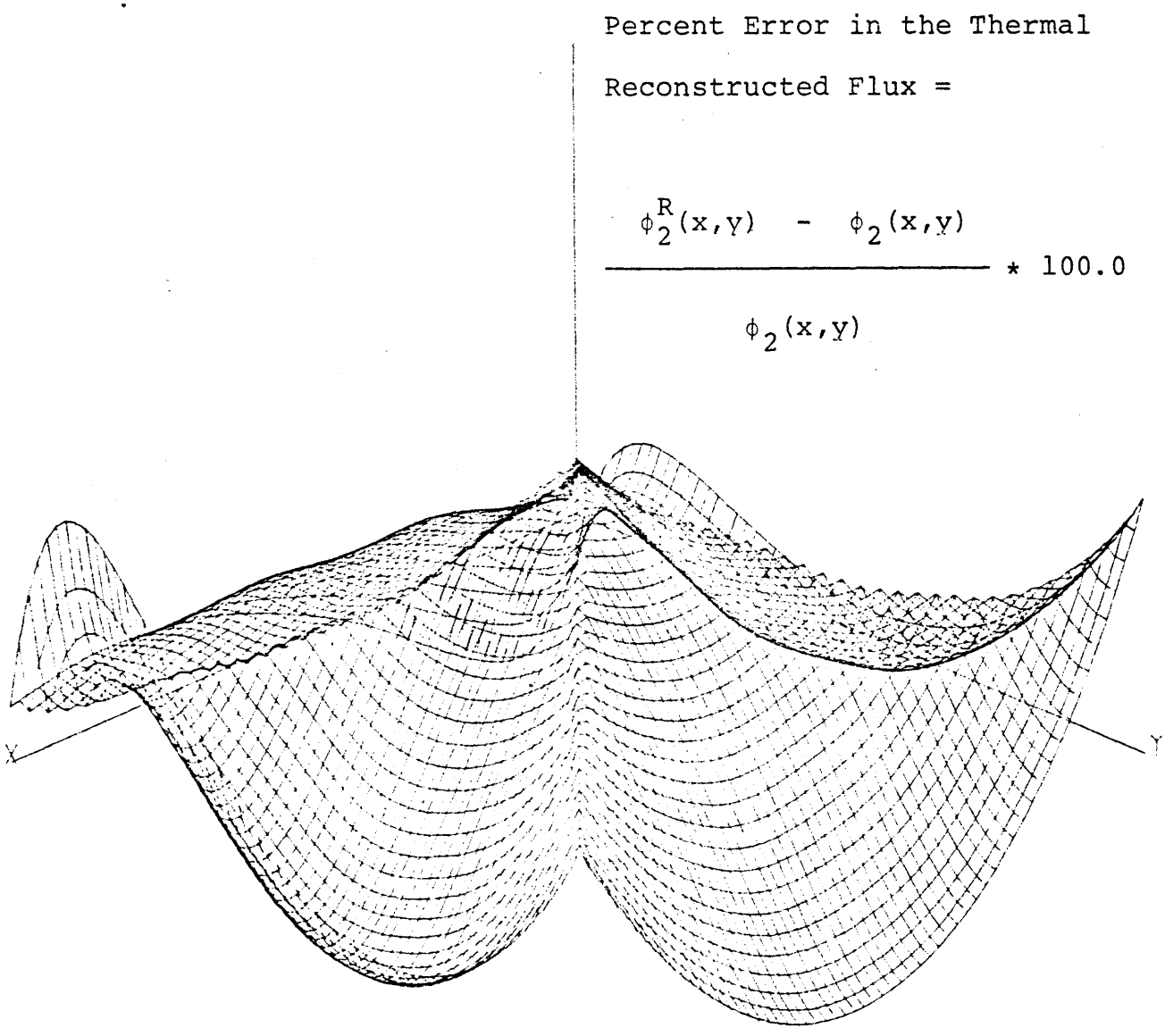

Figure A19.14: Percent Error in the Thermal Reconstructed Flux from FORTE for Node 15 of Benchmark Problem 6 (FORTE input data from QUANDRY-ADF-AXS/CAMPANA)

A19.4 Benchmark Problem 6 Error Plots II (Reference corner point, surface-averaged and volume-averaged form function data for FORTE calculated directly from the reference form functions in Appendix 16, i.e., these reference form functions are based on extended assembly calculations.)

For the two fueled nodes 11 and 15 next to the steel baffle in benchmark problem 6, FORTE was tested by inputting reference corner point, surface-averaged and volume-averaged form function data. This data was derived directly from the reference form functions in Appendix 16. The form functions in Appendix 16 are based on extended assembly calculations.

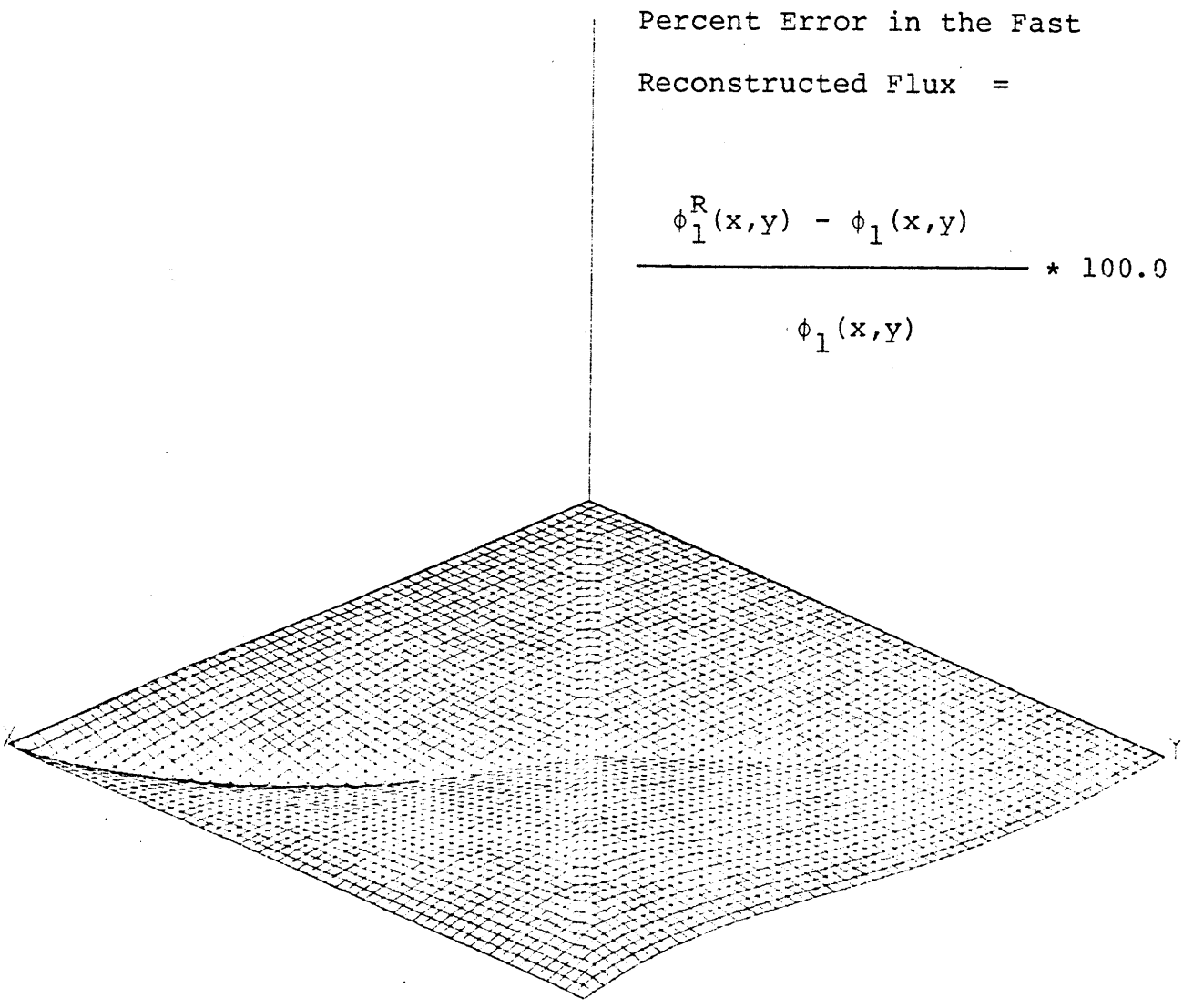

Figure A19.15: Percent Error in the Fast Reconstructed Flux from FORTE for Node 11 of Benchmark Problem 6 (FORTE input data from Reference Form Functions in Appendix 16)

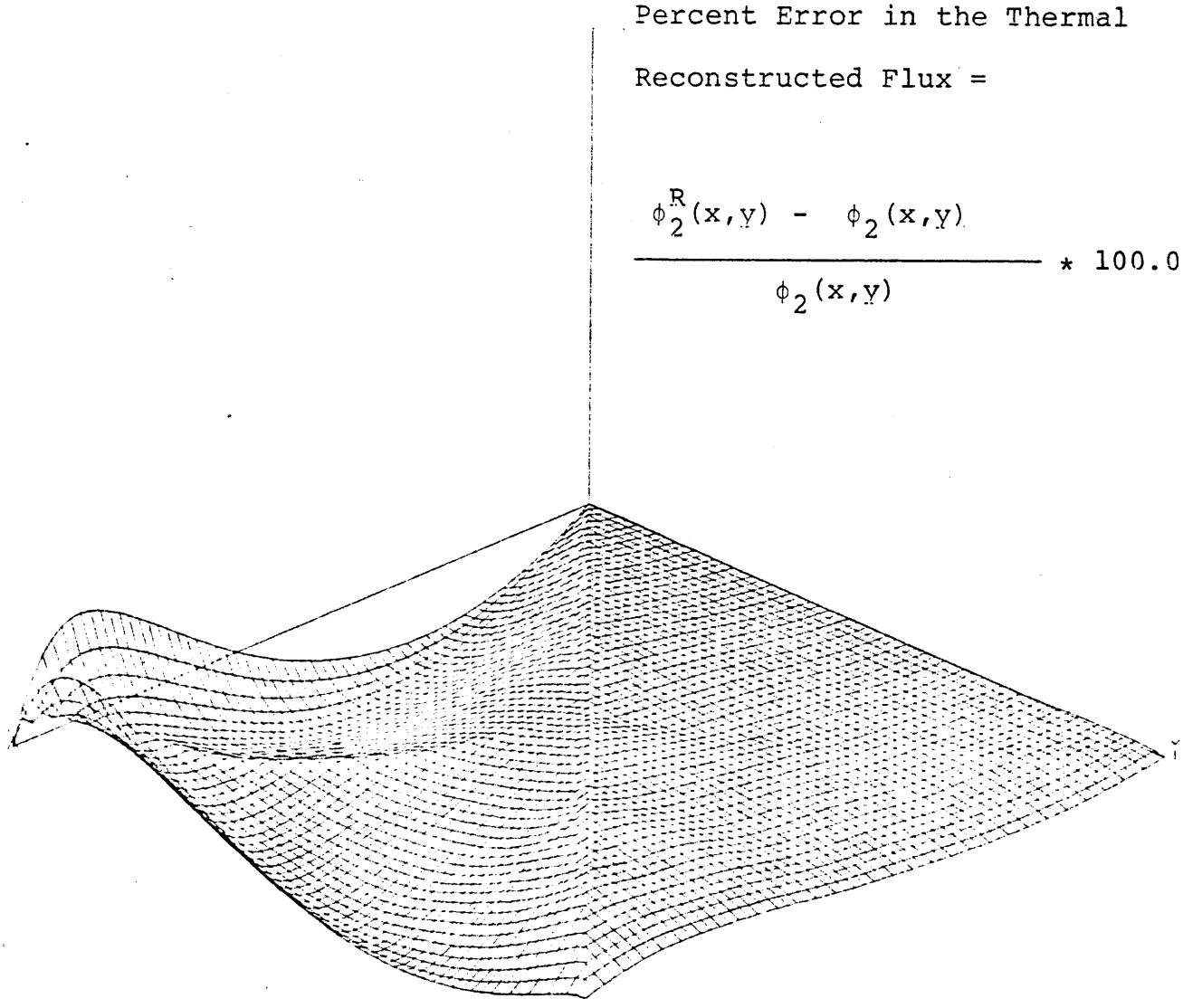

Figure A19.16: Percent Error in the Thermal Reconstructed Flux from FORTE for Node 11 of Benchmark Problem 6 (FORTE input data from Form Functions in Appendix 16)

Percent Error in the Fast Reconstructed Flux =

$$\frac{\phi_1^R(x,y) - \phi_1(x,y)}{\phi_1(x,y)} * 100.0$$

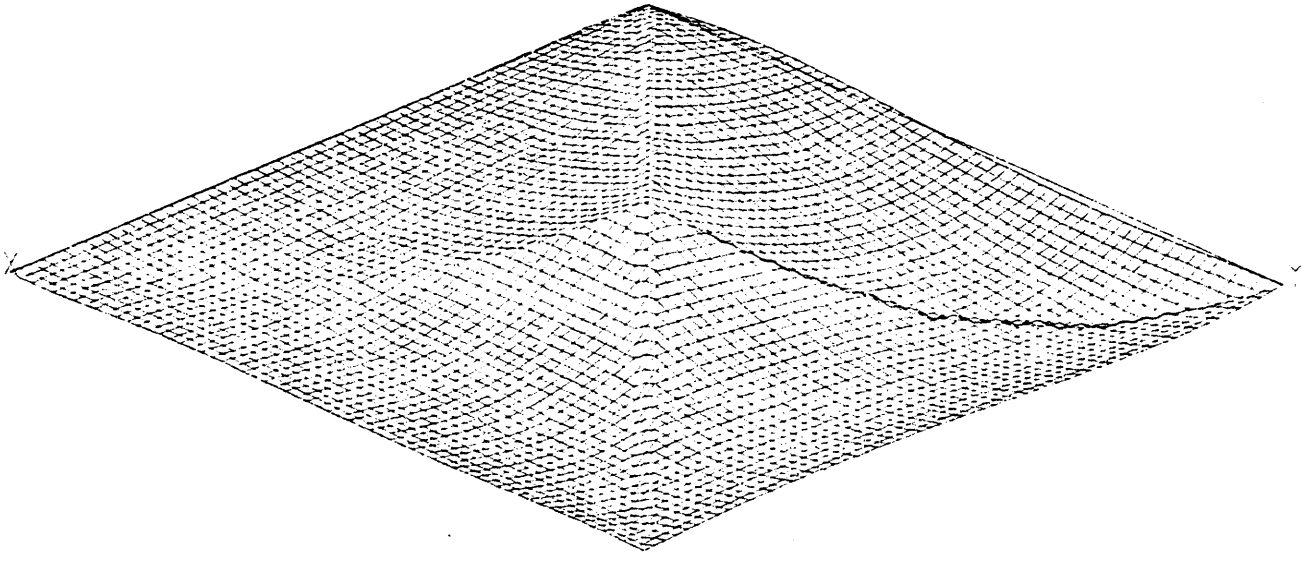

Figure A19.17: Percent Error in the Fast Reconstructed Flux from FORTE for Node 15 of Benchmark Problem 6 (FORTE input data from Form Functions in Appendix 16)

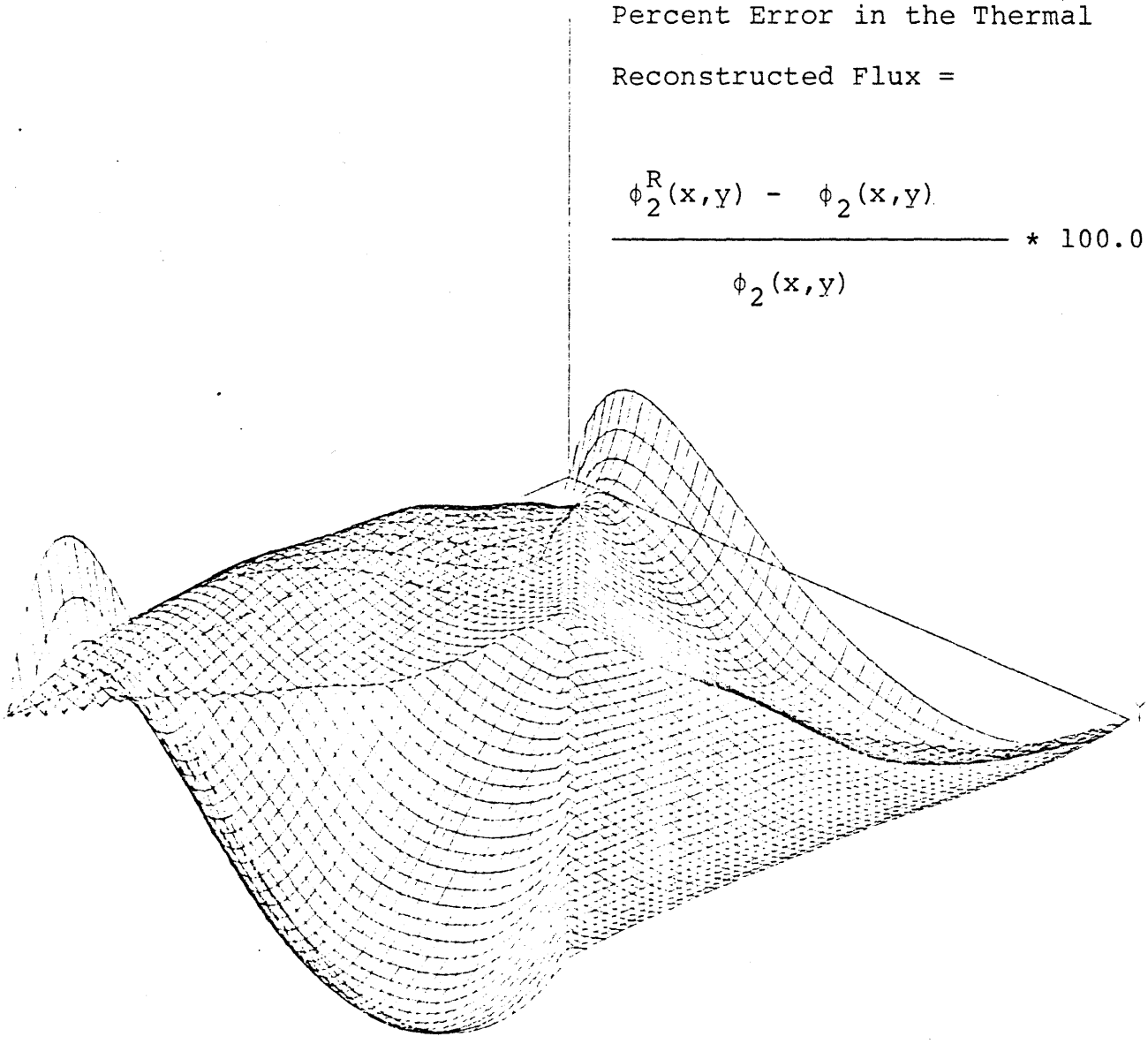

Figure A19.18: Percent Error in the Thermal Reconstructed Flux from FORTE for Node 15 of Benchmark Problem 6 (FORTE input data from Form Functions in Appendix 16)

A19.5 Benchmark Problem 6 Error Plots III (Reference corner point, surface-averaged and volume-averaged form function data for FORTE calculated directly from the reference form functions in Appendix 15, i.e., these reference form functions are based on assembly fluxes derived from assembly calculations employing zero-net-current boundary conditions.)

For the fueled node 11 at the jag in the baffle of benchmark problem 6, FORTE was tested by inputting reference corner point, surface-averaged and volume-averaged form function data. This data was derived directly from the reference form functions in Appendix 15. The form functions in Appendix 15 are based on assembly fluxes which come from assembly calculations employing zero-net-current boundary conditions.

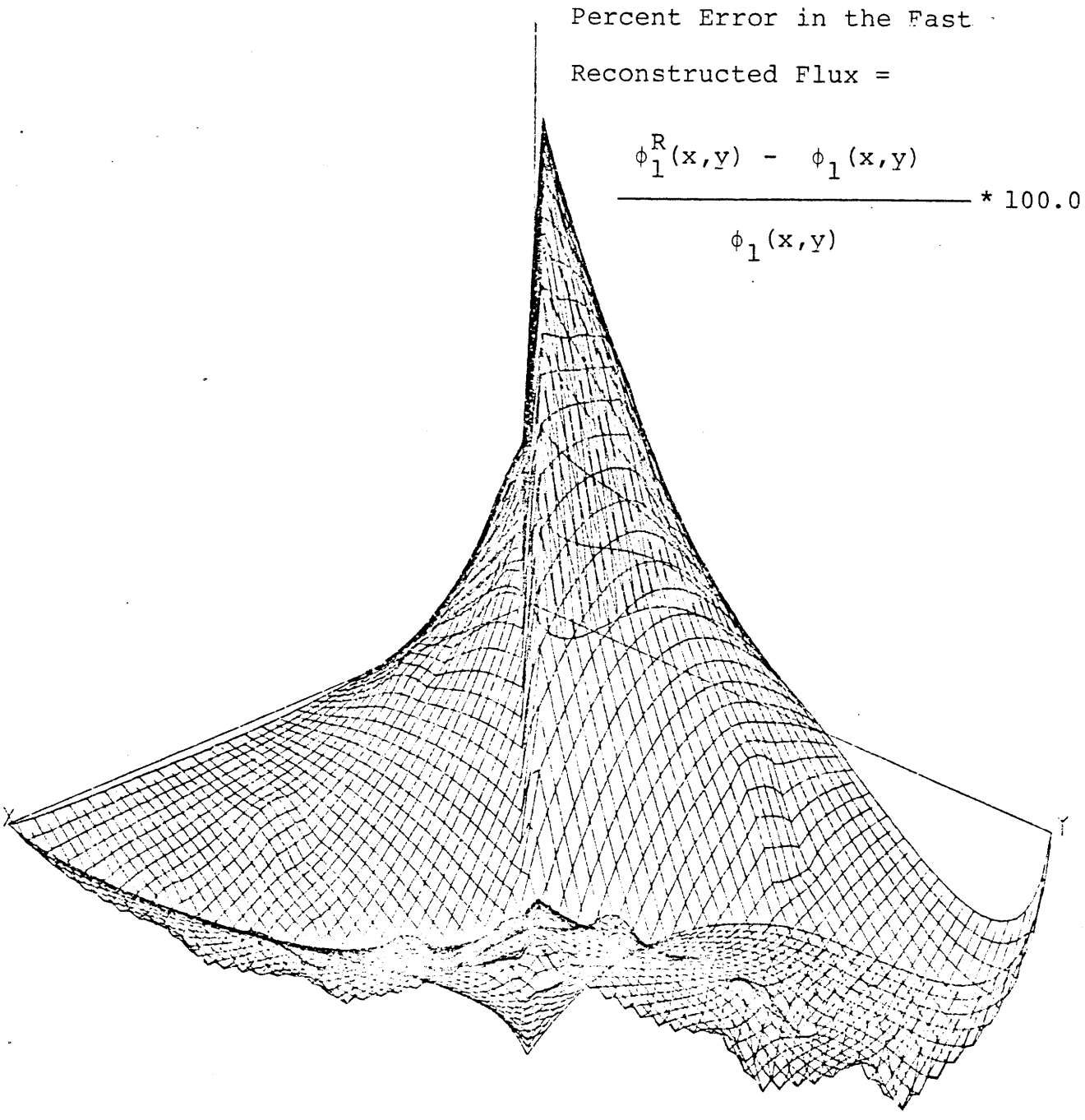

Figure A19.19: Percent Error in the Fast Reconstructed Flux from FORTE for Node 11 of Benchmark Problem 6 (FORTE input data from Form Functions in Appendix 15)

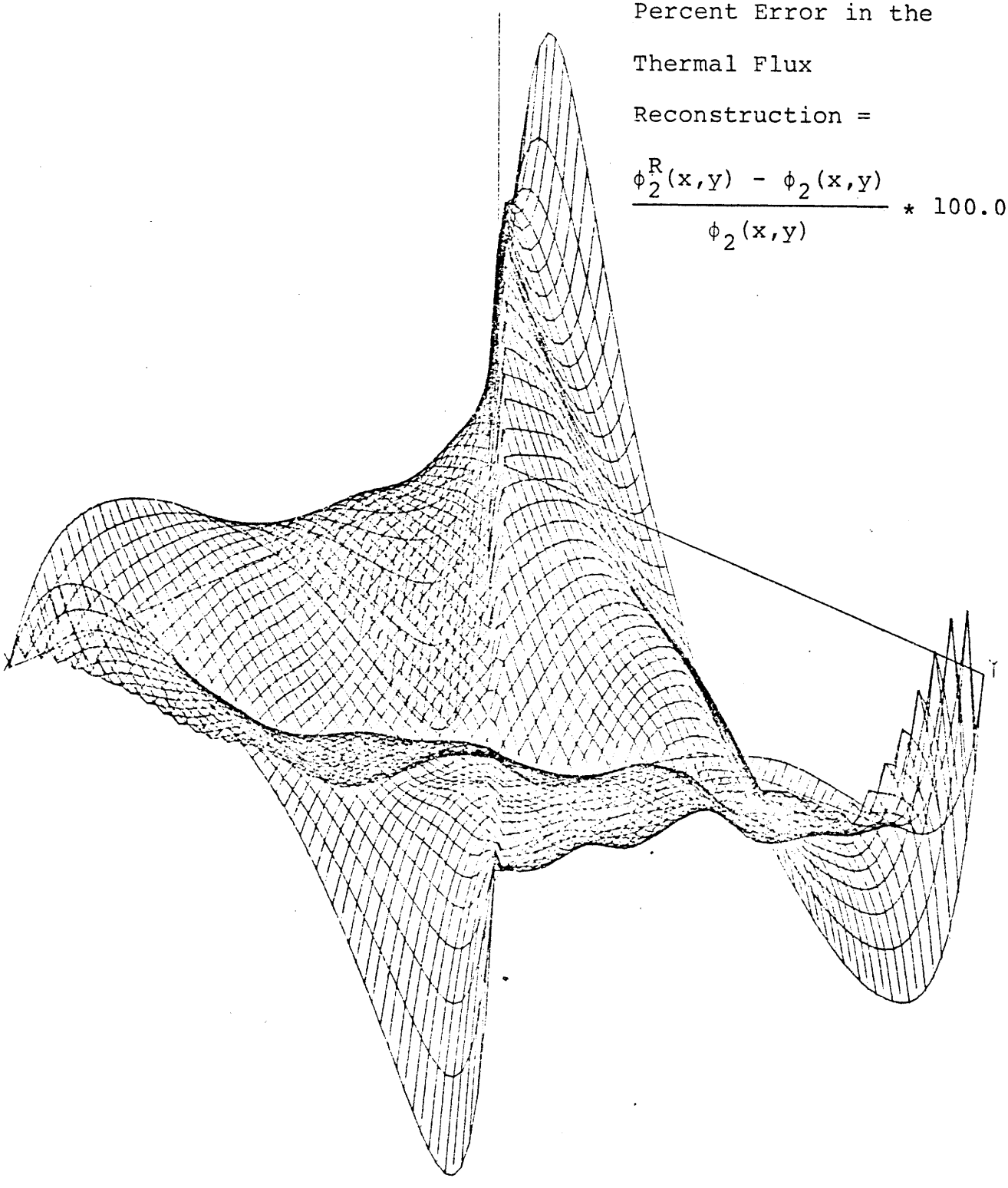

Figure A19.20: Percent Error in the Thermal Reconstructed Flux from FORTE for Node 11 of Benchmark Problem 6 (FORTE input data from Form Functions in Appendix 15)

Appendix 20

RECONSTRUCTED FORM FUNCTION PLOTS FROM FORTE

A20.0 Introduction

A20.1 Benchmark Problem 5 Reconstructed Form Function Plots (QUANDRY-ADF-AXS/CHIME input data for FORTE)

A20.2 Benchmark Problem 7 Reconstructed Form Function Plots (QUANDRY-ADF-AXS/CHIME input data for FORTE)

A20.3 Benchmark Problem 6 Reconstructed Form Function Plots I (QUANDRY-ADF-AXS(from extended assembly calculations)/CAMPANA input data for FORTE)

A20.4 Benchmark Problem 6 Reconstructed Form Function Plots II (Reference corner point, surface-averaged and volume-averaged form function data for FORTE calculated directly from the reference form functions in Appendix 16, i.e., these reference form functions are based on extended assembly calculations.)

A20.5 Benchmark Problem 6 Reconstructed Form Function Plots III (Reference corner point, surface-averaged and volume-averaged form function data for FORTE calculated directly from the reference form functions in Appendix 15, i.e., these reference form functions are based on assembly fluxes derived from assembly calculations employing zero-net-current boundary conditions.)

A20.0 Introduction

This appendix contains plots of the fast and thermal reconstructed form functions from the FORTE code. The symbol, $F_g^R(x,y)$, is used for the reconstructed form function in group g. Form functions are presented for some of the nodes in benchmark problems 5, 6 and 7.

The twenty plots in this appendix correspond on a one-to-one basis with the twenty error plots in Appendix 19. Thus the plots in Appendix 19 illustrate the percent error in the (approximate) reconstructed form functions displayed in this appendix. Hence the remarks in Appendix 19 concerning the source of the input data for the FORTE code also apply to this appendix. This means that the corner point, surface-averaged and volume-averaged form function values in sections 20.1, 20.2 and 20.3 are derived from inexpensive QUANDRY-ADF-AXS runs and from CHIME or CAMPANA heterogeneous corner point flux interpolations. Thus the results in sections 20.1, 20.2 and 20.3 do not rely on information from the expensive global heterogeneous flux calculations.

In section 20.4 and 20.5 FORTE is tested by inputting reference corner point, surface-averaged and volume-averaged form function data. The difference is that the form functions in section 20.4 are based on extended assembly calculations and the form functions in section 20.5 are based on assembly calculations with zero-net-current boundary conditions.

A20.1 Benchmark Problem 5 Reconstructed Form Function Plots (QUANDRY-ADF-AXS/CHIME input data for FORTE)

Benchmark problem 5 is the infinite checkerboard of unrodded fuel type 1 and fuel type 2 assemblies. The sketch below gives the boundary conditions and node numbering for this problem. The flux reconstruction was performed in node 5.

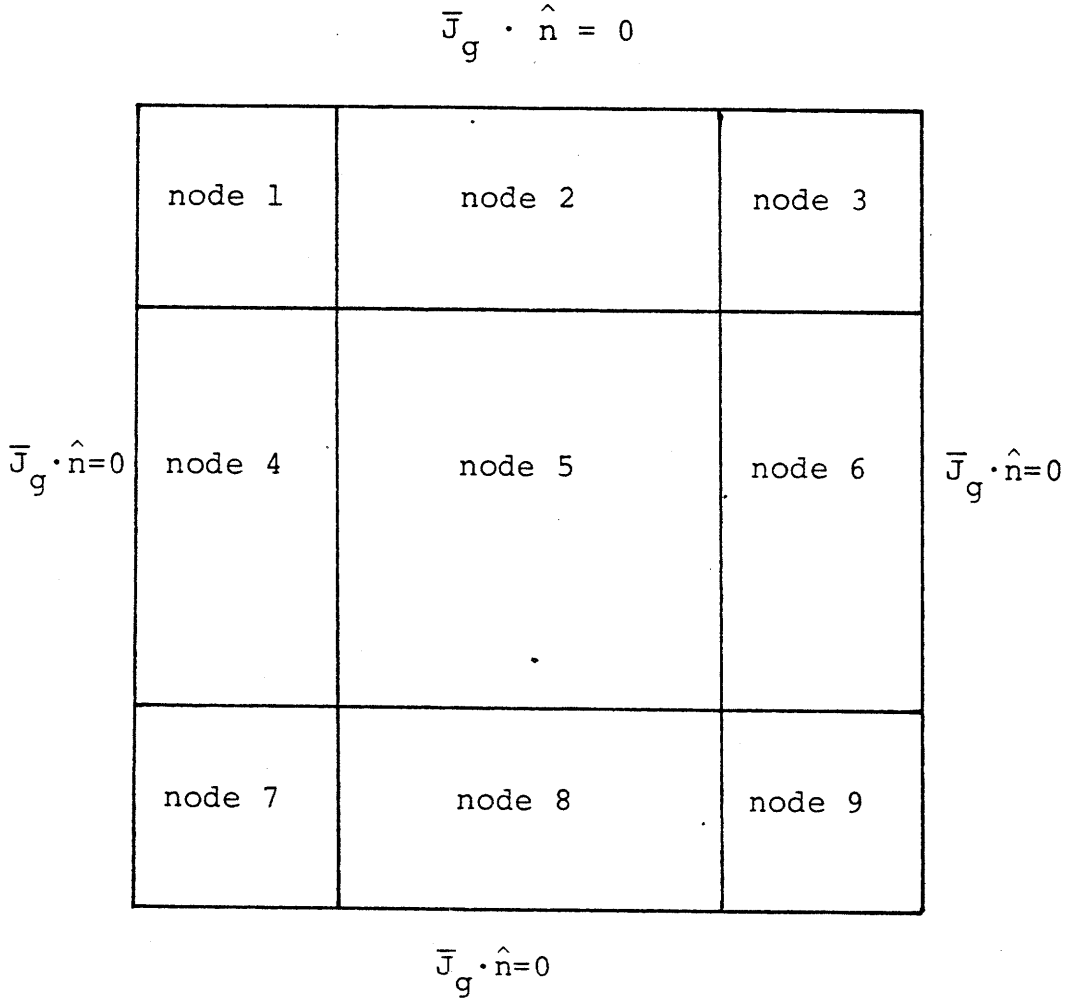

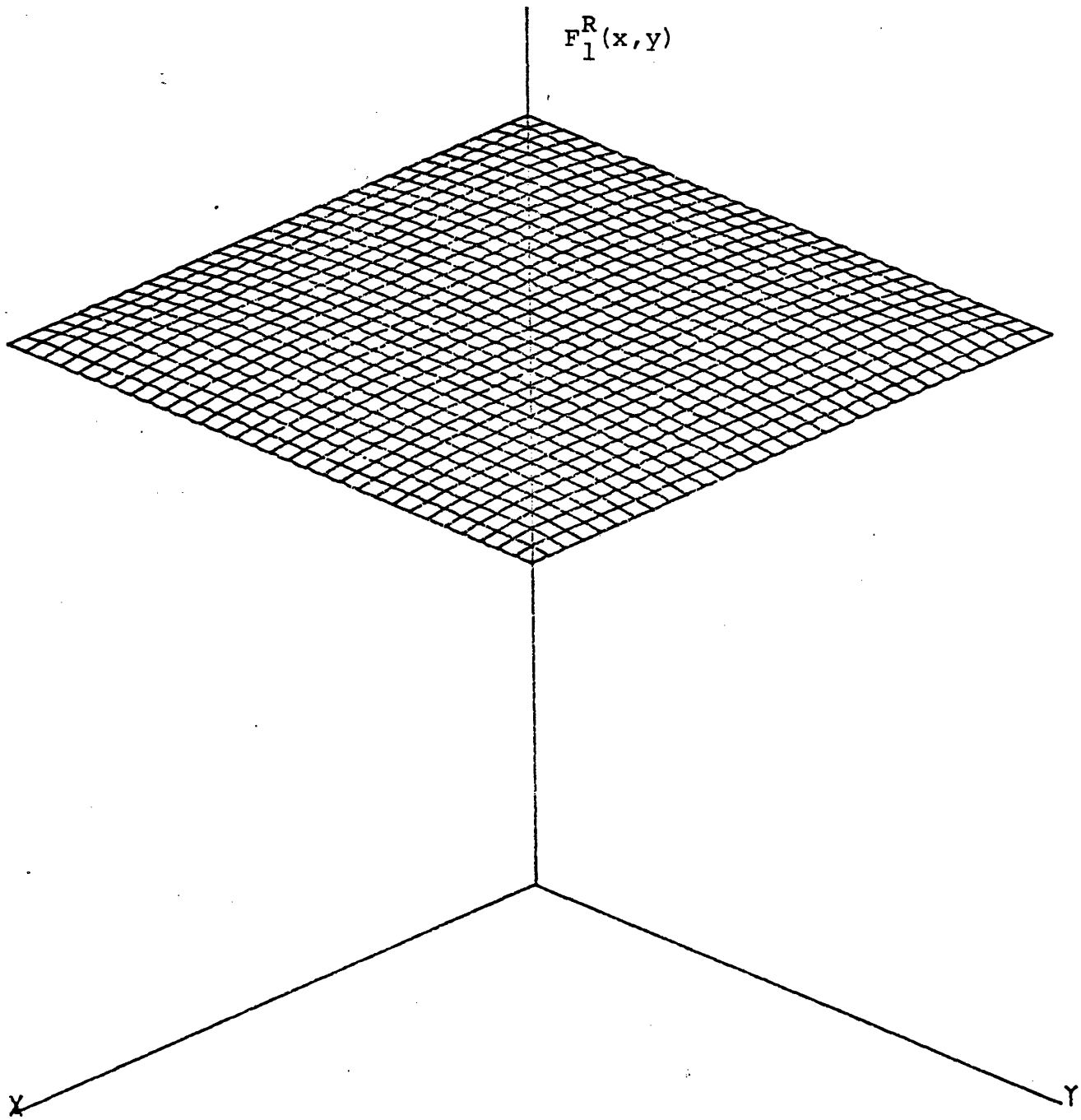

Figure A20.1: The Reconstructed Fast Form Function from FORTE for Node 5 of Benchmark Problem 5 (FORTE input data from QUANDRY-ADF-AXS/CHIME)

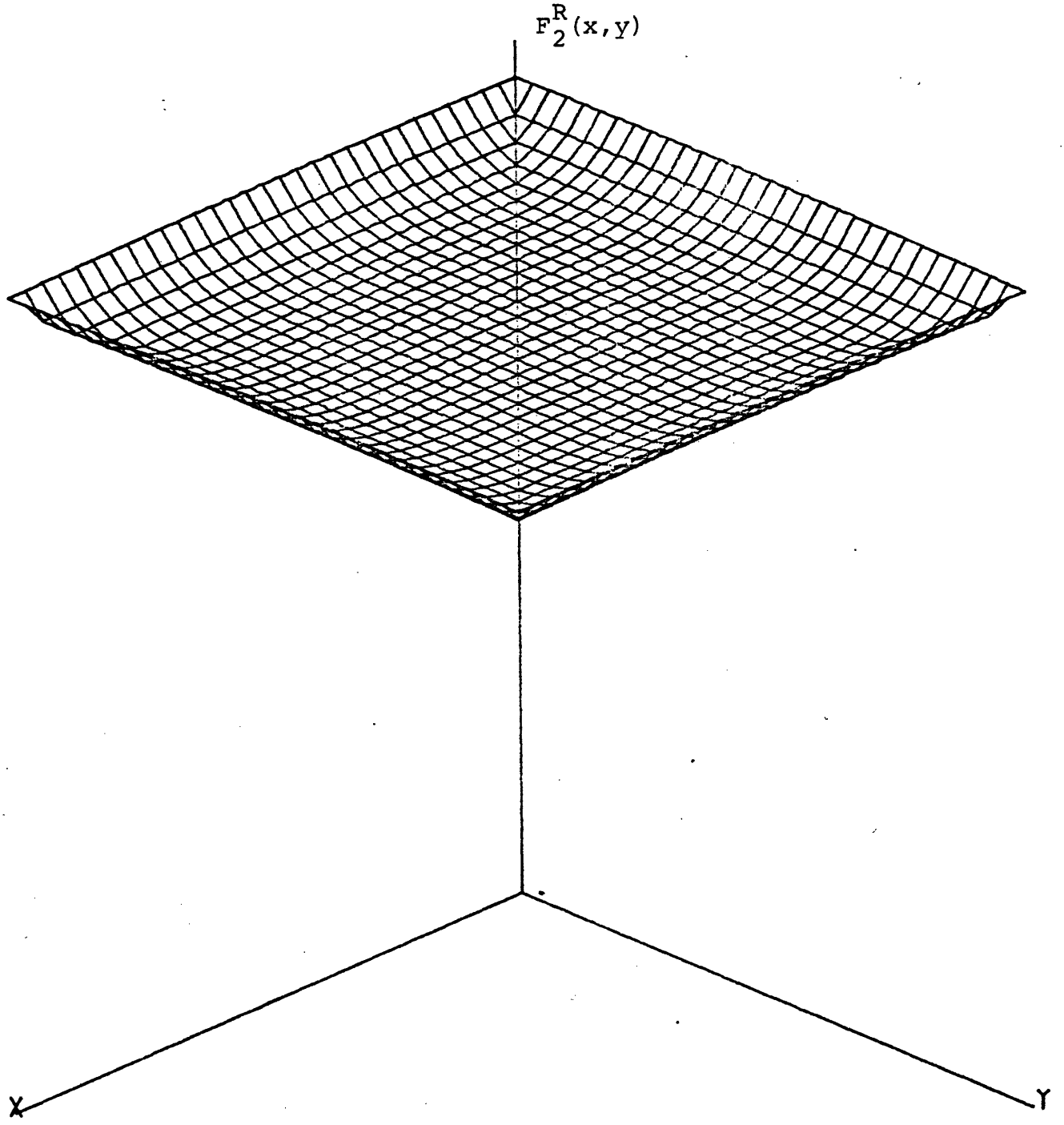

Figure A20.2: The Reconstructed Thermal Form Function from FORTE for Node 5 of Benchmark Problem 5 (FORTE input data from QUANDRY-ADF-AXS/CHIME)

A20.2 Benchmark Problem 7 Reconstructed Form Function Plots (QUANDRY-ADF-AXS/CHIME input data for FORTE)

Benchmark problem 7 is a 3-by-3 node problem. The center node 5 is an unrodded fuel 1 assembly and the other 8 nodes are homogeneous fuel type 2. The sketch below gives the boundary conditions and node number for the problem. FORTE was used to reconstruct the form functions in the fast and thermal group for node 5 of this problem.

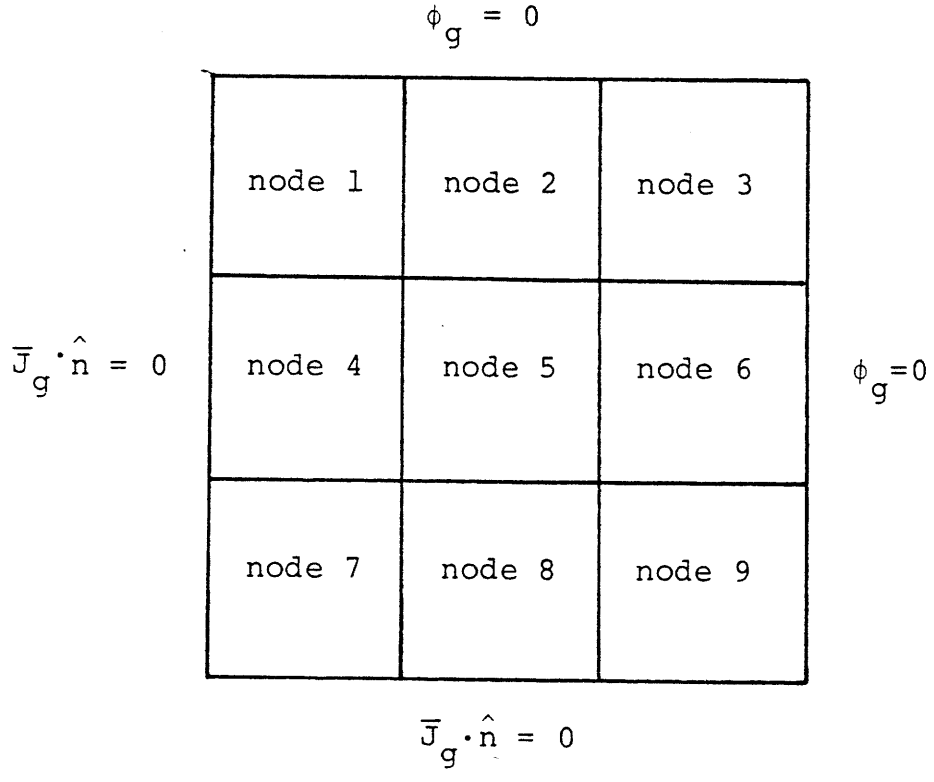

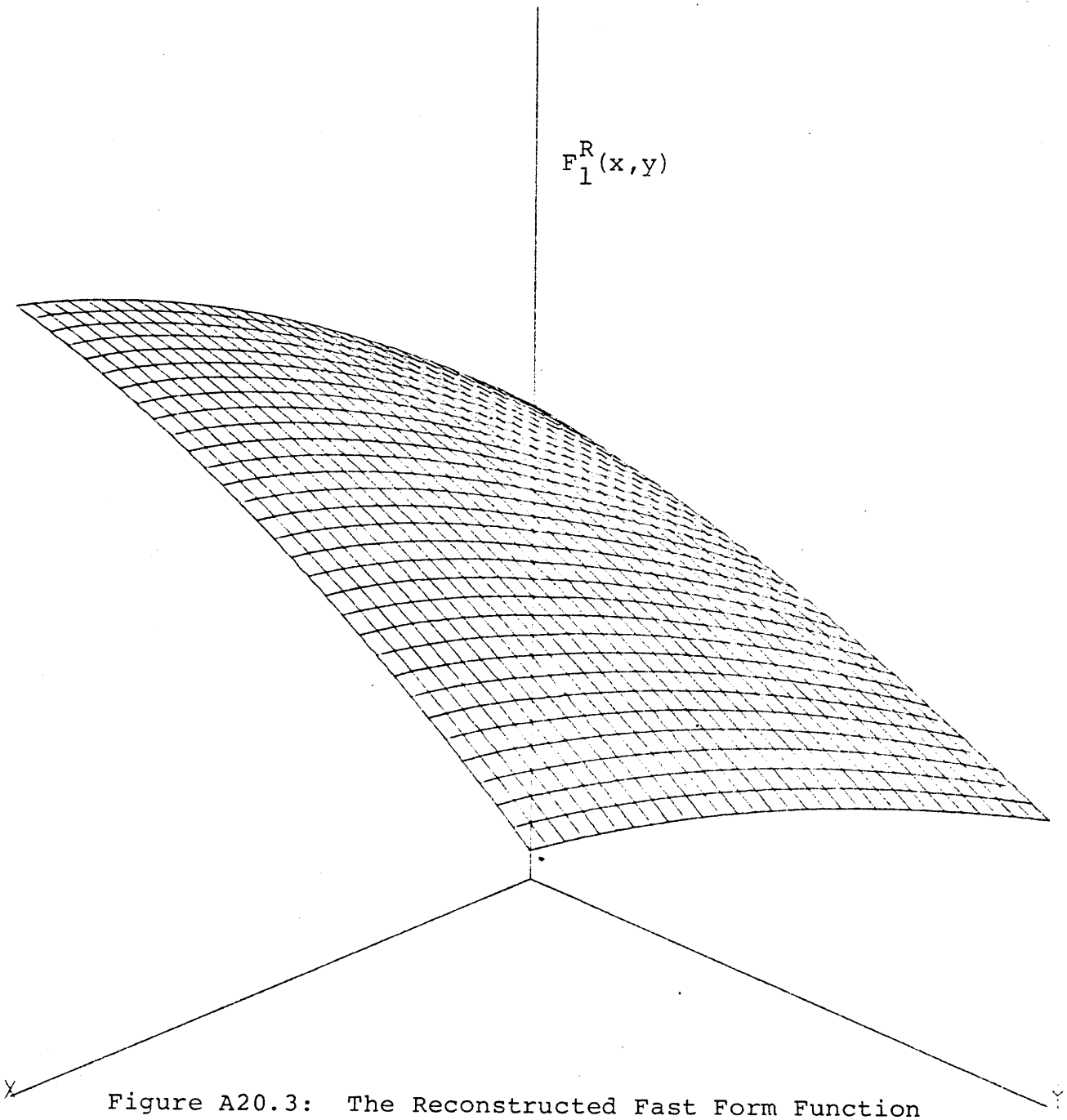

Figure A20.3: The Reconstructed Fast Form Function from FORTE for Node 5 of Benchmark Problem 7 (FORTE input data from QUANDRY-ADF-AXS/CHIME)

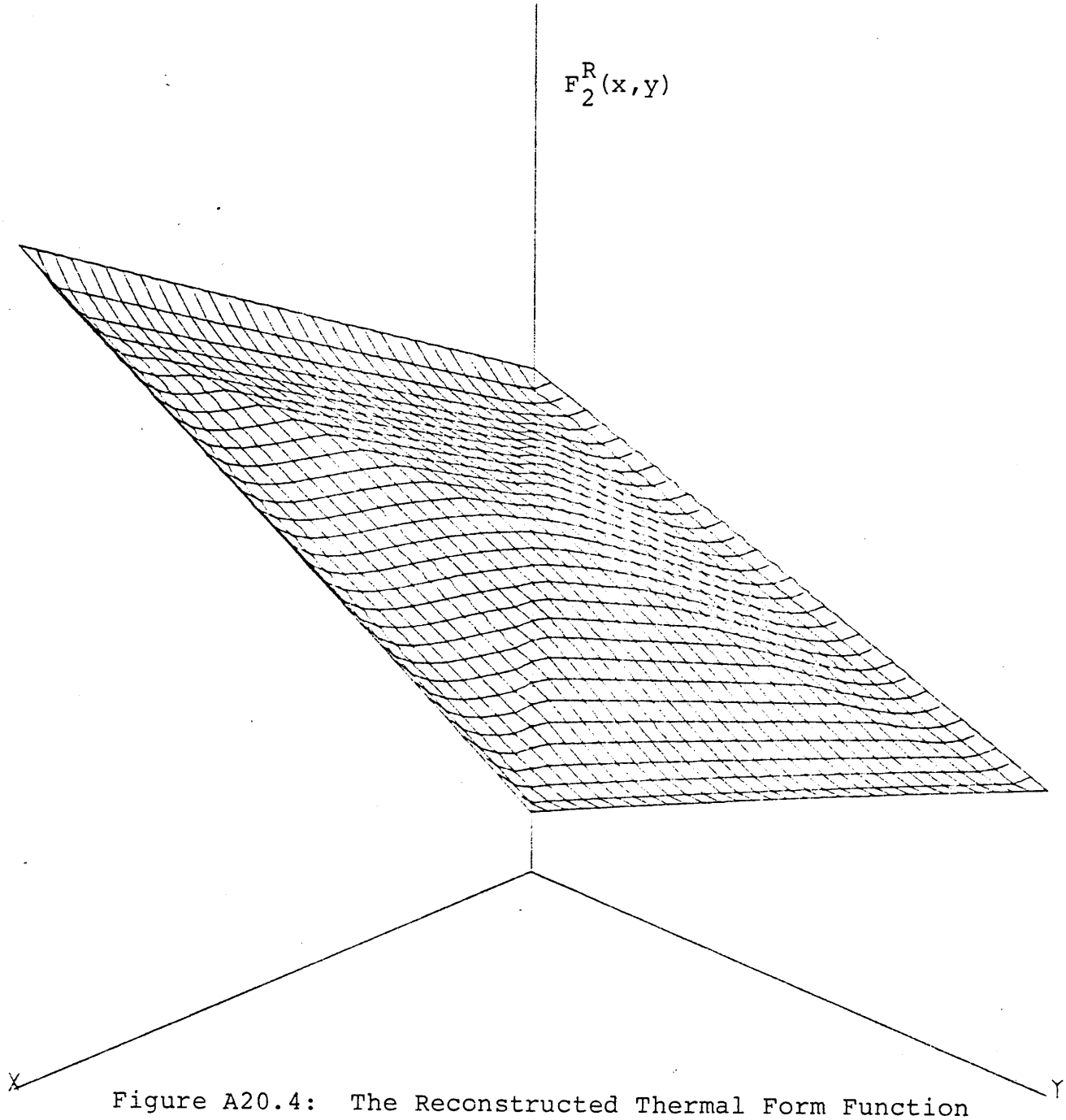

Figure A20.4: The Reconstructed Thermal Form Function from FORTE for Node 5 of Benchmark Problem 7 (FORTE input data from QUANDRY-ADF-AXS/CHIME)

A20.3 Benchmark Problem 6 Reconstructed Form Function Plots I (QUANDRY-ADF-AXS(from extended assembly calculations)/CAMPANA input data for FORTE)

Benchmark problem 6 is the 4-by-4 quarter core with an explicitly represented steel baffle. The sketch below gives the boundary conditions and node numbering for the problem. FORTE was used to reconstruct the form functions in nodes 10, 11, 13, 14 and 15 of this problem.

$\phi_g = 0$

	node 1	node 2	node 3	node 4	
	node 5	node 6	node 7	node 8	
$\bar{J}_g \cdot \hat{n}=0$	node 9	node 10	node 11	node 12	$\phi_g=0$
	node 13	node 14	node 15	node 16	

$\bar{J}_g \cdot \hat{n}=0$

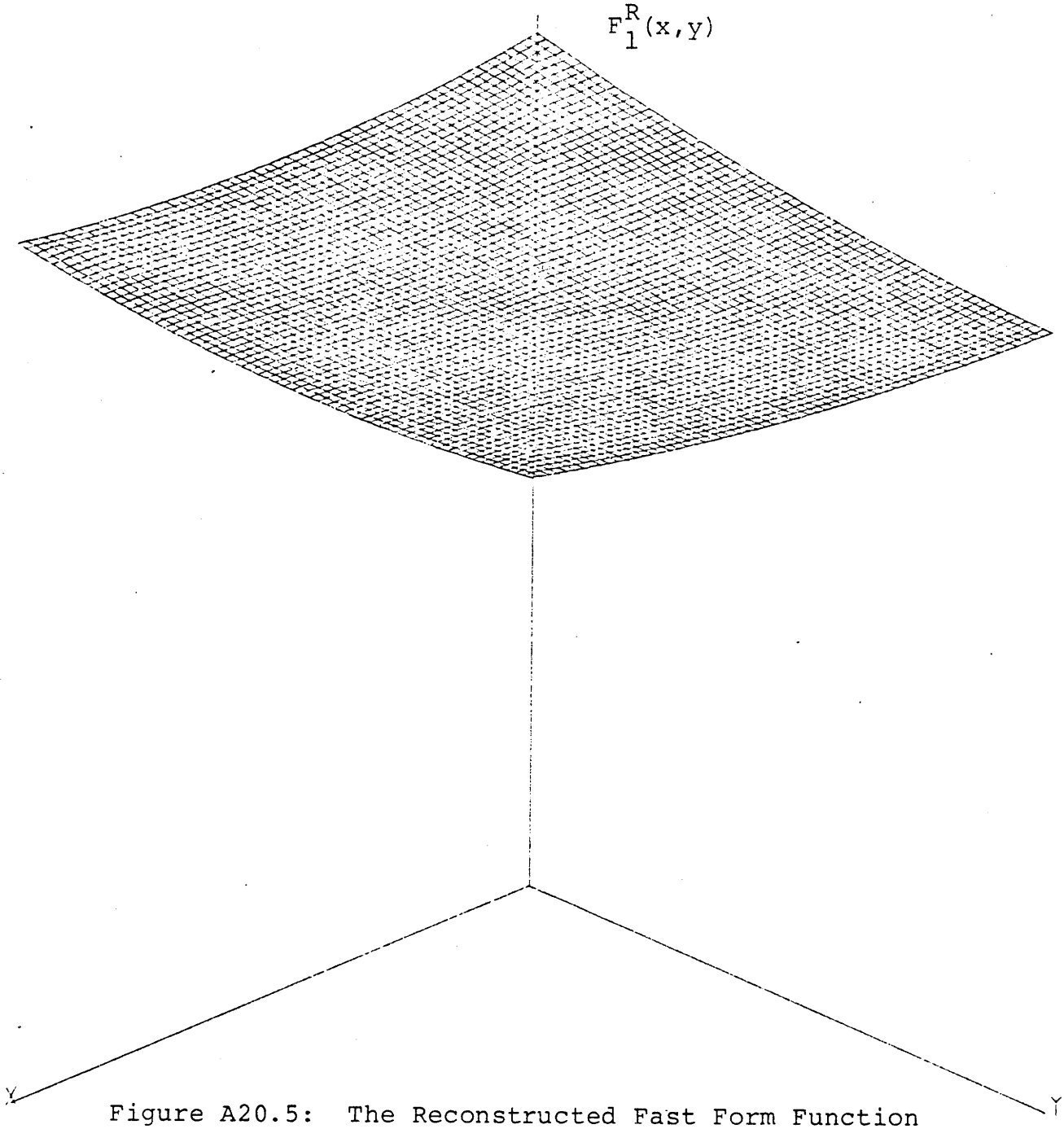

Figure A20.5: The Reconstructed Fast Form Function from FORTE for Node 10 of Benchmark Problem 6 (FORTE input data from QUANDRY-ADF-AXS/ CAMPANA)

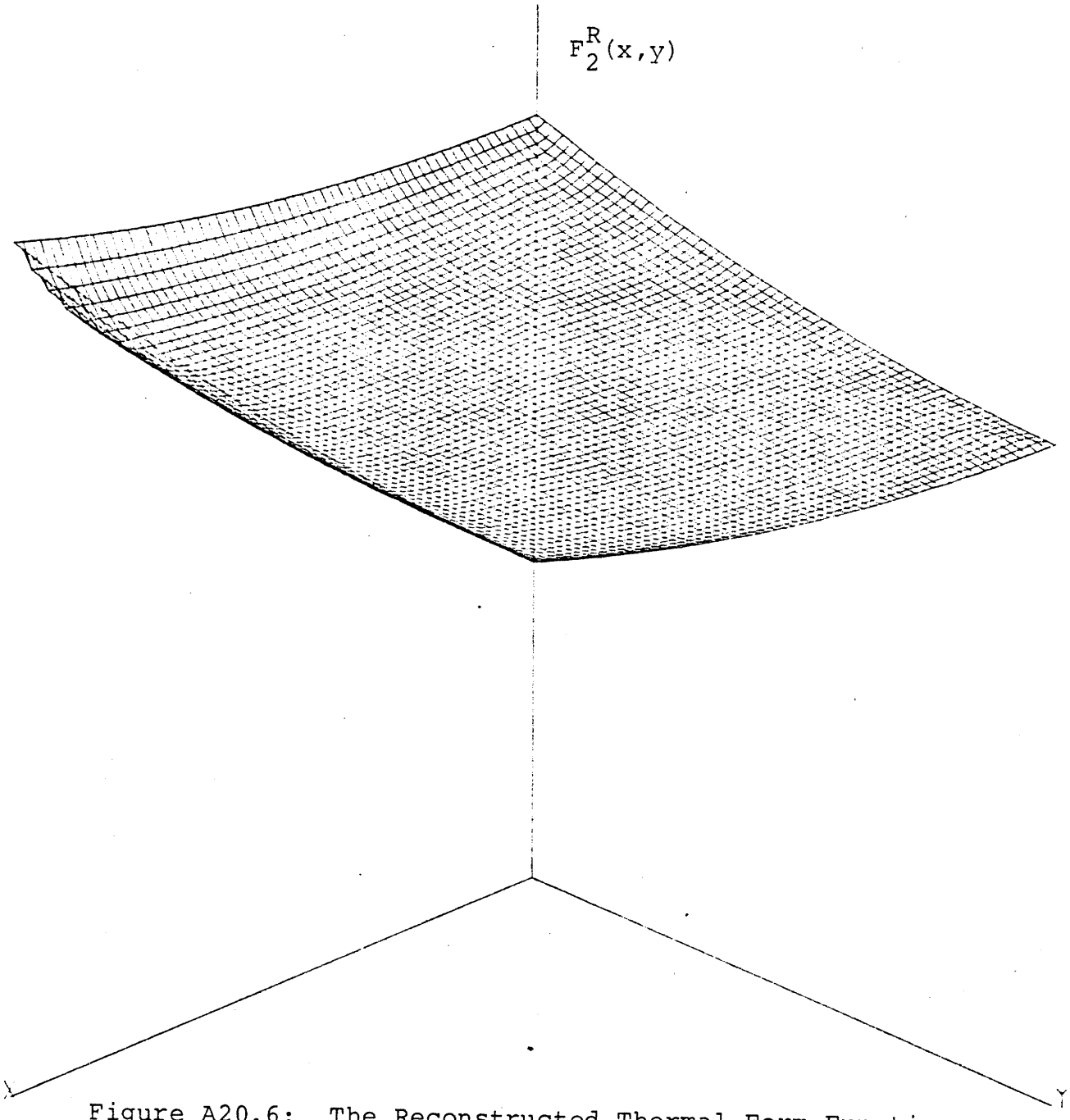

Figure A20.6: The Reconstructed Thermal Form Function from FORTE for Node 10 of Benchmark Problem 6 (FORTE input data from QUANDRY-ADF-AXS/ CAMPANA)

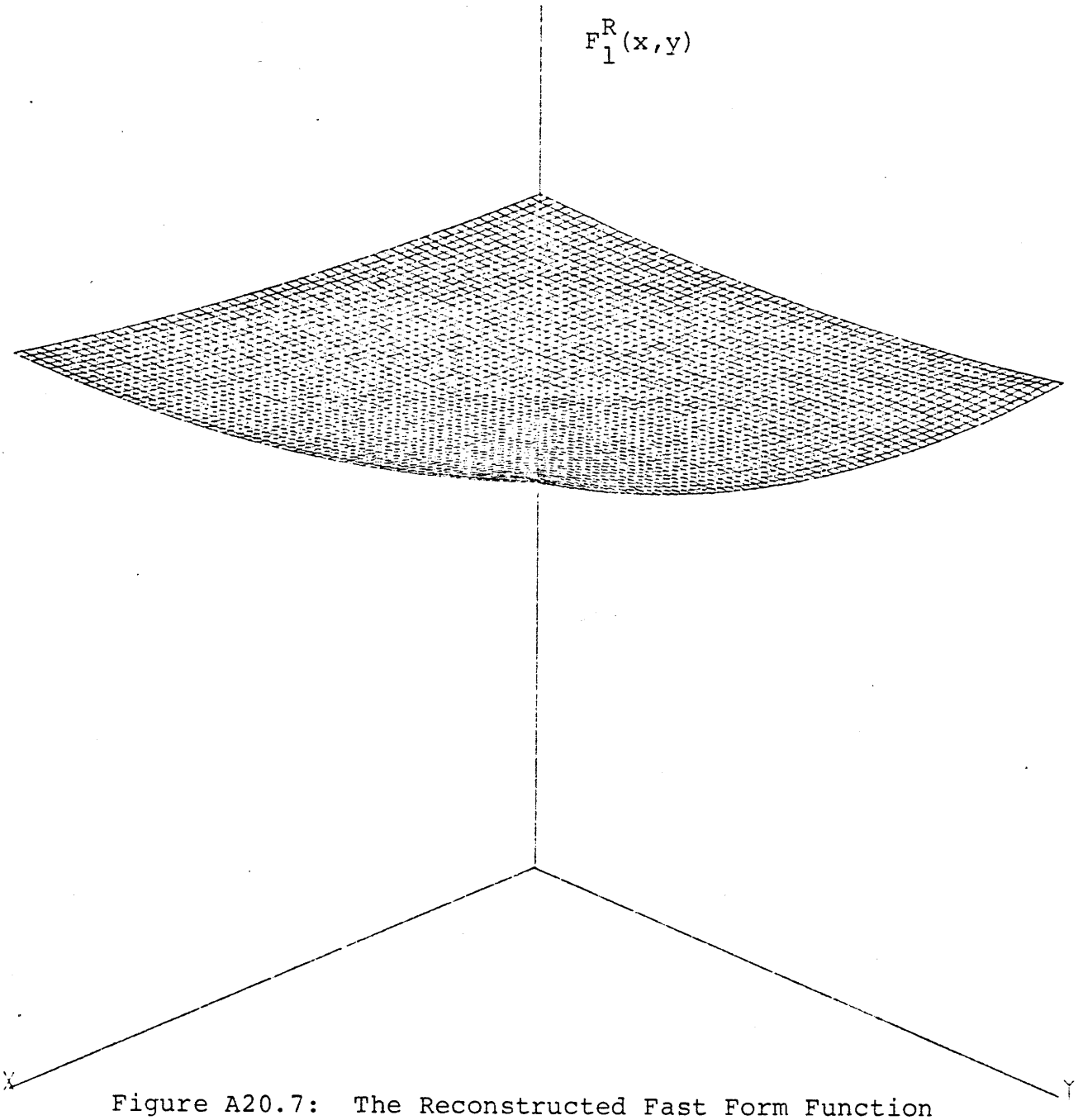

Figure A20.7: The Reconstructed Fast Form Function from FORTE for Node 11 of Benchmark Problem 6 (FORTE input data from QUANDRY-ADF-AXS/ CAMPANA)

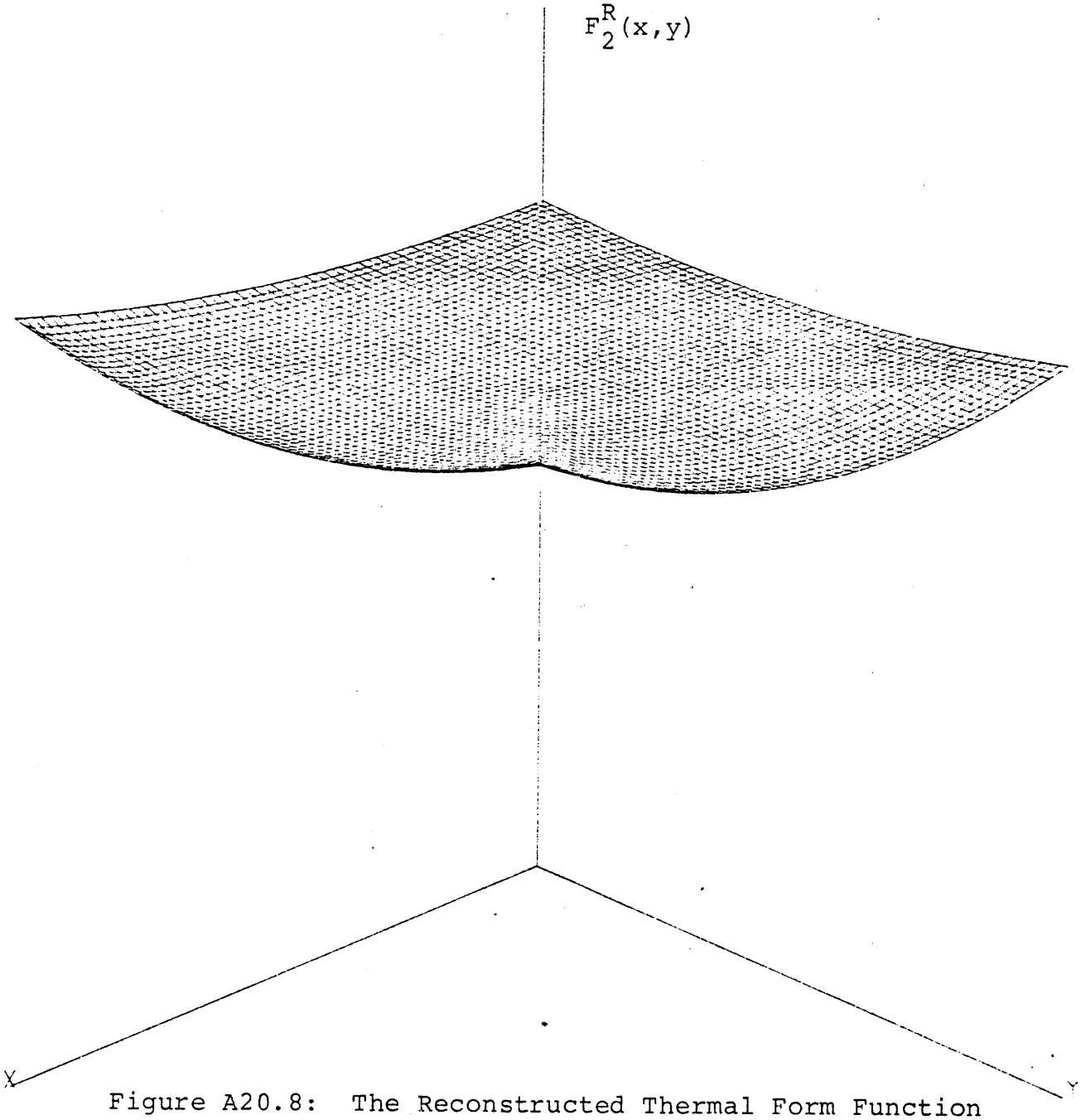

Figure A20.8: The Reconstructed Thermal Form Function from FORTE for Node 11 of Benchmark Problem 6 (FORTE input data from QUANDRY-ADF-AXS/ CAMPANA)

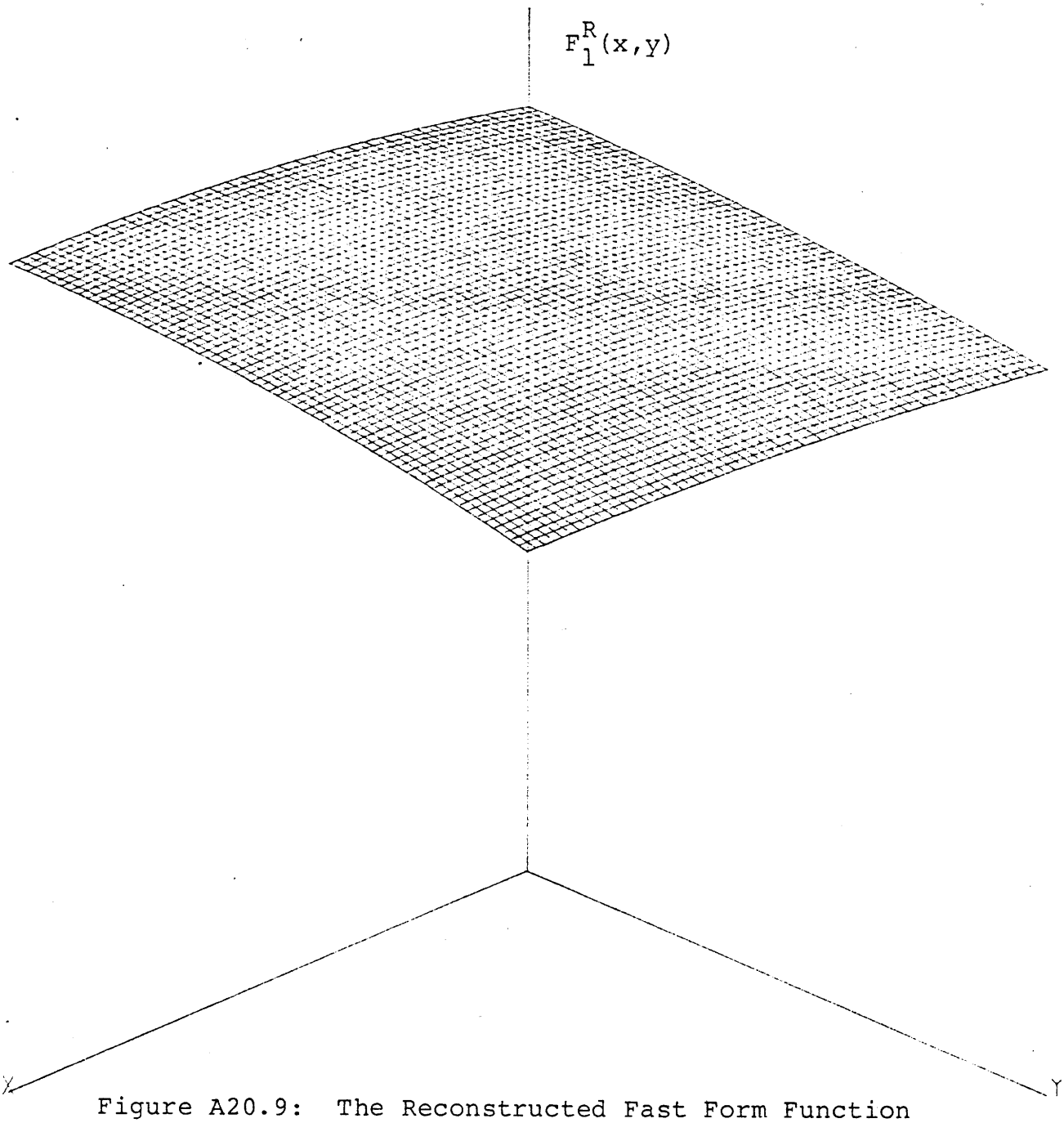

Figure A20.9: The Reconstructed Fast Form Function from FORTE for Node 13 of Benchmark Problem 6 (FORTE input data from QUANDRY-ADF-AXS/ CAMPANA)

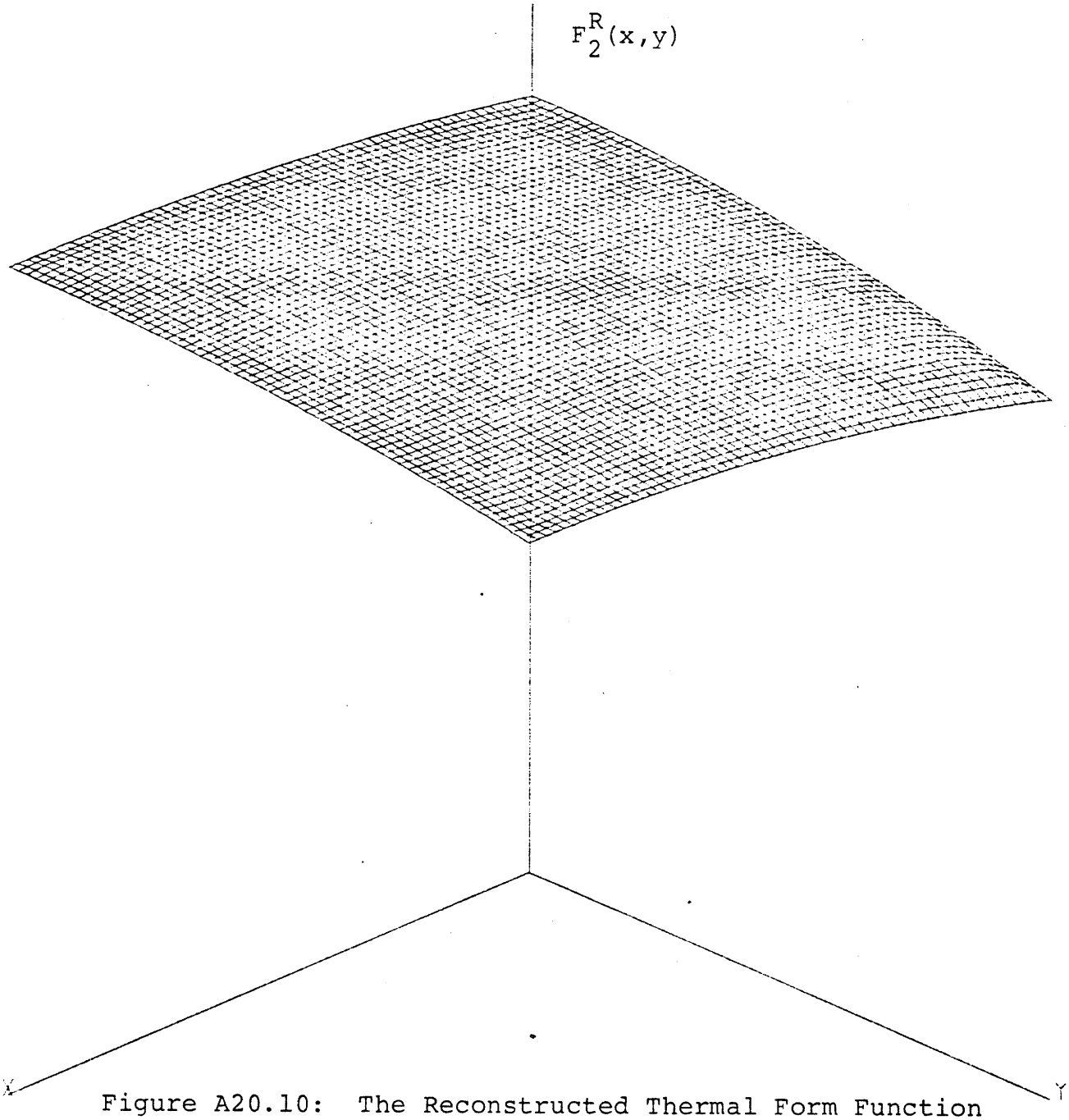

Figure A20.10: The Reconstructed Thermal Form Function from FORTE for Node 13 of Benchmark Problem 6 (FORTE input data from QUANDRY-ADF-AXS/ CAMPANA)

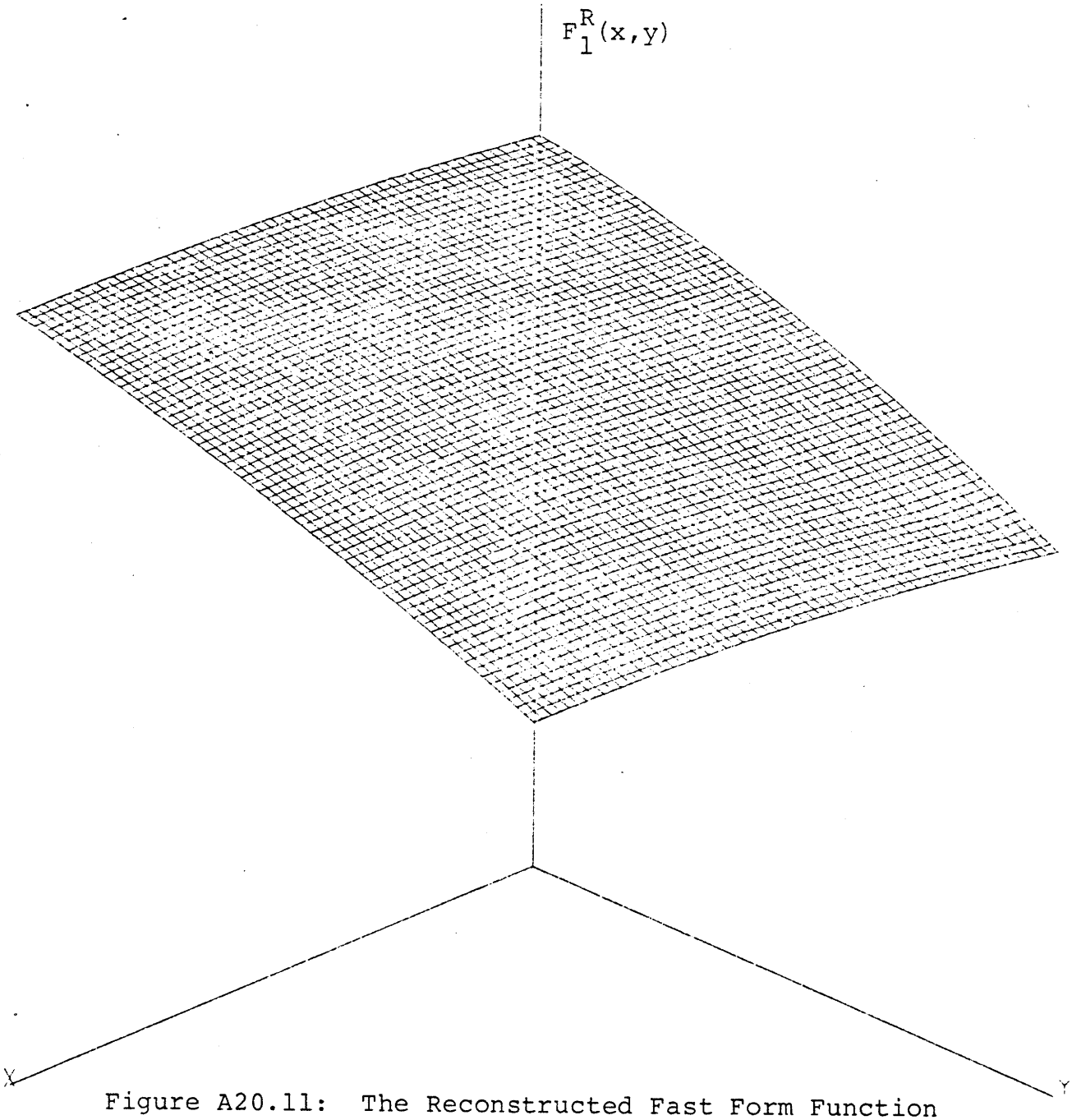

Figure A20.11: The Reconstructed Fast Form Function from FORTE for Node 14 of Benchmark Problem 6 (FORTE input data from QUANDRY-ADF-AXS/ CAMPANA)

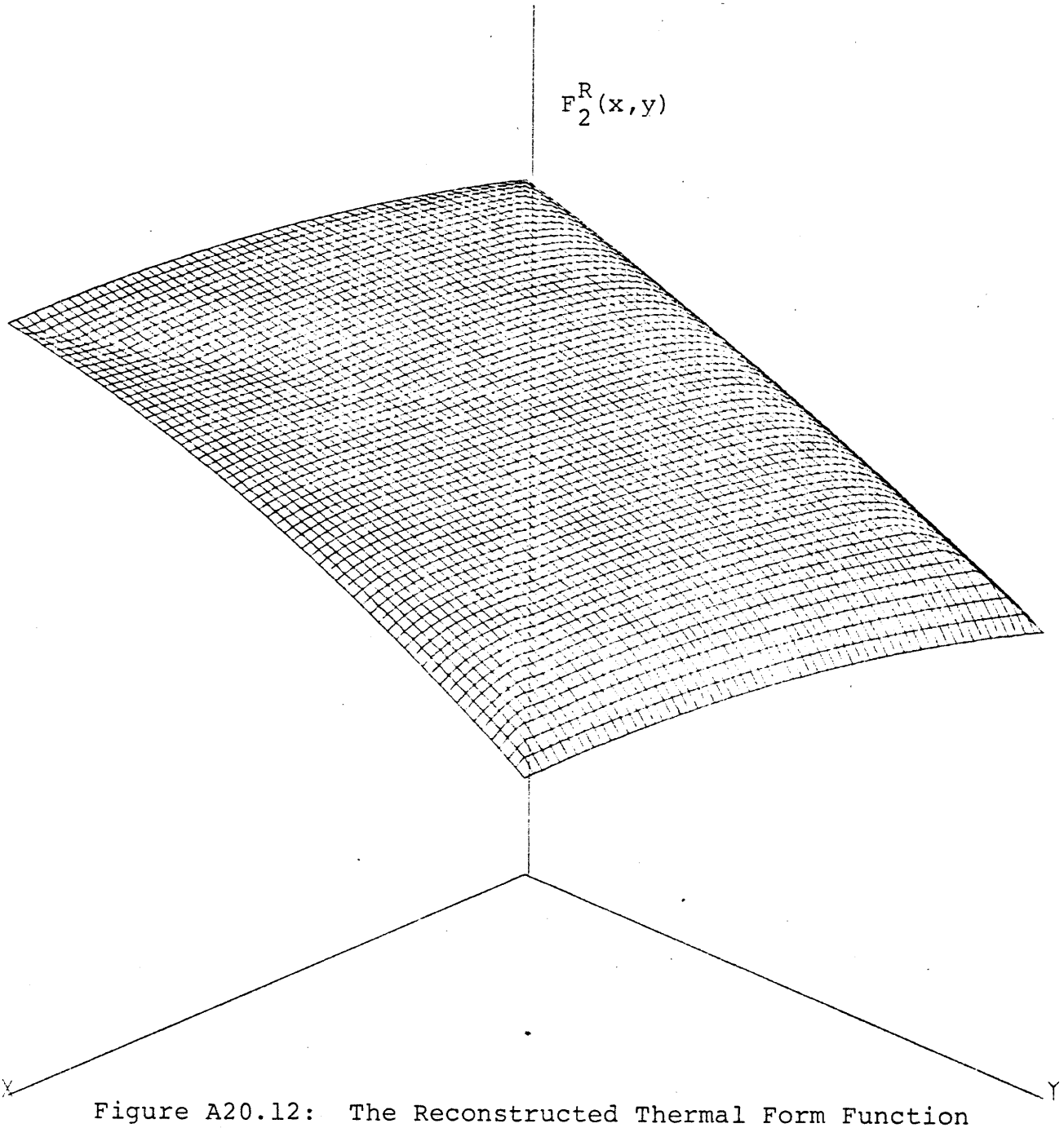

Figure A20.12: The Reconstructed Thermal Form Function from FORTE for Node 14 of Benchmark Problem 6 (FORTE input data from QUANDRY-ADF-AXS/ CAMPANA)

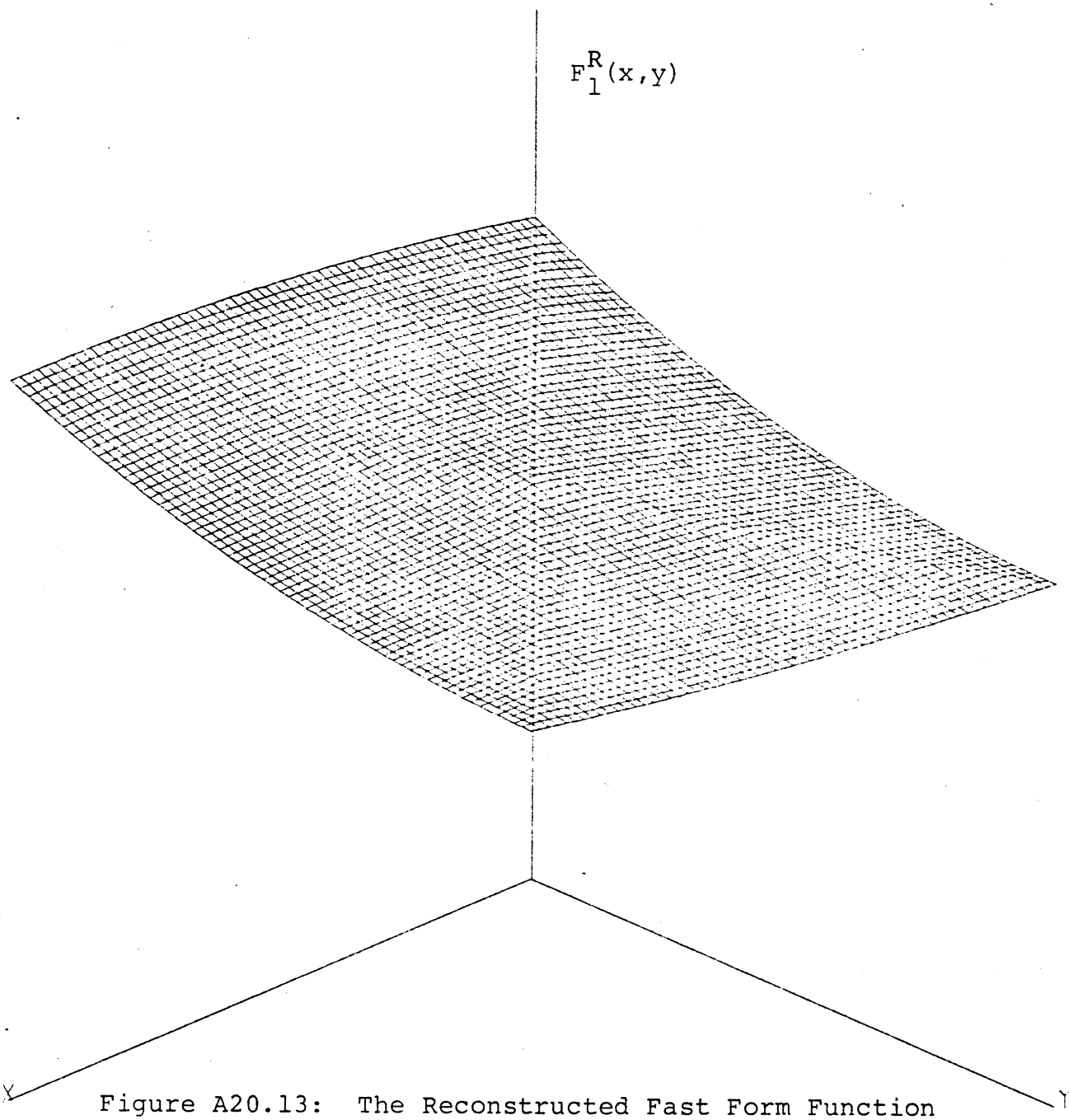

Figure A20.13: The Reconstructed Fast Form Function from FORTE for Node 15 of Benchmark Problem 6 (FORTE input data from QUANDRY-ADF-AXS/ CAMPANA)

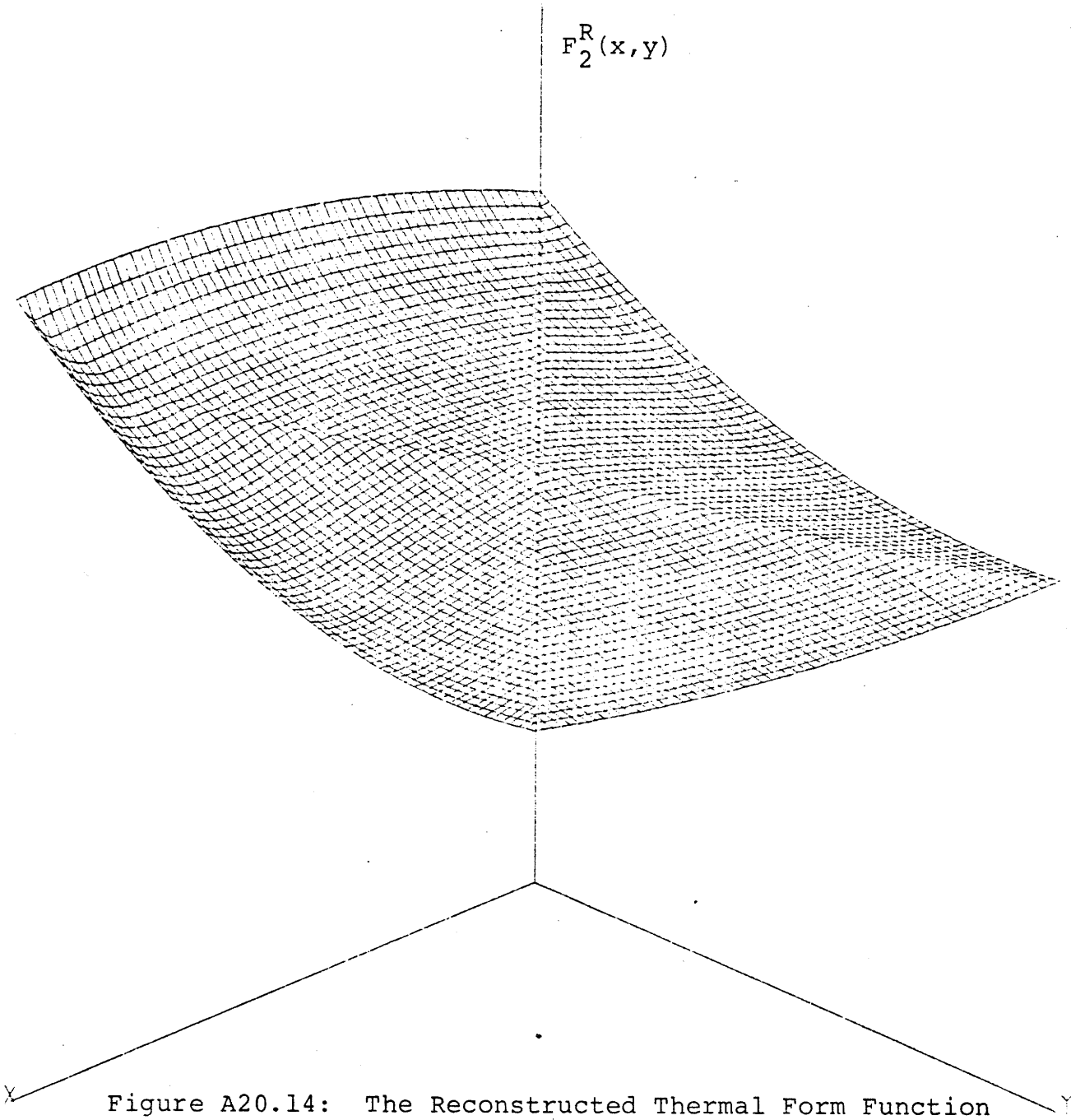

Figure A20.14: The Reconstructed Thermal Form Function from FORTE for Node 15 of Benchmark Problem 6 (FORTE input data from QUANDRY-ADF-AXS/ CAMPANA)

A20.4 Benchmark Problem 6 Reconstructed Form Function Plots II (Reference corner point, surface-averaged and volume-averaged form function data for FORTE calculated directly from the reference form functions in Appendix 16, i.e., these reference form functions are based on extended assembly calculations.)

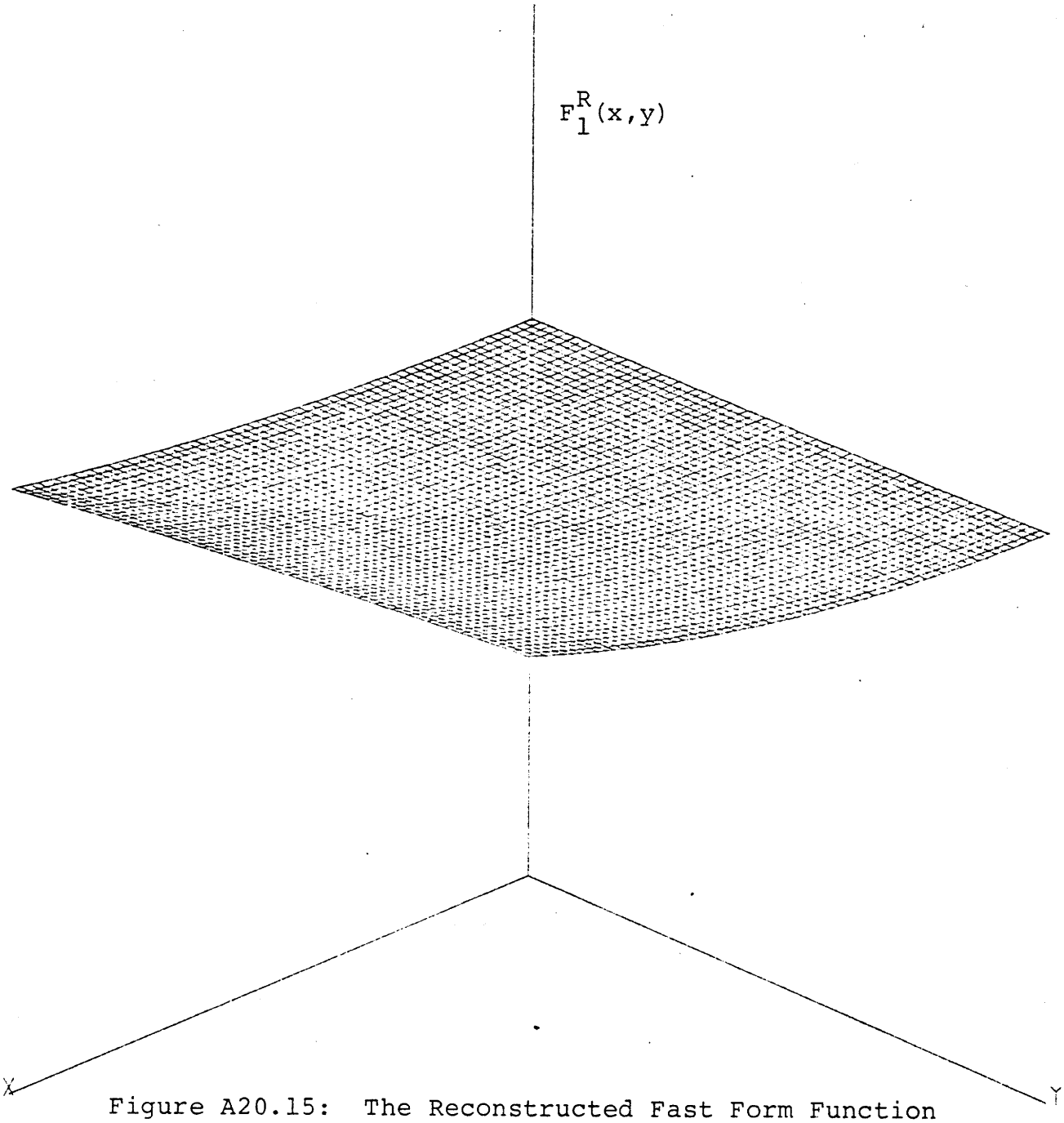

Figure A20.15: The Reconstructed Fast Form Function from FORTE for Node 11 of Benchmark Problem 6 (FORTE input data from Reference Form Functions in Appendix 16)

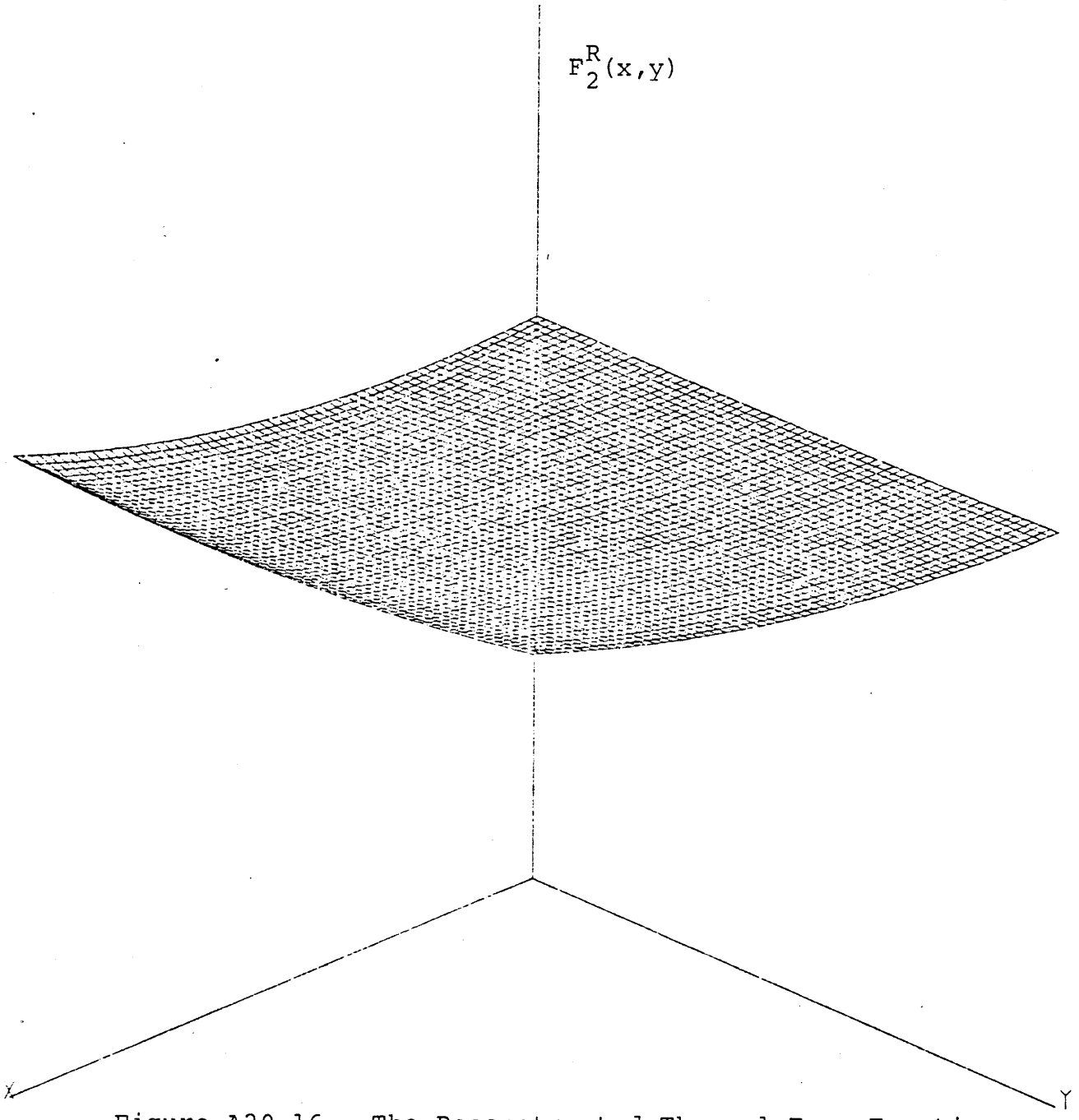

Figure A20.16: The Reconstructed Thermal Form Function from FORTE for Node 11 of Benchmark Problem 6 (FORTE input data from Reference Form Functions in Appendix 16)

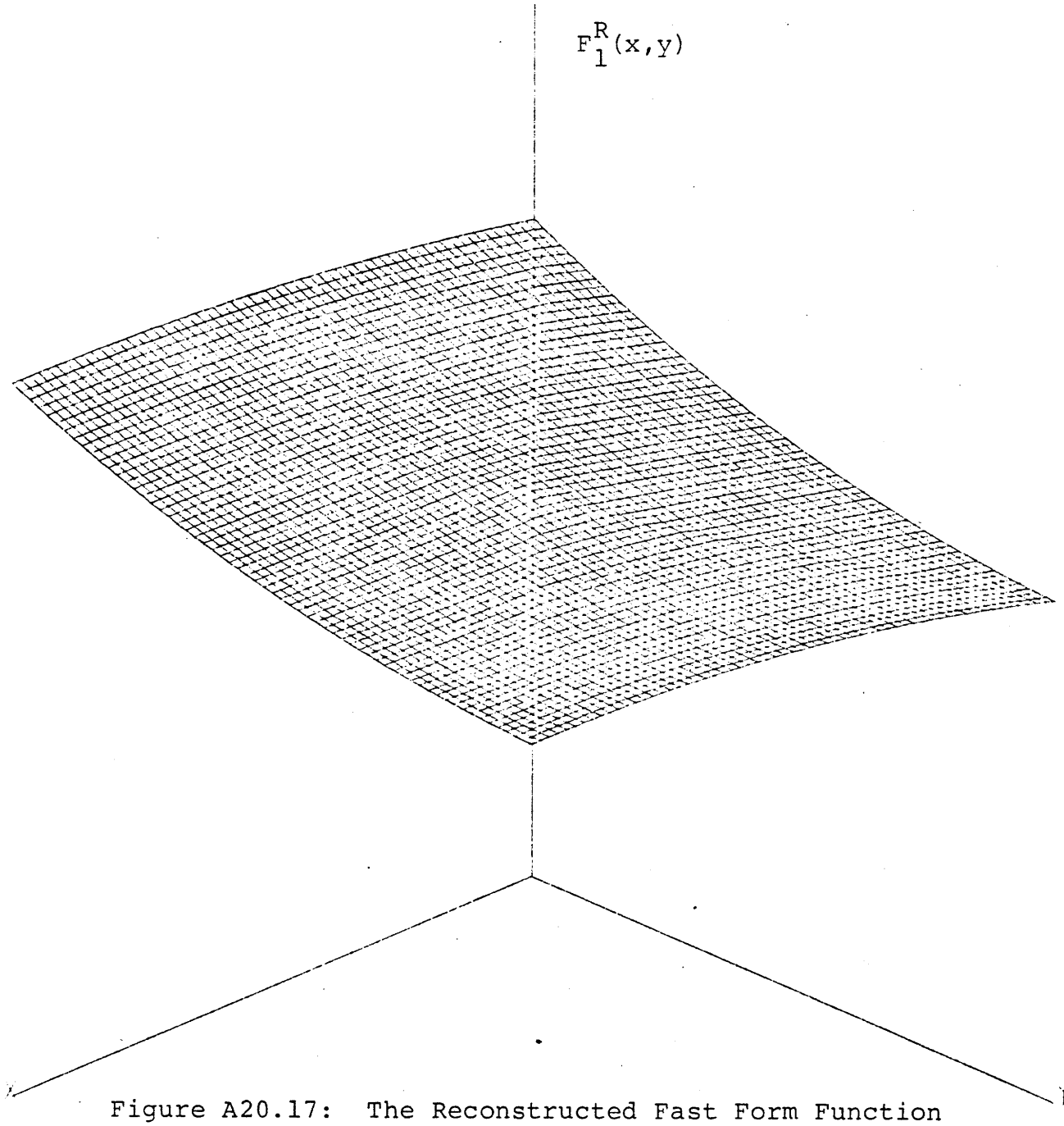

Figure A20.17: The Reconstructed Fast Form Function from FORTE for Node 15 of Benchmark Problem 6 (FORTE input data from Reference Form Functions in Appendix 16)

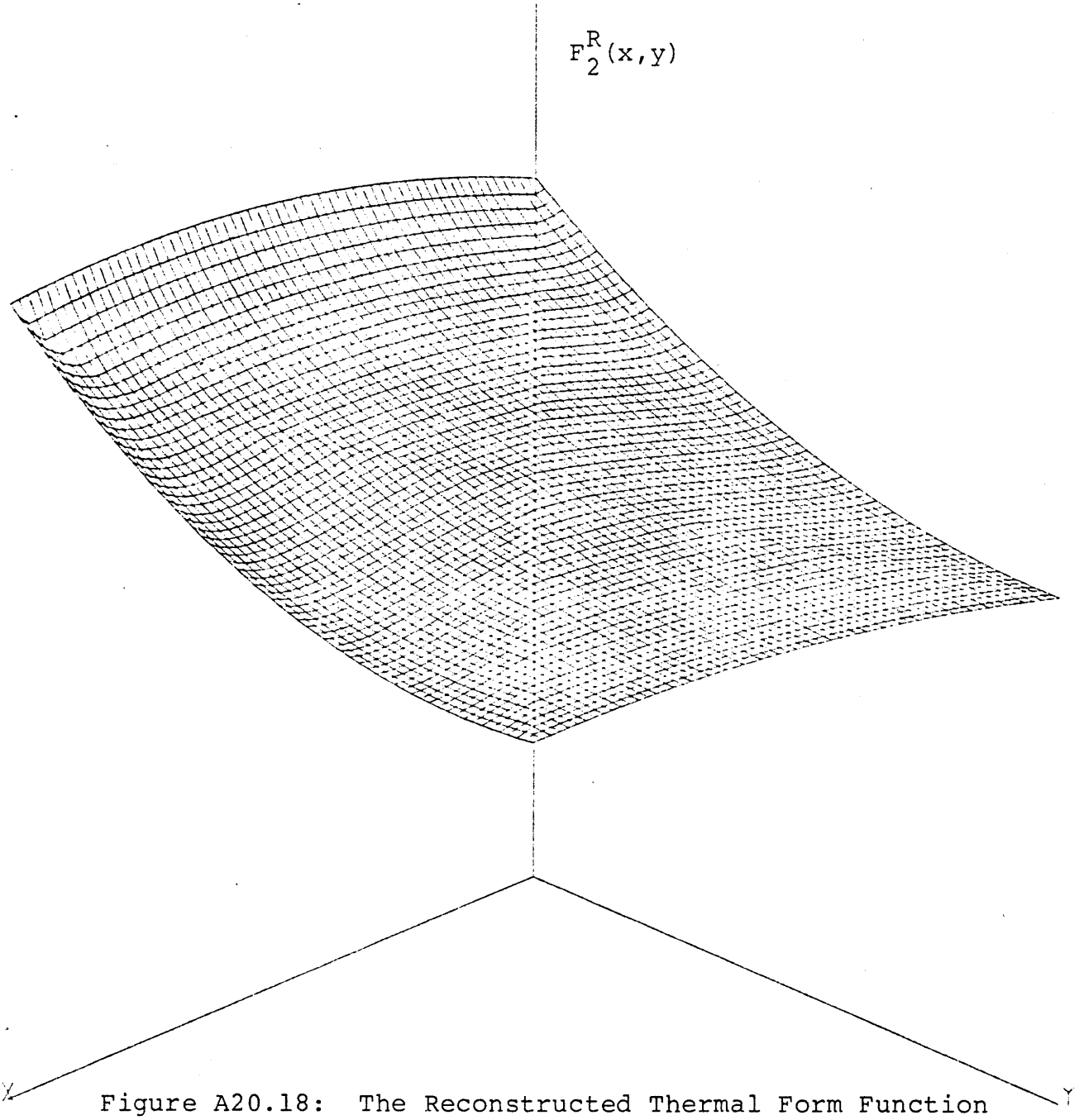

Figure A20.18: The Reconstructed Thermal Form Function from FORTE for Node 15 of Benchmark Problem 6 (FORTE input data from Reference Form Functions in Appendix 16)

A20.5 Benchmark Problem 6 Reconstructed Form Function Plots III (Reference corner point, surface-averaged and volume-averaged form function data for FORTE calculated directly from the reference form functions in Appendix 15, i.e., these reference form functions are based on assembly fluxes derived from assembly calculations employing zero-net-current boundary conditions.)

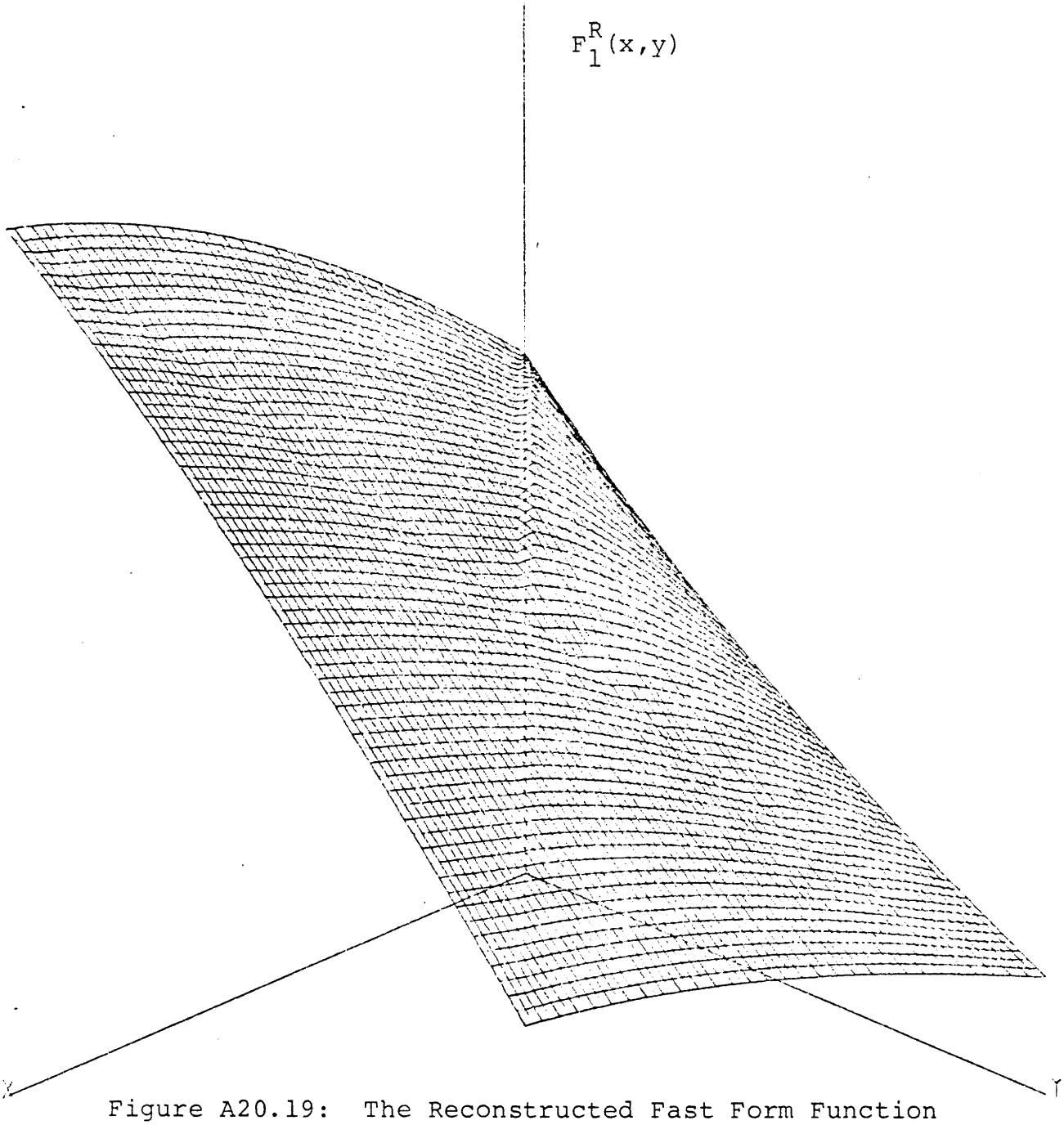

Figure A20.19: The Reconstructed Fast Form Function from FORTE for Node 11 of Benchmark Problem 6 (FORTE input data from Reference Form Functions in Appendix 15)

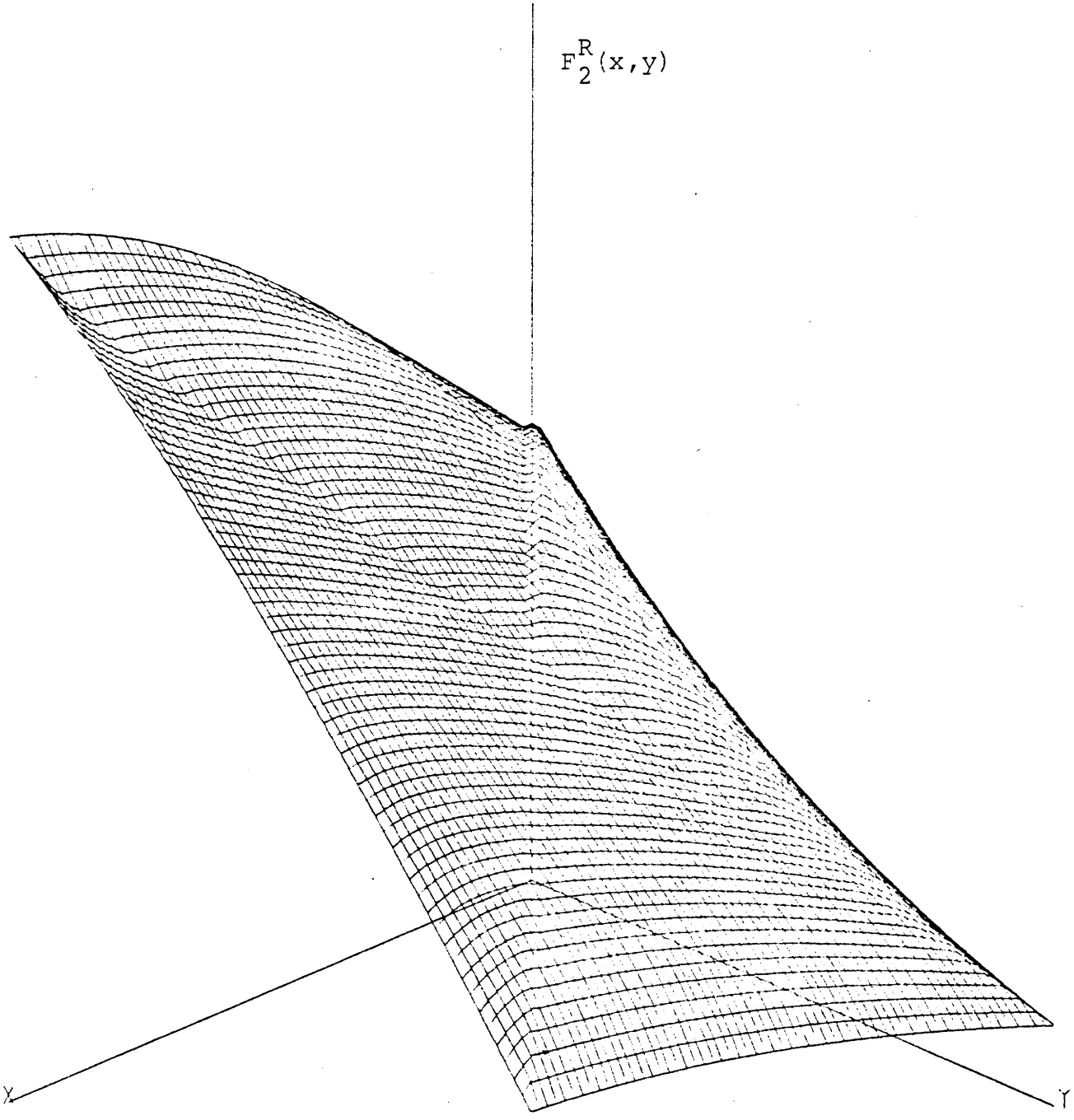

Figure A20.20: The Reconstructed Thermal Form Function from FORTE for Node 11 of Benchmark Problem 6 (FORTE input data from Reference Form Functions in Appendix 15)